Photo-Excited Processes, Diagnostics and Applications

Edited by

A. Peled

Kluwer Academic Publishers

PHOTO-EXCITED PROCESSES, DIAGNOSTICS AND APPLICATIONS

This page intentionally left blank

Photo-Excited Processes, Diagnostics and Applications

Fundamentals and Advanced Topics

Edited by

A. Peled
Holon Academic Institute of Technology, Israel

KLUWER ACADEMIC PUBLISHERS
NEW YORK, BOSTON, DORDRECHT, LONDON, MOSCOW

eBook ISBN: 1-4020-2610-2
Print ISBN: 1-4020-7527-8

©2004 Springer Science + Business Media, Inc.

Print ©2003 Kluwer Academic Publishers
Dordrecht

All rights reserved

No part of this eBook may be reproduced or transmitted in any form or by any means, electronic, mechanical, recording, or otherwise, without written consent from the Publisher

Created in the United States of America

Visit Springer's eBookstore at: http://www.ebooks.kluweronline.com
and the Springer Global Website Online at: http://www.springeronline.com

CONTENTS

PREFACE xiii

CHAPTER 1
HIGH-RESOLUTION PHOTOEMISSION IN LOW DIMENSIONAL CONDUCTORS **1**
L. Perfetti, M. Grioni and G. Margaritondo

1. Introduction 1
   1.1. Notions on high correlation 1
   1.2. Polaronic effects in quasi-1D 2
   1.3. Photoemission experiments 3
   1.4. A Fermi-Liquid System 5
2. Peierls conductors 7
   2.1. Structural and transport properties 7
   2.2. Nesting condition in a typical Peierls system: $K_{0.3}MoO_3$ 9
   2.3. The symmetry of the electronic bands and the effects of CDW fluctuations 10
   2.4. Limits of the weak coupling theory 12
3. A simplified model for systems with large interactions 13
4. The polaron liquids 16
   4.1. Experimental evidences of heavy carriers 16
   4.2. The CDW instability 19
5. Conclusions 22

CHAPTER 2
OPTICAL ABSORPTION, PHOTOEXCITATION AND EXCITONS IN SOLIDS: FUNDAMENTAL CONCEPTS **25**
Jai Singh, I.-K. Oh and Safa O. Kasap

1. Introduction to optical properties 25
2. Lattice or reststrahlen absorption and infrared reflection 29
3. Free Carrier Absorption (FCA) 30
4. Band-to-band fundamental absorption 34
5. Excitonic absorption in crystalline solids 38
6. Absorption in amorphous semiconductors 39
7. Excitonic processes in quantum wells 44
8. Excitonic photoluminescence in amorphous semiconductors 50
9. Conclusions 53

CHAPTER 3
DYNAMIC WAVEGUIDES AND GRATINGS IN PHOTO-REFRACTIVE CRYSTALS **57**
V. I. Vlad, E. Fazio, M. J. Damzen and A. Petris

1. Overview of the photorefractive effect and materials 57
   1.1. Photoexcited processes in photorefractive crystals (PRC) 57
   1.2. Photorefractive crystals 63
2. Spatial solitons and dynamic waveguides in PRC 64
   2.1. Photorefractive spatial solitons 64
   2.2. Analytical solutions of the soliton propagation in PRC with optical activity and absorption 66
   2.3. Experiments with spatial solitons in sillenite crystals 74
3. Dynamic gratings in PRC 79
   3.1. Two-wave mixing 79
   3.2. Inharmonic thin gratings 79
   3.3. Harmonic thin gratings 84
4. Dynamic gratings and adaptive interconnection by double phase conjugation in PRC 88
   4.1. Double phase conjugation (DPC) 88
   4.2. Efficient adaptive coupling of two lasers by DPC 89
   4.3. Phase conjugate reflectivity and the coupling transmission efficiency 90
   4.4. Robustness of the DPC interconnection to beam direction changes and to transmitted information 95
5. Conclusions 97

CHAPTER 4
HOLOGRAPHIC TIME OF FLIGHT **101**
Ivan Biaggio

1. Introduction 101
2. Theory of Holographic Time of Flight 106
3. Review of mobility investigations performed using HTOF 114
4. Conclusions 118

CHAPTER 5
MODELS FOR LASER ABLATION **121**
S. I. Anisimov, N. M. Bityurin and B. S. Luk'yanchuk

1. Introduction 121
2. Thermal model 122
   2.1. Qualitative results 122
   2.2. Dynamics of laser ablation: Calculations assisted by the moments method 125
3. Bulk photothermal model 135

4. Photochemical ablation 139
5. The role of mechanical stresses 142
6. Sub-picosecond laser ablation: Metals and the two-temperature model 145
7. Sub-picosecond ablation in Dielectrics 149
8. Photophysical ablation 152
9. Conclusion 155

CHAPTER 6
DEVELOPMENT AND APPLICATIONS OF UV EXCIMER LAMPS **161**
Ian W. Boyd, Jun-Ying Zhang and U. Kogelschatz

1. Introduction 161
2. Excimer formation in gas discharges 162
   2.1. Rare gas excimers, halogen excimers and rare gas halide exciplexes 162
   2.2. Excimer lamps utilising silent discharge excitation 163
3. Applications of incoherent excimer radiation 166
   3.1. VUV cleaning of surfaces 167
   3.2. High dielectric constant materials 167
      3.2.1. Ta_2O_5 formed by photo-assisted sol-gel processing 170
      3.2.2. Thin Ta_2O_5 film deposited by photo-CVD 171
         3.2.2.1. Growth and characterization of Ta_2O_5 film 171
         3.2.2.2. Mechanism for reduction in the leakage current of Ta_2O_5 films by UV annealing 177
      3.2.3. Other high dielectric constant materials 179
   3.3. Photo-induced deposition of dielectric materials 183
   3.4. Low dielectric constant materials: polyimide and porous silica 185
   3.5. UV oxidation of Si, Ge and SiGe 188
   3.6. UV-induced metallization 190
   3.7. Surface modification of polymers 193
   3.8. UV curing with excimer lamps: printing machines 194
4. Conclusions 195

CHAPTER 7
SYNCHROTRON - RADIATION - EXCITED STRUCTURAL CHANGES AND CHEMICAL BEAM EPITAXY OF SILICON-BASED MATERIALS **201**
H. Akazawa

1. Beamline instrumentation and diagnostic tools for synchrotron radiation excited material processing 201
   1.1. Characteristics of synchrotron-radiation-excited processing 201
   1.2. Configuration of the beamline for material processing 202
   1.3. In-situ monitoring by time-of-flight mass spectroscopy 203
   1.4. In-situ monitoring by spectroscopic ellipsometry 204

2. Radiation effects in a-SiO_2 204
2.1. Surface phenomena 204
2.2. Evaporation vs. compositional change 205
2.3. Temperature-dependent composition of SiO_x 206
2.4. Creation and annihilation of defects during irradiation 207
2.5. Precipitation of nanocrystalline Si in SiO_x matrix 207
2.6. The basic photolytic and thermal processes 208
3. Radiation effects in a-SiN_x:H 210
3.1. Change in compositional structure and refractive index 210
3.2. Microscopic models for the network rearrangement 212
4. Radiation effects in a-Si:H 213
4.1. Layered structure of crystalline and amorphous components 213
4.2. The processes of photolytic network rearrangement 215
5. Elementary processes in synchrotron radiation excited homoepitaxy of Silicon 216
5.1. Thermal interaction of Si_2H_6 with Si(100) surface probed by TOFMS 216
5.2. Interaction of photolysis products with the Si(100) surface 217
5.3. Detection of mSiH_x(a) and (-SiH_x-) by in-situ SE 218
5.4. Dependence of the crystallinity of Si films on photon flux 220
6. Conclusion 222

CHAPTER 8
THIN NITRIDE FILMS DEPOSITED BY REACTIVE PULSED LASER ABLATION **225**
Armando Luches and Anna Paola Caricato

1. Introduction 225
2. Refractory-metal nitrides for hard coatings and microelectronic applications 229
2.1. Laser deposition of Titanium nitride films: methods and results 230
2.2. Growth of Vanadium nitride (VN and V_2N) films 232
2.3. Laser deposition of Zirconium nitride films 234
2.4. Deposition of Tantalum, Molybdenum and Tungsten nitrides 234
3. Laser deposition of crystalline Aluminum nitride films 235
4. The case of Titanium Aluminum nitride 241
5. Laser deposition of cubic Boron nitride films 242
6. Conclusions 246

CHAPTER 9
LIQUID PHASE PHOTODEPOSITION PROCESSES FROM COLLOID SOLUTIONS **251**
Aaron Peled and Nina Mirchin

1. Introduction 251
2. Features of PDCS systems 253

2.1. Basic features 253
2.2. Specific PDCS processes 254
3. Photoreactor systems considerations 256
3.1. Main requirements of a LPPD system 256
3.2. Microscopic observations of LPPD 257
3.3. Fundamental diagnostic parameters of photodeposition 259
4. Controlling photodeposition parameters in liquids 263
4.1. Processing parameters 263
4.2. Properties of the light source 263
4.3. Substrate surface influence 264
4.4. Dependencies of the Quasi Linear Deposition Rate 264
4.4.1. Temperature dependence 265
4.4.2. Light intensity dependence 265
4.4.3. Spectral or photon energy dependence 265
4.4.4. Chromophore and ion source concentration dependencies 267
5. Basic theory of liquid phase photodeposition 268
5.1. The photolytic model of photodeposition in liquid media 269
5.2. The redox model of photodeposition at a semiconductor/liquid interface 271
6. Applications of photodeposition processes 272
6.1 Photodeposition of optical arrays – parallel recording 272
6.2 Laser photodeposition writing – serial recording 273
6.3 Write-Erase features by photodeposition in colloid solutions 275
7. Comparison with gas phase photodeposition 275
7.1. Advantages of liquid phase photodeposition 275
7.2. Shortcomings of liquid phase photodeposition 276
8. Conclusions 276

CHAPTER 10
CARBON ALLOTROPES CREATED BY INTENSE IRRADIATION OF FROZEN HYDROCARBONS **281**
M. Okoshi and M. Hanabusa

1. Introduction 281
2. Reviewing laser synthesis in frozen gases 283
3. Pulsed laser deposition of diamond-like carbon films using excimer lasers 284
4. The production of carbon allotropes by a femtosecond laser 287
4.1. Diamond-like carbon films produced by a femtosecond laser 287
4.2. Synthesis of microcrystals 291
5. Synchrotron radiation used for ablation of frozen acetone 293
6. Free electron laser used for ablation of frozen acetone 295
7. Conclusions 298

CHAPTER 11
EXCIMER LASER MACHINING FOR 3D-SURFACE STRUCTURING 301
K. Zimmer and A. Braun

1. Introduction 301
2. Instrumentation for 3D-surface structuring 302
   2.1. General setup 302
   2.2. Imaging characteristics 304
3. Remarks on excimer laser materials processing 305
   3.1. Ablation of polymers 305
   3.2. Etching of dielectric materials 306
   3.3. Roughness of laser machined surfaces 307
4. Machining techniques for 3D-surfaces 308
   4.1. Overview of basic techniques and masks used in 3D-machining 308
   4.2. The approach of 3D-surface machining 311
      4.2.1. One dimensional scanning 311
      4.2.2. Two dimensional scanning 312
      4.2.3. Gray scale techniques 313
      4.2.4. Combinations of gray scale and contour mask techniques 314
   4.3. Design of masks for 3D-machining 314
      4.3.1. Contour masks 314
      4.3.2. Gray scale masks 315
      4.3.3. Masks for producing interference patterns 319
5. Some laser 3D-machining techniques and their applications 319
   5.1. Laser machining for the microsystems technology 319
   5.2. Stationary regimes 320
      5.2.1. Step and repeat techniques 320
      5.2.2. Gray scale masks for 3D-machining 320
      5.2.3. Sub-micrometric structuring 322
   5.3. Scanned mask regimes 323
      5.3.1. General considerations of mask scanning 324
      5.3.2. Application of scanning contour masks 326
      5.3.3. Hybrid masks 329
   5.4. Laser direct writing using a small spot 330
6. Replication and transfer of laser machined surfaces 332
7. Conclusions 335

CHAPTER 12
MICROFABRICATION OF TRANSPARENT MATERIALS BY LASER PROCESSING 339
Yoshizo Kawaguchi, Hiroyuki Niino and Akira Yabe

1. Introduction 339
2. Microfabrication of transparent materials by pulsed-laser irradiation 340
   2.1. Direct interaction between the substrate and the pulsed laser 340

2.2. Indirect interaction between the substrate and a conventional pulsed laser 343
2.2.1. LIPAA process 343
2.2.2. LIBWE process 344
3. Microetching of transparent materials by the LIBWE process 347
3.1. Micropatterning of fused silica 347
3.2. Characteristics of the LIBWE process with various organic solutions 348
3.3. Mechanism of the LIBWE process 351
4. Conclusions 353

Index 359

This page intentionally left blank

PREFACE

Photo-Excited Processes, Diagnostics and Applications

Fundamentals and Advanced Topics

The great innovations in microelectronics, optoelectronics and photonics during the past two decades have clearly shown that successful technological advancements require the bridging of ideas between physics, chemistry, materials science, electronics, photonics and optoelectronic engineering. In particular, much can be learned from the advancements in microelectronics if one wishes to make a similar impact on technology and scientific progress in the field of photo-excited processes (PEP).

Over the past decade, this nomenclature has expanded to include, first, Applications to become PEPA, and more recently Diagnostics, thus evolving to PEPDA. Today, PEPDA has become a well accepted discipline with several regular international conferences such as ICPEPA, COLA and CLEO or dedicated symposia at EMRS and MRS annual meetings. The PEPDA combined subjects seem to have gained their own distinctive character at the first ICPEPA conference held in Japan in 1992. Since then, the research of *photo-excited processes* has developed more rapidly with a sequence of conferences, enhancing the research aimed at prospective uses of photonic, electronic and material excitations.

The research in photo-excited processes usually involves, in one form or another, the multitude of interactions between photons, electrons and atoms. One finds, for example, scientists who confine themselves to studying only the interactions between photons and electrons in order to create useful physical optical effects such as dynamic holograms. There are also those who look for direct ways of using photon-excited electrons to deposit or ablate atoms on surfaces for various electronic and electro-optic purposes. Thus, photo-excited-processes encompass a wide spectrum of sciences and disciplines ranging from physics and optoelectronics to materials science and photochemistry. It is for this reason that the goal set for this book was to choose a number of concepts and techniques, from fundamentals to advanced applications, and present all of them together to provide a "snap-shot" of the PEPDA fields. The reader can find herein a blend of topics such as physics of quantum excitations, optical advances and photochemical processing of materials in various phases. New concepts for diagnosing, processing of materials and micro-structuring of devices, using beams of photons are also included.

Each chapter in this book has been written as a stand-alone contribution, and is thus comprehensive on its own, without the need for other chapters as prerequisites. They have been written seeking to close the gap between the various disciplines that constitute PEPDA. Each chapter is nonetheless an integral part of the photo-excitation domain as the authors perceive it from their own point of view and experience. We first bring the fundamental concepts of physical excitations, followed

by materials engineering processes excited by photons and culminating with applications for microstructuring.

The specific topics addressed in this book by authors from many countries, appear sequentially as follows: Chapter 1 by *Margaritondo* et al., deals with Angle Resolved Photoelectron Spectroscopy (ARPES) used as a powerful tool for the investigation of low dimensional systems. By measuring the single particle electron spectra directly as a function of momentum and energy, ARPES can determine the band structure. Chapter 2 written by *Singh* et al., on optical absorption, photoexcitation and excitons in solids, treats the classical and quantum concepts from an entirely novel and updated point of view and emphasizes the exciton theory and its applications to materials, including quantum wells and amorphous solids. *Vlad* et al., in Chapter 3 present a rigorous treatise on nonlinear processes for creating soliton dynamic waveguides in photorefractive crystals (PRC). Two-wave mixing and self-diffraction in dynamic harmonic and inharmonic gratings with high diffraction efficiencies and beam amplifications are described. The optical phase conjugation in PRC with high phase conjugate reflectivity and high coupling transmission efficiency, useful in potential adaptive photonic devices is detailed. Chapter 4 authored by *Biaggio*, describes the Holographic Time of Flight (HTOF) method for the all-optical, contact-less investigation of charge carrier mobilities in non-centrosymmetric insulators and semiconductors. This chapter provides a detailed theoretical analysis of the HTOF method, discusses which experimental parameters are important, and also reviews some current applications.

Anisimov et al., bring the most important physical mechanisms and current theoretical models of laser ablation in Chapter 5. These are the surface vaporization model, bulk models for polymer ablation, photophysical ablation model and the two-temperature model for subpicosecond ablation of metals. Chapter 6 by *Boyd* and colleagues, gives a comprehensive review on the development and applications of UV excimer lamps towards thin film processing and surface structuring. *Akazawa* gives an overview in Chapter 7 on in situ diagnostics of synchrotron-radiation-excited structural changes and chemical beam epitaxy for silicon-based materials technology. In-situ monitoring tools such as high-resolution time-of-flight mass spectroscopy and spectroscopic ellipsometry are described. Chapter 8 is a review by *Luches* et al., on the synthesis and deposition of thin films of metal nitrides, using the reactive pulsed laser ablation (RPLD) technique. Thin films deposition of transition-metal nitride, aluminum nitride and boron nitride are described in detail. *Peled* et al., devote Chapter 9 to photo-deposition covering the current knowledge on photo-excited processes in liquid phases, with particular emphasis on film deposition from colloid systems. In Chapter 10, *Okoshi* et al., present new results on laser-irradiated frozen hydrocarbons for obtaining carbon allotropes. Sources used are excimer lasers, femtosecond lasers, synchrotron radiation and a free electron laser.

Micro-structuring implemented by laser ablation, employing contour, gray scale and hybrid masks, is described in Chapter 11 by *Zimmer* et al. Methods are described for high precision machining of 3D-structures with small surface roughness, using excimer lasers in conjunction with mask projection. New methods for micro-

fabrication of fused silica and other transparent materials by pulsed-laser irradiation are reviewed in Chapter 12 by *Kawaguchi* et al. Particular attention is given to the laser-induced backside wet etching – LIBWE and laser-induced plasma-assisted ablation – LIPAA processes.

The book will be useful to scientists and engineers who have a strong interest in photo-electronic device development for microelectronics and photonics. In spite of our efforts to provide a wide coverage, some topics of importance have inevitably been missed. I hope that there will be successors to this volume in the future where additional new exciting advancements will be covered, thus making the present book one of the first in a series dedicated to PEPDA.

Aaron Peled
Editor

This page intentionally left blank

CHAPTER 1

HIGH-RESOLUTION PHOTOEMISSION IN LOW DIMENSIONAL CONDUCTORS

L. Perfetti, M. Grioni and G. Margaritondo*

*Faculté Sciences de Base, Ecole Polytechnique Fédérale de Lausanne (EPFL), CH-1015 Lausanne, Switzerland (*Author for correspondence, E-mail: giorgio.margaritondo@epfl.ch)*

ABSTRACT: This chapter describes how strongly correlated quasi one-dimensional conductors are investigated by Angle Resolved Photoelectron Spectroscopy (ARPES). Low dimensional Peierls conductors deviate from the usual Fermi liquid picture and display the signatures of strongly renormalized carriers. A coherent interpretation of the spectroscopic results can be developed in the framework of the strong coupling electron-phonon theory. This interpretation, based on a polaronic approach, justifies several otherwise unexplainable features of the ARPES lineshapes.

1. Introduction

1.1. *Notions on high correlation*

Strongly correlated systems exhibit a large variety of many-body phenomena, mostly related to the electronic motion in the outermost orbitals of the atoms constituting each material. The microscopic behavior of these electrons is governed by three competing elements: the intrinsic itineracy, the inter-electron Coulomb repulsion and the electron-phonon interaction [1].

The first element is a direct consequence of the relatively high density characterizing a solid system. This implies that an electron placed within an outermost orbital can tunnel from one site to the neighboring sites. The strength of the itineracy can be denoted by the resonance transfer energy t between two neighboring orbitals – whose reciprocal is the tunneling time. In a many-electron system, the free motion of an electron is strongly affected by the Coulombic repulsion energy U. This increases when two electrons happen to be in the same site. Its strength is denoted by the energy cost for a charge fluctuation that places on the same orbital two electrons originally far away from each other. This correlation introduces strong repulsive and exchange interactions that induce magnetic effects and could even localize the electrons leading to the Mott insulating groundstate. Finally, one has to consider the coupling between an electron and the surrounding lattice. Due to this interaction, an electron can induce a local lattice distortion and a large polarization of the surrounding medium. If this local deformation is sufficiently big, the electron may even be confined in a self-trapped state. Otherwise, it will be free to move together with its polarization. The strength of this coupling is denoted by the energy lowering ε^* induced by a singly occupied site.

The interplay of these three competing properties of the electrons – expressed by the tendency to delocalization t, the constraining U and the deformation ε^* –

Aaron Peled (ed.), Photo-Excited Processes, Diagnostics and Applications (PEPDA), 1–24, 2003.
© 2003 *Kluwer Academic Publishers. Printed in the Netherlands.*

may generate complex and exotic groundstates. Their effects are especially important in low dimensional structures. Roughly speaking, with fewer degrees of translational freedom electrons have fewer ways to avoid their mutual interaction. As a consequence, the ordinary metallic state is generally unstable with respect to states for which the translational or spin rotational symmetries are broken. These instabilities lead to gap formation in the charge or spin energy spectrum, followed by the development of superstructures such as charge density waves (CDW) or spin density-waves (SDW). The transitions from the undistorted metallic state to a CDW is primarily interpreted in terms of $t \rightarrow \varepsilon^*$ competitions. Similarly, different magnetic properties are related to $t \rightarrow U$ competitions, while the stabilization of a CDW with respect to a magnetic SDW is determined by $\varepsilon^* \rightarrow U$ competitions.

In the following discussion, we investigate the interplay of low dimensionality and strong coupling in layered CDW materials. We show that in materials that belong to the family of the Peierls conductors, such as $K_{0.3}MoO_3$ and $(TaSe_4)_2I$, the carriers are heavily dressed by the lattice deformation. Based on this experimental observation, we suggest a polaronic interpretation for the peculiar and still debated spectral properties of these compounds.

1.2. *Polaronic effects in quasi-1D*

There is at present a general agreement on the effects that phonons have on the carrier dynamics in 3D conductors [2]. The main point is that free electrons, moving much faster than ions, can screen very effectively the phonon modes. Due to this efficient screening, electrons do not induce a large polarization of the lattice. For this reason, electron-phonon coupling can usually be treated as a weak perturbation. The conducting carriers are not very different from the bare electrons and can be correctly described by light quasiparticles [2]. A different approach must be used in molecules. For a given isolated orbital, t is strictly zero and the unscreened electron-phonon interaction has large effects. As the coupling strength increases, a substantial molecular distortion lowers the energy of the outermost orbitals. The real electron is dressed by vibrational modes and its wavefunction has very limited resemblance with the bare (non-interacting) particle.

This theory can be directly extended to the case of a single electron moving inside a highly polarizable medium. Here, the dressed electron is a polaron – i.e., a heavy carrier moving coherently with the lattice deformation in a narrow effective band. This model has been extensively used to describe the motion of the thermally excited carriers in doped semiconductors [3]. More generally, it applies when the carrier density is sufficiently small to neglect polaron-polaron interactions. Little can be said about a strongly coupled system with a metallic density of electrons. One can suspect that for this system the screening would be large enough to disregard the polaronic effects. As an example, metallic *Pb* exhibits a strong electron-phonon coupling but can be described in terms of light conducting charges. This simple concept may not work if the dimensionality of the material is reduced. In the so-called quasi one-dimensional (1D) conductors, neither the molecular approach,

nor a conventional quasiparticle picture correctly describes the physics of the carriers dressing. Indeed, low dimensional conductors are a bridge between the typical band materials and the molecular crystals. In band conductors the itinerancy is large and ε^* is a small correction, whereas ε^* is generally dominant in molecular crystals. Interestingly, the $t \rightarrow \varepsilon^*$ competition becomes more uncertain if the dimensionality is lowered [4].

This observation must be a consequence of the anisotropic electron tunneling. Peierls materials have metallic atoms arranged in chain-like structures. Generally, the partially filled band is formed by highly directional orbitals. As a consequence, the transfer integral along the chains, defined as $t_{\parallel}$, is at least one order of magnitude larger than the perpendicular $t_{\perp}$. The conduction and the screening are very anisotropic. Transport perpendicular to the 1D chains is strongly reduced, and may be totally incoherent. In this case the $t \rightarrow \varepsilon^*$ competition is ill defined. Along the chains $t_{\parallel}$ is much larger than ε^*, whereas perpendicular to them $t_{\perp}$ is much smaller. Consequently, the usual approach disregarding multi-phonon processes may not be correct. One must then deal with a largely unexplored situation in which the electron and phonon degrees of freedom are so interconnected that separation of the variables is impossible.

1.3. *Photoemission experiments*

Angle Resolved Photoelectron Spectroscopy (ARPES) is a powerful technique for the investigation of low dimensional systems. In a typical ARPES experiment, the layered crystals under investigation are mounted on a cryostat and cleaved at the base pressure of 10^{-11} mbar. Their orientation is performed in advance by X-ray measurements and then checked in-situ by low-energy electron diffraction (LEED). A beam of photons – usually produced by a synchrotron – impinges on the sample and induces the photoemission process. The outgoing photoelectrons are analyzed by a spectrometer that simultaneously resolved their energy and momentum. At present, commercial devices achieve energy resolution and angular resolution better than 10 meV and 0.5 degrees. Under suitable assumptions, this technique provides a direct picture of the single particle removal spectral function and can determine important quantities such as the band structure, the Fermi Surface (FS) and the temperature-dependent energy gap of an ordered phase.

The existence of a FS is a typical characteristic of a metal. In an ARPES experiment, this property corresponds to the fact that an experimentally observed electron band crosses the Fermi level. However, many experiments have revealed that the spectral features of Peierls conductors are quite unusual. No evidence of the Fermi edge is visible in the photoemission spectrum of these metals [5]. As shown in Figure 1, this corresponds to a vanishing spectral weight near the chemical potential for a Peierls conductor, in sharp contrast with the finite signal for a conventional conductor. Different mechanisms have been proposed as possible explanations. The CDW fluctuations must be considered: they induce, above the transition temperature T_p, a pseudogap reminiscent of the actual gap in the low temperature insulating phase. However, the deep pseudogaps observed by photoemission are

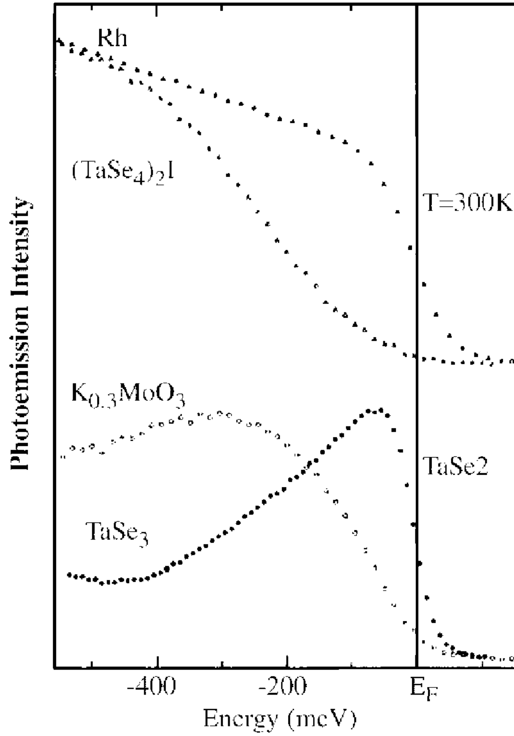

Figure 1. Angle integrated photoemission spectra of the $K_{0.3}MoO_3$ and $(TaSe_4)_2I$ measured at a temperature just above the Peierls transition (ref. [5]). For comparison the spectra of 2D (2H-$TaSe_2$) and 3D (Rh) metals are shown for the same temperature. All spectra are normalized at their maximum intensity.

usually much larger than the low temperature energy gap Δ_0 derived by transport and optical measurements.

An additional effect related to the low dimensionality can explain the suppressed ARPES signal near the Fermi level. Theory has indicated that 1D systems, due to strong electronic correlations, are not Fermi liquids [6]. The quasiparticle picture fails and the theoretical single particle excitations shows evidence of a decoupling of the charge and spin degrees of freedom. The elementary excitations are collective, boson-like modes that lead to a many-body quantum state commonly referred to as the "Luttinger liquid". This theoretical picture, although interesting, faces some difficulties. In the case of the Peierls conductors, the large pseudogaps can be justified only within an extreme and probably unphysical range of parameters such as the "stiffness" of the Luttinger condensate.

Some recent work [7, 8] suggests that a strong electron-phonon coupling could account for the anomalous spectral properties experimentally observed. The transfer of spectral weight towards higher binding energies, technically defined as polaronic renormalization, is clearly enhanced by the low dimensionality of the Peierls

systems. Due to the unresolved problems affecting this approach, the interpretations of the experimental data are mainly phenomenological. Nonetheless, some crucial quantities can be extrapolated quite directly from the ARPES intensity maps. We discuss an efficient method to extract the single particle gap, as well as the phonon dressing of polarons and the spatial coherence length of single particle excitations. The results are systematically compared with bulk-related properties such as optical conductivity, *dc* resistivity and spin susceptibility. The ensemble of these measurements provides a picture of the polaronic liquid state and of its CDW instability.

1.4. *A Fermi-Liquid System*

Before treating complex quasi-1D conductors, we must try to understand single particle excitations in materials that can be considered as Fermi Liquids (FL). ARPES investigations of "standard" metals have verified the theoretical predictions and identified the quasiparticle signatures [9]. As an example, layered 1T-$TiTe_2$ exhibits the typical FL properties and provides an ideal situation in which bands with clear 2D character cross the Fermi level. The weak interlayer dispersion minimises the perturbing effects of the finite photoelectron mean free path and gives direct access to the photohole lifetime.

Figure 2 illustrates an ARPES scan measured at T = 13 K along the high symmetry ΓM direction of the Brillouin zone. The spectra are remarkable for the large contrast between the narrow and intense quasiparticle peak and the very weak background. Both the width and the intensity of the signal exhibit a strong angular dependence. These variations reflect the dispersion of the *Ti d* band across the Fermi level [10, 11].

We can evaluate the quasiparticle scattering rate from the spectral linewidths of the Energy Distribution Curves (EDC). Figure 3 shows the EDC measured at the Fermi wavevector kF for temperatures ranging between 237 K and 13 K. Upon cooling, the spectrum becomes sharper due to the steeper Fermi-Dirac distribution and to the weaker electron-phonon scattering. From a fitting procedure whose details are discussed in ref. [10] we can extract the temperature dependence of the spectral linewidth. Figure 4 shows the half-width at half maximum (HWHM) of the underlying Lorentzian lineshape. Notice that Γ(T) decreases almost linearly down to 70 K and saturates for temperatures lower than 60 K. The residual linewidth Γ_0 = 17 meV is attributed to the extrinsic photoelectron broadening of the photoemission process. Apart from this factor, Γ(T) can be well reproduced by the Migdal-Eliashberg expression [2]:

$$\Gamma(\mathrm{T}) = 2\pi\int_0^\infty \alpha^2 F(\omega)[n(\omega) + f(\omega)]d\omega. \quad (1)$$

Here $n(\omega)$ and $f(\omega)$ are the Bose-Einstein and the Fermi-Dirac distributions and $\alpha^2F(\omega)$ is the Eliashberg coupling function. Within the Debye model, $\alpha^2F(\omega) = \lambda(\omega/\omega_0)^2$ and the electron-phonon scattering is fully described by the coupling parameter λ and the cut-off frequency ω_0 of the phonon-spectrum. The best agree-

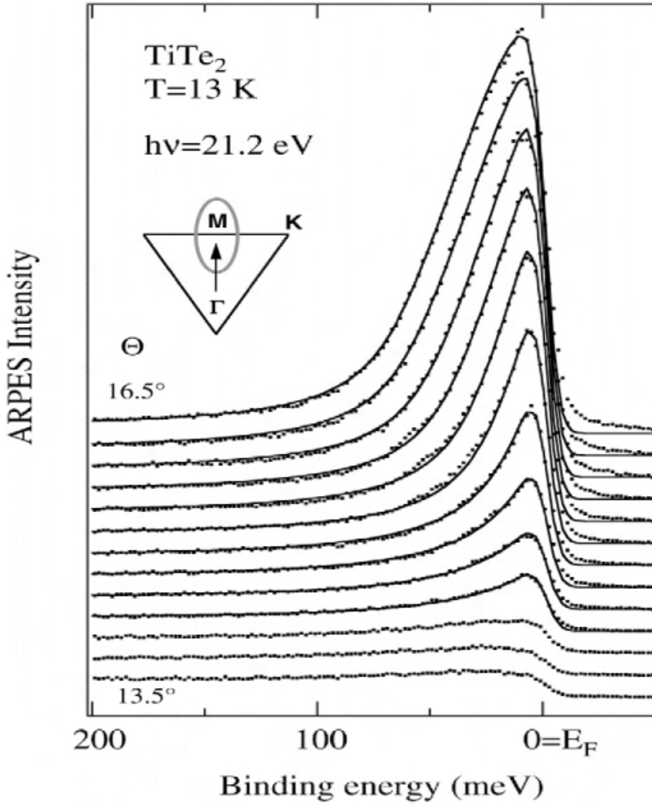

Figure 2. High-resolution ARPES spectra of 1T-$TiTe_2$ measured near the FS crossing along the high-symmetry ΓM direction ($\theta = 0$ is normal emission). The lines are the results of Fermi-liquid-based fits to the data with the parameters discussed in ref. [10]. The inset shows a portion of the Brillouin zone with the relevant ellipsoidal electron pocket.

ment over the entire temperature range is obtained for $\lambda = 0.22$, and $\hbar\omega_0 = 20$ meV.

These results are meaningful especially when compared to the electrical resistivity – see Figure 4. The in-plane resistivity $\rho_{ab}(T)$ exhibits a typical metallic behavior and – apart from the offset Γ0 – the same temperature dependence as the quasiparticle linewidth Γ. The transport relaxation time τ tracks the spectroscopic lifetime revealing a direct connection between macroscopic properties and quasiparticles motion.

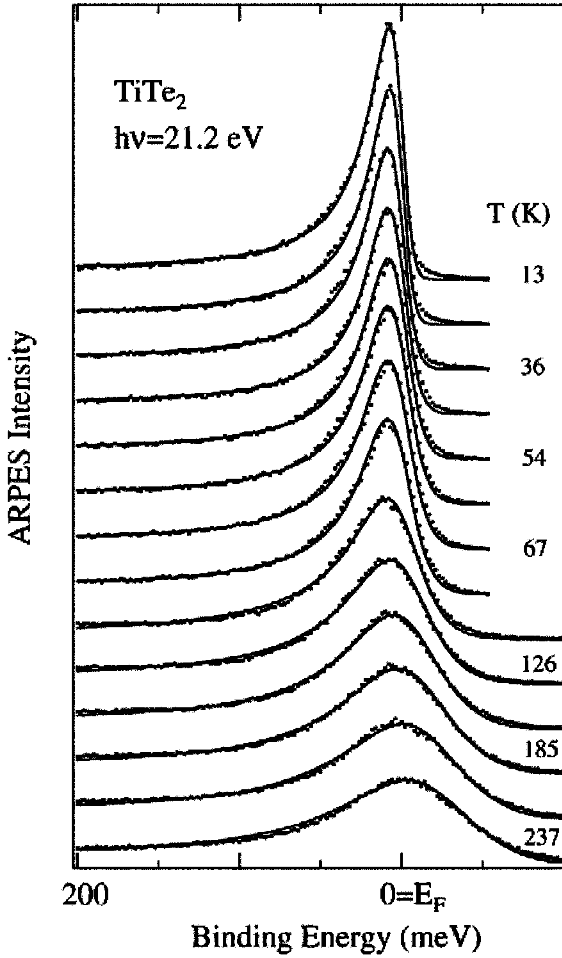

Figure 3. ARPES spectra of 1T-$TiTe_2$ measured at the Fermi surface at different temperatures (ref. [10]). The lines are the result of a Fermi liquid fit with a temperature-dependent self-energy describing electron-phonon scattering.

2. Peierls conductors

2.1. *Structural and transport properties*

The transport physics of quasi-1D Peierls conductors was thoroughly explored during the past twenty years. In the ground state, these materials exhibit a periodic modulation of the charge density and a gap in the spectrum of single particle excitations. The CDW is driven by electron-phonon interactions and appears as a metal-insulator transition occurring at the finite Peierls temperature T_p. This correlated

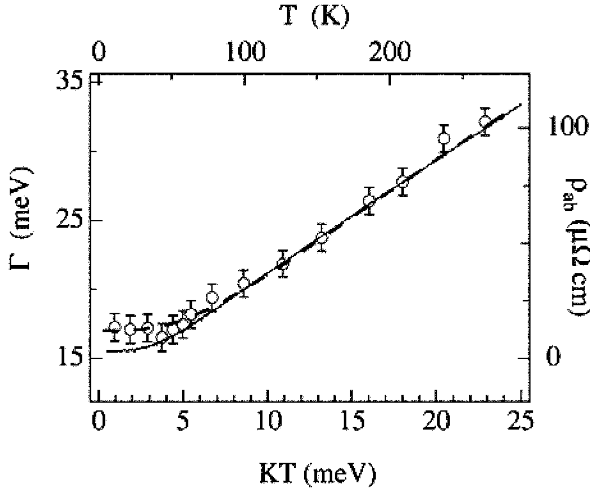

Figure 4. Comparison (ref. [10]) of the temperature-dependent spectral linewidth Γ (HWHM) (open symbols) from $\rho_{ab}(T)$ (solid line). The dashed line illustrates the theoretical prediction for an electron-phonon coupling parameter $\lambda = 0.22$ plus a constant term $\Gamma_0 = 17$ meV. Notice the offset between the two vertical scales.

phase has been studied by measuring the optical response [12], thermodynamic quantities [13], transport coefficients [14] and structural and magnetic properties [15, 16].

Most of these experiments agree with the scenario originally proposed 50 years ago by Peierls [17] who showed that a metallic chain is unstable at T = 0 due to tendency to a periodic distortion of the lattice. This instability results from the large effects of the interactions in a system with a highly degenerate Fermi surface. Indeed, the FS of a 1D metal is formed by two parallel sheets at a distance from each other equivalent to twice the Fermi wavevector. This peculiar topology leads to a modulation of the charge density with wavevector $Q_{CDW} = 2k_F$ [18].

Below the critical temperature, a gap opens in the single particle excitation spectrum and the material becomes insulating. At the mean field level, the system undergoes a transition to a fully ordered CDW state at a finite temperature T_{MF}. This temperature is determined by the strength of the electron-phonon coupling and within the set of approximations usual for the BCS theory of superconductivity one finds a gap $2\Delta_0 = 3.5\ k_B\ T_{MF}$. In the ideal 1D systems, thermodynamic fluctuations prevent a transition to a state with long-range order from occurring at a finite temperature. However, real materials are only approximately 1D. The three dimensional CDW transition is stabilized by the interaction between different metallic chains and this happens at a temperature smaller than the gap energy [19]. Thus, we can identify the CDW formation at T_p as a transition from a metallic phase with strong fluctuations in individual chains to the statically distorted 3D groundstate. As a consequence, the Peierls systems exhibit a metallic phase different from that of usual conductors. Electron-phonon correlations are very strong

rearing a fluctuating pseudogapped regime extending over a broad temperature range [20].

2.2. *Nesting condition in a typical Peierls system: $K_{0.3}MoO_3$*

The molybdenum blue bronze $K_{0.3}MoO_3$ is considered a reference compound for the study of the Peierls instability. It has double chains of Mo_6 octhaedra that run along the crystallographic **b** direction and support conducting bands with strong 1D character. The interaction between adjacent double chains splits these bands into bonding *B* and antibonding *AB* subbands that are doped by charge transfer from the K^+ ions [21, 22]. These bands generate two pairs of open Fermi surface sheets perpendicular to the ΓY direction (**b**) with distinct Fermi wavevectors k_F^B and k_F^{AB}. The metallic state is unstable below T_p = 180 K: a CDW brings the crystal to the insulating phase.

Figure 5(a) shows the ARPES spectra acquired along ΓY with large angular acceptance along the perpendicular direction. Both, the dispersive *B* band and the flatter *AB* band are well resolved [7]. Approaching the crossing wavevectors they produce a weakly but still detectable FS. One can estimate the values of k_F^B and k_F^{AB} from the wavevector dependence of the Momentum Distribution Curve (MDC) I(k, E_F), i.e. a constant energy cut at $E = E_F$ of the measured intensity map. As shown in Figure 5(b), the bonding and the antibonding bands cross near the edge of the

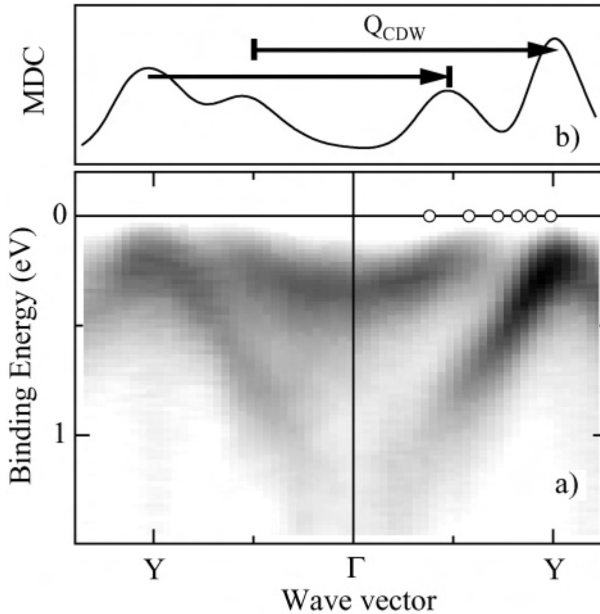

Figure 5. ARPES intensity map of the $K_{0.3}MoO_3$ (ref. [7]) showing the band structure along ΓY (T = 180 K, $\hbar\omega$ = 21 eV). (b) Momentum distribution curve (MDC) extracted from (a) at binding energy E = 30 meV (ΔE = 60 meV), showing the alternate nesting of the FS sheets.

first Brillouin Zone (BZ) and near 0.5 ΓY. Within the experimental uncertaintiy, *B* and *AB* are perfectly nested by the CDW wavevector (0.73 **b*** + 0.5 **c***). This result is in agreement with the FS mapping reported by Gweon [23] and corroborates the occurrence of a $k_F^B + k_F^{AB}$ instability as suggested by band structure calculations [21].

2.3. *The symmetry of the electronic bands and the effects of CDW fluctuations*

When taken with polarized photons, the ARPES spectra reflect the symmetry of specific electronic states. If the crystal has a mirror plane σ, the photohole wavefunction can be classified as even or odd. The photoelectrons ejected along this plane have always even symmetry since an odd wavefunction would have a node in the plane and consequently zero probability amplitude at the detector. If the vector potential lies within σ, the dipole operator contains only even components. In this geometry only initial states with even wavefunctions are detectable [24].

Symmetry-resolved band mapping can be achieved for the blue bronze, since the measured photocurrent is strongly anisotropic and polarization dependent. We show in Figure 6 an intensity map acquired as a function of the inter-chains wavevector $k_\perp$ for $k_\parallel$ = 0.58 ΓY. The perpendicular dispersion is very weak < 0.1 eV and consistent with an open Fermi surface. With the light polarized within the mirror plane, the intensity of the *B* band is maximum for $k_\perp$ = 0, whereas the signal of the *AB* band is zero. Therefore, the two bands have opposite reflection symmetries: even for *B* and odd for *AB*. These are, in the 2D limit, the symmetry properties of the bonding and antibonding combinations of 1D orbitals predicted by band structure calculations [21]. Notice that the antibonding band at $k_\parallel$ = 0.58 ΓY, appearing for $k > k_F^{AB}$ = 0.5 ΓY, is necessarily an *umklapp* process by the CDW potential. Since the map of Figure 6 has been acquired in the undis-

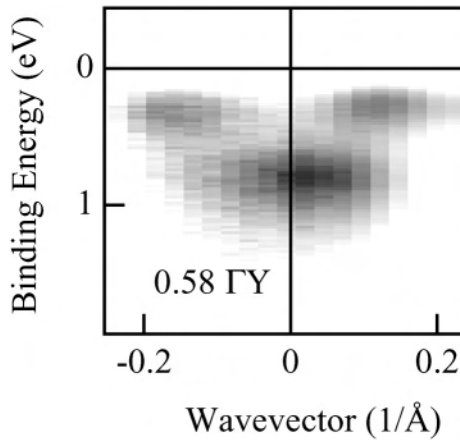

Figure 6. ARPES intensity maps of $K_{0.3}MoO_3$ (ref. [7]) measured perpendicular to the chains, for $k_\parallel$ = 0.58 ΓY (T = 180 K, $\hbar\omega$ = 21 eV). Darker regions correspond to a larger intensity.

torted metallic phase, the observation of *AB umklapp* reveals the effects of strong CDW fluctuations.

These "shadow" bands are expected to appear even when the CDW potential is incommensurate with respect to the lattice. The Peierls system $(TaSe_4)_2I$ is a good candidate for the confirmation of this notion. $(TaSe_4)_2I$ has strong anisotropic properties due to quasi-1D electronic bands formed on $TaSe_4$ chains [25]. The rearrangement of Se_4 units creates an effective unit cell containing 4 Ta-Ta bonds with $c = 4d = 12.824$ Å. In a purely ionic picture the bands are quarter-filled but the charge transfer is incomplete, thus $k_F > \pi/c$. Below $T_p = 263$ K, the system is in a CDW state with a small deviation from commensurability. The bands are effectively doped and X-ray scattering experiments measure a periodic distortion with wavevector modulation $Q_{CDW} = 1.085\ 2\pi/c$.

A dense sampling of the low binding energy window near π/c shows that two periodicities are present in the band structure of this crystal, see Figure 7. The turning points at the top and at the bottom of the ARPES intensity plot do not coincide. The lower edge turns at $k = \pi/c$, while the upper edge turns at $k = k_F = 1.085\ \pi/c$. This result is direct experimental evidence that ARPES detects both the lattice as well as the incommensurate CDW periodicity.

A simple model that evaluates the spectral weight under the influence of two incommensuate potentials is discussed in ref. [26]. A more detailed analysis must considers the specific properties of the material. In particular, the $(TaSe_4)_2I$ lineshape can be decomposed into two Gaussians of identical width, separated by 0.17 eV. The presence of two chains per unit cell [25] suggests a two-leg ladder of $TaSe_4$ as the basic building block of the system. The two ARPES features are associated with the bonding *B* and antibonding *AB* ladder states. One faces, therefore, the

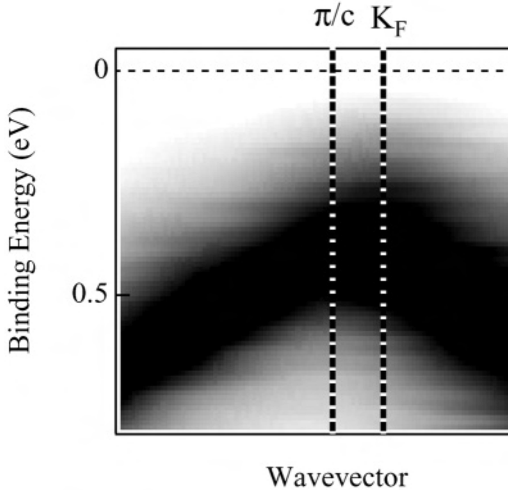

Figure 7. Detailed view of the region near the zone boundary in $(TaSe_4)2I$ (ref. [26]). For clarity, the raw intensity map has been normalized to the same peak intensity, and interpolated with respect to energy and wavevector.

problem of determining the electronic structure of a two-band model with incommensurability induced by slight doping. This system may be in a regime for which each of the two potentials couples to one band separatedly leaving one of the electronic periodicities commensurate with the crystal lattice. Commensurability is important because for a single chain it implies the stabilization of the CDW groundstate. For two chains the situation is more complex. In the limit of non-pinning in the transverse direction, the doping effects of the bonding and antibonding bands are independent and the Fermi wavevectors $k_F^{B,AB}$ depend on the amount of doping. Clearly, the most favorable situation occurs when all doping electrons go into one band and the other remains commensurate.

2.4. *Limits of the weak coupling theory*

The weak coupling theory of the CDW transition can describe many properties of the Peierls conductors [18]. Nonetheless, the fluctuating gap models cannot reproduce the ARPES lineshapes. The weak coupling approach would require a spectral function peaking at the gap energy for $k = k_F$. The situation revealed by the experimental data is quite different. The $(TaSe_4)_2I$ spectrum in Figure 8 exhibits the *A* and *AB* contributions at k_F. It is evident that both bands peak at higher energies than the half-gap value. Instead, the Gaussian tail of the *AB* band coincides with Δ_0 = 120 meV [8].

This displacement of spectral weight stresses the importance of interactions. Both

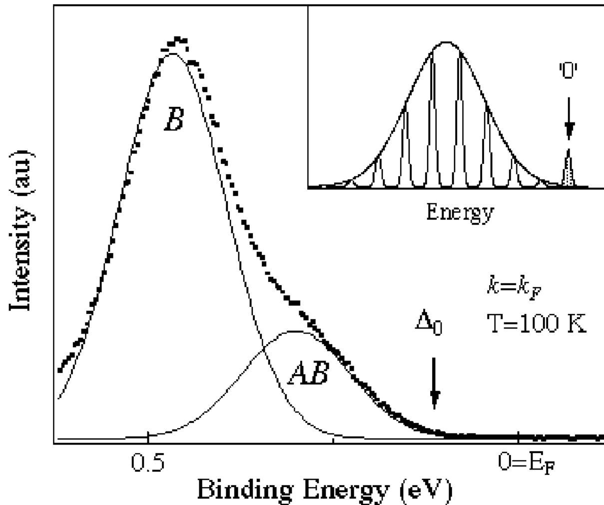

Figure 8. High-resolution ARPES spectrum of $(TaSe_4)_2I$ (ref. [8]) at 100 K and $k = k_F$ ($\hbar\omega$ = 24 eV). The lineshape can be reproduced by two Gaussian lines. The extrapolation of the leading edge coincides with the energy gap Δ_0 = 0.12 eV. Inset: Schematic spectral function of an electron coupled to a harmonic oscillator in the strong-coupling limit. The 'zero-phonon' line ('0') also lies under the Gaussian envelope: here, it was arbitrarily rescaled to enhance its visibility. Its weight is exponentially reduced with the coupling strength.

many-body correlations and electron-phonon interactions transfer spectral weight from the coherent quasiparticle peak to incoherent structures at higher binding energies. In $(TaSe_4)_2I$ and $K_{0.3}MoO_3$ there is no evidence for strong electronic correlations. On the other hand, electron-phonon interactions are important in a CDW system. Therefore, the broad ARPES lineshapes of these Peierls conductors can be interpreted as the spectra of electrons strongly coupled to the lattice [7, 8].

3. A simplified model for systems with large interactions

In the strong coupling regime, one should completely reconsider the coupling with the lattice. A model that ignores the phonon dispersion can be set up with three parameters: the frequency of the phonon, the strength of the coupling and its range. The finite frequency of the lattice vibrations constitutes the main difference between the electron-phonon and the Coulomb interaction. Hence, the retardation of the lattice relaxation must be taken into account. For a dispersionless phonon mode, the quantum that determines a scattering process has energy $\hbar\omega_0$. If $\hbar\omega_0 \ll t$ the phonons cannot follow the motion of the electrons but can produce a “static” potential due to the frozen lattice distortion. This is called the adiabatic limit. On the other hand, when $\hbar\omega_0 \gg t$ the phonons can follow the motion of the electrons instantaneously producing interaction without retardation just as the Coulombic force. None of these extreme situations is verified in real solids but most inorganic crystals are in the adiabatic regime.

When the coupling is strong, the charge carriers are surrounded by a fairly large deformation field of the lattice. For a moving small polaron, there is a continuous exchange of momentum between the electron and the polarizable medium. The electron mass is renormalized by interactions and could be large enough to trap the carriers in a self-induced lattice distortion. Calculations indicate that this process is strongly dependent on the characteristics of the interaction and is a gradual crossover in the case of a long range coupling [28].

The physics of these single particle models has been explored by Monte Carlo simulations [29]. Due to the prohibitive computational effort, the possible many-body extensions – namely polaron liquids – are still largely unexplored. It is likely that the self-energy of a polaron is strongly altered by the presence of other carriers. All theoretical treatments are affected by an initial problem. Since the two coupled systems – electrons and phonons – strongly affect each other, the best starting point of many-body calculations it not obvious. The commonly used approach was proposed by Migdal in 1958 [30]. The justification of the procedure requires to some extent knowledge of the solution. The first step is a treatment of the phonons with electronic states that do not contain phonon effects. The main idea behind it is that phonons alter the electronic states only within an energy distance equivalent the Debye energy from the Fermi Surface. These are a small fraction of the electrons in the system. On the other hand, the electron influence upon the phonons is averaged over all occupied states of the electron gas. This average is only negligibly influenced by the few electrons at the FS. These arguments are formalized by the

Migdal theorem, which provides an efficient way to calculate the renormalized propagator.

The remarkable success of this approach to describe the 3D metallic states makes the Migdal theorem a hallmark of the electron-phonon theory. Nonetheless, its applicability relies mainly on the assumption that electrons are affected by phonons only near the Fermi level. This hypothesis may not be correct in low dimensional materials where the conduction is too anisotropic to provide an efficient screening. If the coupling with the lattice is strong, the multiphonon electronic dressing could affect electrons well below E_F. The lattice and electronic degrees of freedom mix strongly and the Migdal theorem may break down.

In place of a Fermi liquid, a new state develops that can be called a polaron liquid. This dense polaronic phase could be subject to different instabilities, namely a CDW transition. As compared with ordinary insulators, the CDW is quite an exotic phase mainly due to the strong effects that it can have on the relaxation of an excited state. The relevant materials have an adiabaticity ratio $t/\hbar\omega_0 > 10$, so that the electron dynamics is faster than the lattice field. Just after an electronic excitation takes place, a single particle is in a free state extending over the crystal. Only after the lattice relaxation is complete, the hole becomes a very massive quasiparticle. As a result, the itineracy of the single particle excitations depends substantially on the timescale of the probe. A fast probe, like photoemission, produces single particle states that "feel" the frozen lattice dispersion. At the opposite limit, an adiabatic perturbation would generate a response that can be described in terms of heavy quasiparticles dispersing along narrow polaronic bands. In a rigorous treatment of the electronic response, one would calculate exactly the single particle propagator. However, this formidable many-body problem has not yet been solved and one must resort to a heuristic approach to interpret the experimental ARPES results.

The starting point for this approach is the tight binding Hamiltonian [2]:

$$H = t\sum_{j,\delta}\bar{c}_j + {}_{\delta}c_j + \frac{\hbar\omega_0}{\sqrt{2N}}\sum_{j,q}\bar{c}_j c_j e^{iqm}\gamma(q)(d_q + \bar{d}_{-q}) + \hbar\omega_0\sum_q\left(\bar{d}_{-q}d_q + \frac{1}{2}\right). \tag{2}$$

In these notations, c_j destroys an electron on the j site, m is the lattice coordinate, d_q destroys a phonon of wavevector q and energy $\hbar\omega_0$ and $\gamma(q)$ represents the interacting potential. One can perform a canonical transformation that shifts the ions to a new equilibrium positions.

In a more general sense one changes the base of the phonon states in order to diagonalize H in the limit of $t = 0$. The atomic limit ($t = 0$) describes a localized electronic state coupled to oscillators of energy $\hbar\omega_0$ [2]. Its solution yields the Green function dependence on the coupling strength. In this context, the range of the electron phonon interaction is unimportant and we suppose $\gamma(q)$ to be equal to a constant g. The single particle propagator acquires an extra phase

$$\Phi(t) = g^2(1 - e^{(-\hbar\omega_0 t)}), \tag{3}$$

that describes the polarization field. The resulting spectral density consists of a series

of delta functions spaced exactly $\hbar\omega_0$ apart. The distribution of peak heights follows the Poisson law:

$$A(\omega) = 2\pi e^{-g^2} \sum_{l=0}^{\infty} \frac{g^{2l}}{l!} \delta(\hbar\omega + g^2\hbar\omega_0 - l\hbar\omega_0). \tag{4}$$

Without interactions, this would reduce to a single delta peak at the energy of the atomic level. When interactions are turned on, there is a finite probability for excited states with l phonons. These states are virtually present in the quasiparticle and produce excited Frank-Condon satellites in the excitation spectrum.

The spectral function derived from equation 4 is shown in Figure 9(a, b) for two different values of the coupling constant. In the weak coupling regime $g < 1$, the fundamental peak $l = 0$ has the largest intensity and higher l peaks become very rapidly smaller. For strong coupling $g > 1$, the peak strength increases with l up to values of approximately $l \approx g^2$, and then it decreases again. Therefore, one can interpret g^2 as the average number of phonons $\langle n \rangle$ dressing a quasiparticle in the ground state [31].

Difficulties arise when the electronic dispersion is large, and the band is partially filled. After the canonical transformation, the kinetic term becomes a complicated mixture of electron and phonon operators. An analytical solution can be obtained only approximating this term with an averaged transfer integral t'. Notice however that t' (or rather $4t'$) is different from the polaronic bandwidth and it does not represent the exponentially suppressed polaronic hopping. Indeed, a hole is no longer a good excitation but carries a consistent cloud of phonons with intrinsic dynamics and finite spatial extension. In the adiabatic regime, the lattice relaxation is very slow and the electrons on a short timescale are delocalized. As a result, the ARPES signal follows the non-renormalized frozen lattice bands and $t' \approx t$.

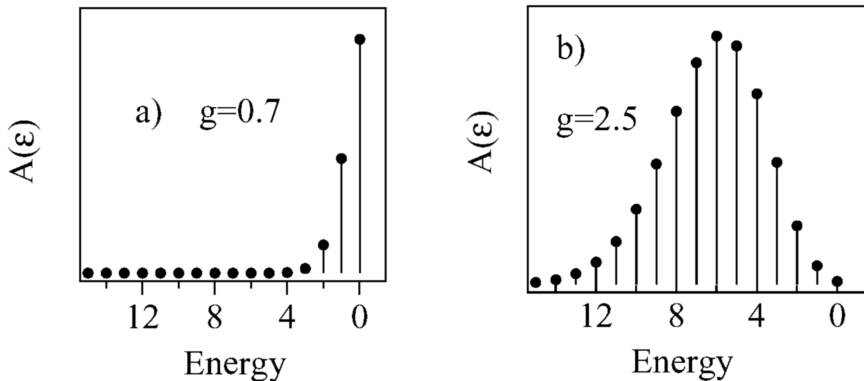

Figure 9. The spectral function of a weakly coupled localized state (a) and strongly coupled (b) to a local stretching mode. The energy is expressed in unit of $\hbar\omega_0$ and is shifted by a relaxation term $g^2\hbar\omega_0$ that rescales the quasiparticle energy to the origin of the plot.

With the introduction of an effective kinetic term, the Hamiltonian becomes purely electronic. With this simplification, the photohole propagator can be expressed by [32]:

$$G(k, \omega) = \frac{1}{2\pi N} \sum_{k'} \int G_0(k', \omega')\sigma(k' - k, \omega' - \omega)d\omega', \tag{5}$$

where $G_0(k', \omega')$ is the bare propagator of an electron with a resonance transfer integral equal to t', and

$$\sigma(k, \omega) = ie^{-g^2} \sum_{l=0}^{\infty} \frac{g^{2l}}{l!} I_l(k) \left(\frac{1}{\omega - l\omega_0 + i\delta} - \frac{1}{\omega - l\omega_0 - i\delta} \right), \tag{6}$$

$$I_l(k) = \frac{1}{g^{2l}} \sum_m I_l(m)e^{ikm}, \tag{7}$$

$$I_l(m) = \left(\frac{1}{2N} \sum_q |\gamma(q)|^2 e^{-iqm} \right)^l, \quad g^2 = I_1(m)|_{m=0}. \tag{8}$$

Figure 10(a) shows the ARPES structure of a polaronic quasiparticle dressed by $\langle n \rangle = g^2 \approx 5$ phonons. As expected, the spectral weight is transferred from the zero-phonon peak to the excited Frank-Condon satellites. In the strong-coupling adiabatic limit , $\hbar\omega_0 \ll 1$, the satellites merge into a single Gaussian peak. The separation between the peak maximum and the zero-phonon line is $\varepsilon^* \approx \langle n \rangle \hbar\omega_0$, proportional to the average number of phonons dressing the electron. The quasiparticle weight is exponentially suppressed and the spectrum is mostly incoherent.

The range of the interaction $I_1(m) = g^2 e^{(-m/r)}$ determines the wavevector dependence of this signal. For a strictly local interaction, the spectral weight is uniformly distributed in k space. For a more realistic non-local interaction, i.e., $r = 30$ Å, the resulting momentum distribution curve defines a coherence length $l = 1/\Delta k$ of the order of the size of the phonon cloud – see Figure 10(b). When the coherence length is larger than the unit cell, the spectral weight is distributed along the frozen lattice band (Figure 10(c)) and the ARPES maps should be interpreted as the superposition of narrow polaronic bands that fill the reciprocal space with uneven intensity, Figure 5(a) [33, 34].

4. The polaron liquids

4.1. *Experimental evidences of heavy carriers*

The most direct signature of heavy renormalization is given by the ARPES data. The observation of displaced Gaussian lineshapes, Figure 8, is consistent with the assumption that the charge carriers are small polarons [7, 8]. Indeed, a large coupling would transfer most of the spectral weight from the "zero-phonon" peak to vibra-

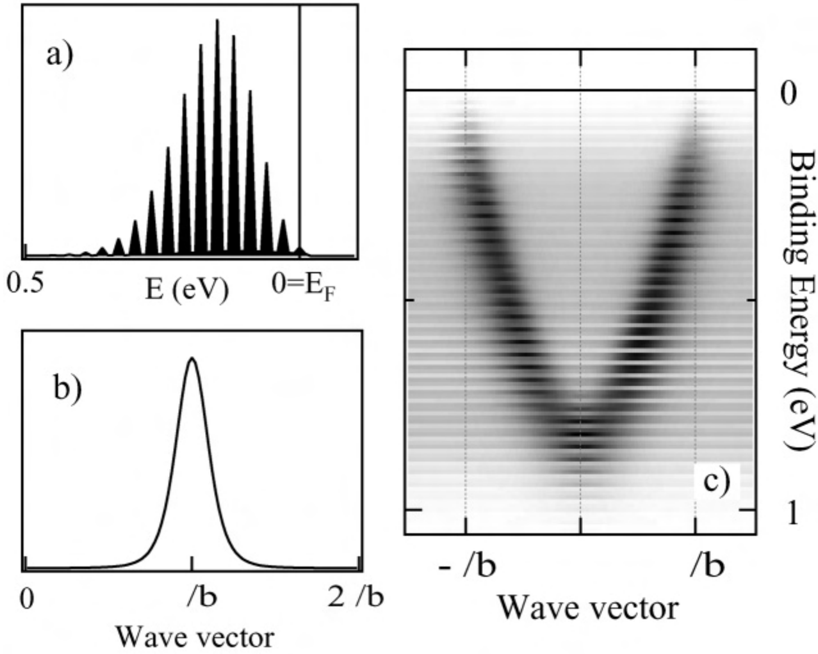

Figure 10. (a) Calculated spectrum and (b) momentum distribution (E = 30 meV) of a polaronic quasiparticle at the Fermi surface [7]. The electron is dressed by $\langle n \rangle = 5$ phonons with energy 30 meV and the range of the *e-ph* interaction is 30 Å. (c) Momentum-dependent spectral weight distribution. We used a lattice constant value b = 7.5 Å, and we choose the underlying 'frozen lattice' dispersion to reproduce a typical experimental ARPES intensity map.

tional satellites. In a solid, of course, the interaction with a continuum of vibrational states together with other broadening mechanisms smear out the satellite structure. Only the Gaussian envelope is observed, and the weight of the leading peak reflects the small overlap of the photohole with the real quasiparticle. In the small polaron limit, this overlap is exponentially suppressed and the spectrum becomes an incoherent peak at $\varepsilon^* \approx \langle n \rangle \hbar\Omega^*$. Here Ω^* is an averaged phonon frequency of the electron-phonon system which in Peierls conductors is typically in the range of 10–50 meV. From the energy separation between the quasiparticle energy and the maximum of the spectrum we can attempt a rough estimate of the polaronic cloud. ARPES data on $(TaSe_4)_2I$ and $K_{0.3}MoO_3$ place ε^* in the 0.15–0.2 eV range. Depending on Ω^*, the resulting $\langle n \rangle$ would vary between 5 and 10. Both numbers are compatible with the formation of small polarons in a strongly coupled regime.

Optical data provide an independent evidence of heavy quasiparticles. We show in Figure 11 the real part of the optical conductivity $\sigma(\omega)$ measured in $K_{0.3}MoO_3$ at T = 200 K. The light is polarized along the chain axis and spans the spectral range below 1 eV ($\approx 10^4$ cm^{-1}) [12]. We can identify several distinct components, which are well reproduced within the phenomenological Lorentz-Drude approach [35]. The

main feature at $2\Delta = 1000\ cm^{-1}$ (≈ 120 meV) is associated with the Peierls pseudogap which is already quite deep at this temperature. At low frequencies, the spectrum exhibits a rather complex behaviour. Besides the peak attributed to the quasi-pinned collective mode at about 3 cm^{-1}, there are two distinct zero-frequency modes. The first narrow Drude represents the collective contribution of the sliding CDW segments while the second broad Drude reflects the response of the uncondensed quasiparticles.

The spectral weight of the quasiparticle component can be scaled with respect to the total spectral weight up to the threshold of the interband transition [7]. The integral [35] of $\sigma(\omega)$ leads to a plasma frequency $\Omega_p^{tot} = 25600\ cm^{-1}$ while spectral weight arguments applied to the quasiparticle component yield $\Omega_p^{QP} = 4100\ cm^{-1}$. From the conductivity sum rule we find:

$$\left(\frac{\Omega_p^{tot}}{\Omega_p^{Q}}\right)^2 = \left(\frac{n^{tot}}{n}\right)\left(\frac{m^*}{m_e}\right) = 39. \tag{9}$$

Notice that m^* is the effective mass of the polaronic quasiparticle and should not be confused with the (much larger) mass of the fluctuating CDW segments. Using $n/n^{tot} \approx 0.7$ at 200 K derived from the spin susceptibility [16], we obtain the polaron effective mass $m^* \approx 28\ m_e$. The same arguments apply to the optical conductivity of $(TaSe_4)_2I$, ref. [8]. Following step by the step the procedure aforementioned for $K_{0.3}MoO_3$, we estimate the effective mass of the $(TaSe_4)_2I$ carriers to be $m^* \approx 10\ m_e$.

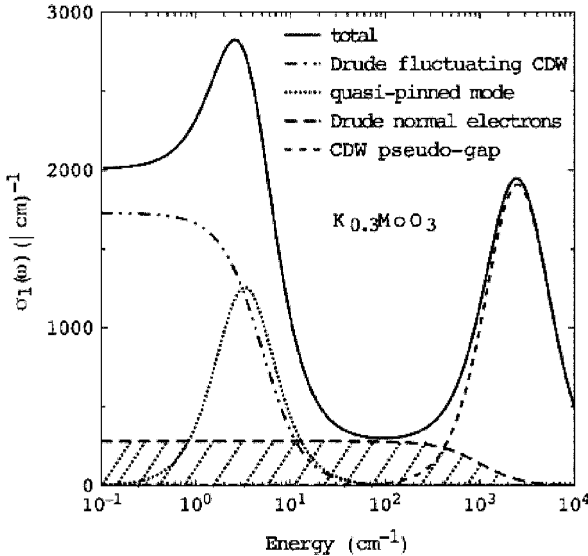

Figure 11. Optical conductivity in $K_{0.3}MoO_3$ at T = 200 K, along the chain direction, ref. [7, 12]. The components of the calculation are shown separatedly and the contribution from the polaronic quasiparticles is highlighted by the dashed surface.

4.2. *The CDW instability*

At high density, namely in the liquid phase, these polarons form a metallic and correlated state that fluctuates strongly above T_p and yields at low temperature the CDW groundstate. Several properties such as the wide bandwidths and the nested FS are consistent with a description based on delocalized electrons. However, the separation of the energy scales between the Peierls gap and the large spectral weight suppression near E_F can be explained only in the framework of large interactions. This is highlighted by the non-trivial evolution of the spectral density across the Peierls transition. We show in Figure 12(a) the angle integrated photoemission signal of $(TaSe_4)_2I$ at 265 K and 100 K. With increasing CDW amplitude, some of the spectral weight transfers to higher binding energy depleting the region near the Fermi level. It is evident in Figure 12(b) that drastic changes occur over a range much larger than Δ_0 leading to the strong temperature dependence of the ARPES signal up to 0.6 eV.

The coexisting effects of CDW fluctuations and heavy dressing can be illustrated and to some extent disentangled by the momentum resolved intensity maps. We show in Figure 13, the ARPES maps of the band structure around π/c, at T_p = 265 K and 100 K. At the higher temperature, in the metallic phase a very

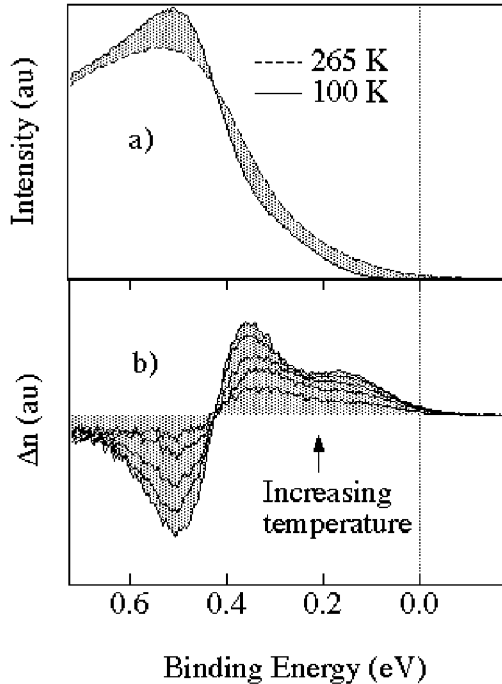

Figure 12. (a) Angle integrated photoemission intensity I(E, T) of $(TaSe_4)_2I$ at 265 K and 100 K ($\hbar\omega$ = 24 eV). The transfer of spectral weight is marked by a dashed area. (b) Temperature evolution of I(E, T)-I(E, 100 K), for 120 K < T < 265 K.

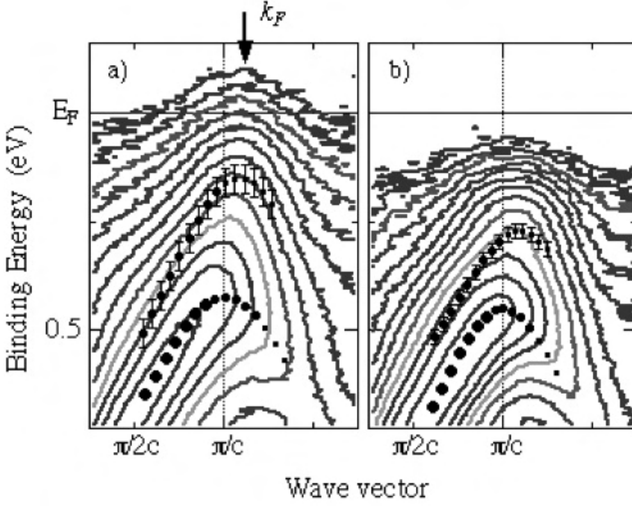

Figure 13. ARPES intensity maps of $(TaSe_4)_2I$ (ref. [8]) at 265 K (a), and 100 K (b), around Z = (π/c), normalized to beam current and acquisition time ($\hbar\omega$ = 24 eV). The lines measure constant ARPES intensity, in a logarithmic scale. The dispersion features of *B* and *AB* are estimated from Gaussian fits as in Figure 8, and their intensities are indicated by the size of the symbols.

weak intensity spills across the Fermi level, whereas at 100 K the leading edge coincides with the half-gap energy. An estimation of the spectral shift can be done with a careful MDCs analysis. The starting point is the MDC measured at the Fermi level at the transition temperature. Below T_p both the intensity and the line-shape of the MDC are preserved if the cut is performed (Figure 14(a)) at a higher binding energy Δ(T). Figure 14(b) shows that Δ(T) behaves as a phenomenological order parameter and saturates at low temperature. The extrapolated value Δ(T) = 120 meV is consistent with the Peierls half- gap determined by transport and optics measurements [8].

The MDC extracted at the Fermi level at T = 265 K is the fingerprint of a QP on the Fermi surface, Figure 14(a). Even if the intensity is quite small and the spectrum is featureless around this energy, the MDC exhibits a Lorentzian line-shape centered at $k = k_F$. However, the properties of this signal are quite unusual. Besides its extremely small intensity, the broad linewidth $\Delta k = 0.1$ Å^{-1} indicates a very short coherence length $\lambda = 1/\Delta k = 10$ Å , close to just 3 times the Ta-Ta distance 3 $d_{(Ta\text{-}Ta)}$ = 9.6 Å. This value is much shorter than the coherence length of the carriers in a typical metal, 10^2–10^3 Å and is also shorter than the spatial scale of the CDW fluctuations ≈ 50 Å near T_p. On the other hand, it is close to the CDW period that determines in the strong coupling regime the coherence of the polaronic cloud.

Similar results in the related Peierls compound $K_{0.3}MoO_3$ shows, Figure 15(a) that the extracted Δ_0 = 60 meV is consistent with the half-gap value measured by means of bulk sensitive techniques [12]. The temperature dependence of the ARPES

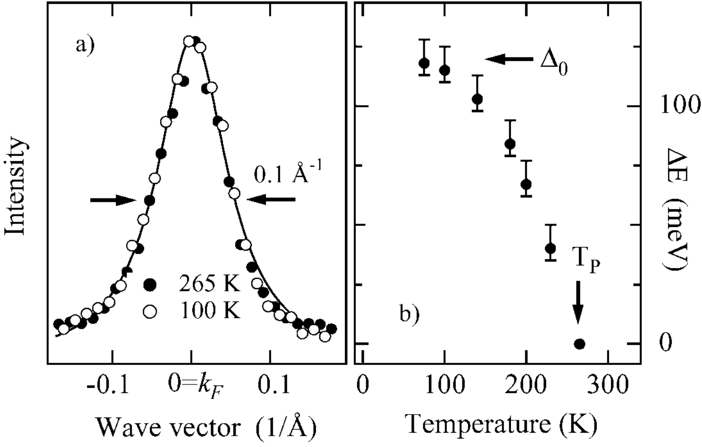

Figure 14. (a) Momentum distribution curves measured in $(TaSe_4)_2I$, ref. [8], at $E = 0$ (265 K) and $E = 0.12$ eV (100 K); the solid curve is a Lorentzian with FWHM = 0.1 $Å^{-1}$. (b) Temperature-dependent position of the energy window producing identical MDCs as in (a). The error bars reflect the uncertainties associated with different normalization procedures.

intensity reflects also the effects of the CDW fluctuations. As previously mentioned, the fluctuating order parameter induces a pseudogap which persists up to high temperatures. Figure 15(b) compares the ARPES intensity at the Fermi surface with the spin susceptibility from ref. [16]. The increase of χ_{spin} above T_p reflects the progressive filling of the metallic pseudogap. Within the experimental uncertainty, $I(k_F^B, E = 0)$ exhibits the same temperature dependence and therefore also reflects the temperature dependent pseudogap. In spite of the unusual lineshape,

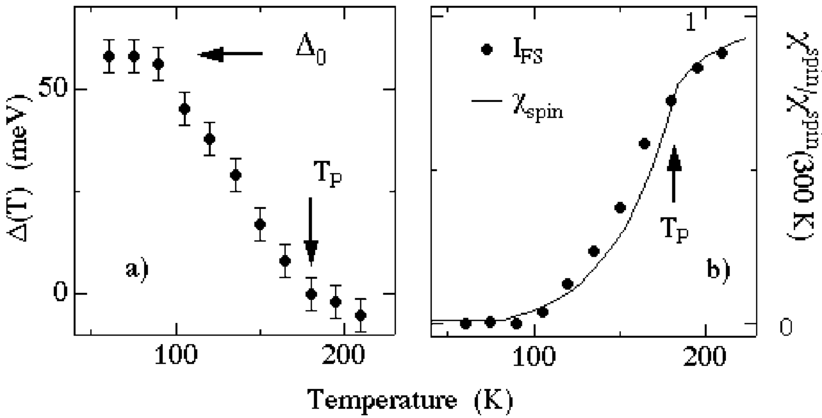

Figure 15. (a) Single particle gap extracted from the MDC analysis of the $K_{0.3}MoO_3$, ref. [7]. The shifts are measured from $T_P = 180$ K. (b) The ARPES intensity I_{FS} at Fermi surface ($E = 0$, $k = k_F^B$) is superimposed on the spin susceptibility from ref. [16].

the ARPES result suggests that the photoemission intensity at the Fermi level reflects the density of electronic states. In the CDW phase, on the other hand, the leading edge of the spectrum traces the energy gap. These observations are incompatible with standard weak coupling description but are certainly consistent with the strong coupling theory discussed above.

5. Conclusions

Angle Resolved Photoemission Spectroscopy is a powerful probe to detect and characterize the quasiparticle excitations in solids. This is illustrated by detailed analysis of model Fermi liquids systems like 1T-$TiTe_2$. Here a coherent photoelectron signal disperses along an electronic band and crosses the Fermi level. The ARPES lineshape is investigated as a function of the temperature and fitted with a Fermi liquid model. Both the extrinsic photoelectron broadening and the quasiparticle scattering rate are extracted from the spectral linewidths. These latter compare exceptionally well with resistivity measurements and are correctly reproduced by the Eliashberg-Migdal theory.

The physics of the quasi one-dimensional Peierls conductors is far more complex. Strong electron-phonon interactions influence deeply the electronic properties. Our discussion dealt with the spectroscopic results for $K_{0.3}MoO_3$ and the related $(TaSe_4)_2I$. It was shown that the ARPES signal disperses according to band structure calculations and hints a 'hidden' Fermi surface. Some predictions of the weak-coupling CDW theory are experimentally confirmed. The Fermi surface is nested by the CDW wavevector, the metallic phase is pseudogapped and a real gap develops in the CDW ground state. Pre-transitional fluctuations are revealed by the temperature evolution of the photoemission intensity at the Fermi level. Their presence is further confirmed by the observation of shadow bands above the transition temperature.

We showed in detail the effect of two incommensurate periodic potentials on the electronic band structure of $(TaSe_4)_2I$. Even if the incommensurate CDW disrupts the translational symmetry, the spectral weight concentrates near the unperturbed band structure. A correct reproduction of the experimental data can be obtained by neglecting higher order superlattice *umklapp* processes and taking explicitly into account the ladder structure of this Peierls material.

The weak-coupling approach may correctly reproduce the band structure but completely fails to describe the spectral lineshape. The gap parameter is not associated with a peak in the spectrum at k_F but rather to the leading edge of the 'pseudogapped' tail. The ARPES signal is too broad to be a coherent quasiparticle excitation and suggests that important multi-phonon processes determine the spectral function. The data can be interpreted in a strong coupling framework in which the quasiparticles are small polarons dressed by a large lattice deformation. From the optical weight of the quasiparticle screening one can extract the effective mass of the polarons becoming ≈ 10 electronic masses. The mostly incoherent spectra, exhibit simultaneously strong renormalization and frozen lattice dispersion. The large itineracy of the holes is not shared by the heavy polaronic carriers

but is mainly an effect of the retardation and of the sizable range of the electron-phonon interaction. A spectroscopic signature of the quasiparticles can still be observed in the momentum distribution curve extracted at the Fermi level. Following its temperature evolution, one can extract a gap parameter in agreement with *dc*-resistivity and optical conductivity measurements.

Acknowledgements

We thank all other co-workers involved in our studies on this subject, S. Mitrovic, A. Reginelli, L. Forro, R. Gaal, L. Degiorgi, H. Höchst and J. Voit, for their essential collaboration. The work was supported by the Swiss National Science Foundation and by the Ecole Polytechnqiue Fédérale de Lausanne. The measurements were mostly performed at the Ecole Polytechnique Fédérale de Lausanne and at the Synchrotron Radiation Center (SRC) of the university of Wisconsin-Madison.

References

1. N. Tsuda, K. Nasu, A. Fujimori and K. Siratori, *Electronic Conduction in Oxides* (Berlin: Springer Verlag, 2000).
2. G. D. Mahan, *Many-Particle Physics* (New York: Plenum, 1981).
3. S. Chakraborty, M. Sadhukhan, D. K. Modak, K. K. Som, H. S. Maiti and B. K. Chaudhuri, *Philosophical Magazine* B **71**, 1125 (1995).
4. H. Fehske, J. Loos and G. Wellein, *Physical Review* B **61**, 8016 (2000).
5. B. Dardel, D. Malterre, M. Grioni, P. Weibel and Y. Baer, F. Lévy, *Phys. Rev. Lett.* **67**, 3144 (1991).
6. M. Grioni and J. Voit, *Electron Spectroscopies Applied to Low-Dimensional Materials*, edited by H. P. Hughes and H. I. Starnberg (Dordrecht: Kluwer, 2000).
7. L. Perfetti, S. Mitrovic, G. Margaritondo, M. Grioni, L. Forro, L. Degiorgi and H. Höchst, *Phys. Rev.* B **66**, 075107 (2002).
8. L. Perfetti, H. Berger, A. Reginelli, L. Degiorgi, H. Höchst, J. Voit, G. Margaritondo and M. Grionil, *Phys. Rev. Lett.* 87, 216404 (2001).
9. R. Claessen, R. O. Anderson, J. W. Allen, C. G. Olson, C. Janowitz, W. P. Ellis, S. Harm, M. Kalning, R. Manzke, and M. Skibowski, *Phys. Rev. Lett.* **69**, 808 (1992).
10. L. Perfetti, C. Rojas, A. Reginelli, L. Gavioli, H. Berger, G. Margaritondo, M. Grioni, R. Gaàl, L. Forrò and F. Rullier Albenque, *Phys. Rev.* B **64**, 115102 (2001).
11. G.-H.Gweon, J. D. Denlinger, J. W. Allen, R. Claessen, C. G. Olson, H. Höchst, J. Marcus, C. Schlenker and L. F. Schneemeyer, *J. of Electron Spectrosc.* **117**, 481 (2001).
12. A. Schwartz, M. Dressel, B. Alavi, A. Blank, S. Dubois, G. Grüner, B. P. Gorshunov, A. A. Volkov, G. V. Kozlov, S. Thieme, L. Degiorgi and F. Lévy, *Phys. Rev.* B **52**, 5643 (1995).
13. R. S. Kwok, G. Grüner and S. E. Brown, *Phys. Rev. Lett.* **65**, 365 (1990).
14. W. Brütting, P. H. Nguyen, W. Rieß and G. Paasch, *Phys. Rev.* B **51**, 9533 (1995).
15. R. M. Fleming and L. F. Schneemeyer, D. E. Moncton, *Phys. Rev.* B **31**, 899 (1985).
16. D. C. Johnston, *Phys. Rev. Lett.* 52, 2049 (1984).
17. R. E. Peierls, *Quantum Theory of Solids* (London: Oxford University Press, 1955).
18. G. Grüner, *Density Waves in Solids* (Reading, MA: Addison-Wesley, 1994).
19. N. Shannon and R. Joynt, *Solid State Comm.* **115**, 411 (2000).
20. P. A. Lee, T. M. Rice and P. W. Anderson, *Phys. Rev. Lett.* **31**, 462 (1973).
21. M.-H. Whangbo and L. F. Schneemeyer, *Inorg. Chem.* **26**, 2424 (1986).
22. E. Canadell and M.-H. Whangbo, *Chem. Rev.* **91**, 965 (1991).

23. G.-H. Gweon, J. W. Allen, R. Claessen, J. A. Clack, D. M. Poirier, P. J. Benning, C. G. Olson, W. P. Ellis, Y. X. Zhang, L. F. Schneemeyer, J. Marcus and C. Schlenker, *J. Phys.: Condens. Matter* **8**, 9923 (1996).
24. H. Lüth, *Surfaces and Interfaces of Solid Materials* (New York: Springer-Verlag, 1993).
25. P. Gressier, M.-H. Whangbo, A. Meerschaut and J. Rouxel, *Inorg. Chem.* **23**, 1221 (1984).
26. J. Voit, L. Perfetti, F. Zwick, H. Berger, G. Margaritondo, G. Grüner, H. Höchst and M. Grioni, *Science* **290**, 501 (2000).
27. V. Vescoli, F. Zwick, J. Voit, H. Berger, M. Zacchigna, L. Degiorgi, M. Grioni and G. Grüner, *Phys. Rev. Lett.* **84**, 1272 (2000).
28. A. H. Romero, D. W. Brown and K. Lindenberg, *Phys. Rev.* B **59**, 13728 (1999).
29. A. S. Alexandrov and P. E. Kornilovitch, *Phys. Rev. Lett.* **82**, 807 (1999).
30. A. B. Migdal, *Sov. Phys. JETP* **7**, 996 (1958).
31. J. M. Robin, *Phys. Rev.* B **56**, 13634 (1997).
32. G. J. Kaye, *Phys. Rev.* B **57**, 8759 (1998).
33. D. S. Dessau, T. Saitoh, C.-H. Park, Z.-X. Shen, P. Villella, N. Hamada, Y. Moritomo and Y. Tokura, *Phys. Rev. Lett.* **81**, 192 (1998).
34. V. Perebeinos and P. B. Allen, *Phys. Rev. Lett.* **85**, 5178 (2000).
35. F. Wooten, *Optical Properties of Solids* (New York: Academic Press, 1972).

CHAPTER 2

OPTICAL ABSORPTION, PHOTOEXCITATION AND EXCITONS IN SOLIDS: FUNDAMENTAL CONCEPTS

Jai Singh[1, *], I.-K. Oh[1] and Safa O. Kasap[2]

[1] *Faculty of Technology and Industrial Education (TIE), B-41 Northern Territory University, Darwin, NT 0909, Australia;* [2] *University of Saskatchewan, Saskatoon, Canada*

(*Author for correspondence, Email: jai.singh@ntu.edu.au)

ABSTRACT: Starting with the optical properties, this chapter covers a wide range of topics associated with the photoexcitation of solids. Lattice absorption and reflection, free carrier and band to band absorptions are summarized in sections 2–4. The excitonic absorption in the crystalline and amorphous solids is reviewed in sections 5 and 6, respectively, where the newly developed concept of the effective mass of charge carriers in amorphous solids is also introduced. Excitonic processes in quantum wells are described in the section 7, where rates of various processes are presented. Finally section 8 reviews the recent advances in the study of photoluminescence in amorphous semiconductors.

1. Introduction to optical properties

The well known simple relation $n = (\varepsilon_r)^{1/2}$ between the refractive index n and relative permittivity ε_r is very useful in relating the dielectric properties to the optical properties over the same frequency range. The *complex refractive index* N, with real part n and imaginary part K, is related to the complex relative permittivity $\varepsilon_r = \varepsilon_r' - j\varepsilon_r''$ by

$$\mathrm{N} = n - jK = \sqrt{\varepsilon_r} = \sqrt{(\varepsilon_r' - j\varepsilon_r'')} \tag{1}$$

That is by

$$n^2 - K^2 = \varepsilon_r' \quad \text{and} \quad 2nK = \varepsilon_r'' \tag{2}$$

Optical properties of materials are typically reported either by showing the frequency dependences of n and K or ε_r' and ε_r''. Figure 1(a) shows the dependencies of n and K on the normalized frequency ω/ω_o for a simple single electronic dipole oscillator in which ω_o is the resonance frequency of the oscillator and γ is the loss coefficient. It is seen that n and the extinction coefficient K peak close to $\omega = \omega_o$. If a material has a $\varepsilon_r'' \gg \varepsilon_r'$, then $\varepsilon_r \approx -j\varepsilon_r''$ and $n = K \approx \sqrt{(\varepsilon_r''/2)}$. The reflectance R is given by

$$R = \left| \frac{1 - n + jK}{1 + n - jK} \right|^2 = \frac{(1-n)^2 + K^2}{(1+n)^2 + K^2}. \tag{3}$$

Aaron Peled (ed.), Photo-Excited Processes, Diagnostics and Applications (PEPDA), 25–55, 2003.
© 2003 *Kluwer Academic Publishers. Printed in the Netherlands.*

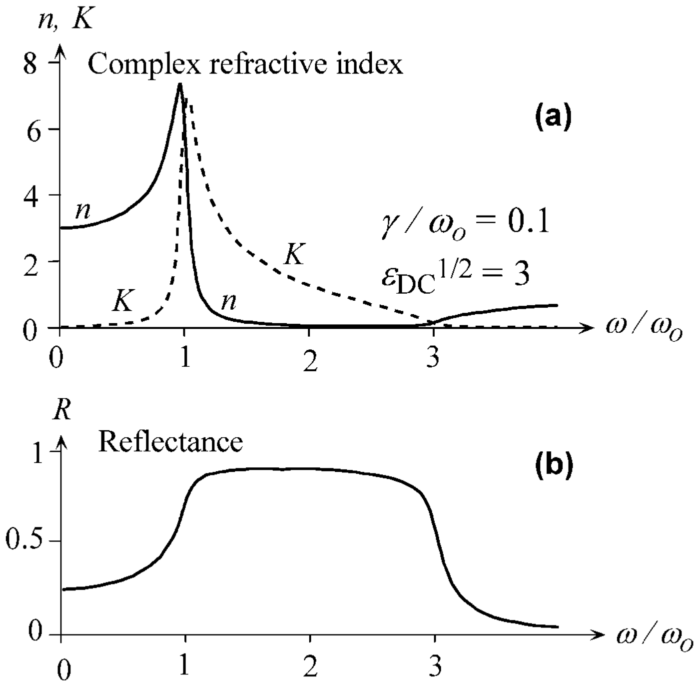

Figure 1. The dipole oscillator model. (a) Refractive index and extinction coefficient vs. normalized frequency. (b) Reflectance vs. normalized frequency.

Notice that whenever K is large, for example over a range of wavelengths, the absorption is strong, and the reflectance is almost unity. The light is then reflected, and any light in the medium is highly attenuated. Figure 1(b) shows the dependence of the reflectance R on the frequency. It is observed that R reaches its maximum value at a frequency slightly above $\omega = \omega_o$, and then remains high until ω reaches nearly $3\omega_o$, thus the reflectance is substantial while absorption is strong.

Normal dispersion region is the frequency range below ω_o where n falls as the frequency decreases, that is, n decreases as the wavelength λ increases. Anomalous dispersion region is the frequency range above ω_o where n decreases as ω increases. Below ω_o, K is small and if $\varepsilon_{\mathrm{DC}}$ is $\varepsilon_r(0)$, the DC permittivity is:

$$n^2 \approx 1 + (\varepsilon_{\mathrm{DC}} - 1)\frac{\omega_o^2}{\omega_o^2 - \omega^2}; \qquad \omega < \omega_o. \tag{4}$$

Since, $\lambda = 2\pi c/\omega$, defining $\lambda_o = 2\pi c/\omega_o$ as the resonance wavelength, then

$$n^2 \approx 1 + (\varepsilon_{\mathrm{DC}} - 1)\frac{\lambda_o^2}{\lambda_o^2 - \lambda^2}; \qquad \lambda > \lambda_o. \tag{5}$$

While intuitively useful, the above dispersion relation is far too simple. More

rigorously, we have to consider the dipole oscillator quantum mechanically which means a photon excites the oscillator to a higher energy level, see, for example, Fox [1] or Simmons and Potter [2]. The result is that we would have a series of $\lambda^2/(\lambda^2 - \lambda_i^2)$ terms with various weighting factors f_i that add to unity, where λ_i represent different resonance frequencies. The weighting factors f_i involve quantum mechanical matrix elements. In practice the dispersion relationships can be quite complicated. For example, the Sellmeier dispersion equation is an empirical expression for the wavelength λ dependence of n that is in the form of a series of $\lambda^2/(\lambda^2 - \lambda_i^2)$, where λ_i is a constant, i.e.

$$n^2 = 1 + \frac{A_1\lambda^2}{\lambda^2 - \lambda_1^2} + \frac{A_2\lambda^2}{\lambda^2 - \lambda_2^2} + \frac{A_3\lambda^2}{\lambda^2 - \lambda_3^2} + \dots \tag{6}$$

where A_1, A_2, A_3 and λ_1, λ_2 and λ_3 are constants, called Sellmeier coefficients, that are determined by fitting this expression to the experimental data. Higher terms involving A_4 and higher A coefficients can generally be neglected in representing n vs. λ behavior over typical wavelengths of interest. Such dispersion relationships are essential in designing photonic devices such as waveguides. Table 1 lists Sellmeier coefficients of some materials as examples.

There are various dispersion relationships that inherently take account of various contributions to the optical properties, such as the electronic and ionic polarization and interaction of photons with free electrons. For example, for many semiconductors and ionic crystals, two useful dispersion relations are

$$n^2 = A + \frac{B\lambda^2}{\lambda^2 - C} + \frac{D\lambda^2}{\lambda^2 - E}, \tag{7}$$

$$n^2 = A + \frac{B}{\lambda^2 - \lambda_o^2} + \frac{C}{(\lambda^2 - \lambda_o^2)^2} + D\lambda^2 + E\lambda^4, \tag{8}$$

where A, B, C, D and E are constants particular to a given material. Table 2 provides typical examples.

Figure 2 shows the complex relative permittivity and the complex refractive index of crystalline silicon in terms of photon energy $h\nu$. For photon energies below the bandgap energy, both ε_r'' and K are negligible and n is close to 3.7. Both ε_r''

Table 1. Sellmeier coefficients. The λ_1, λ_2, λ_3 are in μm.

Material	A_1	A_2	A_3	λ_1	λ_2	λ_3
SiO_2 (fused silica)	0.696749	0.408218	0.890815	0.0690660	0.115662	9.900559
SiO_2-13.5%GeO_2	0.711040	0.451885	0.704048	0.0642700	0.129408	9.425478
Barium fluoride	0.3356	0.506762	3.8261	0.057789	0.109681	46.38642
Sapphire	1.023798	1.058264	5.280792	0.0614482	0.110700	17.92656
Diamond	0.3306	4.3356		0.175	0.106	

Table 2. Parameters from Eqs. (7) and (8) for selected materials (Si data from [3]; others from [4]).

Material	λ_o (μm)	A	B (μm)^2	C (μm)$^{-4}$	D (μm)$^{-2}$	E (μm)$^{-4}$
Silicon	0.167	3.41983	0.159906	–0.123109	1.269×10^{-6}	-1.951×10^{-9}
MgO	0.11951	2.95636	0.021958	0	-1.0624×10^{-2}	-2.05×10^{-5}
LiF	0.16733	1.38761	0.001796	-4.1×10^{-3}	-2.3045×10^{-3}	-5.57×10^{-6}
AgCl	0.21413	4.00804	0.07900	0	-8.5111×10^{-4}	-1.976×10^{-7}

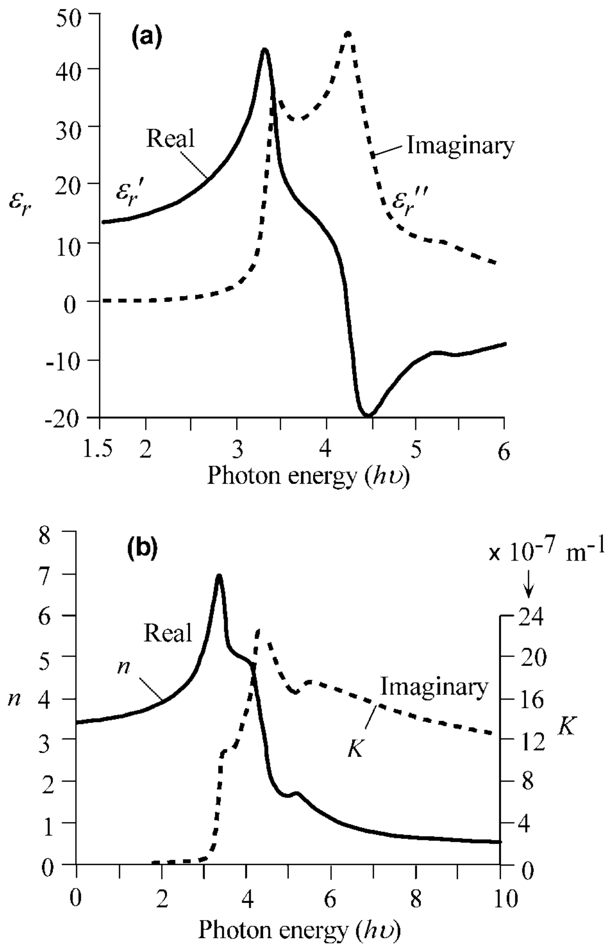

Figure 2. (a) Complex relative permittivity of a silicon crystal as a function of photon energy plotted in terms of real (ε_r') and imaginary (ε_r'') parts. (b) Optical properties of a silicon crystal vs. photon energy in terms of real (n) and imaginary (K) parts of the complex refractive index [5].

and K increase and change strongly as the photon energy becomes greater than 3 eV; far beyond the bandgap energy of 1.1 eV. Notice that both ε_r' and n peak at $h\nu \approx 3.5$ eV, which corresponds to a direct photoexcitation process, electrons excited from the valence band to the conduction band, as discussed later. The optical constants n and K can be determined by measuring the reflectance from the surface of a material as a function of polarization and angle of incidence, and using Fresnel's equations.

Knowing the frequency dependence of the real part ε_r' of the relative permittivity of a material, we can determine the frequency dependence of the imaginary part ε_r''; and vice versa by using *Kramers-Kronig relations*. The transform requires that we know the frequency dependence of either the real or imaginary part over as wide a range of frequencies as possible, ideally from dc to infinity, and that the material is *linear*, i.e. it has a relative permittivity that is independent of applied field. The *Kramers-Kronig relations* for the relative permittivity are

$$\varepsilon_r'(\omega) = 1 + \frac{1}{\pi} P \int_0^\infty \frac{\omega' \varepsilon_r''(\omega')}{\omega'^2 - \omega^2} d\omega' \qquad (9a)$$

and

$$\varepsilon_r''(\omega) = -\frac{2\omega}{\pi} P \int_0^\infty \frac{\varepsilon_r'(\omega')}{\omega'^2 - \omega^2} d\omega' \qquad (9b)$$

where ω' is the integration variable, P represents the Cauchy principal value of the integral and the singularity at $\omega = \omega'$ is avoided.

2. Lattice or reststrahlen absorption and infrared reflection

In the infrared wavelength region, ionic crystals reflect and absorb light strongly due to the resonance interaction of the electromagnetic (EM) wave field with the transverse optical phonons. The dipole oscillator model based on ions driven by an EM wave results in

$$\varepsilon_r = \varepsilon_r' - j\varepsilon_r'' = \varepsilon_{r\infty} + \frac{\varepsilon_{r\infty} - \varepsilon_{ro}}{\left(\frac{\omega}{\omega_T}\right) - 1 + j\frac{\gamma}{\omega_T}\left(\frac{\omega}{\omega_T}\right)}, \qquad (10)$$

where ε_{ro} and $\varepsilon_{r\infty}$ are the relative permittivity at $\omega = 0$ (very low frequencies) and $\omega = \infty$ (very high frequencies) respectively, γ is the loss coefficient per unit reduced mass representing the rate of energy transfer from the EM wave to optical phonons and ω_o is a resonance frequency that is related to the "spring" constant between the ions, and by definition the frequency ω_T is

$$\omega_T^2 = \omega_o^2 \left(\frac{\varepsilon_{r\infty} + 2}{\varepsilon_{ro} + 2}\right). \qquad (11)$$

The loss, ε_r'' and the absorption are maxima when $\omega = \omega_T$, and the wave is attenuated by the transfer of energy to the transverse optical phonons, thus the EM wave couples to the transverse optical phonons. At $\omega = \omega_L$, the wave couples to the longitudinal optical phonons. Figure 3 shows the optical properties of AlSb [6] in terms of n, K and R vs. wavelength. The extinction coefficient K and reflectance R peaks occur over about the same wavelength region, corresponding to the coupling of the EM wave to the transverse optical phonons. At wavelength close to $\lambda_T = 2\pi/\omega_T$, n and K peak, and there is a strong absorption of light which corresponds to the EM wave resonating with the TO lattice vibrations, then R rises sharply.

3. Free Carrier Absorption (FCA)

An electromagnetic wave with sufficiently low frequency oscillations can interact with free carriers in a material and thereby drift the carriers. This interaction results in an energy loss from the EM wave to the lattice vibrations through the carrier scattering processes. Based on the Drude model, the relative permittivity $\varepsilon_r(\omega)$ due to N free electrons per unit volume is given by

$$\varepsilon_r = \varepsilon_r' - j\varepsilon_r'' = 1 - \frac{\omega_p^2}{\omega^2 - \dfrac{j\omega}{\tau}}\,; \qquad \omega_p^2 = \frac{Ne^2}{\varepsilon_o m_e}\,, \tag{12}$$

where ω_p is a *plasma frequency* which depends on the electron concentration, τ is the relaxation time of the scattering process, i.e. the mean scattering time. For metals where the electron concentration is very large, ω_p is of the order of $\sim 10^{16}$ rad s^{-1}, UV frequencies, and for $\omega > \omega_p$, $\varepsilon_r \approx 1$, the reflectance becomes very small. Metals lose their free-electron reflectance in the UV range, thus becoming UV transparent. The reflectance does not fall to zero because there are other absorption processes such as interband electron excitations or excitations from core levels to energy bands. Plasma edge transparency where the reflectance almost vanishes can also be observed in doped semiconductors. For example, the reflectance of doped InSb has a plasma edge wavelength that decreases with increasing free carrier concentration [7]. Equation (12) can be written in terms of the conductivity σ_o at low frequencies (DC) as

$$\varepsilon_r = \varepsilon_r' - j\varepsilon_r'' = 1 - \frac{\tau\sigma_o}{\varepsilon_o[(\omega\tau)^2 + 1]} - j\frac{\sigma_o}{\varepsilon_o\omega[(\omega\tau)^2 + 1]}\,. \tag{13}$$

In metals, σ_o is high. At frequencies where $\omega < 1/\tau$, the imaginary part $\varepsilon_r'' = \sigma_o/\varepsilon_o\omega$, is normally much more than 1, and $n = K \approx \sqrt{(\varepsilon_r''/2)}$ so that the free carrier attenuation coefficient α is then given by

$$\alpha = 2k_oK \approx \frac{2\omega}{c}\left(\frac{\varepsilon_r''}{2}\right)^{1/2} \approx (2\sigma_o\mu_o)^{1/2}\omega^{1/2}. \tag{14}$$

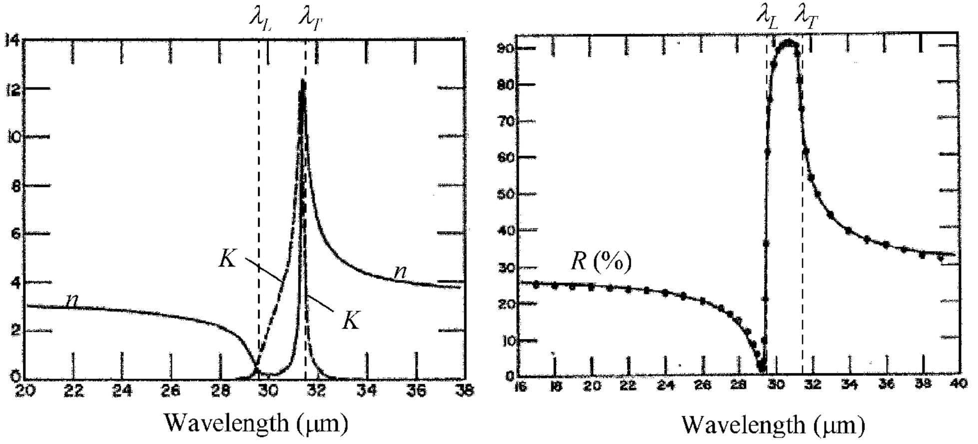

Figure 3. Infrared refractive index n, extinction coefficient K (left), and reflectance R (right) of AlSb. Note: The wavelength axes are not identical, and wavelengths λ_T and λ_L corresponding to ω_T and ω_L respectively, are shown as dashed vertical lines; data from Turner and Reese [6].

Furthermore, the reflectance can be calculated also using $n = K = \sqrt{(\varepsilon_r''/2)}$ which leads to the well-known *Hagen-Rubens* relation [8]

$$R \approx 1 - 2\left(\frac{2\omega\varepsilon_o}{\sigma_o}\right)^{1/2}. \tag{15}$$

In semiconductors one encounters typically $\sigma_o/\varepsilon_o\omega < 1$, since the free electron concentration is small, and we can treat n as constant due to various other polarization mechanisms, e.g. electronic polarization. Since $2nK = \varepsilon_r''$, the absorption coefficient is [9]

$$\alpha = 2k_oK \approx \frac{2\omega}{c}\left(\frac{\varepsilon_r''}{2n}\right) = \frac{\sigma_o}{nc\ \varepsilon_o[(\omega\tau)^2 + 1]}, \tag{16}$$

At low frequencies where $\omega < 1/\tau$, we have $\alpha(\lambda) \sim \sigma_o/n(\lambda)$ so that α should be controlled by the DC conductivity, and hence the amount of doping. Furthermore, α will exhibit the frequency dependence of the refractive index n, i.e. $\alpha(\lambda) \sim 1/n(\lambda)$, thus n would typically be determined by the electronic polarization of the crystal.

At high frequencies where $\omega > 1/\tau$,

$$\alpha \sim \frac{\sigma_o}{\omega^2} \sim N\lambda^2 \tag{17}$$

α is proportional to N, the free carrier concentration, and λ^2. Experimental observations on FCA in doped semiconductors are in general agreement with these

predictions. For example, α increases with N, whether N is increased by doping or by carrier injection [10]. However, not all semiconductors show the simple $\alpha \sim \lambda^2$ behavior. A proper account of the field-driven electron motion and scattering must consider the fact that τ will depend on the electron's energy. The correct approach is to use the Boltzmann transport equation [11] with the appropriate scattering mechanism. FCA can be calculated by using a quantum mechanical approach based on second order time dependent perturbation theory with Fermi-Dirac statistics [12].

Absorption due to free carriers is commonly written as $\alpha \sim \lambda^p$, where the index p depends primarily on the scattering mechanism, though it is also influenced by the compensation doping ratio, if the semiconductor has been doped by compensation, and the free carrier concentration. In the case of lattice scattering one has to consider scattering from acoustic and optical phonons. For acoustic phonon scattering $p \approx 1.5$, for optical phonon scattering $p \approx 2.5$, and for impurity scattering, $p \approx 3.5$. The observed free carrier absorption coefficient will then have all three contributions,

$$\alpha = A_{\text{acoustic}}\lambda^{1.5} + A_{\text{optical}}\lambda^{2.5} + A_{\text{impurity}}\lambda^{3.5} \tag{18}$$

Inasmuch as α for FCA depends on the free carrier concentration N, it is possible

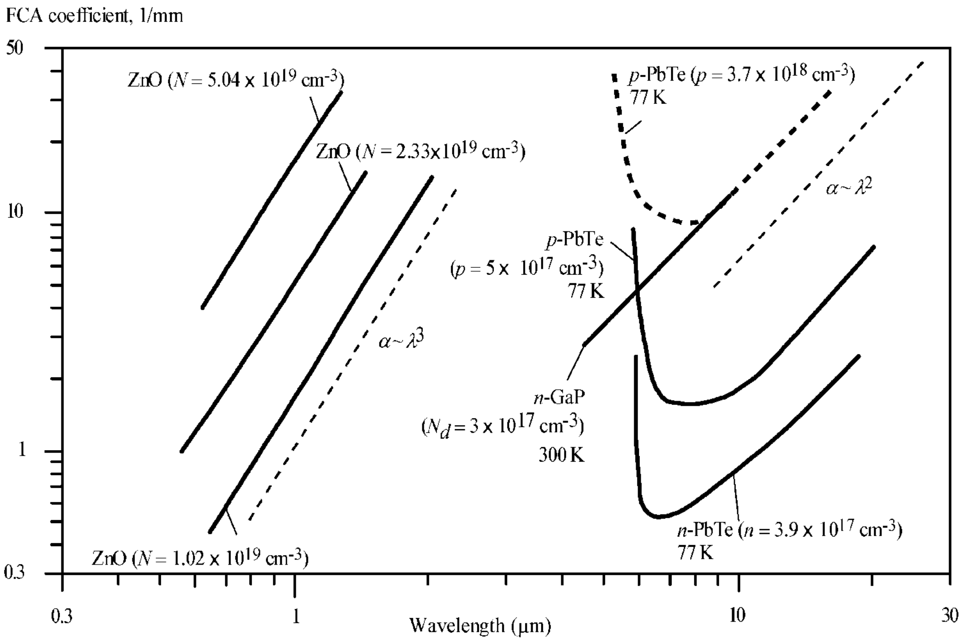

Figure 4. Free carrier absorption in n-GaP at 300 K [14], p and n type PbTe [15] at 77 K and In doped n-type ZnO at room temperature [16].

to evaluate the latter from the experimentally measured α, given its wavelength dependence and p as discussed by Ruda [13].

Free carrier absorption in p-type Ge demonstrates how the FCA coefficient α can be dramatically different than what is expected from Eq. (18). Figure 5 (a) shows the wavelength dependence of the absorption coefficient for p-Ge over the wavelength range from about 2 to 30 μm [17]. The observed absorption is due to excitations of electrons from the spin-off band to the heavy hole band, and from spin-off band to the light hole band, and from the light hole band to the heavy hole band as marked in the figure.

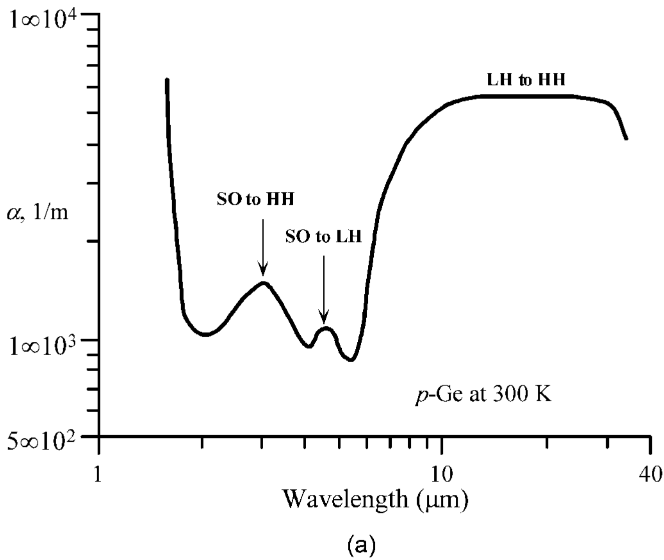

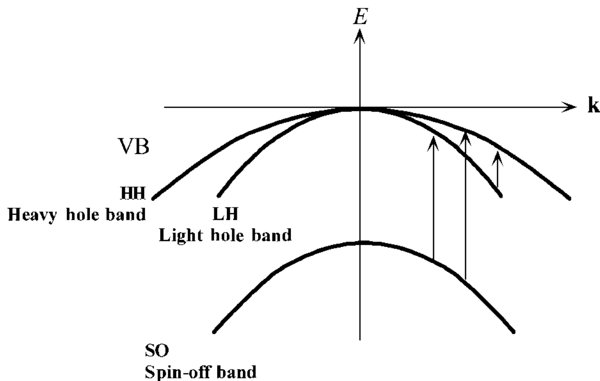

Figure 5. (a) Free carrier absorption due to holes in p-Ge [17]. (b) The valence band of Ge has three bands; heavy hole band, light hole band and a spin-off band.

4. Band-to-band fundamental absorption

Band-to-band absorption, or fundamental absorption, of radiation is due to the photoexcitation of an electron from the valence band to the conduction band. There are two types of band-to-band absorption corresponding to direct and indirect transitions.

A direct transition is a photoexcitation process in which no phonons are involved. The photon momentum is negligible compared with the electron momentum so that when the photon is absorbed to excite an electron from the valence band (VB) to the conduction band (CB), the electron's k-vector does not change. A direct transition on E-k diagram is a vertical transition from an initial energy E and wavevector k in the VB to a final energy E' and wavevector k' in the CB where $k' = k$ as shown in Figure 6(a). The energy $(E' - E_c)$ is the kinetic energy $(\hbar k)^2/(2m_e^*)$ of the electron with an effective mass m_e^*, and $(E_v - E)$ is the kinetic energy $(\hbar k)^2/(2m_e^*)$ of the hole left behind in the VB. The ratio of the kinetic energies of the photogenerated electron and hole depends inversely on the ratio of their effective masses.

The absorption coefficient α is derived from the quantum mechanical transition probability from E to E', the occupied density of states at E in the VB from which electrons are excited, and the unoccupied density of states in the CB at $E + h\nu$. Thus α depends on the joint density of states at E and $E + h\nu$, and we have to suitably integrate this joint density of states. Near the band edges, the density of states can be approximated by a parabolic band, and α rises with the photon energy following

$$\alpha h\nu = A(h\nu - E_g)^{1/2} \tag{19}$$

where the constant $A \approx [(e^2/(nch^2m_e^*)](2\mu^*)^{3/2}$ in which μ^* is a reduced electron and hole effective mass, n is the refractive index, and E_g is the direct bandgap, minimum $E_c - E_v$ at the same k value. Experiments indeed show this type of behavior for photon energies above E_g and close to E_g as shown Figure 6(b) for a GaAs crystal [18] and in (c) for a CdTe crystal [19]. The extrapolation to zero photon energy gives the direct bandgap E_g, which is about 1.40 eV for GaAs and 1.46–1.49 eV for CdTe. For photon energies very close to the bandgap energy, the absorption is usually due to exciton absorption, especially at low temperatures, and is discussed later in this chapter.

In indirect bandgap semiconductors such as Si and Ge, the photon absorption for photon energies near E_g requires the absorption and emission of phonons during the absorption process as illustrated in Figure 7(a). The absorption onset corresponds to a photon energy of $(E_g - h\vartheta)$, which represents the absorption of a phonon with energy $h\vartheta$. For the latter α is proportional to $[h\nu - (E_g - h\vartheta)]^2$. Once the photon energy reaches $(E_g + h\vartheta)$, then the photon absorption process can also occur by phonon emission for which the absorption coefficient is larger than that for phonon absorption. The absorption coefficients for the phonon absorption and emission

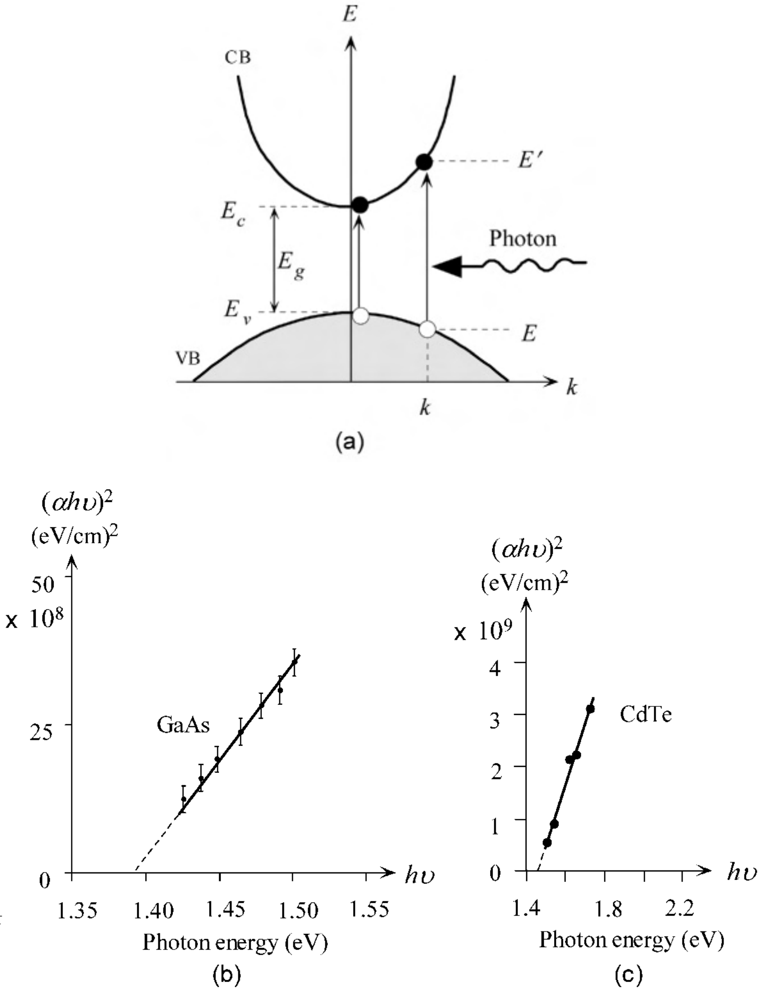

Figure 6. (a) A direct transition from the valence band (VB) to the conduction band (CB) by the absorption of a photon. (b) and (c) Absorption behavior represented as $(\alpha h\nu)^2$ vs. photon energy $h\nu$ near the band edge for single crystals of (b) *p*-type GaAs, from [18] and (c) CdTe , from [19].

processes are given by [20],

$$\alpha_{\text{absorption}} = A[f_{\text{BE}}(h\vartheta)][h\nu - (E_g - h\vartheta)]^2; \quad h\nu > (E_g - h\vartheta) \tag{20}$$

and

$$\alpha_{\text{emission}} = A[(1 - f_{\text{BE}}(h\vartheta)][h\nu - (E_g + h\vartheta)]^2; \quad h\nu > (E_g + h\vartheta) \tag{21}$$

where A is a constant, and $f_{\text{BE}}(h\vartheta)$ is the Bose-Einstein distribution function at the

phonon energy $h\vartheta$, i.e. $f_{BE}(h\vartheta) = [\exp(h\vartheta/k_BT) - 1]^{-1}$, where k_B is the Boltzmann constant and T is the temperature.

As we increase the photon energy in the range $(E_g - h\vartheta) < h\nu < (E_g + h\vartheta)$, the absorption is controlled by $\alpha_{absorption}$ and the plot of $\alpha^{1/2}$ vs. $h\nu$ has an intercept of $(E_g - h\vartheta)$.

On the other hand, for $h\nu > (E_g + h\vartheta)$, the overall absorption coefficient is $\alpha_{absorption} + \alpha_{emission}$, but at slightly higher photon energies than $(E_g + h\vartheta)$, $\alpha_{emission}$ quickly dominates over $\alpha_{absorption}$ since $[f_{BE}(h\vartheta)] \gg [(1 - f_{BE}(h\vartheta)]$. Figure 7(b) shows the behavior of $\alpha^{1/2}$ vs. photon energy for Ge at two temperatures for $h\nu$ near band

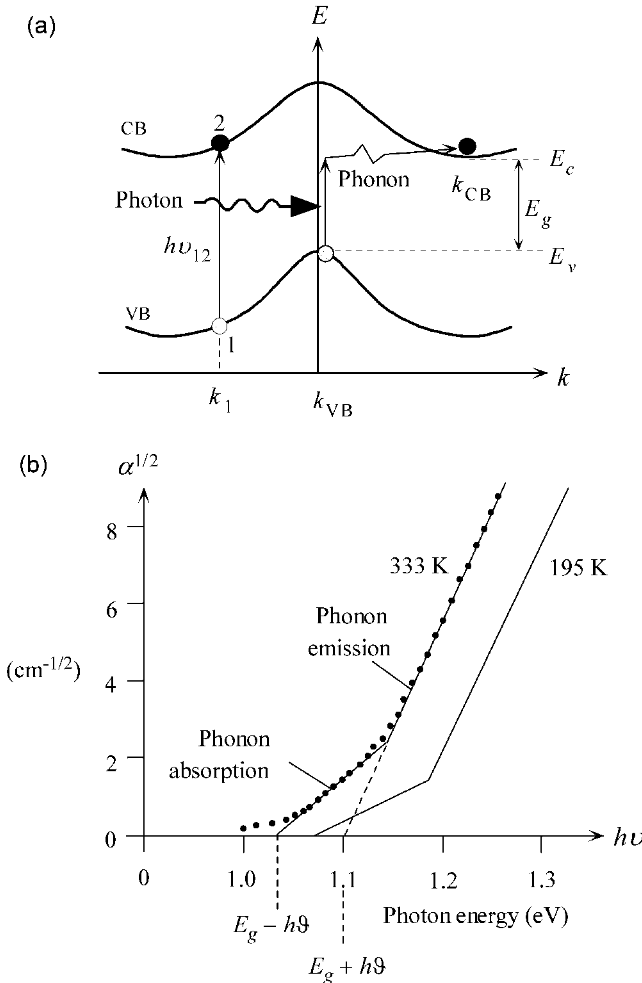

Figure 7. (a) Indirect transitions across the bandgap involve phonons. Direct transitions in which dE/dk in the CB is parallel to dE/dk in the VB lead to peaks in the absorption coefficient. (b) Fundamental absorption in Si at two temperatures. The overall behavior is well described by Eqs. (20) and (21).

edge absorption. At low temperatures, $f_{\mathrm{BE}}(h\vartheta)$ is small and $\alpha_{\mathrm{absorption}}$ decreases with decreasing temperature as apparent in Figure 7(b). Equations (20) and (21) intersect the photon energy axis at $(E_g - h\vartheta)$ and $(E_g + h\vartheta)$, which can be used to obtain E_g.

Examination of the extinction coefficient K or ε_r'' vs. photon energy for Si in Figure 2 shows that absorption peaks at certain photon energies, $h\nu \approx 3.5$ and 4.3 eV. These peaks are due to the fact that the joint density of states function peaks at these energies. The absorption coefficient peaks whenever there is a direct transition in which the E vs. **k** curve in the VB is parallel to the E vs. **k** curve in the CB as schematically illustrated in Figure 7(a) where a photon of energy $h\nu_{12}$ excites an electron from state 1 in the VB to state 2 in the CB in a direct transition $\mathbf{k}_1 = \mathbf{k}_2$. Such transitions where E vs. **k** curves are parallel at a photon energy $h\nu_{12}$ result in a peak in the absorption vs. photon energy behavior and can be represented by the condition that

$$(\nabla_{\mathbf{k}}E)_{\mathrm{CB}} - (\nabla_{\mathbf{k}}E)_{\mathrm{VB}} = 0 \tag{22}$$

The above condition is normally interpreted as the joint density of states reaching a peak value at certain points in the Brillouin zone called van Hove singularities. Identification of peaks in K vs. $h\nu$ involves the examination of all E vs. **k** curves of a given crystal that can participate in a direct transition. The silicon ε_r'' peaks at $h\nu \approx 3.5$ eV and 4.3 eV correspond to Eq. (22) being satisfied at points L, along $\langle 111 \rangle$ in **k**-space, and X along $\langle 100 \rangle$ in k-space, at the edges of the Brillouin zone.

In *degenerate semiconductors*, the Fermi level E_F is in a band, for example, in the CB for a degenerate *n*-type semiconductor. Electrons in the VB can only be excited to states above E_F in the CB rather than to the bottom of the CB. The absorption coefficient then depends on the free carrier concentration since the latter determines E_F. Fundamental absorption is then said to depend on *band filling*, and there is an apparent shift in the absorption edge, called the Burstein-Moss shift. Furthermore, in degenerate indirect semiconductors, the indirect transition may involve a non-phonon scattering process, such as impurity or electron-electron scattering, which can change the electron's wavevector **k**. Thus in degenerate indirect bandgap semiconductors, absorption can occur without phonon assistance and the absorption coefficient becomes

$$\alpha \sim [\mathrm{h}\nu - (E_g + \Delta E_F)]^2 \tag{23}$$

where ΔE_F is the energy depth of E_F into the band measured from the band edge.

Heavy doping of degenerate semiconductors normally leads to a phenomenon called bandgap narrowing and bandtailing. *Bandtailing* means that the band edges at E_v and E_c are no longer well defined cut-off energies and there are electronic states above E_v and below E_c whose density of states falls sharply with energy away from the band edges. Consider a degenerate direct band gap *p*-type semiconductor. One can excite electrons from states below E_F in the VB where the band is nearly parabolic to tail states below E_c where the density of states decreases exponen-

tially with energy into the bandgap, away from E_c. Such excitations lead to α depending exponentially on $h\nu$, a dependence that is called the *Urbach rule* [21, 22],

$$\alpha = A\ \exp[\Gamma(h\nu - E_0)], \tag{24}$$

where A, Γ and E_0 are all constants. The Urbach rule was originally reported for alkali halides. It has been observed for many ionic crystals, degenerately doped crystalline semiconductors and almost all amorphous semiconductors. While exponential bandtailing can explain the observed Urbach tail of the absorption coefficient vs. photon energy, it is also possible to attribute the absorption tail behaviour to strong internal fields arising, for example, from ionized dopants or defects.

5. Excitonic absorption in crystalline solids

There are two types of excitons that can be formed in non-metallic solids: Wannier or Wannier-Mott excitons and Frenkel excitons. The energy of a Wannier exciton or Wannier-Mott exciton is given by [23]

$$E_x = E_g + \frac{\hbar^2 K^2}{2M} - E_n, \tag{25}$$

where E_g is the band gap energy, $\hbar K$ linear momentum and M ($= m_e^* + m_h^*$) effective mass associated with the center of mass and E_n is the exciton binding energy given by

$$E_n = \frac{\mu_x e^4 \kappa^2}{2\hbar^2 \varepsilon^2} \frac{1}{n^2}, \tag{26}$$

where μ_x is the reduced exciton mass, e electronic charge, $\kappa = 1/4\pi\varepsilon_0$, ε static dielectric constant of the solid and n principal quantum number associated with the internal excitonic states $n = 1$ (s), 2 (p), etc. (see Figure 8). According to Eq. (25) the excitonic states are formed within the band gap below the conduction band edge. However, as the exciton binding energy is very small, e.g. a few meV in bulk Si and Ge crystals, exciton absorption peaks can only be observed at very low temperatures. Using the joint density of states approach, the absorption coefficient associated with the excitonic states is obtained as [24]

$$\alpha\omega = A_x(\hbar\omega - E_x)^{1/2}, \tag{27}$$

with the constant $A_x = \dfrac{4\sqrt{2}e^2|p_{xv}|^2}{nc\sqrt{\mu_x}\hbar^3}$, where p_{xv} is the transition matrix element between the valence and excitonic bands. Eq. (27) is similar to the case of direct band transitions discussed above and valid only for the photon energies, $\hbar\omega \geq E_x$. There is no absorption below the excitonic ground state in pure crystalline solids.

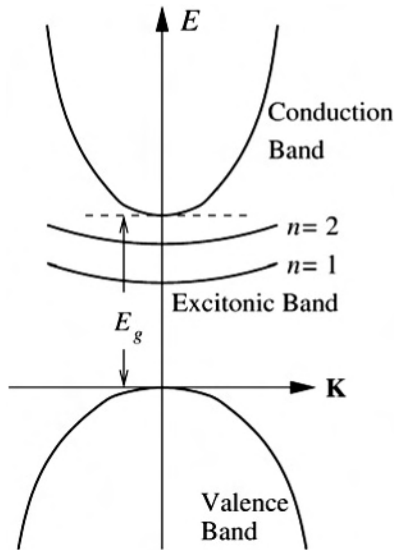

Figure 8. Schematic illustration of excitonic bands for $n = 1$ and 2 in semiconductors. E_g represents the energy gap.

The description of Wannier-Mott excitons presented above is valid for inorganic semiconductors like Si, Ge, GaAs, because in these materials the large overlap of inter-atomic electronic wavefunctions enable the electrons and holes to be far apart but bound in an excitonic state. For this reason these excitons are also called large radii orbital excitons. Excitons formed in organic crystals are called Frenkel excitons. In organic semiconductors/insulators or molecular crystals, the intermolecular separation is large and hence the overlap of inter-molecular electronic wavefunctions is very small and electrons remain tightly bound to individual molecules. Therefore, the electronic energy bands are very narrow and closely related to individual molecular electronic energy levels. In such solids, the absorption of photons occurs close to the individual molecular electronic states and excitons are also formed within the molecular energy levels [23]. Such excitons are therefore also called molecular excitons. For details of the theory of Wannier and Frenkel excitons, readers may like to refer to reference [23].

6. Absorption in amorphous semiconductors

The energy band gap in amorphous semiconductors does not have sharp valence and conduction band edges at its ends. Instead, each band consists of extended states and tail states divided by a mobility edge. Thus, the conduction band in an amorphous semiconductor has a mobility edge, usually denoted by an energy E_c, above which all states are delocalized extended states and below which all states are

localized tail states. Likewise, the valence band has a mobility edge denoted by E_v, below which all hole states are delocalized extended states and above all are localized hole tail states. These states are schematically shown in Figure 9. Thus, unlike in crystalline solids described above, the absorption of photons in intrinsic amorphous solids can also occur for photon energies $\hbar\omega \leq E_0$ as well due to the presence of the tail states in the forbidden gap. Here E_0 represents the energy of the optical gap, which is usually close to the energy of the mobility edge, E_c. For optical transitions caused by photons of energy $\hbar\omega \geq E_0$ in amorphous semiconductors, the approach of joint density of states is not applicable. One has to consider the product of the densities of both conduction and valence extended electronic states in calculating the absorption coefficient [24, 25]. Assuming that these densities of states depend on the square root of the energy, leads to an absorption coefficient, α, which depends on the photon energy as:

$$[\alpha\hbar\omega]^{1/2} = B^{1/2}[\hbar\omega - E_0], \tag{28}$$

where, if one assumes the transition matrix element to be constant, one gets the constant B as [24, 25]

$$B = \left[\frac{1}{nc\ \varepsilon_0}\left(\frac{e}{m_e^*}\right)^2\left(\frac{L(m_e^* m_h^*)^{3/2}}{2^2\hbar^3}\right)\right], \tag{29}$$

where m_e^* and m_h^* are the effective masses of electron and hole, respectively, L is the average inter-atomic separation in the sample and n is the refractive index. Plotting $[\alpha\hbar\omega]^{1/2}$ as a function of $\hbar\omega$ gives a straight line that is usually referred

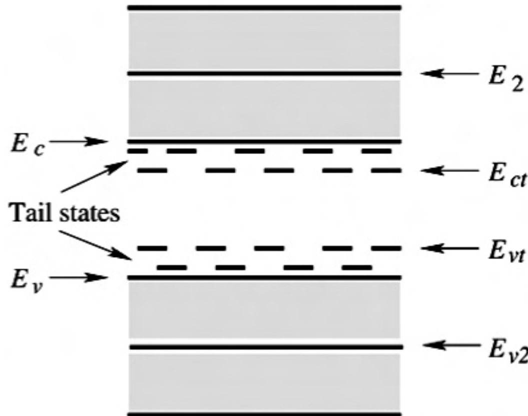

Figure 9. Schematic illustration of the electronic energy states, E_2, E_c, E_{ct}, E_{vt}, E_v and E_{v2}, in amorphous semiconductors. The shaded region represents the extended states. Energies E_2 and E_{v2} correspond to the center of the conduction and valence extended states E_{ct} and E_{vt} and represent the end of conduction and valence tail states, respectively.

to as Tauc's plot from which one can determine the optical gap energy E_0 experimentally. Equation (28) is also known as Tauc's relation and B as Tauc's constant. The experimental data of many amorphous semiconductors and chalcogenides fit to Eq. (28) very well, but not all. Deviations from Tauc's relation have been observed. For instance, some experimental data in a-Si:H fit much better to a cubic root relation given by [26]:

$$[\alpha\hbar\omega]^{1/3} = C[\hbar\omega - E_0], \tag{30}$$

and therefore the cubic root has been used to determine the optical gap E_0. Here C is another constant.

If one considers that the transition matrix element is photon energy independent, one finds that the cubic root dependence on photon energy can be obtained only when the densities of states of the valence and conduction bands depend linearly on energy. Using such density of states, the cubic root dependence has been explained by Mott and Davis [26]. Another approach [27] to get the cubic root dependence has been suggested. Using Eq. (28), Sokolov et al. [27] have modeled the cubic root dependence on photon energy by considering the fluctuations in the optical band gap due to structural disorders. For getting the cubic root dependence they finally assume that the fluctuations are constant over the range of integration and then the integration of Eq. (28) over the optical gap energy produces a cubic root dependence on the photon energy. Although their approach shows a way of getting the cubic root dependence as the integration over the optical gap is carried out by assuming constant fluctuations, Sokolov et al.'s model is little different from the linear density of states model suggested by Mott and Davis [26].

Cody [27] has shown an alternative approach using a photon energy dependent transition matrix element. Thus the absorption coefficient is obtained as [24, 25]:

$$[\alpha\hbar\omega] = B'(\hbar\omega)^2(\hbar\omega - E_0)^2, \tag{31}$$

where

$$B' = \frac{e^2}{nc\,\varepsilon_0}\left[\frac{(m_e^* m_h^*)^{3/2}}{2\pi^2\hbar^7\nu\rho_A}\right]Q_a^2 \tag{32}$$

and Q_a is the average separation between the excited electron and hole pair in an amorphous semiconductor. ν is the number of valence electrons per atom and ρ_A atomic density per unit volume.

Equation (31) suggests that $[\alpha\hbar\omega]$ depends on the photon energy in the form of a polynomial of order 4. Then, depending on which term of the polynomial may be more significant in which material, one can get square, cubic or fourth root dependence of $[\alpha\hbar\omega]$ on the photon energy. In this case Eq. (31) may be expressed as:

$$[\alpha\hbar\omega]^x \propto (\hbar\omega - E_0), \tag{33}$$

where $x \leq 1/2$. Thus in a way any deviation from the square root or Tauc's plot may be attributed to the energy dependent matrix element [24, 25].

Another problem is how to determine the constants B [Eq. (28)] and B' [Eq. (32)], which involve the effective masses of electron and hole. In other words, how to determine the effective mass of charge carriers in amorphous solids? Recently, a simple approach [24, 29] has been developed to estimate the effective mass of charge carriers in amorphous solids. Accordingly, different effective masses of the charge carriers are obtained in the extended and tail states. The approach applies the concepts of tunneling and effective medium and one obtains the effective mass of an electron in the conduction extended states, denoted by m^*_{ex}, and in the tail states, denoted by m^*_{et}, as:

$$m^*_{ex} \approx \frac{E_L}{2(E_2 - E_c)a^{1/3}}\, m_e, \tag{34}$$

and

$$m^*_{et} \approx \frac{E_L}{(E_c - E_{ct})b^{1/3}}\, m_e, \tag{35}$$

where

$$E_L \approx \frac{\hbar^2}{m_e L^2}. \tag{36}$$

Here $a = N_1/N < 1$, N_1 is the number of atoms contributing to the extended states, $b = N_2/N < 1$, N_2 is the number of atoms contributing to the tail states, such that $a + b = 1$ ($N = N_1 + N_2$) and m_e is the free electron mass. The energy E_2 in Eq. (34), corresponds to the energy at which the imaginary part of the dielectric constant becomes maximum (see Figure 9).

Likewise, the hole effective masses m^*_{hx} and m^*_{ht} in the valence extended and tail states are obtained, respectively, as:

$$m^*_{hx} \approx \frac{E_L}{2(E_v - E_{v2})a^{1/3}}\, m_e, \tag{37}$$

and

$$m^*_{ht} \approx \frac{E_L}{(E_{vt} - E_v)b^{1/3}}\, m_e, \tag{38}$$

where E_{v2} and E_{vt} are energies corresponding to the half width of valence extended states and the end of the valence tail states, respectively, see Figure 9.

Using Eqs. (34) and (35) and the values of parameters involved, different effective masses of an electron are obtained in the extended and tail states. Considering,

for example, the density of weak bonds contributing to the tail states as 1 at.%, i.e. $b = 0.01$ and $a = 0.99$, the effective mass and energy E_L, thus calculated for hydrogenated amorphous silicon (a-Si:H) and germanium (a-Ge:H) are given in Table 3:

Table 3. Effective mass of electrons in the extended and tail states of a-Si:H and a-Ge:H calculated using Eqs. (34) and (35) for $a = 0.99$, $b = 0.01$ and $E_{ct} = E_{vt} = E_c/2$. E_L is calculated from Eq. (36). All energies are given in eV. Note that as the absorption coefficient is measured in cm^{-1}, the value of speed of light is used in cm/s.

	L (nm)	E_2	E_c	E_L	$E_c - E_{ct}$	m^*_{ex}	m^*_{et}
a-Si:H	0.235 [30]	3.6 [31]	1.80 [32]	1.23	0.9	0.34	6.3
a-Ge:H	0.245 [30]	3.6	1.05 [33]	1.14	0.53	0.22	10.0

According to Eqs. (34), (35), (37) and (38), for sp^3 hybrid amorphous semiconductors such as a-Si:H and a-Ge:H, the electron and hole effective masses are expected to be the same. In these semiconductors, as the conduction and valence bands are two equal halves of the same electronic band their widths are the same and that gives equal effective masses for electron and hole [24, 34]. This is one of the reasons of using $E_{ct} = E_{vt} = E_c/2$, which gives equal effective masses for electrons and holes in the tail states as well. This is different from crystalline solids where m^*_e and m^*_h are usually not the same. This difference between amorphous and crystalline solids is similar to, for example, having direct and indirect crystalline semiconductors but only direct amorphous semiconductors.

Using the effective masses from Table 3 and Eq. (29), B can be calculated for a-Si:H and a-Ge:H. The values thus obtained with the refractive index $n = 4$ for a-Si:H and a-Ge:H are $B = 6.0 \times 10^6$ cm^{-1} eV^{-1} for a-Si:H and $B = 4.1 \times 10^6$ cm^{-1} eV^{-1} for a-Ge:H, which are an order of magnitude higher than those estimated from experiments [28]. However, considering the quantities involved in B [Eq. (29)] this can be regarded as a good agreement.

The value of the constant B' in Eq. (32) can also be calculated now theoretically, provided Q_a is known. Using the atomic density of crystalline silicon and four valence electrons per atom, Cody [28] has estimated $Q_a^2 = 0.9$ Å^2, which gives $Q_a \approx 0.095$ nm, less than half the inter-atomic separation of 0.235 nm in a-Si:H, but of the same order of magnitude. Using $\nu = 4$, $\rho_A = 5 \times 10^{28}$ m^{-3}, $Q_a^2 = 0.9$ Å^2, and extended state effective masses, we get $B' = 4.6 \times 10^3$ cm^{-1} eV^{-3} for a-Si:H and 1.3×10^3 cm^{-1} eV^{-3} for a-Ge:H. Cody has estimated an optical gap, $E_0 = 1.64$ eV for a-Si:H, which using in Eq. (31), we get $\alpha = 1.2 \times 10^3$ cm^{-1} at a photon energy of, $\hbar\omega = 2$ eV. This agrees reasonably well with $\alpha = 6.0 \times 10^2$ cm^{-1} used by Cody. If we use inter-atomic spacing in place of Q_a in Eq. (32), we get $B' = 2.8 \times 10^4$ cm^{-1} eV^{-3}, and then the corresponding absorption coefficient becomes 3.3×10^3 cm^{-1}. This suggests that for an estimate one may use the inter-atomic spacing in place of Q_a, if the latter is unknown. Thus, both the constants B and B' can be determined theoretically, a task not possible earlier due to lacking knowledge of the effective masses in amorphous semiconductors.

The absorption of photons of energy less than the band gap energy, $\hbar\omega < E_0$ in amorphous solids involves the localized tail states and hence does neither follow Eq. (28) nor (31). Instead, the absorption coefficient depends on photon energy exponentially as given in Eq. (24) giving rise to Urbach's tail. Abe and Toyozawa [35] have calculated the interband absorption spectra in crystalline solids, introducing the Gaussian site diagonal disorders and applying the coherent potential approximation. They have shown that Urbach's tail occurs due to static disorders (structural disorders). However, the current stage of understanding is that Urbach's tail in amorphous solids occurs due to both thermal effect and static disorders [28].

7. Excitonic processes in quantum wells

There has been enormous progress in the field of semiconductor nanostructures in the last two decades due to the development of recent state-of-the-art techniques in the epitaxial crystal-growth of materials such as molecular-beam epitaxy (MBE) and metal-organic chemical vapor deposition. These techniques have made it possible to design semiconductor devices with high precision on an atomic scale and produce high quality low-dimensional systems such as quantum wells (QWs), superlattices, quantum wires (QWRs), and quantum dots (QDs) [36]. These low-dimensional semiconductor systems have important applications in optoelectronic devices, e.g., light detectors, LASERs and LEDs. Many physical properties of optoelectronic devices fabricated by such low-dimensional semiconductor systems are determined from information on excitonic processes. The binding energy of 1s exciton, $E_b(d)$ in d-dimensional (d = 1, 2, 3) semiconductors is given by: $E_b(d) = E_b[2/(d-1)]^2$ [37], where E_b is the exciton's binding energy in the 1s state in bulk (d = 3) obtained from Eq. (26) with $n = 1$. Thus, in low dimensions as the binding energy increases, excitonic states can be observed even at the room temperature and excitons play a very important role in the opto-electronic properties of such materials. Excitonic processes in these semiconductor nanostructures is influenced significantly by the interaction with phonons, excitons and charge carriers [23]. These interactions affect the formation [38, 39], relaxation [40, 41], dephasing [42], and localization [43] of excitons.

As an exciton consists of an electron in the conduction band bound with a hole in the valence band through their Coulomb interaction, the exciton-phonon interaction consists of the electron-phonon and hole-phonon interactions. In non-centrosymmetric and polar crystals of III–V and II–VI semiconductors, excitons interact with acoustic phonons through the deformation potential (DP) and piezoelectric (PE) couplings and with optical phonons through the polar (PO) coupling [40]. In general, since the conduction band near the minimum is isotropic, the electron-acoustic phonon interaction obtained from DP has a non-zero contribution only from longitudinal acoustic (LA) phonons. However, as the valance band is anisotropic, the hole-phonon interaction is non-zero with both LA and transverse acoustic (TA) phonons [40]. With the PE coupling, both LA and TA phonon

interactions are non-zero for electrons and holes. Exciton-optical phonon interaction is non-zero only with the longitudinal optical (LO) phonons [44]. Considering these interactions, the rate of formation of an exciton with wave vector $\mathbf{K}_{\|}$ from a free electron-hole pair through a phonon emission in λ-mode via DP ($J = D$), PE ($J = P$), and PO ($J = O$) couplings is obtained as [38, 39, 45]

$$W^J_{\lambda+} = \frac{1}{A_0}\frac{2\pi}{\hbar}\sum_{\mathbf{q}_{\|},\, q_z,\, \mathbf{k}_{\|}} |C^{\lambda}_J F^J_{\lambda+}(\mathbf{q}_{\|}, q_z, \mathbf{k}_{\|})|^2 f^h_{\alpha_h(\mathbf{K}_{\|}+\mathbf{q}_{\|})-\mathbf{k}_{\|}} f^e_{\alpha_e(\mathbf{K}_{\|}+\mathbf{q}_{\|})+\mathbf{k}_{\|}}$$

$$\times (f^{ex}_{\mathbf{K}_{\|}} + 1)(n^{\lambda}_{\mathbf{q}} + 1)\delta(E_x - E_{e-h} + \hbar\omega_{\mathbf{q},\lambda}), \tag{39}$$

where f^h, f^{ex}, f^e, and $n^{\lambda}_{\mathbf{q}}$ are the occupation numbers of hole, electron, exciton, and phonon, respectively. E_x and E_{e-h} are exciton and electron-hole pair energies, respectively and $\omega_{\mathbf{q},\lambda}$ is the frequency of a λ-mode phonon with wave vector $\mathbf{q}$.

The rate of formation of an exciton is plotted in Figures 10(a) and (b) as a function of $\mathbf{K}_{\|}$ at T_{e-h} = 20, 50, and 80 K and lattice temperature of 4.2 K, for two different charge carrier densities $n_{e-h} = 1 \times 10^{10}$ cm^{-2} and $n_{e-h} = 5 \times 10^{10}$ cm^{-2}, respectively. The rate of formation of excitons by emitting acoustic phonons first increases with $\mathbf{K}_{\|}$ to a peak value and then decreases. The rate of formation decreases

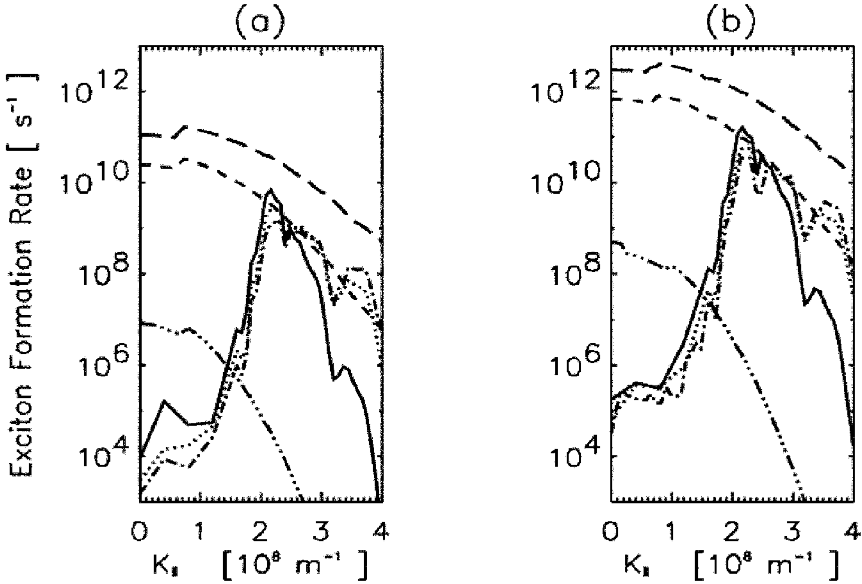

Figure 10. The formation rate of an exciton in GaAs quantum wells is plotted as a function of center-of-mass wavevector $\mathbf{K}_{\|}$ for L_z = 80 Å, T = 4.2 K, (a) $n_{e-h} = 1 \times 10^{10}$ cm^{-2} and (b) $n_{e-h} = 5 \times 10^{10}$ cm^{-2}. The solid, dotted, and dash-dotted curves correspond to the formation rate due to acoustic phonon emission at T_{e-h} = 20, 50, and 80 K, respectively. The dash-dot-dot-dot, dashed, and long-dashed curves correspond to the formation rates due to LO phonon emission at T_{e-h} = 20, 50, and 80 K, respectively [39].

with increasing T_{e-h}, but at a certain $\mathbf{K}_{\|}$ after the peak value, the rate increases with increasing T_{e-h}. Such a dependence of the formation rate of excitons on carrier temperature via acoustic phonons is different from that via LO phonons, where it increases with increasing T_{e-h} for all $\mathbf{K}_{\|}$ [38].

Figure 11 shows the rate of formation of an exciton due to LO phonons as a function of charge carrier density n_{e-h}, from 1×10^8 to 5×10^8 cm^{-2} at T_{e-h} = 60 K for three different well widths. The calculated results of the formation rate shows a square-law dependence for the formation rate of an exciton on the carrier density, n_{e-h}, i.e., $W(n_{e-h}) = bn^x_{e-h}$ ($x \approx 2$). This provides a theoretical confirmation of the observed experimental square-law dependence of the photoluminescence on excitation density obtained by Strobel et al. [46].

As discussed above, an exciton formed from a free electron-hole pair has initially a non-zero $\mathbf{K}_{\|}$. These excitons are hot and will first relax nonradiatively to $\mathbf{K}_{\|} = 0$ by emitting phonons and then recombine radiatively by emitting photons. There are two different relaxation processes, one involving intraband transitions and the other interband transitions.

In the intraband processes, an exciton relaxes from an initial state to another state within the same band by emitting a phonon. The net phonon emission rate of an λ-mode phonon with wavevector $\mathbf{q}$ can be written as [40, 47]

$$\frac{\partial n^\lambda_{\mathbf{q}}}{\partial \mathbf{t}} = \sum_{J,\mathbf{K}_{\|}} W^J_\lambda(\mathbf{q}_{\|}, q_z)\Big\{\big[(f^{ex}_{\mathbf{K}_{\|}-\mathbf{q}_{\|}} + 1)f^{ex}_{\mathbf{K}_{\|}}(n^\lambda_{\mathbf{q}} + 1) - (f^{ex}_{\mathbf{K}_{\|}} + 1)f^{ex}_{\mathbf{K}_{\|}-\mathbf{q}_{\|}}n^\lambda_{\mathbf{q}}\big]$$
$$\times\, \delta\big(E(\mathbf{K}_{\|} - \mathbf{q}_{\|}) - E(\mathbf{K}_{\|}) + \hbar\omega_{\mathbf{q},\lambda}\big) - \big[(f^{ex}_{\mathbf{K}_{\|}+\mathbf{q}_{\|}} + 1)f^{ex}_{\mathbf{K}_{\|}}n^\lambda_{\mathbf{q}}$$
$$- (f^{ex}_{\mathbf{K}_{\|}} + 1)f^{ex}_{\mathbf{K}_{\|}+\mathbf{q}_{\|}}(n^\lambda_{\mathbf{q}} + 1)\big] \times \delta\big(E(\mathbf{K}_{\|} + \mathbf{q}_{\|}) - E(\mathbf{K}_{\|}) - \hbar\omega_{\mathbf{q},\lambda}\big)\Big\}. \quad (40)$$

The maximum rates of LA and TA phonon emission in GaAs QWs, thus calculated from Eq. (40) for DP and PE couplings, are listed in Table 4.

In Figure 12, the phonon emission rates are plotted as a function of exciton temperature. The rate of LO phonon emission increases as exciton temperature increases from 5 K to 200 K. However, the rate of acoustic phonon emission increases first rapidly for exciton temperature $5 < T_{ex} < 17$–19 K at exciton

Table 4. Phonon emission rates due to DP and PE couplings for GaAs/$Al_{0.3}Ga_{0.7}$ As QWs with well width L_z = 80 Å, phonon energy E_{ph} = 0.2 meV, exciton density $n_{ex} = 5 \times 10^{10}$ cm^{-2}, exciton temperature T_{ex} = 20 K, and lattice temperature T = 4.2 K [40]. Here the angle θ is measured from the z-axis, which is assumed to be perpendicular to the quantum well wall and ϕ is the azimuth angle in the x-y (quantum well) plane.

	LA Phonon		TA Phonon	
	DP	PE	DP	PE
Max. rate	2.1×10^9 s^{-1}	1.1×10^7 s^{-1}	5.4×10^9 s^{-1}	3.1×10^7 s^{-1}
θ	7°	61°	4°	90°
ϕ	–	45°	–	45°

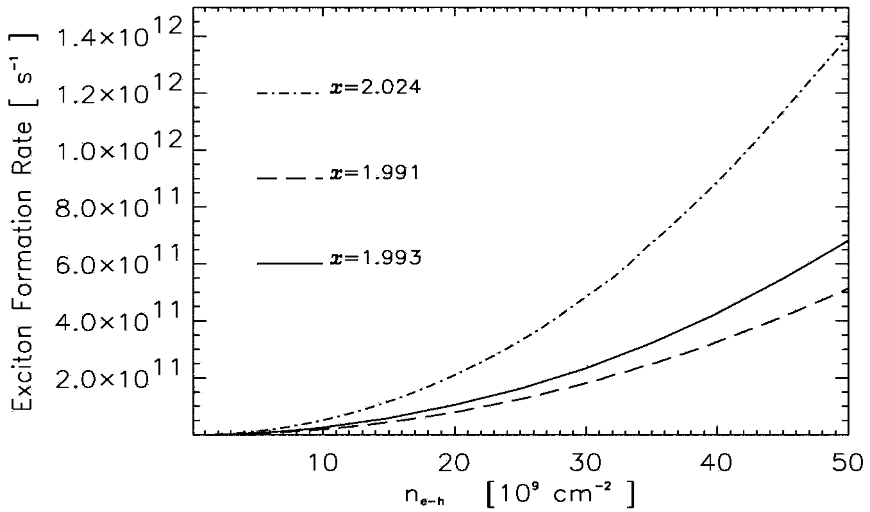

Figure 11. The formation rate of an exciton in GaAs quantum wells as a function of carrier density n_{e-h} at T_{e-h} = 60 K for three different well widths: L_z = 80 Å (dash-dot curve), L_z = 150 Å (solid curve), L_z = 250 Å (dashed curve) at $\mathbf{K}_{\|} = 0$. The number x in the figure is obtained from curve fitting of $W(n_{e-h}) = bn^x_{e-h}$ [38].

densities in the range of 5×10^9 to 8×10^{11} to cm^{-2}, and then it decreases for 17–19 < T_{ex} < 200 K. The LO phonon emission rate is dominant at higher exciton temperatures, whereas the acoustic phonon emission rate is dominant at lower temperatures.

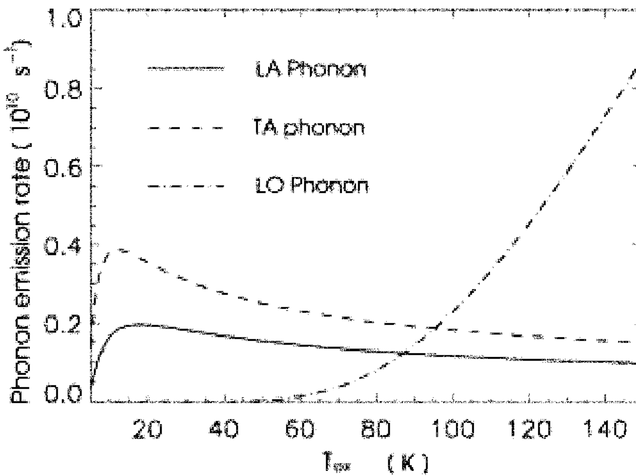

Figure 12. Phonon emission rate, as a function of T_{ex} for GaAs/$Al_{0.3}Ga_{0.7}As$ QWs with L_z = 80 Å, $n_{ex} = 5 \times 10^{10}$ cm^{-2}, and T = 4.2 K [40].

Table 5. Rates of excitonic relaxation processes in GaAs quantum wells.

Processes	Rates
LA phonon emission due to excitonic relaxation via DP coupling	2.1×10^9 s^{-1} [40]
LA phonon emission due to Excitonic relaxation via PE coupling	1.1×10^7 s^{-1} [40]
TA phonon emission due to excitonic relaxation via DP coupling	5.4×10^9 s^{-1} [40]
TA phonon emission due to excitonic relaxation via PE coupling	3.1×10^7 s^{-1} [40]
LO phonon emission due to excitonic relaxation via PO coupling	1.3×10^9 s^{-1} [40]
Heavy hole-exciton formation assisted by LO phonon	3.3×10^{10} s^{-1} [38]
Light hole-exciton formation assisted by LO phonon	2.7×10^{10} s^{-1} [38]
Heavy hole-exciton formation assisted by acoustic phonon	2.1×10^9 s^{-1} [39, 45]
Dephasing of free excitons	$1.7–9.7 \times 10^9$ s^{-1} [42]
LO phonon assisted relaxation of excitons due to intersubband transition	3.28×10^{12} s^{-1} [41]
Localization of free excitons due to interface roughness	1.07×10^{11} s^{-1} [49]

The rates of several excitonic relaxation processes occurring in GaAs quantum wells are listed in Table 5.

In semiconductor QWs, depending on the well width and structure of the confinement potential, there can be several electron and hole subbands through which the exciton formation and relaxation may occur. For example, in GaAs/$Al_xGa_{1-x}As$ QWs, there are two electron subbands ($n_e = 1, 2$) and two heavy hole subbands ($n_h = 1, 2$) at well width $L_z \approx 48–82$ Å. An exciton formed in an upper subband can relax to lower subbands by emitting phonons. This is called interband relaxation process [41].

An interband relaxation of a higher order exciton 1 s (n_ee, n_eh) to any lower order free electron-hole pair (n_e'e, n_e'h) by emitting phonons can be a multi-channel process. For example, when an 1 s (2e, 2h) exciton formed in $n_e = n_h = 2$ subbands relaxes to a (1e, 1h) free electron-hole pair in $n_e = n_h = 1$ subbands, it can do so in one step as ($n_e = n_h = 2 \rightarrow n_e = n_h = 1$) or in two steps with 2 possibilities ($n_e = n_h = 2 \rightarrow n_e = 1, n_h = 2 \rightarrow n_e = n_h = 1$) or ($n_e = n_h = 2 \rightarrow n_e = 2, n_h = 1 \rightarrow n_e = n_h = 1$). However, the orthogonality of subband states does not allow a direct excitonic relaxation from 1 s (2e, 2h) to (1e, 1h) by emitting an LO phonon. The relaxation rate of 1 s (2e, 2h) exciton state to (1e, 2h) electron-hole pair state by LO phonon emission decreases with increasing the center-of-mass wavevector $\mathbf{K}_{\|}$ and decreasing exciton density N_{ex}, and the maximum rate occurs at $\mathbf{K}_{\|} = 0$ [41]. At a crystal temperature of $T = 8$ K and exciton temperature $T_{ex} = 20$ K in QWs of width 130 Å, the relaxation times are 305 fs at an exciton density of $N_{ex} = 1 \times 10^{10}$ cm^{-2}, 616 fs at $N_{ex} = 5 \times 10^9$ cm^{-2}, and 3.11 ps at $N_{ex} = 1 \times 10^9$ cm^{-2}, respectively. The corresponding times for relaxation from 1 s (2e, 1h) to (1e, 1h) are obtained as 304 fs, 614 fs, and 3.10 ps. These relaxation times for exciton densities in the range of $N_{ex} = 5–10 \times 10^9$ cm^{-2} are in a good agreement with those obtained by Pal and Vengurlekar [48], but these are not times of relaxation directly from 1 s (2e, 2h) to (1e, 1h) due to the orthogonality condition.

In QWs, inevitably there are atomic scale structural disorders at the interfaces which give rise to roughness in the interfaces and modify the physical properties.

The interface roughness influences the optical properties and plays a very important role in the dynamics of excitons in QWs. The fine structures and splitting in the PL signals of excitons are examples of effects at the interface roughness causing the localization of an exciton. When such a QW is subjected to photons of energy greater than the band gap of the well material, the following excitonic processes may occur: (1) a free exciton with non-zero wavevector $\mathbf{K}_{\|}$ is formed and relaxes non-radiatively to $\mathbf{K}_{\|} \sim 0$ before recombining radiatively to the ground state, (2) a free exciton is formed and then gets localized non-radiatively in a state of the interface roughness potential by emitting phonons, and (3) the localized exciton formed due to the interface roughness in (2) gets transferred non-radiatively to another localized state.

The rate of localization of a 1 *s* free exciton as a function of the well width in the range of L_z = 50–150 Å for b = 100 Å at $n_{ex} = 5 \times 10^9$ cm^{-2}, T_{ex} = 15 K, and T = 4.2 K is shown in Figure 13. The rates of localization show a non-monotonic behaviour with respect to L_z [49].

The energy eigenvalue of a localized exciton as a function of L_z is plotted in Figure 14 for four different roughness lateral sizes b by assuming that the well width fluctuation is 1 ML ($a/2$ = 2.83 Å) [49]. The binding energy in relatively narrow QWs is found to be larger than in wider QWs, because the penetration of the subband wavefunctions ϕ_e and ϕ_h into the barrier region becomes large for narrow QWs. As a result, the effective interaction of charge carriers with potential fluctuations at the interface of narrow QWs becomes larger compared with that of wider QWs.

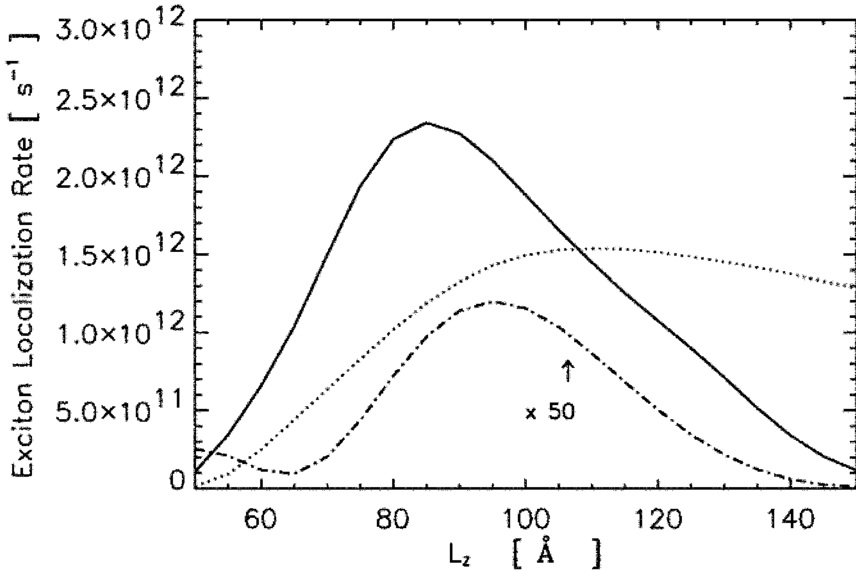

Figure 13. Localization rate as a function of L_z for $n_{ex} = 5 \times 10^9$ cm^{-2}, b = 100 Å, =15 K, T_{ex} = 15 K and T = 4.2 K. The solid curve is at $|\mathbf{K}_{\|}| = 0$, dotted curve at $|\mathbf{K}_{\|}| = 0.52 \times 10^8$ m^{-1}, and dash-dotted curve at $|\mathbf{K}_{\|}| = 1 \times 10^8$ m^{-1} [49].

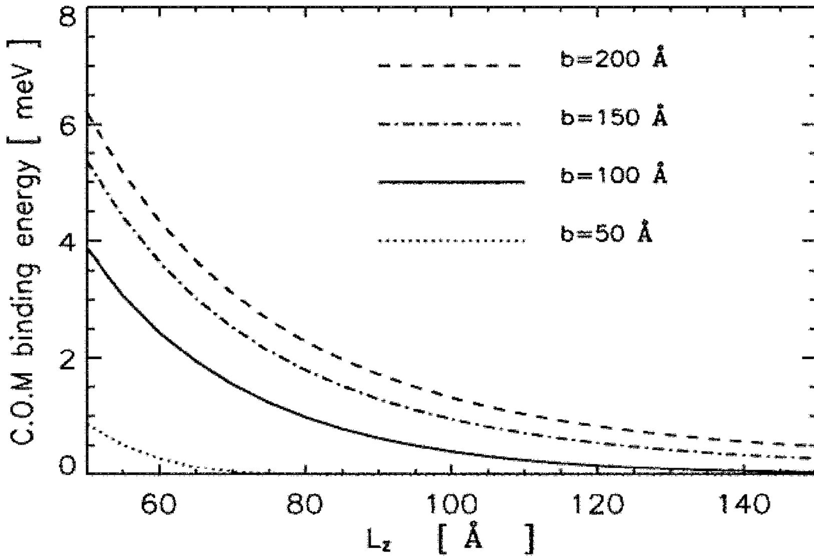

Figure 14. The C.O.M binding energy as a function of L_z in the plane QWs due to interface roughness for four different b [49].

In addition to interaction with phonons, excitons also interact with other charge carriers and excitons, leading to some other excitonic reactions in QWs. Under high excitation density, bi-excitons are formed. Although it is difficult to observe bi-excitons in bulk GaAs, they have been observed in GaAs QWs [50–52] because of the binding energy enhancement due to confinement. Excitons can also interact with other excess charge carries, electrons and holes, in doped quantum wells leading to the formation of charged excitons or trions [53–54]. It is not possible to present a lengthy discussion on this topic here, but interested readers may like to refer to the original papers.

8. Excitonic photoluminescence in amorphous semiconductors

The phenomenon of emitting a photon by radiative recombination of photo-excited charge carriers is called photoluminescence. Such recombinations usually occur either from the bottom of the conduction band or excitonic band, giving rise to free carrier or excitonic photoluminescence, respectively. In experiments where the energy of exciting photons is higher than the band gap, excited charge carriers first relax non-radiatively to the conduction band edge and then recombine radiatively. The non-radiative recombination or relaxation occurs through the lattice interaction by emitting phonons as charge carriers relax to their band edges. The non-radiative relaxation is much faster, usually in the picosecond (ps) range whereas radiative recombination takes place on a nanosecond (ns) time scale. In semi-

conductors with strong charge carrier-lattice interaction, excitons can get self-trapped due to their interaction with the lattice [23]. The self-trapped exciton (STE) state lies usually at a lower energy in comparison to the free exciton (FE) state. In terms of the adiabatic potential energy surfaces (APES), $V(q)$, plotted as a function of the interaction coordinate q, the STE is formed due to a lattice deformation in the direction of q. A barrier exists between the minimum of FE and STE states. An exciton should tunnel the barrier at low temperatures to get self-trapped. APES associated with the free exciton and self-trapped exciton states are shown in Figure 15 schematically. Photoluminescence from both FE and STE states have been observed [23] and in some materials both can co-exist.

Photoluminescence from amorphous semiconductors and glasses has recently attracted more attention [54–60]. This is because as stated in section 6, amorphous semiconductors do not have a translational symmetry, therefore it is believed that the formation of exciton states is not possible in such semiconductors. As the lowest energy states are the tail states, the radiative recombination from the tail states, which are localized, can only occur when the exited charge carriers tunnel the distance between them before recombination. This is called radiative tunneling (RT) [32] and accordingly only a broad photoluminescence band may be observed in amorphous solids. However, contrary to the RT model, using the quadrature frequency resolved spectra (QFRS) technique, a double peak PL lifetime distribution has been observed in a-Si:H [54–58]. Ambros et al. [54] have found two life time peaks: i) a short living photoluminescence peak for ≈ 10 μs, and ii) a long living peak for ≈ 1 ms. Recently Ishii et al. [59] and Aoki [60] have observed a similar double peak lifetime distribution also in a-Ge:H using the QFRS technique (shown in Figure 16), and found that the long lifetime photoluminescence occurs at 10^{-4} s and the short life time one at 1 μs.

Recently, using the effective mass approximation, Singh et al. [29] have developed a theory of Wannier-Mott excitons in real coordinates space applicable to

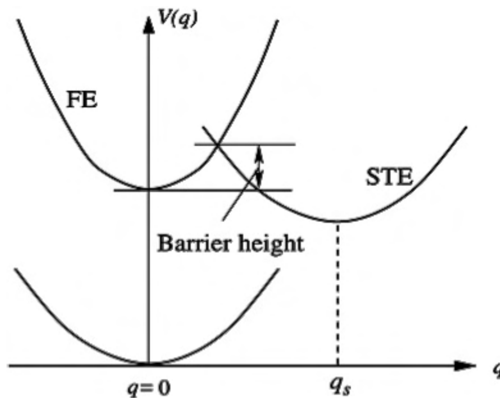

Figure 15. Adiabatic potential energy surfaces (APES), $V(q)$, of the ground state (valence band), free exciton band (FE) and self-trapped exciton (STE) state as a function of the interaction coordinate q. q = 0 represents the minimum of APES for FE and q_s that of STE.

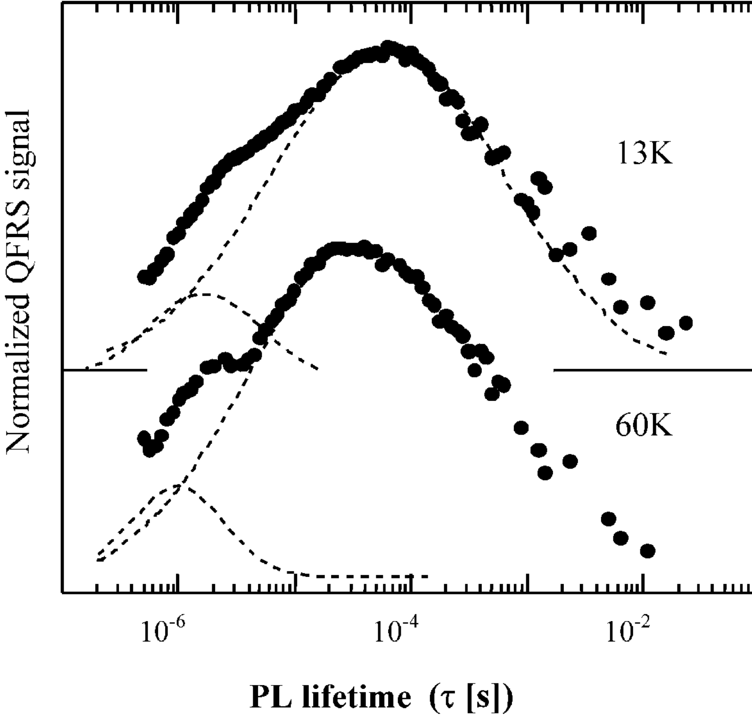

Figure 16. Photoluminescence lifetime distribution in a-Ge:H at T = 13 K and $G \approx 2 \times 10^{20}$ cm^{-3} s^{-1}. Dashed curves are convoluted ones [59, 60].

amorphous solids. Accordingly, the short and long living components of the photoluminescence peaks occur due to the radiative recombination of singlet and triplet excitons, respectively. The radiative recombination of singlet excitons is spin allowed whereas that of triplet excitons is spin forbidden. Therefore, the radiative recombination of singlets has a large oscillator strength and is faster. The energy of excitonic states as a function of spin (singlet or triplet) is obtained as:

$$E_n(S) = -\frac{\mu_x e^4 \kappa^2}{2\hbar^2 \varepsilon'(S)^2} \frac{1}{n^2}, \tag{41}$$

where $E_n(S)$ is the energy of an excitonic state in its spin state S (= 0 for singlet and 1 for triplet) and principal quantum number n (1, 2, . . . or s, p, . . . states), μ_x the exciton's reduced mass and $\varepsilon'(S)$ is given by:

$$\varepsilon'(S) = \varepsilon \left[1 - \frac{(1-S)}{A} \right]^{-1}, \tag{42}$$

Here ε is the static dielectric constant of the solid and A is the ratio of the magnitude of the Coulomb and exchange interactions between the electron and

hole in an exciton. For a-Si:H and a-Ge:H, A is estimated to be 10, which gives the ground state singlet-triplet energy splitting as [31]:

$$\Delta E_x \approx 0.2\ C_M, \tag{43}$$

where $C_M = \mu_x e^4 \kappa^2 / 2\hbar^2 \varepsilon^2$. Assuming that both the electron and hole in an exciton are excited in their extended states for a-Si:H and a-Ge:H and using the corresponding effective masses from Table 3, we get the excitonic reduced mass $\mu_x = 0.17\ m_e$ for a-Si:H and $\mu_x = 0.11\ m_e$ for a-Ge:H. Using the static dielectric constant $\varepsilon = 12$ for a-Si:H [28], we get $C_M = 16.12$ meV and for a-Ge:H we have $C_M = 5.87$ meV with $\varepsilon = 16$ [61]. This gives the energy difference between singlet and triplet excitonic states from Eq. (41) as $\Delta E_{ex} = 3.22$ meV for a-Si:H, and 1.17 meV for a-Ge:H. This agrees with the experimental values estimated by Aoki [60] as 3.0 meV in a-Si:H and 0.8 meV in a-Ge:H.

The excitonic Bohr radii of singlet [a_{ex} ($S = 0$)], and triplet [a_{ex} ($S = 1$)] states have also been estimated from Eq. (41) for a-Si:H and a-Ge:H. We thus find that:

$$a_{ex}(S = 0) = \frac{5}{4} a_{ex}(S = 1), \tag{44}$$

and

$$a_{ex}(S = 1) = \frac{\mu\varepsilon}{\mu_x} a_0; \quad a_0 = \frac{\hbar^2}{\kappa \mu e^2}, \tag{45}$$

where a_0 is the Bohr radius and μ reduced mass of the electron in a hydrogen atom. Thus, the Bohr radius of a singlet excitonic state is larger than that of a triplet excitonic state, which is expected because the binding energy of a triplet state is larger than that of a singlet state.

9. Conclusions

A wide range of optical properties of solids is presented in this chapter. Starting with the classical considerations used in studying these properties in condensed matter, band-to-band absorption is presented using the quantum mechanical concepts. Excitonic absorption in crystalline solids and absorption in amorphous solids are also described. A simple approach to determine the effective mass of charge carriers in amorphous solids is given and applied to study the absorption, excitonic states and photoluminescence in amorphous semiconductors. Several excitonic processes occurring in quantum wells and their rates are also presented.

Acknowledgements

This work was supported by the Australian Research Council's large grants scheme (2000–2002). One of the authors (SK) thanks the Northern Territory University for a visiting fellowship allowing him to collaborate with the co-authors of this chapter.

References

1. M. Fox, *Optical Properties of Solids* (Oxford: Oxford University Press, 2001).
2. J. H. Simmons and K. S. Potter, *Optical Materials* (San Diego: Academic Press (2000).
3. D. F. Edwards and E. Ochoa, *Appl. Optics* **19**, 4130 (1980).
4. W. L. Wolfe, 'Properties of Optical Materials', in W. G. Driscoll and W. Vaughan (eds.), *The Handbook of Optics* (New York: McGraw-Hill, 1978).
5. D. E. Aspnes and A. A. Studna, *Phys. Rev.* **B27**, 985 (1983).
6. W. J. Turner and W. E. Reese, *Phys. Rev.* **127**, 126 (1962).
7. W. G. Spitzer and H. Y. Fan, *Phys. Rev.* **106**, 882 (1957).
8. E. Hagen and H. Rubens, *Ann. Phys.* **14**, 986 (1904).
9. R. J. Elliott and A. F. Gibson, *An Introduction to Solid State Physics and Its Applications* (London: MacMillann Press Ltd., 1974).
10. H. B. Briggs and R. C. Fletcher, *Phys. Rev.* **91**, 1342 (1953).
11. C. R. Pidgeon, *Handbook on Semiconductors*, Vol. 2, *Optical Properties of Solids*, Ed. M. Balkanski (Amsterdam: North Holland Publishing, 1980), Ch. 5. pp. 223–328.
12. H. E. Ruda, *J. Appl. Phys.* **72**, 1648 (1992).
13. H. E. Ruda, *J. Appl. Phys.* **61**, 3035 (1987).
14. J. D. Wiley and M. DiDomenico, *Phys. Rev.* **B1**, 1655 (1970).
15. H. R. Riedl, *Phys. Rev.* **127**, 162 (1962).
16. R. L. Weihler, *Phys. Rev.* **152**, 735 (1966).
17. W. Kaiser, R. J. Collins and H. Y. Fan, *Phys. Rev.* **91**, 1380 (1953).
18. I. Kudman and T. Seidel, *J. Appl. Phys.* **33**, 771 (1962).
19. A. E. Rakhshani, *J. Appl. Phys.* **81**, 7988 (1997).
20. R. H. Bube, *Electronic Properties of Crystalline Solids* (San Diego: Academic Press, 1974), Ch. 11.
21. F. Urbach, *Phys. Rev.* **92**, 1324 (1953).
22. J. Pankove *Phys. Rev.* **140**, A2059 (1965).
23. J. Singh, *Excitation Energy Transfer Processes in Condensed Matter* (New York: Plenum, 1994).
24. J. Singh and K. Shimakawa, *Advances in Amorphous Semiconductors* (London: Taylor & Francis, 2003).
25. J. Singh, *Nonlinear Optics* **29**, 119 (2002).
26. N. F. Mott and E. A. Davis, *Electronic Processes in Non-Crystalline Materials* (Oxford: Clarendon Press, 1979).
27. A. P. Sokolov, A. P. Shebanin, O. A. Golikova and M. M. Mezdrogina, *J. Phys.: Cond. Matter* **3**, 9887 (1991).
28. G. D. Cody, *Semiconductors and Semimetals* **B21**, 11 (1984).
29. J. Singh, K. Shimakawa and T. Aoki, *Phil. Mag.* **B82**, 855 (2002).
30. K. Morigaki, *Physics of Amorphous Semiconductors* (London: World Scientific, 1999).
31. L. Ley, *The Physics of Hydrogenated Amorphous Silicon II*, Eds. J. D. Joannopoulos and G. Lukovsky (Berlin, Springer: 1984), p. 61.
32. R. A. Street, *Hydrogenated Amorphous Silicon* (Cambridge: Cambridge University Press, 1991).
33. T. Aoki, H. Shimada, N. Hirao, N. Yoshida, K. Shimakawa and S. R. Elliott, *Phys. Rev.* **B59**, 1579 (1999).

34. J. Singh, *J. Materials Science* **14**, 171 (2003).
35. S. Abe and Y. Toyozawa, *J. Phys. Soc. Jpn.* **50**, 2185 (1981).
36. C. Weisbuch, H. Benisty and R. Houdré, *J. Lumin.* **85**, 271 (2000).
37. X.-F. He, *Phys. Rev.* **B43**, 2063 (1991)
38. I.-K. Oh, J. Singh, A. Thilagam and A. S. Vengurlekar, *Phys. Rev.* **B 62**, 2045 (2000) and references therein.
39. I.-K. Oh and J. Singh, *Superlattices and Microstructures* **30**, 221 (2001) and references therein.
40. I.-K. Oh and Jai Singh, *J. Lumin.* **85**, 233 (2000) and references therein.
41. I.-K. Oh, J. Singh, and A. S. Vengurlekar, *J. Appl. Phys.* **91**, 5796 (2002) and reference therein.
42. I.-K. Oh and J. Singh, *Superlattices and Microstructures* **30**, 287 (2001) and references therein.
43. E. Runge and R. Zimmermann, *Ann. Physik (Leipzig)* **7**, 417 (1998) and references therein.
44. G. D. Mahan, 'Polarons in heavily doped semiconductors', in J. T. Devreese (ed.), *Polarons in Ionic Crystals and Polar Semiconductors* (Amsterdam: North-Holland, 1972).
45. I.-K. Oh and J. Singh, *Int. J. Mod. Phys.* **B15**, 3660 (2001).
46. R. Strobel, R. Eccleston, J. Kuhl and K. Köhler, *Phys. Rev.* **B43**, 12564 (1991).
47. I.-K. Oh and J. Singh, *J. Lumin.* **87–89**, 219 (2000)
48. B. Pal and A. S. Vengurlekar, *Appl. Phys. Lett.* **79**, 72 (2001).
49. I.-K. Oh and J. Singh, submitted.
50. R. C. Miller, D. A. Kleinman, A. C. Gossard, and O. Munteanu, *Phys. Rev.* **B25**, 6545 (1982).
51. D. Birkedal, J. Singh, V. G. Lyssenko, J. Erland and J. M. Hvam, *Phy. Rev. Lett.* **76**, 672 (1996).
52. J. Singh, D. Birkedal, V. G. Lyssenko and J. M. Hvam, *Phys. Rev.* **B53**, 15909 (1996).
53. G, Finkelstein, H. Strikman and I. Bar-Joseph, *Phys. Rev. Lett.* **74**, 976 (1995).
54. J. Singh, *Nonlinear Optics* **18**, 171 (1997) and references there in.
55. S. Ambros, R. Carius and H. Wagner, *J. Non-Cryst. Sol.* **137–138**, 555 (1991).
56. R. Stachowitz, M. Schubert and W. Fuhs, *J. Non-Cryst. Sol.* **227–230**, 190 (1998).
57. F. Boulitrop and D. J. Dunstan, *J. Non-Cryst. Sol.* **77–78**, 663 (1985).
58. T. M. Searle, M. Hopkinson, M. Edmeades, S. Kalem, I. G. Austin and R. A. Gibson, *Disordered Semiconductors*, Ed. M. A. Kastner, G. A. Thomas and S. R. Ovshinsky (New York,: Plenum, 1987), p. 357.
59. S. Ishii, M. Kurihara, T. Aoki, K. Shimakawa and J. Singh, *J. Non-Cryst. Sol.* **266–269**, 721 (2000). (An error was detected in determining in this paper, which has been corrected in 61.)
60. T. Aoki, in *Proc. 11th International School on Condensed Matter Physics*, held in Varna, Bulgaria, 1–4 September, 2000, p. 57.
61. G. A. N. Conwell and J. R. Pawlik, *Phys. Rev.* **B13**, 787 (1976).

This page intentionally left blank

CHAPTER 3

DYNAMIC WAVEGUIDES AND GRATINGS IN PHOTOREFRACTIVE CRYSTALS

V. I. Vlad[1, *], E. Fazio[2], M. J. Damzen[3], A. Petris[1]

[1] *The Institute of Atomic Physics, NILPRP – Romanian Center of Excellence in Photonics and RACASP, R-76900 Bucharest, Romania;*

[2] *Università di Roma "La Sapienza" and INFM, Dipart. Energetica, I-00161 Roma, Italy;*

[3] *The Blackett Laboratory, Imperial College, London SW7 2BZ, United Kingdom*

*(*Author for correspondence, E-mail: vlad@ifin.nipne.ro)*

ABSTRACT: This chapter is an overview of the photorefractive effect, the important photorefractive nonlinear processes and common photorefractive materials. In Section 2, the formation of steady-state spatial solitons by laser beam propagation through photorefractive crystals (PRC) with optical activity and absorption is theoretically and experimentally described. The spatial soliton features, which characterize the dynamic waveguide built in PRC, are analyzed. The soliton polarisation dynamics reaches a stable behavior under high external electric fields. Two-wave mixing and self-diffraction in dynamic harmonic and inharmonic gratings, induced by lasers in PRC, are presented in Section 3. The diffraction efficiency and beam amplification can reach high values, with promising potential in optical interconnections and storage. Dynamic and adaptive gratings by double phase conjugation (DPC) in PRC are discussed in Section 4. High phase conjugated reflectivity, high coupling transmission efficiency and robust interconnections of mutually incoherent lasers are achieved in DPC using Rh:$BaTiO_3$ crystals.

1. Overview of the photorefractive effect and materials

1.1. *Photoexcited processes in photorefractive crystals (PRC)*

The photorefractive effect is a process, in which the refractive index of an optical material is changed, when illuminated by light. The photorefractive effect is commonly understood by the band transport model [1–8]. According to this model, a photorefractive material contains deep and shallow levels in the forbidden bandgap due to impurities or defects in that material. In Figure 1, this model is illustrated for the case of a deep level associated with a donor and the shallow level-trap, to an acceptor. It is assumed that the donor concentration is greater than the acceptor, such as when the shallow acceptors are completely filled by electrons.

It is also assumed that the donor level is deep in the bandgap and consequently, the thermal excitation is neglected.

When the photorefractive material is illuminated by light with a high photon energy, the deep donors are photoionized and free carriers are raised into the conduction band. If additionally, nonuniform light distributions, such as focused laser beams or intensity interference patterns are used, the free electrons move into the conduction band by diffusion, drift and photovoltaic transport processes. Another important process in these materials is the recombination of the free carriers with

Aaron Peled (ed.), Photo-Excited Processes, Diagnostics and Applications (PEPDA), 57–100, 2003.
© 2003 *Kluwer Academic Publishers. Printed in the Netherlands.*

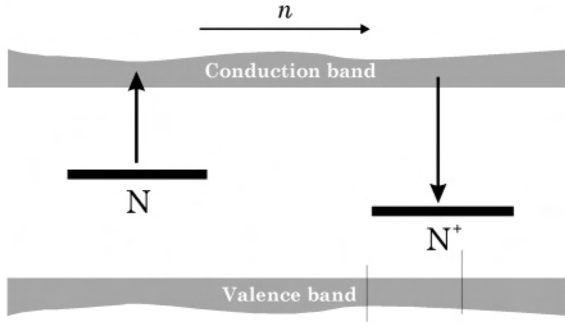

Figure 1. A simplified diagram of the standard band model of photorefraction.

ionized deep traps. At equilibrium, these processes lead to the generation of a nonuniform space charge distribution, which yields an electric field. The space charge electric field changes the refractive index by electrooptic effects. For the linear electrooptic effect case, the refractive index change is given by:

$$\Delta n = \frac{1}{2} n^3 r_{eff} E_{sc} \tag{1}$$

where n is the linear refractive index, r_{eff} is the effective linear electrooptic coefficient, which depends on the orientation of the crystal and the polarization of light, and E_{sc} is the space charge electric field.

A simple mathematical description of this standard model of the photorefractive effect may be sought by considering a bell-shaped, particularly, Gaussian laser beam intensity,

$$I(x) = I_0 f(x); \quad f(x) = f(-x); \quad f(0) = 1; \quad f(x) \xrightarrow[x \to \infty]{} 0 \tag{2}$$

which illuminates the material, as in Figure 2a.

At steady state, the standard single-carrier single-trap model, without photovoltaic effect, gives the following space charge field expression [2–5]:

$$E_{sc} = \frac{E_0 - \left(\frac{k_B T}{e}\right) \frac{\partial}{\partial x} \left[\frac{I(x)}{I_B}\right]}{1 + \left[\frac{I(x)}{I_B}\right]}, \tag{3}$$

where E_0 is the external electric field, k_B is the Boltzmann constant, T is the temperature, e is the elementary charge and I_B is the light background intensity, i.e., the noise intensity detected in the dark. By combining Eqs. (1)–(3), one can realize that the refractive index changes with the spatial gradient of the intensity distribution, rather than with the intensity alone. Therefore, homogeneous illumination

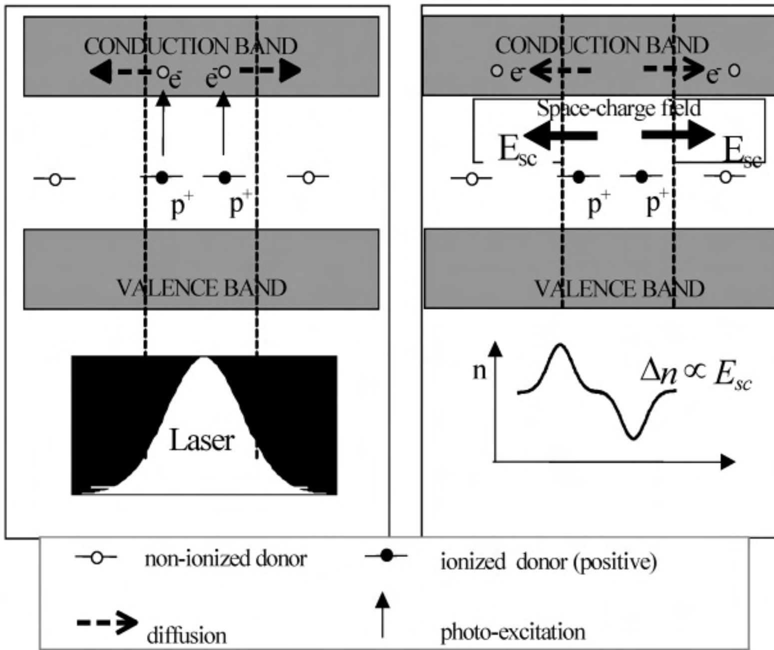

Figure 2a. Schematically illustration of the photoexcited processes in a photorefractive crystal: the laser beam ionizes more donor atoms at its center, where the intensity is higher. The ionized donors remain in their fixed positions, but the generated electrons which are non-uniformly distributed in the conduction band, diffuse from the region of higher concentration to the lower concentration. Consequently, a space charge field develops, which modulates the PRC refractive index by the Pockel's effect.

washes out the refractive index distribution in the photorefractive material and resets it to the initial conditions.

If the carrier transport is dominated by drift, at high external electric fields, E_{sc} takes the form [3–5]:

$$E_{sc} = \frac{E_0}{1 + \dfrac{I(x, z)}{I_B}}, \tag{4}$$

which depends non linearly on the ratio of the light and dark intensities. This dependence is used in the generation of photorefractive spatial solitons.

If we assume now that the illumination of the photorefractive material is by the interference pattern of two beams, i.e., by a grating with the intensity showed in Figure 2b, it is given by:

$$I(x) = I_0 \left(1 + m \cos \frac{2\pi x}{\Lambda} \right), \tag{5}$$

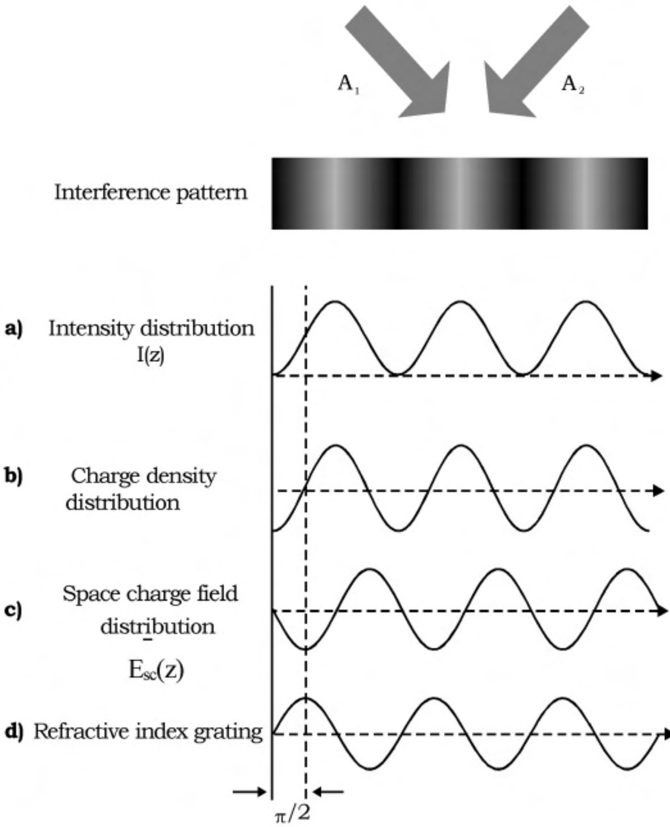

Figure 2b. The formation of a refractive index grating by light-induced redistribution of charge.

where Λ is the grating period and m is the modulation depth. Following the carrier excitation and spatial transport, due to diffusion and drift, the interference pattern given by Eq. (5) produces a refractive index grating.

The refractive index grating diffracts the two interfering beams, which in turn change the interference pattern and the refractive index grating. The interaction between the laser beams and the photorefractive material develops dynamically. This process in photorefractive materials is referred to as two-wave mixing [3–5]. An application of this dynamic mixing process, with spatial modulation, is dynamic holography.

In the framework of the single-carrier, single-trap model, E_{sc} obtained from Eq. (5) can be written, in steady state, for small modulation depths and for negligible photovoltaic effect, as [2–5]:

$$E_{sc} = m \frac{iE_q(E_D - iE_0)\sigma_p}{E_q + E_D - iE_0\sigma_d + \sigma_p}, \tag{6}$$

In Eq. (6), E_0 is the external electric field, $E_D = (k_BT/e) \times (2\pi/\Lambda)$ is the diffusion field, σ_p is the photoconductivity of the material under the illumination, σ_d is the dark conductivity, $E_q = eN_E/K\varepsilon$ is the trap-limited field, ε is the dielectric constant, $N_\varepsilon = N_A(N_D - N_A)/N_D$ is the effective trap density and N_D and N_A are the deep donor and the shallow acceptor concentrations, respectively. The trap-limited field is the maximum field that can be generated by the redistribution of charges with density N_E.

If the carrier transport is dominated by diffusion and $\sigma_p \gg \sigma_d$, E_{sc} takes the form:

$$E_{sc} = i2\pi m \frac{k_BT}{e\Lambda_D} \times \frac{\Lambda_D/\Lambda}{1 + (\Lambda_D/\Lambda)^2}, \tag{7}$$

where

$$\Lambda_D = 2\pi \sqrt{\frac{k_BT}{e^2}} \times \sqrt{\frac{\varepsilon}{N_E}} = 2\pi \sqrt{\frac{k_BT}{e^2}} \times \frac{n}{\sqrt{N_E}}, \tag{8}$$

is the Debye screening length. For a fringe period $\Lambda \ll \Lambda_D$, E_{sc} is approximately independent on the fringe period, while for $\Lambda \gg \Lambda_D$, E_{sc} is inversely proportional to it. For $\Lambda = \Lambda_D$, E_{sc} reaches a maximum. The maximum field is determined by the ratio of the dielectric constant to the effective trap density of the photorefractive material and by the controllable material temperature, as $T^{-1/2}$.

The space charge field, given by Eq. (6) or Eq. (7), is a complex number. This means that the space charge field is spatially de-phased (shifted) with respect to the intensity pattern of the interference fringes, see Figure 2b. The phase shift of the space charge field is exactly $\pi/2$ when the transport of the carriers is governed by diffusion, i.e., when the external field is absent. Thus, this effect is a *non-local* one. The crystal should be lacking inversion symmetry, otherwise there is no preference for the phase shift direction.

When the carrier transport is dominated by drift and for $\sigma_p \gg \sigma_d$, the space charge field has the following form :

$$E_{sc} \propto m \times \Lambda_E \left[1 + \left(\frac{2\pi\Lambda_E}{\Lambda} \right)^2 \right]^{1/2}, \tag{9}$$

where $\Lambda_E = \mu\tau_R E_0$ is the drift length, μ is the charge carrier mobility and τ_R is the charge carrier recombination lifetime. If $\Lambda \ll 2\pi\Lambda_E$, i.e., for large external field and small angle between the interfering beams, in the first approximation, $E_{sc} \propto m\Lambda/2\pi$, i.e., the space charge field is independent of the external field and proportional to the grating period. For large grating periods, $\Lambda \gg 2\pi\Lambda_E$, in the first approximation, $E_{sc} \propto m\Lambda_E$, i.e., the space charge field is proportional to the external electric field.

The asymmetry of the refraction index grating formation leads to an one-way flow of energy between the two coupling beams. The weaker beam is amplified by

the asymmetric two-wave mixing, while the stronger beam works as a pump beam. The direction of energy flow depends on crystal orientation, polarization of light, and whether the carriers are electrons or holes. The amplified beam grows exponentially unless the pump beam is depleted, and the gain coefficient is defined as [5]:

$$\gamma = 2\pi\Delta n \times \frac{\sin\varphi}{\lambda\cos\theta}, \tag{10}$$

where φ is the phase shift, λ is the wavelength and 2θ is the angle between the coupled waves in the material. The gain coefficient γ_a, vanishes when the phase shift is zero, even when the nonlinear refractive index grating exists. To produce a finite phase shift, one can displace laterally the interference pattern with a speed comparable to the response time of the material [3]. The gain coefficients of some photorefractive materials are much larger than those typical of laser active media and one can easily obtain an oscillation if high gain photorefractive materials are introduced into optical resonators.

When the laser beam is incident onto photorefractive materials, the transmitted beam spreads widely in the direction of amplification, so called beam fanning. The fanned beam is the scattered light pumped by the input beam itself by two-wave mixing. Consequently, the fanning beam has the direction for which the scattered light is amplified efficiently. For high gain photorefractive materials, the energy of the incident beam can be almost totally transferred to the fanning beam.

An important feature of Eq. (6) is that the refractive index change is proportional to the modulation depth of the intensity distribution m, rather than the intensity itself, unless the illumination is so low that $\sigma_p \sim \sigma_d$. One important consequence is that the gain coefficient of the two-wave mixing does not depend on the pump intensity, see Eq. (10). This is quite different from other nonlinear optical amplifications e.g., optical parametric amplification and stimulated scattering, where the gain coefficients are proportional to the pump intensity. Therefore, efficient multiple-wave mixing can be obtained even with low intensity pump beams. One can explain this by considering that the refractive index change is not caused by carrier excitation, but rather by the redistribution of the ionized photorefractive centers. The high light intensity is however important for increasing the response speed.

The photo-excitation should be greater than thermal excitation, because the thermal excitation erases the recorded refractive index gratings. Eq. (6) shows that, at a low intensity, the refractive index change increases linearly as the intensity increases. At an intensity for which the photoconductivity exceeds the dark conductivity, the index change saturates to a steady state value. This saturation regime can be reached in many photorefractive materials by illumination with low-power c.w. laser beams.

For the same approximation of Eq. (6), the response time of the refractive index grating formation can be deduced from [5]:

$$\frac{1}{\tau} = \frac{1}{\tau_{di}} \times \frac{E_M}{E_q} \times \frac{E_q + E_D - iE_0}{E_M + E_D - iE_0}, \tag{11}$$

where $\tau_{di} = \varepsilon/\sigma$ is the dielectric relaxation time and $E_M = (K\mu\tau_R)^{-1}$ is the *mobility field*, which is the electric field that drives an electron a distance $1/K$ during its lifetime. The real part of Eq. (11) gives a photorefractive response rate and the imaginary part is related to the frequency of transient oscillations at space charge formation. The response time is basically determined by the dielectric time constant, which is inversely proportional to the intensity of illumination. The more intense is the illumination, the faster is the formation of the refractive index grating.

When two pairs of beams are interacting in the photorefractive material, they form at least three distinct dynamic gratings in a nonlinear process, so-called four-wave mixing [5, 6, 9]. The multiple-wave mixing processes are analyzed by the coupled wave theory [9]. Applications of multi-wave mixing in photorefractive materials can be found in image amplification, optical phase conjugation and in optical information processing.

Real materials however, exhibit a more complex behavior, and often do not behave as the above simple model predicts [7, 8, 10]. The photovoltaic effect for instance, was not considered above, although it is a dominant transport process of carriers in some ferroelectric oxides such as $LiNbO_3$ [1–4, 11].

1.2. *Photorefractive crystals*

The most useful photorefractive materials are classified into four groups:

(a) ferroelectric oxides such as $LiNbO_3$, $BaTiO_3$, $Sr_xBr_{1-x}Nb_2O_6$ (SBN), $KNbO_3$;
(b) cubic oxides, sillenites such as $Bi_{12}SiO_{20}$ (BSO), $Bi_{12}GeO_{20}$ (BGO), $Bi_{12}TiO_{20}$ (BTO);
(c) compound semiconductors e.g. GaAs, InP; and
(d) organic materials e.g. polymers and crystals.

These materials have a large potential for the experimentalists, since their parameters can be controlled, in principle, by doping and other treatment processes of material science. In spite the fact that it is not easy to obtain very reproducible photorefractive materials, one could give some average numbers, which may guide the modeling of the photoexcited processes in these materials and the applications which are developing for these materials.

The main parameters of photorefractive materials extensively used in our works are shown in Table 1, where α is the absorption coefficient, ρ_0 – optical rotating power, E_g – the bandgap energy and R^* – the conjugated reflectivity. λ_0 is the laser wavelength for which the photorefractive crystals are used optimally in non-linear processes such as spatial soliton propagation and wave mixing.

Some of these parameters have a noticeable variation as a function of laser wavelength, as shown in Table 2 for the BSO crystals ($r_{max} = r_{41}$), which require adjustments when devices are swapped or when another wavelength is used for inter-action monitoring.

Finally, some good reviews on photorefractive organic materials, such as polymers and crystals are described in many papers, e.g. in Refs. [12, 13].

Table 1. Parameters of typical photorefractive materials.

	$LiNbO_3$:Fe	$BaTiO_3$	BSO	BTO	GaAs:Cr	GaP	InP:Fe
λ_0 [nm]	515	515	515	633	1064	633	1064
n	2.3 (ordinary)	2.44 (ordinary)	2.615	2.25	3.5	3.45	3.29
α [cm^{-1}]	0.5	0.3	1.7	0.5	0.7–1	2	2
ρ_0 [mm^{-1}]			38.6	6.3			
r_{max} [pm/V]	31	1640	4.5	5.2	1.43	1.07	1.34
E_g [eV]	3.2–3.7	3	3.25	3.5	0.82	1.1	1.35
μ [cm^2/Vs]	~0.8	0.5	~1	~1	8500	110	4600
$\mu\tau_R$ [cm^2/V]	5.2×10^{-13} (0.03%Fe)	$\sim10^{-10}$	$(5–8)\times10^{-7}$	2.4×10^{-8}	10^{-7}	1.7×10^{-8}	1.6×10^{-7}
σ_d [Ωcm]$^{-1}$	10^{-8}–10^{-19}	10^{-12}	10^{-15}	10^{-15}	3×10^{-8}		
γ [cm^{-1}]	~10	~30	2.5–5	10–15	0.3–6		4
R^* [%]		10^2	10^{-4}–2.7	30	0.14–1		0.01–1

Table 2. Some BSO parameters as a function of laser wavelength.

BSO	λ_0 = 488 nm	515 nm	633 nm
n	2.65	2.615	2.53
ρ_0 [mm^{-1}]	45.5	38.6	21.4
r_{41} [pm/V]	4.52	4.51	4.41

2. Spatial solitons and dynamic waveguides in PRC

2.1. *Photorefractive spatial solitons*

Steady-state spatial solitons were proved to exist recently at low laser intensity, which lead to one-dimensional and two-dimensional compensation of diffraction by refractive index modulation in photorefractive crystals [14–24].

The steady-state solitons were first predicted by Segev et al. [14, 15] and by Christodoulidis and Carvalho [16]. They assumed that the focused signal beam is incoherently superimposed on a collimated background beam, into PRC. The background ensures a constant pumping of electric charges and provides the dependence of the refractive index change on the average light intensity in steady-state conditions. This system may reach a stable modification of the refractive index, which can lead to the stable soliton formation in the signal beam propagation. In order to obtain the spatial soliton, the signal beam is propagating perpendicular to an external electric field, which creates a dominant drift regime for the photorefractive effects. The static electric field is decreased inside the crystal by screening in the region of the focused signal beam, which has a narrow Gaussian spatial

distribution. The resulting electric space-charge field induces a spatial refractive index modulation in the form of a dynamic waveguide, which preserves the soliton shape of the propagating signal beam. Thus, the soliton can be thought as a wave, which changes dynamically the properties of the nonlinear propagation medium, particularly PRC, in such a way that it compensates the diffraction and maintains the initial wavefront in a certain space-time range. The theory of steady-state solitons in PRC was further developed by Crosignani et al. [17, 18].

Experimental observation of (2+1)D (two-dimensional) and (1+1)D (one-dimensional) steady-state solitons and self-focusing in PRC were given by by Shih et al. [19, 22], Iturbe Castillo et al. [20, 21], Kos et al. [23], Chen et al. [24], Fressengeas et al. [25], Wolfensberger et al. [26]. Segev et al. [27] and Crosignani et al. [28] wrote good reviews on the major achievements in the field. Soliton interaction also is largely investigated too, see for example the review by C. Denz et al. [29].

Many photorefractive crystals such as the sillenites and organic non-linear materials show considerable optical activity [4], which complicates the wave propagation in these anisotropic non-linear media. Singh and Christodoulidis [30] and Krolikowski et al. [31] developed theoretical models and numerical calculations for studying wave propagation and possible (1+1)D soliton formation in these complex media.

Analytical and numerical results within a theoretical model for (2+1)D soliton propagation in PRC with strong optical activity and experimental results proving the generation of (1+1)D and (2+1)D solitons in $Bi_{12}SiO_{20}$ (BSO) crystals [32, 33, 36–39], at high external electric fields are presented in this section.

Herriau et al. have correlated the relatively large absorption with good photorefractive properties [34] and Blair et al. have demonstrated its importance in spatial soliton formation [35]. Consequently, absorption is considered here in the treatment of spatial solitons [36–39]. The dependence of the soliton features on different controllable parameters is also derived. Experimental results, as well as numerical simulations in BSO crystals, confirm the analytical solutions and the importance of optical activity and absorption in soliton formation.

The photorefractive solitons possess the following properties, which make them attractive for all-optical light control.

1. They can occur at low intensity in PRC. However, the shorter the laser impulse is, the higher is the required signal beam intensity.
2. The spatial solitons are controllable by the signal-to-background intensity ratio and by the external electrical field.
3. The spatial solitons show relative stability to the signal beam shape changes, moderate losses and diffusion. This stability maintains the light confinement in micro-channels, i.e. the high resolution in an array of soliton devices.
4. The spatial solitons can interact, if their waveguides are parallel and closely spaced. They attract each other if they are in phase and repel each other if they are in anti-phase. This property can provide important functions as optical switching and routing.

5. They can provide dynamic waveguiding and control of strong optical beams at wavelengths outside PRC sensitivity band, by weak soliton beams, which create the waveguide.
6. The optical activity, which can be thought as a pair of counter-rotating circular polarized waves, adds interesting features for applications.

2.2. *Analytical solutions of the soliton propagation in PRC with optical activity and absorption*

The light propagation in a non-linear anisotropic material with optical activity and absorption can be described by the wave equation for the electric vector of the optical field [5, 7, 18]:

$$\nabla^2\vec{E}(\vec{r}, t) - \frac{1}{c^2}\left[\hat{\varepsilon} \otimes \frac{\partial^2\vec{E}}{\partial t^2} + \frac{g}{k}\left(\vec{\nabla} \times \frac{\partial^2\vec{E}}{\partial t^2}\right)\right] - \frac{n_0}{c}\alpha\frac{\partial\vec{E}}{\partial t} = 0, \tag{12}$$

where c is the light velocity in vacuum, $\hat{\varepsilon}$ is the symmetric dielectric permittivity tensor of the anisotropic material, "$\otimes$" is the tensor-vector multiplication, $g = 2\rho_0/k$ is the gyration constant, ρ_0 is the optical rotating power, n the refractive index, α the absorption constant and k is the wave vector inside the material.

Considering the classical solution of the form:

$$\vec{E}(\vec{r}, t) = \vec{A}(\vec{r}) \times e^{i(kz - \omega t)}, \tag{13}$$

and introducing the slowly varying envelope approximation (SVEA), Eq. (12) becomes:

$$2ik\frac{\partial\vec{A}}{\partial z} + \frac{\partial^2\vec{A}}{\partial x^2} + \frac{\partial^2\vec{A}}{\partial y^2} - k^2\vec{A} + k^2\hat{\varepsilon} \otimes \vec{A} + ik^2 g(\vec{e}_z \times \vec{A}) +$$
$$k^2\frac{g}{k}(\vec{\nabla} \times \vec{A}) + ik\alpha\vec{A} = 0. \tag{14}$$

In a simplified single species model, the photorefractive effect consists of photoionization of some donors and a refractive index modulation by the resulting electric space-charge field, including carrier transport and recombination. In the steady state and drift dominated transport conditions, the space charge field as a function of light intensity is described by Eq. (4) [15–18, 23, 24]. Crosignani et al. [28] found that, in both (1+1)D and (2+1)D cases, the dependence of the dielectric permittivity tensor on the optical field intensity is given by the following good approximation:

$$\hat{\varepsilon} = [\vec{E}_0\hat{R}n^2]\left[1 + \left(\frac{\vec{A}}{\sqrt{I_B}}\right)^2\right]^{-1} + \hat{\varepsilon}_d, \quad \hat{\varepsilon}_d = \begin{bmatrix} \varepsilon_{xx} & 0 \\ 0 & \varepsilon_{yy} \end{bmatrix}, \tag{15}$$

where E_0 is the external electric field applied perpendicularly to the optical beams, along the 0X axis, $\hat{R}$ is the electro-optic tensor of the anisotropic material, I_B the background intensity and $\hat{\varepsilon}_d$ is the dielectric permittivity tensor in the dark, recalling also that $\varepsilon_d = n^2$.

For a dispersionless optical activity, one can take in Eq. (14): $\vec{\nabla} \times \vec{A} = 0$, as justified in [4]. Then, one can diagonalise the permittivity tensor in Eq. (14) by an anti-clockwise rotation of the optical field plane. For cubic PRC and for a coincidence of the optical field axis (z-axis) with one of the principal directions of the index ellipsoid, one finds [17, 25]:

$$\varepsilon_{xx} = \varepsilon_{yy} = 1, \quad \varepsilon_{xy} = \frac{c_1}{1 + |\vec{A}|^2/I_B}, \quad c_1 = n^2 r_{41} E_0 = \frac{1}{n^2}\Delta \mathrm{n} \rightarrow \varphi' = \frac{\pi}{4}, \tag{16}$$

with Δn being the refractive index change due to the photorefractive effect, due to induced birefringence.

The rotation of the light electric vector by the optical activity is more conveniently described by the wave equation in cylindrical coordinates, scaled to the non-linear birefringence coefficient, c_1:

$$\xi = \rho \cos \varphi; \quad \eta = \rho \sin \varphi; \quad \zeta = c_1 kz; \quad \rho = \sqrt{\xi^2 + \eta^2} = \sqrt{c_1 k}\,\sqrt{x^2 + y^2};$$
$$\varphi = \arctan(y/x).$$

Moreover, the optical field components, normalized to the background amplitude, can define a new vector with components (u, v), which consist of fast factors, functions of φ, and slow envelopes, u_1, v_1, rotating and pulsating during propagation according to:

$$|\vec{u}| = \begin{vmatrix} u \\ v \end{vmatrix} = \begin{vmatrix} A_x/\sqrt{I_B} \\ A_y/\sqrt{I_B} \end{vmatrix} \approx \sqrt{\frac{2}{\pi}} \begin{bmatrix} \cos(\varphi/2) & \sin(\varphi/2) \\ -\sin(\varphi/2) & \cos(\varphi/2) \end{bmatrix} \begin{vmatrix} u_1 \\ v_1 \end{vmatrix}, \tag{17}$$

With these assumptions and notations, Eq. (14) can be written as [37]:

$$2i\frac{\partial \vec{u}}{\partial \zeta} + \frac{\partial^2 \vec{u}}{\partial \rho^2} + \begin{bmatrix} (1 + u^2 + v^2)^{-1} & 0 \\ 0 & \mu(1 + u^2 + v^2)^{-1} \end{bmatrix} \begin{bmatrix} u_1 \\ v_1 \end{bmatrix} + i\left(\frac{g_1}{c_1}\right)(\vec{e}_z \times \vec{u}) = 0 \tag{18}$$

where μ takes the values 0 or –1 for the two important orientations of the crystal, i.e., with the electric field along the [001] and [110] directions, respectively and $g_1 = 2[\rho_0 - (\alpha/2)]/k$ is the effective gyration constant, which includes the effects of linear optical absorption.

To separate the induced birefringence and optical activity, one can rotate the normalized optical vector, $\vec{u}$, in the reference frame of the optical activity by an angle $g_1\zeta/c_1 = g_1 kz$, i.e. transforming it into a new vector by the vector $\vec{\Phi}(\rho, \zeta)$

product with an axial vector $\vec{\gamma}(\rho, \zeta)$:

$$\vec{u} = \begin{vmatrix} u \\ v \end{vmatrix} = \vec{\Phi}(\rho, \zeta) \times \vec{\gamma}(\varphi, \zeta), \tag{19}$$

One can restrict the form of the axial vector $\vec{\gamma}(\varphi, \zeta)$ by the condition:

$$2i\vec{\Phi} \times \frac{\partial \vec{\gamma}}{\partial \zeta} + i\delta[\vec{e}_z \times (\vec{\Phi} \times \vec{\gamma})] = 0, \tag{20}$$

which eliminates the rotating term from Eq. (18) and leads to the solution [32, 36]:

$$\gamma(\varphi, \zeta) \approx e^{-\alpha z/2} |\cos \theta|^{-1}, \tag{21}$$

with $\theta = (1/2)[\varphi - 2\varphi' + (g_1/c_1)\zeta - 2\zeta_0] = (1/2)[\varphi + g_1 kz - (\pi/2)]$.

In Eq. (21), one can take $\varphi' = \pi/4$ for cubic crystals and the initial phase of the optical activity $\zeta_0 = 0$, from suitable boundary conditions to ensure the continuity with the Gaussian input beam. The axial vector $\gamma(\varphi, \zeta)$ leads to transverse oscillations so called "breathing" of the propagating wave with the spatial period:

$$\lambda_b = \frac{2\lambda}{g_1} = \frac{2\pi}{\rho_0 - (\alpha/2)}, \tag{22}$$

When $\cos \theta = 0$, the modulus of this axial vector is singular, but the light field is limited by other factors in the solutions, which compensate this behavior and ensure power conservation, as shown later.

Using the transformation (19) and the condition (20) in Eq. (18), it becomes:

$$2i\frac{\partial \vec{\Phi}}{\partial \zeta} + \frac{\partial^2 \vec{\Phi}}{\partial \rho^2} + \begin{bmatrix} (1 + u^2 + v^2)^{-1} & 0 \\ 0 & \mu(1 + u^2 + v^2)^{-1} \end{bmatrix} \begin{bmatrix} \Phi_x \\ \Phi_y \end{bmatrix} = 0. \tag{23}$$

The transformation of the Φ-vector components back into amplitude components of the light electric field can be found from:

$$\begin{bmatrix} A_x \\ A_y \end{bmatrix} = \sqrt{\frac{2I_B r}{\pi}}\, \gamma(\varphi, \zeta) \begin{bmatrix} \sin \theta & -\cos \theta \\ \cos \theta & \sin \theta \end{bmatrix} \begin{bmatrix} \Phi_x \\ \Phi_y \end{bmatrix}. \tag{24}$$

Proceeding further to solve the propagation equations, some piecewise linearizations of the space-charge characteristic permittivity function of the photorefractive crystals are first performed.

(a) At *low light intensity levels*, the intensity dependent factor from Eq. (15) can be approximated by $(1 - I/I_B) = 1 - r\,(I/I_0)$, where I_0 is the maximum input intensity and $r = I_0/I_B$. The resulting solutions of Eq. (23) are as follows [32, 36, 37].

Case 1: $\mu = 0$, when the external electric field is oriented along the [001] direction, the optical field components are:

$$\begin{bmatrix} A_x \\ A_y \end{bmatrix} = \sqrt{\frac{2I_B r}{\pi}}\,\gamma(\varphi,\zeta)\begin{bmatrix} \sin\theta & -\cos\theta \\ \cos\theta & \sin\theta \end{bmatrix} \times$$

$$\begin{bmatrix} \exp\{-[\rho_1^2 w_0^2/(w_0^4 + 4\zeta^2)]\} \cdot [\pi^2(w_0^4 + 4\zeta^2)]^{-1/4} \\ e^{i\zeta'/2}\sqrt{2}\cosh^{-1}(\sqrt{2}\,\rho_1)\exp\{-[\rho_1^2/(w_0^2 + 4\zeta^2/w_0^2)]\} \cdot [\pi^2(w_0^4 + 4\zeta^2)]^{-1/4} \end{bmatrix} \quad (25)$$

where

$$\rho_1 = \sqrt{\frac{2r}{\pi}}\,\gamma(\varphi, z) \times \rho = \sqrt{\frac{2r}{\pi}}\,e^{-\alpha z/2}\left|\cos\left(\frac{1}{2}\right)\left(\varphi + g_1 kz - \frac{\pi}{2}\right)\right|^{-1} \times \rho = \frac{\rho}{(\Delta\rho)_1}$$

w_0 is the input Gaussian beam width and $(\Delta\rho)_1 = (\sqrt{\pi/2r})/\gamma$ is the normalized beam width for $r \ll 1$. The wave defined by (25) has a confined "breathing" core and a weak diffraction part in both components. The total intensity of this wave, which is in a good approximation:

$$I(\rho, \varphi, \zeta') \approx \left(\frac{2}{\pi^2 w_0^2}\right) I_B(r\gamma^2)\exp\left(-\frac{2\rho_1^2}{w_0^2}\right)[1 + 2\cosh^{-2}(\sqrt{2\rho_1})], \quad (26)$$

has a soliton behavior given by the function "$\cosh^{-2}(\sqrt{2\rho_1})$". The approximation holds for the short tested BSO crystals, which have large absorption. In Eq. (26), jumps of the γ-function, when $\cos\theta = 0$, are balanced by the exponential factor, so that the total intensity preserves the soliton-like shape. The initial conditions, which impose the continuity of the signal and the soliton beams at the crystal input face, lead to the relation, $w_0 \approx 6r/\pi^{3/2}$ and constrain the signal beam width, w_0, to small values. Both conditions are restrictive for (2+1)D soliton formation.

Thus, the soliton propagation is maintained in the presence of optical activity and absorption. The increase of optical activity at a given absorption constant decreases the soliton breathing period, and an increase in the absorption constant at a given optical activity, slightly increases the soliton breathing period, with a simultaneous increase of the soliton width.

In the calculation of the soliton width, one can consider the maximum width of the hyperbolic secant at the maximum values of the cosine-function and approximate it by a Gaussian function. Then, one can combine this Gaussian function with the Gaussian factor from Eq. (26) in order to obtain the maximum soliton width:

$$(\Delta\rho_t)^{-2} \approx (\Delta\rho_{1\,\max})^{-2} + \left(\frac{\sqrt{\pi}w_0}{\gamma\sqrt{r}}\right)^{-2}, \quad (27)$$

We observe that the soliton maximum width is smaller than the Gaussian input beam and decreases also with an increase of the beam intensity ratio, r. All trans-

verse variables were normalized by the factor $k\sqrt{n^2 r_{41} E_0} = (2\pi n^2/\lambda_0)\sqrt{r_{41} E_0}$. Thus, one obtains the following maximum soliton width:

$$w_{s\,\max} = \frac{\Delta\rho_t}{k\sqrt{n^2 r_{41} E_0}}, \tag{28}$$

From Eq. (28), one can deduce that the better is the soliton confinement, the higher is the external electric field.

Case 2: $\mu = -1$
This is when the electric field is oriented along the [110] direction. Here, the wave amplitudes are:

$$\begin{bmatrix} A_x \\ A_y \end{bmatrix} = \sqrt{\frac{2I_B r}{\pi}}\,\gamma(\varphi, \zeta')\begin{bmatrix} \sin\theta & -\cos\theta \\ \cos\theta & \sin\theta \end{bmatrix}\begin{bmatrix} e^{-i\zeta'/2}\psi_x(\rho_1, z) \\ e^{i\zeta'/2}\psi_y(\rho_1, z) \end{bmatrix}, \tag{29}$$

which define breathing soliton waves along both axes, with a soliton beam intensity given by

$$\begin{aligned} \mathrm{I} &= A_x^2 + A_y^2 \\ &= \frac{1}{\sqrt{\pi} w_0} I_B \times r\gamma^2(\varphi, \zeta')\left\{\frac{16}{9} \times \frac{1}{[\ln(|\tan\mathrm{h}(\rho_1/2)|) - \cosh\rho_1]^2} + \frac{1}{(\cosh\rho_1)^2}\right\} \end{aligned} \tag{30}$$

For this crystal orientation, the y-component is a transverse modulated, breathing soliton and the x-component is a deformed version of the former case due to the logarithmic term. The same initial conditions, as in the previous case, lead to a relation between the input beam width and the beam intensity ratio r, namely: $w_0^2 = \pi/2r$, which confirms the restrictive conditions for (2+1)D solitons observed in experiments with other materials e.g., SBN crystals [28].

At the first maximum, the breathing soliton waveguide (channel), defined in Eq. (30), has the following normalized width:

$$(\Delta\rho)_{1\,\max}\left(r, \frac{\alpha}{2\rho_0}\right) = \sqrt{\frac{\pi}{2r}}\,\frac{2\rho_0 - \alpha}{\sqrt{\alpha^2 + (2\rho_0 - \alpha)^2}} \times \exp\left\{\frac{\alpha}{2\rho_0 - \alpha}\left[\arctan\left(\frac{\alpha}{2\rho_0 - \alpha}\right) + \frac{\pi}{4}\right]\right\}, \tag{31}$$

The maximum soliton width can be derived here, as in (28), by de-multiplication:

$$w_{s1} = \frac{(\Delta\rho)_{1\,\max}}{k\sqrt{n^2 r_{41} E_0}}, \tag{32}$$

In the total intensity, expressed by Eq. (30), the optical activity is included in γ and leads to breathing. The total intensity decreases strongly with the propagation distance due to the large absorption, which is also included in γ. The difficult detection is a reason why sillenite crystals longer than a few millimeters are not practically used. The absorption leads also to a progressive decrease of diffraction compensation by the non-linearity. However, for usual sillenite crystal lengths of 0.2–1 cm and absorption of 0.5–2 cm^{-1}, the soliton confinement is reasonable good [37].

Using Eqs. (22), (28) and (32), one can calculate the period of the transverse modulation, as well as the soliton width in the first half-period, and realize that they are slightly increasing with the absorption increase, for strong optical activity. For typical parameter values given below an external field of E_0 = 30 KV/cm, the calculated "breathing" period can increase, for BSO crystals, from 0.8 cm, without absorption to approx. 1 cm for $\alpha = 1.7$ cm^{-1}. For BTO crystals, the "breathing" period increases from 5.7 cm, without absorption, to 7.3 cm with $\alpha = 0.5$ cm^{-1}. For a BSO crystal length of 2 mm and absorption coefficient $\alpha = 1.7$ cm^{-1} the soliton width increases by some 17%. According to Eq. (31), the higher is optical activity, the smaller is the soliton width. One can remark another positive feature of the complicated behavior of solitons in PRC with optical activity and absorption: the soliton width increases due to absorption compensation when the width decreases in the focusing region, at least for the first half-period of the breathing. The half-period of the breathing is approx. 5 mm for BSO crystals. Thus, the beam confinement is even improved in the experiments with the commonly used BSO and BTO crystals.

(b) In the case of a *high signal to background intensity ratio*, the intensity dependent factor from Eq. (15), which is proportional to the spatial charge field in the photorefractive crystal can be written as:

$$E_{sc} \sim \frac{1}{1 + (I/I_B)} \sim \frac{1}{(I/I_B)} = \frac{I_0}{r \times I}; \qquad r = \frac{I_0}{I_B}, \tag{33}$$

and the equations of the field (Φ_x, Φ_y) taken from [32, 36, 37] are:

$$\begin{aligned} 2i\frac{\partial \Phi_x}{\partial \zeta'} + \frac{\partial^2 \Phi_x}{\partial \rho^2} + \frac{\mu}{(2r/\pi)\gamma^2[\Phi_x^2 + \Phi_y^2]}\Phi_x = 0, \\ 2i\frac{\partial \Phi_y}{\partial \zeta'} + \frac{\partial^2 \Phi_y}{\partial \rho^2} + \frac{1}{(2r/\pi)\gamma^2[\Phi_x^2 + \Phi_y^2]}\Phi_y = 0. \end{aligned} \tag{34}$$

Case 1: $\mu = 0$

Assuming that the usual crystal length is small, ensuring small soliton attenuation and that the perturbation term along the propagation axis is negligible, the solution of Eq. (34) is a soliton-like wave with total intensity [37]:

$$I(\rho, \varphi, \zeta') \approx \left(\frac{2}{\pi^2 w_0^2}\right) I_B(r\gamma^2)\exp\left(-\frac{2\rho_3^2}{w_0^2}\right) [1 + 2\cosh^{-2}(\sqrt{2}\rho_3)], \tag{35}$$

where

$$\rho_3 = \frac{\rho}{(\Delta\rho)_3} = \frac{\rho}{\sqrt{2r/\pi} \times \gamma} \approx \left[\sqrt{\frac{\pi}{2r}}\, e^{\alpha z/2} \cos\left(\frac{1}{2}\phi + \frac{1}{2} g_1 kz - \frac{\pi}{4}\right)\right] \rho.$$

The total intensity in Eq. (35) is apparently similar to that obtained for the previous case, at low intensity. However, the dependence of ρ_3 on the axial function γ is inverted here. The soliton-like propagation is maintained here in the presence of optical activity and absorption. The higher is optical activity, the smaller is the soliton breathing period, for a given absorption constant. The increase of absorption coefficient, at a given optical activity, slightly increases the soliton breathing period.

We should mention here that for propagation distances, which make $\gamma \to \infty$, the solution (35) cannot hold and the y-component should be replaced by the linear diffraction solution derived directly from Eq. (34) leading to:

$$I(\rho, \varphi, \zeta') \approx 2\exp\left(-\frac{2\rho^2 w_0^2}{w_0^4 + 4\zeta'^2}\right) \times [\pi^2(w_0^4 + 4\zeta'^2)]^{-1/2}. \tag{36}$$

Thus, at the corresponding equally spaced z-points, the wave intensity looses the confinement and tends to the linear diffraction limit, with its width growing up to:

$$\Delta\rho = w_0 \sqrt{1 + \frac{4\zeta'^2}{w_0^4}}\,, \tag{37}$$

This periodic, very localized intensity jumping does not disturb significantly the soliton confinement.

The soliton width is obtained by combining the width of the hyperbolic secant, which can be well approximated by a Gaussian function, and the width of the Gaussian factor of Eq. (35). Thus, from Eq. (35), we obtain the maximum normalized soliton width as:

$$(\Delta\rho_t)^{-2} \approx (\Delta\rho_{3s})^{-2} + \left(w_0\gamma\sqrt{\frac{r}{\pi}}\right)^{-2} = \left(\frac{2\pi}{r\gamma^2}\right)[1 + (\sqrt{2}w_0)^{-2}], \tag{38}$$

We may observe here that the soliton width is smaller than the Gaussian input beam, as expected, and increases also with the increase in the beam intensity ratio, r. As all transverse variables are normalized, one can calculate the soliton width by de-multiplication: $w_{s\,\max} = (\Delta\rho_t)/k\sqrt{n^2 r_{41} E_0}$. As in (28) one can deduce that the higher is the external electric field, the better is the soliton confinement.

Similar initial conditions for the case of low intensity, lead to the relation

$w_0 = 6r/\pi^{3/2}$ and constrain the signal beam width, w_0, to small values. Both conditions are restrictive for (2+1)D soliton formation.

Case 2: $\mu = -1$
In this case, one can derive the optical field components as in ref. [37]:

$$\begin{bmatrix} A_x(\rho_3, \varsigma') \\ A_y(\rho_3, \varsigma') \end{bmatrix} = \sqrt{\frac{2I_B r}{\pi}}\, \gamma(\varphi, \zeta')e^{-S_1(\rho_3)} \begin{bmatrix} \sin\theta & -\cos\theta \\ \cos\theta & \sin\theta \end{bmatrix} \times$$
$$\begin{bmatrix} e^{-i\varsigma'/2}\cos S_2(\rho_3) & e^{-i\varsigma'/2}\sin S_2(\rho_3) \\ -e^{i\varsigma'/2}\sin S_2(\rho_3) & e^{i\varsigma'/2}\cos S_2(\rho_3) \end{bmatrix} \begin{bmatrix} \psi_x(0) \\ \psi_y(0) \end{bmatrix}, \tag{39}$$

where

$$S_1(\rho_3) = \left| \frac{1 - \cosh^2 2\beta + \sin^2 2\alpha}{(\cosh 2\beta + \cos 2\alpha)^2} \right|; \quad S_2(\rho_3) = \left| \frac{2\sin 2\alpha \times \sinh 2\beta}{(\cosh 2\beta + \cos 2\alpha)^2} \right|.$$

α, β are parameters, which are proportional to ρ_3 and depend on the initial conditions. With the same initial conditions as in previous case, one can find, see ref. [25]:

$$\alpha = -\beta = \sqrt{\frac{\pi}{2}}\frac{\rho_3}{2\psi_0} = \frac{\pi}{4}\frac{\rho}{\psi_0\gamma\sqrt{r}} = \left(\frac{\pi}{4}\right)^{1/4}\frac{\rho}{\gamma\sqrt{rw_0}},$$

and the resulting (2 + 1)D wave intensity is:

$$I_S(\rho_3, z) = \frac{1}{\sqrt{\pi}} \times I_B \times \frac{r\gamma^2(\varphi, z)}{w_0} \times e^{-2S_1(\rho_3)}, \tag{40}$$

which describes a breathing soliton with the same period as in the previous cases.

For propagation distances, which make $\gamma \to \infty$, this solution cannot hold and it should be replaced by the linear diffraction solution derived directly from Eq. (34), as for Eq. (36). At the corresponding equal spaced z-points, the wave intensity looses the confinement and tends to the linear diffraction limit, with its width growing up to: $\Delta\rho = w_0\sqrt{1 + 4\zeta'^2/w_0^4}$. This periodic behavior disturbs only slightly the soliton confinement, in most propagation processes.

The normalized widths of the wave component envelopes are:

$$\rho_{3x} \equiv 2\alpha = \frac{\rho}{\Delta\rho_{3x}}; \quad \rho_{3y} \equiv -2\beta = -\frac{\rho}{\Delta\rho_{3y}}; \quad \Delta\rho_{3x} = |\Delta\rho_{3y}| = \left(\frac{4}{\pi}\right)^{1/4}\gamma\sqrt{rw_0}, \tag{41}$$

The proportionality of the wave widths in Eq. (41) to $\sqrt{r}$ corresponds well with the experimental findings shown below. The same initial conditions introduce the constraints: r higher than 1, but close to unity and $w_0^3 = r/\pi^{3/2}$, which guide the experimental observation of these soliton waves.

Finally, when considering the (1+1)D case, one finds [37]:

$$2\alpha = 0; \quad S_2(\rho_3) = 0; \quad S_1(\rho_3) = th^2\rho_{3y}$$

and

$$I_S(\rho_{3y}, \zeta') \cong \frac{2}{\pi} I_B r\gamma^2(\varphi, \zeta') \frac{1}{\cosh^2(\rho/\Delta\rho_{3y})}; \quad \Delta\rho_{3y} = \frac{\gamma\sqrt{r}}{\pi};$$
$$\Delta\rho_{3x} \to \infty. \tag{42}$$

2.3. *Experiments with spatial solitons in sillenite crystals*

The (1+1)D soliton propagation of laser beams inside photorefractive BSO crystals has been experimentally demonstrated using the set-up shown in Figure 3 [37]. The BSO crystal was 8 mm long and biased by a static electric field along its [001] crystallographic direction which corresponds to the $\mu = 0$ condition. It was simultaneously illuminated by the focused Gaussian signal beam at $\lambda = 514$ nm and by the uniform background beam intensity, I_B. In order to avoid electric discharge in air due to the high static electric fields, up to 40 kV/cm, the crystal was kept in an insulating liquid cell. A laser beam, orthogonally polarized with respect to the background, was focused with a cylindrical lens onto the crystal, providing a (1+1)D light beam, which consists of a light "sheet" with a thickness of 15 μm at the crystal input face. Beyond the crystal, a focusing lens images the output signal beam on a CCD camera with a magnification factor of about 20.

The complete recording of the soliton formation and its propagation is given in Figure 4, where experimental images for several external electric fields and propagation distances are shown. At 0 kV/cm, as well as for 20 kV/cm, the signal beam is enlarged by diffraction. For the 20 kV/cm bias, self-focusing occurs, which leads to a smaller beam width as compared to the 0 bias case, at the 8 mm propagation distance. One can observe that the soliton is formed only for electric fields

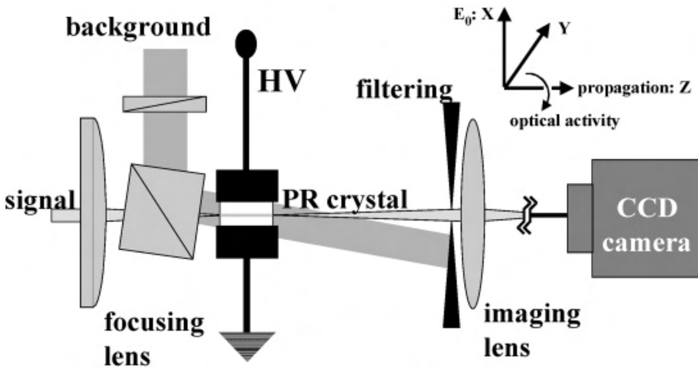

Figure 3. The experimental setup for soliton waveguide formation and observation in PRC.

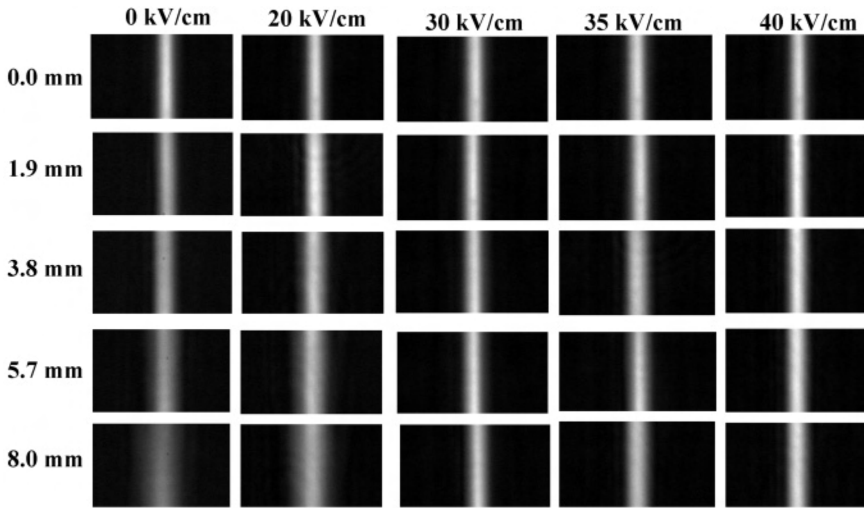

Figure 4. Experimental images of signal wave propagation and soliton formation in a BSO crystal, for several external electric fields – horizontal axis, and propagation distances – vertical axis.

in excess of 30 kV/cm, for which the signal beam maintains the same width along the entire propagation distance.

For electric fields higher than 35 kV/cm, the soliton breathing becomes evident, see Figure 5a, and confirms the above described analytical results [37]. In Figure 5b, the normalized experimental beam waists are shown versus the signal/background

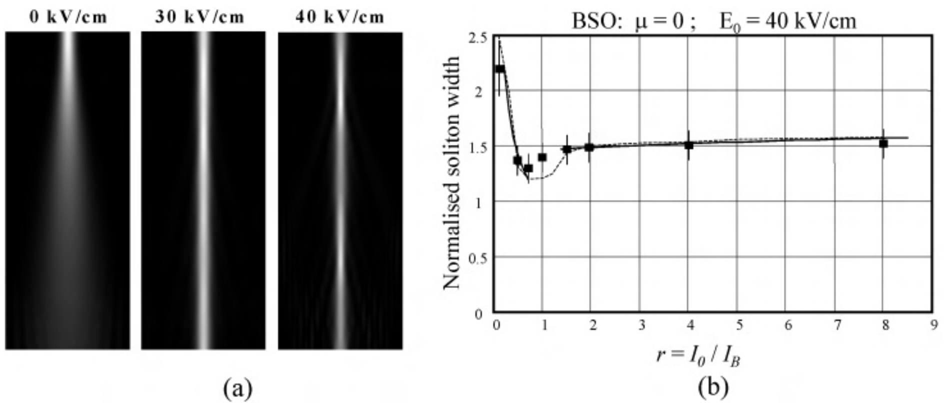

Figure 5. (a) The simulation of signal wave propagation in a BSO crystal, for different external electric fields and large propagation distance, i.e., six diffraction lengths, which show soliton formation and breathing occurrence at 30 and 40 kV/cm). (b) The normalized experimental beam waist versus the signal/background intensity ratio, r, at E_0 = 40 kV/cm, together with the analytical solutions-solid lines, and with the numerical solutions of Eq. (14) – dashed line. The normalized waists scales as $(I_0/I_B)^{1/2}$ for low r = $I_0/I_B < 1$, but scales as $0.06(I_0/I_B)^{1/2}$ + bias, for high $r = I_0/I_B > 2$.

intensity ratio, r, at $E_0 = 40$ kV/cm, together with the analytical solutions (solid lines) and with numerical solutions of Eq. (14) (dashed line). It is interesting to note that the normalized waists scales as $(I_0/I_B)^{-1/2}$ for low I_0/I_B (in this case < 1), while it scales as $0.06(I_0/I_B)^{1/2}$ + bias, for high I_0/I_B (> 2). The numerical simulations derive from the use of a BPM code, which was described in [33].

For the same external electric field, both the numerical integration and the experimental data show a minimum (1+1)D soliton width at $r \approx 0.8$. The experimental data show that the breathing period is not constant, but depends on the experimental conditions, as analytically described. The agreement between the analytical, numerical and experimental data is good.

The first experimental observation of (2+1)D spatial solitons in BSO crystals was reported in refs. [38, 39]. The scheme of the experimental set-up was similar to that shown in Figure 3, except for the background beam, which was expanded using a telescope with a spatial filter, and then sent after a long path, to the sample along its [110] crystallographic direction-denoted Y in the following discussion. It ensures the homogeneous illumination of the crystal and it is incoherent with respect to the signal beam. Two Pockels cells, one for the background and one for the signal beam, are used to adjust the intensities of the two beams and their polarisations. The BSO crystal was again 8 mm long, corresponding to 4.6 difraction lengths along the Z direction, collinear to the [110] crystallographic direction and biased along the [001] direction-X direction with a static electric field variable up to 53 kV/cm.

In Figure 6a, the intensity profiles of the polarization components, X – parallel and Y – orthogonal to the direction of the bias field, are also presented. The X-profiles have been intensified in order to resolve the specific features inside. The Y component, the one that experiences the photorefractive nonlinearity, is strongly confined, driving almost the whole dynamics of the beam. The X component is not confined, but experiences a nonlinear rotation speed, in the center of the beam. The beam central part becomes darker, at 35 kV/cm and brighter again, at 45 kV/cm. At 53 kV/cm, the polarization is homogeneous across the soliton beam and almost the same spatial intensities distributions occur in the Y- and X- components.

In order to analyze completely the soliton polarization dynamics, the Stokes parameters, $S_0 = I_x + I_y$; $S_1 = I_x - I_y$; $S_2 = 2\sqrt{I_x I_y}\cos\phi$; $S_3 = 2\sqrt{I_x I_y}\sin\phi$, have been calculated, at the crystal output plane. Here, $I_x = |A_x|^2$, $I_y = |A_y|^2$ and ϕ is the dephasing of the X- and Y-polarization components. A good three-dimensional visualization of the polarization dynamics can be obtained on the Poincaré sphere with the radius equal to the total signal intensity, S_0 (as shown for example in M. Born and E. Wolf, Principles of Optics, 7th Ed., Cambridge Univ. Press, 1999). In Figure 7, the trajectory of the tip of the polarization vector, defined by the components (S_1, S_2, S_3), is shown with propagation time (distance) as parameter and for different biases.

The dynamics of the S_3 parameter allows one to analyze the final polarization state of the beam. Starting from the equatorial plane, where $S_3 = 0$ and the signal polarization is linear, the polarization trajectory evolves in the Northern hemisphere.

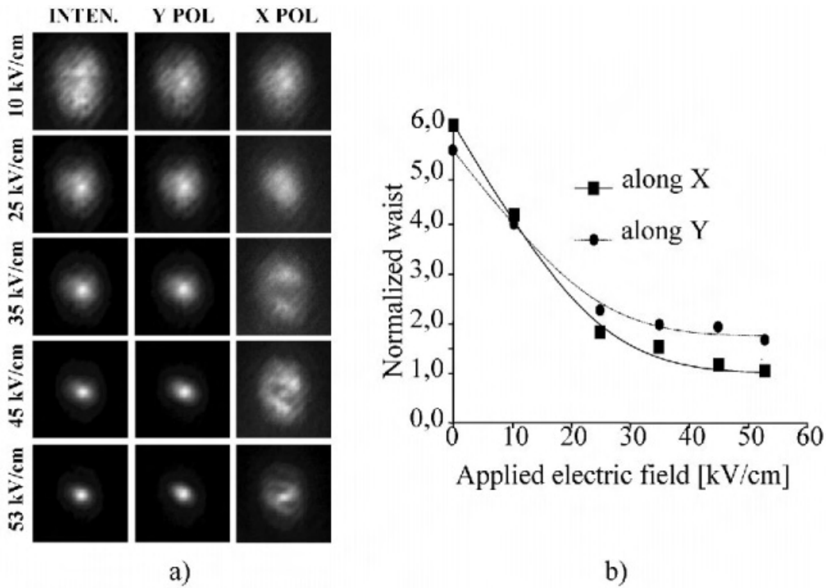

Figure 6. (a) Signal beam total intensity distribution (first column), Y and X component intensity distributions (marked above the corresponding columns) are shown at several external electric fields (biases). (2+1)D spatial solitons in BSO crystals are formed only at 45 kV/cm, when the input and output beam widths are equal. (b) The normalized width of signal beam total intensity in BSO crystal vs. external electric field.

This means that the signal becomes elliptically polarized and with left-handed rotation of the ellipse major axis in the propagation, due to the optical activity of BSO crystals. One can remark that, above 35 kV/cm, the polarization trajectory goes fast, after one loop, to a limit cycle, which characterize a stable, almost-periodical behavior of the soliton polarization dynamics. For this stable behavior, the values of S_3 parameter are concentrated in a limited interval, corresponding to the final limit cycle of the soliton polarization state.

The correspondence between the experimental and numerically calculated Stokes parameters is good, see Figure 8, showing a slight discrepancy only for biases around 20-25 kV/cm. These discrepancies are mainly connected to the process of the polarization homogenization across the beam profile. In fact, the acceleration of the polarization rotation is not constant across the beam but depends on its profile and needs a high bias or a longer propagation to homogenize across the beam. Thus, for bias values between 15 and 40 kV/cm, the exact determination of the beam polarization state is difficult.

The above studied solitons, which are self-created dynamic optical waveguides, and their interactions are more general, have additional controllable features than the conventional ones, due to the presented polarization dynamics.

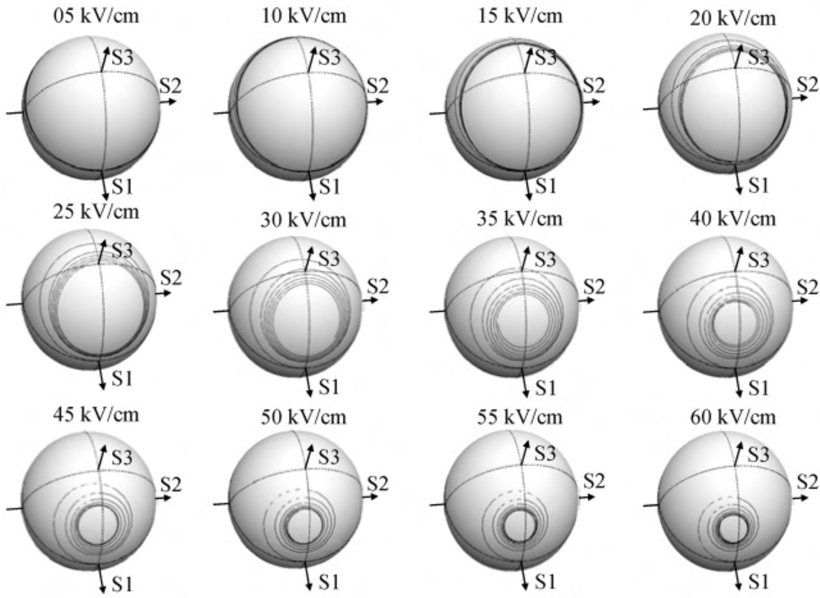

Figure 7. The dynamics of the polarization state of the signal beam on the Poincaré sphere vs. propagation time (distance) and for several external electric fields.

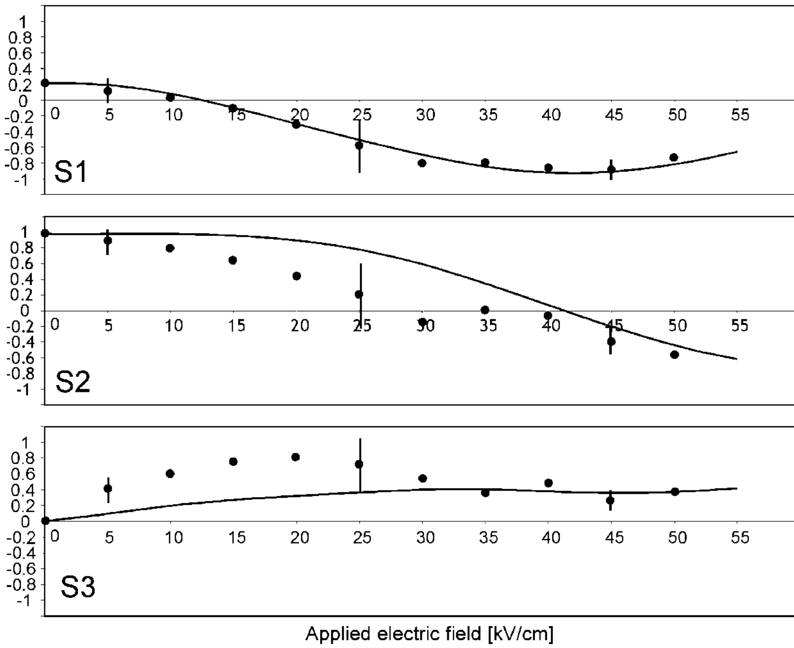

Figure 8. The experimental values of the Stokes parameters (the points), at the output plane of the crystal and their numerical calculations (the lines) versus the external electric field.

3. Dynamic gratings in PRC

3.1. *Two-wave mixing*

In two-wave mixing, two light waves diffract on the dynamic grating induced by their mutual interaction in a non-linear material. When switching off the light beams, the dynamic grating will disappear after a lifetime that depends on the specific properties of the non-linear material and the recording process, in contrast to a permanently recorded grating. For a linear recording process, the diffraction in the phase gratings is characterized by the numerical values of two parameters, namely the phase correlation of the diffraction orders, $Q = 2\pi\lambda d/n\Lambda^2$ and the amplitude of the phase modulation, $\varphi = 2\pi\Delta nd/\lambda^2$ [40]. λ is the incident light wavelength, d is the crystal thickness, n is the refractive index of the crystal and Δn is the modulation amplitude of the refractive index. These parameters can be used also in the case of weak nonlinearity of the recording materials (PRC).

In the Bragg diffraction regime, characteristic for thick gratings, $Q \geq 10$ and $Q/\varphi \geq 10$ [41, 42]. Due to the Bragg condition, only one diffracted beam (first-order) appears for each incident beam. The interference of the zero diffraction order, i.e., the non-diffracted light of one beam, with the first diffraction order of the other beam results in an energy transfer between the interfering beams. In the Raman-Nath diffraction regime, characteristic for thin gratings, $Q \geq 0.5$ and $Q \times \varphi \leq 1$. In this case, many diffraction orders may appear for each incident beam [43–45] and their number and intensity depend on the phase modulation of the grating.

Two-wave mixing in photorefractive crystals for strong unequal intensity beams has been intensively studied in the past [4, 6, 8, 40, 46, 47]. In these works, the thick dynamic gratings in the Bragg regime were mostly investigated.

When the intensities of the incident beams are strongly unequal, the induced phase grating is *harmonic*, like an incident light interference pattern. For small angles between the incident beams, the l diffraction order of one beam is superimposed and is mixed with the $(l + 1)$ diffraction order of the other beam. For incident beams with comparable intensities, the modulation of the interference pattern is large, i.e., close to 1 and the phase grating induced in photorefractive crystals becomes *inharmonic* [48–53]. In this case, for dynamic photorefractive thin gratings, an additional mixing of diffraction orders produced by the grating harmonics may appear [54–57].

In the following section, laser beam self-diffraction in inharmonic and harmonic photorefractive dynamic gratings, at small angle between the incident interfering beams, is presented [58, 59]. The results can be used in real-time holography and interferometry, optical amplification, image and beam processing, optical memory, optical computing and optical interconnects [5].

3.2. *Inharmonic thin gratings*

To model the wave mixing in thin photorefractive gratings, we consider the harmonic fringe pattern produced by the interference of two beams, S and R, with complex

amplitudes $A_S = A_{S0}e^{iK_{xS}x}$, $A_R = A_{R0}e^{iK_{xR}x}$, which are incident on a photorefractive crystal. The spatial distribution of the light intensity in this pattern is given by:

$$I = I_{R0} + I_{S0} + 2\sqrt{I_{R0}I_{S0}} \cos (Kx) = I_0 \left[1 + m \cos \left(\frac{2\pi x}{\Lambda} \right) \right], \tag{43}$$

Here K_{xR} and K_{xS} are the wave numbers of the incident beams, A_{S0}, A_{R0} are their amplitudes, respectively, I_{S0} and I_{R0} are the light intensities of the incident beams, $I_0 = I_{S0} + I_{R0}$ is the average light intensity of the fringe pattern, and Λ is the fringe spacing. $K = |\mathbf{K}| = 2\pi/\Lambda$ is the wave-number of the interference pattern and $\boldsymbol{K} = \boldsymbol{K}_{xR} - \boldsymbol{K}_{xS}$ is the wave-vector. m $= 2\sqrt{p}/(1 + p)$ is the fringe contrast and $p = I_{S0}/I_{R0}$ is the beam intensity ratio.

The diffusion space charge field, E_{sc}, generated in the photorefractive crystal without external electric field, is inharmonic [48]:

$$E_{sc} = \frac{m_1 E_D \sin (Kx)}{1 + m_1 \cos (Kx)} ; \tag{44}$$

where E_D is the diffusion field and m_1 is the effective modulation ratio inside the crystal, given by [40]:

$$m_1 = \frac{m}{1 + \Sigma} ; \tag{45}$$

$\Sigma = \sigma_d/\sigma_p$ is the ratio of dark conductivity, σ_d and photoconductivity, σ_p. Usually, $\sigma_d \ll \sigma_p$, thus $m_1 \approx m$. If the values of the fringe contrast and fringe spacing allow a space-charge field to be sustained by the traps concentration of the crystal, the inharmonicity of E_{sc} is determined by Eq. (44) alone. The Fourier series of the right-hand term of Eq. (44) is [48]:

$$E_{sc} = -2E_D \sum_{h=1}^{\infty} \left[\left(\frac{1}{m^2} - 1 \right)^{1/2} - \frac{1}{m} \right]^h \sin (hKx) = -2E_D \sum_{h=1}^{\infty} (-\sqrt{p})^h \sin (hKx), \tag{46}$$

which shows that the relative amplitudes of the Fourier components of E_{sc} depend on the contrast m only. Thus the inharmonicity of E_{sc} becomes significant for large values of the contrast.

The space charge field given by Eq. (46), yields an inharmonic spatial modulation of the refractive index of the photorefractive crystal by the Pockel's, linear electro-optic effect:

$$\Delta n = \frac{1}{2} n^3 r_{eff} E_{sc} = \sum_{h=1}^{\infty} (\Delta n)_h \sin (hkx). \tag{47}$$

In Eq. (47), r_{eff} is the effective electro-optic coefficient of the photorefractive crystal and $(\Delta n)_h = n^3 r E_D (-\sqrt{p})^h$. Eq. (47) shows that for a harmonic fringe pattern, incident on a photorefractive crystal, the resulting phase grating is inharmonic.

For small modulation depths, $m \ll 1$, only one Fourier component of the space-charge field needs to be taken into account. In this case, the space-charge field distribution is harmonic, and the refractive index grating has the same spatial frequency and de-phasing of $\pi/2$ with respect to the fringe distribution [56, 57].

When E_{sc} and the refractive index grating does not have the sinusoidal form of the incident interference pattern, i.e., for an inharmonic grating, the recording becomes nonlinear [56, 57]. In this case, E_{sc} has a spectrum of spatial harmonics with frequencies that are multiples of the incident pattern. The necessary number of harmonics to be considered for a correct description of the grating depends on the nonlinearity strength [60]. For sillenites crystals, characterized by very small electro-optic coefficients, the diffraction regime is controlled only by the value of Q. For a given crystal and laser wavelength, Q can be modified by changing Λ and consequently, the diffraction regime can be controlled by Λ, i.e. by the angle between the interfering beams.

To a first approximation, one can take into consideration only the fundamental grating and the second spatial harmonic, discarding the contribution of higher spatial harmonics. Thus, the interference pattern in the photorefractive crystal produces the space charge electric field [56, 57]:

$$E_{sc} \approx E_{sc1} \cos\left[Kx + \left(\frac{\pi}{2}\right)\right] + E_{sc2} \cos\left[2Kx + \left(\frac{\pi}{2}\right)\right], \tag{48}$$

Here E_{sc1} and E_{sc2} are the electric field amplitudes of the first and the second spatial harmonics, respectively. The phase modulations corresponding to these harmonics are:

$$\varphi_1 = \frac{\pi d r n^3 E_{sc1}}{\lambda}; \quad \varphi_2 = \frac{\pi d r n^3 E_{sc2}}{\lambda}. \tag{49}$$

The transmission, T, of the thin phase grating, produced by the space charge electric field (48), is given by:

$$T = \exp i\left\{\varphi_1 \cos\left[Kx + \left(\frac{\pi}{2}\right)\right] + \varphi_2 \cos\left[2Kx + \left(\frac{\pi}{2}\right)\right]\right\}. \tag{50}$$

Since the incident optical field can be written as:

$$(A_S + A_R)_{in} = A_{S0} \exp(iK_S x) + A_{R0} \exp(iK_R x), \tag{51}$$

the optical field after the grating takes the form:

$$(A_S + A_R)_{out} = (A_S + A_R)_{in} \times T, \tag{52}$$

Considering now $\varphi_1, \varphi_2 \ll 1$, the following approximations hold:

$$\cos(\varphi \sin Kx) \approx J_o(\varphi) \quad \text{and} \quad \sin(\varphi \sin Kx) \approx 2J_1(\varphi) \sin Kx. \tag{55}$$

where $J_l(\varphi)$ is the Bessel function of the first kind and l-th order. One can further approximate $J_0(\varphi) \approx 1$; $J_1(\varphi) \approx \varphi/2$, to obtain finally for the output field:

$$(A_S + A_R)_{out} = \left[A_{S0} + A_{R0}\frac{\varphi_1}{2}\right]\exp(iK_S\, x) + \left[A_{R0} - A_{S0}\frac{\varphi_1}{2}\right]\exp(iK_R\, x) + \left[A_{S0}\frac{\varphi_1}{2} + A_{R0}\frac{\varphi_2}{2}\right]\exp[i(K_S - K)x] + \left[-A_{R0}\frac{\varphi_1}{2} - A_{S0}\frac{\varphi_2}{2}\right]\exp[i(K_R + K)x] + \left[A_{S0}\frac{\varphi_2}{2}\right]\exp[i(K_S - 2K)x] + \left[-A_{R0}\frac{\varphi_2}{2}\right]\exp[i(K_R + 2K)x]. \tag{54}$$

The amplitudes of the first self-diffraction order of the beams S and R, in the third and the fourth terms of Eq. (54), are not affected by higher harmonics of the inharmonic phase grating from Eq. (50). In the direction of these self-diffraction orders, only the first and second harmonic of the phase grating can diffract the incident optical field. The assumption φ_1, $\varphi_2 \ll 1$ leads to a dominant role of the first diffraction order of each harmonic.

The important result of this analysis is that each self-diffraction order is the result of an order mixing produced by the linear diffraction of the incident beams on two successive harmonics of the grating.

The amplitudes of the first Fourier harmonics of the space-charge field can be calculated from Eq. (46):

$$E_{sc1} = -2E_D(-\sqrt{p}) = 2E_D\sqrt{p}, \quad \text{and} \quad E_{sc2} = -2E_D(-\sqrt{p})^2 = -2E_D p. \tag{55}$$

When $A_{S0} = A_{R0}$, m and p are equal to 1 and the amplitudes of all Fourier components of E_{sc} are equal, though with alternating signs. In this case, the amplitudes of the first self-diffraction order of the beams S and R, are given by:

$$A_{S,\,1} = \frac{1}{2}A_{S0}(q_1 + q_2) = \frac{1}{2}A_{S0}\frac{\pi d}{\lambda}rn^3(2E_D - 2E_D) = 0,$$

$$A_{R,\,1} = -\frac{1}{2}A_{S0}(q_1 + q_2) = 0. \tag{56}$$

Similarly, one can show that the amplitudes of all the orders of self-diffraction for the beams S and R are zero, when the modulation index of the grating is $m = 1$.

This model of self-diffraction in thin gratings was tested in an experimental study in inharmonic gratings induced in a photorefractive $Bi_{12}TiO_{20}$ (BTO) crystal, with $m = 1$ [55]. The experimental set-up is shown in Figure 9.

A linearly polarized He-Ne laser beam with $\lambda = 632.8$ nm, was split into two beams, which were superimposed in a BTO crystal of thickness $d = 8.6$ mm, inducing

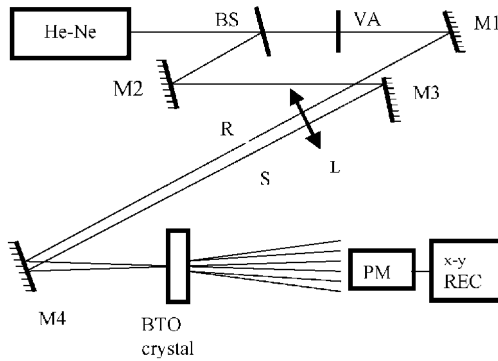

Figure 9. The experimental set-up for the study of self-diffraction in inharmonic photorefractive thin gratings.

a dynamic phase grating. The angle between the interfering beams was $\beta = 7'40''$, leading to a grating spatial period of $\Lambda = 0.285$ mm. With this spatial period, the self-diffraction is in the Raman-Nath regime. To ensure $m = 1$, the power of the incident beams was set to $P_{inc, R, S} = 2.4$ mW by a variable attenuator (VA). The power of the self-diffraction orders and their temporal evolutions have been monitored with a power-meter (PM) and an x-y recorder (x-y REC).

The temporal dependencies of the first, second and third self-diffraction orders of one incident beam were measured and recorded. The temporal evolution of the first two self-diffraction orders is shown in Figure 10 a–b. The third order has a similar evolution [58].

The entire dynamics spans 20–25 minutes from the beginning of the grating recording. The time evolution of the self-diffraction orders shows that their power increased to maximum values, after time intervals that are longer, as the self-diffraction orders are higher. After the maxima, the self-diffraction orders strongly decrease and finally vanish, confirming the prediction of the above theoretical model of self-diffraction in thin photorefractive gratings.

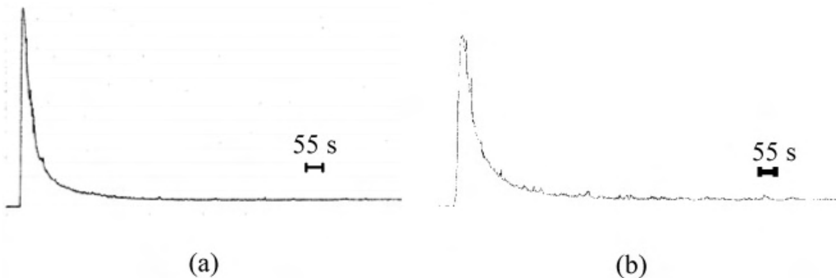

Figure 10. Experimental temporal evolution of the power of the first (a) and second (b) self-diffraction orders in BTO crystals. The scale on the time axis (horizontal) is 1 cm = 55 sec; the signal plotted on vertical axis is proportional to the optical power. The signal is 10 times higher in (b) than in (a).

There are some effects that tend to decrease the modulation index inside the crystal, from the input value $m = 1$. Among them, one can mention the non-zero dark conductivity of the crystal [40], the energy exchange between the beams passing through the crystal, the optical activity of the crystal, the incoherent background produced by internal reflections and light scattering in the crystal and the mechanical stability of the set-up.

These effects were analyzed in [58, 61–63] and they are possible reasons of the remnant non-zero intensity of the self-diffraction orders, in the steady state, for $m = 1$ at the input.

3.3. *Harmonic thin gratings*

In this section, laser beam self-diffraction at small angles (Raman-Nath diffraction regime) on light induced harmonic gratings in rhodium-doped barium titanate ($Rh:BaTiO_3$) and barium titanate ($BaTiO_3$) crystals is presented [59]. Recently, it has been demonstrated that $Rh:BaTiO_3$ crystals have high sensitivity and large two-wave mixing efficiency, for red and near-infrared wavelengths [64–66].

Let us consider that a harmonic fringe pattern, see Eq. (43), illuminates the photorefractive crystal. In the case of low fringe modulation $m \ll 1$, without an external electrical field, the space charge field of Eq. (44) becomes harmonic (see also Eqs. 7, 8) [40]:

$$E_{sc}(x) = m \frac{k_B T}{e} \frac{2\pi\Lambda}{\Lambda^2 + \Lambda_D^2} \sin(Kx) \approx m \frac{k_B T}{e} \frac{2\pi}{\Lambda} \sin(Kx). \tag{57}$$

The modulation amplitude of E_{sc} depends on the diffusion field only when the fringe period obeys $\Lambda \gg \Lambda_D$, corresponding to the case when the trap density is large enough to allow trapping of all the photoexcited charge carriers. This space-charge field creates the refractive index spatial modulation of the photorefractive crystal, as in Eq. (47). The effective electro-optic coefficient of the photorefractive crystal, r_{eff}, depends on the angle of E_{sc} relative to the c-axis, θ_c, and on the angle of propagation of the incident beam relative to the c-axis, $\alpha_{.c.}$ For the extraordinary beam light polarisation, in barium titanate crystals, the effective electro-optic coefficient is [5]:

$$r_{eff}(\theta_c, \alpha_c) = r_{13} \cos\theta_c \cos^2\alpha_c - 2r_{42} \sin\theta_c \sin\alpha_c \cos\alpha_c + r_{33} \cos\theta_c \sin^2\alpha_c. \tag{58}$$

Assuming that the interfering beams are incident symmetrically in the crystal and at a small angle to the crystal normal, $(\beta_i/2) \ll 1$, one can set $\alpha_c \approx 90°$ and $\theta_c \cong 0°$. In this case, from Eq. (58), one obtains $r_{eff}(\theta_c, \alpha_c) \approx r_{33}$.

To a first approximation, the modulation index m, and the amplitude of the refractive index modulation Δn_e (for e – polarisation), are constant for the propagation inside the crystal. In the Raman-Nath regime and for the harmonic grating with $\varphi \ll 1$, and $J^2_{l+1}(\varphi) << J^2_l(\varphi)$, the intensities of the zero and the first self-

diffracted orders, on the side of the stronger beam, R, are given by:

$$I^{(R)}_{0,\,\text{out}} \approx T_a I^{(R)}_{in}, \tag{59}$$

$$I^{(R)}_{1,\,\text{out}} \approx T_a I^{(R)}_{in} J_1^2(\varphi) \approx T_a I^{(R)}_{in} (\varphi/2)^2, \tag{60}$$

where I_{in} is the intensity of the incident beam and T_a is the transmission amplitude of the crystal. The intensity ratio of these orders is then given by:

$$\eta_1 = \frac{I^{(R)}_{1,\,\text{out}}}{I^{(R)}_{0,\,\text{out}}} \approx \frac{\varphi^2}{4} = \frac{1}{4}\left(\frac{2\pi d}{\lambda} \times \frac{1}{2} n^3 r_{eff} E_{sc}\right)^2 \propto \frac{m^2 d^2}{\Lambda^2}, \tag{61}$$

which can be considered as the diffraction efficiency of the self-diffraction process, when materials with different absorption are compared.

The experimental set-up for self-diffraction in Rh:$BaTiO_3$ and $BaTiO_3$ [59] was similar to that used in the study of self-diffraction on inharmonic gratings, shown in Figure 9. The full angle between the incident He-Ne laser beams, R and S, e-polarized, was $\beta = 20'$ in air, corresponding to a grating period inside the crystal of $\Lambda \cong 0.1$ mm.

Several barium titanate crystals, with Rh doping concentration and thickness shown in the Table 3, were used in these experiments.

The diffraction efficiency of Eq. (61) vs. the grating modulation index is shown in Figure 11, for undoped $BaTiO_3$ and for the 120 ppm Rh doped crystals. One can observe that the diffraction efficiency for $BaTiO_3$ crystal varies quadratically with the modulation index. This behavior follows closely the dependence of Eq. (61) up to $m \approx 0.2$. For the 120 ppm Rh doped crystal, the diffraction efficiency increased much faster with m than predicted by Raman-Nath theory, using the value of $r_{33} \sim 100$ pm/V [68] and that measured in the undoped crystal in the same experiments. An unusually high diffraction efficiency of 5% was found for $m = 1$, which is 150 times the corresponding experimental value for the undoped crystal.

In Figure 12, the results of the self-diffraction in $BaTiO_3$ and Rh:$BaTiO_3$ crystals from Table 3 are shown. In these measurements, the ratio between the incident intensities was fixed to $p = 0.0056$ leading to a modulation index of $m = 0.15$.

The diffraction efficiency for different crystals was normalized to the square of their thickness d^2, to ensure comparable values in the graph. The experiments were done for two opposite directions of the c-axis, with respect to the incident beams,

Table 3. The doping concentration, thickness and diffraction parameter Q of the crystals used in self-diffraction experiments in $BaTiO_3$ and Rh:$BaTiO_3$ crystals.

$BaTiO_3$ crystal Rh concentration	Nominally undoped	120 ppm Rh	400 ppm Rh	2400 ppm Rh	3200 ppm Rh
Thickness, d (mm)	2	2.16	5	2.6	3.5
Q	0.33	0.36	0.83	0.43	0.59

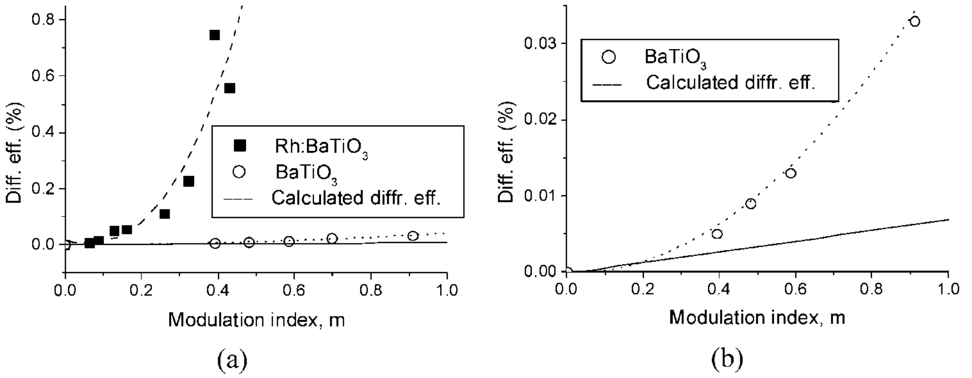

Figure 11. (a) The diffraction efficiency vs. *m*, for $BaTiO_3$ (dashed) and for 120 ppm Rh doped crystal (dotted), with comparable thickness. Raman-Nath quadratic prediction is plotted with a solid line. (b) The diffraction efficiency for $BaTiO_3$ (dashed) and Raman-Nath prediction (solid line) at a more convenient scale.

R and S. In one case, the effective modulation index increased inside the crystal, by the energy transfer from the weak to the strong beam, while in the other case, the modulation index decreased. In Figure 12a, one observes the large increase of the normalized diffraction efficiency with Rh-concentration in the crystals. The crystal with a maximum concentration of 3200 ppm showed a decrease and very different values of the diffraction efficiency for the above mentioned orientations of the c-axis. This difference may be attributed to the very strong fanning of the beams, which is observed inside this crystal. All other crystals yielded a monotonic increasing dependence of the diffraction efficiency with Rh-concentration and similar values of the diffraction efficiency for the opposite orientations of the c-axis.

Due to the differences in the ionization cross-sections of the charge states involved, an additional absorption grating could be induced in the photorefractive crystal. The presence of the absorption grating in two-beam coupling experiments in $BaTiO_3$ was previously reported [69, 70]. In $BaTiO_3$ crystals, the refractive index grating can be eliminated if the c-axis of the crystal is aligned perpendicularly to the plane of incidence of the interfering beams ($\theta_c = 90°$, $\alpha_c = 90°$). For this geometry, r_{eff} and the change in the refractive index are zero, see Eq. (58), independently of the polarization of the incident beams. This experimental geometry was used to observe and evaluate the contribution of a possible absorption grating in the unusually high diffraction efficiency reported in Rh-doped barium titanate crystals [59]. The experiment has been performed for both polarizations, extraordinary and ordinary states of the incident beams, for all Rh:$BaTiO_3$ crystals in Table 3. In all situations, the self-diffraction orders were not observed for the entire range of modulation index *m*. This experiment showed that the contribution of a possible absorption grating to the self-diffraction efficiency is negligible. Thus, the large differences in the diffraction efficiency between the Rh-doped and the undoped crystals are due to other effects.

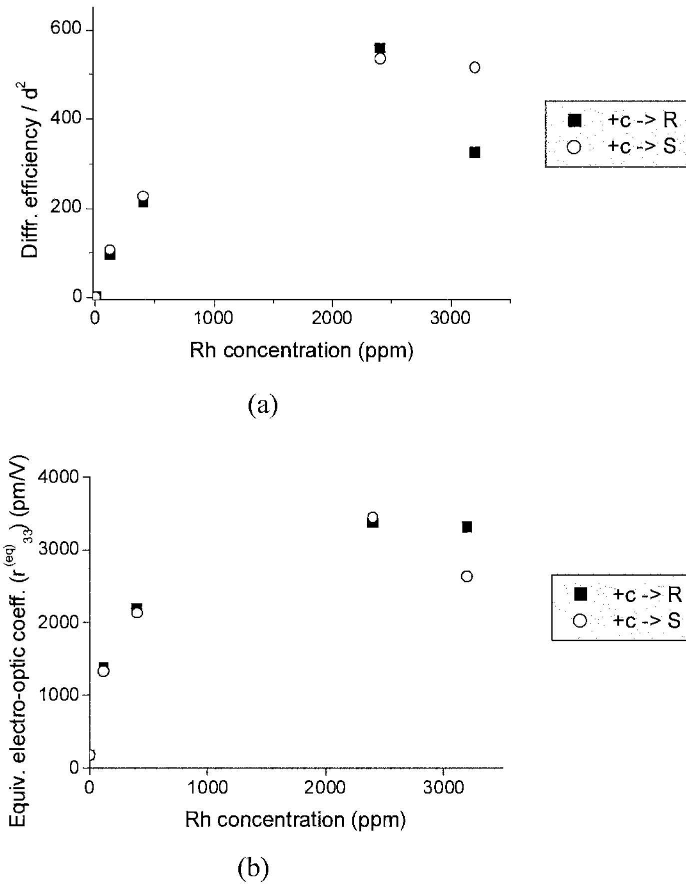

Figure 12. (a) The normalized diffraction efficiency for barium titanate crystals with various Rh concentrations. (b) The "equivalent" electro-optic coefficient $r^{(eq)}{}_{33}$, of $Rh:BaTiO_3$ vs. Rh-doping concentration obtained from self-diffraction experiments.

In the case of low fringe modulation $m \ll 1$, for an appropriate crystal c-axis orientation, amplification of the weak beam occurs. However, in the Raman-Nath self-diffraction regime, set by a large grating period Λ, the gain coefficient [5, 8, 45]:

$$\gamma_a \approx \frac{(2\pi)^2 n^3}{\lambda} \times \frac{k_B T}{e} \times r_{eff} \times \frac{1}{\Lambda} = \frac{4}{m}\sqrt{\eta_1}, \tag{62}$$

is small and the intensity of the weak beam is expected to be slightly increased.

The value of the gain coefficient, calculated using experimental diffraction efficiency data for 120 ppm $Rh:BaTiO_3$ and Eq. (62), is 2.4 cm^{-1}. This value is much larger than γ_a = 0.2 cm^{-1}, calculated for Λ = 0.1 mm and r_{33} = 100 pm/V [3]. On

the other hand, the results obtained for γ_a, of two-beam coupling in the Bragg regime, for the same crystal [59, 67], are in good agreement with the theoretical predictions. Thus, we can assert that much higher amplifications than expected from the two-beam coupling theory are possible in self-diffraction at small angles between the input beams in $Rh{:}BaTiO_3$ crystals.

The diffraction efficiency from Eq. (61) or alternatively, the gain coefficient from Eq. (62), can be taken for calculating an “equivalent” electro-optic coefficient, $r^{(eq)}{}_{33}$, using the experimental data of self-diffraction at small angles between incident beams. The dependence of this parameter on Rh concentration, for the crystals in Table 3, is shown in Figure 12b. In this graph, the “equivalent” electro-optic coefficient shows similar values for both orientations of the c-axis, except for the case of the highest doped crystal, for which the differences are due to the strong fanning observed in this crystal.

4. Dynamic gratings and adaptive interconnection by double phase conjugation in PRC

4.1. *Double phase conjugation (DPC)*

Optical phase conjugation is a nonlinear process that can generate a time-reversed replica of an incident light wave [5, 6, 9] and plays an important role in adaptive optics for dynamic correction of the disturbed wavefronts. Photorefractive materials may be used for efficient optical phase conjugation of wavefronts at very low light intensities thus showing a great potential for adaptive laser beam coupling and interconnections [5, 71, 72].

Initially, optical phase conjugation in PRC was obtained in four-wave mixing configurations. In these cases, two counter-propagating beams were pumping the crystal region, in which a signal (third) beam was diffracted by the generated dynamic gratings into a conjugate (fourth) beam [9]. More recently, self-pumped phase conjugation (SPPC) in PRC, in which a single incident laser beam is responsible for the generation of the conjugated wavefront, was demonstrated [68]. Another important nonlinear process in photorefractive optics is the mutually pumped phase conjugation (MPPC), in which two incident laser beams mutually pump the photorefractive material and produce two phase conjugate wavefronts [5]. Several configurations of MPPC have been demonstrated and investigated, namely the Bird-wing, Bridge, British I and II, Double-Phase-Conjugation (called also Double-Phase-Conjugation Mirror (DPCM)), and others [73–80]. The mutual coherence of the two pump beams considerably changes the efficiency of MPPC [81–83]. The DPC configuration (Figure 13a) is the best one for coupling mutually incoherent input beams [81–83]. In a DPC, each conjugated beam is generated by the other pump beam by diffraction on a common shared grating induced in PRC, and not by each pump beam itself. This fact is essential for finding and tracking a laser source by another one in a bi-directional link. Moreover, the DPC reconfigures itself, if small direction changes of incident beams occur, within some specified angular

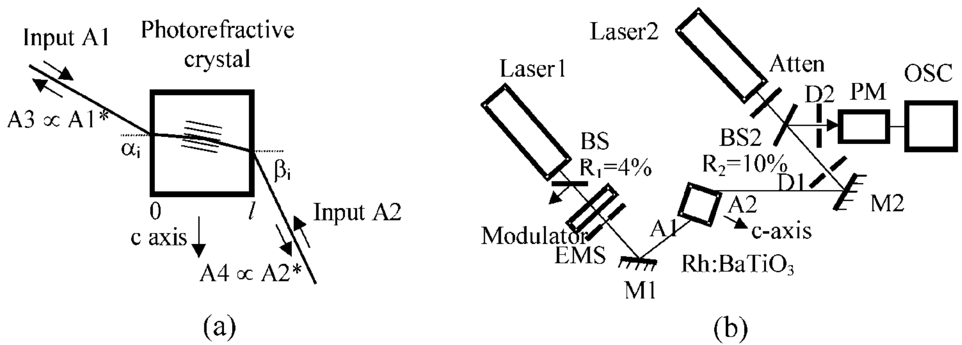

Figure 13. (a) Adaptive coupling using DPC configuration in a photorefractive crystal; (b) The experimental setup for coupling of two lasers by DPC in Rh:$BaTiO_3$.

range in the crystal (Figure 13a). The phase conjugation provided by a DPC is an all-optical solution to the problem of bi-directional adaptive interconnection of two independent laser sources, ensuring the finding of each source by the other one and their reciprocal tracking in a very robust link. The coupling of two or more incoherent laser beams is important for optical communications, optical interconnects and multi-beam coupling into an optical fiber.

Among photorefractive materials, Rh:$BaTiO_3$ crystal is one of the most interesting due to its large electro-optic coefficient and good sensitivity in the red and near-infrared [67, 84] with promising applications in laser diode pumped DPC. Here, results of a study [85] on adaptive interconnection of two lasers using DPC in Rh:$BaTiO_3$ crystals are presented.

4.2. *Efficient adaptive coupling of two lasers by DPC*

In the DPC configuration, see Figure (13a), the beams A1 and A2, from two separate lasers of the same frequency are incident on the opposite faces of a photorefractive crystal with c-axis oriented as shown in Figure (13). Because the input beams are mutually incoherent, they cannot couple directly with each other in the crystal. Randomly scattered light, fanned from beam A1, travels across beam A1, coherently couples with this beam and writes a multitude of refractive index beam fanning gratings in the photorefractive crystal. A similar process occurs with beam A2, i.e., light fanned from this beam coherently couples with beam A2 and writes another set of beam-fanning gratings. Each input beam tends to erase most of the beam-fanning gratings produced by another.

However, A2 is incident at Bragg angle for a small set of beam-fanning gratings produced by A1. The diffracted beam is A3, which is the phase conjugate replica of the beam A1. A3 efficiently couples with beam A2, since they are mutually coherent. The result of a similar diffraction process of the beam A1 on the beam-fanning gratings induced by A2 is the beam A4, which is the phase conjugated replica of A2. Since the gratings written by two pairs of beams A3, A2 and A4, A1,

respectively, have an optimal overlapping, the conjugated beams A3, A4 grow in strength reinforcing a common shared grating (SG), which fulfills the Bragg diffraction condition for both input beams. The other beam-fanning gratings are washed out. In this way, diffraction from the common grating is responsible for the generation of A3 and A4, phase conjugated beams of the mutually incoherent input beams, A1 and A2, respectively.

The overall efficiency of the DPC configuration is evaluated using two parameters: *the phase conjugate reflectivity*, R^*, for the two input beams and *the coupling transmission efficiency*, T, for these beams. With the notations used in Figure (13a) for the beams, these parameters are defined as the following ratios of the corresponding beam powers:

$$R_1^* = \frac{P_{A3}(0)}{P_{A1}(0)}, \quad R_2^* = \frac{P_{A4}(l)}{P_{A2}(l)}, \tag{63}$$

$$T_1^* = \frac{P_{A4}(l)}{P_{A1}(0)}, \quad T_2^* = \frac{P_{A3}(0)}{P_{A2}(l)}, \tag{64}$$

$P_{A1}(0)$, $P_{A2}(l)$ are the powers of the input beams A1 and A2, incident on the opposite sides of the crystal, and $P_{A3}(0)$, $P_{A4}(l)$ are the powers of the conjugated beams A3 and A4, respectively. An experimental set-up, used to study the interconnection of two low power He-Ne or diode lasers, which are mutually-incoherent, by DPC, in Rh:$BaTiO_3$, is shown in Figure (13b) [85]. The input beams, A1 and A2, are e-polarized to take advantage of the maximum electro-optic coefficient of the crystal. The power of the input beams was P_{A1} = 2.55 mW, P_{A2} = 1.35 mW and their diameter, 1.2 mm at $1/e^2$ of the maximum power level. A fraction of the beams A3 and A4, conjugated to the input beams A1 and A2, is extracted with the beam splitters BS1 and BS2, respectively. A power-meter (PM) and an oscilloscope (OSC) do the measurement and the monitoring of the temporal evolution of the conjugate beams. Two apertures (D1 and D2), with diameters equal to the incident laser beams are placed in the set-up in order to measure only the conjugated beams, blocking the contribution of any other diffracted components and of stray scattered light. A shutter (EMS) is used to switch on and off the beam A1. The Rh:$BaTiO_3$ crystal used in [85] had the dimensions 5 × 5 × 5 mm with a 400 ppm Rh doping concentration. The small signal absorption coefficient, measured with a low intensity e-polarized probe beam, was α_o = 1.4 cm^{-1}. The optimum incidence angles of the two input beams for DPC were found at α_i = 30°30′, for the beam A1 and β_i = 60°30′, for the beam A2, ensuring a crossing angle of the beams, inside the crystal, of 171°.

4.3. *Phase conjugate reflectivity and the coupling transmission efficiency*

In Figure 14, the time evolution of the conjugated beam (A4) power, for different input beam (A2) powers is shown [85].

In these recordings, at time $t = 0$, the beam A2 is unblocked and at a time

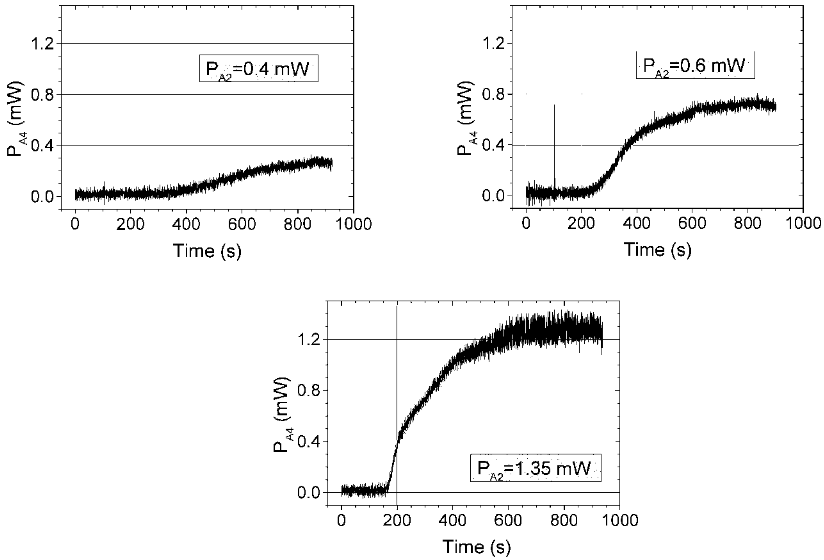

Figure 14. The time evolution of the conjugated beam (A4) power.

t = 100s the beam A1 is switched on, so that growth of the common shared grating (SG), which ensures a coupling channel, can start. A delay occurs between the moment when both beams are switched on and the beginning of SG growth, due to the necessary fanning development and the SG creation. In Figure 14, one can observe that the coupling channel more rapidly starts to grow at higher powers of the beam A2.

The phase conjugate reflectivity $R_2^* = P_{A4}/P_{A2}$, for the weaker input beam A2, and the coupling transmission efficiency of the DPC device, $T_1 = P_{A4}/P_{A1}$, for the stronger beam A1 were measured. The functions R_2^* and T_1 vs. A2 beam power are shown in Figure 15 a,b. The second parameter is very important for an interconnection, since it measures the efficiency of signal transfer between one light source channel to the other. In Figure 15, one can observe that the maximum coupling transmission efficiency reaches ~50%, at maximum power of A2, with a corresponding phase conjugate reflectivity of 95%, for a ratio of the input beams powers of 1.9.

The maximum phase conjugate reflectivity obtained in this experiment was 121% for input beams ratio of 4.25, with a 29% coupling transmission efficiency [85]. These parameters are probably the best in all experiments for bi-directional coupling of incoherent laser beams by phase conjugation in Rh:$BaTiO_3$ crystals, using a similar configuration [84] or bird-wing configuration [89]. In ref. [89], the coupling transmission efficiency was 6%, a typical value expected for this configuration. In the ref. [84] was reported 26% maximum coupling transmission efficiency with 80% reflectivity in DPC at 800 nm, using a Rh:$BaTiO_3$ crystal with the absorption coefficient for this wavelength, $\alpha_0 = 1.4$ cm^{-1} (similar to the crystal used in the set-up from Figure 13b).

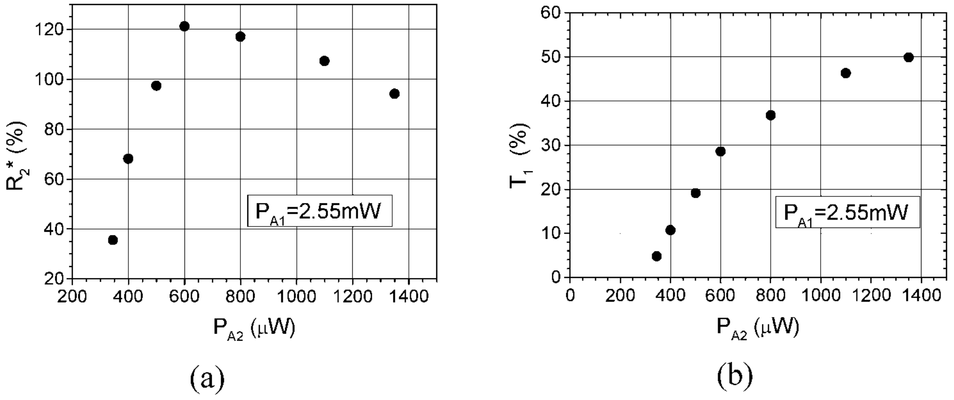

Figure 15. The efficiency of the DPC device: (a) the phase conjugate reflectivity, $R_2^* = P_{A4}/P_{A2}$; (b) the coupling transmission efficiency, $T_1 = P_{A4}/P_{A1}$.

To use this efficient laser coupling in a bi-directional link, we checked the possible presence of the gratings, which are induced by each incident beam by its own back-scattered light [85]. For the interconnection, these gratings lead to cross-talk (i.e. components of signal 1 are transferred into the signal 2 and vice versa), which affects negatively the performance [81, 83]. The experimental results from [85] show clearly that these gratings were not significant in the coupling and the conjugate of each input beam was produced by the other input beam only.

To evaluate the coupling efficiency of the link between the lasers, provided by the DPC in Rh:$BaTiO_3$, when only the SG is present, a simple theoretical model of DPC neglecting absorption [76] can be used. In this case, the phase conjugate reflectivity and the coupling transmission efficiency were calculated, by solving analytically the coupled wave equations that describe the spatial evolution of the input and conjugated beam amplitudes. R^* and T depend on the photorefractive coupling strength, $\gamma_a l$, which is the product of the photorefractive coupling coefficient, γ_a, and the interaction length l, and on the ratio of the input beam powers, $q = P_{A1}/P_{A2}$, for equal c.w. laser beam widths. In Rh:$BaTiO_3$ crystal, with no external electric field, the coupling constant is real:

$$\gamma_a = \frac{2\pi n_1}{\lambda \cos\theta}, \tag{65}$$

where λ is the wavelength of the incident light, n_1 is the amplitude of the refractive index modulation produced by the photorefractive effect and 2θ is the angle between the coupling beams inside the crystal.

Weiss, Sternklar and Fischer [76], found that T is symmetric and given by:

$$T_1 = T_2 = T = \frac{1}{4}[a^2(q^{-1/2} + q^{1/2}) - (q^{-1/2} + q^{1/2})^2], \tag{66}$$

where the parameter a is related to the coupling coefficient, γ_a, by the transcendental equation:

$$\tanh(\gamma_a l a/4) = a \tag{67}$$

In the DPC process, the phase conjugate reflectivities for the two incident beams are [47]:

$$R_1^* = T/q, \quad R_2^* = Tq. \tag{68}$$

The operation range of the DPC configuration is set by the following limits of q:

$$\left(\frac{1+a}{1-a}\right)^{-1} < q < \left(\frac{1+a}{1-a}\right). \tag{69}$$

Solving graphically the transcendental equation (Eq. 67), the parameter a is obtained for different coupling strengths, (al [85]. Figure 17 shows plots of the coupling transmission efficiency, T of Eq. (66) and the phase conjugation reflectivity R_2^* of Eq. (68) versus q, together with the experimental results from [85]. Comparing the theory with the experiment, the coupling strength of the crystal in the DPC configuration is found by best fit: $\gamma_a l = 5.2$. The theoretical curves show that *the maximum values for T* and R^* cannot be attained simultaneously and provide the range of the ratio q for DPC operation, for a given coupling strength, $\gamma_a l$. For $\gamma_a l = 5.2$, the maximum transmission efficiency predicted by theory is $T \sim 55\%$ for $q \sim 1$. The experimental values of T were limited in [85] by the available laser power (P_{A2}) to a maximum value of ~50%, for $q = 1.9$, see Figure 15(b). This value is well supported by the theoretical curve for $\gamma_a l = 5.2$, see Figure 16(a). The maximum phase conjugate reflectivity given by theory for $\gamma_a l = 5.2$ is 125% at $q \sim 3.6$. The maximum value of R_2^*, measured in these experiments, was about 121%, quite close to the maximum of this theoretical curve, which is rather flat with respect to q, see Figure 16(b).

Eq. (69) limits the operation range of the DPC interconnection from [85] in the interval $0.14 < q < 7.1$, for $\gamma_a l = 5.2$, in agreement with the experimental data from that experiment. Comparing experimental results with the simple analytical expressions for T and R_2^* provided by the DPC theoretical model, is useful for the evaluation of the coupling efficiency and the operation range of DPC interconnection devices. The nonlinear absorption cannot be totally ignored in $Rh:BaTiO_3$, at $\lambda = 633$ nm, and the theoretical modeling is more complicated when accounting for it, though there are not yet analytical solutions for this more general case. On the other hand, the results for the coupling strength, obtained by the simple model described above, are consistent with those obtained in two beam coupling experiments in [67].

The upper limit of the coupling transmission efficiency in DPC experiments depends on losses due to absorption in the crystal and Fresnel reflections from the crystal surfaces. Subtracting these losses, it was estimated that the maximum

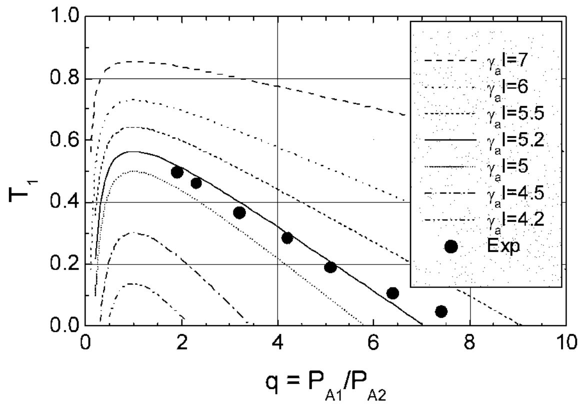

(a)

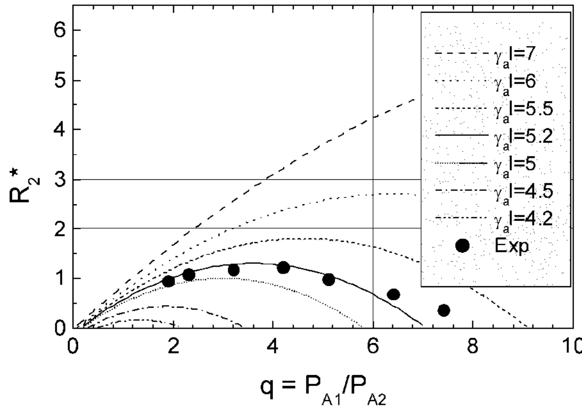

(b)

Figure 16. The coupling transmission efficiency of the phase conjugation process, T_1 (a) and the phase conjugate reflectivity, R_2^* (b), vs. the power ratio, q, of the two incident input beams. Theoretical predictions: dashed and dotted lines; experimental results: dots. The coupling strength of the crystal in the DPC configuration corresponds most closely to $\gamma_a l = 5.2$.

coupling transmission efficiency measured experimentally in [85] is close to the maximum transmission allowed by the crystal.

In DPC configuration, self-pumped phase conjugation (SPPC) can occur for each input beam when part of their fanning reaches a crystal corner and totally reflects, forming an internal loop with a self-conjugation process. This is a parasitic effect for the DPC bi-directional link due to power loss outside the interconnection, which decreases the coupling transmission efficiency T. In the above described DPC theoretical model, Eq. (67) has nontrivial real solutions for $\gamma_a l > 4$. This limit sets the minimum DPC threshold [5, 76]. In comparison, the SPPC

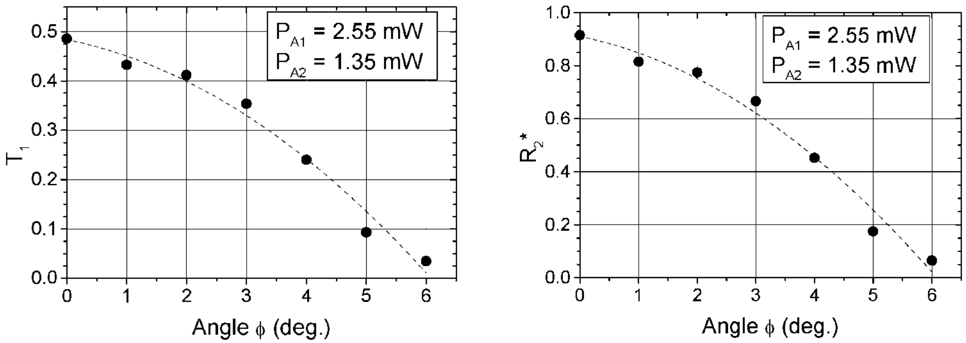

Figure 17. The DPC coupling efficiency versus the angle of A2 beam, ϕ, in the plane (V). The lines are eyes guiding only.

theoretical treatment [90] leads to a coupling strength threshold for this process of $\gamma_a l = 4.68$. Thus, the theoretical results show that DPC is the winner in the competition with SPPC. In DPC experiments, the SPPC process is stronger for the input beam A1, which is incident at a smaller angle with respect to the crystal c-axis [85]. To reduce SPPC, one may displace the incidence position of the beam A1 farther from the crystal corners. We observed also [85] that, when A2 is too weak, the SPPC cannot be suppressed and the DPC onset is no longer observed for long times. This observation is compatible with the DPC range of operation provided by the theoretical prediction (Eq. (69)) and the experimental data from [85].

4.4. *Robustness of the DPC interconnection to beam direction changes and to transmitted information*

The DPC was efficiently used in a large in-plane angular range ~10° [71, 81, 82, 84], as long as good overlapping and low SPPC were ensured. For DPC interconnections of an array of sources, it is important to determine also the alignment requirements for out-of-plane angular changes of the input beams. These changes occur when one input beam is rotated with respect to the plane formed by the other and the crystal c-axis (horizontal plane, H). Rotating the beam A2 in the vertical plane, (V), by an angle ϕ, and preserving the incidence angles (α_i and β_i, respectively) of the beams in the plane (H), T and R_2^* decrease in a similar manner vs. ϕ and become very small for $\phi > 6°$ [85], see Figure 17.

Taking into account the positive and negative values of ϕ, one may realize that DPC can operate efficiently in an angular range of ~10° in the (V) plane. We can conclude that a DPC interconnection is robust for incident beam angular misalignments. This property can be used for DPC interconnections of modern array sources with a large input angular range e.g., centimeter sizes at distances of ~10 cm from the photorefractive crystals.

The most interesting potential application of bi-directional interconnection using DPC is information transmission. This leads to the investigation of the reciprocal

influence of the input beam modulation and the DPC interconnection. This problem was dealt with for the following two cases:

(a) The stronger beam, A1, was modulated after both unmodulated beams created the optimum interconnection channel. A binary modulation source, at 2 kbit/s with 50% duty cycle of a light square wave, was employed. This source provided a strong modulation in which the crystal was illuminated during half the time with only one beam, see Figure 18(a, b) [85]. When the modulation is switched on, at t ~ 500 s, the coupling efficiency does not change, indicating a stable interconnection. Once the interconnection is fully established, the modulation frequency of the input beam can be as high as possible, without optical limitations of the crystal

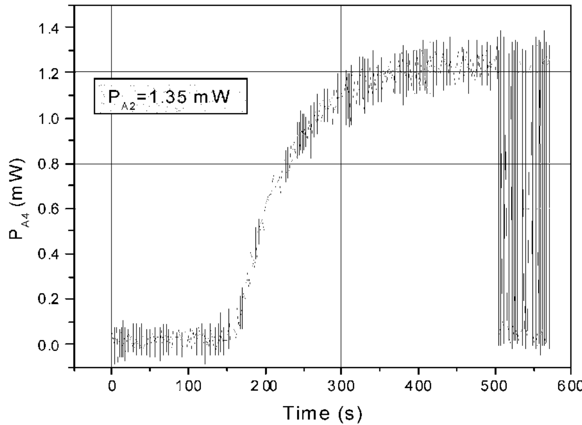

(a)

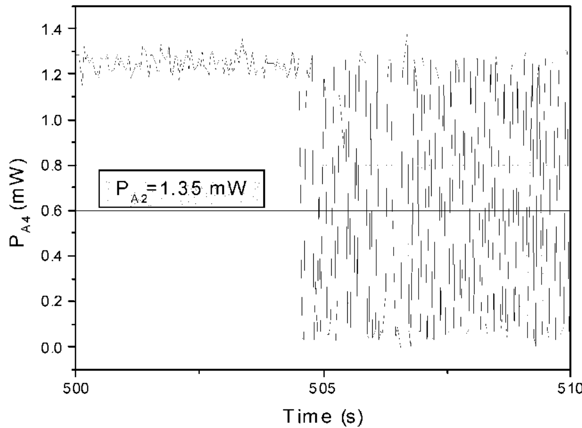

(b)

Figure 18. (a) The influence of the input beam modulation on the coupling transmission efficiency; (b) a magnified view of the modulation switching from graph (a).

parameters. Moreover, the higher the modulation frequency is, the smaller the coupling efficiency change becomes, due to the large time constants of the crystal response, at these low light power levels.

(b) The modulated input beams were introduced together into the crystal from the starting moment of the DPC coupling. In this case, the DPC interconnection develops like in case (a), but with a slightly longer onset and rise time and with a slightly smaller final value of the coupling transmission efficiency.

The influence of the DPC adaptive coupling on the input beam modulation was studied, too, by comparing the waveforms of modulated A1 input beam and of the output A4 beam [85]. No observable changes induced by the DPC channel on these waveforms were found.

5. Conclusions

The photorefractive effect is an important photo-excited nonlinear process, with complex behavior and great potential applications. This chapter developed theoretically and showed the experimental occurrence of spatial solitons by laser beam propagation in photorefractive crystals exhibiting a large optical rotating power and absorption. The soliton polarization dynamics reaches a stable behavior at high external electric fields. These spatial solitons create dynamic waveguides in PRC with controllable parameters and can interact, which is important for optical switching, routing and storage. Two-wave mixing and self-diffraction in dynamic harmonic and inharmonic gratings, induced by lasers in PRC, were thoroughly studied. The high-modulated phase gratings induced in PRC are inharmonic and show significant changes in the self-diffraction spectra. Experimental data, obtained with BTO crystals, are in agreement with the theoretical predictions. In Rh:$BaTiO_3$ crystals, the measured diffraction efficiencies and beam amplifications are one to three orders of magnitude larger than in the case of undoped crystals. This may point to their use in applications as real-time holography, interferometry, storage and interconnections.

Optical phase conjugation in PRC was also described. High phase conjugate reflectivity, high coupling transmission efficiency and robust interconnection of mutually incoherent lasers can be achieved in DPC, using Rh:$BaTiO_3$ crystals.

References

1. A. Ashkin, G. D. Boyd, J. M Dziedzic, R. G. Smith, A. A. Ballman, J. J Levinstein and K. Nassau, A*ppl. Phys. Lett.* **9**, 72 (1966).
2. N. V. Kukhtarev, V. B. Markov, S. G. Odulov, M. S. Soskin and V. L. Vinetskii, *Ferroelectrics* **22**, 949 (1979).
3. P. Gunter, J.-P. Huignard (Eds.), *Photorefractive Materials and Their Applications*, Vol. I and II (Springer Verlag, 1988).
4. M. P. Petrov, S. I. Stepanov and A. V. Khomenko, *Photorefractive Crystals in Coherent Optical Systems* (Springer Verlag, 1991).

5. P. Yeh, *Introduction to Photorefractive Nonlinear Optics* (New York: Wiley, 1993).
6. P. Yeh and C. Gu (Eds.), 'Landmark Papers on Photorefractive Nonlinear Optics', *World Scientific* (1995).
7. D. D. Nolte (Ed.), *Photorefractive Effects and Materials* (Kluwer Academic Publishers, 1995).
8. L. Solymar and D. J. Webb, A. Grunnet-Jepsen, *The Physics and Applications of Photorefractive Materials* (Clarendon Press, 1996).
9. M. Cronin-Golomb, B. Fischer, J. O. White and A. Yariv, *IEEE J. Quantum Electron.* **QE-20**, 12 (1984).
10. F. P. Strohkendl, J. M. C. Jonathan and R. W. Hellwarth, *Opt. Lett.* **11**, 312 (1986).
11. A. M. Glass, D. von der Linde and T. J. Negram, *Appl. Phys. Lett.* **25**, 233 (1974).
12. W. E. Moerner and S. M. Silence, *Chem. Rev.* **94**, 127 (1994).
13. S. M. Silence, D. M. Burland and W. E. Moerner, 'Photorefractive Polymers', in D. D. Nolte (ed.), *Photorefractive Effects and Materials* (Kluwer Academic Publishers, 1995), p. 266.
14. M. Segev, G. C. Valley, B. Crosignani, P. di Porto and A. Yariv, *Phys. Rev. Lett.* **73**, 3211 (1994).
15. M. Segev, M. Shih and G. C. Valley, *J. Opt. Soc. Am.* B **13**, 706 (1996).
16. D. N. Christodoulides and M. I. Carvalho, *J. Opt. Soc. Am. B* **12** 1628 (1995); *Opt. Lett.* **19**, 1714 (1994).
17. B. Crosignani, M. Segev, D. Engin, P. di Porto, A. Yariv and G. J. Salamo, *J. Opt. Soc. Am.* B **10**, 446 (1993).
18. B. Crosignani, P. di Porto, A. Degasperis, M. Segev and S. Trillo, *J. Opt. Soc. Am.* B **14**, 3078 (1997).
19. M. Shih, M. Segev, G. C. Valley, G. Salamo, B. Crosignani and P. di Porto, *Electron. Lett.* **31**, 826 (1995).
20. M. D. Iturbe Castillo, P. A. Marquez Aguilar, J. J. Sanchez Mondragon, S. Stepanov and V. Vysloukh, *Appl. Phys. Lett.* **64**, 406 (1994).
21. M. D. Iturbe Castillo, J. J. Sanchez Mondragon, S. Stepanov, M. B. Klein and B. A. Wechsler, *Opt. Commun.* **118**, 515 (1995).
22. M. Shih, P. Leach, M. Segev, M. H. Garrett, G. Salamo and G. C. Valley, *Opt. Lett.* **21**, 324 (1996).
23. K. Kos, H. Meng, G. Salamo, M. Shih, M. Segev and G. C. Valley, *Phys. Rev.* E **53**, R4330 (1996).
24. Z. Chen, M. Mitchell, M. Shih, M. Segev, M. H. Garrett and G. C. Valley, *Opt. Lett.* **21**, 629 (1996).
25. N. Fressengeas, D. Wolfensberger, J. Maufoy and G. Kugel, *J. Appl. Phys.* **85**, 2062 (1999).
26. D. Wolfensberger, N. Fressengeas, J. Maufoy and G. Kugel, *J. Appl. Phys.* **89**, 2511 (2001).
27. M. Segev, B. Crosignani, G. J. Salamo, G. C. Duree, Jr, P. di Porto and A. Yariv, 'Photorefractive Spatial Solitons', in D. D. Nolte (ed.), *Photorefractive Effects and Materials* (Boston: Kluwer Academic Publishers, 1995), p. 221.
28. B. Crosignani, P. di Porto, M. Segev, G. J. Salamo and A. Yariv, *Riv. del Nuovo Cimento* **21**, 1 (1998).
29. C. Denz, J. Petter, C. Weilnau and M. Ahles, *CLEO/Europe-EQEC Digest, Munich*, 163 (2001); *Proc. SPIE* **4829** (ICO-19, Florence, 2002), p. 513.
30. S. R. Singh and D. N. Christodoulidis, *J. Opt. Soc. Am.* B **13**, 719 (1996).
31. W. Krolikowski, N. Akhmediev, D. R. Andersen and B. Luther-Davies, *Opt. Commun.* **132**, 179 (1996).
32. V. I. Vlad, V. Babin, M. Bertolotti, E. Fazio and M. Zitelli, *OSA Annual Meeting, Santa Clara, 1998, Paper ThCC7*, 143 (1999); *Proc. Romanian Academy* **A1**, 25 (2000).
33. E. Fazio, F. Mariani, A. Funto, M. Zitelli, M. Bertolotti, V. Babin and V. I. Vlad, *J. Optics* **A3**, 466 (2001) and *Proc. SPIE* **4430**, 411 (2001).
34. J. Herriau, D. Rojas, J. P. Huignard, J. Bassat and J. Launay, *Ferroelectrics* **66**, 1 (1986).
35. S. Blair, K. Wagner and R. McLeod, *J. Opt. Soc. Am.* **B13**, 2141 (1996).
36. V. I. Vlad, V. Babin, M. Bertolotti and E. Fazio, *Proc. SPIE* **4430**, 418 (2001).
37. E. Fazio, V. Babin, M. Bertolotti and V. I. Vlad, *Phys. Rev* E **66**, 016605 (2002).
38. E. Fazio, W. Ramadan, A. Belardini, A. Bosco, M. Bertolotti, A. Petris and V. I. Vlad, *Phys. Rev* E **67**, 026611 (2003).

39. E. Fazio, V. Babin, A. Petris, A. Belardini, M. Bertolotti and V. I. Vlad, *Proc. SPIE (ICO-19, Florence)* **4829**, 909 (2002) and *J. Optics* **A** (2003).
40. H. J. Eichler, P. Gunter, D. W. Pohl, *Laser Induced Dynamic Gratings*, Springer Series in Optical Sciences, vol. 50 (Berlin: Springer Verlag, 1985).
41. M. G. Moharam, T. K. Gaylord and R. Magnusson, *Opt. Commun.* **32**, 19 (1980).
42. M. G. Moharam, T. K. Gaylord and R. Magnusson, *Opt. Commun.* **32**, 14 (1980).
43. R. Magnusson, T. K. Gaylord, *J. Opt. Soc. Am.* **67**, 1165 (1977).
44. N. Korneev, D. Mayorga, S. Stepanov, A. Gerwens, K. Buse and E. Kraetzig, *Appl. Phys.* B **66**, 393 (1998).
45. A. Apolinar-Iribe, N. Korneev and J. Sanchez-Mondragon, *Opt. Lett.* **23**, 877 (1998).
46. N. V. Kukhtarev, V. B. Markov, S. G. Odulov, M. S. Soskin and V. L. Vinetskii, *Ferroelectrics* **22**, 949 (1979).
47. S. I. Stepanov and M. P. Petrov, 'Nonstationary Holographic Recording for Efficient Amplification and Phase Conjugation', in P. Gunter and J.-P. Huignard (eds.), *Photorefractive Materials and Their Applications I* (Berlin: Springer-Verlag, 1989)
48. M. G. Moharam, T. Gaylord, R. Magnusson and L. Young, *J. Appl. Phys.* **50**, 5642 (1979).
49. M. P. Petrov, S. Miridonov, S. I. Stepanov and V. Kulikov, *Opt. Commun.* **31**, 301 (1979).
50. T. Y. Chang and P. Yeh, *J. Opt. Soc. Am.* **A3**(13), 33 (1986).
51. E. Ochoa, F. Vachss and L. Hesselnik, *J. Opt. Soc. Am.* **A3**(2), 181 (1986).
52. F. Vachss and L. Hesselnik, *J. Opt. Soc. Am.* **A5**(5), 690 (1988).
53. L. B. Au and L. Solymar, *J. Opt. Soc. Am.* **A7**(8), 1554 (1990).
54. V. I. Vlad, A. Petris and I. Apostol, *Ro. Repts. Phys.* **46**, 586 (1994).
55. A. Petris, I. Apostol and V. I. Vlad, *Proc. SPIE* **2461**, 280 (1995).
56. M. P. Petrov, V. M. Petrov, Y. S. Raptis, L. P. Xu and E. Anastassakis, *J. Appl. Phys.* **79**(6), 2846 (1996).
57. M. P. Petrov, V. M. Petrov, I. S. Zouboulis and L. P. Xu, *Opt. Commun.* **134**, 569 (1997).
58. A. Petris and V. I. Vlad, *Proc. SPIE* **4430**, 460 (2001).
59. A. Petris, M. J. Damzen and V. I. Vlad, *Opt. Commun.* **176**, 223 (2000).
60. E. Serrano, M. Carrascosa and F. Agullo-Lopez, *J. Opt. Soc. Am.* B **13**(11), 2587 (1996).
61. A. Bledowski, J. Otten and K. H. Ringhofer, *Opt. Lett.* **16**(9), 672 (1991).
62. U. van Stevendaal, K. Buse, H. Malz, H. Veenhuis and E. Kratzig, *J. Opt. Soc. Am.* B **15**(12), 2868 (1998).
63. O. Kobozev, S. Shandarov, A. Kamshilin and V. Prokofiev, *J. Opt. A: Pure Appl. Opt.* **1**, 442 (1999).
64. G. W. Ross, P. Hribek, R. W. Eason, M. Garett and D. Rytz, *Opt. Commun.* **11**, 60 (1993).
65. A. Wechsler, M. B. Klein, C. C. Nelson and R. N. Schwarz, *Opt. Lett.* **19**, 536 (1994).
66. M. Kaczmarek and R. W. Eason, *Opt. Lett.* **20**, 1850 (1995).
67. L. Corner, R. Ramos-Garcia, A. Petris and M. J. Damzen, *Opt. Commun.* **143**, 165 (1997).
68. S. Ducharme and J. Feinberg, 'Electro-optic and Photorefractive Materials', in P. Gunter (ed.), *Springer Proceedings in Physics*, vol. 18 (Berlin: Springer-Verlag, 1987).
69. R. M. Pierce, R. S. Cudney, G. Bacher and J. Feinberg, *Opt. Lett.* **15**, 414 (1990).
70. R. S. Cudney, R. M. Pierce, G. Bacher and J. Feinberg, *J. Opt. Soc. Am.* B **8**, 1326 (1991).
71. M. Snowbell, N. Strasman, B. Fischer and M. Cronin-Golomb, *J. Lightwave Technol.* **13**, 55 (1995).
72. S. Weiss, M. Segev, S. Sternklar and B. Fischer, *Appl. Opt.* **27**, 3422 (1988).
73. M. D. Ewbank, *Opt. Lett.* **13**, 47 (1988).
74. A. M. C. Smout and R. W. Eason, *Opt. Lett.* **12**, 498 (1987).
75. D. Wang, Z. Zhang, Y. Zhu, S. Zhang and P. Ye, *Opt. Commun.* **73**, 495 (1989).
76. S. Weiss, S. Sternklar and B. Fischer, *Opt. Lett.* **12**, 114 (1987).
77. B. Fischer, S. Sternklar and S. Weiss, *IEEE J. Quantum Electron.* **QE-25**, 550 (1989).
78. Q. B. He, P. Yeh, C. Gu and R. Neurgaonkar, *J. Opt. Soc. Am.* B **9**, 114 (1992).
79. P. Yeh, *Appl. Optics* **28**, 1961 (1989).
80. Qi-Chi He, *IEEE J. Quantum Electron.* **QE-24**, 2507 (1988).
81. S. C. De La Cruz, S. MacCormack, J. Feinberg, Q. Byron He, H. K. Liu and P. Yeh, *J. Opt. Soc. Am.* B **12**, 1363 (1995).
82. M. Gruneisen, E. Seeberger, J. Milevski and K. Koch, *Opt. Lett.* **16**, 596 (1991).

83. Q. B. He and P. Yeh, *Appl. Phys.* B **60**, 47 (1995).
84. M. Kaczmarek, P. Hribek and R. W. Eason, *Opt. Commun.* **136**, 277 (1997).
85. A. Petris, M. J. Damzen and V. I. Vlad, *Opt. Commun.* **205**, 437 (2002).
86. M. Cronin-Golomb, B. Fischer, J. O. White and A. Yariv, *IEEE J. Quantum Electron.* **QE-20**, 12 (1984).
87. M. P. Petrov, S. L. Sochava and S. I. Stepanov, *Opt. Lett.* **14**, 284 (1989).
88. G. Martel, N. Wolffer, J. Y. Moisan and P. Gravey, *Opt. Lett.* **20**, 937 (1995).
89. S. MacCormack, J. Feinberg and M. H. Garrett, *Opt. Lett.* **19**, 120 (1994).
90. K. R. MacDonald and J. Feinberg, *J. Opt. Soc. Am.* **73**, 548 (1983).

CHAPTER 4

HOLOGRAPHIC TIME OF FLIGHT

Ivan Biaggio
Department of Physics, Lehigh University, Bethlehem, PA 18015, U.S.A.
E-mail: biaggio@lehigh.edu

ABSTRACT: The Holographic Time of Flight (HTOF) method for the all-optical, contact-less investigation of charge transport in non-centrosymmetric insulators and semiconductors is based on the instantaneous photoexcitation of a spatially modulated distribution of charge carriers and on the linear electro-optic (Pockels) effect to visualize a charge-displacement by its associated refractive index change. It can be used with a free-carrier density so low that it does not otherwise have any detectable influence on the optical properties of a material, and with short free carrier lifetimes of the order of nanoseconds or less. HTOF is an especially striking example of how several independent linear and nonlinear light-matter interaction mechanisms can join to deliver a peculiar wave-mixing effect that is directly determined by a seemingly unrelated microscopic parameter: the free-carrier mobility. This chapter reviews the HTOF method and provides a detailed theoretical treatment that will be invaluable to experimentalists interested in applying this method to new materials. The author discusses the experimental parameters that influence the HTOF results and presents the basic assumptions and experimental conditions that allow the characterization of charge transport in the bulk of a material, with a sub-nanosecond time resolution only limited by the duration of the laser pulses, and for transport lengths down to a fraction of a micrometer.

1. Introduction

By illuminating a dielectric material with a pulsed laser it is possible to optically excite free electrons or holes, either from donor centers in the energy band gap between valence and conduction band, or directly by interband transitions. This leads to a transient increase in the number of free charge carriers, and therefore of the conductivity. Transient studies of current initiated by optical excitation of charge carriers lead to several ways to study charge transport processes in insulators and semiconductors.

Homogenous charge-carrier photoexcitation in the bulk of a sample can be achieved by photoionization of impurity centers with energy levels inside the energy band gap. The analysis of such a homogenous photoconductivity transient gives some information on the charge transport properties, but generally delivers only indirect information on the charge-carrier mobility.

On the other hand, the optical excitation of a packet of charges localized at the surface of a sample, either by interband excitation or by charge-carrier injection, is at the basis of conceptually simple methods to measure drift mobilities [1]. These methods rely on the observation of the drift of a charge-carrier packet in an applied electric field by its controlled photoexcitation and the detection of its time-of-arrival after a well-defined transport length. A well-established tool to

Aaron Peled (ed.), Photo-Excited Processes, Diagnostics and Applications (PEPDA), 101–120, 2003.
© 2003 *Kluwer Academic Publishers. Printed in the Netherlands.*

measure drift-mobilities is the time-of-flight (TOF) method [2–6], which has been extensively used in developing photoconductors for the printer and photocopier industry [7]. In this method, an optically excited thin sheet of free charge carriers drifts across a sample under the influence of an applied electric field. The time of arrival of the charge carriers at the other side of the sample is normally determined by measuring the current as a function of time. As long as the charge carrier packet is drifting inside the sample, a current flows in an external circuit. When the charge-carrier packet reaches the electrode at the other side of the sample, the current falls to zero. By measuring this current transient it is possible to determine the transit time of the charge packet, and hence the carrier-mobility. But for the TOF measurements to be readily interpretable in terms of carrier mobility, the transit time must be shorter than the free-carrier lifetime.

The above is a fundamental condition that determines the applicability of TOF methods for the study of charge-transport in many materials. Its main consequences are: (1) It can be difficult to produce samples so thin that charge carriers have the time to drift from one side of the sample to the other side during their lifetime; (2) Thinner samples rise the sensitivity to surface states and defects; (3) Even if the mobility and applied field were large enough to allow the transit of the charge carriers during their lifetime, the time-resolution of the electronic current measurement itself would need to be shorter than the transit time; (4) For low-mobility materials, the carrier mobility can only be determined by applying strong electric fields, and no data can be obtained for the mobility at low fields.

These difficulties could be solved by (1) setting the transport length independently from the sample thickness, (2) increasing the time-resolution with which charge-transport can be observed, and (3) increasing the sensitivity with which charge displacement is detected. It turns out that all these requirements can be fulfilled by controlled optical excitation and detection and by a compromise between the homogenous and the localized photoexcitation of charge-carriers we mentioned above.

By using the interference pattern of two intersecting laser beams to photoexcite charge carriers it is possible to obtain a spatially sinusoidal modulation in the free charge carrier density. This can lead to a characterization of charge transport using a short transport length – corresponding to the spatial period of the interference pattern – provided that one can follow the time evolution of the free-carrier density distribution.

A first possibility of detecting the amplitude of a sinusoidally modulated spatial distribution is realized when the optical properties of the material are directly modified by the presence of the charge carriers themselves. Since the carrier distribution is modulated in space like a plane-wave, the corresponding modulation in optical properties corresponds to an absorption or refractive index grating, which can be detected by diffraction of a probe-beam incident at the Bragg angle [8]. This technique, although practicable, has some disadvantages: (1) One generally needs a high carrier concentration to modify the optical properties in a detectable way; this could result in a number of ambiguities in the interpretation of experimental results, e.g. because of the strong space-charge field induced by the diffusion

of the carriers, heating, heat diffusion, etc. (2) This method of detection is only sensitive to the amplitude of the charge-carrier modulation. It is not particularly sensitive to charge-carrier *movement*; the signal would not be sensitive to a drift of the charge carrier distribution in an applied electric field, unless special techniques related to homodyne detection were used. (3) There are other effects that can lead to the same signal dynamics as the ones induced by charge transport; as an example, after pulsed excitation, one would observe an exponentially decaying signal because of carrier diffusion, but these temporal dynamics could also be caused by other effects, such as the decay by thermal diffusion of a temperature grating, or the relaxation of excited states.

A second possibility that is only sensitive to charge carrier movement can be implemented in non-centrosymmetric materials, where several new holographic methods have been developed during the last decade of the 20th century which rely on the refractive index modulation induced by space-charge electric fields [9–21]. The motivation for these studies was the interest in the charge transport properties of *photorefractive crystals*, a class of materials with potential for several applications of dynamic holography and holographic data storage [22]. Despite this interest and the fundamental role played by charge transport in the holographic properties of these materials, very little data was available on the intrinsic charge-carrier mobility because the low density of charge-carriers, their small mobility, and their limited lifetime before trapping in some kind of deep or shallow traps, limited the application of conventional mobility-measurement techniques. As a result, various schemes were developed where the photorefractive properties of these non-centrosymmetric materials were used to study charge transport. The basic principle involves the fact that charge transport inside a spatially modulated carrier density leads to a space-charge electric field, which then modulates the refractive index of the material by the linear electro-optic effect, also known as Pockels effect. The resulting refractive index modulation corresponds to a holographic grating in the bulk of the sample which can be detected by the diffraction of a probe beam.

Since both charge-carrier excitation and detection of charge carrier movement can be done optically, all such techniques amount to examples of four-wave mixing. This wave-mixing approach to charge-transport investigation can be used both for continuous wave excitation and for pulsed excitation of charge-carriers.

From the study of the space-charge dynamics under continuous wave excitation it is possible to measure the photoconductivity by purely optical means. This has its own advantages because it allows a determination of the photoconductivity and the anisotropy of the mobility tensor in the bulk of irregularly shaped samples, without using any applied electric fields and with no need for electric current measurements [19].

By confining the charge-carrier photoexcitation to a time interval so short that it does not allow for any significant charge transport, it is possible to temporally separate the charge-carrier photoexcitation process from the charge-transport process. This leads to a simplification of the theoretical analysis, and to the possibility of determining carrier mobilities by measuring the evolution of a charge carrier distribution photoinduced by a short, spatially modulated light flash.

This is at the origin of the Holographic Time of Flight (HTOF) method. The name comes from the observation that diffusion and drift of a spatial sinusoidal pattern of charge carriers in the bulk of a non-centrosymmetric sample, instead of a thin sheet at the surface as in conventional TOF, leads to a refractive index grating: an hologram [9, 20]. In HTOF, the current, following the evolution of the space-charge, is measured optically by diffracting a probe beam from the space-charge-induced refractive-index grating caused by the separation of the free carriers from their excitation point. When the transport length, i.e. the spatial period of the photo-excited charge pattern, is long and the mobility is small, charge-transport can be observed using a continuous wave probe beam. For short transport lengths – which can be as small as a fraction of a micrometer – and for larger mobilities, charge migration can be followed using a delayed probe pulse in a pump & probe four-wave mixing set-up [14, 15, 20] (see Figure 1). This allows the contact-less observation of charge-displacement with picosecond time resolution – from nanoseconds down to the duration of the optical pulses used – and the measurement of the charge-carrier mobility during the first few pico- or nanoseconds after photoexcitation, over transport lengths of one micrometer or less, before the first trapping event takes place.

Two variants of HTOF can be implemented. When the charge-separation is induced by drift in an external electric field we have the case of *drift-mode* HTOF [9], represented schematically in Figure 2. This is the technique that most closely parallels conventional Time-of-Flight. In drift-mode HTOF the space-charge field reaches a maximum when the mobile carrier distribution has drifted by half of its spatial period, to a position of anti-coincidence with the immobile distribution of

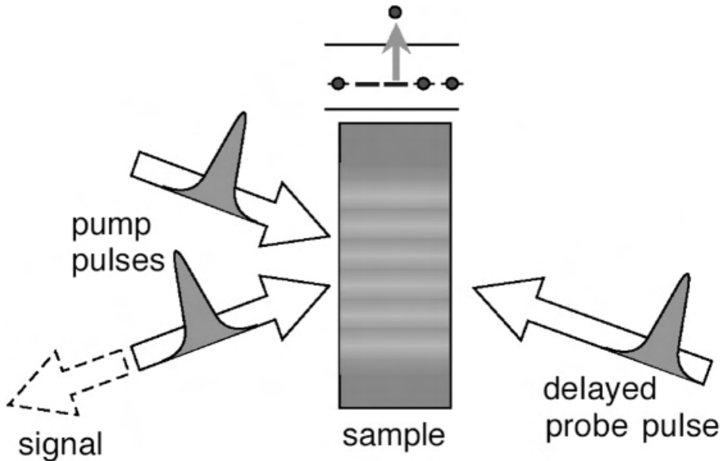

Figure 1. Principle of impulsive photoexcitation of a modulated charge carrier distribution and pump & probe measurement of its time-evolution. The interference pattern between two short pulses excites a sinusoidal charge carrier distribution from donor centers in the energy-band gap, and a delayed probe pulse detects the refractive-index grating resulting from the space-charge field induced by charge-transport. The beams are arranged in a typical Degenerate Four Wave Mixing set-up.

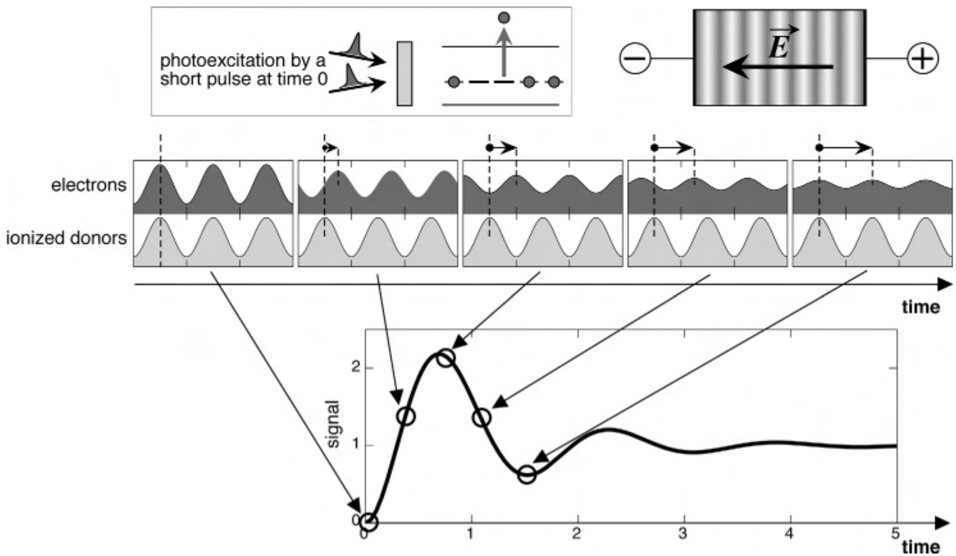

Figure 2. Graphical representation of the working principles of HTOF in drift mode, with a schematic representation of photoexcitation by a modulated intensity pattern inside a sample with an applied electric field. The drift of the negatively charged photoexcited electron distribution with respect to the positively charged static ionized donor distribution is shown, together with the resulting time-dependence of the HTOF signal. Note how the HTOF signal directly tracks the charge *displacement*, not just the modulation of the charge-density.

the donors from where it was photoexcited. Further drift causes a decrease of the space-charge field until coincidence is reached again and so on. HTOF was first demonstrated in drift-mode with relatively large transport lengths of the order of 100 μm by Partanen et al. [9, 11], where it was used to determine the average electron mobility caused by shallow traps in $Bi_{12}SiO_{20}$ [12].

Since HTOF starts from a sinusoidally modulated space-charge distribution, charge-separation can also be caused simply by thermal diffusion, which tends to make the photocarrier distribution homogenous. This effect is exploited by *diffusion-mode* HTOF [20], although this name was not used initially [14, 15]. This technique is represented schematically in Figure 3. In diffusion-mode HTOF, the carrier migration leads to an exponential build-up of the signal of the form $1 - \exp(-t/\tau_0)$. When the spatial modulation period of the carrier distribution is small enough, the build-up time τ_0 corresponds to the carrier diffusion time and gives the mobility. Diffusion-mode HTOF was first used in a pump & probe, degenerate four wave mixing set-up to determine the intrinsic electron mobility in $KNbO_3$ [14, 15].

In the following, we first present the basic assumptions and principles that allow an implementation of HTOF, and provide a detailed discussion of the influence of various experimental parameters. Then, we review some of the work that has been performed with HTOF. A description of the details of the actual experimental

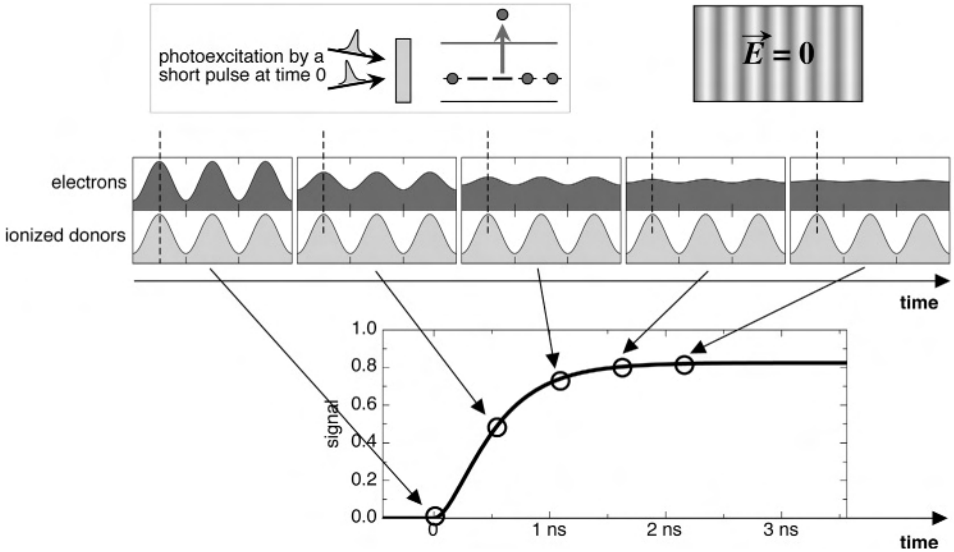

Figure 3. Graphical representation of the working principles of HTOF in diffusion mode, with a schematic representation of photoexcitation by a modulated intensity pattern inside a sample. No electric field is applied. The diffusion of the negatively charged photoexcited electron distribution with respect to the positively charged static ionized donor distribution is shown, together with the resulting time-dependence of the HTOF signal.

setups is not included in this chapter. Besides the fact that we discuss the required experimental parameters in depth, which should allow an easy experimental realization, the references given already provide all the necessary experimental arrangements in enough detail.

Readers familiar with photorefractive materials and the models used to describe their optical response [22] may recognize some features of the theoretical results and the discussion of the experimental parameters presented below. However, this similarity is only superficial and can lead to a misinterpretation of what is taking place. In the following, no attempt is made to use the concepts and definitions of the conventional photorefractive theory based on quasi-continuous wave illumination. Trying to do this would only be a source of confusion in the present case, where illumination is only used to establish an initial condition for the charge-carrier density and charge transport takes place subsequently in the dark.

2. Theory of Holographic Time of Flight

The optical excitation of free charge carriers and the optical detection of their movements can achieve its full potential for mobility measurements when the experimental parameters are chosen in such a way that the influence of charge-displacement on

the measured signal is maximized. By confining the charge-carrier photoexcitation to a time interval so short that it does not allow for any significant charge transport, it is possible to temporally separate the photoexcitation process from the transport process. This leads to a simplification of the theoretical analysis, and to the possibility of determining the absolute mobility of photoexcited charge carriers by measuring the evolution of a charge carrier distribution photoinduced by a short optical pulse.

The following is a slightly modified form of the treatments first published in Refs. [11] and [14], with many additional details regarding the assumptions made and their range of validity. We also add a previously unpublished analysis of the effects of an applied electric field on the signal amplitude and a discussion of the main features of the HTOF signal.

Four basic assumptions enable a simple and compact analysis of the photoexcitation and transport mechanisms giving rise to the observed signal. They are the precondition for a Holographic Time of Flight measurement, and we assume them to be true for the analysis that follows:

1. The photoexcitation pulses are so short that no charge transport takes place during the pulse duration.
2. Only one type of mobile carrier is excited by photoionization of impurity centers with energies in the gap between valence and conduction band. Photoexcitation takes place in the bulk of the material.
3. The density of photoexcited carriers is so small that there are no saturation effects during photoexcitation and that the space-charge field that is built up by subsequent charge transport has a negligible influence on the transport dynamics itself.
4. The average lifetime τ of the photoexcited carriers is a constant, i.e. the distribution of any trapping centers can be assumed to be homogenous.

The first requirement can be fulfilled by selecting an appropriate laser source with short enough pulses.

The second requirement can be fulfilled by choosing an appropriate photoexcitation wavelength that maximizes the probability for photoexcitation of one particular carrier, and also by targeted doping of the material. One should note that this requirement does not forbid simultaneous photoexcitation of electrons and holes as long as there is a large enough difference between their respective mobilities and only the contribution of one carrier is observed on a given time scale.

The third requirement of a small density of carriers is met by reducing the energy in the interference pattern used for impulsive photoexcitation. This can be easily done because the detection of charge displacement by the electro-optic effect allows a much greater sensitivity than other methods of optical detection that rely on the change of optical properties introduced by the free-carrier density itself.

The fourth requirement is met in the presence of a spatially homogeneous distribution of traps in addition to the donor centers providing the photoexcited carriers, a common occurrence. Further, if retrapping in the original donors was a signifi-

cant contribution to the free carrier lifetime τ, one could help satisfying this requirement by reducing the contrast in the interference pattern that photoexcites the carriers, and by the enforcement of the third requirement mentioned above.

It is important to note that the above assumptions can be largely satisfied by adjusting experimental parameters that can be easily controlled, such as wavelength, pulse-length, pulse-energy and contrast in the optical interference pattern. When requirements (1)–(4) are met, the nature of the impurity centers from which the free carriers are excited, or the nature of the trapping centers that limit their lifetime, are not important in the analysis. One should also note that, among the above assumptions and in the following, we do not consider the influence of the probe beam used to detect the space-charge dynamics. First, any probe beam with an homogenous intensity could only provide a homogenous free carrier background that does not affect the space-charge modulation amplitude introduced by the excitation pulses. Second, if the probe is a short pulse with the same characteristics as the pulse used to photoexcite charge carriers, any effect it might have will happen *after* it generated a diffracted signal pulse from the refractive index modulation. An additional observation is that any homogenous, continuous wave illumination during a pump and probe experiment would only provide a negligible number of photons in the time interval of interest [20].

We are interested in the description of the evolution of a free-carrier modulation from the moment it was created, to the point when it reaches a steady state. For the sake of simplicity we consider photoexcitation of only one type of carrier, and assume that they are electrons. Then the photoexcited electron distribution that is left in the crystal after the photoexcitation pattern has been switched off at time $t = 0$ is of the form

$$n(z, t) = n_0(t) + \frac{1}{2}[n_1(t)e^{ik_{sp}z} + c.c.], \tag{1}$$

Where $n_1(t)$ is a complex amplitude and the initial conditions $n_0(t = 0)$ and $n_1(t = 0)$ are given by the average energy and the contrast of the interference pattern used to photoexcite the carriers. The "+ *c.c.*" stands for the addition of the complex-conjugate expression. k_{sp} is the modulus of the wavevector, pointing in the z-direction, that describes the sinusoidal interference pattern. Under the assumptions mentioned above, the time evolution $n(z, t)$ is governed by free carrier lifetime, diffusion, and drift,

$$\frac{\partial n(z, t)}{\partial t} = -\frac{n(z, t)}{\tau} + \left[\frac{\mu k_B T}{e}\right]\frac{\partial^2 n(z, t)}{\partial z^2} + \mu E\frac{\partial n(z, t)}{\partial z}. \tag{2}$$

Here τ is the free-carrier lifetime, μ is the free-carrier mobility, k_B is Boltzmann's constant, T is the absolute temperature, e is the unit charge, and E is a static electric field along the z-direction. The "+" sign in front of the last term comes from the assumption that the drifting charges are negative.

Substitution of (1) into (2) leads to separate equations for $n_0(t)$ and $n_1(t)$ with

the solutions

$$n_0(t) = n_0^0 e^{-t/\tau}, \quad n_1(t) = n_1^0 e^{-\Gamma t}, \tag{3}$$

Where $\Gamma = 1/\tau + 1/\tau_D + i\omega$,

$$\tau_D = \frac{e}{k_{sp}^2 \mu k_B T}, \tag{4}$$

is the diffusion time, and $\omega = \mu E k_{sp}$ is the rate of change of the spatial phase caused by drift in the applied field.

Substituting (3) into (1) one finds

$$n(z, t) = n_0^0 e^{-t/\tau} \left[1 + \frac{n_1^0}{n_0^0} e^{-t/\tau_D} \cos(k_{sp} z + \omega t) \right], \tag{5}$$

which shows that the average carrier density decays exponentially with the free carrier lifetime, the modulation in the charge-distribution decays exponentially with the diffusion time, and the phase of the charge distribution changes linearly with the drift velocity μE.

Immediately after photoexcitation, the space charge corresponding to the free charge carriers $[-en(z, t = 0)]$ is exactly compensated by the ionized centers from where they were excited, which have a charge density $+en(z, t = 0)$. The evolution of the free electron density described by (5) then uncovers the space-charge field of the ionized donors. As already mentioned above, the trapping mechanism behind the free carrier lifetime does not need to be described in any special way provided that its effect is just to transform a mobile free carrier described by the mobility μ into an immobile carrier. If the carrier was captured by a shallow trap, we assume that there is no significant thermal re-excitation during the time scale of the experiment (the opposite case of a thermal re-excitation much faster than the time-scale of the experiment would be taken into account by an effective trap-limited mobility). The density of trapped charge carriers at any given time after photoexcitation is then simply given by $\partial n_T(z, t)/\partial t = -n(z, t)/\tau$, and it is essentially the time-integral of (5).

The space-charge electric field is found from the Gauss equation and the balance of the charge densities of ionized donors, moving electrons, and trapped electrons,

$$\frac{\partial E_{sc}(z, t)}{\partial z} = \frac{e}{\epsilon\epsilon_0} [n(z, t = 0) - n(z, t) - n_T(z, t)], \tag{6}$$

where ϵ is the effective dielectric constant in the z-direction [23, 24] and ϵ_0 is the permittivity of vacuum. The resulting space-charge field is $E_{sc}(z, t) = [E_{sc}(t)\exp(ik_{sp}z) + c.c.]/2$ and it is spatially modulated like a plane wave, with the complex amplitude

$$E_{sc}(z, t) = E_{sc}^{\infty}[1 - e^{-\Gamma t}], \tag{7}$$

and a steady state value

$$E_{sc}^{\infty}(t) = n_1^0 \frac{e}{ik_{sp}\epsilon\epsilon_0}\left[1 + \frac{1/\tau}{1/\tau_D + i\omega}\right]^{-1}, \tag{8}$$

In a non-centrosymmetric material, this electric field induces a spatial refractive index modulation – a holographic grating – with an amplitude that is linearly proportional to the absolute value of (7). A probe pulse diffracted from this refractive index grating has an energy proportional to the modulation amplitude of the refractive index, and therefore to $|E_{sc}(t)|^2$. A measurement of the probe energy as a function of its delay time after charge-carrier photoexcitation allows a direct observation of the evolution of the space-charge field. In the following we discuss the material parameters that can be extracted from this measurement.

From the form of (7) we see that Γ is a "build-up rate" that contains all the essential features describing the time-dependence of the space-charge field. Its real part corresponds to a buildup time $\tau_0 = 1/\mathrm{Re}[\Gamma]$. Its imaginary part $\omega = \mu E k_{sp}$ arises because of the applied electric field, and introduces an oscillatory behavior in the time-dynamics.

More insight into the physical mechanism can be gained by writing the full time and space dependence of the space-charge field that can be derived from (7):

$$E_{sc}(z, t) = |E_{sc}^{\infty}| \, [\sin(k_{sp}z + \theta) - e^{-t/\tau_0} \sin(k_{sp}z + \theta - \omega t)]. \tag{9}$$

Where θ is defined by $E_{sc}^{\infty} = |E_{sc}^{\infty}| e^{i(\theta - \pi/2)}$ and represents a spatial shift of the space-charge field modulation that is introduced by the applied electric field. Even without an applied field, the space-charge field modulation is phase-shifted by $\pi/2$ with respect to the optical interference pattern. For the sake of completeness, we also give explicit expressions for the amplitude and the phase shift of the space-charge field:

$$|E_{sc}^{\infty}| = \frac{n_1^0 e}{k_{sp}\epsilon\epsilon_0}\left[1 + \frac{\tau_D}{\tau}\frac{2 + \tau_D/\tau}{1 + (\omega\tau_D)^2}\right]^{-1/2}, \tag{10}$$

$$\theta = \arctan\left[\frac{\tau_D}{\tau}\frac{\omega\tau_D}{1 + \tau_D/\tau + (\omega\tau_D)^2}\right], \tag{11}$$

The space-charge field described by (9) consists of a time independent component with a constant phase shift of $\pi/2 + \theta$ with respect to the light intensity modulation and of a component drifting with velocity $\omega/k_{sp} = \mu E$. The amplitude of the latter decays exponentially with the time-constant τ_0. At time $t = 0$ these two components exactly compensate each other. For later times the second component decays and acquires a phase shift, leading to an increasing space-charge field amplitude.

The time dynamics of the space charge field is plotted in Figure 4 for various values of the imaginary part of the buildup rate. Comparing the dashed curve with

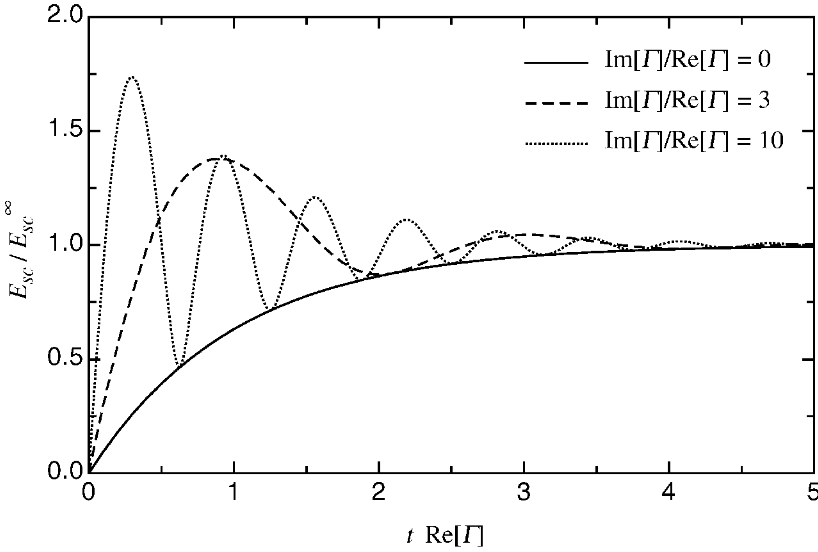

Figure 4. Evolution of the space-charge field amplitude in a HTOF experiment. Curves are shown for different imaginary parts Im[Γ] = ω of the buildup rate Γ. The time axis is in units of the buildup time τ_0 = Re[Γ]$^{-1}$ and the curves are normalized to the final space charge field amplitude.

the solid curve we see that clear oscillations in the time-dynamics of the space-charge field appear when $\omega\tau_0 > 3$. The oscillation period is related to the drift-velocity and the period of the spatial interference pattern. The steady state value of the space-charge field (8) depends on the balance between free-carrier lifetime, diffusion-time, and drift velocity, as described by the term inside the square brackets of Eq. (8). Note that the $\omega = 0$ curve , corresponding to no applied field, describes the position of the minima of the curves with $\omega > 0$.

The above result is the full solution for the time evolution of the space-charge field from the moment a sinusoidally modulated free-carrier density is created to the point where the free-carrier density does not change anymore, either because the effect of diffusion has died away, or because there are no free carriers left. This process has the final result of creating a space-charge modulation that is left in the material, while we assumed as an initial condition the absence of any space-charge fields. It is beyond the theoretical model presented here to describe the relaxation processes that lead to the slow disappearance of such a space-charge field because of thermal excitation or a homogenous illumination [22]. The details of these relaxation processes are irrelevant for the interpretation of HTOF data as long as they restore the sample to its initial state before a new measurement takes place. It is possible to accelerate the restoration of a homogenous distribution of charge by illuminating the sample homogenously between successive pulsed exposures [20].

To analyze the dependence of the space-charge field amplitude and dynamics from the experimental parameters it is useful to introduce some dimensionless quanti-

ties. One is the wavevector k_0 of the space-charge modulation for which the free-carrier lifetime equals the diffusion time (4). The influence of the applied field can then be described by $\omega_0 = \mu E k_0$, and the dimensionless parameter used to plot the curves in Figure 4 can be written as $\omega\tau_0 = \omega_0\tau(k_0/k_{sp} + k_{sp}/k_0)^{-1}$. We thus see that the condition of a large $\omega\tau_0$ is easier to fulfill for $k_{sp} = k_0$. This is the wavevector to be selected in order to observe the oscillatory time dynamics of the space-charge field with the smallest possible applied field. At shorter wavevectors the applied field must be larger because of the increased influence of a limited free carrier lifetime. At larger wavevectors the applied field must be larger because of the adverse effect of a short diffusion time.

The wavevector k_0 also plays an important role in the case where no electric field is applied and $\omega = 0$. Figure 5 shows the exponential build-up time τ_0 and the steady-state value of the space-charge field as a function of the spatial period of the optical interference pattern. The buildup time is proportional to $[1 + (k_{sp}/k_0)^2]^{-1}$ and it is constant, given by the free carrier lifetime, for large spatial periods. It is dominated by diffusion and proportional to the square of the spatial period for $k_{sp} > k_0$. At $k_{sp} = k_0$, $\tau_0 = \tau/2 = \tau_D/2$. The space-charge field amplitude is proportional to $(k_0/k_{sp} + k_{sp}/k_0)^{-1}$ and it peaks at $k_{sp} = k_0$, reaching its maximum value $n_1^0 e/(2k_{sp}\epsilon\epsilon_0)$. An applied electric field not only introduces an oscillation of the space-charge field amplitude in time during the buildup, but also increases the final, steady state value of the space-charge field. However, as can be seen from Figure 5(b), this effect can only be seen for large spatial periods of the photoexcited electron distribution, where $k_{sp} \ll k_0$, because otherwise diffusion dominates. In this range the steady-state amplitude of the space-charge is a constant independent from the spatial period.

It is interesting to analyze this enhancement effect of the applied field further. Figure 6 shows the ratio between steady-state electric field amplitude with and without applied field as a function of the spatial period and for the same three applied fields used in Figure 5(b). The dashed line in Figure 6 gives the maximum enhancement possible, which is equal to 2 at $k_{sp} = k_0$ and tends to $(k_0/k_{sp})^2$ at large grating spacings. This ratio can be calculated from (10) in the limit of large spatial modulation periods, that is when $\tau_D \gg \tau$, and for the practical case of small applied fields when $\omega\tau \ll 1$. Both limits are easy to fulfill. The result is:

$$\frac{|E_{sc}^{\infty}(E)|}{|E_{sc}^{\infty}(E=0)|} \approx \sqrt{1 + (\omega\tau_D)^2} = \sqrt{1 + \left(\frac{eE}{k_B T k_{sp}}\right)^2} . \tag{12}$$

That is, in this limit the magnitude of the electric field induced enhancement of the space-charge amplitude depends only on the applied field itself and on two easy to control experimental parameters: the sample temperature and the wavevector of the optical interference pattern. Moreover, it does not depend on any material parameter. This means that a measurement of the enhancement at large spatial modulation periods can provide a local, independent way to measure the electric field that is actually present inside the sample where the measurement is performed. This is important because a precise knowledge of the applied field is

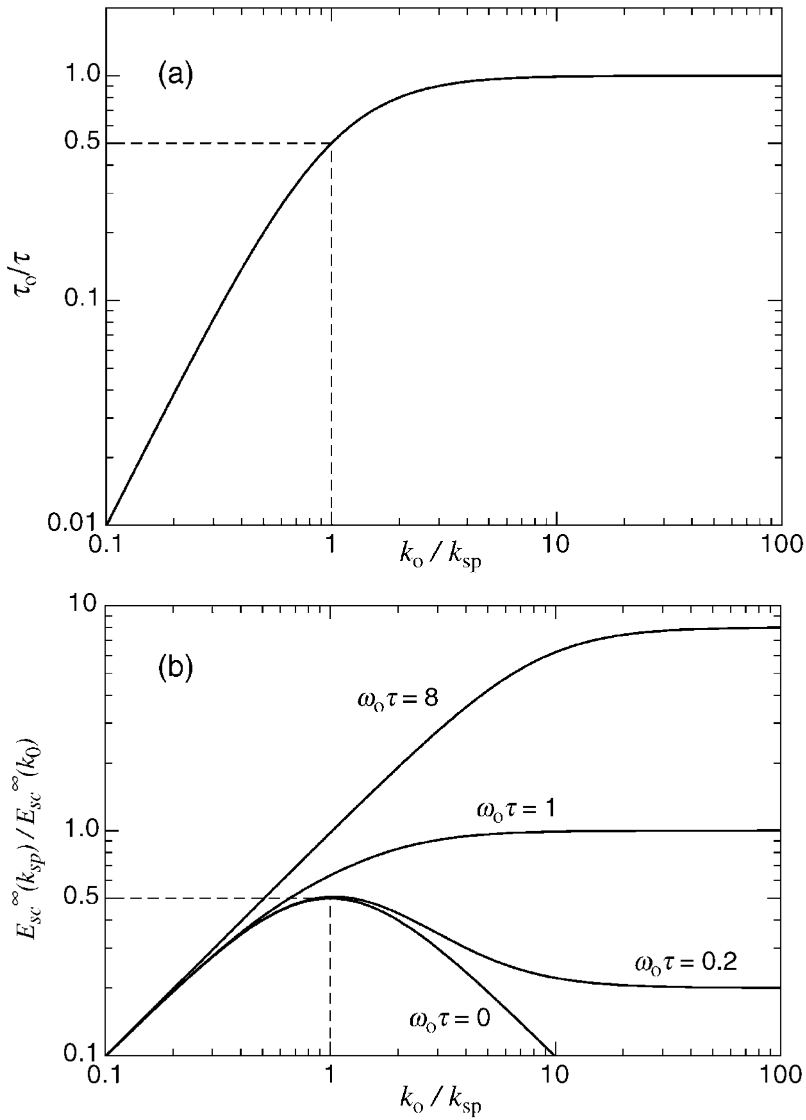

Figure 5. (a) Exponential rise time of the space-charge field amplitude, observed in the absence of any applied electric fields, vs. the spatial period of the optical interference pattern. (b) Steady-state space-charge field amplitude vs. the modulation period of the optical interference pattern for various applied electric fields given in terms of the dimensionless parameter $\omega_0\tau$.

necessary in order to calculate the free-carrier mobility from a measurement of ω, and it is well known that the electric field externally applied to a bulk photoconductor can be screened by accumulation of charges in trapping sites near the contacts and by the effects of an inhomogeneous illumination.

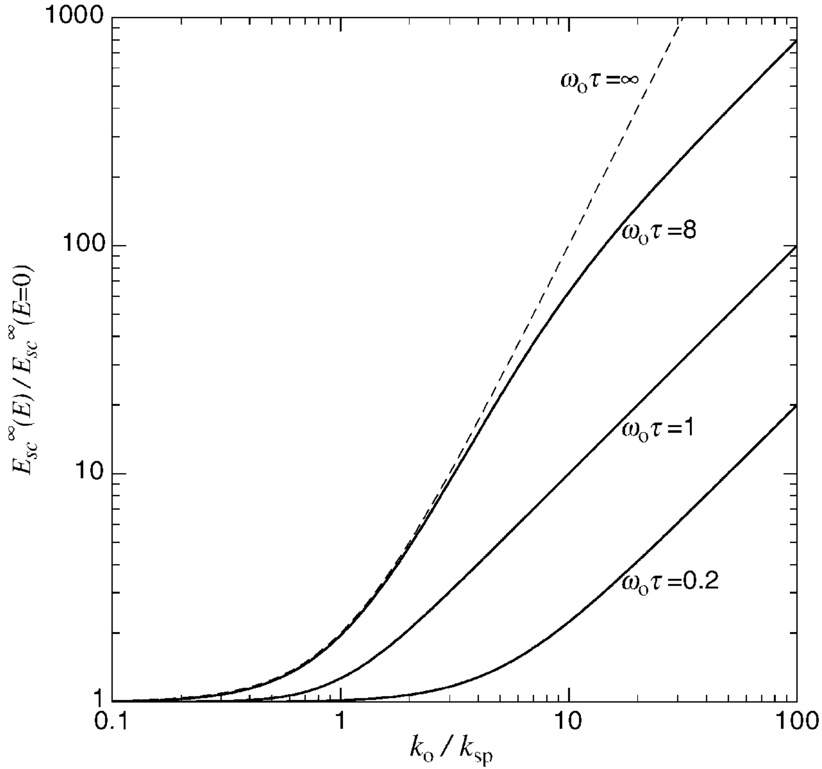

Figure 6. Enhancement of the steady-state space-charge field amplitude for applied electric fields E of different magnitudes, represented by the dimensionless parameter $\omega_0\tau$. The enhancement is given with respect to the space-charge field amplitude at $E = 0$ and as a function of the modulation period of the optical interference pattern.

3. Review of mobility investigations performed using HTOF

Two different ways of measuring charge carrier mobility emerge from the above discussion. The first is the use of an interference pattern with $k_{sp} > k_0$ to determine the rise-time of the space-charge field amplitude without applying any external field. In this limit, the rise time is given by the diffusion time (4) and the mobility can be readily determined. To check the validity of this interpretation, one can measure the rise time as a function of k_{sp} and confirm the expected quadratic dependence. The second one is to use an interference pattern with $k_{sp} \approx k_0$, apply an external electric field along z, and determine the drift velocity from a measurement of the oscillation frequency of the space-charge field amplitude. Obviously, other spatial modulations can be used if one can apply a strong enough electric field. In any case it is best to determine the size of the applied field inside the sample by a direct measurement, such as the determination of the enhancement factor plotted in Figure 6 .

The time-dependence of a space-charge field caused by diffusion of photo-excited carriers after impulsive illumination was first observed in Refs. [25, 26]. In both experiments it could be assumed that no transport took place during the photoexcitation pulse and a space-charge field buildup like that in Figure 4 was observed. However, the potential of developing the experimental technique into a controlled method for measuring mobility was not realized. In Ref. [25] the observed signal was assigned to diffusion and a mobility was calculated from it, but the authors miscalculated the influence of the free-carrier lifetime, which in their case determined the exponential time-constant of the build-up, and the resulting mobility value was too large by more than an order of magnitude [20].

HTOF was first implemented in a controlled way to determine the average mobility of electrons being continually trapped and re-excited thermally from shallow traps while drifting under the influence of an external electric field in the sillenite photoconductor $Bi_{12}SiO_{20}$ [9, 11]. The oscillatory time-dependence displayed in Figure 4 was indeed observed, even though with a relatively strong damping. This allowed the determination of the imaginary part ω of the build-up rate, and consequently of the mobility (μ = ~0.2 cm_2 V^{-1} s^{-1}). The experimental parameters where such that a *trap-limited* mobility was determined. In $Bi_{12}SiO_{20}$, the free-carrier lifetime before recombination into a shallow trap can be as small as ~20 ns [11], but in this material, charge carriers travel over distances as large as 100 μm while being continuously trapped and thermally re-excited from shallow traps before they finally recombine into a deeper trap [27]. The drift-mode HTOF experiments of Ref. [11] were performed with a spatial modulation of the interference pattern close to 90 μm and over a time scale of about 100 μs. The trap-limited mobility measured on these space and time scales is thermally activated, and depends exponentially on sample temperature. This was confirmed by temperature dependent HTOF measurements, where an activation energy of ~0.3 eV was determined [12].

Because of the large drift length corresponding to this trap limited mobility, it should also be possible to determine its value by conventional time of flight experiments, as was the case for $Bi_{12}GeO_{20}$, a material similar to $Bi_{12}SiO_{20}$, in Ref. [28]. In that work the observed mobility varied from sample to sample in the range between 0.2 and 1 cm^2 V^{-1} s^{-1}, as expected from a mobility that depends on impurity concentration. This trap limited mobility cannot give any information on the intrinsic properties of a charge-carrier.

The strength of HTOF in this situation is highlighted by the fact that it would be extremely difficult to extend the kind of time of flight experiments of Ref. [28] in such a way that the intrinsic electron mobility can be determined in $Bi_{12}SiO_{20}$ despite the nanosecond free-carrier lifetime. HTOF, however, can be applied to this task simply by changing the transport length. In a first attempt, HTOF in drift mode was applied with a continuous wave detection of the evolving space-charge field, but the low amount of probe-beam photons diffracted by the space-charge field, and the limited time response of the photomultiplier used to detect them, complicated the analysis [29]. These problems can be avoided by replacing the continuous wave detection by an appropriately time-delayed probe pulse in a pump and probe

setup [14, 15, 20]. This was done in Ref. [20], where the spatial modulation period of the interference pattern was chosen to be a fraction of a micrometer, and the evolution of the space-charge field was followed by a pump and probe technique in the first few nanoseconds after impulsive photoexcitation of the sinusoidal charge-carrier density. For the work in Ref. [20], HTOF in diffusion-mode was used. This removed the difficulty of controlling and determining the effective value of the applied field inside the sample, and easily allowed the investigation of the electron mobility as a function of sample temperature [20, 30]. It was found that the electron mobility determined in this way, $\mu = {\sim}3.4\ cm^2\ V^{-1}\ s^{-1}$ at room temperature, was in fact the intrinsic mobility of the charge carriers in $Bi_{12}SiO_{20}$, before their first encounter with a trap or an impurity. From the measurement and analysis of the temperature dependence of the intrinsic mobility it was shown that it corresponds to the mobility of *large polarons* [20, 30, 31]. Large polarons are formed in ionic crystals when a free electron polarizes the lattice around it and the electron drifts accompanied by the lattice polarization it induces. A discussion of these results is beyond the task of this review, but it should be noted that the high time resolution and controlled short transport lengths that are possible with HTOF were instrumental in the direct measurement of the intrinsic electron mobility and in the development of a fundamental understanding of the mechanisms limiting the charge-carrier mobility in this material.

HTOF in diffusion-mode was first used in Ref. [14] to investigate the electron mobility in $KNbO_3$, a ferroelectric perovskite. Ref. [14] gives experimental evidence for the dependence of the space-charge field amplitude and risetime from the spatial modulation period that is predicted in Figure 5. In Ref. [15], the HTOF measurements were extended towards shorter spatial modulations and applied to several samples with different doping. The risetime data in Ref. [15] contains a data point taken at a spatial period of 0.12 μm and it confirms the prediction of Figure 5(a). The electron mobility was determined to be $\sim 0.5\ cm^2\ V^{-1}\ s^{-1}$ [15], while a 4 ns free-carrier lifetime was observed. It is a surprising fact that the free-carrier lifetime was found to be the same for several different samples, as though it was also an intrinsic property of the material. The reason for this behavior is unknown. Ref. [15] also provides experimental data and numerical simulations for the saturation effects that occur when the energy density in the laser pulses used to excite the charge carriers becomes too large.

HTOF in drift mode was first applied to the investigation of charge-carrier mobility in organic photoconducting polymers in Refs. [32] and [16]. Characteristic of these experiments is that the oscillatory behavior of the space-charge field depicted in Figure 4 was not observed. After the first peak the space-charge field slowly relaxed to its final steady-state value. In these experiments, the drift velocity was estimated dividing the spatial period by the time corresponding to the first observed peak in the diffracted signal amplitude. The oscillatory behavior was not observed because in a polymer, like in many amorphous materials, there is no such thing as the sharp value of the free-carrier mobility which was assumed in the theory presented in the previous section. Charge-transport in these materials is *dispersive* [7, 33, 34]. This means that the distribution of trapping centers is such that many

different thermal excitation times are possible, and that a drifting charge-carrier can be captured in many different kinds of traps. Depending on the transport length, the probability that a drifting carrier is trapped in a trap with a long thermal excitation time is different and the resulting apparent mobility is different. Dispersive charge transport occurs when the dependence of the trap density from the thermal excitation energy of the trap follows an exponential law [34]. In a conventional time of flight experiment, dispersive charge transport deforms the current transient by stretching the current decay over many time-decades, but it is still possible to identify a transition point that can be used to assign a mobility value [34]. In HTOF, different "components" of the photoexcited charge-carrier distribution drift with a different velocity and the superposition of the contribution of all components hides the oscillatory behavior; the time corresponding to the first peak in the signal was used to obtain a mobility value in all experiments published to date. But for dispersive charge transport it is difficult to relate this definition of a HTOF mobility to the TOF mobility determined in a time of flight experiment [16]. The reason is to be found both in the different transport lengths and in the different effective transit time definitions used in the two experiments.

The hole mobility in a photorefractive polymer was also investigated by drift-mode HTOF in Ref. [35]. Also in this case no oscillations in the space-charge field amplitude could be observed because of the effect of dispersive charge transport in the polymer, and only the time position of the first peak was used to evaluate the experiments, which showed that background illumination changes the value of the mobility [35].

A comparison between conventional time-of-flight and HTOF mobility measurements in an organic glass showing dispersive charge transport was published in Ref. [36]. Here again, no oscillations could be observed in the HTOF trace and the time of the first peak was used to determine a mobility. As expected, this mobility value and that obtained in a conventional TOF experiment were different, but their respective electric field dependence was the same [36]. Additional HTOF investigations in an organic glass were performed in Ref. [37]. As mentioned above, for dispersive charge transport the relationship between the drift velocity measured by the time delay of the first peak in a non-oscillating HTOF trace and the actual distribution of mobilities is not a-priori clear. But one of the big advantages of HTOF with respect to conventional time of flight is the relative ease with which the transport length can be controlled. This fact was exploited in Ref. [38] to study the relationship between the drift velocity determined by the position of the first peak in HTOF and the transport length set by the spatial period of the interference pattern. In addition, the relationship of the resulting HTOF mobility to that determined by conventional time of flight was studied [38]. Because of the nature of dispersive charge transport, both mobilities depend on the transport length. These works complement a previously published analysis of the relationship between HTOF and conventional time of flight measurements [17] in materials showing dispersive charge transport, and give some additional background facts that are useful for the interpretation of HTOF measurements in this class of materials.

As the measurements discussed above demonstrate, the fact that the transport

length can be easily tuned in HTOF could make it an important tool for the study of dispersive charge transport. However, there is still much work to be done in the theoretical analysis of the influence of dispersive charge transport in HTOF measurements.

In none of the drift-mode HTOF experiments published to date was the internal electric field determined with the method described in the previous section. In Ref. [11] the internal electric field was determined by electro-optic measurements. In the other experiments discussed above the internal electric field was not determined independently. One measurement of the enhancement factor given by Eq. (12) appears in Ref. [39] where it was found that the internal electric field was half of that applied in the particular experimental configuration used, but it was not coupled to a drift-mode HTOF experiment.

4. Conclusions

Holographic Time of Flight is a modification of Four-Wave Mixing for the detection of charge transport in insulating or semiconducting materials. In this method, two pump pulses impinge on the material at the same time, and produce a spatial sinusoidal intensity pattern. Free charge carriers are then photoexcited from levels in the energy gap between valence and conduction band. This free carrier distribution is spatially modulated like the interference pattern, and is then free to diffuse or drift in an applied field. This leads to the creation of a space-charge electric field after the pump pulses have left the crystal. In an appropriate experimental configuration, this space-charge field will lead to a periodic refractive index modulation that diffracts a probe beam incident at the Bragg angle. Good time resolutions are obtained by using pump and probe techniques, where the space-charge field caused by charge migration is detected by diffraction of a time-delayed probe pulse, to generate a signal pulse.

Holographic Time of Flight techniques offer two distinct advantages over regular time of flight methods: (1) The length scale determining the time dynamics of transport is the period of the sinusoidal excitation pattern, – instead of the sample thickness like in conventional time-of-flight – and can be easily controlled by changing the crossing angle between laser beams, with a lower limit of a fraction of a micrometer. (2) The movement of the photoelectrons is measured optically, allowing a higher time resolution, only limited by the length of the optical pulses employed. Additional advantages can be summarized as follows. (3) The migration of a small concentration of charge carriers – of the order of 10^{14} cm^{-3} – already gives a detectable refractive index change. (4) The detected signal has a very characteristic signature that can be easily distinguished from other effects not connected to transport, such as temperature gratings and excited states gratings, allowing for a better identification of the charge-displacement signal. For example, after pulsed excitation, the non-local response due to charge migration is initially zero, leading to a time-delayed response easily distinguishable from other local responses which are initially strong and decay later, like local heating or excited

states. (5) Drift in an electric field of a sinusoidal carrier-distribution with constant amplitude is readily visible because the sum of the space-charge field of the mobile carriers and the space-charge field of the ionized donor centers oscillates in time. Finally, for diffusion-mode HTOF we can add that (6) no electrodes are needed, (7) no particular sample shapes are required, and (8) no uncertainties are introduced because of possible internal electric field variations caused by trapped space-charge.

References

1 . S. M. Vaezi-Nejad, 'Instrumentation Aspects and Applications of Charge Transport Measurement Techniques', *Measurement* **17**(4), 267–277 (1996).
2. J. R. Haynes and W. Shockley, 'The Mobility and Life of Injected Holes and Electrons in Germanium', *Phys. Rev.* **81**(5), 835 (1951).
3. W. E. Spear, *Proc. Phys. Soc. London, Sect. B* **70**, 669 (1957).
4. W. E. Spear, *Proc. Phys. Soc. London, Sect. B* **76**, 826 (1960).
5. R. G. Kepler, 'Charge Carrier Production and Mobility in Anthracene Crystals', *Phys. Rev.* **119**, 1226 (1960).
6. F. K. Dolezalek, in *Photoconductivity and Related Phenomena*, J. Mort and D. M. Pai (eds.) (Elsevier/Noth Holland, 1976).
7. D. M. Pai and B. E. Springett, 'Physics of Electrophotography', *Rev. Mod. Phys.* **65**(1), 163 (1993).
8. R. I. Devlen and E. A. Schiff, 'Optically Detected Photocarrier Transport in Amorphous Silicon: A Review', *J. of Non-Cryst. Solids* **141**, 106–118 (1992).
9. J. P. Partanen, J. M. C. Jonathan and R. W. Hellwarth, 'Direct Determination of Electron Mobility in Photorefractive $Bi_{12}SiO_{20}$ (BSO) by Holographic Time-of-Flight Technique', *Appl. Phys. Lett.* **57**(23), 2404–2406 (1990).
10. G. Pauliat, A. Villing, J. C. Launay and G. Roosen, 'Optical Measurements of Charge-Carrier Mobilities in Photorefractive Sillenite Crystals', *J. Opt. Soc. Am.* **B7**(8), 1481–1486 (1990).
11. J. P. Partanen, P. Nouchi, J. M. C. Jonathan and R. W. Hellwarth, 'Comparison Between Holographic and Transient-Photocurrent Measurements of Electron Mobility in Photorefractive $Bi_{12}SiO_{20}$', *Phys. Rev.* **B44**, 1487–1491 (1991).
12. P. Nouchi, J. P. Partanen and R. W. Hellwarth, 'Temperature Dependence of the Electron Mobility in Photorefractive $Bi_{12}SiO_{20}$', *J. Opt. Soc. Am.* **B9**(98), 1428–1431 (1992).
13. P. Nouchi, J. P. Partanen and R. W. Hellwarth, 'Simple Transient Solutions for the Photoconduction and the Space-Charge Field in a Photorefractive Material with Shallow Traps', *Phys. Rev.* **B47**(23), 15581–15587 (1992).
14. I. Biaggio, M. Zgonik and P. Günter, 'Photorefractive Effects Induced by Picosecond Light Pulses in Reduced $KNbO_3$', *J. Opt. Soc. Am.* **B9**(8), 1480–1487 (1992).
15. M. Ewart, I. Biaggio, M. Zgonik and P. Günter, 'Pulsed-Photoexcitation Studies in Photorefractive $KNbO_3$', *Phys. Rev.* **B49**(8), 5263–5273 (1994).
16. G. G. Malliaras, V. V. Krasnikov, H. J. Bolink and G. Hadziioannou, 'Holographic Time-of-Flight Measurements of the Hole-Drift Mobility in a Photorefractive Polymer', *Phys. Rev.* **B52**(20), R14324–R14327 (1995).
17. G. G. Malliaras, H. Angerman, V. V. Krasnikov, G. ten Brinke and G. Hadziiannou, 'The Influence of Disorder on the Space Charge Filed Formation in Photorefractive Polymers', *J. Phys. D: Appl. Phys.* **29**, 2045–2048 (1996).
18. D. Mahgerefteh, D. Kirillov, R. S. Cudney, G. D. Bacher, R. M. Pierce and J. Feinberg, 'Anisotropy of the Hole Drift Mobility in Barium Titanate', *Phys. Rev.* **B53**(11), 7094–7098 (1996).
19. P. Bernasconi, I. Biaggio, M. Zgonik and P. Günter, 'Anisotropy of the Electron and Hole Drift Mobility in $KNbO_3$ and $BaTiO_3$', *Phys. Rev. Lett.* **78**, 106 (1997).

20. I. Biaggio, R. W. Hellwarth and J. P. Partanen, 'Band Mobility of Photoexcited Electrons in $Bi_{12}SiO_{20}$', *Phys. Rev. Lett.* **78**, 891-894 (1997).
21. P. Bernasconi, G. Montemezzani, I. Biaggio and P. Günter, 'Characterization of the Bipolar Mobility in Polar Materials by Interband Photoexcitation', *Phys. Rev.* **B56**, 12196–12200 (1997).
22. P. Yeh, 'Introduction to Photorefractive Nonlinear Optics', Wiley series in *Pure and Applied Optics* (John Wiley & Sons, 1993).
23. P. Günter and M. Zgonik, 'Clamped-Unclamped Electro-Optic Coefficient Dilemma in Photorefractive Phenomena', *Opt. Lett.* **16**(23), 1826–1828 (1991).
24. M. Zgonik, R. Schlesser, I. Biaggio, E. Voit, J. Tscherry and P. Günter, 'Material Constants of $KNbO_3$ Relevant for Electro- and Acousto-Optics', *J. Appl. Phys.* **74**, 1287 (1993).
25. J. M. C. Jonathan, G. Roosen and P. Roussignol, 'Time-Resolved Buildup of a Photorefractive Grating Induced in $Bi_{12}SiO_{20}$ by Picosecond Light Pulses', *Opt. Lett.* **13**, 224 (1988).
26. M. Zgonik, I. Biaggio, U. Bertele and P. Günter, 'Degenerate Four-Wave Mixing in $KNbO_3$: Picosecond and Photorefractive Nanosecond Response', *Opt. Lett.* **16**, 977–979 (1991).
27. I. Biaggio and G. Roosen, 'Influence of Shallow Traps on the Enhancement of the Photorefractive Grating Amplitude by a High-Frequency Alternating Electric Field: A Probabilistic Analysis', *J. Opt. Soc. Am.* **B13**(10), 2306–2314 (1996).
28. A. Ennouri, M. Tapiero, J. P. Vola and J. P. Zielinger, 'Determination of the Mobility and Transport Properties of Photorcarriers in $Bi_{12}GeO_{20}$ by the Time-of-Flight Technique', *J. Appl. Phys.* **74**(4), 2180–2191 (1993).
29. P. Nouchi, J. P. Partanen and R. W. Hellwarth, *OSA Technical Digest Series – Optical Society of America*, Vol. 12, in Conference on Lasers and Electro-Optics, 1992 (Washington, D.C., 1992), p. 84.
30. M. Wintermantel and I. Biaggio, 'Temperature Dependent Electron Mobility and Large Polaron Interpretation in $Bi_{12}SiO_{20}$', *Phys. Rev.* **B67**, 165108 (2003).
31. R. W. Hellwarth and I. Biaggio, 'Mobility of an Electron in a Multi-Mode Polar Lattice', *Phys. Rev.* **B60**(2), (1999).
32. G. G. Malliaras, V. V. Krasnikov, H. J. Bolink and G. Hadziioannou, 'Transient Behavior of Photorefractive Gratings in a Polymer', *Appl. Phys. Lett.* **67**, 455 (1995).
33. H. Baessler, G. Herrmann, N. Riehl and G. Vaubel, *J. Phys. Chem. Solids* **30**, 1579 (1969).
34. H. Scher, M. F. Shlesinger and J. T. Bendler, 'Time-Scale Invariance in Transport and Relaxation', *Physics Today* **44**(1), 26–34 (1991).
35. J. Wolff, S. Schluter, U. Hofmann, D. Haarer and S. J. Zilker, 'Speed Enhancement of Photorefractive Polymers by Means of Light-Induced Filling of Trapping States', *J. Opt. Soc. Am.* **B16**, 1080 (1999).
36. S. J. Zilker, M. Grasruck, J. Wolff, S. Schloter, A. Leopold, M. A. Kol'chenko, U. Hofmann, A. Schreiber, P. Strohriegl, C. Hohle and D. Haarer, 'Characterization of Charge Generation and Transport in a Photorefractive Organic Glass: Comparison between Conventional and Holographic Time-of-Flight Experiments', *Chem. Phys. Lett.* **306**, 285 (1999).
37. U. Hofmann, M. Grasruck, A. Leopold, A. Schreiber, A. Schloter, C. Hohle, P. Strohriegl, D. Haarer and S. J. Zilker, 'Correlation between Dispersivity of Charge Transport and Holographic Response Time in an Organic Photorefractive Glass', *J. Phys. Chem.* **B104**, 3887 (2000).
38. A. Leopold, M. Grasruck, U. Hofmann, M. A. Kol'chenko and S. J. Zilker, 'Length Scales of Charge Transport in Organic Photorefractive Materials', *Appl. Phys. Lett.* **76**, 1644 (2000).
39. I. Biaggio, 'Photorefractive Effects Induced by Short Light Pulses', Ph.D. Thesis No. 10009, Fig. 5.26, ETH Zurich, Switzerland (1993).

CHAPTER 5

MODELS FOR LASER ABLATION

S. I. Anisimov[1], N. M. Bityurin[2, 3] and B. S. Luk'yanchuk [3]

[1] *L. D. Landau Institute for Theoretical Physics, Russian Academy of Sciences, 142432 Chernogolovka, Moscow Region, Russia, E-mail: anisimov@itp.ac.ru;* [2] *Institute of Applied Physics Russian Academy of Sciences, 603950 Nizhnii Novgorod, Russia, E-mail: bit@appl.sci-nnov.ru;* [3] *Data Storage Institute, Agency for Science, Technology and Research, Singapore 117608, E-mail: Boris_Lukiyanchuk@dsi.a-star.edu.sg*

ABSTRACT: Physical mechanisms and theoretical models of laser ablation are discussed in this chapter. Among the basic models we present the surface vaporization model, bulk models for polymer ablation, e.g., photothermal and photochemical, photophysical ablation model and a two-temperature model for subpicosecond ablation of metals. For various mechanisms typical associated phenomena are qualitatively analyzed and methods for studying them quantitatively considered. Calculations of ablation kinetics for various materials are presented and compared with experimental data.

1. Introduction

Irradiation of solid surfaces with intense laser pulses leading to removal of material is called ablation. Pulsed laser ablation is of great interest to technological applications and fundamental physics. The great majority of researches e.g., refs. [1–8], utilize the term "laser ablation" to describe the damage of a solid material, similar to evaporation or sublimation, usually complicated by the occurrence of a condensed phase in the disintegration products. However, we do not consider it appropriate to use the term "laser ablation" to all kinds of laser-induced material removal processes, e.g. for laser-induced chemical etching [8] and laser induced "crumbling" of materials through the formation of microcracks [9].

Many authors also emphasize that laser ablation has a fluence threshold, i.e. an appreciable removal of the material takes place only for $\Phi > \Phi_{th}$ see, for instance, refs. [10–12]). Some authors claim that the term "laser ablation" has been adopted to describe situations with explosive vaporization of the underlying material, when it reaches its vaporization temperature, see e.g. discussion [13]. Many models have been developed to describe ablation processes, but each pertains only to a separate component of the interaction thus applicable only in limited conditions.

The pioneering investigations of laser ablation were performed almost 40 years ago [14–18], see also [19, 20] and references cited therein. The aim of this chapter is to outline the fundamental works on modeling laser ablation. Some of the most important results were discussed recently in our papers [21–23]. Because of the breadth of the problem, we do not discuss here physical processes within the plume of the ablation products.

Aaron Peled (ed.), Photo-Excited Processes, Diagnostics and Applications (PEPDA), 121–159, 2003.
© 2003 *Kluwer Academic Publishers. Printed in the Netherlands.*

2. Thermal model

2.1. *Qualitative results*

The first investigations of laser ablation [14–18] primarily dealt with the response of the absorbing media to radiation of cw lasers and lasers with millisecond pulses, where the quasi-stationary ablation regime achieved main attention. Relying on these investigations, the so-called ‘thermal model’ of laser evaporation [14, 15, 18] was formulated in the 1960s, not undergoing substantial changes since then.

Since the early 1980s ablation research was pursued primarily with laser pulse durations in the nanosecond range [8]. Then, during the last decade, increasingly more attention has been paid to the ablation produced by ultrashort laser pulses in the picosecond and femtosecond range, see refs. [24–27], for which the quasi-stationary model is not applicable.

There is always the question of the laser ablation mechanism [28]. In particular, it is vital to understand whether experimental data can be interpreted by the ‘thermal model’ or other mechanisms, such as photochemical bond breaking, non-equilibrium molecular excitation, which may play an important role in the process. This endeavor requires the verification if the laser ablation rate obeys the conventional ‘thermal’ behavior.

The kinetics of thermal evaporation of condensed bodies is described by the relationship

$$v = v_0 \exp\,[-T_a/T] \tag{2.1}$$

The constants v_0 and T_a in formula (2.1) are listed in reference data e.g. [29]. The derivation of formula (2.1) and a comprehensive discussion may be found in [30].

During laser pulse irradiation, the temperature T and the laser ablation rate v vary with time. The dependences $T(t)$ and $v(t)$ are determined in experiments and the laser ablation mechanism can be found by analyzing these dependences in Arrhenius coordinates: $\ln(v) = f(1/T)$, for which a straight line corresponds to the thermal process.

However, the difficulty is that direct measurements of $T(t)$ and $v(t)$ are extremely hard to accomplish in experiments with short laser pulses. As a rule, researchers determine another dependence, namely, the layer thickness h of the material removed per pulse as a function of fluence Φ [8]:

$$h = h(\Phi), \qquad h = \int_0^\infty v(t)\,dt, \qquad \Phi = \int_0^\infty I(t)\,dt, \tag{2.2}$$

where $I(t)$ is the intensity of the incident laser radiation. The integral curve $h = h(\Phi)$ depends only slightly on the change in the ablation mechanism. The experimental data can be satisfactorily described employing conservation laws, which do not take into account the kinetics of the process investigated.

The qualitative behavior of the $h = h(\Phi)$ dependence is easy to analyze. For materials strongly absorbing the laser radiation, these dependences exhibit three characteristic regions: the subthreshold process, $\Phi < \Phi_{th}$, the ablation in the immediate vicinity of the threshold $\Phi \approx \Phi_{th}$, and the region of developed ablation $2.5\ \Phi_{th} < \Phi < 5\ \Phi_{th}$.

In typical cases, the surface temperature T peaks at some point in time t_{max}, of the order of the pulse length τ_ℓ, and varies smoothly in the vicinity. Furthermore, in many cases of practical interest one can consider $T_a \gg T$ in formula (2.1). This inequality determines in fact the range of applicability of formula (2.1). That is why the integral of the laser ablation rate, which appears in expression (2.2), can be calculated by the saddle-point method.

The layer thickness of the material removed by one pulse is given by:

$$h = A \exp\left(-\frac{T_a}{T_{max}}\right), \quad A \approx \sqrt{\frac{2\pi T_{max}}{T_a}}\, v_0 t_\ell. \tag{2.3}$$

In the range of temperatures typical to laser ablation, the weak temperature dependence of the parameter A can be neglected. In the majority of laser ablation experiments, the fluence $\Phi = I_0 t_\ell$ is varied by changing the intensity with neutral density filters or focusing, while the pulse shape is kept constant. In this case, for subthreshold fluences $\Phi < \Phi_{th}$, we can assume with a good accuracy that $T_{max} \propto \Phi$ and transform relationship (2.3) to the Arrhenius form

$$h = A \exp\,[-B/\Phi], \tag{2.4}$$

where A and B are constants. The presence of 'Arrhenius tails' (see in Figure 1) is quite often regarded as a strong argument in favor of the thermal mechanism in laser ablation, see for instance in ref. [31].

Above the threshold of laser ablation $\Phi > \Phi_{th}$, for relatively short laser pulses and high radiation absorption coefficients an intermediate region of linear dependence of the evaporated layer thickness vs. fluence is found, which follows from the energy balance [8]:

$$h = \beta(\Phi - \Phi_{th}), \quad \beta \approx \frac{1 - R}{L}, \tag{2.5}$$

where R is the surface optical reflection coefficient, and L is the latent heat of vaporization per unit volume of the solid.

Lastly, the screening of the evaporating surface by the plume of the ablation products exerts a significant influence on the ablation process at high laser fluences $2.5\ \Phi_{th} < \Phi < 5\ \Phi_{th}$. Assuming the optical thickness of the screening plume to be proportional to the mass evaporated, one can show that the fluence that finds its way to the solid surface, taking into account the radiation absorption in the plume, is given by $\Phi_a = \Phi \exp[-\alpha_g h]$, where α_g is the effective radiation absorption coefficient of the vapor normalized to the density of the solid. We substitute Φ_a for Φ

in formula (2.4) and solve the resultant equation for Φ to obtain

$$\Phi = B \exp[\alpha_g h] \ln^{-1} [A/h], \tag{2.6}$$

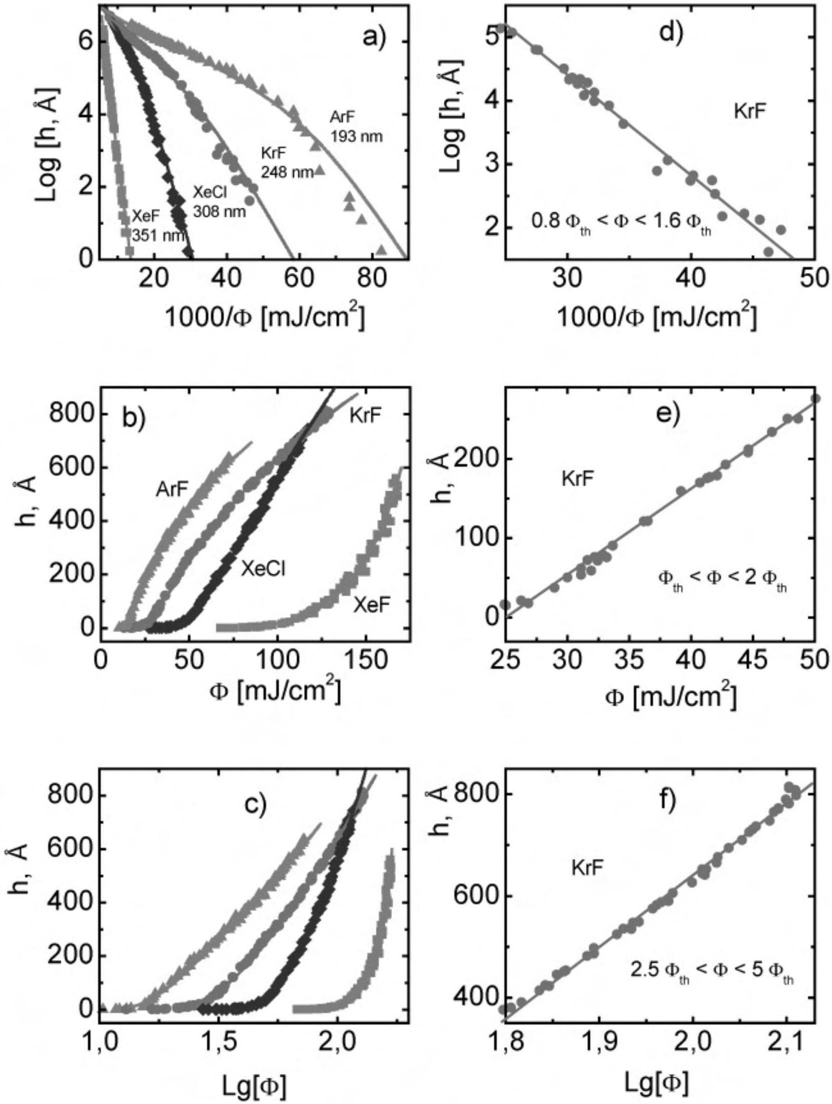

Figure 1. The thickness of polyimide ablated by excimer ArF, KrF, XeCl and XeF laser irradiation, reproduced from Ref. [31], in Arrhenius (a), linear (b), and logarithmic (c) coordinates. The dashed lines represent the best approximation by interpolation of formula (2.6). (d–f) Enlarged views of the regions, where experimental points follow the Arrhenius (2.4), linear (2.5), and logarithmic (2.7) dependences (straight dashed lines).

Equation (2.6) was proposed in ref. [32] as an interpolation formula for describing the dependence of the ablated thickness on laser fluence over a wide range of fluences. Figure 1 shows that this equation agrees well with available experimental data.

For small fluences, Eq. (2.6) reduces to Eq. (2.4). For high fluences, where plays a significant role, it leads to a logarithmic dependence

$$h = \frac{1}{\alpha_s} \ln \left(\frac{\Phi}{\Phi_s} \right), \quad \Phi_s = \frac{B}{\ln (\alpha_s A)} . \tag{2.7}$$

Other screening models were considered in Refs. [16, 33].

Although all three characteristic dependences – the Arrhenius dependence (2.4) in the subthreshold range, the linear one (2.5) in the vicinity of the threshold, and the logarithmic one (2.7) in the screening region – were derived using qualitative considerations, these dependences also follow from an extended consideration of the dynamics of the process in the framework of the thermal model [34]. These three ranges are conveniently analyzed more closely by using the proper coordinates in which the $h(\Phi)$ dependences are represented by straight lines (Figure 1d–1f).

As shown below the integral curves have a weak dependence on the detailed kinetics of the laser ablation. The registration of the time variation of the surface temperature of the material experiencing ablation would be most informative. These data, however, are hard to obtain. Paper [35] is an exceptional case where the surface temperature of polyimide was measured for ablation produced by the nanosecond pulse of an excimer laser.

2.2. *Dynamics of laser ablation: Calculations assisted by the moments method*

The accurate calculation of temperatures during laser ablation is of great importance. This problem is however rather complicated. Calculations based on the solution of the linear heat conduction equation are usually oversimplified and sometimes inappropriate even for qualitative estimates. The moments method in contrast, seems to be suited best for quantitative calculations of laser ablation. This method permits the reduction of the complex nonlinear problem of solving partial differential equations to an integration of a set of ordinary differential equations. By this method it is easy to take into account the temperature dependences of optical and thermal properties of the material, the effects caused by radiation absorption in the vapor, the phase transitions i.e., evaporation, melting, structural transitions, and also the particular laser pulse shape [34, 36, 37].

We consider here the transient laser ablation in the one-dimensional case. This case is realized when a target is irradiated by a sufficiently short laser pulse. Let the plane ablation front travel in the z-direction with a velocity $v = v(t)$. The heat conduction equation written in the ablation-front frame of reference is:

$$\frac{\partial H}{\partial t} = v \frac{\partial H}{\partial z} + \frac{\partial}{\partial z} \left(\kappa \frac{\partial T}{\partial z} \right) - \frac{\partial I}{\partial z} \equiv B[T], \tag{2.8}$$

where

$$H(T) = \rho \int_{T_\infty}^{T} c(T_1)\, dT_1, \tag{2.9}$$

is the enthalpy per unit volume of the solid, $c(T)$ is its specific heat capacity, $\kappa(T)$ is the thermal conduction coefficient, and T_∞ is the initial temperature. The density ρ of the solid is assumed to be constant, and $B[T]$ denotes the right-hand side of Eq. (2.8).

The absorbed laser radiation intensity distribution in the bulk of a solid is defined by the equation

$$\frac{\partial I}{\partial z} = -\alpha I, \qquad I|_{z=0} = I_s, \tag{2.10}$$

Here, α is the absorption coefficient, and I_s is the absorbed laser radiation intensity at the ablation front ($z = 0$).

The intensity I_s at the ablation front depends on the temporal profile of the laser pulse $I = I(t)$, the surface temperature $T_s = T(z = 0, t)$, and the layer thickness of an evaporated material: $h(t) = \int_0^t v(t_1)dt_1$, which screens the ablation front:

$$I_s = I(t)A(T_s) \exp [-\alpha_g h], \tag{2.11}$$

where $A(T_s) = 1 - R(T_s)$ is the absorptivity, R is the reflectivity, and α_g is the absorption coefficient of the vapor (ablation products) normalized to the solid density. The velocity of the ablation front is defined by formula (2.1) in which $T = T_s(t)$ should be substituted.

All optical and thermal parameters in equations (2.8)–(2.11) and also the pre-exponential factor in formula (2.1) may generally depend on temperature.

The heat conduction equation (2.8) should be completed with initial and boundary conditions. The boundary condition at the ablation front relates the heat flux J_s at the phase interface to the expenditure of energy for evaporation [15]:

$$\kappa \frac{\partial T}{\partial z}\Big|_{z=0} = v[L - H_s + H_s^{(v)}] \equiv -J_s. \tag{2.12}$$

Here, L is the latent heat of vaporization per unit volume of the solid, $H_s = H(T_s)$ is the enthalpy of a unit volume of the solid at the phase interface, $H_s^{(v)} = \rho\int_{T_\infty}^{T_s} c^{(v)}(T_1)dT_1$ is the vapor formation enthalpy referred to a unit volume of the solid, and $c^{(v)}(T)$ is the heat capacity of the vapor at constant pressure. The second boundary condition $T|_{z\to\infty} = T_\infty$ and the initial condition $T|_{t\to 0} = T_\infty$ are obvious.

In view of the relationship (2.9), the boundary condition (2.12) can be rewritten as

$$\frac{\partial H}{\partial z}\Big|_{z=0} = -\frac{J_s}{\chi_s}, \tag{2.13}$$

where $\chi = \kappa/c\rho$ is the thermal diffusivity, and $\chi_s = \chi(T_s)$. The model described by Eqs. (2.8)–(2.13) does not take into account some effects, such as the density variation $\rho = \rho(T)$ caused by the thermal expansion of the solid. However, the discarded effects are usually small, and therefore the model outlined in the foregoing is appropriate for the quantitative investigation of transient ablation.

The basic idea of the moments method was outlined in detail in the monographs [38–40]. The application of this technique to solve nonlinear heat equations for thermal laser ablation was discussed in [34, 36, 37]. We introduce two moments of the enthalpy distribution:

$$M_0(t) = \int_0^\infty H(z, t)dz, \qquad M_1(t) = \int_0^\infty zH(z, t)dz, \tag{2.14}$$

Integration of the heat equation, with appropriate boundary conditions, yields the following system of equations

$$\frac{dM_0}{dt} = -vH_s + J_s + I_s = -v(L + H_s^{(v)}) + I_s, \qquad \frac{dM_1}{dt} = -vM_0 + \int_{T_\infty}^{T_s} \kappa(T)\, dT + \frac{I_s}{\alpha}, \tag{2.15}$$

The proper choice of the trial function is of crucial importance to the moments method. In refs. [33, 35, 36] the adopted function was

$$H_p(z, t) = \frac{1}{1 - \alpha\ell} \left\{ \left[H_s - \frac{J_s\ell}{\chi_s} \right] \exp\,[-\alpha z] - \left[\alpha\ell H_s - \frac{J_s\ell}{\chi_s} \right] \exp\left[-\frac{z}{\ell} \right] \right\}. \tag{2.16}$$

A trial function of the form (2.16) satisfies the boundary conditions for $z = 0$, $z = \infty$ and ensures the fulfillment of the obvious condition $H_p(z = 0, t) \equiv H_s(t)$. The first term in expression (2.16) describes the variation of the enthalpy distribution related to the radiation penetration depth, while the second term describes the effects related to thermal conduction. The function $\ell(t)$ is the enthalpy distribution spatial scale, i.e., the heated layer thickness or the characteristic thermal length.

Substituting expression (2.16) into Eq. (2.14) we get the following expressions for the moments:

$$M_0 = (\ell + \alpha^{-1})H_s - \frac{\alpha^{-1}\ell J_s}{\chi_s}, \qquad M_1 = (\ell^2 + \ell\alpha^{-1} + \alpha^{-2})H_s - (\ell + \alpha^{-1})\,\frac{\alpha^{-1}\ell J_s}{\chi_s}. \tag{2.17}$$

Next, one should introduce expressions (2.17) into Eqns. (2.15) to obtain the differential equations for the functions $T_s(t)$ and $\ell(t)$. The J_s and H_s quantities are related to T_s by equations (2.9) and (2.12). It is worth noting that we need not solve analytically these equations for the derivatives $d\ell/dt$ and dT_s/dt if we use

high-level software, such as 'Mathematica' [41], to solve numerically the resultant equations.

In the particular case of constant thermal and optical characteristics these equations can be written in an explicit form [21]:

$$\frac{dT_s}{dt} = F(T_s, \ell), \qquad \frac{d\ell}{dt} = \Psi(T_s, \ell). \tag{2.18}$$

The functions F and Ψ in the above equations are defined by the formulas

$$F = \alpha v T_L \frac{(2q+1)\frac{1}{\xi} - \left(1 + \frac{\xi}{\alpha\ell}\right)\theta_s - 2}{2 + \alpha\ell + \Pi}, \tag{2.19}$$

$$\Psi = \frac{\chi}{\ell} \frac{\alpha\ell\left[q - q_s(1-\xi) + (1 + \alpha\ell + \Pi)\left(1 - q - \frac{1}{\xi}\right) + (1 + \theta_s\xi)(1 + \Pi)\right]}{(1 + \theta_s\xi)(2 + \alpha\ell + \Pi)}, \tag{2.20}$$

where

$$T_L = \frac{L}{c}, \quad \Pi = \frac{T_a T_L}{(T_L + T_\infty)^2}\frac{v\ell}{\chi}, \quad \theta_s = \frac{T_s}{T_L}, \quad \xi = \frac{\alpha\chi}{v}, \quad q = \frac{I_s}{c\rho v T_s}. \tag{2.21}$$

are dimensionless parameters. One may note that in Eqs. (2.19)–(2.21) and later on, T denotes the increase in temperature, i.e. the surface temperature is now defined as $T = T_s + T_\infty$.

The system of equations for the surface temperature and the heated layer thickness should be complemented with the equation describing the variation of the ablation layer thickness:

$$\frac{\mathrm{d}h}{\mathrm{d}t} = v = v_0 \exp\left[-\frac{T_a}{T_s + T_\infty}\right], \tag{2.22}$$

which is required for describing the screening effect. Therefore, the problem reduces to a system of three ordinary differential equations for the functions $T_s(t)$, $\ell(t)$ and $h(t)$, which should be numerically integrated with the corresponding initial conditions. This approach proves to be more flexible and convenient for the analysis of the experimental data than the direct numerical solution of the boundary-value problem employing finite difference or finite element methods. An investigation of different problems on laser ablation, performed in refs. [34, 36, 37], reveals that the moments method maintains an accuracy of about 20–30% and allows an easy inclusion of the temperature variations of $c(T)$, $\kappa(T)$, and $A(T)$.

Figure 2 gives an example of the computational investigation of the ablation kinetics in polyimide exposed to radiation of excimer lasers with different wave-

lengths. The temperature dependences of the thermal parameters of the material are given in the Figure's caption. The laser pulse shape was modeled by the function

$$I(t) = I_0 \frac{t}{t_\ell} \exp\left[-\frac{t}{t_\ell}\right], \tag{2.23}$$

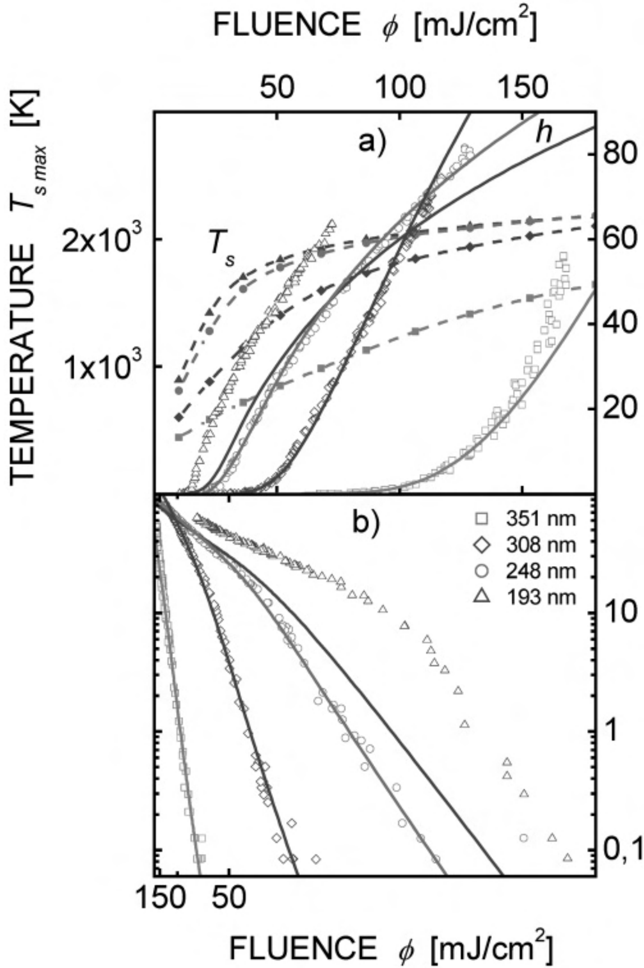

Figure 2. Laser ablation of polyimide [34]. Calculation by the moments method (solid curves) and from experimental data [31] in conventional (a) and Arrhenius (b) coordinates. Parameters of calculations: $t_\ell = 6.13$ ns (the FWHM of the laser pulse is 15 ns); $v_0 = 3 \times 10^6$ cm s^{-1}; $T_a = 15.7 \times 10^3$ K = 1.51 eV; $T_\infty = 300$ K; $c = 2.55 - 1.59 \exp[(300 - T)/460]$ J g^{-1} K^{-1}; $c_g = 2.55$ J g^{-1} K^{-1}; $\kappa = 1.55 \times 10^{-3} \times (T/300)^{0.28}$ W cm^{-1} K^{-1}; $\rho = 1.42$ g cm^{-3}; $L/\rho = 500$ J g^{-1}; $\alpha_g = 0.45\,\alpha$; $\lambda = 193$ nm (triangles), $A = 0.93$, $\alpha = 4.25 \times 10^5$ cm^{-1}; $\lambda = 248$ nm (circles), $A = 0.88$, $\alpha = 3.1 \times 10^5$ cm^{-1}; $\lambda = 308$ nm (diamonds), $A = 0.89$, $\alpha = 10^5$ cm^{-1}; $\lambda = 351$ nm (squares), $A = 0.9$, $\alpha = 0.32 \times 10^5$ cm^{-1}. The dashed lines represent the calculated peak surface temperature.

with the fluence and the characteristic time related by the formula $\Phi = I_0 t_\ell$. We note that the full width at half maximum (FWHM) of the laser pulse is $t_{\mathrm{FWHM}} \approx 2{,}445\ t_\ell$. For brevity the pulse shape given by (2.23) will be referred to as the "excimer" pulse.

One can realize from Figure 2 that the dependences of the removed layer thickness h on the fluence Φ for the 350, 308, and 248 nm wavelengths are adequately described by our formalism using the thermal model with surface evaporation. Notice that the temperature at the ablation front in Figure 2 agrees well with that measured in Ref. [35]. However, for the 193-nm radiation, the computations and experimental data diverge significantly, probably since the ablation mechanism is more complex than the purely thermal approximation.

Similar calculations employing the moment's method were carried out for the laser ablation of metals. In Ref. [36], for instance, a study was made on ablation of indium exposed to a laser pulse with a duration of $t_{\mathrm{FWHM}} = 15$ ns. It turned out that the calculated results involving the thermal model agreed nicely with the experimental data throughout the nanosecond range [24, 42]. However, the ablation mechanism proves to be more complicated for subpicosecond pulses e.g. $t_{\mathrm{FWHM}} = 0.5$ ps. Some of the calculated results on the laser heating dynamics and indium ablation are given in Figure 3.

The investigation of the system of Eq. (2.18) is a conventional problem of the nonlinear theory of oscillations [43]. This system of equations has a single singular point $T_s = T_{s0}$, $\ell = \ell_s$, which corresponds to the so-called *stationary evaporation wave* [15, 17, 18], where $F = \Psi = 0$. The parameters of the stationary wave are conveniently written implicitly by

$$v_s = v_0 \exp\left[-\frac{T_a}{T_\infty + T_{s0}}\right], \qquad I_s = c\rho v_s(T_{s0} + T_L), \qquad \ell_s = \frac{\chi}{v_s}. \tag{2.24}$$

Here the temperature T_{s0} and the heated layer thickness ℓ_s in (2.24) are independent of the absorption coefficient α. The moments method and the successful choice of the trial function (2.16) lead to results which coincide with the exact solution not only for short, but for also for long times, $t \to \infty$. Therein presumably lies the cause of the good accuracy of the method, typically of 20–30% [34, 36, 37].

Several parameters of the stationary evaporation wave are shown in Figure 4. One can see from the plots that the lengths ℓ and $z_{\max}$ decrease while the temperatures T_{s0}, $T_{\max}$ and the subsurface superheating $\Delta T = T_{\max} - T_{s0}$ grow with increasing radiation intensity. The lengths ℓ and $z_{\max}$ differ greatly in scale, thus the point $z_{\max}$ is located near the evaporating surface, and these lengths are therefore plotted on different scales in Figure 4c. We stress also that the surface evaporation model is applicable here only in the temperature range $T < T_c$, where T_c is the critical temperature. As the critical temperature is approached, the enthalpy of the phase transition decreases and then vanishes at the critical point. To investigate the laser ablation at the critical and higher temperatures, one should use the hydrodynamics models.

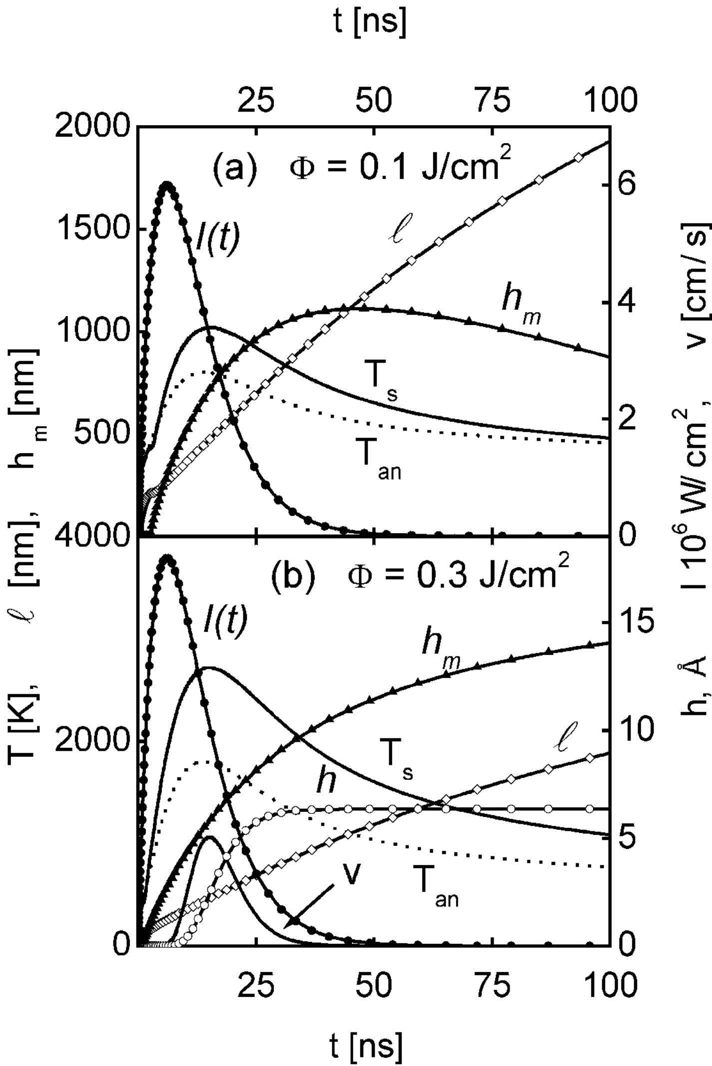

Figure 3. Calculated results on laser heating and ablation of an indium target in the subthreshold region (the FWHM of the laser pulse is 15 ns) [36]. Shown are the laser pulse profile $I(t)$, the surface temperature T_s, the heated layer thickness ℓ, the location of the melting front h_m, the ablation rate v, and the ablation layer thickness h of the material. The dotted lines represents the temperature determined by solving the linear heat equation

$$T_{an} = T_\infty + \frac{\alpha A}{\rho c} \int_0^t I(t - t_1)\ e^{a^2 D t_1}\ erfc\sqrt{\alpha^2 D t_1} dt_1 . \qquad (2.25)$$

The thermal parameters in the equation are constant and equal to the corresponding values at room temperature T_∞. The temperature dependences of the parameters c, κ, α and A used in the calculations were reported in Ref. [36].

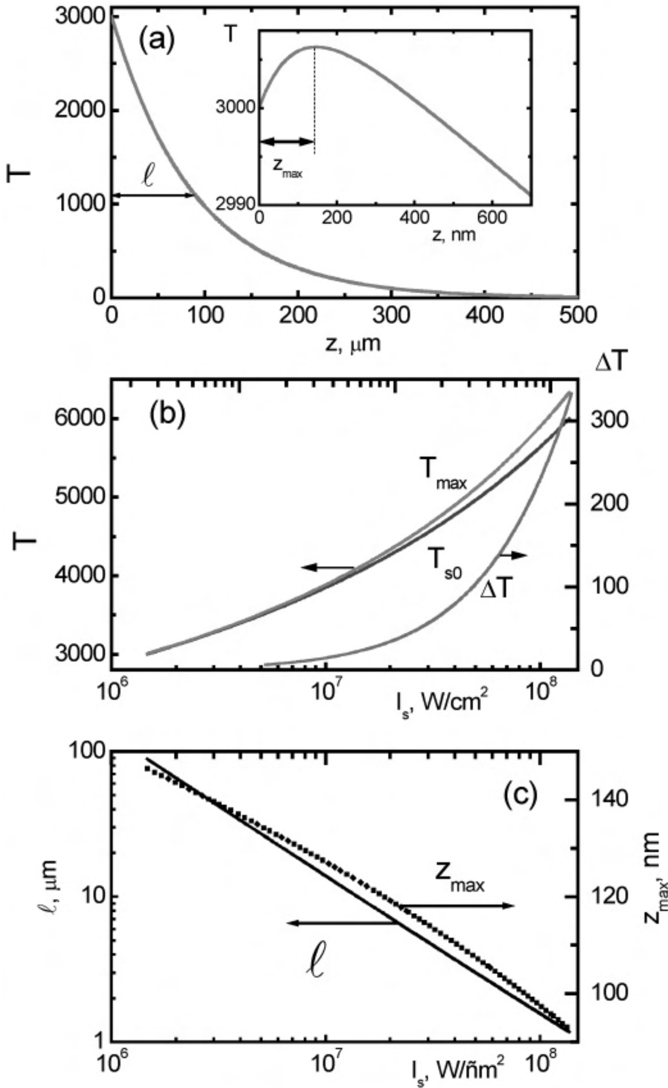

Figure 4. Parameters of the stationary evaporation wave calculated for $v_0 = 10^6$ cm s^{-1}, $T_a = 3 \times 10^4$ K, $T_\infty = 300$ K, $c = 1$ J g^{-1} K^{-1}, $\kappa = 1$ W cm^{-1} K^{-1}, $\rho = 1$ g cm^3, $L/\rho = 10^4$ J g^{-1}, and $\alpha = 10^5$ cm^{-1}: (a) temperature distribution in the wave for $T_{s0} = 3000$ K (the inset shows an enlarged view of the temperature peak neighborhood); (b) surface temperature T_{s0}, peak temperature T_{max}, and the superheating $\Delta T = T_{max} - T_{s0}$ as the functions of intensity I_s; (c) characteristic thermal length ℓ and location of the temperature peak z_{max} as functions of intensity Is.

The stability investigation of the singular point (2.25) is performed by conventional techniques of non-linear theory [43]. This analysis [21] indicates that the singular point, a node or a focus, is stable, and the stationary evaporation wave is

therefore an attractor to which the solution is attracted from any initial conditions. The bifurcation boundary, which separates the nodes and the foci, is shown in Figure 5(a) in the $\{I_s, \alpha\}$ – parameter plane. In the case when the state is a focus, transient oscillations occur at the initial stage of the process. The phase portrait and the oscillation dynamics of the ablation rate and heated layer thickness for this system are shown in Figure 5(b–d), respectively. These oscillations may be of importance [10].

When pulsed laser ablation is investigated, the intensity of the incident radiation depends on time. In this case, Eqs. (2.20) should be solved simultaneously with Eq. (2.23) and the intensity I_s at the ablation front is given by formula (2.11). The layer thickness of the material removed during a laser pulse is defined by the integral

$$h = v_0 \int_0^{t \gg t_\ell} \exp\left[-\frac{T_a}{T_\infty + T_s(t)}\right] dt, \tag{2.26}$$

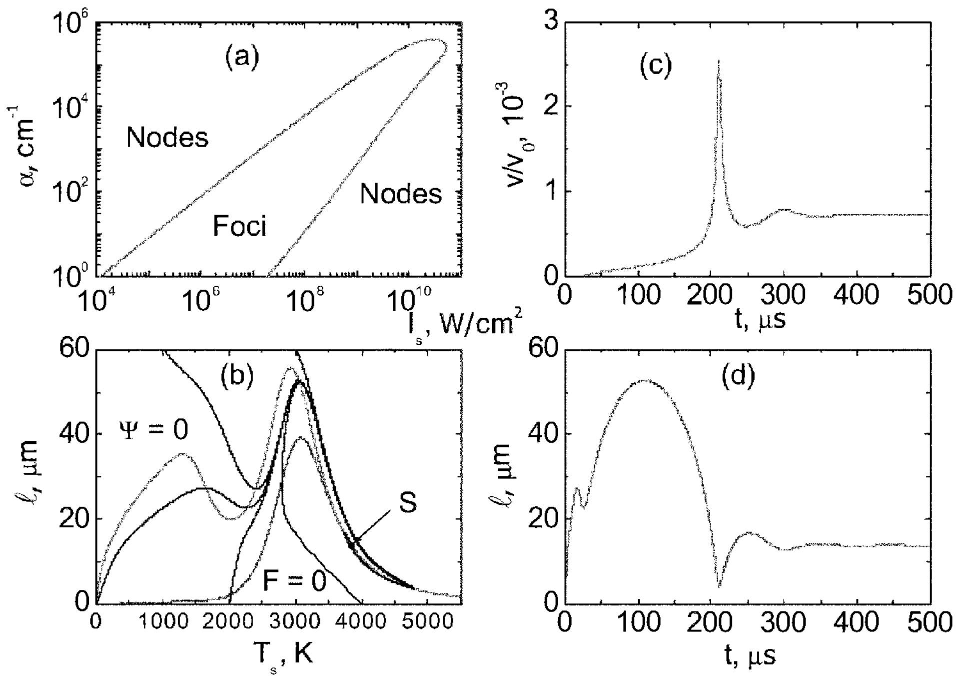

Figure 5. (a) Bifurcation boundary in the plane of parameters $\{\alpha, I_s\}$, which separates stationary states of the node and focus type; the thermal parameters are the same as in Figure 4. (b) Phase portrait of the system for $\alpha = 10$ cm^{-1}, $I_s = 10^7$ W cm^{-2}, and stationary wave parameters $T_{s0} = 3848$ K, $\ell_s = 13.8$ μm. (c) Temporal variation of the laser ablation rate. (d) Temporal variation of the heated layer thickness ℓ.

The expression (2.26) is understood as an intermediate asymptotic. Should the integration in expression (2.26) be extended to infinity, the integral would diverge, since for $t \to \infty$ the temperature $T_s \to 0$, thus the ablation rate $v = v_0 \exp[-T_a/T_\infty] > 0$ becomes a finite though very small. The intermediate asymptotic technique is well developed and widely used for problems of physics of combustion and chemical kinetics [44–46].

It can be shown [34, 37] that the dependence $h(\Phi)$ has three characteristic ranges in the case when the optical and thermal parameters are constant, i.e., the sub-threshold case – for $\Phi < \Phi_{th}$, near-threshold for $\Phi > \Phi_{th}$, $\Phi \approx \Phi_{th}$, and screening, $2.5\ \Phi_{th} < \Phi < 5\ \Phi_{th}$. The asymptotic behavior of the curves in these ranges is well described by formulas (2.4), (2.5), and (2.7), and the general dependence follows the interpolation formula (2.6).

The lowering of the threshold Φ_{th} by shortening the laser pulse can also be considered as a characteristic feature of thermal ablation. The ablation threshold may also vary significantly with the form of the laser pulse [36]. The peak surface temperature grows by shortening the laser pulse, while the time at which this temperature and heated layer thickness ℓ are attained decreases [21].

Some special cases when the integral kinetics of laser ablation departs from the discussed above are noteworthy. These departures may be caused by the temperature dependences of the optical and thermal parameters of the material. We shall highlight here deviations of two types: (i) the slope of the $h(\Phi)$ dependence flattens out, and (ii) the $h(\Phi)$ dependence steepens in the form of "jumps". Responsible for the special feature of the first type is, for instance, the lowering of the heating rate in the vicinity of the melting point [36] and also the growth of the heat capacity with temperature [37]. The jumps in the ablation rate may arise for instance due to the temperature dependence of the absorptivity $A(T)$. For example, one can consider the increase of absorptivity at temperatures $T > T_j$ [21].

An interesting feature of the laser ablation for the case considered above is the occurrence of an "intermediate threshold" attained when the laser ablation rate experiences a rapid change. When the switching temperature T_j is relatively low, the absorption jumps have a minor effect on the $h(\Phi)$ curves shapes. But as T_j increases, the changes in the ablation rate become almost jump-like [21]. Jumps of this type are frequently observed in experiments, see for instance, ref. [8], but have not yet received a satisfactory explanation. In paper [11], attention was drawn to the fact that the intermediate jumps can be attributed to ablation upon cessation of the laser pulse, provided the ablation front catches up with the temperature peak in the layer beneath the surface. In papers [48–50] the appearance of jumps in the ablation rate at a specific fluence value were tentatively explained by an "explosive vaporization" mechanism, i.e., boiling of the overheated material. A similar acceleration in ablation can arise by the development of instabilities of the plane ablation front [47]. The relation between volume and surface effects in ablation processes was discussed in refs. [47, 51].

3. Bulk photothermal model

The thermal ablation model does not consider any chemical modification of the material. However for some materials, e.g. polymers, these chemical transformations can strongly influence the ablation process. Polymers are composed of long macromolecules consisting of sequences of monomers. The inherent feature of polymeric materials is the hierarchy of bonds between the molecular groups. There are strong, covalent, bonds connecting adjacent molecular groups of the same chain, and weak, molecular bonds between neighboring groups that belong to different polymer chains. Removal of molecular groups from the material surface during ablation proceeds through breaking covalent intra chain bonds. On the other hand, the removal of polymer chain as a whole from the surface is possible as a result of breaking of all weak bonds, which connect this chain with the surrounding material. If the chain is long enough, this process is suppressed, because the combined energy of the weak bonds is greater than a single strong bond.

These problems were recently discussed in detail in the review paper [23] and here we discuss briefly the so-called volume photothermal model of laser ablation following refs. [52–55]. The basic idea of this model is that laser ablation proceeds through a bulk reaction, which results in the creation of broken bonds.

Let us consider a single-step, thermally activated reaction $A \to B$. Here A is associated with elements of the initial virgin material, while B denotes the reaction products of broken bonds. N_A and N_B stand for the number density of species A and B, $n_A = N_A/N_0$ and $n_B = N_B/N_0$ are the fractions of unbroken and broken bonds, and N_0 is the initial number density of the bonds. The chemical kinetics equation reads then:

$$\frac{\partial n_B}{\partial t} = V\,\frac{\partial n_B}{\partial z} + (1 - n_B)k_0 \exp\left(-\frac{E_b}{k_B T}\right). \tag{3.1}$$

Here k_0 is a constant, E_b is the activation energy and V is the ablation velocity. Eq. (3.1) is given in the reference frame of the ablation front. The heat equation has the usual form, similar to Eq. (2.8)

$$\frac{\partial T}{\partial t} = V\,\frac{\partial T}{\partial z} + \frac{1}{\rho c_p}\frac{\partial}{\partial z}\left(\kappa\frac{\partial T}{\partial z}\right) + Q. \tag{3.2}$$

The heat source term Q however, contains an additional term that takes into account the heat effect of the chemical reaction. For nanosecond pulses we have

$$Q = \frac{\alpha I}{c_p\rho} - \frac{\Delta H_b N_0(1 - n_B)k_0 \exp\left(-E_b/k_B T\right)}{c_p\rho}, \tag{3.3}$$

where ΔH_b is the enthalpy of each strong bond, which is broken according to Eq. (3.1).

The total energy of the “weak” bonds between the chain and environment for a

short enough chain is proportional to its length. In the model under consideration the ablation is caused by removal of sufficiently short polymer chains. The velocity of ablation can be approximated similarly to Eq. (2.1) by

$$V = V_0 \exp\left(-\frac{E_a}{k_B T_s}\right). \tag{3.4}$$

where E_a denotes the activation energy for removing a short polymer chain. In the case of degradation of the polymer by random chain scission, either due to photochemical or photothermal reactions, the average chain length is about $\sim 1/n_B$ after several steps. Neglecting molecular-mass distributions of polymer chains one can estimate E_a as

$$E_a = E_m/n_s. \tag{3.5}$$

Here n_s is the surface value $n_s(\mathrm{t}) = n_B(0, t)$ and E_m stands for the energy of the weak bonds per “monomer”. A monomer here refers to the molecular group between neighboring-along-the-chain bonds, which can be broken. Thus the ablation velocity is given in this case by:

$$V = V_{0m} \exp\left[-\frac{E_m}{k_B n_s T_s}\right]. \tag{3.6}$$

Eq. (3.6) provides a sharp dependence of the ablation rate on the number density of broken bonds at the boundary. Following Refs. [54, 55], we employ equation (3.6) with the boundary condition:

$$\kappa(T) \left.\frac{\partial T}{\partial z}\right|_{z=0} = \rho \Delta H_m V, \tag{3.7}$$

where ΔH_m stands for the enthalpy of evaporation of weak bonds per ‘monomer’. The boundary conditions at infinity are

$$T|_{z\to\infty} = T_\infty, \quad n_B|_{z\to\infty} = 0. \tag{3.8}$$

This generic model permits various modifications and simplifications. For example, instead of equation (3.6), which gives the Frenkel-Wilson type boundary condition, one can use the Stefan type boundary condition, where a position of the interface is fixed with a certain critical value, n_{cr} of broken bonds [52, 53]:

$$n_s = n_{cr}. \tag{3.9}$$

This condition can be considered as an approximation of (3.6) with a very sharp dependence of the velocity on the fraction of broken bonds at the surface. If the length of the chain at the surface becomes shorter than n_{cr} and if E_m can be neglected,

we obtain the condition (3.9). In this case the enthalpy of evaporation can also be neglected, i.e.

$$\kappa(T)\,\frac{\partial T}{\partial z}\bigg|_{z=0} = 0. \tag{3.10}$$

In what follows the surface evaporation thermal model, without the chemical modification is referred to as model I. The volume model with a chemical modification and with Stefan type condition (3.9) is referred to as model II, while the volume model of Frenkel-Wilson type with the boundary condition (3.4) is referred to as model III.

The analysis of the stationary ablation within the Stefan-type bulk photothermal model has been performed in Ref. [52]. It was shown that a stationary wave in this model is similar to the stationary laser surface evaporation wave, but with a renormalized activation energy $E_a' = 2E_b/3$. A more rigorous analysis [53] shows that E_a' slightly depends on the laser intensity, changing from $E_a' = 2E_b/3$ at small intensities to $E_a' = E_b$ at high intensities.

For the *stationary regime*, the surface evaporation model resembles the volume model above in several aspects though it is not its limiting case. For example, in the volume model a maximum of temperature is always reached at the surface. Here, instead of the formation of a subsurface temperature maximum, observed in surface models [15], the temperature distribution near the surface flattens out. One can in fact subdivide two spatial regions, along the z-axes. In the reaction region, the absorbed energy goes into the enthalpy of the decomposition reaction. In the conduction region the reaction rate is small and absorption is balanced by changes in temperature. The size of the reaction region, for high velocities, is of the order of $1/\alpha$.

The volume model II yields the following time dependence of the ablated depth h near the onset of ablation, as detailed in Ref. [53]:

$$h(t) = U_0(t - t_{cr})^{1/2}, \qquad U_0 = \text{const} \approx \left(\frac{2D_T}{e^{-\alpha^2 D_T t_{cr}}/erfc\sqrt{\alpha^2 D_T t_{cr}} - 1}\right)^{1/2}. \tag{3.11}$$

The square root dependence in (3.11) leads to an infinite velocity at the moment $t = t_{cr}$. The total thickness of ablated material versus fluence near ablation threshold is given in [53] by a square-root function

$$h_e \propto \left(\frac{\phi - \phi_{th}}{\phi_{th}}\right)^{1/2}. \tag{3.12}$$

We have mentioned already that the experimental data on mass-loss kinetics of polyimide irradiated by KrF excimer laser [31] demonstrate “Arrhenius tails” near the ablation threshold. However, the bulk models II and III cannot explain these tails, if we assume layer-by-layer ablation as the only cause for mass loss. Nevertheless, it has been suggested in [53, 56] that these tails may originate from

the depletion of the volatile species, which result from the same bulk reaction $A \rightarrow B$. This reaction breaks the bonds, destroys the polymer chains, and may simultaneously create trapped volatile species. Below ablation threshold, the volatile species are responsible for mass loss, which requires out-diffusion of trapped species and occurs on μs or even ms time scales. As volatile species and broken bonds are produced in a pyrolytic reaction, this results in an Arrhenius tail. Above the threshold, the volatile species leave the material together with the ablation products. When ablation ceases, some of the volatile species still exist below the surface and leave the material later. This results in an additional mass loss, M (per unit area), which does not necessarily contribute to the ablated depth

$$M = m_v N_0 \int_0^{\infty} n_B(z)dz, \tag{3.13}$$

where m_v is the mass of volatile products produced per broken bond. To compare the theoretical curves with the available experimental data on mass-losses kinetics we introduced the notion of an equivalent "depth" h_M

$$h_M \equiv \frac{M}{\rho} = \frac{m_v}{m_t} \int_0^{\infty} n_B(z)dz. \tag{3.14}$$

Here m_t is the initial mass per virgin bond, $\rho = m_t N_0$, and h_M contributes to the total effective "depth" $h = h_A + h_M$. The above picture is not in contradiction with recent experimental spectroscopic findings [57, 58].

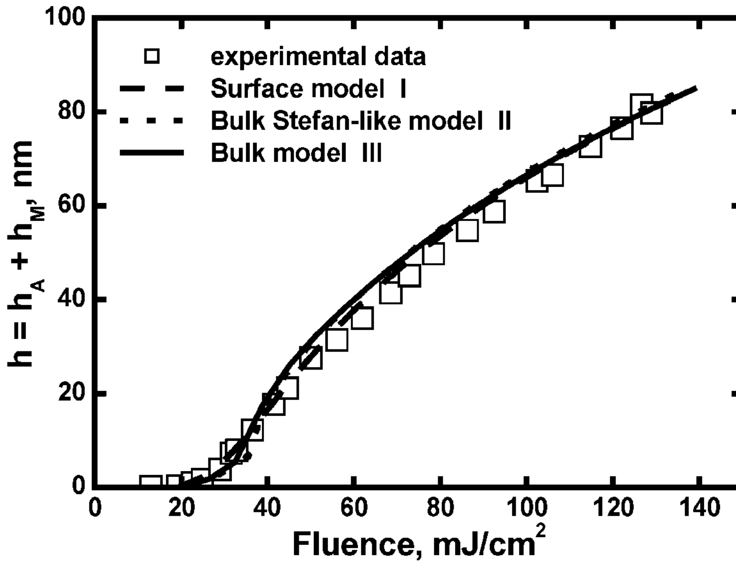

Figure 6. Ablation kinetics of polyimide by KrF excimer laser. Experimental mass-loss data are taken from Ref. [31].

We carried out the calculation of laser ablation kinetics of nanosecond pulses with mass losses. Figure 6 shows the mass losses kinetics curve for all three considered models compared to the experimental data of Ref. [31]. From the curves it is hard to distinguish between the models using only the experimental data on ablation kinetics for nanosecond pulses. These models however yield large differences in the dynamics of ablation as discussed in depth in [23].

Now the ablated depth is measured besides the mass loss method also by profilometry such as optical interferometry, mechanical stylus [59] and atomic force microscope (AFM) [60]. These measurements show that ablation starts *sharply* at a fluence $\phi = \phi_{th}$. Similar conclusions were drawn from reflectivity [61] or acoustic response measurements [62].

We believe that the bulk models outlined above provide the explanation for the discrepancies between the mass-loss and profilometry experiments data. It implies that the latter measure real layer-by-layer material ablation whereas the former takes into account the mass-loss provided by the depletion of volatile species as well. The mass-loss from the bulk of the material may influence the surface morphology even below the threshold fluence. In polymers with flexible chains like PMMA, this may result in an essential decrease of the thin polymer film thickness due to free volume relaxation [63]. In polymers with hard chains like polyimide this relaxation should be hindered. In polyimide phenomena like "hump" and "dent" formation are observed [64]. These impede accurate AFM measurements of ablation kinetics near the threshold.

4. Photochemical ablation

The development of VUV laser sources [65, 66] with wavelength shorter than commonly used F_2 lasers [67] provides new opportunities for laser treatment of materials with greater accuracy and lateral resolution. In particular, VUV ablation of polymers is one of the promising areas using the newly developed laser technique [68]. From the very beginning of UV laser ablation modeling, it was believed that polymer ablation is dominated by direct photochemical main-chain scission [69]. Comprehensive investigations [70] have shown, however, that, at least for the largely studied and used polymer – PMMA, only by VUV the direct photochemical main-chain scission becomes truly relevant to the laser ablation process. In photochemical laser ablation the accompanying modification of material can be important. Thus, first we consider modification of a material by the UV laser light without ablation.

Let us consider a laser beam propagating along the z-axis and the half-space $z > 0$ being occupied initially by a homogeneous dielectric medium. First we consider the simplest photochemical reaction

$$A \xrightarrow{\hbar\omega} B. \qquad (4.1)$$

Here A stands for the element of the initial material, and B denotes the product of the photochemical reaction. The kinetics of modification caused by reaction

(4.1) is described by the equations:

$$\frac{\partial N_A}{\partial t} = -\frac{\eta_A \sigma_A}{\hbar\omega} N_A I; \qquad \frac{\partial I}{\partial z} = -\alpha I;$$
$$\alpha = \sigma_A N_A + \sigma_B N_B, \qquad N_A + N_B = N_0. \tag{4.2}$$

Here N_A and N_B are the number densities of A and B species, respectively, I is the light intensity, η_A is the quantum yield, σ_A and σ_B are the absorption cross-sections, and α is the optical absorption coefficient. This model describes irreversibly induced darkening, for $\sigma_A > \sigma_B$ or bleaching for $\sigma_A < \sigma_B$. We do not need a differential equation for N_B since the conservation law requires N_0 = const. The initial and boundary conditions are:

$$N_A(z, 0) = N_0, \quad N_B(z, 0) = 0, \quad I(0, t) = I_s(t). \tag{4.3}$$

One may consider instead of (4.1) a more general model, which consists of two successive photochemical reactions, $A \xrightarrow{\hbar\omega} B \xrightarrow{\hbar\omega} C$. In contrast to (4.1) this model can describe a nonmonotonous change of the absorption coefficient. In a similar way, three, four etc., successive or branching reactions can be taken into account to describe the modification of the material.

This type of models was analyzed in [71–75] for transient absorption during pulsed laser permanent modification of polymers by UV lasers. Similar problems were considered in laser physics, plasma physics and in photochemical kinetics [76–77]. In [78] such models were applied to investigate the photo-aging of polyvinyl chloride (PVC). These models allow analytical solutions, see, e.g. [23]). The set of partial differential equations can be reduced to ordinary differential equations, describing the propagation of a non-deformable profile, or wave of modification [78, 80]) with a time dependent velocity.

For example, the model given by Eqs. (4.2), (4.3) can be reduced to the following ordinary differential equation

$$\frac{dn_A}{d\xi} = (1 - \beta)(1 - n_A)n_A - \beta n_A \log(n_A) \tag{4.4}$$

with boundary condition

$$n_A(\xi = 0, t) = \exp(-\tau). \tag{4.5}$$

Here we introduced the dimensionless variables

$$n_A = \frac{N_A}{N_0}, \quad \tau = \frac{\eta_A \sigma_A}{\hbar\omega}\int_0^t I_s(t_1)dt_1, \quad \xi = \sigma_A N_0 z, \quad \beta = \frac{\sigma_B}{\sigma_A}. \tag{4.6}$$

The value of parameter β controls the type of the irreversible optical modification, such as bleaching for $\beta < 1$ or darkening for $\beta > 1$. The solution of equations (4.4)–(4.5) is shown in Figure 7. One can see the propagating wave of the photochemical modification along the ξ coordinate. The time dependent velocity of the wave of modification is given by:

$$V_{\mathrm{mod}} = \frac{1}{(1 - \beta)[1 - \exp(-\tau)] + \beta\tau} . \tag{4.7}$$

During ablation, part of the material is removed from the surface of the sample, thus laser ablation provides the problem of photochemical modification with a moving interface. There are two approaches to formulate this problem. The first is similar to the Frenkel-Wilson approach in the theory of melting front propagation [8]. This approach for the photochemical theory of UV etching was developed in Ref. [79].

The second is the Stefan-type approach [79, 81–83], which relates the position of the ablation front to the critical number density of broken bonds, N_{cr}. It gives an expression for the etch depth, h_e per single pulse, as a function of laser fluence for the model of Eq. (4.2), as detailed in [83, 23]:

$$h_e = \frac{1}{\alpha_P} \ln\left[1 + \frac{\alpha_P(\Phi - \Phi_{th})(1 - R)}{\hbar\omega\kappa_{ph}}\right] . \tag{4.8}$$

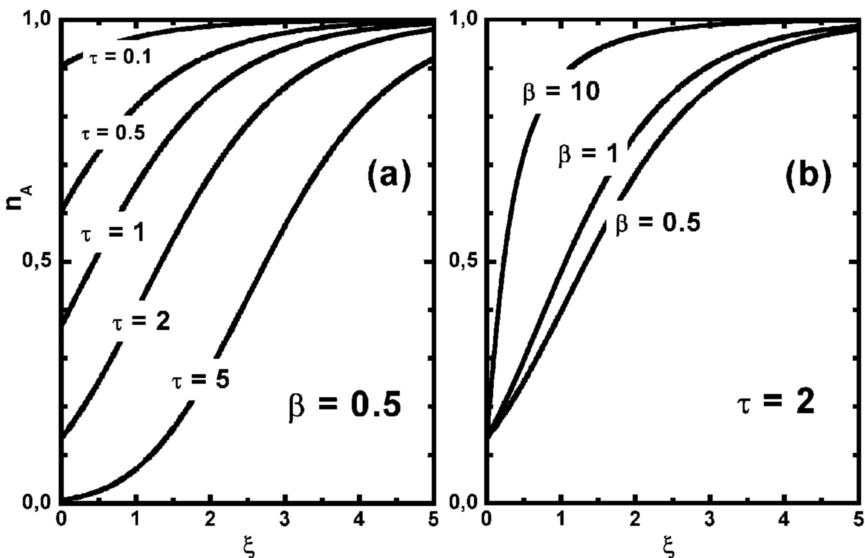

Figure 7. Wave of the typical photochemical reaction; the profiles $n_A = n_A(\xi)$ are obtained by integration of equation (4.4) for the parameter $\beta = 0.5$ (a), and for the parameter $\tau = 2$ (b). For $\beta < 1$ one gets the bleaching effect and with $\beta > 1$ the darkening effect. The profile of n_B can be obtained from $n_B = 1 - n_A$.

Here κ_{ph} is the number density of photons, which should be absorbed at the particular point to produce a critical number density of broken bonds. R is the reflection coefficient and α_p refers to the Lagrange extinction coefficient of the plume. For the model of Eq. (4.2) where N_B is associated with the number density of broken bonds

$$\kappa_{ph} = \int_0^{N_{cr}} \frac{\alpha(N_B)}{\Psi(N_B)}\, dN_B = \frac{N_{cr}}{\eta_A}(1 + \tilde{\gamma}), \quad \text{where} \quad \tilde{\gamma} = \beta \left[\frac{1}{\delta} \ln\left(\frac{1}{1-\delta}\right) - 1 \right],$$

$$\beta = \frac{\sigma_B}{\sigma_A} \quad \text{and} \quad \delta = \frac{N_{cr}}{N_0}.$$

If the absorption coefficient α is constant,

$$\kappa_{ph} = \frac{\Phi_{th}(1-R)\alpha}{\hbar\omega}, \quad \text{and} \quad h_e = \frac{1}{\alpha_P} \ln\left[1 + \frac{\alpha_P(\Phi - \Phi_{th})}{\alpha\Phi_{th}}\right]. \tag{4.9}$$

This equation coincides with the formula obtained in Ref. [84].

For multiple-pulses irradiation this model predicts a *logarithmic* dependence of the etch depth on laser fluence if the fluence is much higher than the apparent threshold, and a linear dependence for fluences much smaller than the apparent threshold.

5. The role of mechanical stresses

Mechanical stresses caused by laser irradiation of polymers can strongly influence the laser ablation dynamics of these materials. Some authors consider mechanical stresses among the main driving forces of laser ablation in PMMA [89–93]. Specially designed photosensitive polymers were reported to be ablated by "explosive decomposition" [94] for which mechanical stresses are expected to play an important role.

The stresses can be thermo-elastic, due to thermal expansion, but they can also be provided by low-molecular products of either photochemical or photothermal bulk reactions. These species may result in quasi-stationary stresses due to an increase in the total molecular volume. The well-known example is depolymerization of PMMA. The polymerization of PMMA is accompanied by an up to 20% volume contraction [95], thus depolymerization should be accompanied by an expansion. On the other hand, for the small, light fragments and volatile species, consisting of simple molecules like CO, CN, CH_2 of number density N_ℓ, may be treated as an ideal gas, causing an average inner pressure

$$p = \zeta N_1 k_B T, \tag{5.1}$$

with $\zeta < 1$, i.e., only a fraction of the total number of these species will contribute to p.

In the simplest case of uniaxial acoustic approximation when only the stress tensor component σ_{zz} is relevant, the equation of thermoelasticity reads:

$$\frac{\partial^2 \alpha_{zz}}{\partial^2 t} = c_s^2 \frac{\partial^2(\sigma_{zz} - p)}{\partial z^2} - \frac{E_Y}{3(1 - 2\mu)} \frac{\partial^2}{\partial t^2} [\alpha_V(T - T_0)]. \quad (5.2)$$

Here α_V is the volume thermal expansion coefficient, E_Y is the Young's modulus, μ is the Poisson ratio, and c_s is the sound velocity. Equation (4.2) should be solved together with the boundary conditions :

$$\sigma_{zz}(t, z = 0) = p(t, z = 0), \quad \sigma_{zz}(t, z = \infty) = 0. \quad (5.3)$$

Here p is the quasistationary pressure, for which the volatile species obeys Eq. (5.1).

Stress can influence both the bulk photothermal bond breaking and material removal from the surface due to a change in the corresponding activation energies in formulas (2.1), (3.1), (3.4). A simple estimate of this influence is provided by Zhurkov's formula, see e.g. ref. [96], which yields a linear decreasing of the activation energy under stresses. For example, in the case of a simple photothermal model we can write :

$$E_a(\sigma) = E_a - \gamma\sigma, \quad E_b(\sigma) = E_b - \gamma\sigma. \quad (5.4)$$

In polymers, γ may have values up to 10^{-21} cm^3, e.g., for PMMA $\gamma = 1.7 \times 10^{-21}$ cm^3 [96]. Formula (5.4) is valid for tensile stress, i.e. when $\sigma > 0$. In the opposite case, of compressive stress, the relations (5.4) are not obvious, since then a decrease in the activation energy by chain breaking is also possible due to local plastic deformations [97]. Relations (5.4) are thus valid only if $E > \gamma\sigma$. In the opposite case, $E_a < \gamma\sigma$, the chain breaking process will proceed independently of temperature with a preexponential frequency, thus here the "sublimation" boundary condition of the type (3.4) is not valid.

The example of the simple bulk photothermal model in the quasi-stationary case, when transient stresses can be neglected was considered in [23]. Typically it is valid if the pulse duration, t_p, is large enough: $t_p > 1/\alpha c_s$. Here α is the absorption coefficient and c_s is the sound velocity. For short pulses when $t_p < 1/\alpha c_s$ nonstationary effects, caused by transient stresses are important. These stresses may result in spallation, i.e. in the removal of part of the material due to propagation of the rarefaction wave, as demonstrated in ref. [91], where the whole PMMA film was removed from the substrate by this mechanism.

Transient stresses can also provide bulk chain degradation. Some possible nonstationary effects when photophysical phenomena are accompanied by transient stresses are considered in refs. [98, 99], along with some possible effects of the recoil pressure on the generation of broken bonds. Some results of the calculations are shown in Figure 8.

When using the bulk photothermal model in the form studied in section 3 by applying it to specific materials, the effect of stresses should be estimated if it is

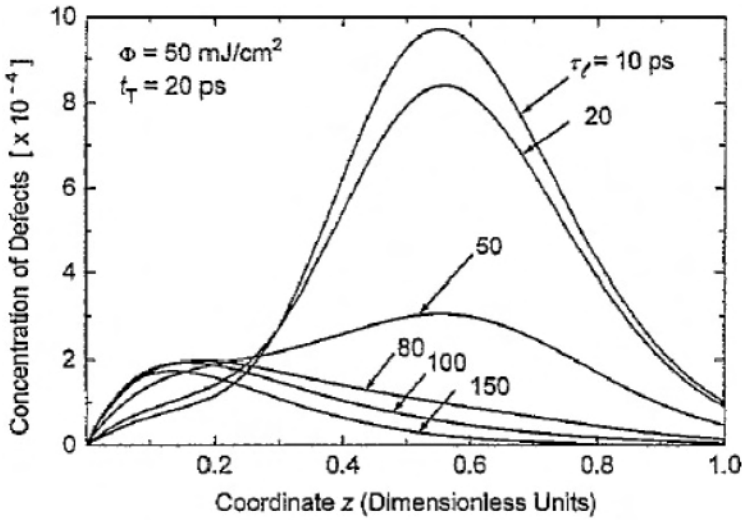

Figure 8. Spatial distribution of defects generated by acoustic waves due to transient thermal stresses. Thermal relaxation time t_T = 20 ps. The density number of defects is normalized to the total density number of the chromophores. The coordinate is given in units $1/\alpha$. The parameters are the same as in [99].

significant. For example, it was shown in Ref. [100] that for polyimide near ablation threshold, both nonstationary thermoelastic stresses and quasistationary stresses resulting from pressure provided by heated volatile species, can be neglected if $\gamma < 3 \times 10^{-21}$ cm^3 and $\zeta \times m < 0.1$. Here we assume that the bulk photothermal reaction produces m volatile species per single chain break.

There is some contradiction between data on photochemical modification of PMMA well below and near ablation threshold [92, 101]. With small laser fluences, UV photon absorbed by the Ester group results in a cleavage of this group with a small quantum yield ~0.01, of the main chain scission [102–104]. With fluences close to the ablation threshold the chain scission process initializing depolymerization is much more effective [101]. A possible explanation of this phenomenon is that inner mechanical stresses increase the quantum yield of photochemical chain breaking. Moreover, the activation energy of the initial pure thermal chain breaking, which creates the end radicals initiating the unzipping process, can decrease due to arising mechanical stresses.

Up to this point we considered some averaged macro-stresses. However at the moment of emerging of monomer during unzipping or at the moment of cleavage of a particular side group and escape of volatile species, the occurring micro-stresses can be large enough to provide some chemical changes of adjacent molecules. Molecular dynamic simulations of some of these processes are performed in papers [90, 105, 106]. Another interesting problem is related to ablation in the presence of outer stresses [107–110]. Here ablation is unstable resulting in surface pattering and cracks formation.

6. Sub-picosecond laser ablation: Metals and the two-temperature model

When employing shorter laser pulses, i.e., subpicosecond pulses in ablation kinetics, features appear which the conventional thermal model can no longer describe. These features relating to the energy absorption, the electron-phonon interaction, the mechanism of transferring material to the vapor – gas state, and vapor expansion, are described in refs [111–116].

A two-temperature model for the description of transition phenomena in a non-equilibrium electron gas and lattice under subpicosecond laser irradiation was proposed more than 30 years ago [15, 17, 117]. For a detailed comparison of this model with experiment, various characteristics should be measured with a subpicosecond temporal resolution, which is an intricate task [118–122].

The electron-phonon interaction dynamics was investigated by Fal'kovskiï et al. [123]. This research supports the validity of the basic ideas underlying the two-temperature model, enabling one to determine the electron-phonon interaction constant, and permits several kinetic coefficients to be expressed in terms of microscopic metal characteristics.

The two-temperature model describes the energy transfer inside a metal by applying the coupled heat conduction equations for the temperatures of electrons T_e and the lattice T_i:

$$c_e \frac{\partial T_e}{\partial t} = c_e v \frac{\partial T_e}{\partial z} + \frac{\partial}{\partial z}\left(\kappa_e \frac{\partial T_e}{\partial z} \right) + Q - \mu(T_e - T_i), \tag{6.1}$$

$$c_i \frac{\partial T_i}{\partial t} = c_i v \frac{\partial T_e}{\partial z} + \frac{\partial}{\partial z}\left(\kappa_i \frac{\partial T_i}{\partial z} \right) + \mu(T_e - T_i). \tag{6.2}$$

Here, c_e and c_i are the specific heat capacities of the electrons and lattice, respectively; κ_e and κ_i are the corresponding thermal conductivity coefficients, and the parameter $\mu = c_e/\tau$ characterizes the rate of energy exchange [W cm^{-3} K^{-1}] between the electron and lattice subsystems where τ is the characteristic exchange time for the electron subsystem.

The laser energy absorbed by the electrons is described by

$$Q = \frac{\partial I}{\partial z} = \alpha I, \qquad I(0, t) = I_s(t), \tag{6.3}$$

where α is the absorption coefficient, and I_s is the radiation intensity at the metal surface ($z = 0$). The quantity $I_s(t) = I(t)A$ in Eq. (6.3) depends on the laser pulse shape $I(t)$, and the absorptivity $A = 1 - R$ of the material. In the case of an ultrashort laser pulse, the plume is produced after the pulse and has no effect on the ablation process. Thus, it is no screening effect associated with plume.

The heat conduction equations (6.1) and (6.2) are written in the ablation front frame of reference and thus the ablation front travels with a velocity $v = v(t)$ relative to the immobile material. This formulation is slightly different from the

conventional two-temperature model [47, 124], from which several small parameters in (6.1), (6.2), were omitted. Here, we take advantage of this form, because it is convenient for the analysis of a stationary evaporation wave.

The boundary conditions that specify the energy fluxes at the surface $z = 0$ are:

$$-\kappa_e \frac{\partial T_e}{\partial z}\Big|_{z=0} = J_e, \tag{6.4}$$

with J_e given by the Richardson law

$$J_e = -k_0 b_0 (T_\infty + T_{es})^2 \exp\left[-\frac{T_u}{T_\infty + T_{es}}\right], \tag{6.5}$$

where b_0 is the Richardson constant, and T_u the work function. The factor $k_0 = k_B(T_\infty + T_{es})/e$ in Eq. (6.5) is used to convert the energy flux density J_e into energy units [W cm^{-2}].

Similarly, the thermal flux related to energy losses due to material removal by ablation is given by a formula similar to expression (2.12):

$$-\kappa_i \frac{\partial T_i}{\partial z}\Big|_{z=0} = J_i = -\rho v L, \tag{6.6}$$

The two other evident boundary conditions, for $z = \infty$ and the initial conditions for $t = 0$ are

$$T_e|_{z=\infty} = T_i|_{z=\infty} = T_e|_{t=0} = T_i|_{t=0} = 0. \tag{6.7}$$

As in Section 2, the subscript “s” is used for denoting the temperature at the surface $z = 0$, i.e. $T_e|_{z=0} = T_{es}$, $T_i|_{z=0} = T_{is}$. The quantity T_{es} arises in the Richardson law, while the quantity T_{is} arises in the laser ablation rate

$$v = v_0 \cdot \exp\left[-\frac{T_a}{T_\infty + T_{is}}\right]. \tag{6.8}$$

To make the model suitable for analysis of experimental data, specific temperature dependencies of the coefficients c_e, c_i, κ_e, κ_i, A, α and μ must be sought. For instance, the electron heat capacity is a linear function of the electron temperature, $c_e = \beta T_e$, and the lattice heat capacity c_i is practically constant above the Debye temperature $T > T_D$. When calculations include melting process and other structural phase transitions, the effective lattice heat capacity c_i depends on the lattice temperature T_i. Finally, the electron heat conductivity κ_e depends on the temperatures T_e and T_i [122, 134]. The reflection coefficient R and the absorption constant α also depend on the temperatures T_e and T_i. Specifically, for semiconductors, the reflection coefficient R varies linearly with electron temperature T_e [122].

The majority of the above-given temperature dependences may be taken into account in the calculations in the same manner as done in the one-temperature thermal model employing the moments method [34]. To illustrate the main features of the two-temperature model, we consider a simplified problem in which all the coefficients are assumed constant.

The two-temperature model equations (5.1) and (5.2) apply when the classical Fourier laws describing the electron and phonon thermal energy transfer can be used. This implies that the model is appropriate for times much longer than τ_e. The time τ_e itself depends on the electron temperature, on the energy density in a laser pulse, and in typical cases it amounts to several hundreds femtoseconds [122].

The assumption of diffusive electron energy transfer (6.1) implies that the variations in the electron temperature distribution occur over spatial scales greater than the electron mean free path ℓ_e. For shorter lengths, the electron transport becomes primarily ballistic [125]. For various metals, the quantity $\ell_e \approx v_F \tau_e$, where v_F is the Fermi electron velocity, differs by more than one order of magnitude. For nickel, as an example, the electron mean free path ℓ_e is several tens of nanometers, whereas for gold some hundreds of nanometers [126, 127].

Calculations using a simplified two-temperature model [118, 119, 124, 128, 129], where the convective terms $v\nabla T_{e,\,i}$ were omitted, do not allow one to calculate the layer thickness of the material removed by laser pulse irradiation. To achieve this, one should take advantage of the complete model given by Eqs. (6.1), (6.2) and extend the calculations to longer times, of the order of 10^3 laser pulse duration. The late stage of the process was investigated in ref. [130] employing the moments method.

The trial functions for the temperatures $T_e(z, t)$ and $T_i(z, t)$ were chosen as:

$$
\begin{aligned}
T_e &= \frac{1}{1 - \alpha\ell_e}\left[\left(T_{es} - \frac{\ell_e}{\kappa_e}J_e\right)e^{-\alpha z} - \left(T_{es}\alpha\,\ell_e - \frac{\ell_e}{\kappa_e}J_e\right)e^{-z/\ell_e}\right] \\
T_i &= \frac{1}{1 - \alpha\ell_i}\left[\left(T_{is} - \frac{\ell_i}{\kappa_i}J_i\right)e^{-\alpha z} - \left(T_{is}\alpha\,\ell_i - \frac{\ell_i}{\kappa_i}J_i\right)e^{-z/\ell_i}\right]
\end{aligned} \tag{6.9}
$$

These functions automatically satisfy the boundary conditions for $z = 0$ and $z = \infty$. The trial solutions contain four unknown functions: the characteristic surface temperatures $T_{es}(t)$ and $T_{is}(t)$ the characteristic scales of lengths $\ell_e(t)$, $\ell_i(t)$.

Next we introduce four moments for electron and lattice temperatures:

$$
M_0 = \int_0^\infty T_e dz, \quad M_1 = \int_0^\infty T_e z dz, \quad N_0 = \int_0^\infty T_i dz, \quad N_1 = \int_0^\infty T_i z dz, \tag{6.10}
$$

The differential equations for the moments are obtained by integrating the input equations (6.1) and (6.2), see [21, 130]. The subsequent calculation involves the substitution of the trial functions (6.9) into Eqs. (6.10) and the differential equations for moments. The result is a system of four ordinary differential equations for $T_{es}(t)$, $T_{is}(t)$ and $\ell_e(t)$, $\ell_i(t)$.

Figure 9 shows the dynamics of metal heating by a laser pulse with duration t_p = 1 ps and a fluence of Φ = 0.15 J cm^{-2}, where the pulse shape is described by Eq. (2.21). Referring to Figure (9a), it is seen that the electron temperature T_e "detaches" from the lattice temperature T_i during the laser pulse and peaks at $t \approx 1.8$ ps. The characteristic lattice heating time is sufficiently large, following from the relation $c_i/\mu \gg c_e/\mu = \tau$, and the phonon temperature peaks at $t \approx 27.2$ ps. In this case, the characteristic scale lengths ℓ_e and ℓ_i in Figure (9b), increase in time according to the thermal conduction law, i.e. are proportional to $\sqrt{i}$. For longer times, the distinction between ℓ_e and ℓ_i is insignificant, while for $t \approx 100$ ps the difference is still appreciable; $\ell_e > \ell_i$ since $\kappa_e > \kappa_i$.

The results presented in Figure 9 show that the method describes adequately the features of the problem, found for instance, in Ref. [124].

One can see from Figure (10a) that the ablation is completed in a time of the order of 1 ns, which is approximately 10^3 times longer than the laser pulse. In traditional experiments, the layer thickness of the material ablated in a laser pulse is measured as a function of the energy density of the pulse.

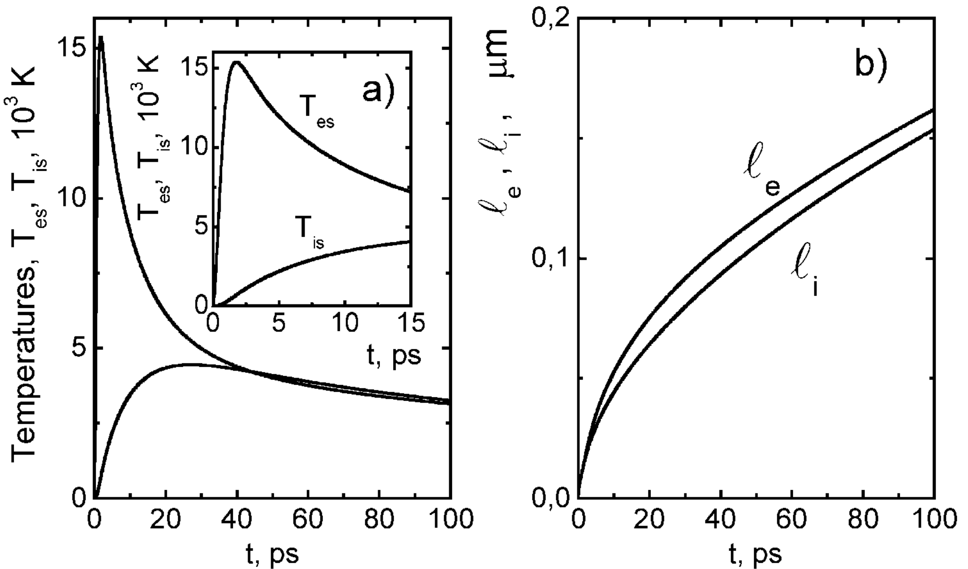

Figure 9. Dynamics of metal heating by a t_p = 1 ps laser pulse with fluence Φ = 0.15 J cm^{-2}. (a) Electron and lattice temperatures are T_{es} and T_{is} (the inset shows an enlarged view of the initial stage of the process). (b) Characteristic spatial scales $\ell_e(t)$ and $\ell_i(t)$ of the electron and lattice temperature distributions. Parameters of the calculations are: c_e = 0.04035 J cm^{-3} K^{-1}, c_i = 2.43 J cm^{-3} K^{-1}, κ_e = 2.37 W cm^{-1} K^{-1}, κ_i = 1 W cm^{-1} K^{-1}, relaxation time τ = 1 ps ($\mu = c_e/\tau$), density ρ = 2.688 g cm^{-3}, latent heat of evaporation L = 10,860 J g^{-1}, the factor in formula (6.8) is v_0 = 414,000 cm s^{-1}, activation energy T_a = 35,240 K, the work function in expression (6.5) is T_u = 49,300 K, the Richardson constant b = 120.4 A cm^{-2} K^{-2}, the initial temperature T_∞ = 300 K, the absorption coefficient α = 1.516 10^5 cm^{-1}, and absorptivity A = 1.

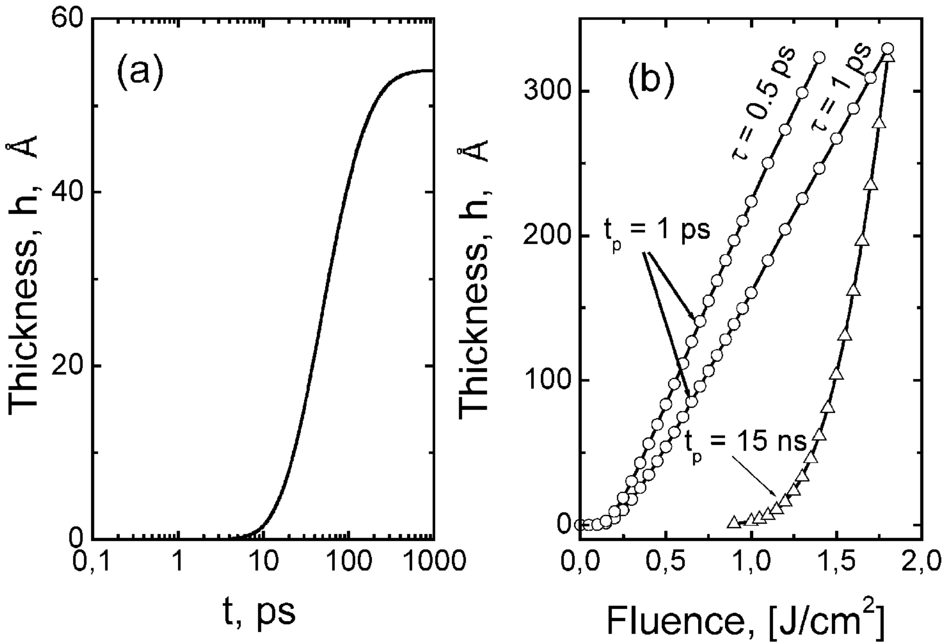

Figure 10. (a) The thickness of removed material as a function of time. Pulse duration of t_p = 1 ps with an energy density of Φ = 500 mJ cm^{-2}. (b) Layer thickness of the material removed in one pulse as a function of pulse energy density for one long and two short laser pulses. Parameters used for the calculation are the same as in Figure 9.

The typical dependence of ablation kinetics on the laser pulse duration is illustrated in Figure (10b). For a long, nanosecond laser pulse, the ablation is insensitive to the lattice – electrons energy exchange rate. For $\tau \leq 1$ ps, the curves coincide with the results following from the thermal ablation model with a single temperature for the lattice and electrons. For short, picosecond laser pulses, the corresponding curves are sensitive to the characteristic relaxation time τ. When $\tau \to 0$, typical to the case of a purely thermal model, the curves show a faster growth of the ablation layer thickness in comparison to the experimental results [36].

Another effect evident in Figure (10b) is the lowering of the ablation threshold when shortening the laser pulse [8].

7. Sub-picosecond ablation in Dielectrics

It is perceived now that the threshold ablation of transparent dielectrics by ultra-short laser pulses (USLP) coincides with the onset of ionization [131, 134]. In dielectrics, however, one cannot use the two-temperature model, because the energy distribution of electrons cannot be described as quasi-stationary. Instead one should examine the kinetic equation for the electron energy distribution.

We consider here dielectrics with a ionization potential ε_i = 10–12 eV. Seed electrons are provided either by a direct transition from the ground state to the conduction band or by transition through intermediate bounded excited states. If $\gamma_A^2 = 2\omega^2 m\varepsilon_I/(eE)^2$, where γ_A is the adiabatic or Keldysh parameter [129], the direct transition from the ground state to the conduction band can be interpreted as a multi-photon transition with a rate $W \propto I^K$. Here m and e are the mass and the charge of electron respectively, E is the electric field, I is the laser intensity, $K = \langle \varepsilon_I(1 + 1/2\gamma_A^2)\rangle$ and the brackets stand for the integer part of a number. Impact ionization can be described by Boltzmann-type kinetics equation [136, 137] for the electron energy distribution function. In the case of wide bandgap materials several simplifications lead to a Fokker-Planck equation for the electron energy distribution function [128–129]. Both approaches provide a similar equation for the time dependence of the number density of free electrons, $N_e(t)$, [137, 138], which for a rectangular laser pulse at the surface gives:

$$\frac{dN_e}{dt} = W + \Theta(t - t_{\text{delay}})\,\frac{1}{t_{\alpha v}}\,(N_e - W\,t_{\text{delay}}), \quad \Theta(\xi) = \begin{cases} 0, & \text{if } \xi < 0 \\ 1, & \text{if } \xi \geq 0 \end{cases}. \tag{7.1}$$

Here W is the rate of multi-photon ionization and t_{av} is the characteristic time of avalanche ionization. Equation (7.1) suggests that during the time interval t_{delay} the impact ionization can be neglected and an increase in the number density of free electrons is provided solely by multiple photon ionization. It was estimated in [138] that $t_{\text{delay}} \cong 0.2t_{av}$. Ionization results in a strong absorption of laser light during the pulse, conveying energy from the laser to the solid, facilitating ablation.

For highly absorbing dielectrics, ablation due to heating can occur at a fluence which is smaller than that needed for the development of avalanche ionization. In what follows we assume that radiation is absorbed in a material by chromophores [139], i.e., that the first electronic transition occurs in a bound state, which is typical for polymers. Near ablation threshold ionization does not play a significant role in energy transfer and can thus be neglected. The examples considered below are related for instance to the near threshold ablation of Polyimide by subpicosecond pulses at a wavelength 248 nm. Here the initial linear absorption at the wavelength of irradiation is very strong. With ultra-short laser pulses we cannot employ the approximation of a constant absorption coefficient, α = const., thus we must consider the transient response of the medium. Since an important feature of such a response is the saturation of energy levels, the absorption of radiation in a dielectric will be described by multilevel models of this medium and we shall take into account stimulated emission and nonradiative relaxation. A set of rate equations for the populations of the energy levels for a three-level model is given by:

$$\frac{\partial n_1}{\partial t} = V\,\frac{\partial n_1}{\partial z} - \frac{\sigma_{12}}{\hbar\omega}\,I(n_1 - n_2) + \frac{n_2}{t_{21}}, \tag{7.2}$$

$$\frac{\partial n_2}{\partial t} = V\,\frac{\partial n_2}{\partial z} + \frac{\sigma_{12}}{\hbar\omega}\,I(n_1 - n_2) - \frac{\sigma_{23}}{\hbar\omega}\,In_2 - \frac{n_2}{t_{21}} + \frac{n_3}{t_{32}}, \tag{7.3}$$

$$n_1 + n_2 + n_3 = n_0. \tag{7.4}$$

Here n_1, n_2, and n_3 are the populations of the corresponding levels and n_0 is the number density of chromophores in the medium, taken in our calculations as $n_0 = N_0$. σ_{ij} are the cross-sections of the corresponding transitions and t_{21}, t_{32} are the nonradiative relaxation times of the electronically excited states. In equation (7.3) the stimulated emission is ignored for the transitions between the third and second level. The transition to the third level can be attributed also to the photoionization of chromophores from the excited state. As discussed in [140, 141], this model for a medium response enables good fitting of the experimental data for two-pulse ablation of Polyimide. The absorption coefficient is given by:

$$\alpha = \sigma_{12}(n_1 - n_2) + \sigma_{23}n_2. \tag{7.5}$$

In what follows we consider surface photothermal model (model I) and bulk photothermal model (model III) for laser ablation of polymers. These models for nanosecond pulses were considered in Section 3. The definition of the models is given just below formula (3.10).

For subpicosecond pulses the heat source term in equation (3.2), instead of (3.3), should be rewritten as follows:

$$Q = \frac{\hbar\omega}{\rho c_p(T)}\left(\frac{n_2}{t_{21}} + \frac{n_3}{t_{32}}\right) - \frac{\Delta H_b N_0(1 - n_B)k_0 \exp\left(-E_b/k_B T\right)}{c_p\rho}. \tag{7.6}$$

For a surface photothermal model we should take (7.6) with $k_0 = 0$.

We compare next the features of *the dynamics* of laser ablation predicted by surface and bulk photothermal models of laser ablation of polymers considered in section 3 [55]. In the numerical calculations below the Gaussian USLP with a pulse duration of 500 fs is considered. It is seen in Figure 11(a) that the ablation velocity maxima for the *surface* model practically coincides in time with the surface temperature maxima. In contrast, the delay time between the maximum heating of the surface of the material and the beginning of *bulk* laser ablation can be longer by an order of magnitude as compared to the thermal relaxation time, see Figure 11(a, b).

The beginning of ablation for the surface model is governed by a thermal relaxation time, whereas in the bulk model the beginning of ablation is governed by the thermally activated chemical reaction time of polymer chains scission. The time delay of the ablation after the end of the laser pulse for the surface and bulk mechanisms may differ by an order of magnitude [55]. The time of the beginning of ablation after the end of the laser pulse can be fixed, for example, by using a pump-probe technique [144–146]. The only existing data of time resolved experiments have been published in ref. [142]. Two-pulse ablation experiments with subpicosecond ablation of polyimide at 248 nm provided an estimation for the thermal relaxation time of about 30–50ps. It was mentioned, however [142], that within a time span of 200 ps after the single 500 fs pulse with a fluence above

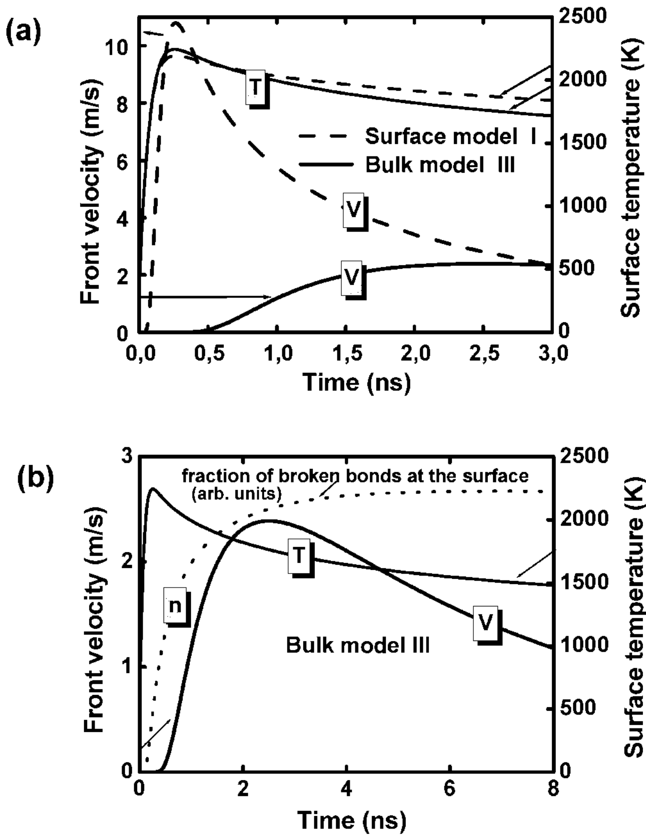

Figure 11. Dynamics of laser ablation for a single 500 fs laser pulse with fluence F_p = 50 mJ/cm^2 for two ablation models. (a) Ablation front velocity and surface temperature versus time for surface models (I) and bulk model (III) (b) Ablation front velocity, surface temperature and fraction of broken bonds versus time according to the bulk model III.

the ablation threshold there was no evidence of material removal from the surface. The above analysis hints for a bulk model because the delay time between the end of the pulse and ablation appears to be significantly longer than the thermal relaxation time. It should be noted, however, that additional experiments are needed to confirm this.

8. Photophysical ablation

A photophysical model of laser ablation has been suggested in [147–149]. The main idea is that the activation energy for breaking a covalent bond within excited molecules on the surface is smaller than the activation energy for breaking a bond of the molecules in the ground state. Despite the obvious physical reasons, until now

there is no direct evidence that the photophysical mechanism really works. Some effect, which can be interpreted as a photophysical ablation, however, recently has been shown in [150].

We consider the effect of USLP on a dielectric, which can be described by a two-level medium. The laser frequency is assumed to be in resonance with the electronic transition discarding the induced radiation effect. The aim of this section is to compare the predictions of the photothermal and photophysical surface evaporation models in laser ablation.

Both models describe the material response in a similar way:

$$\frac{\partial n^*}{\partial t} = V\frac{\partial n^*}{\partial z} + (n_0 - n^*)\frac{I\sigma_{12}}{\hbar\omega} - \frac{n^*}{t_{21}}, \tag{8.1}$$

$$\frac{\partial I}{\partial z} = -I\sigma_{12}(n_0 - n^*), \tag{8.2}$$

$$\frac{\partial I}{\partial t} = V\frac{\partial I}{\partial z} + \frac{1}{c_p(T)\rho}\frac{\partial}{\partial z}\left[\kappa(T)\frac{\partial I}{\partial z}\right] + \frac{n^*}{t_{21}\rho c_p(T)}, \tag{8.3}$$

with the initial and boundary conditions

$$n^*|_{t=0} = 0, \qquad T|_{t=0} = T_\infty, \tag{8.4}$$

$$I|_{z=0} = I_0(t), \qquad n^*|_{z\to\infty} = 0, \qquad T|_{z\to\infty} = T_\infty. \tag{8.5}$$

The coordinate frame is taken at the ablation front, I is the laser intensity, T is the temperature, n_0 is the number density of chromophores, n^* is the number density of the excited chromophores, ω is the laser and electronic transition frequency, σ_{12} is the corresponding absorption cross-section and V is the ablation velocity. t_{21} is the thermal relaxation time, $\kappa(T)$ is the thermal conductivity and $c_p(T)$ is the specific heat of the material.

The difference between the photophysical surface model and the surface photothermal model can be observed by inspecting the relation for the velocity of the ablation front and the boundary condition for temperature:

$$V = \left(1 - \frac{n_s^*}{n_0}\right)V_0 \exp\left(-\frac{E_a}{k_B T_s}\right) + \frac{n_s^*}{n_0}V_0^* \exp\left(-\frac{E^*}{k_B T_s}\right), \tag{8.6}$$

$$\kappa\frac{\partial T}{\partial z}\bigg|_{z=0} = \left(1 - \frac{n_s^*}{n_0}\right)\rho\Delta H_s V_0 \exp\left(-\frac{E_a}{k_B T_s}\right) + \frac{n_s^*}{n_0}\rho\Delta H_s^* V_0^* \exp\left(-\frac{E^*}{k_B T_s}\right), \tag{8.7}$$

where E_a and E^* denote the ablation activation energies for the ground and excited states, respectively. The subscript s refers to the ablation front at $z = 0$ and ΔH_s and ΔH_s^* are the transition enthalpies. ΔH_s^* was estimated as $\Delta H_s^* = \Delta H_s E^*/E$.

Numerical calculations are performed for t_{21} = 30 ps with $c_p \approx 2\ J\ g^{-1}\ K^{-1}$, ΔH_s = 700 *mJ/g* and $D_T \approx 10^{-3}$ cm^2/s. Figure 12(a) exhibits the time dependence of the ablation velocity for the photothermal model and for photophysical models with different E^*.

Since the pulse duration is considerably shorter than the relaxation time, ablation starts after the laser pulse. Relaxation of excited species results in an increase of temperature. The ablation velocity, according to the photothermal model, depends monotonically on the surface temperature. This leads to a relatively rapid increase in the velocity resulting from the temperature increase due to electronic relaxation. This rise is followed by a slow decrease of temperature due to the penetration of the ablation front into a colder part of the sample and by heat diffusion, see the "photothermal" curve in Figure 12(a). The ablation velocity demonstrates different behavior in the photophysical model. The sharp ablation velocity maximum for the three upper curves in Figure 12(a) is not connected to the time dependence of the surface temperature but to the decrease in the concentration of the excited electrons because it is proportional to the population of the excited states on the surface. When the population of the excited states vanishes, the velocity of the ablation front reaches its pure photothermal value.

The dynamics of a single USLP laser ablation, which proceeds photophysically, is essentially different from the case of pure photothermal ablation. The most important feature of photophysical ablation is that the time delay between the end

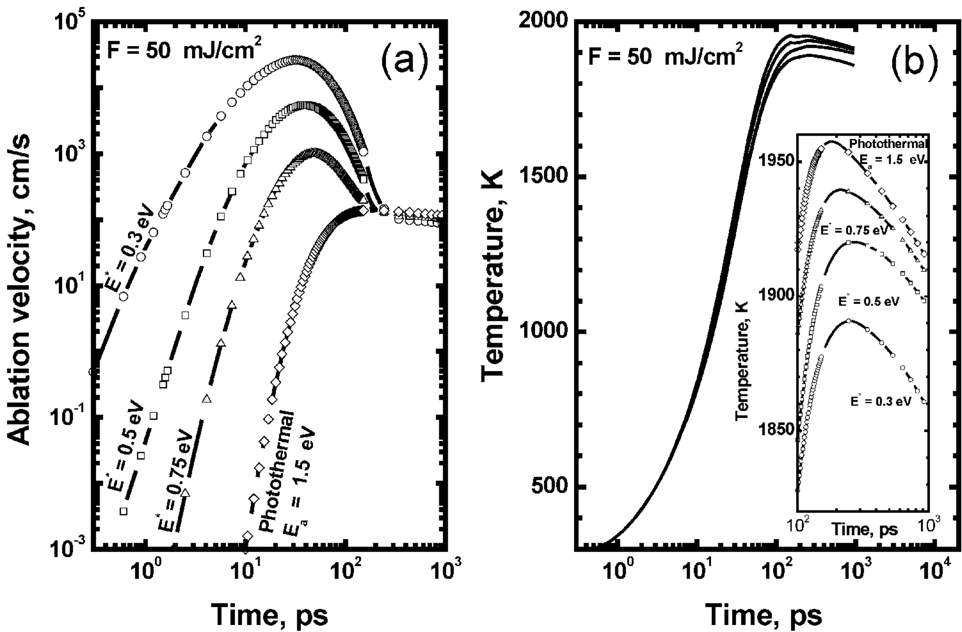

Figure 12. Dynamics of laser ablation for a single laser pulse with fluence 50 mJ/cm^2. The photophysical ablation with different E^* and pure photo-thermal ablation. For all curves E_a = 1.5eV. (a) Ablation velocity vs. time. (b) Surface temperature vs. time.

of the USLP and the commencing ablation is shorter than the thermal relaxation time, though, the resulting ablated depths can be similar if the activation energy of the pure photothermal process is not very high.

Finally, investigations [149] show that the electronic relaxation time significantly influences the efficiency of the photophysical ablation. Thus an increase in the relaxation time results in an essential increase of the etched depths in the case of photophysical ablation and slightly decreases the efficiency in pure photothermal ablation. As a result, photophysical ablation mechanism can be recognized in materials with long relaxation times and with high activation energy of pure photothermal ablation.

9. Conclusion

We stress again that many models have been developed to describe laser ablation but there are no models yet that *completely* describe this process. Each model has some limitations and is applicable only for specific conditions. This review does not pretend to be exhaustive. As already noted, laser ablation has been the subject of several thousand publications, and it is unrealistic to cover all those works in a single review.

Although laser ablation is an extremely intricate process, many aspects of this process are reasonably clear from the physical standpoint and allow a rather close quantitative description, which we endeavored to demonstrate in this review. The thermal model and two-temperature model are well confirmed by experiment. The basic problem however is that the models employed in the theory of laser ablation rely on complex nonlinear systems of partial differential equations. Solutions of these equations call for using numerical methods this however hampers the interpretation of the experimental results.

We demonstrated nevertheless in the present review, that it is possible to obtain a reasonably complete description of laser ablation by invoking reduced models that involve the solution of nonlinear ordinary differential equations systems. The reduction can be performed by taking advantage of the moment's method or special solutions of the partial differential equations, the solutions possessing specific symmetries. These models prove to be expedient for the quantitative analysis of the experimental results and allow a better understanding of the physics of the ablation phenomenon.

Acknowledgements

The authors express their appreciation to N. Arnold, D. Bäuerle, M. C. Castex, T. C. Chong, M. H. Hong, D. von der Linde, A. Malyshev, B. Rethfeld for discussions of the issues raised in this review. Special thanks are due to Prof. Aaron Peled for his helpful comments. The Russian Foundation for Basic Research supported this work through grants No. 01-02-16136 and No. 02-02-17745.

References

1. D. C. Paine and J. C. Bravman (Eds.), *Laser Ablation for Material Synthesis, MRS Symp. Proc.*, vol. 191 (Pittsburgh, Pennsylvania, 1990).
2. J. C. Miller and R. F. Haglund, Jr. (Eds.), 'Laser Ablation – Mechanisms and Applications', *Lecture Notes in Physics*, vol. 389 (Berlin: Springer, 1991).
3. E. Fogarassy and S. Lazare (Eds.), 'Laser Ablation of Electronic Materials – Basic Mechanisms and Applications', *Proc. E-MRS*, vol. 4 (Elsevier: North-Holland, 1992).
4. J. C. Miller (Ed.), 'Laser Ablation – Principles and Applications', *Springer Series Mater. Sci.*, vol. 28 (Berlin: Springer, 1994).
5. E. Fogarassy, G. Geohegan and M. Stuke (Eds.), *Laser Ablation, Proc. E-MRS*, vol. 55 (Amsterdam: North-Holland, 1996).
6. R. Russo, D. Geohegan, K. Murakami and R. Haglund (Eds.), 'Laser Ablation', *Appl. Surf. Sci.* (North-Holland, Amsterdam, 1998), pp. 127–129.
7. C. R. Phipps (Ed.), 'High-Power Laser Ablation', *Proc. SPIE 3343* (1998); *Proc. SPIE 3885* (2000); *Proc. SPIE 4065* (2000); *Proc. SPIE 4760* (2002).
8. D. Bäuerle D., *Laser Processing and Chemistry*, 3 Ed. (Berlin: Springer-Verlag, 2000).
9. V. V. Novozhilov, *Dokl. Akad. Nauk SSSR* **270**, 831 (1983).
10. E. N. Sobol, *Phase Transformations and Ablation in Laser-Treated Solids* (New York: Wiley, 1995).
11. D. Bäuerle, B. Luk'yanchuk, P. Schwab, X. Z. Wang and E. Arenholz, *Laser ablation: Fundamentals and Recent Developments*, In Ref. [3], p. 39.
12. D. Bäuerle, B. Luk'yanchuk, N. Bityurin and S. Anisimov, 'Pulsed-laser Ablation', in L.D. Laude (Ed.), *Excimer Lasers* (Dordrecht: Kluwer Academic Publishers, 1994), p. 39.
13. J. H. Yoo, S. H. Leong, X. L. Mao and R. E. Russo, *Appl. Phys. Lett.* **79**, 444 (2001).
14. M. A. El'yashevich, S. I. Anisimov, G. S. Romanov, L. I. Grechihin, L. Ya. Min'ko, G and I. Bakanovich, *Breakdown of Metals Exposed to Laser Radiation, Report No. KEA -14* (Minsk: Physics Institute, Belarussian SSR Academy of Sciences, 1963).
15. S. I. Anisimov, Ya. A. Imas, G. S. Romanov and Yu. V. Khodyko, *Action of High-Power Radiation on Metals* (Springfield, VA: National Technical Information Service, 1971).
16. J. F. Ready, *Effects of High-Power Laser Radiation* (New York: Academic Press, 1971).
17. S. I. Anisimov, A. M. Bonch-Bruevich, M. A. El'yashevich, Ya. A. Imas, N. A. Pavlenko and G. S. Romanov, *Zh. Tekh. Fiz.* **36**, 1273 (1966).
18. S. I. Anisimov, *Teplofiz. High Temp.* **6**, 110 (1968).
19. B. Ya. Lyubov and E. N. Sobol, In: *Effect of Concentrated Energy Flows on Materials*, Ed. by N. N. Rykalin (Moscow: Nauka, 1985), p. 226.
20. B. Ya. Lyubov and E. N. Sobol, *J. Eng. Phys. Thermophys.* **45**, 670 (1983).
21. S. I. Anisimov and B. S. Luk'yanchuk, *Physics – Uspekhi* **45**, 293 (2002).
22. S. I. Anisimov, 'Ablation of Metals with Femtosecond Laser Pulses', In A. Guenther (Ed.), *International Trends in Applied Optics* (Washington, DC: Optical Society of America; Bellingham, WA: SPIE, 2002).
23. N. Bityurin, B. S. Luk'yanchuk, M. H. Hong and T. C. Chong, *Chem. Rev.* **103**, 519 (2003).
24. S. Preuss, A. Demchuk and M. Stuke, *Appl. Phys.* **A 61**, 33 (1995).
25. J. Krueger and W. Kautek, *Appl. Surf. Sci.* **96–98**, 430 (1996).
26. A. Rosenfeld and E. E. B. Campbell, *Appl. Surf. Sci.* **96–98**, 439 (1996).
27. A. Cavalleri, K. Sokolowski-Tinten, J. Bialkowski and D. von der Linde, *Appl. Phys. Lett.* **72**, 2385 (1998).
28. R. F. Haglund Jr., 'Mechanisms of Laser-Induced Desorption and Ablation', in J. C. Miller and R. F. Haglund, Jr. (Eds.), *Laser Ablation and Desorption* (San Diego: Academic Press, 1998), p. 15.
29. D. E. Gray (Ed.), *American Institute of Physics Handbook*, 3rd edition (New York: McGraw-Hill, 1972).
30. Ya. I. Frenkel, *Kinetic Theory of Liquids* (Oxford: Clarendon Press, 1946).
31. S. Küper, J. Brannon and K. Brannon, *Appl. Phys.* **A 56**, 43 (1993).

32. B. Luk'yanchuk, N. Bityurin, S. Anisimov and D. Bäuerle, 'Photophysical Ablation of Organic Polymers', in L. D. Laude (Ed.), *Excimer Lasers*, NATO ASI Series, vol. E 256 (Dordrecht: Kluwer Academic Publishers, 1994), p. 59.
33. Yu. V. Afanasiev and O. N. Krokhin, *Sov. Phys. JETP* 2**5**, 639 (1967).
34. N. Arnold, B. Luk'yanchuk and N. Bityurin, *Appl. Surf. Sci.* **127–129**, 184 (1998).
35. D. P. Brunco, M. Q. Thompson, C. E. Otis and P. M. Goodwin, *J. Appl. Phys.* **72**, 434 (1992).
36. N. Arnold, B. Luk'yanchuk, N. Bityurin and D. Bäuerle, *Laser Physics* **8**, 47 (1998).
37. N. Arnold, B. Luk'yanchuk and N. Bityurin, *Proc. SPIE* **3343**, 484 (1998).
38. Yu. V. Vorob'ev, *Moments Method in Applied Mathematics* (New York: Gordon & Breach Sci. Publ., 1962).
39. A. A. Samarskii, V. A. Galaktionov, S. P. Kurdyumov and A. P. Mikhailov, *Blow-up in Quasilinear Parabolic Equations* (Berlin: De Guyter, 1995).
40. D. Zwillinger, *Handbook of Differential Equations* (Boston: Academic Press, 1989).
41. S. Wolfram, *The Mathematica Book*, 4th ed. (Champaign, IL: Wolfram Media, 1999).
42. T. Goetz and M. Stuke, *Appl. Phys.* **A 64**, 539 (1997).
43. A. A. Andronov, A. A. Vitt and S. E. Khaikin, *Theory of Oscillators* (New York: Dover, 1987).
44. Ya. B. Zeldovich, G. I. Barenblatt, V. B. Librovich and G. M. Makhviladze, *The Mathematical Theory of Combustion and Explosions* (New York: Consultants Bureau, 1985).
45. G. Barenblatt, *Scaling, Self-Similarity, and Intermediate Asymptotics* (Cambridge: Cambridge Univ. Press, 1996).
46. D. A. Frank-Kamenetski, *Diffusion and Heat Transfer in Chemical Kinetics* (New York: Plenum Press, 1969).
47. S. I. Anisimov and V. A. Khokhlov, *Instabilities in Laser – Matter Interaction* (Boca Raton, FL: CRC Press, 1995).
48. J. H. Yoo, S. H. Jeong, X. L. Mao, R. Greif and R. E. Russo, *Appl. Phys. Lett.* **76**, 783 (2000).
49. N. M. Bulgakova and A. V. Bulgakov, *Appl. Phys.* **A 73**, 199 (2001).
50. Q. Lu, S. S. Mao, X. L. Mao and R. E. Russo, *Appl. Phys. Lett.* **80**, 3072 (2002).
51. F. V. Bunkin and M. I. Tribelskii, *Sov. Phys. Uspekhi* **23**, 105 (1980).
52. N. Bityurin, N. Arnold, B. Luk'yanchuk and D. Bäuerle, *Appl. Surf. Sci.* **127**, 164 (1998).
53. N. Arnold and N. Bityurin, Appl. Phys. **A 68**, 615, (1999).
54. N. Bityurin, *Proc. SPIE.* **4423**, 197 (2001).
55. N. Bityurin and A. Malyshev, *J. Appl. Phys.* **92**, 605 (2002).
56. M. Himmelbauer, N. Bityurin, B. Luk'yanchuk, N. Arnold and D. Bäuerle, *Proc. SPIE* **3093**, 220 (1997).
57. E. E. Ortelli, F. Geiger, T. Lippert, J. Wei and A. Wokaun, *Macromolecules* **33**, 5090, (2000).
58. T. Lippert and J. T. Dickinson, *Chem. Rev.* **102**, 453 (2003).
59. S. V. Babu, G. C. D'Couto and F. D. Egitto, *J. Appl. Phys.* **72**, 692 (1992).
60. M. Himmelbauer, E. Arenholz and D. Bäuerle, *Appl. Phys.* **A 63**, 87 (1996).
61. G. Paraskevopoulos, D. L. Singleton, R. S. Irwin and R. S. Taylor, *J. Appl. Phys.* **70**, 1938 (1991).
62. R. S. Taylor, D. L. Singleton and G. Paraskevopoulos, *Appl. Phys. Lett.* **50**, 1779 (1987).
63. N. Bityurin, S. Muraviov, A. Alexandrov and A. Malyshev, *Appl. Surf. Sci.* **110**, 270 (1997).
64. M. Himmelbauer, E. Arenholz, D. Bäuerle and K. Schichler, *Appl. Phys.* **A 63**, 337 (1996).
65. P. E. Dyer, G. A. Oldershaw and D. J. Schudel, *J. of Phys. D – Appl. Phys.* **26**, 323 (1993).
66. M. Lapczyna and M. Stuke, *Appl. Phys.* **A 66**, 473 (1998).
67. L. Museur, W. Q. Zheng, A. V. Kanaev and M. C. Castex, *IEEE J. Sel. Topics Quantum. Electron.* **1**, 900 (1995).
68. D. Riedel and M. C. Castex, *Appl. Phys.* **A 69**, 375 (1999).
69. H. H. G. Jellinek and R. Srinivasan, *J. Phys. Chem.* **88**, 3048 (1984).
70. M. C. K. Tinone, K. Tanaka and N. Ueno, *J. Vac. Sci. Technol.* **13**, 1885 (1995).
71. G. H. Pettit and R. Sauerbrey, *Appl. Phys. Lett.* **58**, 793 (1991).
72. G. H. Pettit and R. Sauerbrey, *Appl. Phys.* **A 56**, 51 (1993).
73. G. H. Pettit, M. N. Ediger, D. W. Hahn, B. E. Brinson and R. Sauerbrey, *Appl. Phys.* **A 58**, 573 (1994).

74. T. Lippert, L. S. Bennett, T. Nakamura, H. Niino, A. Ouchi and A. Yabe, *Appl. Phys.* **A 63**, 257 (1996).
75. P. E. Dyer, D. M. Karnakis and G. A. Oldershaw, *Appl. Surf. Sci.* **86**, 1 (1995).
76. H. Mauser, *Z. Naturforsch.* **22 B**, 569, (1967).
77. H. Mauser, *Z. Naturforsch.* **34 C**, 1264 (1979).
78. N. M. Bityurin, *Ph.D. Thesis*, Inst. Appl. Phys., USSR Ac. Sci., Gorkii, USSR, 1988.
79. N. Bityurin, *Appl. Surf. Sci.* **138–139**, 354 (1999).
80. N. M. Bityurin, V. N. Genkin and V. V. Sokolov, *Sov. J. Polymer Sci.* **24 A**, 748 (1982).
81. M. C. Castex, N. Bityurin, C. Olivero, S. Muraviov, N. Bronnikova and D. Riedel, *Appl. Surf. Sci.* **168**, 175 (2000).
82. M. C. Castex and N. Bityurin, *Appl. Surf. Sci.* 197–198, 805, (2002).
83. N. Bityurin and M. C. Castex, *J. Appl. Phys.* (2003) (to be published).
84. K. Schildbach, *Proc. SPIE* **1279**, 60, (1990).
85. K. A. Valiev, L. V. Velikov, Yu. I. Dorofeev and V. E. Skurat, *Chemistry of High Energy* **22**, 352 (1988).
86. J. C. White, H. G. Craighead, R. E. Howard, L. D. Jackel, R. E. Beringer, R. W. Epworth, D. Henderson and J. E. Sweeney, *Appl. Phys. Lett.* **44**, 22 (1984).
87. K. Kudo, T. Iwabuchi, K. Muton, T. Miyata, R. Sano and K. Tanaka, *Jap. J. Appl. Phys.* **29**, 2572 (1990).
88. G. D. Mahan, H. S. Cole, Y. S. Liu and H. R. Philipp, *Appl. Phys. Lett.* **53**, 2377 (1988).
89. B. J. Garrison and R. Srinivasan, *Appl. Phys. Lett.* **44**, 849 (1984).
90. M. S. Kitai, V. L. Popkov and V. A. Semchishen, *Makromol. Chem. Macromol. Symp.* **37**, 257 (1990).
91. D. E. Hare, J. Franken and D. D. Dlott, *J. Appl. Phys.* **77**, 5950 (1995).
92. R. Srinivasan, B. Braren and K. G. Casey, *Appl. Phys.* **68,** 1842 (1990).
93. D. E. Hare and D. D. Dlott, *Appl. Phys. Lett.* **64**, 715 (1994).
94. L. S. Bennet, T. Lippert, H. Furutani, H. Fukumura and H. Masuhara, *Appl. Phys.* **A 63**, 327 (1996)
95. G. Odian, *Principle of Polymerization*, 2nd ed. (New York: Wiley, 1970), p. 258.
96. G. M. Bartenev, *Stability and Mechanisms of Polymer Destructio*n (Moscow: Khimia, 1984) (in Russian).
97. Ya. B. Zeldovich and Yu. P. Raizer, P*hysics of Shock Waves and High-Temperature Hydrodynamic Phenomena* (New York: Academic Press, 1966, 1967).
98. N. Bityurin, A. Malyshev, B. Luk'yanchuk, S. Anisimov and D. Bäuerle, *Proc. SPIE* **2802**, 103 (1996).
99. B. Luk'yanchuk, N. Bityurin, S. Anisimov, A. Malyshev, N. Arnold and D. Bäuerle, *Appl. Surf. Sci.* **106**, 120 (1996).
100. A. Malyshev, *Ph.D. Thesis*, Inst. Appl. Phys. Russian Ac. Sci., N. Novgorod, 2002.
101. G. B. Blanchet, P. Cotts and C. R. Fincher Jr., *J. Appl. Phys.* **68**, 2975 (2000).
102. Yu. A. Mikheev, T. S. Popravko and D. Ya. Toptygin, *Doklady AN SSSR* **210**, 148 (1973).
103. A. Gupta, R. Liang, F. D. Tsay and J. Moacanin, *Macromolecules* **13**, 1696 (1980).
104. S. Küper and M. Stuke, *Appl. Phys.* **A 49**, 211 (1989).
105. L. V. Zhigiley, P. B. Kodali and B. J. Garrison, *J. Phys. Chem.* **B 102**, 2845 (1998).
106. L. V. Zhigiley, E. Leveugle, B. J. Garisson, Ya. G. Yingling and M. I. Zeifman, *Chem. Rev.* **102**, 321 (2003).
107. K. Tonyali, L. C. Jensen and J. T. Dickinson, *J. Vac. Sci. Technol.* **A 6**, 941 (1988).
108. T. Bahners and E. Schollmeyer, *J. Appl. Phys.* **66**, 1884 (1989).
109. E. Arenholz, M. Wagner, J. Heitz and D. Bäuerle, *Appl. Phys.* **A 55**, 119 (1992).
110. N. Bityurin, E. Arenholz, N. Arnold and D. Bäuerle (to be published).
111. Yu. V. Afanasiev, B. N. Chichkov, N. N. Demchenko, V. A. Isakov and I. N. Zavestovskaya, *J. Russ. Laser Res.* **20**, 89 (1999).
112. Yu. V. Afanasiev, B. N. Chichkov, V. A. Isakov, A. P. Kanavin and S. A. Uryupin, *J. Russ. Laser Res.* **20**, 189 (1999).
113. Yu. V. Afanasiev, B. N. Chichkov, N. N. Demchenko, V. A. Isakov, I. N. Zavestovskaya, *J. Russ. Laser Res.* **20**, 489 (1999).

114. Yu. V. Afanasiev, B. N. Chichkov, V. A. Isakov, A. P. Kanavin and S. A. Uryupin, *J. Russ. Laser Res.* **21**, 34 (2000).
115. Yu. V. Afanasiev, B. N. Chichkov, V. A. Isakov, A. P. Kanavin and S. A. Uryupin, *J. Russ. Laser Res.* **21**, 505 (2000).
116. J. Hohfeld, *Ultrafast Electron-, Lattice- and Spin-Dynamics in Metals* (Berlin: VWF Verlag fur Wissenshaft und Forcschung, 1998).
117. S. I. Anisimov, B. L. Kapeliovich and T. L. Perel'man, *Sov. Phys. JETP* **39**, 375 (1974).
118. J. G. Fujimoto, J. M. Liu, E. P. Ippen and N. Blombergen, *Phys. Rev. Lett.* **53**, 1873 (1984).
119. X. Y. Wang, D. M. Riffle, Y.-S. Lee and M. C. Downer, *Phys. Rev.* **B 50**, 8016 (1994).
120. C.-K. Sun, F. Vallee, L. H. Acioli, E. P. Ippen and J. G. Fujimoto, *Phys. Rev.* **B 50**, 15337 (1994).
121. R. H. M. Groeneveld, H. Sprik and A. Lagendijk, *Phys. Rev.* **B 51**, 11433 (1995).
122. J. Hohlfeld, J. G. Müller, S. -S. Wellershoff and E. Matthias, *Appl. Phys.* **B 64**, 387 (1997).
123. L. A. Fal'kovskiï and E. G. Mishchenko, *JETP* **88**, 84 (1999).
124. S. I. Anisimov and B. Rethfeld, *Izv. Ross. Akad. Nauk Ser. Fiz.* **61** 1642 (1997).
125. A. P. Kanavin, I. V. Smetanin, V. A. Isakov, Yu. V. Afanasiev, B. N. Chichkov, B. Wellegehausen, S. Nolte, C. Momma and A. Tünnermann, *Phys. Rev.* **B 57**, 14698 (1998).
126. J. Güdde, J. Hohlfeld, J. G. Müller and E. Matthias, *Appl. Surf. Sci.* **127–129**, 40 (1998).
127. S.-S. Wellershoff, J. Hohlfeld, J. Güdde and E. Matthias, *Appl. Phys.* **A 69** (Suppl.) S99 (1999).
128. S. I. Anisimov, B. I. Makshantsev and A. V. Barsukov, *Opt. Acoust. Rev.* **1**, 251 (1991).
129. B. Rethfeld, A. Kaiser, M. Vicanek and G. Simon, *Appl. Phys.* **A 69** [Suppl.], S109 (1999).
130. B. S. Luk'yanchuk, S. I. Anisimov and Y. F. Lu, *Proc. SPIE* **4423**, 141 (2001).
131. B. C. Stuart, M. D. Feit, A. M. Rubenchik, B. W. Shore and M. D. Perry, *Phys. Rev. Lett.* **74**, 2248 (1995).
132. A. A. Oraevsky, L. B. DaSilva, M. D. Feit, M. E. Glinsky, B. M. Mammini, K. L. Paquette, M. D. Perry, A. M. Rubenchik, W. Small IV and B. C. Stuart, *Proc. SPIE*, **2391**, 423 (1995).
133. B. C. Stuart, M. D. Feit, S. Herman, A. M. Rubenchik, B. W. Shore and M. D. Perry, *JOSA* **B 13**, 459 (1996).
134. B. C. Stuart, M. D. Feit, A. M. Rubenchik, B. W. Shore and M. D. Perry, *Phys. Rev.* **B 53**, 1749 (1996).
135. L. V. Keldysh, *Sov. Phys. JETP* **20**, 1307 (1965).
136. A. Kaiser, B. Rethfeld, M. Vicanek and G. Simon, *Phys. Rev.* **B 61**, 11437 (2000).
137. B. Rethfeld, A. Kaiser, M. Vicanek and G. Simon, *Proc. SPIE*, **4423**, 250 (2000).
138. N. Bityurin and A. Kuznetsov, *J. Appl. Phys.* **93**, 1567 (2003).
139. J. Guillet, *Polymer Photophysics and Photochemistry* (Cambridge: Cambridge University Press, 1985).
140. N. Bityurin and A. Malyshev, *Appl. Surf. Sci.* 127–129, 199 (1998).
141. A. Yu. Malyshev and N. M. Bityurin, *Quantum Electronics* **29**, 134 (1999).
142. S. Preuss, M. Spaeth, Y. Zhang and M. Stuke, *Appl. Phys. Lett.* **62**, 3049 (1993).
143. J. K. Frisoli, Y. Hefetz and T. F. Deutsch, *Appl. Phys.* **B 52**, 168 (1991).
144. A. Rosenfeld, D. Ashkenasi, H. Varel, M. Wähmer and E. E. B. Cambell, *Appl. Surf. Sci.* **127–129**, 76 (1998).
145. R. Stoian, D. Ashkenasi, A. Rosenfeld and E. E. B. Campbell, *Phys. Rev.* **B 62**, 13167 (2000).
146. R. Stoian, M. Boyle, A. Thoss, A. Rosenfeld, D. Ashkenasi, G. Korn, I. V. Hertel and E. E. B. Campbell, In: *Technical Digest CLEO'2001* (Baltimore, MD, Baltimore Convention Center, May 6–11, 2001), p. 577.
147. B. Luk'yanchuk, N. Bityurin, S. Anisimov and D. Bäuerle, *Appl. Phys.* **A 57**, 367 (1993).
148. B. Luk'yanchuk, N. Bityurin, S. Anisimov, N. Arnold and D. Bäuerle, *Appl. Phys*. **A 62**, 397 (1996).
149. B. Luk'yanchuk, N. Bityurin, A. Malyshev, S. Anisimov, N. Arnold and D. Bäuerle, *Proc. SPIE* **3343**, 58, (1998).
150. V. P. Aksenov, G. N. Mikhailova, J. Boneberg, P. Leiderer and H. J. Muenzer, *Proc. SPIE* **4423**, 70 (2001).

CHAPTER 6

DEVELOPMENT AND APPLICATIONS OF UV EXCIMER LAMPS

Ian W. Boyd[1, *], Jun-Ying Zhang[2] and Ulrich Kogelschatz[3]

[1] *Electronic and Electrical Engineering, University College London, Torrington Place, London WC1E 7JE, United Kingdom;* [2] *Structure Research Laboratory, University of Science and Technology of China, Academia Sinica, Hefei, Anhui, 230026, PR China;*
[3] *Retired from ABB Corporate Research, Baden, Switzerland*
*(*Author for correspondence, E-mail: i.boyd@ee.ucl.ac.uk)*

ABSTRACT: The principles and properties of ultraviolet (UV) and vacuum ultraviolet (VUV) radiation generated by decaying excimer complexes are discussed. Excimer lamps offer very high intensity (before saturation effects start to limit the spontaneous emission) narrow-band radiation, at various UV and VUV wavelengths, are highly efficient (with no self absorption), and can provide high photon fluxes over large areas. For large-scale industrial applications silent (dielectric-barrier) discharges using simple geometric configurations are therefore possible. Applications of these sources include photo-deposition of large area or patterned thin metal films, of high- and low-dielectric-constant insulating layers, low-temperature oxidation of Si, SiGe and Ge, and annealing, curing, cleaning, etching and microstructuring of surfaces, demonstrating that these low cost systems can provide an interesting alternative to excimer lasers for industrial large-scale low-temperature materials processing.

1. Introduction

Monochromatic photons, especially in the ultraviolet spectral range, can selectively initiate photochemical reactions in gas streams, in liquids and on surfaces. Many of these processes have been demonstrated for the first time in research laboratories using UV lasers. For industrial applications where large fluid flows or surface areas need to be treated, however, cheaper and more robust wavelength-selective photon sources are required. With the recent introduction of excimer lamps new tools for large-scale low-temperature photo-processing are now emerging. The advantages of these lamps include efficient generation of UV and VUV radiation in pre-selected narrow wavelength ranges, high photon fluxes, a variety of different geometrical shapes and extended operating lifetimes.

Novel applications of UV excimer lamps include cleaning of large substrates, curing of resins, adhesives and paints, surface modification, oxidation of Si, Ge and SiGe, deposition of large area or patterned thin films, such as metals, semiconductors, or extremely high- to low-dielectric constant insulators, etching and microstructuring of polymer surfaces, and annealing to improve optical and electrical properties. Using short wavelengths even room temperature reactions can be initiated. VUV photons are also utilised on a very large scale in plasma display panels and in mercury-free fluorescent lamps. In these applications internal phosphor coatings are used to convert the VUV excimer radiation to visible light.

Aaron Peled (ed.), Photo-Excited Processes, Diagnostics and Applications (PEPDA), 161–199, 2003.
© 2003 *Kluwer Academic Publishers. Printed in the Netherlands.*

2. Excimer formation in gas discharges

2.1. *Rare gas excimers, halogen excimers and rare gas halide exciplexes*

Non-equilibrium discharges in high density rare gases at a pressure level around or above atmospheric pressure have the interesting ability to efficiently convert electron kinetic energy to electronic excitation energy and rapidly funnel that excitation to a few low-lying atom and excimer levels. These systems have been intensively studied with pulsed electron beam pumping and pulsed discharge excitation for excimer laser applications [1–3]. Simple and efficient excimer lamps can also be built using different types of gas discharges to induce excimer formation in certain gas mixtures. The fluorescence radiation of decaying excimer complexes is normally restricted to specific narrow wavelength ranges. Theoretical predictions of the fluorescence efficiency of rare gas excimer radiation lie in the range 45–80% [2, 4–9]. At particle densities of about 10^{25} m^{-3} excited species and ions rapidly form excimer complexes. Vibrational relaxation is very fast at elevated pressures and the spectrum is dominated by emission bands originating from the two lowest excimer states. These excimer states do not interact with the ground state and can only decay by radiation. The second excimer continua of the pure rare gases He_2*, Ne_2*, Ar_2*, Kr_2*, and Xe_2* peak at 74 nm, 83 nm, 126 nm, 146 nm and 172 nm, respectively. Table 1 shows the rare gas dimers with their respective peak wavelengths. Typical halfwidths of the observed fluorescence bands are between 10–15 nm. With mixed rare gases the emission can spread over a wider wavelength region due to the formation of heteronuclear diatomic molecules [10–11].

Table 1. Rare gas dimers with corresponding peak wavelengths in nm.

He_2*	Ne_2*	Ar_2	Kr_2*	Xe_2*
74	83	126	146	172

For industrial applications the Xe_2* excimer has become the most important vacuum ultraviolet source because high purity silica tubes with sufficient VUV transmission are available. For shorter wavelengths special window materials, such as LiF, MgF_2 or CaF_2 have to be used. For wavelengths below 100 nm no transparent window materials are available. Of the shorter wavelengths, Ar_2* excimer radiation has in particular achieved importance in intermediate through-flow windowless systems.

The energy of excited rare gas atoms and ions can also be utilized to form halogen excimers, X_2*, or rare gas-halide exciplex complexes of the type RgX*, where Rg stands for a rare gas atom and X for a halogen atom (Rg: He, Ne, Ar, Kr, or Xe, and X: F, Cl, Br or I). In these excimers the bound-free $B \rightarrow X$ transitions are utilised in a similar way to generate spontaneous VUV/UV emission of high efficiency and even smaller bandwidth, typically of 2–4 nm spectral width [12, 13]. Table 2 summarises several excimers and their respective peak wavelengths, while Figure 1 shows selected emission spectra.

Table 2. Halogen and rare gas halide excimers with corresponding peak wavelengths in nm.

F_2*	ArCl*	ArF*	KrCl*	KrF*	XeI*	Cl_2*	XeBr*	Br_2*	XeCl*	I_2*	XeF*
157	175	193	222	248	253	259	282	289	308	342	354

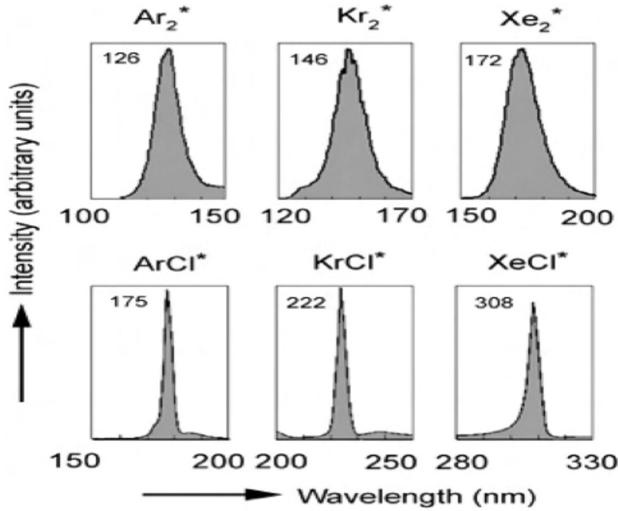

Figure 1. Characteristic emission spectra of excimer lamps (after Refs. [16, 18]).

2.2. *Excimer lamps utilising silent discharge excitation*

In this chapter we concentrate on the excimer lamp systems based on silent discharges (also referred to as dielectric-barrier discharges or DBDs). This type of discharge allows excitation of the gas mixture without having metal electrodes in contact with the aggressive plasma. For practical applications this has proved to be much simpler than with high-energy electron beam generators or pulsed capacitor discharges which tend to be expensive and only operate at low repetition rates. Laboratory type excimer sources based on sealed electrodeless lamps are cheap and have potentially long operating lifetime as reviewed elsewhere [4, 14–19]. These lamps are filled with excimer forming gas mixtures at filling pressures of 0.1–1 bar. In most applications quartz tubes are used which can have protective internal coatings against fluorine attack or functional coatings to reduce the ignition voltage. High purity silica (Suprasil) is transparent down to the wavelength of the powerful Xe excimer lamp operating at 172 nm. To achieve even shorter wavelengths special window materials or windowless geometries can be used [17, 20]. Switch-mode power supplies operating in the range 20 kHz to 15 MHz provide an efficient and reliable way to drive these discharges. Either transformers or resonant circuits are used to step up the voltage to the range of a few kV (peak-to-peak). With recent advances in HV power semiconductor devices these elements may no longer be

required in the future. The use of dielectric-barrier discharges to generate excimer radiation has proved to be a very sound concept [4, 15–19, 21–23]. Their main advantage is simplicity, high efficiency and low cost and lack of internal electrodes. Sealed lamps of various planar and cylindrical geometries can be designed (Figures 2 and 3). The width of the discharge gap ranges from 0.1 mm to several mm and filling pressures from 10^4–5×10^5 Pa. In many cases a third buffer gas (He, Ne) is added to the binary excimer-forming mixture to facilitate ignition and provide additional control over the electron energy distribution. Operating frequencies range from 50 Hz to 15 MHz, applied voltages from a few hundred V to several kV, and when discharge gap widths of a few mm and excimer forming gas mixture pressure around 1 bar are used, voltage amplitudes of a few kV are required for ignition. The so-called planar electrode configuration on the right of Figure 3 uses thin adjacent metal electrodes that are imbedded in or covered by a dielectric. Very fine structured electrodes have been manufactured by screen printing, a fast and economic process by which dielectric layers can also be produced. In this configuration a few hundred volts is sufficient to ignite a surface discharge in the gas mixture. Commercial excimer lamps are now available for 126 nm (Ar_2*), 146 nm (Kr_2*), 172 nm (Xe_2*), 222 nm (KrCl*) and 308 nm (XeCl*) with typical efficiencies from 5–40%. For curing applications, cylindrical XeCl* lamps up to 2 m length are available. Powerful and efficient XeI* and XeBr* lamps radiating at 253 nm [24] and 282 nm [25], respectively, have recently been investigated. Most excimer lamps concentrate their narrow emission around the quoted wavelength. Cooled versions can operate close to room temperature even at high electrical input powers. Phosphors can be used to transform the UV radiation to visible light. This is the basis of mercury-free fluorescent lamps and of flat plasma display panels with up to 1.5 m picture diagonal. In these applications simple glass structures can be used because no UV transmission is required.

Using the co-planar electrode configuration shown in the right of Figure 3, thin (< 10 mm thick) flat, large-area, Hg-free fluorescent lamps have been developed [26–28]. The applications are mainly for backlighting liquid crystal displays for

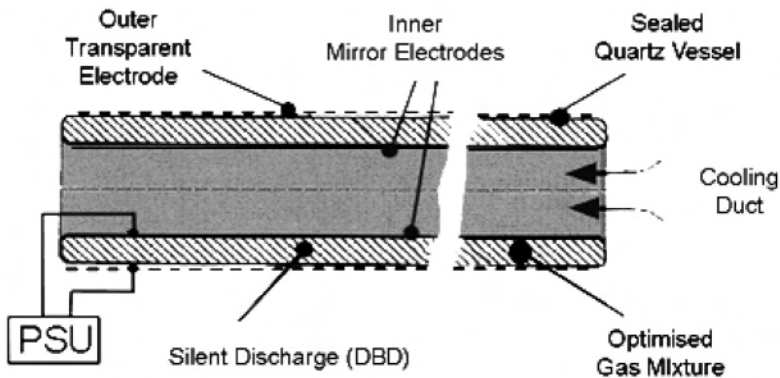

Figure 2. Sealed cylindrical silent-discharge excimer lamp configuration (PSU: power supply unit).

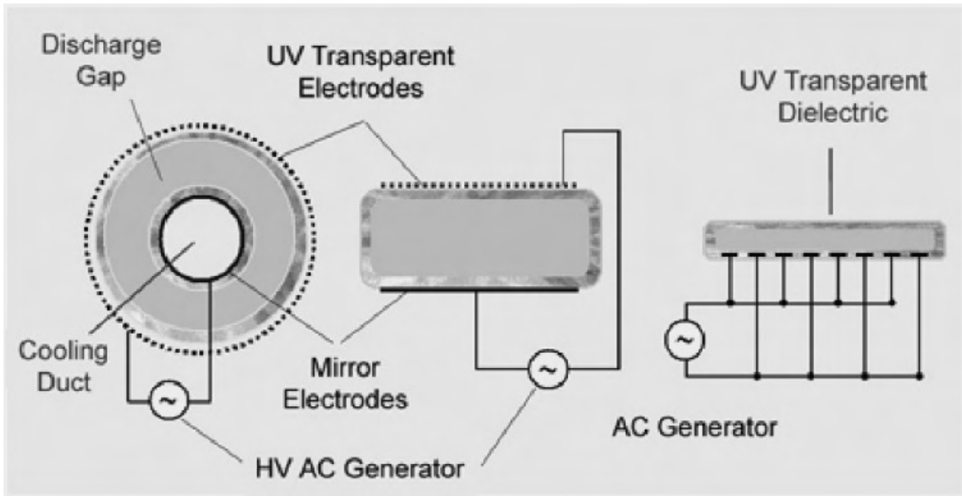

Figure 3. Sealed cylindrical and planar silent-discharge excimer lamp configurations (Ref. [14]).

small automotive displays to large LCD screens. Operating lifetimes up to 100,000 hours have been reported. Since internal phosphor layers are used to convert the VUV Xe excimer radiation to visible light, sealed glass cells are used. If large-area sources are desired for wafer processing or surface treatment this technology could readily be extended to use UV transparent silica vessels or windows. The attractive feature of this is that inexpensive manufacturing techniques have been found to apply electrode structures and dielectric coatings by thick film printing. Based on these significant advances large- area flat VUV sources using excimer radiation at 172 nm can be readily mass-manufactured.

To overcome the limitation of window materials at wavelengths shorter than the 172 nm radiation of xenon excimer also windowless or open configurations have been proposed. A relatively simple configuration can be found in Ref. [15]. In this configuration (Figure 4) the silent discharge is initiated between adjacent tube electrodes covered by a dielectric that can be made of e.g. silica or ceramic. If a rare gas fill is used, the second excimer continuum is generated, and irradiates the substrates without intermediate windows.

A more sophisticated version has been developed at the Institut für Oberflächen-modifizierung (IOM) in Leipzig [20]. This pilot installation with a moving belt (Figure 5) provides powerful radiation at 126 nm by using a through flow argon system. The length of the electrodes is 30 cm, the applied voltage 1.5 kV, the frequency 1 MHz, and the RF power is 2.5 kW. By optimising the seals the Ar flow could be restricted to 5–20 l/h. The maximum tolerable oxygen content was kept below 100 ppm. Since argon gas is not very expensive and the use of technical grade levels is sufficient large industrial installations based on this principle are readily conceivable.

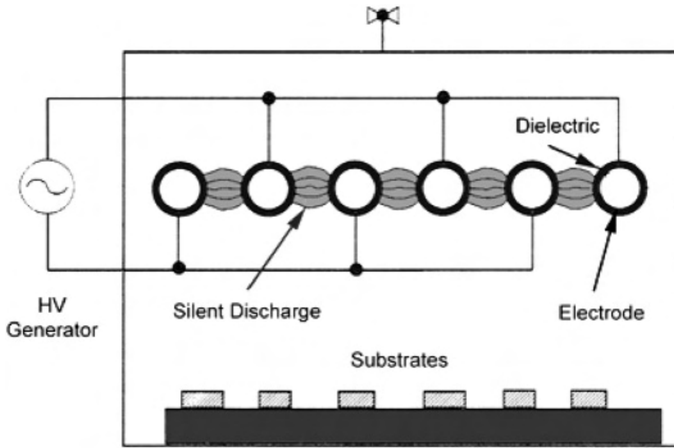

Figure 4. Windowless excimer vacuum ultraviolet source (after Ref. [15]).

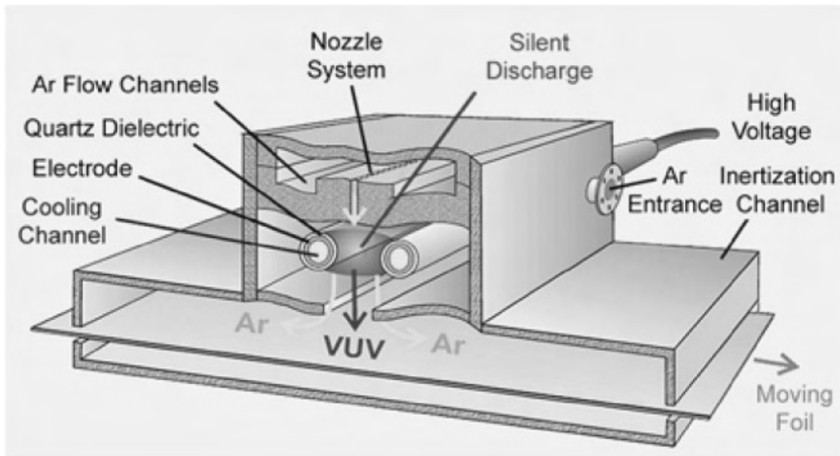

Figure 5. Windowless, Ar excimer UV irradiation system after M. Lenk/R. Mehnert, IOM, Leipzig [20].

3. Applications of incoherent excimer radiation

Soon after the prototypes of excimer lamps [4, 15, 17, 29–31] became available these novel UV sources found a large number of interesting applications [32, 36, 44, 48, 54, 59, 61], including dielectric [32–35] and metallic [36–43] thin film deposition, oxidation of Si, Ge and Si-Ge [44–47], annealing [54–58], surface modification and polymer etching [48-53], degradation of various pollutants [59, 60], as well as large area flat panel displays [61, 62] etc. Single- and multi-layered

films of SiO_2, Si_3N_4, and SiON could be deposited by UV-CVD from different mixtures of silane, oxygen, ammonia, and nitrous oxide gases [32–33, 63–66]. Fine-tuning of the refractive index of these films could be controlled by varying the precursor ratios. Direct irradiation of Si in O_2 at 250 °C was found to induce oxidation rates more than three times greater than those obtained using a typical low pressure Hg lamp at 350 °C [44, 46, 67]. Novel applications toward high- and low-dielectric constant thin films on Si by photo-CVD as well as UV sol-gel processing, have been reported, including Ta_2O_5, TiO_2, Ti-doped Ta_2O_5 and HfO_2, ZrO_2 and PZT. Several of these techniques will be reviewed in the following sections.

3.1. *VUV cleaning of surfaces*

UV cleaning of glass substrates in LCD manufacturing, of reticules for VUV lithography and in wafer processing has become a standard process. The main aim is the removal of residual organic surface contaminants (mainly aliphatic and aromatic hydrocarbons), to improve wetability and to promote adhesion. Xe excimer lamps, whose photon energy is 7.25 eV, are mainly used for this purpose. This is high enough to break most molecular bonds in organic compounds. However, it is not high enough to split the CO_2 molecule, one of the most likely final products. UV cleaning is typically performed in an Ar/O_2 mixture at reduced pressure in the 10–100 mbar range. The Ar carrier gas is transparent to this radiation, while O_2 is strongly absorbing, and splits into the very reactive atomic constituents $O(^3P)$ and $O(^1D)$. Ozone (O_3), formed by a recombination of O atoms with O_2 molecules, also absorbs the radiation and photo-dissociates to yield an excited $O(^1D)$ atom. H_2O molecules resulting from the cleavage of organic compounds of the general form $C_xH_yO_z$ also strongly absorb this radiation, and following excitation, homolyse with the formation of hydroxyl radicals and hydrogen atoms. The gas pressure and oxygen content is optimised to obtain a powerful cleaning process of surface contaminants resulting from the combined attack of direct VUV irradiation and a highly reactive gas mixture containing O_3, $O(^3P)$, $O(^1D)$ and OH radicals. The intermediate molecular fragments are transformed into the stable end-products H_2, H_2O, CO and CO_2, which are carried away in the gas stream. The result is a much cleaner surface with a wetability contact angle of 5°–10° compared with 30°–60° before VUV cleaning depending on the nature of the substrate. Present technology uses arrays of parallel linear cylindrical Xe excimer lamps providing irradiances of typically 10 mW/cm^2. Adhesion improvement can be achieved in 10 s, though thorough surface cleaning may take a little longer.

3.2. *High dielectric constant materials*

As electronic devices scale down, their gate oxide thicknesses must be correspondingly reduced and thickness control becomes a critical issue. If trends continue, then by 2012 the SiO_2 thickness predicted by the semiconductor industry roadmap, will reach atomic dimensions (five Si atomic layers), or less than one nanometre [68] as indicated in Table 3 [69, 70]. For 0.1 μm technology and beyond this gate

Table 3. The projected gate oxide thickness for CMOS integrated circuits for 1997–2012 [69–70].

Technology timeline	1997	1999	2001	2003	2006	2009	2012
Design rule (μm)	0.25	0.18	0.15	0.13	0.10	0.07	0.05
Wafer diameter (mm)	200	300	300	300	300	450	450
Gate dielectric (nm, $\varepsilon = 3.9$) equivalent SiO_2 thickness	4–5	3-4	2-3	2-3	1.5-2	< 1.5	< 1.0
Gate dielectric (nm) Ta_2O_5 thickness $\varepsilon = 19$)	20–25	15–20	10–15	10–15	7.5–10	< 7.5	< 5

thickness must be scaled below 2.0 nm and will present extremely difficult fabrication and reliability problems as well as fundamental quantum mechanical difficulties. However, an insulating film with a dielectric constant higher than that for SiO_2 (see Table 4) can solve this gate dielectric problem, allow the use of a thicker insulating layer with a similar effective capacitance and enable a further decrease in device area. Recently, many high dielectric constant materials have been investigated as possible candidates to replace SiO_2 in dynamic random access memories (DRAMs). Some of these are summarised in Table 4. More detailed thermodynamic stability and Si-compatibility of these dielectrics can be found elsewhere [71–73].

Amongst these dielectrics, much of the focus of current high *k* research involves $PbZr_xTi_{1-x}O_3$ (PZT), $Ba_xSr_{1-x}TiO_3$ (BST), Ta_2O_5, TiO_2, and HfO_2. Tantalum pentoxide (Ta_2O_5) is a promising candidate to replace SiO_2 in several applications because of its compatibility with ULSI processing and its chemical and thermal stability [74–77]. Various storage capacitor configurations with Ta_2O_5 films such as polySi/Ta_2O_5/polySi (SIS), metal/Ta_2O_5/metal (MIM), or MIS, are also used to study its properties [78]. Ta_2O_5 capacitors with TiN/poly-Si top electrodes are suitable for 256 Mbit memory devices [76]. Recently, a large increase in dielectric constant from 20 to >120 in Ta_2O_5 bulk ceramic through the addition of 8% TiO_2 has been shown [79]. Mixed Ta-Ti oxide films have since exhibited dielectric constants > 50 [80–81]. However, neither pure nor doped Ta_2O_5 can be applied to DRAM technology, because of large leakage currents in the as-deposited films due to oxygen deficiency, and defect and impurity contamination present. These can be reduced by post-deposition furnace annealing, with O_2, N_2, H_2, NH_3, O_3, N_2O, etc., rapid thermal (O_2) annealing (RTA), UV generated ozone (UVO), plasma and a number

Table 4. Alternate gate dielectrics for use in silicon MOS transistors [71–73].

Material	*k*	Material	*k*	Material	*k*	Material	*k*
$PbZr_xTi_{1-x}O_3$ (PZT)	1000	Ta_2O_5	25–28	Nd_2O_3	16–20	MgO	9.8
$BaxSr_{1-x}TiO_3$ (BST)	500	$LaAlO_3$	25	Y_2O_3	11–14	Li_2O	8.1–8.8
TiO_2	100	$La_2Be_2O_5$	25	Er_2O_3	12.5–13	$MgAl_2O_4$	8.3–8.6
$LaScO_3$	30	ZrO_2	22	$ZrSiO_4$	12–13	BeO	6.9–7.7
Y_2O_3–ZrO_2	29.7	La_2O_3	21	Al_2O_3	9–12	Ce_2O_3	7.0

of 2-step and more complicated methods [54–56, 82–93]. Since furnace and RTA annealing are carried out at > 700 °C the Ta_2O_5 is crystallised and grain boundaries lead to an increase in leakage [82]. With UVO and plasma annealing, leakage can be significantly reduced compared with other techniques with the films remaining amorphous because of low annealing temperatures (< 400 °C). Table 5 summarises the properties of the Ta_2O_5 films deposited and annealed by different methods. After annealing, the leakage current significantly reduced to the range 10^{-6}–10^{-8} A/cm^2 from around 10^{-3} A/cm^2 in the as-deposited films. A variety of chemical and physical deposition techniques have been used to deposit Ta_2O_5 films [54, 55, 75, 83–89, 94–99]. Each technique has its merit and drawbacks. However, photo-induced processing has in particular received much attention since it operates at low temperatures, which minimises problems such as atom diffusion, dopant redistribution, and defect generation caused by higher temperatures, and the processed surface is not subjected to the damaging ionic bombardment which can occur in plasma-assisted systems.

To date most photo-CVD has been performed with lasers, which, although offering high photon fluences, are very expensive and commercially available systems provide only small area beams (typically only several cm^2). On the other hand, visible and UV radiation is available from high-current arc discharges in Xe and Hg/rare-gas mixtures, emitting broad spectra ranging from 200 nm to several microns. Because many materials absorb wavelengths shorter than about 250 nm, very efficient UV or VUV sources are important for stimulating and initiating chemical processes. Therefore, there is a demand for high power, low cost and selective optical sources, with which larger area samples can be efficiently processed.

Table 5. Properties of Ta_2O_5 deposited and annealed by different methods (J: leakage current density).

Method and annealing conditions	Capacitor structure	*k*	*J* (A/cm^2) at 1 MV/cm	Ref.
Sputtering annealed at 850 °C	Al/Ta_2O_5/Pt Al/Ta_2O_5/p-Si	a) 24 b) 45	a) 10^{-4} b) 10^{-7}	[83]
CVD at 450 °C and RTA annealed at 800 °C in O_2, N_2O	Al/Ta_2O_5/n-Si TiN/Ta_2O_5/n-Si		a) 10^{-3} b) 10^{-8}	[84]
Thermal oxidation and O_2 annealed at 800 °C	Al/Ta_2O_5/p-Si	16–25	a) > 10^{-4} b) 10^{-8}	[85]
CVD at 400–470 °C and O_2 annealed at 700–900 °C	Al/Ta_2O_5/p-Si	19	a) > 10^{-3} b) 10^{-8}	[86–87]
Plasma-CVD at 200–600 °C and N_2 annealed at 700 °C	Al/Ta_2O_5/p-Si	a) 20.3 b) 19.0	a) >10^{-2} b) 10^{-6}	[88]
CVD at 400 °C and plasma annealed at 400 °C	TiN/Ta_2O_5/n-Si		a) 10^{-3} b) 10^{-8}	[82]
Photo-CVD at 250–400 °C and UV annealed at 400 °C	Al/Ta_2O_5/n-Si	a) 24 b) 20	a) 10^{-3}–10^{-7} b) 10^{-8}	[54, 77]

(a): as-deposited films; and (b): annealed films.

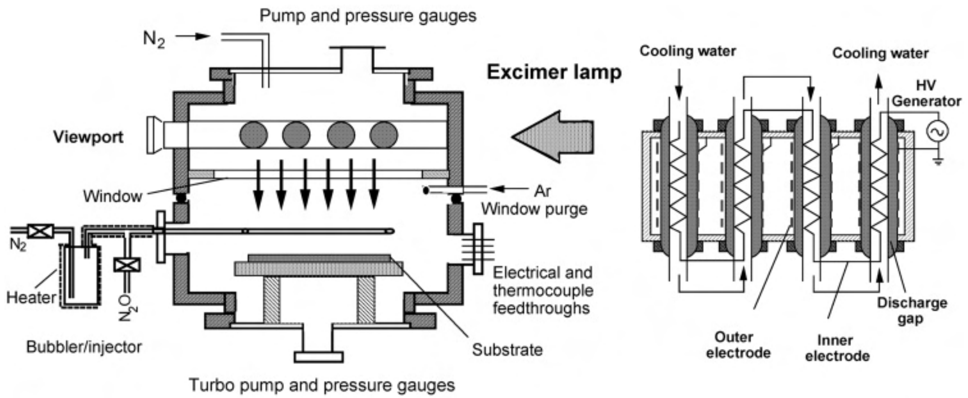

Figure 6. Schematic diagram of photo-CVD system incorporating of an array of excimer UV lamps.

Figure 6 schemes a large area excimer lamp system used in our studies. The complete system comprised a set of two stainless steel chambers (lamp and reactor chambers) separated by a MgF_2 window transparent to the VUV radiation. The lamp chamber consisted of an array of parallel cylindrical lamp tubes (details shown on the right of Figure 6). Excimer UV radiation, from either pure Xe (Xe_2^*, $\lambda = 172$ nm) or a mixture of Kr and Cl (KrCl*, $\lambda = 222$ nm), was generated in the top chamber traversed a low pressure gas mixture within the bottom chamber, and impinged upon the sample with a output power of about 30 mW/cm^2 [56].

n-type (100) orientation c-Si (2–4 Ω·cm resistivity) wafers, cleaned using a standard RCA clean, were used. Substrate temperature was fixed between 100–400 °C and measured with a thermocouple attached to the heater stage. The N_2O oxidizing agent was introduced into the reactor chamber at a fixed flow rate of 20 sccm. The Ta metalorganic precursors, namely tantalum tetraethoxy dimethylaminoethoxide ($Ta(OEt)_4(DMAE)$) and tantalum ethoxide, were vaporised between 100–130 °C in a bubbler/injector and then transported into the reaction chamber by N_2 carrier gas. A full description of this reactor is published elsewhere [56, 100].

The processing chamber could be evacuated to a pressure of 10^{-6} mbar by a turbomolecular pump and filled with the appropriate processing gas mixture. Ultraviolet annealing could be performed at temperatures between 350–400 °C for a pressure of 1000 mbar in high purity (99.999%) O_2 using 172 nm lamps with output powers in the 10–200 mW/cm^2 range, as determined using actinometric techniques [101, 102]. The chemical, structural and optical properties of the films produced were determined by XPS, FTIR and UV spectrophotometry and ellipsometry. Their electrical properties were measured at a frequency of 1 MHz on $Al/Ta_2O_5/Si$ capacitor test structures of area 8×10^{-4} cm^2.

3.2.1. *Ta_2O_5 formed by photo-assisted sol-gel processing*

To form a sol-gel solution, tantalum ethoxide ($Ta(OC_2H_5)_5$) was dissolved in ethanol with a small quantity of water and hydrochloric acid in ethanol. In the sol-gel

process, the reaction involves two simultaneous chemical processes, hydrolysis and polymerisation. The alkoxide hydrolysis and polymerisation reactions occurred over hours, when the colloidal particles and condensing metal species linked together to form a three dimensional network, i.e., a slow polymerisation of the organic compounds took place, leading to gelation. From this sol-gel solution, films of 10–300 nm thickness were prepared on Si (100) substrates by spin-on and then irradiated for various times and temperatures, to form Ta_2O_5 [35].

Table 6 compares the electrical properties in the UV irradiated layers formed at different temperatures with films deposited at 350 °C and UV annealed at 400 °C. The fixed oxide charge density decreases with increasing temperature, from 4.0×10^{11} cm^{-2} at 150 °C to 1.0×10^{11} cm^{-2} at 400 °C, similar to those obtained in layers prepared by plasma-CVD [103], indicating a more ideal reaction between the O and Ta species at the higher temperatures. Subsequent low temperature (400 °C) UV annealing improves this to 8.8×10^{10} cm^{-2}. These values are comparable to those obtained for films annealed at high temperatures between 700 °C and 1000 °C [88, 104]. Breakdown fields were found to be in the range of 2.2–4 MV/cm, depending on processing conditions. The flat-band voltage VFB was negative, indicating the expected presence of positive fixed charges near the Ta_2O_5/Si interface. With increased temperature, the C-V curve shifted towards the positive voltage axis and V_{FB} decreased, indicating a reduction in positive surface charge. At a temperature of 150 °C, the V_{FB} was found to be –1.2 V. As the growth temperature increased to 250 °C and 400 °C the V_{FB} reduced to –0.4 V and –0.2 V, respectively. After UV annealing a further reduction to 0.1 V could be achieved. Clearly, very good electrical properties can be obtained for the Ta_2O_5 layers by this photo-assisted low temperature sol-gel technique.

Table 6. Comparison of the electrical properties of the as grown Ta_2O_5 films at different temperatures together with film deposited at 350 °C and UV annealed at 400 °C.

Temperature (°C)	Fixed charge density (cm^{-2})	Leakage current densityat 1 MV/cm (A/cm^2)	Breakdown field (MV/cm)	Flat-band voltage V_{FB} (V)
150	4.0×10^{11}	4.4×10^{-5}	2.2	–1.2
250	2.6×10^{11}	2.29×10^{-5}	3.0	–0.4
400	1.0×10^{11}	5.2×10^{-7}	3.4	–0.2
UV annealed at 400 °C	8.8×10^{11}	3.0×10^{-8}	4.0	–0.1

3.2.2. *Thin Ta_2O_5 film deposited by photo-CVD*

3.2.2.1. *Growth and characterization of Ta_2O_5 film*

In photo-induced CVD of Ta_2O_5 from tantalum ethoxide ($Ta(OC_2H_5)_5$) and N_2O, the primary photochemistry of the N_2O induced by the 172 nm radiation involves the following reaction:

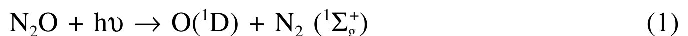

$$N_2O + h\upsilon \rightarrow O(^1D) + N_2\ (^1\Sigma_g^+) \qquad (1)$$

The active oxygen species O (^{1}D) formed subsequently react with the $Ta(OC_2H_5)_5$ causing its dissociation through a series of reactions leading to Ta_2O_5 deposition on the substrate surface. Figure 7 shows Arrhenius plots of the deposition rate of the photolytic (photo-CVD) and pyrolytic (thermal-CVD) deposited Ta_2O_5 films. The growth rate of the thermally deposited films strongly depends on the substrate temperature, is particularly slow and essentially negligible below 400 °C and has a high activation energy of 1.97 eV. For the photo-deposited films the growth rate only slightly increases with temperature and a much lower activation energy of 0.078 eV is obtained, indicating that different reaction mechanisms are operating. This reduced activation energy for the photo-CVD approach provides clear evidence for the reduced importance of substrate temperature and enables substrate temperatures as low as 100 °C to be used. Figure 8 shows a typical XPS spectrum of the films grown at 350 °C. As can be seen, peaks of Ta 4f, Ta 4d, Ta 4p3, Ta 4p1 and O 1s are readily detected whilst that for C 1s (around 285 eV) is very small. The XPS depth profile of a 95 nm thick layer grown at 350 °C is shown in the inset of Figure 8. The O and Ta concentrations distributed throughout the depth of the film are quite uniform. The atomic ratio of O/Ta of about 2.4, is very close to the stoichiometric ratio of 2.5 for Ta_2O_5 and much higher than the 2.0 ratio obtained for films produced by photo-CVD using a low pressure Hg lamp [105].

Figure 9 shows the UV spectral transmittance of Ta_2O_5 films as a function of substrate temperature. The average transmittance of about 90% in the visible region of the spectrum for films grown at temperatures between 250–400 °C is characteristic of very high quality material while higher transmittance of about 98% is observed for layers grown at 150 °C due to the thinner layers obtained at the lower deposited temperature. The onset of the absorption edge shifts to higher wavelengths as the deposition temperature increases, indicating an increase in the thickness.

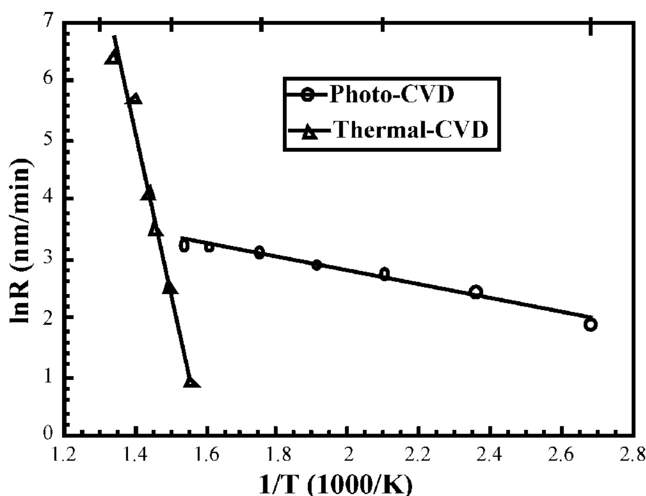

Figure 7. Arrhenius plot of the growth rate of Ta_2O_5 deposited by photo- and thermal-CVD on Si.

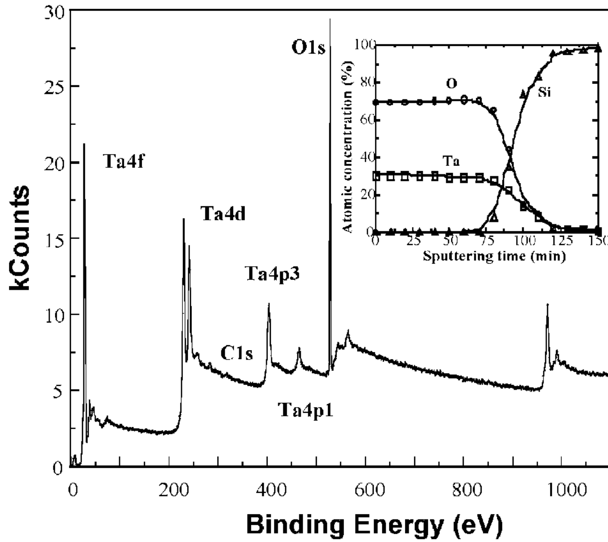

Figure 8. XPS spectrum of films deposited at 350 °C. Inset: XPS depth profile of 95 nm film.

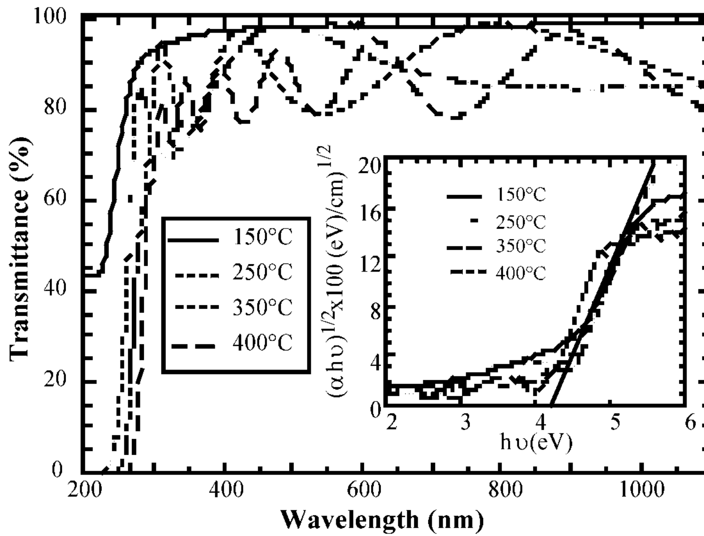

Figure 9. Transmittance spectra of photo-CVD Ta_2O_5 on quartz. Inset shows the plot of $(\alpha h\upsilon)^{1/2}$ vs. hυ.

This is in excellent agreement with the ellipsometry and FTIR measurements. The spectral dependence of the absorption coefficient (α) is given by [106]:

$$\alpha = \frac{B(h\upsilon - E_g)^r}{h\upsilon} \qquad (2)$$

where B is a constant, hυ is the photon energy, E_g is the optical band-gap energy and r can take values of 2, 3, 1/2, or 3/2, depending on the nature of the electronic transitions [106–107]. The change of $(\alpha h\upsilon)^{1/2}$ with hυ has been plotted for the films grown at different substrate temperatures and shown in the inset of Figure 9. An optical band-gap energy of 4.10 eV was obtained for the film grown at 150 °C and of 4.18 ± 0.04 eV for temperatures above 300 °C, which compares closely with films deposited by PLD and ion-beam sputtering [55, 108].

Figure 10 shows the I-V characteristics of the Al/Ta_2O_5/Si MOS capacitors fabricated using the as-deposited films grown at different temperatures (250, 350, 400 °C). The leakage current density clearly decreases as temperature increases, indicating a more ideal reaction between oxygen and tantalum species at the higher deposition temperatures. At a temperature of 400 °C, leakage current densities as low as 2.41×10^{-7} A/cm^2 at 1 MV/cm can be achieved.

The *I–V* plot of the MOS capacitors shows that after UV annealing, as with tantalum oxide formed by photo-assisted sol-gel processing, the leakage current is reduced dramatically (see Table 7). In fact, both leakage current and the fixed oxide charge density decrease with increased anneal time. After 1 hour annealing, the fixed oxide charge density changed from 2.9×10^{11} cm^{-2} for the as-deposited film, to 3.7×10^{10} cm^{-2}, while leakage current densities as low as 1.63×10^{-8} A/cm^2 are achieved – three orders of magnitude lower than for as-deposited layers (2.19×10^{-5} A/cm^2) and comparable to that only previously achieved for high temperatures (600–900 °C) annealed layers [78, 85, 88]. Several effects could cause the reduction and will be discussed in the section 2.1.2.2. In the *I-V* plots it was also observed that current density increased sharply at higher fields for the as-deposited and annealed films, as is seen with CVD deposited layers [103]. This is

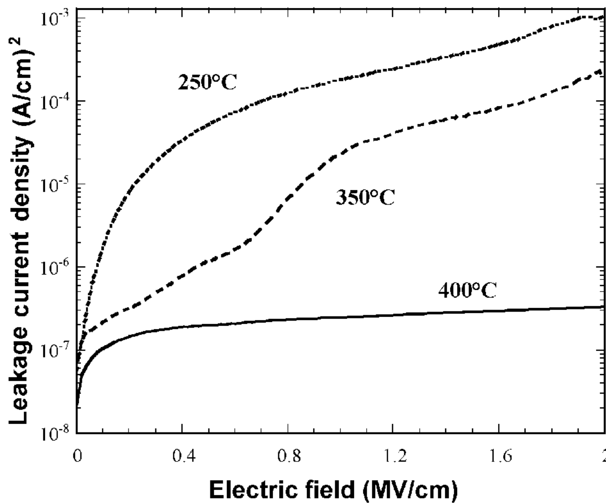

Figure 10. I–V plots of Al/Ta_2O_5/Si MOS capacitors using as-deposited Ta_2O_5 grown at 250, 350, 400 °C.

Table 7. Comparison of electrical properties of photo-CVD Ta_2O_5 films at various annealing times.

Annealing time (h)	Leakage current density at 1 MV/cm (A/cm^2)	V_{FB} (V)	Fixed charge density (cm^{-2})
0	2.19×10^{-5}	–1.8	2.9×10^{11}
0.5	2.55×10^{-6}	–0.8	2.3×10^{11}
1.0	1.63×10^{-8}	–0.1	3.7×10^{10}

due to Fowler-Nordheim (FN) tunnelling, characterised by [109]:

$$J = \frac{q^3E^2}{8\pi h\phi} \exp\left(-\frac{8\pi(2m_{eff}\phi^3)^{1/2}}{3qhE}\right), \tag{3}$$

where J is the current density (A/cm^2), E (V/cm) is the electric field, q is the electron charge, h is Planck's constant, ϕ (eV) is the barrier height at the Ta_2O_5-Si interface, and m_{eff} is the effective mass of electron in oxide. Equation (3) can be simplified as follows:

$$J = aE^2 \exp\left(-\frac{b}{E}\right), \tag{4}$$

where a and b are constants and are given, respectively:

$$a = \frac{q^3}{8\pi h\phi}, \quad b = \frac{8\pi(2m_{eff}\phi^3)^{1/2}}{3qh}$$

A straight line was obtained by a plot of $\ln(J/E^2)$ versus $(1/E)$ for the leakage current measured for the films, indicating that the current is dominated by FN tunnelling and is due to a process such as field emission of trapped electrons into the conduction band of tantalum oxide or by electrons tunnelling from the Fermi level of the metal into the insulator conduction band. A comparison of the leakage current densities in films obtained by different methods is shown in Table 8. For the as-deposited films the leakage current density of photo-CVD layers is much lower than for those grown by thermal and plasma-CVD, with values as low as 2.19×10^{-5} A/cm^2 at 1 MV/cm, two orders of magnitude lower than for as-deposited layers obtained by thermal and plasma-CVD [88, 110]. A subsequent annealing step can significantly reduce the leakage current densities to the order of 10^{-8} A/cm^2 for the films grown by either plasma-CVD or by photo-CVD techniques. However, this was performed at high temperatures (700–800 °C) whilst UV annealing can be carried out at temperatures as low as 400 °C. Figure 11 shows a *C-V* plot of Al/Ta_2O_5/Si capacitors at 1 MHz containing as-deposited and annealed layers. All flat-band voltages (V_{FB}) were negative indicating the presence of positive fixed charges near the Ta_2O_5/Si interface. With no annealing the V_{FB} was found to be –1.4 V. This reduced to –0.7 V and –0.2 V after annealing for 0.5 and 1 hour,

Table 8. Comparison of leakage current densities (J) at 1 MV/cm in different Ta_2O_5 films.

	CVD		Plasma-CVD		Our work	(Photo-CVD)
	As-deposited	Annealing	As-deposited	Annealing	As-deposited	Annealing
J (A/cm^2)	10^{-3}	10^{-8}	10^{-3}	10^{-6}	2.19×10^{-5}	1.63×10^{-8}
T	550 °C	800 °C	500 °C	700 °C	350 °C	400 °C

respectively, indicating a reduction in the *C-V* hysteresis effect and therefore in positive surface charge. The dielectric constant of the films was determined from *C-V* measurements using the usual expression:

$$C = \frac{\varepsilon_o k A}{d}, \tag{5}$$

where C is measured capacitance, ε_o is permittivity in vacuum, k and d are dielectric constant and thickness, and A is area. A value of $k = 24$ was found for the as-deposited film which decreased to 20 after 1 hour anneal due to SiO_2 formation as indicated by XPS and FTIR [54].

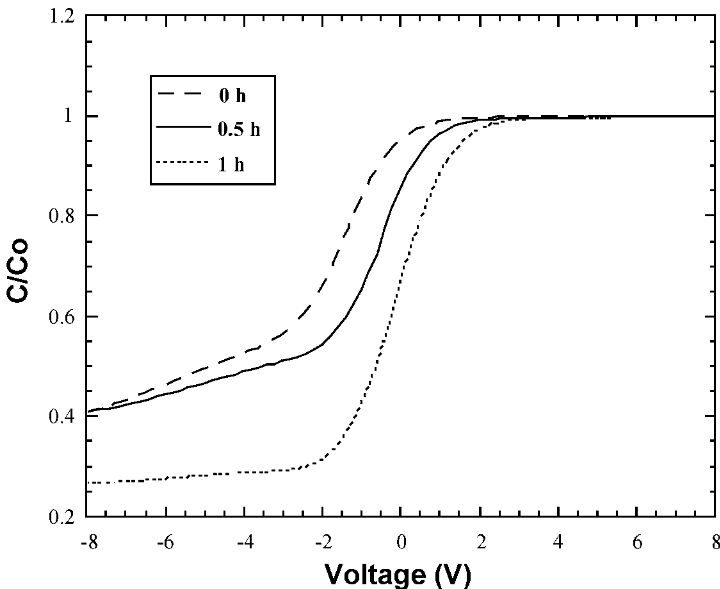

Figure 11. *C-V* characteristics of $Al/Ta_2O_5/Si$ capacitors for as-deposited and annealed films.

3.2.2.2. *Mechanism for reduction in the leakage current of Ta_2O_5 films by UV annealing*

To understand the mechanism for the reduction in leakage current in the Ta_2O_5 layers by UV annealing, the chemical and structure changes were investigated by FTIR. Figure 12 shows the evolution of the FTIR spectra from 400–4000 cm^{-1} for as-deposited and 172 nm annealed photo- CVD layers. A weak absorption band at 800–1000 cm^{-1}, attributed to the presence of suboxides [95], was seen for the as-deposited film. However, after UV annealing, this peak is significantly reduced. In the as-deposited films the H_2O and OH groups, which absorb at 3400 cm^{-1}, have been completely removed. This removal by UV also occurs in PLD films [55].

A peak at 1070 cm^{-1} due to Si-O bond stretching in SiO_2 was observed for films annealed for 1 hour [54], indicating the formation of SiO_2 during the annealing process [111]. Figure 13 shows the spectral transmittance of as-deposited film together with layers annealed in O_2 at pressures of 1 mbar and 1000 mbar. The maximum transmittance in the visible for the as-deposited layer is only 22%, indicating that its composition is a mixture of Ta, Ta suboxide, and tantalum oxide rather than pure oxide. After UV annealing at 1000 mbar and 1 mbar this increases to 95% and 64%, respectively. The annealed films become more transparent as the O_2 pressure is increased due to the greater availability of O atoms at the higher pressures. Under the 172 nm radiation (hυ = 7.2 eV), O_2 is readily dissociated, leading to the formation of active oxygen species, which are strong oxidising agents. These species (including O atoms and O_3) reach the surface and react with any present Ta, suboxides and oxygen vacancies as well as diffuse into the layer to create Ta_2O_5 and remove defects present in the layers. Clearly, the oxygen-rich

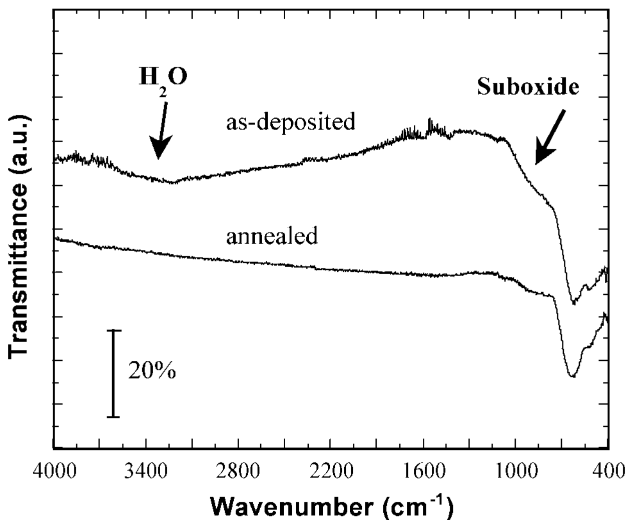

Figure 12. FTIR spectra for Ta_2O_5 films deposited at 350 °C and UV annealed at 400 °C.

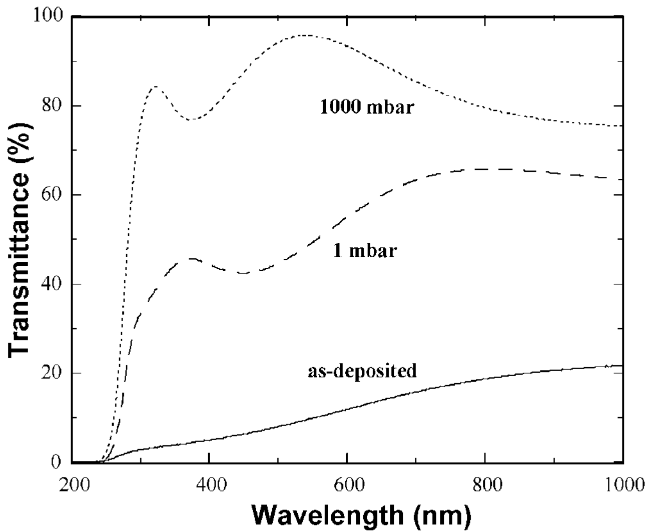

Figure 13. Spectral transmittance of as-deposited film and films annealed at different O_2 pressures.

environments enhance the annealing process, indicating that oxygen plays an important role in the improvement of the layer properties. Another feature of these spectra is that the fall in transmission around the absorption edge becomes sharper at higher annealing pressures, which is also due to the reduction of suboxides present. From the XPS, FTIR, and electrical measurement results, we propose a possible mechanism for the UV annealing effect, which is attributed to the active oxygen species produced by the UV irradiation as follows:

1) O_2 is dissociated under the 172 nm irradiation

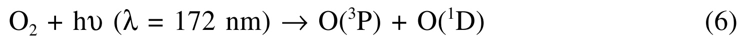

$$O_2 + h\upsilon\ (\lambda = 172\ \text{nm}) \rightarrow O(^3P) + O(^1D) \tag{6}$$

2) Ozone is subsequently formed from the released oxygen atoms by following reaction

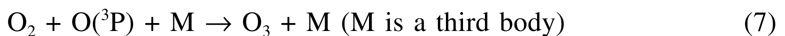

$$O_2 + O(^3P) + M \rightarrow O_3 + M\ (\text{M is a third body}) \tag{7}$$

3) The ozone is then decomposed by the UV light to produce excited state ^1D oxygen atoms.

$$O_3 + h\upsilon\ (\lambda = 172\ \text{nm}) \rightarrow O_2 + O(^1D) \tag{8}$$

The active oxygen species $O(^1D)$ formed by the photolysis of ozone are adsorbed on to and diffuse into the Ta_2O_5 surface, accept electrons, and occupy any vacancies present as shown in Figure 14. The decrease in the number of vacancies in the films leads to the observed reduction of leakage current. On the other hand, the active oxygen species can react with the Si either at the Ta_2O_5/Si interface, or with any Si species that diffuse from the substrate to the Ta_2O_5 surface, leading to

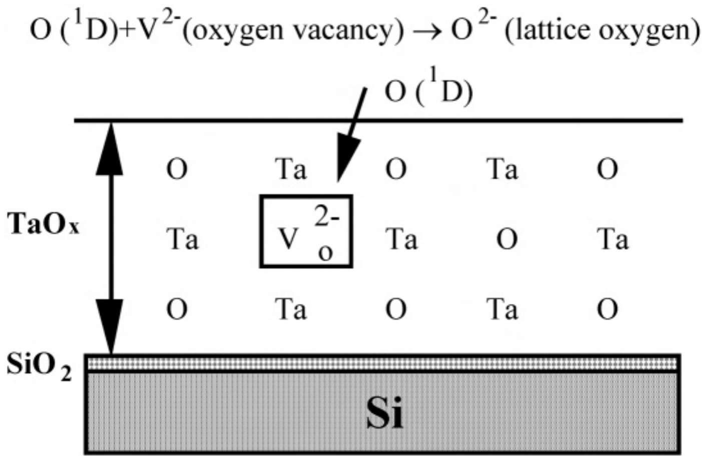

Figure 14. Model of the mechanism for reduction of leakage current of Ta_2O_5 films by UV annealing.

the formation SiO_2 at the interface and the surface of the Ta_2O_5 films. Thus, the most likely contributions to the reduction of leakage current in the tantalum oxide films provided by the UV annealing step are summarised as follows:

(1) The active oxygen species react with and reduce or remove any suboxides present, leading to improved stoichiometry;
(2) The active oxygen species decrease the density of defects and oxygen vacancies;
(3) A thin SiO_2 layer is formed at the Ta_2O_5/Si interface and on the Ta_2O_5 surface by the reaction between the active oxygen and Si, leading to improved interfacial quality [18];
(4) Removal of any impurities present in the as-deposited films and densification of layers;
(5) Improvement of surface morphology and reduction of the as-deposited particle-size.

It can be seen that all of the above processes require the presence of active oxygen species, which therefore play a very important role in the improvement of the layer properties. All of these processes could result in improved layer quality, especially for the reduction of leakage current density although it is not clear at present which of these dominates.

3.2.3. *Other high dielectric constant materials*

Photo-assisted growth of a range of high dielectric constant layers has been demonstrated using excimer UV sources [112–113]. Single- and multi- layer TiO_2 films have been prepared from isopropoxide ($Ti(OC_3H_7)_4$) at low temperatures (80–300 °C) by photo-induced sol-gel processing using a 172 nm lamp [112]. Refractive indices as high as 2.4 were obtained, which compare favourably with

the bulk value of 2.58. The films exhibited good optical properties with 85%–90% transmittance in the visible. PZT layers have also been grown by 172 nm decomposition of a PZT metal-organic sol-gel polymer [113]. Very low leakage current densities (10^{-7} A/cm^2) have been achieved, which compare well with high temperature grown layers. Very recently, nanocrystalline TiO_2 has also been prepared at temperatures as low as 210 °C [114, 115]. Figure 15 shows an AFM image and line measurement of a TiO_2 film deposited on quartz at 350 °C, which reveal that cubic structures have formed with uniform dimensions of about 0.4 μm. AFM images of films deposited on Si at temperatures > 250 °C also revealed that a uniform particle structure with average edge sizes of about 20–30 nm.

Figure 16 shows a typical x-ray diffraction pattern for the TiO_2 films deposited

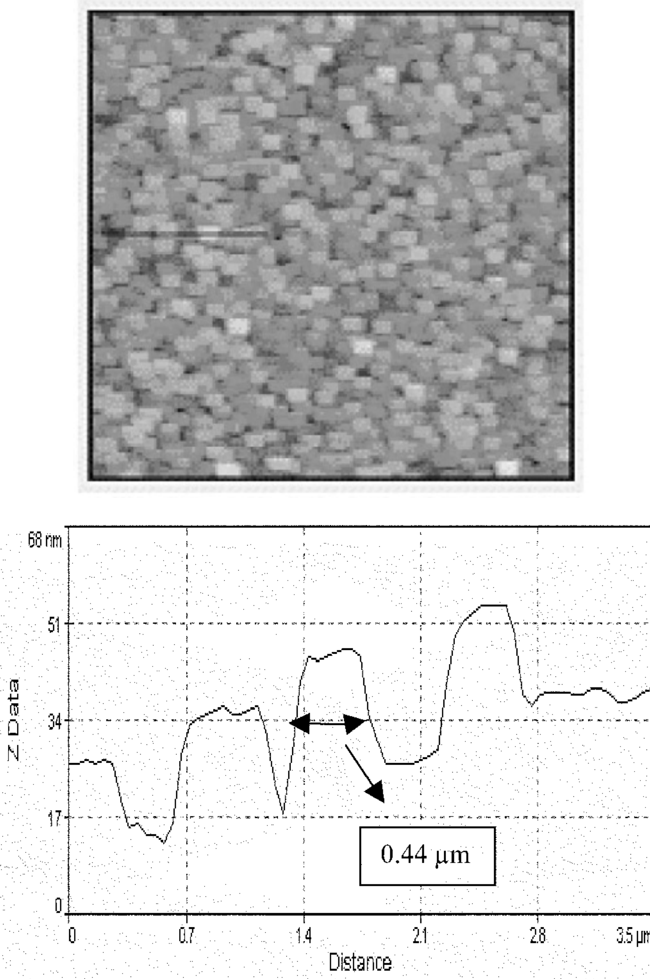

Figure 15. AFM image and line measurement of TiO_2 film deposited on quartz at 350 °C.

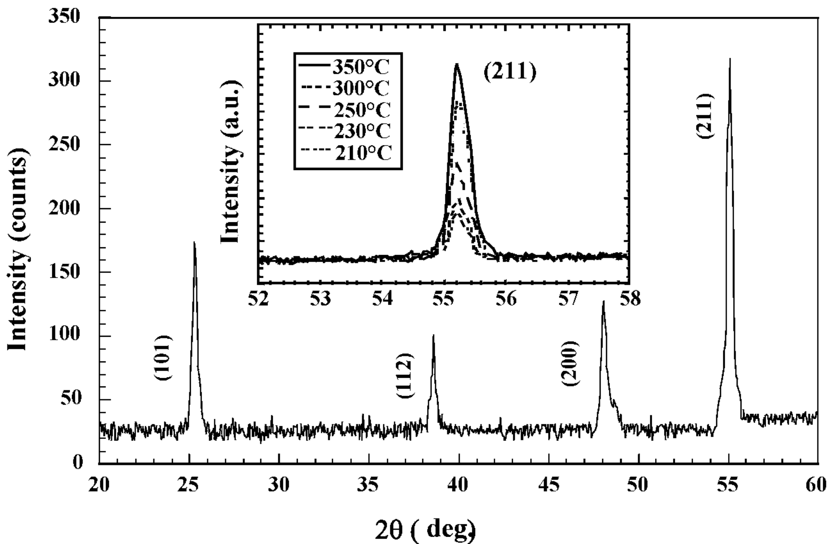

Figure 16. XRD pattern (λ = 0.154054 nm) of TiO_2 deposited at a temperature of 350 °C by photo-CVD. The inset shows the 2θ scan around the (211) peak at various temperatures.

on a Si (100) substrate at 350 °C. The XRD peaks at 25.35°, 38.63°, 48.12°, 55.08° correspond to anatase (101), (112), (200), (211) crystal planes, respectively [116]. No rutile phases were observed in these layers. The XRD pattern also shows that anatase (211) is the preferential growth orientation and that its intensity increases with deposition temperature (see inset of Figure 16), indicating that the TiO_2 becomes more crystalline. It was also found that the initiation of the crystalline anatase phase occurred at a temperature of 210 °C. Table 9 summarizes the equivalent SiO_2 thickness, leakage current density, flat-band shift and fixed oxide charge density of different thicknesses of deposited TiO_2. Clearly thicker layers possess the best electrical properties. For 70 nm films (T_{eq} = 6.8 nm) leakage current densities as low as 8×10^{-6} A/cm^2 were achieved, which are lower than for thermal-CVD material. It was found that low temperature UV annealing could reduce the leakage current density from 10^{-6} A/cm^2 as-deposited films to 10^{-8} A/cm^2. Some possible contributors to the reduction of leakage current have been discussed already in section

Table 9. Equivalent SiO_2 thickness (T_{eq}), and electrical properties of different TiO_2 thicknesses.

Thickness (nm)	T_{eq} (nm) (equivalent to SiO_2 thickness)	Leakage current density (A/cm^2)	Flat-band shift (V)	Fixed oxide charge density (Q_f/q, cm^{-2})
10	1.0	7.0×10^{-4}	–1.6	8.7×10^{11}
20	1.95	7.8×10^{-5}	–1.2	8.0×10^{11}
30	2.9	1.2×10^{-5}	–0.5	5.6×10^{11}
70	6.8	8.0×10^{-6}	–0.4	5.1×10^{11}

3.2.2.1. Moreover, the annealed films exhibited smooth surfaces (Figure 17b) compared with those of the as-deposited layers (Figure 17a) and the clusters of small particles on the as-deposited films disappeared after UV annealing. Their presence could also initiate large leakage currents. Ti-doped Ta_2O_5 and HfO_2 and other thermodynamically stable oxides such as ZrO_2 have been grown by photo-CVD and UV curing of sol gels with excimer lamps [167, 168]. The as-deposited films exhibited an amorphous structure when the Ti/(Ti+Hf) atomic ratio was < 25%, while the crystalline TiO_2 anatase phase was obtained when it was > 25%. The uniformity of the lamp grown films was good, with thickness variations less than two percent across 4-inch wafer.

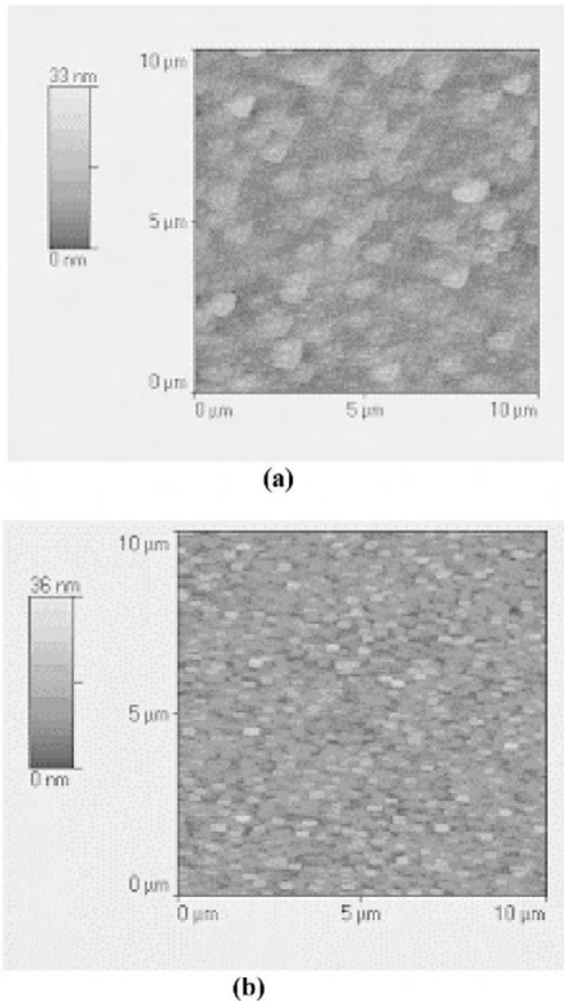

Figure 17. AFM images of TiO_2 films grown on Si 350 °C (a) and annealed at 350 °C by UV lamp (b).

3.3. *Photo-induced deposition of dielectric materials*

Photo-assisted processes have attracted strong interest in recent years by enabling the production of many types of high quality damage-free dielectric and semiconducting film compounds at low temperature. The interest stems from the ability of optical radiation to induce specific chemical reactions in the gas phase or at a surface. The selective, optical production of atoms and/or molecular radical in the gas near a surface considerably reduces any dependence of the process on the substrate temperature and allows deposition to occur at very much lower temperatures than employed in conventional CVD reactors. A variety of materials can be deposited by photo-CVD using optical radiation from lasers or lamps. However, the application of these excimer lamps, with their capability of emitting tuneable wavelengths in the vacuum ultraviolet (VUV) (< 200 nm) to photo-CVD is entirely new. Since most precursor gas molecules exhibit appreciable absorption in the VUV region, a wide range of compounds can be deposited. Current work on the deposition of dielectric and amorphous semiconductors using excimer lamps is listed in Table 10. We have demonstrated the first application of excimer lamps to the deposition of SiO_2, Si_3N_4, SiO_xN_y layers by irradiating silane, nitrous oxide and ammonia mixtures [33, 63, 66]. High deposition rates (500 Å/min) have been achieved by irradiating silane and oxygen mixtures for substrate temperatures as low as 300 °C [32]. A full description of the reactor used has been reported in details elsewhere [33, 123]. P-type silicon (100) substrates up to one inch in diameter were used in these studies. Silane is transparent to 172 nm radiation, and since only the oxidising and reducing agents exhibit a significant absorption cross-section, σ these are readily photochemically dissociated [124]. The following primary reactions are initiated:

$$N_2O + h\upsilon \rightarrow N_2 + \cdot O \; (\sigma = 2 \text{ atm}^{-1} \text{ cm}^{-1}) \quad (9)$$

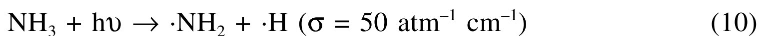

$$NH_3 + h\upsilon \rightarrow \cdot NH_2 + \cdot H \; (\sigma = 50 \text{ atm}^{-1} \text{ cm}^{-1}) \quad (10)$$

$$O_2 + h\upsilon \rightarrow \cdot O + \cdot O \; (\sigma = 20 \text{ atm}^{-1} \text{ cm}^{-1}) \quad (11)$$

Table 10. Deposition dielectric and amorphous semiconductor by photo-induced CVD.

Material	Temperature (°C)	Precursor	Light source (λ)	Reference
a-Si:H	160–250	Si_2H_6, B_2H_6	Kr_2*, Xe_2* (146, 172 nm)	[120]
SiO_2	200–300	SiH_4, N_2O	Xe_2* (172 nm)	[63]
Si_3N_4	200–300	SiH_4, NH_3	Xe_2* (172 nm)	[33]
SiO_xN_y	300	SiH_4, N_2O, NH_3	Xe_2* (172 nm)	[66]
a-SiC:H	150–250	Si_2H_6, fomblin oil	Ar_2*, Kr_2*, Xe_2* (126, 146, 172 nm)	[121]
SiO_2	100–300	SiH_4, O_2	Xe_2* (172 nm)	[32]
a-Si:H	200–400	SiH_4	Ar_2* (126 nm)	[122]

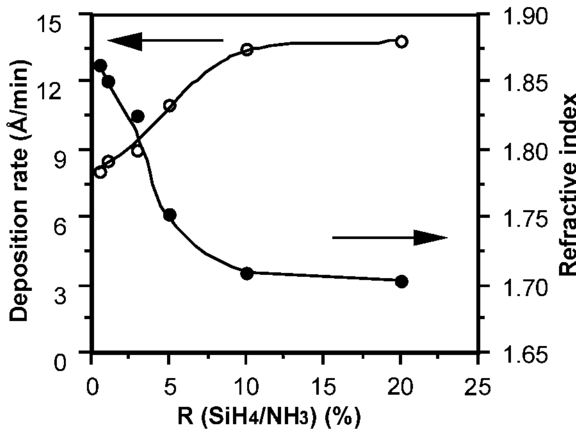

Figure 18. Deposition rate and refractive index of Si_3N_4films vs. SiH_4/NH_3 ratio.

The primary reaction products, such as ·O, ·H and $\cdot NH_2$ radicals, can rapidly react with silane causing its dissociation through a series of reactions, leading to material deposition on the substrate surface. The films obtained exhibited refractive indices and infrared vibration modes similar to those for thermally deposited films. Figure 18 shows the growth rate and refractive indices of Si_3N_4 thin film obtained for various precursor mixtures (SiH_4/NH_3) at a temperature of 300 °C using excimer lamp (172 nm, 10 mW/cm^2, 10 mbar).

The refractive index is strongly dependent upon the silane concentration within the ammonia. Values as high as 1.85 were obtained for low SiH_4/NH_3 ratios. Enhanced deposition rates by using higher photo fluxes from more powerful lamp seems possible. Figure 19 shows the influence of silane to oxygen ratio (R) on deposition rate and refractive index for the SiO_2 films. Tiny differences in R strongly

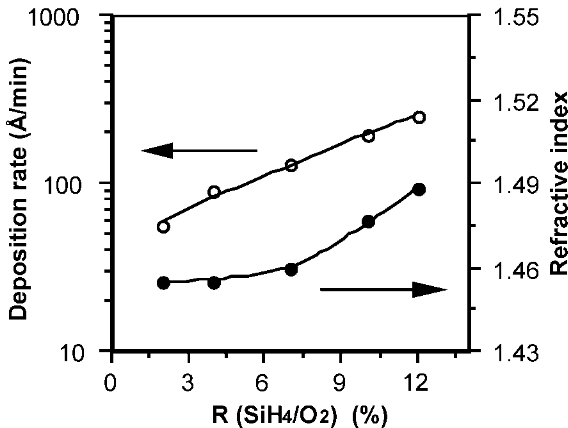

Figure 19. Deposition rate and refractive index of SiO_2 deposited for various precursor ratios R.

alter the growth rate while the refractive index increases with R. The amount of hydrogen incorporated is also influence by the precursor mixture [32]. Very high deposition rates of 100–500 Å/min are obtained for temperatures as low as 300 °C. Optimised conditions at 200 °C produced SiO_2 layers with n = 1.46, etch rates in diluted (1:25) buffered $HF:H_2O$ of 20 Å/min, and electrical breakdown fields of 5–8 MV/cm. These properties are close to those for thermally grown SiO_2 obtained at high temperature [125].

Three oxide-nitride-oxide layers with thicknesses around 100 Å have been also deposited and characterised using SIMS analysis (Figure 20). Four distinct zones can be seen and each layer is readily recognisable. From the bulk of the Si substrate (right), a first oxide layer of thickness about 150 Å is visible. A nitrogen rich layer, of 100 Å in thickness is found next and finally the surface silicon oxide layer appears on the left of the depth profile.

By using $SiH_4/NH_3/N_2O$ as precursors the deposition of SiON can be achieved. Fine-tuning of the refractive index can be obtained by varying the composition of this mixture. A smooth progression from silicon nitride to silicon oxide can be achieved with this method, and therefore good control of the SiO_xN_y stoichiometry during deposition [64].

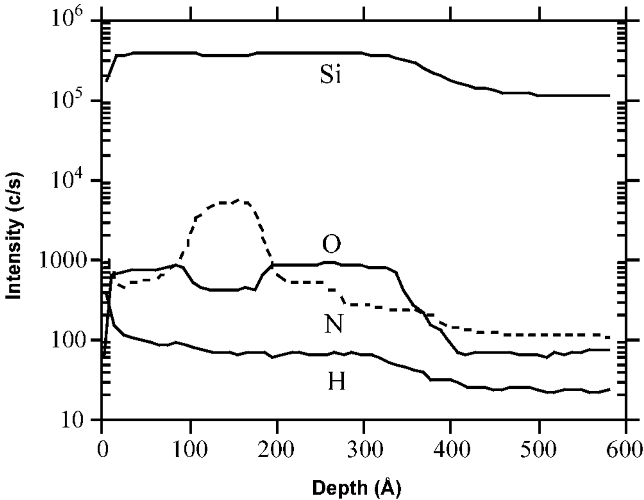

Figure 20. SIMS profile of an oxide-nitride-oxide multilayered structure on silicon.

3.4. *Low dielectric constant materials: polyimide and porous silica*

As feature sizes in integrated circuits reduce to sub-micron dimensions, crosstalk noise, power dissipation and propagation delay at the metal interconnects become significant due to RC coupling. This RC time delay can be reduced either with the incorporation of low permittivity dielectric materials and/or high conductivity metals. Current low-k commercialisation emphasises spin-on glasses (SOGs) and

fluorinated SiO_2, and a number of polymers are under development with k in the range of 2–3. Of these, polymeric films are a promising group that may eventually replace the widely used SiO_2 as an interlayer dielectric to shorten the RC time delays, reduce "cross-talk" between metal lines and decrease power consumption at high signal frequencies [127]. Polyimides are particularly attractive not only because of their low k values but also their ease of application and patterning and high thermal stability [128]. Photo induced deposition of low dielectric constant organic polymers for interlayer dielectrics has highlighted a significant role of photo effects on the curing of polyamic acid films [129]. Compared with conventional furnace processing, the photo-induced curing of the polyimide provided both reduced processing time and temperature. In particular, I-V measurements showed that the leakage current density of the irradiated polymer was over an order of magnitude smaller than for the layers obtained by thermal processing [129]. Figure 21 shows FTIR spectra in the 600–2000 cm^{-1} range for films after an initial pre-bake and only a 150 °C thermal cure for 20 min, and also under otherwise identical conditions, but with additional UV irradiation. Figure 21a shows the characteristic bands of the carboxyl (–COOH) absorption at 1723 cm^{-1}, amide (–CONH–) groups at 1659 and 1546 cm^{-1}, and the amide stretching mode in polyamic acid at 1410 cm^{-1}. After UV curing (Figure 21c) all these bands completely disappear. Simultaneously, a carbonyl group doublet corresponding to an imide moiety appears at 1778 and 1726 cm^{-1} together with the imide C–N absorption at 1379 cm^{-1}. The small absorption at 728 cm^{-1} has been attributed to deformation of the imide ring or the imide carbonyl groups [130]. The bands corresponding to polyimide at 1778, 1726 and

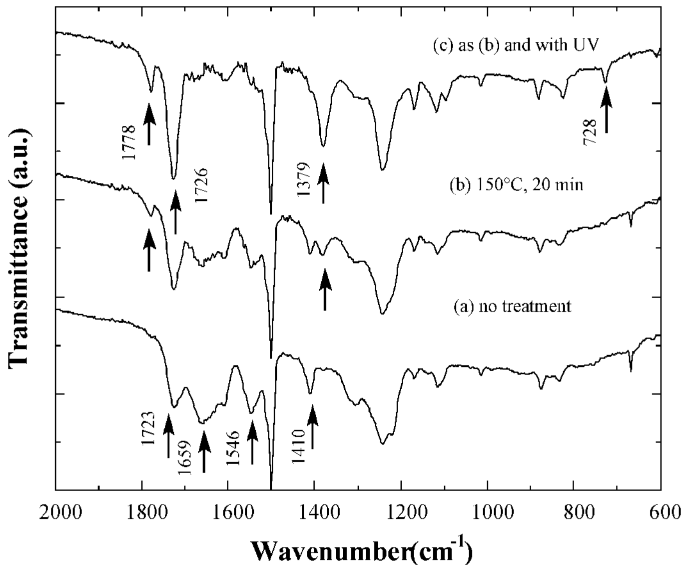

Figure 21. FTIR spectra of polyamic acid films after pre-bake and thermal and UV treatments: (a) initial pre-bake only; (b) thermal cure at 150 °C, 20 min; (c) 150 °C plus irradiation for 20 min by 172 nm lamp.

1379 cm^{-1} for the thermally cured polyamic acid (Figure 21b) are significantly smaller than those obtained by UV curing. Also, the bands related to polyamic acid at 1659, 1546, 1410 cm^{-1} decreased but did not completely disappear. These results indicate that the polyamic acid film is completely transformed to polyimide by the UV curing step at 150 °C, whilst the thermally cured sample is only partly transformed.

The photochemical mechanism initiated by the UV curing of the polyamic acid may involve a two-step process. The absorption of photons in the polyamic acid would firstly cause a photoreaction in the weak bonds in the carboxyl group of the molecule, resulting in the formation of hydroxyl (·OH) and carbonyl (·CO–) radicals. These radicals then react with the amide groups in the polyamic acid precursor by losing H2O to form the polyimide. Figure 22 shows the degree of imidization at different temperatures for both the UV curing and purely thermal curing steps. The degree of imidization was calculated by comparing the 1375 cm^{-1} imide band and the 1500 cm^{-1} aromatic band intensities, which are known to give precise internally consistent measurements [130]. At lower curing temperatures (i.e. < 150 °C) the imidization characteristics of the two curing methods are markedly different. For UV curing, the films start to imidize very significantly, whilst for thermal curing it is very slow. The degree of imidization is 85% for UV curing at 150 °C, and < 20% for the thermal process.

More recent work on low temperature photo-induced deposition of low dielectric porous silica films from TEOS sol-gel solutions using an excimer lamp shows that the dielectric constant of the films strongly depends on irradiation temperature [131]. At room temperature dielectric constant values as low as 1.7 can be

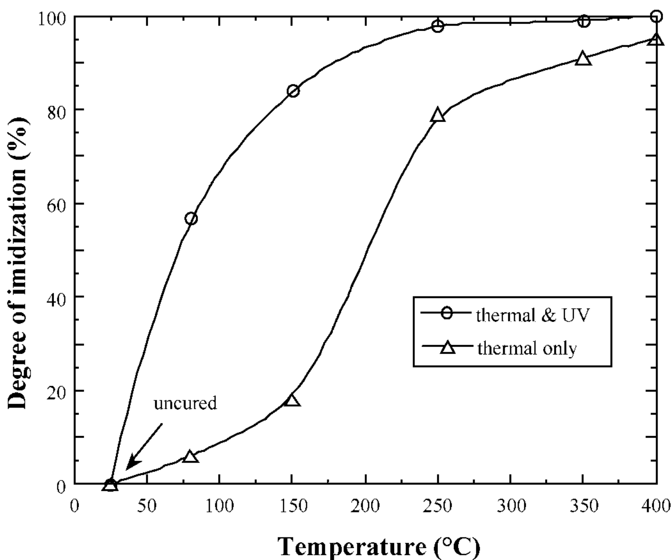

Figure 22. Imidization of polyamic acid film at different curing temperature with and without irradiation.

achieved in the films. The tuneable dielectric constants between 1.7 and 3.6 can readily be obtained by this technique and have high potential applicability as interlayer dielectric layers for advanced ultra-large-scale-integrated devices.

3.5. *UV oxidation of Si, Ge, and SiGe*

The continuous reduction of linear dimensions in microelectronic devices has also imposed a severe limitation on the thermal budgets associated with the various process steps employed in fabrication. Particular attention has been paid to various low-temperature alternatives to traditional thermal oxidation of Si, typically performed at about 1000 °C. The use of excimer lamps can considerably enhance the oxidation rate at low temperatures.

Figure 23 shows the oxide thickness of the films grown at 5 mbar as a function of exposure time compared with previously published data [132] for layers grown using a low pressure mercury lamp, visible radiation, ozone and conventional furnace oxidation. As can be seen, the oxidation rate using the excimer lamp is by far the highest. It is also 90 times greater than thermal oxidation at 612 °C [132]. The thermal oxidation is essentially negligible at 450 °C, even after oxidation times extending to 5 hours while the excimer lamp induced oxidation at 250 °C is more than three times greater than when using a low pressure Hg lamp at 350 °C.

The bond energy of O_2 is approximately 5.1 eV. Therefore, with 172 nm radiation (photon energy 7.2 eV), O_2 can be readily dissociated. The oxygen atoms released can subsequently form ozone which can then be decomposed by further absorption of the VUV light, producing excited state ^{1}D oxygen atoms. The active oxygen species thus formed subsequently react with Si and form SiO_2. It is reasonable to assume that the oxidation process involves: (1) transport of the oxygen

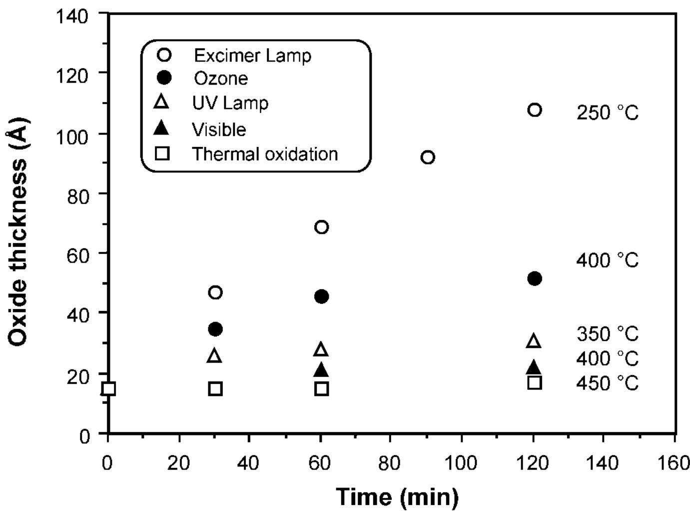

Figure 23. Oxide thickness grown as a function of time for different photon, particle and thermal sources.

species to the oxide surface, (2) diffusion through the oxide, and (3) reaction with Si at the Si-SiO_2 interface, and that the overall reaction rate will be governed by the slowest process. During the initial stages of oxidation, the reaction at the silicon-oxide interface will most likely be the controlling factor, whereas in the later stages when a significant film thickness has formed, the diffusion of reactant through the oxide may become important, as in conventional Si oxidation.

Simple MOS capacitors have been fabricated using 11 nm thick layers with an evaporated Al top contact of area 3.2×10^{-3} cm^2. Table 11 shows the fixed oxide charge density of the as-grown films to be 2.4×10^{11} cm^{-2}. The electrical properties of these films are clearly not comparable with the best high temperature thermal oxide films grown under strict cleanroom conditions. However, even the rapid thermal oxides grown at 950 °C contain fixed oxide charge density in the high 10^{11} cm^{-2} range [133]. It has been recently found that UV-O_3 annealing of Ta_2O_5 films improves their electrical properties significantly [134]. This technique has been applied to our films, which were subsequently annealed in 1 atmosphere of O_2 radiated by a 172 nm excimer lamp at 400 °C. A comparison of the electrical properties of the films after different annealing times is shown in Table 11. After 2 h UV annealing, the fixed oxide charge density decreased from 2.4×10^{11} cm^{-2} for the as-grown material, to 4.5×10^{10} cm^{-2}, which is comparable to that for thermally grown oxide on Si at 1030 °C [133]. It was also found that the Si-O-Si stretching peak shifted to higher wavenumbers after this annealing step (Table 11), indicating a possible increase in film density [135–136]. Very recently, this work has been extended to study to 126 nm irradiation [119, 166], and rates as high as 8 nm/min have been achieved, with leakage current densities down to 5×10^{-8} A/cm^2 for 17 nm thick layers at a field of 1 MV/cm.

The direct photo-oxidation of Ge at temperatures < 400 °C using a 172 nm excimer lamp has also been achieved. An oxidation rate of 0.1 nm/min was obtained which is significantly faster than conventional thermal oxidation. According to FTIR and XPS analysis the oxide layers grown have a composition identical to that of thermally grown GeO_2 [137].

VUV oxidation of SiGe layers have similarly shown rapid oxidation in comparison to the thermal reaction, as well as photon enhanced interdiffusion of Si and Ge atoms, and low temperature formation of Ge nanoclusters [126, 164]. Photoluminescence measurements show that these nanoparticles increase in size as a result of extended UV annealing in O_2 [165].

Table 11. Comparison of electrical properties and position of the Si-O-Si stretching absorption band maximum of UV grown oxides after different annealing times (172 nm lamp, 1000 mbar O_2, 400 °C).

Annealing time (h)	Fixed oxide charge density (cm^{-2})	Leakage current density at 1.0 V (A/cm^2)	Si-O-Si stretching absorption band maximum (cm^{-1})
0	2.4×10^{11}	1.2×10^{-6}	1069
1	7.5×10^{10}	7.0×10^{-7}	1073
2	4.5×10^{10}	9.0×10^{-8}	1075

3.6. *UV-induced metallization*

High specification metallisation of electrically insulating materials is increasingly required in ultra-large scale integrated (ULSI) devices, sensor, multifunctional micro systems, hybrid electronics, optics and display technologies. However, several problems remain with existing metallization techniques that limit their applicability to certain important industrial requirements. Silk-screen printing techniques have a current line and space minimum size limit of 100 μm. Other conventional insulator metallization technologies such as RF sputtering, evaporation or chemical vapour deposition do not lend themselves to low-cost high volume processing due to their requirements for high vacuum, and suffer from problems in metallising non-planar substrates, and they limited by lack of metalorganic or inorganic precursors with sufficiently high pressures, as well as unwanted side reactions, which cause contamination of thin film deposits.

Recently, several reports of metal deposition by laser-induced decomposition of spin-on material of metallo-organic or organometallic compounds have appeared [138, 139]. MOD is a non-vacuum, liquid based, spin-on, spray, or dip-coating method of layer deposition. A metallo-organic precursor, dissolved in suitable solution, is dispensed on to a substrate. It is then decomposed photochemically using a laser in air, O_2, N_2, or other suitable atmosphere to convert it to its constituent metal elements, oxides or other compounds.

Selection of precursors with sufficient optical absorbance at the appropriate wavelength for photo-induced MOD is required in order to initiate the necessary photo-reactions. Various radiation sources such as the Ar ion, excimer, and Nd:YAG lasers, UV lamps and synchrotrons have been used for this process.

Table 12 is a list of different metals and metal oxides that have been deposited by photo-MOD on various substrates over the past few years. Film growth by laser (L-MOD) offers several advantages over other deposition processes. It occurs at ambient temperature and pressure without gas transport or distribution systems, and does not need complicated vacuum equipment. The precursor materials can be synthesized to incorporate a wide variety of metals. However, lasers are very expensive, non-uniform and can only pattern limited areas. Therefore, the use of large-area sources with high photo fluxes for industrial large-area processing is very attractive. Excimer UV lamp-induced decomposition of palladium acetate films has been demonstrated over the past few years [15, 36, 49]. The Pd thin film, even when only a few nanometres thick, acts as an activator for subsequent electroless metal plating process in which a μm thick Cu, Ni or Au layer grows on top of the Pd. Such electroless plating thicknesses provide a level of electrical conductivity that is sufficient for applications involving microcircuits and printed circuit boards. The decomposition mechanism of palladium acetate and the properties of deposited palladium have been studied [36, 37, 48, 49]. Electroless plating of metal films has the potential for low-cost, high-volume, high-selective and low thermal budget metallization processing suitable for industrial applications. This technology could possibly open a new route for rapid, low cost, high-selective, large area metallization processing.

Table12. Photo-induced metallo-organic decomposition (photo-MOD)

Metal or compound	Substrates	Metallo-organic film	Light source (λ)	Reference
Au	Al_2O_3, glass-epoxy, Si	Dimethyl (1,3-diphenyl-1,3 propanedionato)gold, nitrocellulose/ammonium tetrchloroaurate	Hg/Xe deep UV lamp (254/365 nm) Low pressure Hg lamp (185/254 nm)	[140, 141]
Cu	Glass, polymer (ULTEM™), polymer, Si, quartz glass, polyimide, Si, Al_2O_3	$Cu(CH_3CN)_4BF_4$-doped poly(N-vinylpyrolidone), copper formate, copper acetate	Argon laser (532 nm) Argon laser (515 nm), KrF* laser (248 nm), Xe_2* lamp (172 nm), Nd:YAG (1.06 μm)	[36, 142–145]
Pd	Quartz, Al_2O_3, quartz, AlN, polyimide	Palladium acetate	Argon laser (351, 515 nm), ArF*, KrF*, XeCl*, XeF* (193, 248, 308, 351 nm), Ar_2*, Kr_2*, Xe_2* lamps (126, 146, 172 nm), Xe_2*, KrCl*, XeCl* lamps (172, 222, 308 nm), Synchrotron (40–300 nm)	[36–38, 49, 139, 146, 148–152]
Pt	Quartz	Metalorganic Pt compound (Engelhard Industries)	Argon laser (351, 515 nm)	[153–154]
Al_2O_3	Quartz	Aluminium di(i-propoxide) acetoacetic ester chelate	KrCl* lamp (222 nm)	[122]
$LiNbO_3$	Si and sapphire	Lithium neodecanoate, Nb triethoxy-di-neodecanoate	Tungsten lamp (200–1000 nm)	[155]

It is well known that the activity of catalysts for electroless metal deposition depends on the thickness, distribution and purity of the metal nuclei on the non-catalytical surface. The quality of the coating, e.g. the adhesion of the metal layers on the substrate depends decisively on the electrochemical properties of the Pd activator. Therefore, different excimer lamp parameters (wavelength, UV intensity, exposure time), the thickness, morphology and purity of the deposited Pd layers for optimised coating need to be determined [36–38, 49]. Figure 24 shows Pd thickness as a function of exposure time on quartz at different wavelengths (λ = 172 nm), (λ = 222 nm), (λ = 308 nm). The different deposition rates correlate with the different absorption coefficients of wavelengths of UV radiation used. The highest deposition rate was achieved with the shortest wavelength radiation at (λ = 172 nm) due to the higher absorption of palladium acetate in the VUV. Film patterning can be achieved by illuminating the layers through metal contact masks.

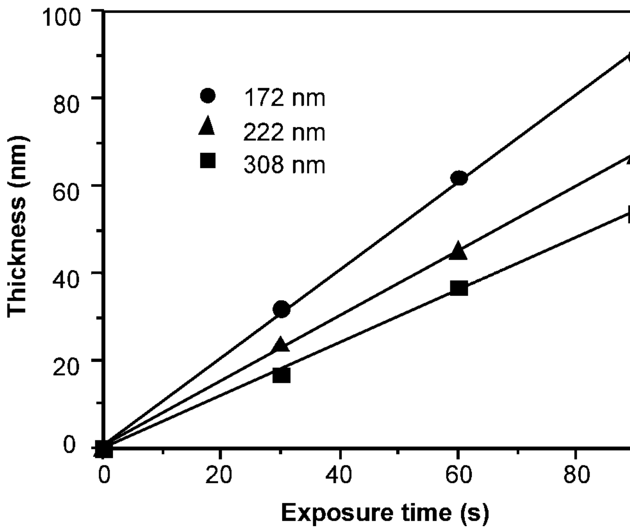

Figure 24. Pd thickness as a function of exposure time on quartz at different wavelengths.

Using the described process, plastics, paper, polymer, cardboard or synthetic fibre can be metal-coated at room temperature without difficulty. The grain size of laser-irradiated Pd is always large and the grains are arranged in clusters. By contrast, excimer UV sources always produce homogeneous and mirror-like layers with previously unattainable quality and adhesion [36, 38]. The edge-quality of these films formed using excimer lamps is much better than that produced by using lasers and was also found to be highly reproducible [36, 49].

This deposition process offers several advantages over the other deposition methods, such as operating at a low temperature, being insensitive to substrate properties, and providing large-area and low cost layers. The use of excimer sources instead of expensive lasers may therefore provide an interesting economical alternative for the manufacture of thin films.

Patterned deposition has been achieved by using metal or quartz contact masks. Figure 25 shows an array of Cu structures formed on a Pd pattern produced by 172 nm radiation for 5 min on an AlN substrate after a 1 min immersion in an electroless Cu bath at 25 °C [43]. The vertical radius of the spots on the top right side in Fig. 25 is 7.5 μm, while the largest radius on the bottom right is 200 μm. The width of the Cu lines comprising the incomplete square on the upper left is 100 μm. The smallest features, just visible between the spots in Figure 25 are dots with a diameter of 1.5 μm. The edge quality of the features formed is remarkably sharp with no metal particles, often present around lines written by focused laser, being detectable in the surrounding areas.

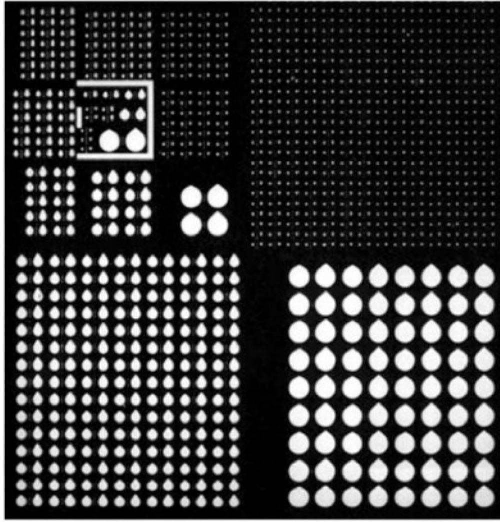

Figure 25. Selectivity of Cu plating on Pd nucleated AlN after immersion in an electroless Cu bath.

3.7. *Surface modification of polymers*

Dry etching of photoresists and various polymers has become an important process step in the fabrication of microelectronic devices. Photo-etching of various polymers e.g. PMMA (poly-methylmethacrylate), PI (polyimide), PET (poly-ethyleneterephthalate), PTFE (polytetra-fluoroethylene) has been demonstrated using different wavelength excimer lamps (172 nm, 222 nm, and 308 nm) [49, 50, 53, 151, 156, 157]. In the case of PTFE, etch rates as high as 1 μm/min have been achieved. These high material removal rates suggest that excimer lamps will also find applications in the microstructuring of large area polymer surfaces.

Polymer surfaces are often smooth and chemically unreactive. Photo-induced etching can lead to physical and chemical alteration of surface properties. This has become a field of considerable technical importance. It can be used to improve the adhesion of coatings as well as wetability, bondability and printability of polymers by changing the morphology and chemical surface properties [158]. The roughness of the UV irradiated area can be controlled by suitable choice of parameters (wavelength, exposure time, gas environment, pressure, etc.) and depends also on the properties of the material to be etched.

Recent work on PET using excimer lamps shows a pronounced increase of surface roughness with rising exposure time [53]. UV irradiation of PET leads to the formation of ripples at the surface. Ripple dimensions and roughness features increase with exposure time. Compared to pulsed excimer laser irradiation at 248 nm and 308 nm [52, 159, 160], the characteristic scale size of the roughness features is much smaller. For the excimer lamp etching of polymers, no threshold fluence and no significant temperature rise was observed [52]. Consequently no thermal

damage such as melting or bubble formation was found in and around the exposed region. The experiments suggest that the etching process with incoherent UV radiation originating from excimer lamps is mainly of photolytic nature.

The application of excimer UV sources has also been demonstrated in several other areas recently, such as UV curing of paints, varnishes and adhesives [21], VUV substrate cleaning and etching [17, 48], and photo-degradation of a variety of pollutants [59].

3.8. *UV curing with excimer lamps: printing machines*

UV curing, polymerization induced by UV irradiation, is a technologically advanced process in which intense UV radiation is used to instantly cure paints, varnishes, coatings, printing inks and adhesives in a wide range of industries. One of the main advantages of these formulations is that no solvents are used and that consequently emissions of volatile organic compounds (VOCs) and other hazardous air pollutants (HAPs) are avoided.

Traditionally, medium pressure Hg lamps doped with various additives are used for UV curing. These have the disadvantage that only a relative small fraction of the radiation (< 20%) is in the UV range. The remainder, in the visible and infrared, is not used in the process. These lamps produce ozone and get very hot (> 800 °C), a property which precludes their use with heat sensitive substrates and which necessitates fast mechanical shutters.

Excimer lamps offer a number of advantages that makes them especially attractive for UV curing. Their radiation output is restricted to a narrow UV wavelength range, which can allow for a perfect match to the absorption spectrum of the photoinitator. They can be instantly switched on and off, eliminating the use of mechanical shutters, and they can be operated at low temperature (cold UV), which enables delicate substrates to be irradiated.

One of the applications where excimer lamps could replace traditional lamps is the UV curing of optical fibre coatings [161]. In this study DeSolite® 950 (DS) series optical fibre coatings were used and three different wavelengths were tested (172, 222, 308 nm), with the best results being obtained with the XeCl* lamp (308 nm).

Another application with promising prospects for high power excimer lamps is their use in printing machines. Experiments with lamps mounted on web and sheet fed offset printing presses in Leipzig at the Institut für Oberflächenmodifizierung showed the potential of these novel UV sources for UV printing [162, 163]. After developing highly reactive offset printing inks and improving their design of the nitrogen blanketing (or inerting) system, which reduces the presence of oxygen and thus production of radicals to several ppm that otherwise would inhibit the desired monomer conversion, maximum curing speeds of 300 m/min in web offset and 8000 sheets/h in sheet offset were reached. These results were obtained with a UV curing unit containing two parallel XeCl excimer lamps with a maximum irradiance of 200 $mW{\cdot}cm^{-2}$ on the web offset printing press and a one-lamp system on the sheet offset printing press. More powerful lamps or more lamps are needed

to reach the maximum mechanical speed of these printing machines (400 m/min, 50,000 sheets/h).

Making use of even shorter wavelengths also opens up new possibilities. With KrCl excimer lamps operating at 222 nm and Xe excimer lamps operating at 172 nm, curing of thin acrylate layers without the use of photoinitiators was demonstrated. With the VUV wavelength of the Xe_2* lamp and the windowless Ar_2* lamp (126 nm) special matting and surface structuring effects were obtained. At 126 nm the radiation penetrates only to a depth of 20–100 nm into polymers, which results in very fine surface structures. Microstructured polyacrylate surfaces show interesting properties such as self-cleaning, drag reduction or layer separation [20].

4. Conclusions

In this chapter, we have shown that the efficient generation of powerful narrow-band incoherent UV excimer radiation covering a significant portion of the UV-VUV range can be achieved utilising transient excimer complexes formed in special gas discharges.

Sealed VUV/UV sources filled with such excimer forming gas mixtures and fitted with external electrodes provide powerful optical tools that can be applied to a wide area of materials processing, including surface modification, etching, deposition, and curing. These sources can be very large area, geometrically flexible, and exhibit long operating lifetimes. As such, in several areas, they are strong competitors to the more expensive excimer laser sources used for much materials processing today. Moreover, they open up new avenues of application not previously available to excimer laser or other laser and lamp sources.

Acknowledgement

This work was partly supported by EPSRC (grants GR/190909 and GR/R97474) and EU (IST-1999-10541 TOPS) project funding.

References

1. S. Watanabe and H. Kashiwagi, *Oyo Buturi* (Japan), **46**, 978 (1977) (in Japanese).
2. Ch. K. Rhodes, Ed., *Excimer Lasers* (New York: Springer, 1979 and 1984).
3. I. S. Lakoba and S. I. Yakovlenko, *Sov. J. Quantum Electron.* **10**, 389 (1980).
4. B. Eliasson and U. Kogelschatz, *Appl. Phys.* **B 46**, 299 (1988).
5. A. P. Gochelashvili, A. V. Dem'yanov, J. Kochetov and L. Yangurazova, *Laser Phys.* **3**, 140 (1993).
6. V. V. Ivanov, K. S. Klopovskii, Yu. A. Mankelevich, A. T. Rakhimov, T. V. Rakhimova, G. B. Rulev and V. B. Saenko, *Laser Phys.* **6**, 654 (1996).
7. F. Vollkommer and L. Hitzschke, *Proc. 8th Int. Symp. Sci. & Technol. Light Sources (LS-8)*, Edited by G. Babucke, Greifswald, Germany, (1998), pp. 51–60.
8. A. Oda, H. Sugarawa, Y. Sakai and H. Akashi, *J. Phys. D: Appl. Phys.* **33**, 1507 (2000).

9. R. J. Carman, B. K. Ward and R. P. Mildren, *Proc. XXV. Int. Conf. on Phenomena in Ionized Gases (ICPIG-XXV)*, Vol. 4, Nagoya, (2001), pp. 331–332.
10. S. Kubodera, M. Honda, M. Kitahara, J. Kawanaka, W. Sasaki and K. Kurosawa, *Jpn. J. Appl. Phys.* **34**, L618 (1995).
11. G. N. Gerasimov, G. A. Volkova, G. N. Zvereva, P*roc. 8th Int. Symp. Sci. & Technol. Light Sources (LS-8)*, Edited by G. Babucke, Greifswald, Germany (1998), pp. 248–249.
12. A. K. Shuaibov, L. L. Shimon and I.V. Shevera, *Instr. Exp. Techn.* **41**, 427 (1998).
13. A. K. Shuaibov, L. L. Shimon, A. I. Dashchenko and I. V. Shevera, *Tech. Phys.* **46**, 207 (2001).
14. U. Kogelschatz, H. Esrom, J.-Y. Zhang and I. W. Boyd, *Appl. Surf. Sci.* **168**, 29 (2000).
15. U. Kogelschatz, *Appl. Surf. Sci.* **54**, 410 (1992).
16. B. Eliasson and U. Kogelschatz, *IEEE Trans. Plasma Sci.* **19**, 309 (1991).
17. U. Kogelschatz, *Pure Appl. Chem.* **62**, 1667 (1990).
18. B. Gellert and U. Kogelschatz, *Appl. Phys.* **B 52**, 14 (1991).
19. U. Kogelschatz, *Proc. XX. Int. Conf. on Phenomena in Ionized Gases (ICPIG-XX)*, Edited by V. Palleschi, D. P. Singh and M. Vasselli, Barga, Italy, 1991, Invited Papers, pp. 218–227.
20. M. Lenk and R. Mehnert, *Proc. Rad. Tech Europe*, Basle (2001), pp. 153–158.
21. U. Kogelschatz, B. Eliasson and H. Esrom, *Materials & Design* **12**, 251 (1991).
22. K. Stockwald and M. Neiger, *Contrib. Plasma Phys.* **35**, 15 (1995).
23. J.-Y. Zhang and I. W. Boyd, *J. Appl. Phys.* **80**, 633 (1996).
24. J.-Y. Zhang and I. W. Boyd, *J. Appl. Phys.* **84**, 1174 (1998).
25. Z. Falkenstein and J. J. Coogan, *J. Phys. D: Appl. Phys.* **30**, 2704 (1997).
26. T. Urakabe, S. Harada, T. Saikatsu and M. Karino, *Proc. 7th International Symposium on the Science and Technology of Light Sources (LS7), Kyoto, Japan*, Edited by R. Italani and S. Kamiya, The Illuminating Engineering Institute of Japan (1995), pp. 159–160.
27. M. Ilmer, R. Lecheler, H. Schweizer and M. Seibold, *SID International Symposium, Long Beach, CA, Digest of Technical Papers*, Vol. XXXI, Edited by J. Morreal (2000), pp. 931–933.
28. M. G. Kwak and J. I. Han, *J. SID* **9**, 165–168 (2001).
29. B. Eliasson, U. Kogelschatz, *Proc. 40 Ann. Gas. Electron. Conf. (GEC 87)*, Atlanta, 174 (1987)
30. B. Gellert, B. Eliasson and U. Kogelschatz, *Proc. 5th Int. Symp. on the Science & Technology of Light Sources (LS-5)*, York (1989), pp. 155 and 181.
31. I. W. Boyd and J.-Y. Zhang, *Nucl. Instrum. Meth. Phys. Res.* **B121**, 349 (1997).
32. P. Bergonzo and I. W. Boyd, *J. Appl. Phys.* **76**, 4372 (1994).
33. P. Bergonzo and I. W. Boyd, *Appl. Phys. Lett.* **63**, 1757 (1993).
34. J.-Y. Zhang, L.-J. Bie, and I. W. Boyd, *Jpn. J. Appl. Phys.* **37**, L27 (1998).
35. J.-Y. Zhang, B.-J. Bie, V. Dusastre and I. W. Boyd, *Thin Solid Films* **318**, 252 (1998).
36. H. Esrom, J. Demny and U. Kogelschatz, *Chemtronics* **4**, 202 (1989).
37. H. Esrom and U. Kogelschatz, *Appl. Surf. Sci.* **46**, 158 (1990).
38. H. Esrom and U. Kogelschatz, *Appl. Surf. Sci.* **54**, 440 (1992).
39. J.-Y. Zhang, Qi Fang, S. L. King and Ian W. Boyd, *Appl. Surf. Sci.* **109/110**, 487 (1997).
40. J.-Y. Zhang, H. Esrom and I. W. Boyd, *Appl. Surf. Sci.* **96–98**, 399 (1996).
41. J.-Y. Zhang and I. W. Boyd, *J. Mat. Sci. Lett.* **16**, 996 (1997).
42. J.-Y. Zhang and I. W. Boyd, *Appl. Phys.* **A 65**, 379 (1997).
43. J.-Y. Zhang and I. W. Boyd, *Thin Solid Films* **318**, 234 (1998).
44. J.-Y. Zhang and I. W. Boyd, *Electronics Letters* **32**, 2097 (1996).
45. V. Craciun, B. Hutton, D. E. Williams and I. W. Boyd, *Electronics Letters* **34**, 71(1998).
46. J.-Y. Zhang and I. W. Boyd, *Appl. Phys. Lett.* **71**, 2964 (1997).
47. V. Craciun, J-Y. Zhang and I. W. Boyd, *NATO Advanced Research Workshop on Fundamental Aspects of Ultrathin Dielectrics on Si-based Devices*, St. Petersburg, Russia (1997), p. 461.
48. H. Esrom and U. Kogelschatz, *Thin Solid Films* **218**, 231 (1992).
49. J.-Y. Zhang, *Thesis*, Karlsruhe University, Germany (1993).
50. H. Esrom, J.-Y. Zhang and U. Kogelschatz, *Mat. Res. Soc. Proc.* **236**, 39 (1992).
51. J.-Y. Zhang, H. Esrom, U. Kogelschatz and G. Emig, *Appl. Surf. Sci*. **69**, 299 (1993).
52. J.-Y. Zhang, H. Esrom, U. Kogelschatz and G. Emig, *J. Adhesion Sci. & Technol.* **8**, 1179 (1994).

53. J.-Y. Zhang, H. Esrom and I. W. Boyd, *Surface and Interface Analysis* **24**, 718 (1996).
54. J.-Y. Zhang, V. Dusastre, D. E. Williams and I. W. Boyd, *J. Phys. D: Appl. Phys.* **32**, L1 (1999).
55. J.-Y. Zhang, Q. Fang, and I. W. Boyd, *Applied Surface Science* **138–139**, 320 (1999).
56. J.-Y. Zhang, B. Lim and I. W. Boyd, *Thin Solid Films* **336**, 340 (1998).
57. V. Craciun, I. W. Boyd, D. Craciun, P. Andreazza and J. Perriere, *J. Appl. Phys.* **85**, 8841 (1999).
58. V. Craciun, D. Craciun, P. Andreazza, J. Perriere and I. W. Boyd, *Appl. Surf. Sci*. **139**, 587 (1999).
59. U. Kogelschatz, 'UV Production in Dielectric Barrier Discharges for Pollution Control', in B. M. Penetrante and S. E. Schultheis (Eds.), NATO ASI Series, Vol. G34, Part B, *Non-Thermal Plasma Techniques for Pollution Control* (Berlin, Springer, 1993), pp. 339–354.
60. R. S. Nohr, J. G. MacDonald, U. Kogelschatz, G. Mark, H.-P. Schuchmann and C. von Sonntag, *J. Photochem. Photobiol. A: Chem.* **79**, 141 (1994).
61. U. Kogelschatz, P*lasma Sources Sci. Technol.* **11**, A1–A6 (2002).
62. S. Mikoshiba, 'Gas-discharge Displays', in John G. Webster (Ed.), *Wiley Encyclopedia of Electrical and Electronic Engineering*, Vol. 8 (New York: Wiley-Interscience, 1999), pp. 233–238.
63. P. Bergonzo, U. Kogelschatz and I. W. Boyd, *Appl. Surf. Sci.* **69**, 393 (1993).
64. P. Bergonzo, U. Kogelschatz and I. W. Boyd, *Proc. SPIE* **2045**, 174 (1994).
65. P. Bergonzo and I. W. Boyd, *Electronics Letters* **30**, 606 (1994).
66. P. Bergonzo and I. W. Boyd, *Microelectronic Engineering* **25**, 345 (1994).
67. G. Eftekhari, *J. Electrochem. Soc.* **140**, 787 (1993).
68. D. A. Muller, T. Sorsch, S. Moccio, F. H. Baumann, K. Evans-Lutterodt and G. Timp, *Nature* **399**, 758 (1999).
69. Semiconductor Industry Association, *The National Technology Roadmap for Semiconductors*, Sematech Austin (1997), pp. 71–78.
70. M. Schulz, *Nature* **399**, 729 (1999).
71. C. A. Billman, P. H. Tan, K. J. Hubbard and D. G. Schlom, *Mat. Res. Soc.* **567**, 409 (1999).
72. Q. X. Jia, X. D. Wu, S. R. Foltyn and P. Tiwari, *Appl. Phys. Lett.* **66**, 2197 (1995).
73. R. Singh, S. Alamgir and R. Sharangpani, *Appl. Phys. Lett.* **67**, 3939 (1995).
74. S. Tanimoto, M. Matsui, K. Kamisako, K. Kuroiwa and Y. Tarui, *J. Electrochem. Soc.* **139**, 320 (1992)
75. Y. Nishimura, K. Tokunaga and M. Tsuji, *Thin Solid Films* **226**, 144 (1993).
76. K. W. Kwon, C. Kang, S. Park, H. Kang, S. T. Ahn, *IEEE Trans Electron Devices* **43**, 919 (1996).
77. J.-Y. Zhang, B. Lim, V. Dusastre and I. W. Boyd, *Appl. Phys. Lett.* **73**, 2299 (1998).
78. H. Shinriki, T. Kisu, S. Kimura, Y. Nishioka, Y. Kawamoto and K. Mukai, *IEEE Trans. Electron Devices* **37**, 1939 (1990).
79. R. F. Cava, W. F. Peck Jr. and J. J. Krajewski, *Nature* **377**, 215 (1995).
80. A. Cappellani, J. L. Keddie, N. P. Barradas and S. M. Jackson, *Sol. State Electron.* **43**, 1095 (1999).
81. R. J. Cava and J. J. Krajewski, *J. Appl. Phys.* **83**, 1613 (1998).
82. S. Kamiyama, H. Suzuki, H. Watanabe, A. Sakai, H. Kimura and J. Mizuki, *J. Electrochem. Soc.* **14**, 1246 (1994).
83. A. Pignolet, G. M. Rao and S. B. Krupanidhi, *Thin Solid Films* **258**, 230 (1995).
84. S. C. Sun and T. F. Chen, *IEEE Electron Device Letters* **17**, 355 (1996).
85. S. W. Park, Y. K. Baek, J. Y. Lee, C. O. Park and H. B. Im, *J. Electronic. Mater.* **21**, 635 (1992).
86. S. Zaima, T. Furuta, Y. Koide and Y. Yasuda, *J. Electrochem. Soc.* **137**, 2876 (1992).
87. S. Kamiyama, P. Lesaicherre, H. Suzuki, A. Sakai, I. Nishiyama and A. Ishitani, *J. Electrochem. Soc.* **140**, 1617 (1993).
88. J. L. Autran, P. Paillet, J. L. Leray and R. A. B. Devine, *Sensors and Actuators* **A 51**, 5 (1993).
89. H. Shinriki and M. Nakata, *IEEE Trans. Electron. Dev.* **38**, 455 (1991).
90. R. A. B. Devine, *Appl. Phys. Lett.* **68**, 1924 (1996).
91. C. Isobe and M. Saitoh, *Appl. Phys. Lett.* **56**, 907 (1990).
92. J.-Y. Zhang and I. W. Boyd, *J. of Mater. Sci. Lett.* **17**, 1507 (1998).
93. P. A. Murawala, M. Sawai, T. Tatsuta, O. Tsuji and S. Fujita, *Jpn. J. Appl. Phys.* **32**, 368 (1993).

94. H.O. Sankur and W. Gunning, *Appl. Opt.* **28**, 2806 (1989).
95. I. L. Kim, J. S. Kim, O. S. Kwon, S. Ahn, J. Chun and W. J. Lee, *J. Electron. Mater.* **24**, 1435 (1995).
96. D. Laviale, J. C. Oberlin and R. A. B. Devine, *Appl. Phys. Lett.* **65**, 2021 (1994).
97. M. Matsui, S. Oka, K. Yamagishi, K. Kuroiwa and Y. Tarui, *Jpn. J. Appl. Phys.* **27**, 506 (1988).
98. S. Oshio, M. Yamamoto, J. Kuwata and T. Matsuoka, *J. Appl. Phys.* **71**, 3471 (1992).
99. T. Aoyama, S. Yamazaki and K. Imai, *J. Electrochem. Soc.* **145**, 2961 (1998).
100. J.-Y. Zhang, I. W. Boyd, M. B. Mooney, P. K. Hurley, B. O'Sullivan, J. T. Beechinor, P. V. Kelly, G. M. Crean and J.-P. Senateur, *Mat. Res. Soc. Proc.* **567**, 397 (1999).
101. J.-Y. Zhang, H. Esrom and I. W. Boyd, *Appl. Surf. Sci.* **109/110**, 482 (1997).
102. J.-Y. Zhang, H. Esrom and I. W. Boyd, *Appl. Surf. Sci.* **138–139**, 315 (1999).
103. G. Q. Lo, D. L. Kwong and S. Lee, *Appl. Phys. Lett.* **60**, 3286 (1992).
104. Atanassova, 'Thin RF Sputtered and Thermal Ta_2O_5 on Si for High Density DRAM Application', *Microelectronics Reliability* **39**, 1185 (1999).
105. K. Yamagishi and Y. Tarui, *Jpn. J. Appl. Phys.* **25**, L306 (1986).
106. J. Tauc, R. Grigorovich and A. Vancu, *Phys. Stat. Sol.* **15**, 627 (1966).
107. J. Tauc, *Amorphous and Liquid Semiconductors* (New York: Plenum, 1974).
108. H. Demiryont, J. R. Sites and K. Geib, *Applied Optics* **24**, 490 (1985).
109. S. M. Sze, *Physics of Semiconductor Devices* (New York: John Wiley & Sons, 1981), p. 403.
110. K. A. McKinley and N. P. Sandler, *Thin Solid Films* **290–291**, 440 (1996).
111. A. Y. Mao, K. A. Son, J. M. White, D. L. Kwong, D. A. Roberts and R. N. Vrtis, *Mat. Res. Soc. Proc.* **567**, 473 (1999).
112. N. Kaliwoh, J.-Y. Zhang and I. W. Boyd, *Surface and Coating Technology* **125**, 424 (2000).
113. J.-Y. Zhang and I. W. Boyd, *Jpn. J. Appl. Phys.* **38**, L393 (1999).
114. J.-Y. Zhang, I. W. Boyd, B. J. O'Sullivan, P. K. Hurley and P. V. Kelly, J.-P. Senateur, *J. Non-Crystalline Solids* **303**, 134 (2002).
115. J.-Y. Zhang, Q. Fang, J. X. Wu, C. Y. Xu, B. J. O'Sullivan, P. K. Hurley, T. L. Leedham, M. A. Audier, J.-P. Senateur and I. W. Boyd, *J. Phys. IV (France)*, **11**, 295 (2001).
116. J. V. Grahn, M. Linder and E. Fredriksson, *J. Vac. Sci. Technol.* **A 16**, 2495 (1998).
117. N. Kaliwoh, J.-Y. Zhang and I. W. Boyd, *Appl. Surf. Sci.* **186**, 426 (2002).
118. Q. Fang, J.-Y. Zhang, Z. M. Wang, J. X. Wu, B. J. O'Sullivan, P. K. Hurley, T. L. Leedham, M. A. Audier, J.-P. Senateur and Ian W. Boyd, *Thin Solid Films* **427**, 391 (2003).
119. J. Zhang and I. W. Boyd, *Appl. Surf. Sci.* **186**, 64 (2002).
120. F. Kessler and G. H. Bauer, *Appl. Surf. Sci*. **54**, 430 (1992).
121. C. Manfredotti, F. Fizzotti, C. Osenga, G. Amato and L. Boarino, *Phys. Stat. Sol. (a)* **135**, 191 (1993).
122. P. Bergonzo, *Thesis*, University College London, 1994.
123. P. Bergonzo, P. Patel, I. W. Boyd and U. Kogelschatz, *Appl. Surf. Sci.* **54**, 424 (1992).
124. J. G. Calvert and J. N. Pitts, *Photochemistry* (New York: Wiley & Sons, 1966).
125. T. T. Chau, S. R. Meija and K. C. Kao, *J. Electrochem. Soc.* **138**, 325 (1991).
126. V. Craciun, I. W. Boyd, A. H. Reader, W. J. Kersten, F. J. Hakkens, P. H. Oosting and D. E. W. Vandenhouldt, *J. Appl. Phys.* **75**, 1972 (1994).
127. P. Singer, *Semiconductor International*, 34 (1994).
128. S.P. Murarka, Solid State Technology **39**, 83 (1996).
129. J.-Y. Zhang and I. W. Boyd, *Optical Materials* **9**, 251 (1998).
130. C. A. Pryde, *J. Polym. Sci., Part A: Polym. Chem.* **27**, 711 (1989).
131. J.-Y. Zhang and I. W. Boyd, *Materials Science in Semiconductor Processing* **3**, 345 (2000).
132. I. W. Boyd, V. Craciun and A. Kazor, *Jpn. J. Appl. Phys.* **32**, 6141 (1993).
133. G. Eftekhari, *J. Electrochem. Soc.* **140**, 787 (1993).
134. H. Shinriki and M. Nakata, *IEEE Tansactions on Electron Devices* **38**, 455 (1991).
135. W. A. Pliskin, *Thin Solid Films* **2**, 1 (1968).
136. I. W. Boyd and J. I. B. Wilson, *J. Appl. Phys.* **62**, 3195 (1987).
137. V. Craciun, B. Hutton, D. E. Williams and I. W. Boyd, *Electronics Letters* **34**, 71 (1998).

138. G. J. Fisanick, M. E. Gross, J. B. Hopkins, M. D.Fennell, K. J. Schnoes and A. Katzir, *J. Appl. Phys.* **57**, 1139 (1985).
139. M. E. Gross, G. J. Fisanick, P. K. Gallagher, K. J.Schnoes and M. D.Fennell, *Appl. Phys. Lett.* **47**, 923 (1985).
140. T. H. Baum, *J. Electrochem. Soc.* **137**, 252 (1990).
141. Y. Ye and R. G. Hunsperger, *Appl. Phys. Lett.* **51**, 2136 (1987).
142. A. Auerbach, *Appl. Phys. Lett.* **47**, 669 (1985).
143. A. Gupta and R. Jagannathan, *Appl. Phys. Lett.* **51**, 2254 (1987).
144. C. T. Lin, H. Y. Lee and M. A. Souto, *J. Mater. Res.* **6**, 760 (1991).
145. C. M. Harish, V. Kumar and A. Prabhakar, *J. Electrochem. Soc.* **135**, 2903 (1988).
146. M. E. Gross, *Chemtronics* **4**, 197 (1989).
147. H. Esrom and G. Wahl, Chemtronics **4**, 216 (1989).
148. Y. Zhang and M. Stuke, Chemtronics **4**, 212 (1989).
149. Y. Zhang and M. Stuke, *Appl. Surf. Sci.* **46**, 153 (1990).
150. H. S. Cole, Y. S. Liu, J. W. Rose, R. Guida, L. M. Levinson and H. R. Philipp, 'Laser Processes for Microelectronic Applications', in J. J. Ritsko, D. J. Ehrlich and M. Kashiswagi (Eds.), *Proc. Electrochem. Soc., 88-10*, Pennington, USA (1988), p. 187.
151. H. S. Cole, Y. S. Liu, J. W. Rose and R. Guida, *Appl. Phys. Lett.* **53**, 2111 (1988).
152. Y. S. Liu and H. S. Cole, *Chemtronics* **4**, 209 (1989).
153. R. C. Sausa, A. Gupta and J. R. White, *J. Electrochem. Soc.* **134**, 2707 (1987).
154. R. C. Sausa, A. Gupta and J. R. White, 'Laser Processes for Microelectronic Applications', in J. J. Ritsko, D. J. Ehrlich and M. Kashiswagi (Eds.), *Proc. Electrochem. Soc., 88-10*, Pennington, USA (1988), p. 172.
155. C. H.-J. Huang and T. A. Rabson, *IEEE Electron Device Letters* **13**, 609 (1992).
156. J.-Y. Zhang, H. Esrom, G. Emig and U. Kogelschatz, *Polymer Surface Modification: Relevance to Adhesion*, edited by K. L. Mittal, VSP, Utrecht, 153 (1996).
157. H. Esrom. J.-Y. Zhang, U. Kogelschatz, *Polymer Surfaces and Interfaces: Characterisation, Modification and Application*, edited by K. L. Mittal, K.-W. Lee, VSP, Utrecht (1997), p. 27.
158. S. Lazare, P. D. Hoh, J. M. Baker and R. Srinivasan, *J. Am. Chem. Soc.* **106**, 4288 (1984).
159. T. Nakata, F. Kannari and M. Obara, *Optoelectronics-Devices & Technology* **8**, 179 (1993).
160. J. E. Andrew, P. E. Dyer, D. Forster and P. H. Key, *Appl. Phys. Lett*. **43**, 717 (1983).
161. J.-Y. Zhang, G. Windall and I. W. Boyd, 'UV Curing of Optical Fibre Coatings Using Excimer Lamps', *Appl. Surf. Sci.* **186**, 568 (2002).
162. R. Mehnert, 'UV Curing Equipment – Monochromatic UV Lamps', in R. Mehnert, A. Pincus, I. Janorski, R. Stowe, A. Bereika, (Eds.), *UV and EB Curing Technology and Equipment*, Chapter IV, John Wiley/SITA (1999), pp. 83–105.
163. R. Mehnert, 'Excimer UV Curing in Printing', *Proc. Rad. Tech. Europe 99*, Berlin, 303 (1999).
164. V. Craciun, I. W. Boyd, B. Hutton and D. Williams, *Appl. Phys. Lett.* **73**, 1261 (1999).
165. J.-Y. Zhang, Q. Fang, A. J. Kenyon and I. W. Boyd, *Appl. Surf. Sci.* **208–209**, 364 (2003).
166. Q. Fang, J.-Y. Zhang and Ian W. Boyd, *Applied Surface Science* **208–209**, 369 (2003).
167. N. Kaliwoh, J.-Y. Zhang and I. W. Boyd, *Appl. Surf. Sci*. **168**, 13–16 (2000).
168. J. J. Yu and I. W. Boyd, *Appl. Phys.* **A 74**, 143 (2002).

This page intentionally left blank

CHAPTER 7

SYNCHROTRON-RADIATION-EXCITED STRUCTURAL CHANGES AND CHEMICAL BEAM EPITAXY OF SILICON-BASED MATERIALS

H. Akazawa

NTT Microsystem Integration Laboratories, 3-1 Morinosato Wakamiya, Atsugi-shi, Kanagawa 243-0198, Japan; E-mail: akazawa@aecl.ntt.co.jp

ABSTRACT: In this chapter an introduction of the significant characteristics of materials processing by synchrotron radiation excitation is given. The instrumentation of a state of the art beamline as well as *in-situ* monitoring techniques are described. The photochemical reactions which follow the initial excitation of the core electronic states of the material vary with the structure, ionicity of the chemical bonds, and form and presence of the vacancies in the network. The specific radiation effects on the material are detailed for a-SiO_2, a-SiN_x:H, and a-Si:H. Details of the microscopic processes involved in the synchrotron-radiation-excited epitaxy of Si film from Si_2H_6 are clarified and used for a better understanding of their growth.

1. Beamline instrumentation and diagnostic tools for synchrotron radiation excited material processing

1.1. *Characteristics of synchrotron-radiation-excited processing*

The effects of synchrotron-radiation (SR)-excitation in processing of materials have only been investigated for a limited number of systems. The energy levels involved distinguish this photo-processing technique by light from other sources. Photons from an electron storage ring have energies in the range from vacuum ultraviolet to x-ray; i.e., they are sufficiently energetic to excite the core-electronic states through one-photon processes, yet it is still possible to keep the temperature in the irradiated region low. Excitation by one photon in this energy range is sufficient to induce processes such as photolysis of gas-phase molecules, photodesorption and photodissociation of adsorbates at surfaces, and rearrangement of the network in bulk material. The quantum efficiency of atomic displacement when a core electron is excited is much greater when a valence electron is excited. Under appropriate conditions, the thermal effect is minimized and the electronic process becomes dominant. This is the great advantage of SR over lasers when we want to elucidate the microscopic mechanisms responsible for the effects of radiation or to fabricate microstructures. For example, atomically controlled superlattices with sharp doping profiles or abrupt interfaces are only achievable through low-temperature epitaxy using excitation by SR photons. SR-beam processing also offers precise controllability of film thickness and selectivity in terms of regions of deposition. The recent progress in the implementation of extremely brilliant synchrotron light sources is rapidly improving the lower throughput.

Aaron Peled (ed.), Photo-Excited Processes, Diagnostics and Applications (PEPDA), 201–224, 2003.
© 2003 *Kluwer Academic Publishers. Printed in the Netherlands.*

In view of the large penetration depth of photons in solid materials, an important feature specific to SR-excited reactions is processing of thin films rather than merely surface phenomena. It is generally accepted that the three major areas of application are deposition, etching, and the induction of structural changes in materials. If the reaction is driven photolytically, the reaction rate or the results is insensitive to the process temperature, and the amount of products saturates steeply in terms of the irradiation time. Although the electronically excited breaking of the chemical bonds is obviously the initial event, our primary interest is whether such local structural change grows up to some macroscopic changes. This sometimes requires additional heating of the substrate. If a thermal activation barrier exists after the electronic process, the reaction rate is temperature dependent. The electronic materials featured in this chapter manifest distinct radiation effects and comparison of them offers insightful information on the underlying kinetics of SR excited processes.

1.2. *Configuration of the beamline for material processing*

A state-of-the-art SR beamline, which was especially designed for materials processing rather than for the study of superficial photochemistry, has been installed at the “super-ALIS” superconducting electron storage ring in the NTT Atsugi Research and Development Center [1].

Figure 1 schematically illustrates the components of beamline 7. The Super-ALIS ring is of the race-track type, providing five extraction ports in each of the 180° bending sections.

Four separate ultrahigh vacuum (UHV) chambers consist the end of apparatus. Synchrotron radiation emitted at a bending magnet is focused by double toroidal mirrors onto the surface of a specimen mounted in the UHV process chamber (base pressure of 5×10^{-10} torr). The energy in the white spectral SR beam is distributed through the range 10–1500 eV, with the maximum flux energy at about 100 eV. At a ring current of 300 mA, the total number of photons is 5.5×10^{17} s^{-1}, and the photon density at the beam center is 1.3×10^{16} s^{-1} mm^{-2}.

The beamline is equipped with a large gas supply and exhausting facilities for performing advanced CVD processes involving multiple substances. Feeding up to four kinds of gases, either in continuous or pulsed mode, can be synchronized with irradiation from the SR beam. Eight 5-meter-long differential pumping stages are placed at the intermediate sections of the beamline (D1–D8). For improved efficiency in differential pumping, the conductance of gas in the upstream direction is reduced by the insertion of two aperture blocks in each beam duct (A1–A5). With an N_2 pressure of 0.1 torr in the reaction chamber, the pressure in the mirror chamber was below 4×10^{-9} torr, which is a durable condition for routinely conducting experiments.

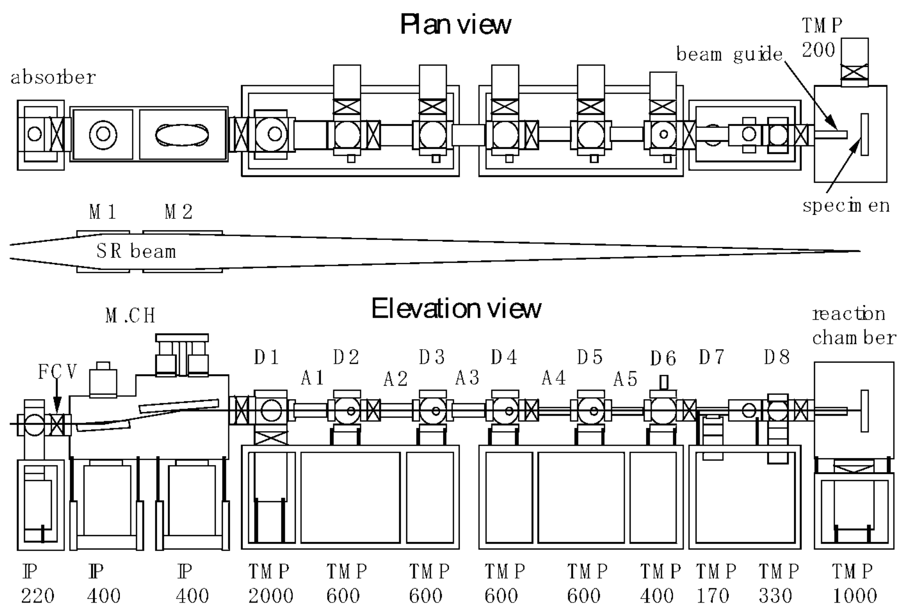

Figure 1. Plan and elevation views of beamline 7 connected to Super-ALIS. (FCV: fast-closing valve, M.CH: mirror chamber, IP: ion pump, and TMP: turbomolecular pump. The numbers indicate the pump-evacuation speeds in 1 s^{-1}. D1–D8 denote differential pumping chambers, and A1–A5 are the beam ducts that connects the chambers.)

1.3. In-situ *monitoring by time-of-flight mass spectroscopy*

Figure 2 is a block diagram of the apparatus for time-of-flight mass spectroscopy (TOFMS) to detect positive ions that are desorbed from solid surfaces [2]. This system can be used in the single-bunch mode of the Photon Factory (PF), which operates on a repetition cycle of 624 ns with a bunch width of 100 ps. The trigger signal is obtained by dividing the reference signal (500 MHZ) by 312. The ions produced by desorption from the solid surface and photolysis in the gas-phase enter the drift tube through the grid mesh and are then detected by a fast-response microchannel plate (MCP). The signals from the MCP are amplified and converted to logic signals by a constant fraction discriminator (CFD). For minimized dead time, the TOF spectra are recorded in the time-inverted mode, where the trigger signal is input to the stop channel and the ion signal is input to the start channel of the biased time-to-amplitude converter (TAC). The spectra thus recorded are stored in a multichannel analyzer (MCA). The time resolution of the photon signal was 270 ps.

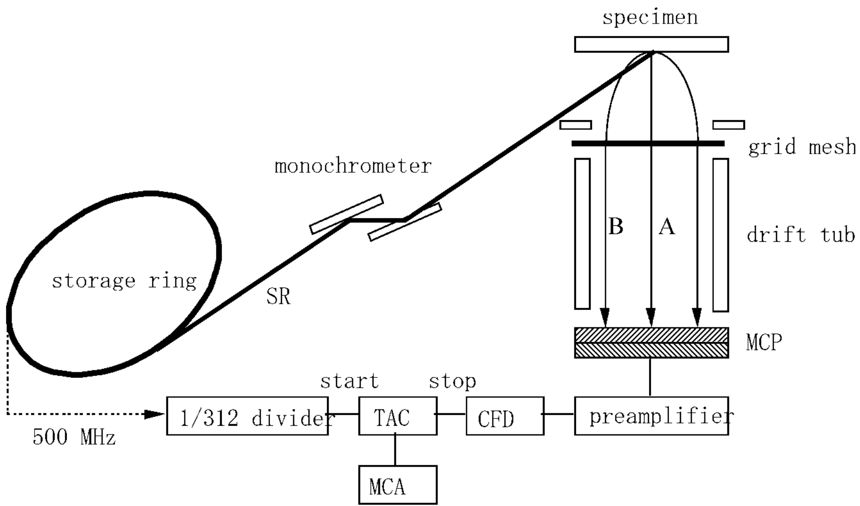

Figure 2. TOFMS detector and signal processing system using the single-bunch operating mode of the PF ring.

1.4. In-situ *monitoring by spectroscopic ellipsometry*

Phase-modulated spectroscopic ellipsometry (SE) [3] is probably the best solution for real-time monitoring of a CVD process, since this technique only involves the use of optical probes and is thus noncontact, nondestructive, and noninvasive and remains applicable in situations where the reactant gas is under high-pressure. In SE, we measure the ratio ρ between the Fresnel reflection coefficients (R_p and R_s) of *p*- and *s*-polarized light incident to the solid surface [4]. The ellipsometric angles Ψ and Δ correspond to the amplitude and phase of ρ defined by $\rho = R_p/R_s = \tan \rho \cdot \exp(i\Delta)$. Although SE is less sensitive to the state of the outermost surface of a film vs. surface-specific techniques, it is reasonably sensitive to the state of the near-surface region. In any case, the nanometer-range resolutions of thickness scales that we are able to grow or etch with photo-excited processing prove that SE provides the best solution [5, 6]. In beamline 7, the polarized light meets the substrate surface at a 72° angle of incidence, and the SE signal samples information from an elliptical region, with major and minor axes 10 and 3-mm long, which is centered within the rectangular area (10 × 18 mm) irradiated by the SR beam [1].

2. Radiation effects in a-SiO_2

2.1. *Surface phenomena*

When a body of a-SiO_2 is bombarded with high-energy electrons, vacuum-ultraviolet photons, or soft x-rays, O^+ ions are ejected from its surface [7] and oxygen

atoms are displaced from the Si-O-Si network. As a result, vacancies are created at sites which were initially occupied by oxygen atoms [8]. When the irradiation temperature is lower than 500 °C, most of these oxygen-vacancy defects are maintained once they are created, as diffusion and desorption of the O_2 molecules reduce the concentration of oxygen atoms in the film and change its net composition into a Si-rich SiO_x [9]. Observation of the elementary Si(LVV) signal at 92 eV in Auger electron spectra and the Si^0 signal in x-ray photoelectron spectra confirmed the formation of Si-Si bonds [10]. At irradiation temperatures above 730 °C, however, the film decomposes through the continuous desorption of SiO product molecules [11].

2.2. *Evaporation vs. compositional change*

The changes in ellipsometric angles Ψ and Δ as monitored from the beginning of the irradiation of a 400-Å-thick film of a-SiO_2 are plotted in Figure 3 for various temperatures of the irradiated area. The Ψ-Δ trajectories start from the origin O(38°, 80°) and show an up – and leftward trend with decreasing thickness. In trajectories where the temperature was above 500 °C, the decreases in Ψ and increases in Δ are almost linear with the period of irradiation. The changes slowed suddenly at 50–60 min, when the a-SiO_2 film was almost gone. The trajectories at $T_s \leqq 500$ °C are short and terminate at points with small Δ-angle coordinates. All trajectories are close to the curve O-A-B. The dotted curve O-X-Y is the trajectory simulated on the assumption of uniform etching of a 400-Å-thick a-SiO_2 film at 800 °C while maintaining the stoichiometric composition of the film. The end

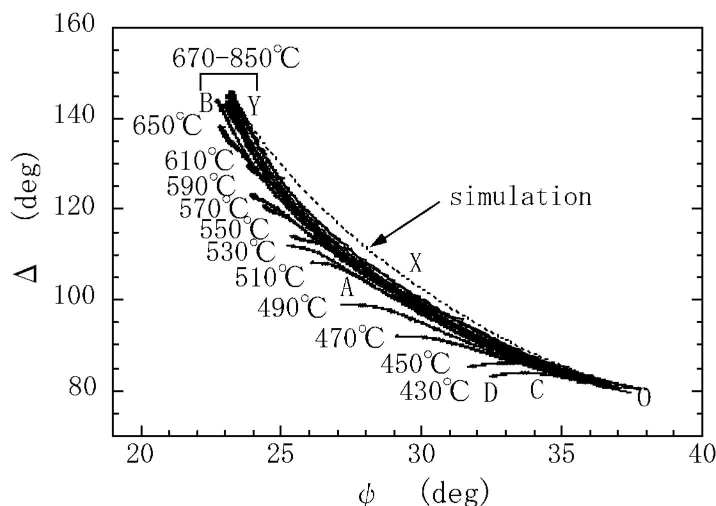

Figure 3. Ψ-Δ trajectories monitored at 3.4 eV with irradiation of an a-SiO_2 film. A trajectory simulated on the assumption of the homogeneous etching of a 400-Å-thick film of SiO_2 at 800 °C is given as the dotted curve, marked O-X-Y. Trace O → A → B is the envelope of all of the traces and trace O → C → D is the trajectory at 430 °C.

points of the trajectories for the 670–850 °C range are all close to the point Y, which defines the optical constant of an atomically clean and flat Si(100) substrate. This means that the SiO_2 film had almost completely been removed in these cases [10].

The changes in the Ψ and Δ angles at $T_s > 500$ °C are due primarily to the decreasing thickness of the overlayer, hence the instantaneous rate of evaporation at any time can be derived from the derivatives of the angles with respect to time. If the dependences of $d\Psi/dt$ and $d\Delta/dt$ on temperature at an early stage of irradiation along with the evaporation rate as evaluated from the depth at the center of the irradiated region are plotted in the Arrhenius manner, all have the same slope, which yields an activation energy of 0.44 eV [12].

Although the outline of the trajectory reflects the thickness of the overlayer, the compositional change is also clearly identifiable in Figure 3. The trajectory at 430 °C, for instance, initially overlaps with the envelope curve O-A-B, but its direction shifts abruptly leftward at the turning point, C. This turning point defines the critical point beyond which the SiO_x film becomes resistant to evaporation. The trace C $\rightarrow$ D, on which Δ is almost constant and Ψ decreases, is mainly a result of structural changes. Thus, in the initial stage of irradiation, SiO_2 is evaporated so that the film remains compositionally stoichiometric SiO_2; this continues until the formation of oxygen vacancies suddenly becomes the predominant process. The eventual termination of a trace at a steady-state position indicates that the composition of the SiO_x film is stable and further decomposition does not occur.

2.3. *Temperature-dependent composition of SiO_x*

The dielectric function of a modified SiO_x can be calculated by assuming an appropriate model structure based on Bruggeman EMA [13]. A double-layered structure consisting of an inner layer, represented by a mixture of SiO_2 with optically thick polycrystalline Si (p-Si), and a surface roughness layer, represented by a mixture of voids with p-Si, reproduced well the experimental spectra. In mixing the dielectric functions of SiO_2 and p-Si, we use the dielectric response of p-Si to represent the response of Si-Si bond units or Si clusters.

It was found that when the volume fraction of p-Si exceeds some threshold value (10–24%), which depends on the temperature of irradiation, the evaporation actually ends, and the SiO_x film is resistant to further decomposition [12]. This is because the valence holes produced by the Auger decay of a core hole are neutralized very rapidly when the density of the valence electrons that originate in Si-Si bonds becomes high enough. Between 610 and 690 °C which is the intermediate temperature range, the volume fraction of SiO_2 in the steady state suddenly drops from 76.7% to 0%. At temperatures higher than 700 °C, no oxides are present in the steady state and the interface is partially exposed. The final double-layered structure in this case consists of 16–30Å-thick inner layer of p-Si and a 5–20Å-thick surface-roughness layer. This process has been studied by *in-situ* monitoring by reflection high-energy electron diffraction (RHEED) [14]. The first change is the appearance of a ring pattern over a halo background, which indicates that Si aggregates, consisting of networks of crystalline Si, are oriented in random directions.

Then, diffraction spots, which indicate that the electrons are being transmitted through three-dimensional islands, are increasingly superimposed on the ring pattern as the Si aggregates merge into islands, which are created by solid-phase crystallization. When the irradiation temperature was higher than 800 °C, the islands of p-Si were flattened and a clear pattern of (2 × 1)-reconstructed Si(100) surface was observed [15].

2.4. *Creation and annihilation of defects during irradiation*

Figure 4 shows how the volume fraction of SiO_2 and the thickness of the layer vary at various temperatures during irradiation. At 470 °C, the composition changed significantly from the beginning of the irradiation period. When the temperature was higher than 690 °C, the material remained stoichiometrically SiO_2 down to a thickness of 80 Å, with the suboxide phase (SiO_x) only prevailing in the subsequent final stage. The experimental results confirm the general trend of a first stage where the SiO_2 film evaporates, as silicon-containing product molecules (SiO) are desorbed, and a second stage where the volume loss is primarily due to preferential desorption of oxygen atoms (molecules). The prolonged maintenance of SiO_2 stoichiometry at the higher temperatures suggests that defects and Si-Si bonds are being annihilated as the sites are decomposed into volatile SiO molecules.

2.5. *Precipitation of nanocrystalline Si in SiO_x matrix*

Systems of Si/SiO_2 and suboxide have various optoelectronic applications. From such systems, nanocrystalline Si (nc-Si) embedded in a matrix of SiO_2 is promising as a material that emits visible light. The widely employed methods for the depo-

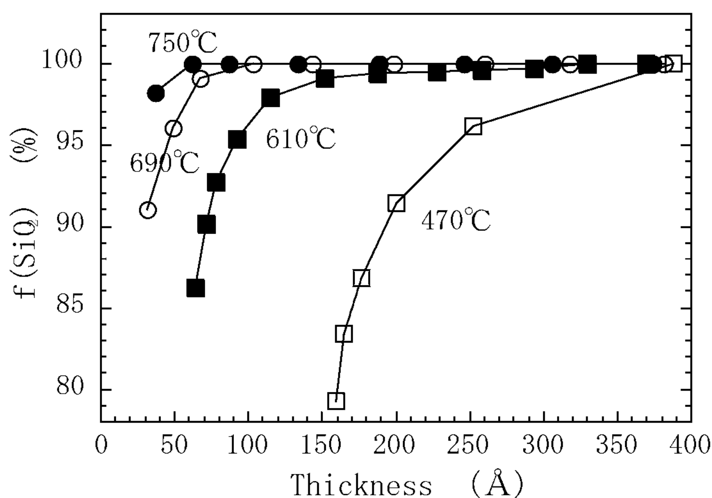

Figure 4. Volume fraction of SiO_2 vs.layer thickness during irradiation of a-SiO_2 at various temperatures.

sition suboxide films are sputtering in an O_2 atmosphere or Si-ion implantation into SiO_2 films [16, 17]. The film of SiO_x thus prepared is then annealed at temperatures above 1000 °C to induce phase-separation into Si and SiO_2 domains. The resulting particles of nc-Si are small, typically less than 5 nm in diameter. Here, we focus on the microscopic structure of SiO_x films produced by irradiating SiO_2 films.

Cross-sectional transmission electron microscopy (XTEM) revealed that irradiation at 300 °C produced an amorphous film with a SiO_2 volume fraction of 90.3% [12]. This observation suggested that the Si_nO_{4-n} (n = 0–4) local composition structures are distributed statistically throughout the SiO_x film [18]. When the temperature of the irradiated area was 470 °C, nc-Si particles with an average length/width of 2–3 nm appeared [14]. These particles were mainly present at the surface and near the SiO_2/Si interface.

The nanocrystals become larger with increasing temperature. This is because the separation of SiO_x into Si and SiO_2 domains is thermally activated [19]. Si aggregate is produced through the aggregation of Si-Si bond units with the desorption of SiO and O_2 species. The remaining reproduced SiO_2 domains are subjected to defect formation, decomposition, through which further aggregation of Si-Si bond units occurs. This sequence of oxygen loss and phase-separation continues until a diffusion-limited equilibrium state has been reached.

When the irradiation temperature is 610 °C, numerous large nanocrystalline domains are distributed throughout the resulting film, as shown by the XTEM image in Figure 5. The nc-Si particles at the surface are relatively small but occur at a high density high enough to form a continuous crystalline overlayer. The grains of nc-Si near the interface are typically about 10 nm in diameter and 20 nm in length and aligned in the direction normal to the surface. The undulation of the interface indicates that solid-phase epitaxy had produced crystalline islands from the oxygen-depleted interfacial SiO_x film.

2.6. *The basic photolytic and thermal processes*

The experimental results described above give us a clear view of the interplay between the basic photolytic and thermal processes. The decomposition of an a-SiO_2 film and the changes of its composition are initiated by the cleavage of Si-O bond

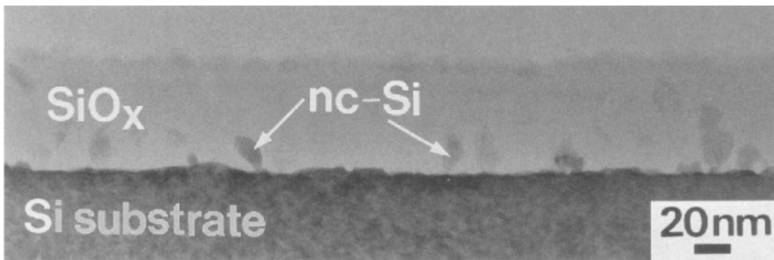

Figure 5. XTEM images of SiO_x films produced by irradiation at 610 °C.

as a result of electronic excitation. The changes to the material's dielectric function can be related to well-known defect-formation processes [20, 21]. The production of an E_1' center with an interstitial oxygen atom (Frenkel pair) is the basic radiation-induced event: In the Devine's notation this is expressed as

$$O_3 \equiv Si\text{-}O\text{-}Si \equiv O_3 + h\nu \rightarrow O_3 \equiv Si \cdot \ {}^{+}Si \equiv O_3 + O + e^{-} \quad (1)$$

where ($\cdot$) denotes an unpaired electron and $\equiv$ denotes the chemical bonds with the three oxygen atoms. The E_1' center is converted into a neutral oxygen vacancy site by the attachment of an electron:

$$O_3 \equiv Si \cdot \ {}^{+}Si \equiv O_3 + e^{-} \rightarrow O_3 \equiv Si\text{-}Si \equiv O_3 \quad (2)$$

Pairs of adjacent Si atoms ($Si \cdot {}^{+}Si$ and Si-Si) are the majority defects, and are responsible for changes in the dielectric response. The Si-Si bonds are distributed homogeneously within the SiO_x film at $T_s \leqq 300$–400 °C. Non-bridging oxygen hole centers (NBOHC) ($O3 \equiv Si\text{-}O \cdot$) constitute another defects, and are produced by the scheme [21]:

$$O_3 \equiv Si\text{-}O\text{-}Si \equiv O_3 + h\nu \rightarrow O_3 \equiv Si\text{-}O + \cdot Si \equiv O_3 \quad (3)$$

The oxygen atom released in scheme (1) may either be incorporated in the Si-O-Si network to create a peroxylinkage ($O3 \equiv Si\text{-}O\text{-}O\text{-}Si \equiv O_3$) or become attached to an NBOHC to create a peroxyradical ($O_3 \equiv Si\text{-}O\text{-}O \cdot$) [22]. A peroxylinkage or peroxyradical is decomposed through the release of an O_2 molecule. The loss of O_2 from the bulk material is the process that leads to a Si-rich composition. Photon-stimulated desorption also contributes to the removal of oxygen atoms at the surface.

We can distinguish between two competing models of the local structure of SiO_x films. In the two-phase model, the film is assumed to consist of regions of Si aggregate and regions of stoichiometric SiO_2. The average volume of the phases in the material determines the index x. In the continuous random network (CRN) model, the local bonding is described statistically in terms of the distributions of five different local bonding environments: $Si\text{-}Si_{4-n}O_n$, with n = 0, 1, 2, 3, and 4 [18]. Since the photon-induced events occur randomly throughout the film, a film of SiO_x that is produced by low-temperature ($T_s \leqq 400$ °C) irradiation of SiO_2 will have the CRN structure.

The configuration in which oxygen atoms are displaced into interstitial positions is metastable. If an interstitial oxygen atom displaced from an E_1' center or NBOHC is able to overcome the potential barrier because of the elevated temperature, it may return to its original position to reproduce the ordinary Si-O-Si network. This leads to the annihilation of Frenkel pairs [23]. However, when the interstitial oxygen atom becomes largely separated from the defect site, we see decomposition of the network. The coordination number of a Si atom at an E_1' center is small, hence such a site is easily decomposed into SiO molecules, and the repetition of this process results in macroscopic-level evaporation of the film. Sooner or later, the

thermal decomposition channel is terminated when the number of Si-Si bonds accumulated in the SiO_x reaches a critical value. On this basis, we can conclude that photo excitation triggers high local structural change, whereas annealing drives two opposing processes that affect the macroscopic restructuring of the network. Annealing makes the network decompose into volatile SiO molecules but also leads to the precipitation of Si nanocrystals.

3. Radiation effects in a-SiN_x:H

3.1. *Change in compositional structure and refractive index*

With the recent progress in technology for advanced optical communications network, techniques for the fabrication of micro-photonic devices have become an important field of research and development. The fundamental principle in the confinement of propagating light within optical waveguides is the selection of appropriate materials for the core and cladding regions. Thus, the application of light to induce structural changes in thin films, i.e., modifying their refractive indices, has been an important technique ever since the pioneering work by Hill et al. [24]. In this section, hydrogenated amorphous silicon nitride (a-SiN_x:H) films are shown to be promising as candidates for the role of a photosensitive material that will allow us to write high-Δ waveguides and fiber Bragg gratings. Since such films contain large molar fractions of H atoms, sufficient space is available to facilitate rearrangement of the atomic network. Excitation by high-energy photons has been found to produce irreversible forms of network restructuring around the photoexcited atoms.

a-SiN_x:H ($x = 1.31$) films between 2500 and 2800 Å thick were deposited on Si(100) substrates by plasma-enhanced CVD from a gaseous mixture of SiH_4 and NH_3. The distinct effects of radiation on a-SiN_x:H and on a-SiO_2 were compared by monitoring the time evolution of the ellipsometric (Ψ, Δ) angles obtained at 3.4 eV and room temperature [25]. In the case of a-SiO_2, the (Ψ, Δ) angles changed slowly but continuously until they reached their respective saturation levels. In the case of a-SiN_x:H, however, the (Ψ, Δ) angles changed sharply as irradiation commenced. The time-constant of the responsible photochemical reaction was 100 s and it almost run its course by 200 s. The changes in the dielectric constant observed in this case are certainly of a photolytic origin.

Linear regression analysis of the (Ψ, Δ) spectra was applied to determine the thickness and compositional structure of the films in terms of the chemical bonds that are contributing to the respective dielectric responses. A reasonable agreement between the experimental and calculated spectra was obtained by using a single-layer (Si_3N_4+c-Si+void) model in which the dielectric functions of stoichiometric silicon nitride (Si_3N_4), crystalline silicon (c-Si), and the void were mixed under the Bruggeman EMA [13]. The void component represents the vacant spaces around hydrogen-terminated defect sites. Si_3N_4 shows very little absorption above 4.8 eV, so the major contribution here is from the c-Si component. The c-Si component also represents the relatively silicon-rich composition of the film

in comparison with a film of Si_3N_4. The probable corresponding microscopic structure is Si-Si bond units that exist in the form -Si-SiH_x (x = 0–3) or as aggregated Si.

The respective volume fractions of the Si_3N_4, void, and c-Si components of the film in its as-grown state were 0.809, 0.149 and 0.042. After irradiation, the corresponding volume fractions became 0.882, 0.093, and 0.025 where these values are average for eight specimens. This means that the composition was brought closer to that of stoichiometric Si_3N_4 by a reduction in the number of chemical sites that are accompanied by voids and in the amount of c-Si. Consequently, the total thickness of the film was reduced by 9.8 ± 2%. As a quantitative basis for discussion, the nominal volumes of the Si_3N_4, c-Si, and void components which would be required to make up the total thickness were calculated. The void volume was reduced by 44 ± 9% from the initial void volume and the c-Si volume was reduced by 49 ± 15% from the initial c-Si volume. These values were not correlated with the temperature during irradiation. The volumetric reduction ratio for Si_3N_4 was, however, an increasing function of temperature, varying from 0.3% at 200 °C to 3% at 870 °C. This thermally activated behavior is consistent with the evaporation rate of stoichiometric Si_3N_4 [15].

Figure 6 illustrates the results at room-temperature for the refractive index n and extinction coefficient k of nonirradiated and irradiated a-SiN_x:H films. Irradiation led to an increased refractive index, regardless of the energy level. Specifically, the refractive index increased from 1.92 to 1.96 with irradiation at 1.96 eV (633 nm). The values remain lower than the 2.00 for stoichiometric Si_3N_4 because of the many H atoms still in the network. The Δn values for the eight specimens ranged from 0.034 to 0.046, which are among the largest values ever reported for silicon-based optical materials. These values are independent of the temperature during

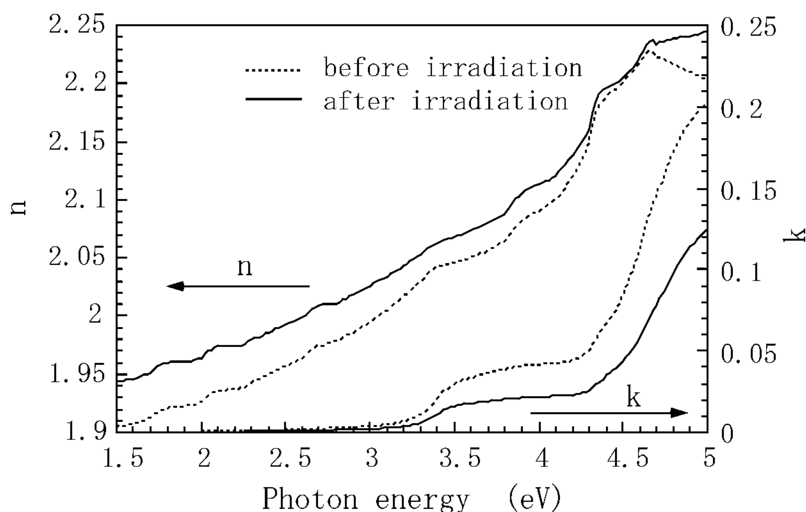

Figure 6. Room-temperature refractive index n and extinction coefficient k of the a-SiN_x:H film before (dotted lines) and after (solid lines) irradiation at 200 °C.

irradiation, further confirming that the change is produced by photolytic reaction kinetics. The decrease in the volume of the c-Si component lowered the k value in the ultraviolet region. The combination of a positive Δn and negative Δk is a unique feature of the a-SiN_x:H system.

Irradiated and non-irradiated samples were also evaluated by Fourier transform infrared spectroscopy. This revealed absorption bands at 3350, 2190, and 830 cm^{-1}, which are assigned to absorption by stretching of N-H, Si-H, and Si-N bonds, respectively. Irradiation led to significantly less absorption by N-H, slightly more absorption by Si-H, and slightly less absorption by Si-N. The numbers of N-H, Si-H and Si-N bonds after irradiation at temperatures above 200 °C is temperature-insensitive [26].

3.2. *Microscopic models for the network rearrangement*

The refractive indices of materials are changed by one or some combination of three known mechanisms [27]. The first is the creation of color centers, where the change in the refractive index is according to the Kramers-Kronig relation. The second is the formation of electric dipoles through retrapping of holes and electrons, which induces a local index change. However, measurements of spin density by electron spin resonance spectroscopy revealed that the number of dangling-bond terminated defects created by irradiation was of the order of 10^{18} cm^{-3}. This only produces a Δn of the order of 10^{-5}. Therefore, the much greater Δn seen in the present system is not explicable in terms of either of these mechanisms.

The third mechanism is a change in the density of the constituent atoms that contribute to polarization. This was originally proposed to account for the change seen in a-SiO_2 with compaction by electron-beam irradiation [28]. The relative change in volume is expressed by the Lorentz-Lorenz relation [29]: $\Delta n/n = -[(n^2 - 1)(n^2 + 2)/6n^2](\Delta v/v + \Delta\alpha/\alpha)$, where v is the molecular volume and α is the molecular polarizability. Assuming that the polarizability is fixed, n = 1.92 and Δv/v = 9.8%, yields Δn/n = 6.77%, which is of the same order as our experimental result, Δn/n = 2%.

It is thus evident that the large volume taken up by the voids around the hydrogen-terminated sites is responsible for the large value of Δn. Electronically exciting the atoms stimulates cross-linking, expressed as

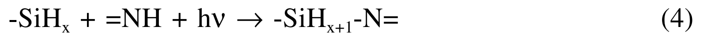

$$\text{-SiH}_x + \text{=NH} + h\nu \rightarrow \text{-SiH}_{x+1}\text{-N=} \qquad (4)$$

is primarily responsible for the compaction. Another bond rearrangement scheme involving the release of H_2 is also possible:

$$\text{-SiH}_x + \text{-NH}_y + h\nu \rightarrow \text{-SiH}_{x-1}\text{-NH}_{y-1}\text{-} + H_2 \qquad (5)$$

Lucovsky et al. [30] have suggested that films of a-SiN_x:H grown by plasma-enhanced CVD may be treated as mixtures of Si_3N_4 and $Si(NH)_2$. $Si(NH)_2$ is iso-structural with SiO_2, but bridging NH groups in the former substance replaces

the bridging oxygen atoms of the latter. This means that the network of $Si(NH)_2$ is readily rearranged by exposure to electronic excitation. Another important point is that the restructured network is more similar to stoichiometric Si_3N_4. This is because Si_3N_4 has a relatively constant structure under exposure to radiation.

Various explanations are possible for the differences between the stability of a-SiO_2 and a-Si_3N_4 under exposure to electronic excitation. The coordination numbers of the atoms in which the network lead to different degrees of structural freedom [31]; in terms of the surrounding Si atoms, the nitrogen atoms in Si_3N_4 are three-fold coordinated while the oxygen atoms in SiO_2 are two-fold coordinated. Obviously, a larger coordination number produces a stronger resistance to the displacement of atoms into interstitial sites. In the case of question here, the simultaneous rupture of three Si-N bonds is unlikely. The Si-N bond also has a greater covalency than the Si-O bond. A greater covalency means faster hopping decay for the valence holes produced by the Auger decay of the core holes than the initial photo-excitation creates [32].

4. Radiation effects in a-Si:H

4.1. *Layered structure of crystalline and amorphous components*

Films of hydrogenated amorphous silicon (a-Si:H) are widely used in electronic and photonic devices such as thin-film transistors and solar cells, and the fundamental properties of these films (for example, conductivity and optical response), are critically dependent on the concentration of hydrogen atoms. The defects created when such films are exposed to light in the range from visible to ultraviolet play a crucial role as contributions to the degradation of solar cells [33, 34]. In this section we focus on the bond exchange and network restructuring when a-Si:H films are irradiated with high-energy photons at low temperatures, such that irreversible changes are produced [35].

a-Si:H films were deposited in various thicknesses (100–800 Å) on Si(100) wafers at 200 °C or 400 °C by SR-CVD from Si_2H_6 gas at a relatively high pressure of 7 $\times 10^{-3}$ torr and a low storage current, between 250 and 300 mA. The structural changes were induced by post-irradiation at higher levels of storage current, between 420 and 470 mA. Typical room-temperature pseudo-dielectric functions before and after irradiation are compared in Figure 7. The $\langle\varepsilon_2\rangle$ spectrum obtained from a film as-deposited at 200 °C (410Å thick) has a single broad peak centered at 3.3 eV, reflecting an amorphous (a-Si) outermost layer (Figure 8(a)) [36, 37]. After only a few minutes of SR-beam irradiation at 200 °C, the peak energy blue-shifted by 0.15 eV and the amplitude between 3 and 4 eV increased; this increase apparently indicates on the densification of the film in the near-surface region [38]. The amorphous layer of a Si film deposited at 400 °C was thin (150Å), reflected in the asymmetrical $\langle\varepsilon_2\rangle$ spectrum (Figure 8(b)). Post-irradiation at 400 °C produced shoulder structures at 3.4 and 4.25 eV, which indicates the regrowth of large crystalline domains that in some cases reach the surface [37]. In a thin film case

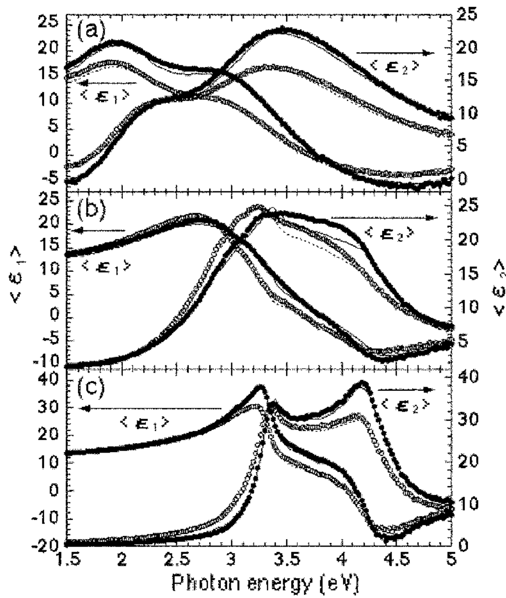

Figure 7. The real and imaginary parts of the pseudo-dielectric functions obtained before (open circles) and after (solid circles) irradiation of a-Si:H films. The dotted and solid curves show calculated spectra for the sample before and after irradiation.

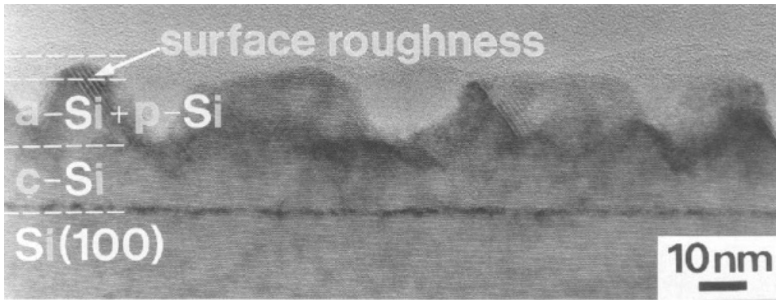

Figure 8. An XTEM image of an a-Si film deposited at 200 °C and post-irradiated at 200 °C.

(Figure 8(c)), the $<\varepsilon_2>$ spectrum resembles that of crystalline Si (c-Si) [39]. Post-irradiation at 400 °C increased the amplitude between the E_1 (3.4 eV) and E_2 (4.25 eV) critical points of band-to-band transitions.

The XTEM image in Figure 8 shows a representative layered structure of the film, consisting of a 140-Å-thick layer of c-Si, a 120-Å-thick outer layer of polycrystalline Si (p-Si) islands, and a 50-Å-thick amorphous surface-roughness layer. For linear-regression analysis of the $<\varepsilon>$ spectra, we used a two-layer model comprised of an (a-Si+void) top layer and (a-Si+c-Si+void) outer layer on a Si(100)

surface with Bruggeman EMA [13]. The epitaxial c-Si layer is not able to be optically discriminated from the substrate.

The thickness contribution and volume fraction of the a-Si, c-Si, and void components in each layer before and after irradiation were optimized to fit the experimental spectra. These calculated spectra are shown in Figure 7, and have a good fit with the measured spectra. For the sample in Figure 8, the best-fit thickness contributions (d_1 and d_2) and volume fractions (f_1 and f_2) of the outer (subscript 1) and top (subscript 2) layers were d_1 = 127.6 Å, d_2 = 53.8 Å, f_1(a-Si) = 0.43, f_1(c-Si) = 0.57, f_1(void) = 0.0, f_2(a-Si) = 0.80, and f_2(void) = 0.20. Once the parameters are obtained, the nominal thicknesses are obtained from the a-Si, c-Si, and void volumes by calculating d_1f_1(a-Si)+d_2f_2(a-Si), d_1f_1(c-Si), and d_1f_1(void)+ d_2f_2(void), respectively. The differential thickness, i.e., the difference between the nominal thickness before and after post-irradiation, was used to evaluate the effect of the radiation.

4.2. *The processes of photolytic network rearrangement*

Slightly ionic Si-H bonds are broken by the direct Auger-stimulated mechanism which is initiated by core electronic excitation [40]. Although photon-stimulated desorption (PSD) is a surface phenomenon, the mechanisms involved are also relevant to the electronically excited bond-breaking processes that occur inside the bulk material [41]. The cross-section for all Si-H bonds contained in the Si-Si network is substantial. Irradiation of a-Si:H films at 200 °C leads to an increase in the volume of a-Si and decrease in the volume of voids. If we assume that these changes are correlated and that the voids correspond to density deficits associated with hydrogen-terminated defect sites, the most likely explanation for these changes is as follows. If a dangling bond site [-$SiH_{x-1}\cdot$] is able to interact with the nearest-neighbor Si chain, a Si-Si bond, which contributes to the amorphous network, is created at the cost of a Si-H bond. This local bond exchange leads to densification is expressed as

$$-SiH_x + -SiH_y + h\nu \rightarrow -SiH_{x-1}\text{-}SiH_{y-1}- + H_2 \quad (6)$$

The reaction (6) will thus trigger the formation of Si ad-molecules into networks. In fact, quadrupole mass spectroscopy yielded strong desorption signals for H_2 but no SiH_x signals.

When a specimen was irradiated at 400 °C, the network was significantly restructured. The volumes of both a-Si and voids decreased and the volume of c-Si increased. This means that recrystallization took the form of thermally assisted conversion of a-Si into c-Si [42]. Irradiation always reduced the void volume, regardless of the temperature. This suggests that vacancies in the network are prerequisite to bond exchange and network restructuring.

5. Elementary processes in synchrotron radiation excited homoepitaxy of silicon

5.1. *Thermal interaction of Si_2H_6 with Si (100) surface probed by TOFMS*

At temperatures below the threshold for H_2 desorption from silicon hydride species on Si(100) surface, the reactive sticking of Si_2H_6 proceeds in a self-limiting manner according to this schemes [43, 44]:

$$Si_2H_6(g) \rightarrow Si_2H_6(a) \tag{7}$$

$$Si_2H_6(a) + 2_ \rightarrow 2SiH_3(a) \tag{8}$$

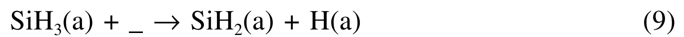

$$SiH_3(a) + _ \rightarrow SiH_2(a) + H(a) \tag{9}$$

where (g) and (a) respectively designate the gas and adsorbate and [_] is a dangling-bond-terminated surface site. Since the hydride coverage was below the limit for detection by *in-situ* SE, TOFMS was used to detect surface species by PSD [2]. Figure 9(a) shows a typical mass spectrum of the positive ions desorbed from a clean Si(100) surface in a UHV. After the signal response to SR photons (time zero), intense H^+ and weak F^+ and HF^+ ion signals appeared. The origin of the F^+ and HF^+ ions is in trace amounts of impurities such as BH_x (dopant) and HF, which could be introduced during the wet pretreatment [45]. Other than the F^+ and HF^+, H^+ was the only desorption product from the clean surface [46, 47]. The high-resolution spectrum for H^+ given in Figure 9(b) is bimodal in structure, having two distinct peaks, designated as α-H^+ and β-H^+.

The different flight times of the species that contribute to the α-H^+ and β-H^+ is ascribed to their bonding to different partner species on the Si surface. To investigate the respective origins, the surface was exposed to Si_2H_6 gas at a saturation dose and then returned to a UHV [48]. Along with the species seen in Figure 9(a), H_2^+ now appears, Figure 9(c). In this case, the yield of α-H^+ increased fivefold but the yield of β-H^+ was almost unchanged, Figure 9(d). The increase in the presence of the species responsible for the α-H^+ peak, with increased chemisorption of Si_2H_6, indicates that these ions were ejected from hydrogen bound to SiH_x(a) and that the ions contributing to the non-affected β-H^+ peak were bonded to other atoms, e.g. in HF or BH_x. Another noteworthy point is that desorption products containing Si atoms were not seen at all. This means that bond breaking occurs exclusively at the slightly ionic Si-H bond and that the entirely covalent Si-Si bond is very rarely or never broken.

PSD from SiH_x(a) relies on the excitation of Si(2p) (100 eV) or Si(2s) (150 eV) electrons. Since the Si-H bond is strongly covalent, Coulombic repulsion between the Si and H atoms of the surface requires that more than two holes be localized within the Si-H bond for a sufficient period after re-excitation of the electrons from the valence orbital [46, 47]. H-F and H-B bonds, on the other hand, have more of an ionic character, leading to much higher yields of H^+ desorption in these cases. The yields of α-H^+ and H_2^+ from the surface are consistent with

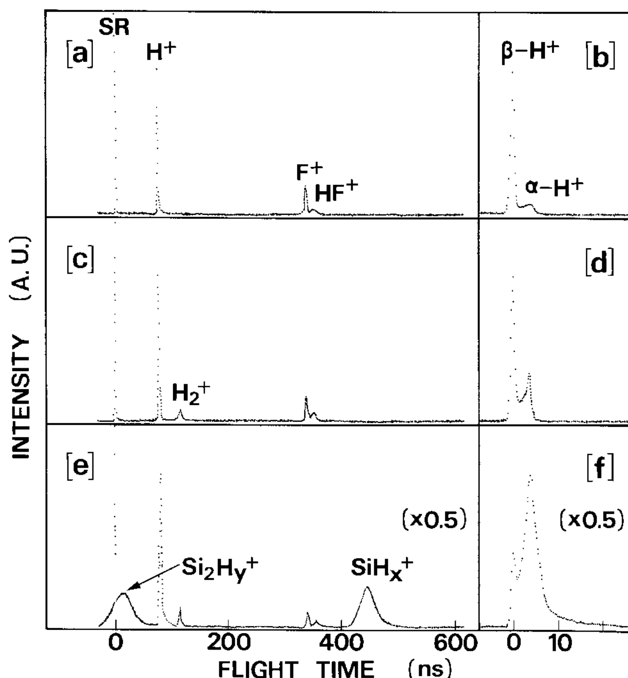

Figure 9. TOFMS spectra obtained from a clean Si(100) surface ((a) and (b)), from a Si(100) surface with chemisorbed Si_2H_6 ((c) and (d)), and during SR-CVD with Si_2H_6 pressure of 5.1×10^{-6} torr ((e) and (f)). The mass number is proportional to the square root of the flight time. (b), (d), and (f) are high-resolution spectra of the regions around the respective H^+ signals.

considerations of thermodynamical stability of hydrides on Si(100). The following is a summary of the PSD channels for α-H^+, β-H^+, and H_2^+.

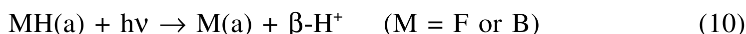

$$MH(a) + h\nu \rightarrow M(a) + \beta\text{-}H^+ \quad (M = F \text{ or } B) \tag{10}$$

$$SiH(a) + h\nu \rightarrow Si(a) + \alpha\text{-}H^+ \tag{11}$$

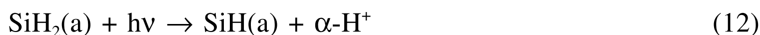

$$SiH_2(a) + h\nu \rightarrow SiH(a) + \alpha\text{-}H^+ \tag{12}$$

$$SiH_2(a) + h\nu \rightarrow Si(a) + H_2^+ \tag{13}$$

5.2. *Interaction of photolysis products with the Si(100) surface*

Consider now the TOFMS spectra obtained during SR-CVD growth, which are given in Figures 9(e) and 9(f). The SiH_x^+ (x = 0–3) and $Si_2H_y^+$ (y = 0–6) signals intensified with the increased pressure of Si_2H_6. The $Si_2H_y^+$ signal is distributed at the 15-ns position in the spectrum, which corresponds to a total flight time of 639 ns. The poor mass resolution was a result of photoionization occurring along the whole SR beam path, flight time consequently varied with position. For the same reason,

the α-H^+ peak is markedly more intense than under UHV and has a tail in the direction of longer flight times.

The yields of α-H^+ and H_2^+ increase linearly with the pressure of Si_2H_6 because they are created by photoionization of the Si_2H_6 molecule. The relative contributions of PSD and the photolysis of Si_2H_6 can be determined from the dependence of the α-H^+ yield on pressure. The yield as obtained by extrapolation to zero pressure is ascribed to PSD from SiH_x(a), whereas the growth in proportion to pressure is ascribed to a gas-phase process.

SR-excited atomic layer epitaxy (SR-ALE) [49, 50] is a digital growth method in which a sequence of gas exposure, evacuation, and SR irradiation of the surface is repeated. Dangling bonds are regenerated by the PSD of ligand (hydrogen or halogen) atoms that have been used to passivate the surface. In SR-excited chemical vapor deposition (SR-CVD) [51, 52], on the other hand, deposition takes place in a period of continuous exposure of the substrate to the SR beam and reactant gas. The kinetic pathways for the deposition of Si atoms by SR-CVD include the photolysis of Si_2H_6 molecules, reactive sticking of fragments thus photo-decomposed, and regeneration of dangling bonds [52]. The question we need to answer is how the Si ad-molecules introduced to the surface are incorporated into the bulk Si crystal. The responsibility of the following process of sequential conversion has been verified:

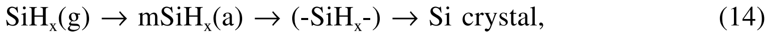

$$SiH_x(g) \rightarrow mSiH_x(a) \rightarrow (\text{-}SiH_x\text{-}) \rightarrow \text{Si crystal}, \qquad (14)$$

where SiH_x(g) denotes photolysis products in the ambient atmosphere, $mSiH_x$(a) indicates multiple layers of silicon hydride at the outermost surface, and (-SiH_x-) is the infant stage of a Si-Si network which is formed beneath the $mSiH_x$(a). Formation of the $mSiH_x$(a) layer indicates that the epitaxial growth in SR-CVD proceeds in a multilayer mode rather than in a layer-by-layer manner.

5.3. *Detection of $mSiH_x(a)$ and (-SiH_x-) by* in-situ *SE*

When a Si(100) surface is simultaneously exposed to Si_2H_6 gas and an SR beam, changes in the ellipsometric angles are detectable by *in-situ* SE [53]. Figure 10 shows how the $\langle\varepsilon\rangle$ spectrum changes in response to Si_2H_6 exposure and evacuation under irradiating the SR beam. The peak amplitudes at the E_1 (3.4 eV) and E_2 (4.25 eV) critical points decreased with exposure of the surface to Si_2H_6 gas and they recovered to their initial levels with evacuation of the gas. This suggests the presence of an overlayer which has a dielectric constant smaller than that of c-Si.

The difference between the optical responses of $mSiH_x$(a) and c-Si is ascribed to the contribution of Si-H bonds [54, 55]. If the dielectric function of the overlayer is much smaller than that of the substrate (ε_s), the pseudo-dielectric function $\langle\varepsilon\rangle$ can be approximated by the equation $\langle\varepsilon\rangle = \varepsilon_s + 4\pi i d\varepsilon_s^{3/2}\lambda^{-1}$, where λ is the wavelength of the light and d is the thickness of the overlayer [56]. Applying this formula near the E_1 critical point energy in Figure 10 yields the value of 3Å for the thickness of the $mSiH_x$(a).

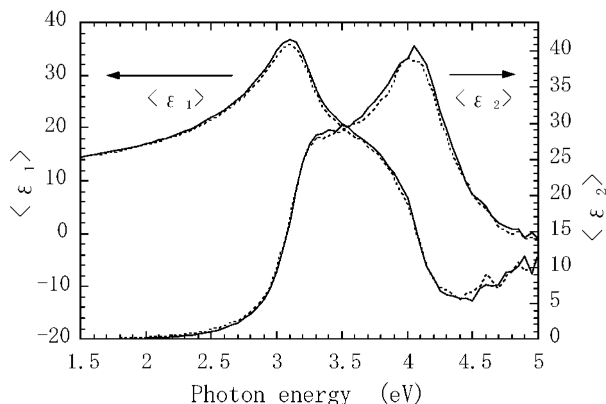

Figure 10. Real and imaginary parts of the pseudo-dielectric functions of Si(100) surface at 200 °C by irradiation under exposure to Si_2H_6 gas at 2×10^{-3} torr (dotted curve) and after evacuation of the gas (solid curve).

Figure 11(a) shows an Ψ-Δ trajectory at 400 °C where Si_2H_6 gas was introduced at a pressure of 3×10^{-3} torr without irradiating the Si(100) surface by the SR beam and then evacuated until the 10^{-7} torr range was reached. The (Ψ, Δ) points are randomly scattered within a very narrow region $|\delta\Psi| < 0.05°$ and $|\delta\Delta| < 0.05°$ around the center (20.22°, 145.72°), which represents the background noise level of the measurement system.

Figures 11(b), 11(c), and 11(d) depict trajectories at 400 °C produced by exposure to Si_2H_6 for 60 s, in the presence of irradiation by the SR beam. Within 10 s of introduction of the gas, the (Ψ, Δ) point moved immediately (trace A → B). At 3.4 eV, the shifts in (Ψ, Δ) were mainly in the Ψ direction. At the lower levels of photon energy (2.3 and 1.5 eV), however, the directions of the shifts had increasingly significant components in the Δ direction. The shift in the Ψ angle, ΔΨ, was –0.15° at 3.4 eV. When the Si_2H_6 gas was removed, the reverse change occurred, along trace C → D (δΨ = 0.15°), but here the relaxation time was longer, 50 s. Since the stationary trajectory during film growth (trace B → C) is orthogonal to these trajectories, the immediate shifts associated with beginning and end of the Si_2H_6 exposure reflect surface phenomena caused by the interaction of photolysis products with the Si(100) surface. A reasonable interpretation is that the surface, initially terminated with dangling-bonds, is immediately passivated by an adlayer of SiH_x(a) which the atmosphere of Si_2H_6 makes possible. The Si adatoms thus produced have dangling bonds and may be incorporated as constituents in the Si-Si crystal network. Trace B → C, in contrast, was identified as corresponding to the build-up of a void-containing (-SiH_x-) network of crystalline character in the near-surface region. The formation of mSiH_x(a) is thus clearly distinguishable from the building up of (-SiH_x-).

The sizes of the immediate shifts, |δΨ| and |δΔ|, provide an index of the abundance of hydride species at the surface. At 1.5, 2.3 and 3.4 eV, the values of these shifts were constant between 1×10^{-4} and 4×10^{-3} torr. This suggests that the

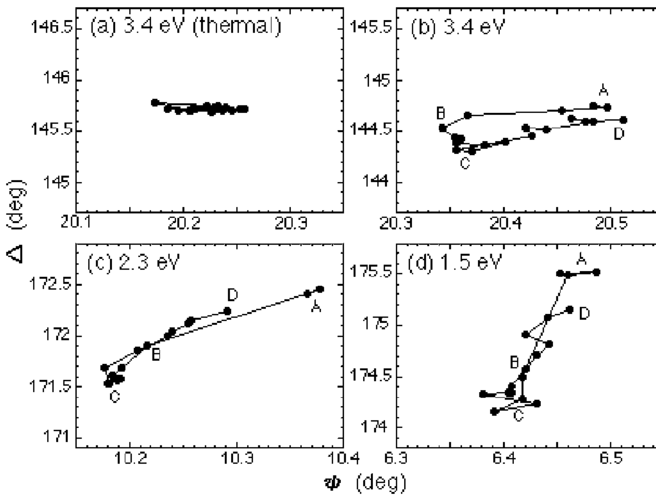

Figure 11. Ψ-Δ trajectories by exposure of Si_2H_6 to Si(100) surface at 3×10^{-3} torr (a) without irradiation and with irradiation at (b) 3.4 eV, (c) 2.3 eV, and (d) 1.5 eV. The (Ψ, Δ) data points were collected every 10 s and trace the sequence indicated by the alphabetical order of the labels. The exposure to Si_2H_6 was terminated at point C.

thickness of the hydride layer is self-limiting such that the layer is monoatomic. Once the monolayer of SiH(a) has been completed, further hydrogenation is possible at higher Si_2H_6 pressures. Above 4×10^{-3} torr, $|\delta\Psi|$ and $|\delta\Delta|$ increased gradually with pressure. Surface hydride chains are able to grow through such insertion reactions as [57]:

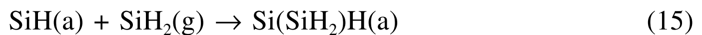

$$SiH(a) + SiH_2(g) \rightarrow Si(SiH_2)H(a) \qquad (15)$$

Such extension of the Si-Si chain network through repeated insertion reactions results in the greater shift in the ellipsometric angles. When random network formation prevails, surface flatness is not preserved, the nucleation rate is increased, and the crystallinty deteriorates.

5.4. *Dependence of the crystallinity of Si films on photon flux*

The growth modes inferred from the kinetic SE data have been categorized into three types, i.e. type I, II, and III, and the type is dependent on the absolute photon flux of the SR beam [58]. During type-I growth, the Si film is entirely epitaxial and its surface is covered by an $mSiH_x(a)$ layer. During type-II growth, the epitaxy is maintained but is now accompanied by the building up of a void-containing ($-SiH_x-$) network on the growing surface. During type-III growth, the epitaxy is terminated halfway.

The type-I mode appears under large photon fluxes (I_R = 420–370 mA). TEM images show that the Si overlayer is entirely crystalline and the Si/Si interface is

smooth [59]. The surface roughness of the Si overlayer is of atomic order. The trajectories are quite confined, never straying far from the starting point, as is illustrated in Figures 11(b), 11(c) and 11(d). This means that the epitaxial layer is not optically distinct from the Si substrate. The deposited Si ad-atoms are instantly incorporated in the Si crystal network and the growth proceeds in a layer-by-layer fashion.

Figure 12 depicts the type-II trajectory produced by intermittent exposure to Si_2H_6 with the surface being irradiated by a medium flux of SR. A 160-Å-thick Si film was grown in each cycle. As already described, we see the formation and decomposition of $mSiH_x(a)$. With regard to the first cycle (GR1), the (Ψ, Δ) point immediately moved to the left with the introduction of the Si_2H_6 gas (trace A $\rightarrow$ B), and immediately moved to the right when the Si_2H_6 gas was evacuated (trace C $\rightarrow$ D). The envelope curve of the traces during stationary growth (line B-C-E), on the other hand, indicates the deposition of a Si-Si network with a degree of crystallinity which differs from that of c-Si.

Trace B $\rightarrow$ C $\rightarrow$ E can be simulated by assuming uniform deposition of films of various compositions. A best-fit result for the B-C-E line was obtained by assuming the growth of a film with p-Si (70%) and void (30%) components, which corresponds to ($-SiH_x-$) in formula (16). As Ψ varied from 22.5° to 21°, a Si film 800 Å thick was grown, but the thickness of the overlayer at point E in Figure 12 is only 50 Å. This disagreement indicates that the void-rich Si overlayer ($-SiH_x-$) is continuously formed from the $mSiH_x(a)$ and is converted to c-Si at the interfacial region. If such recrystallization does not keep up with the supply of Si atoms, a void-containing network gradually builds up [59].

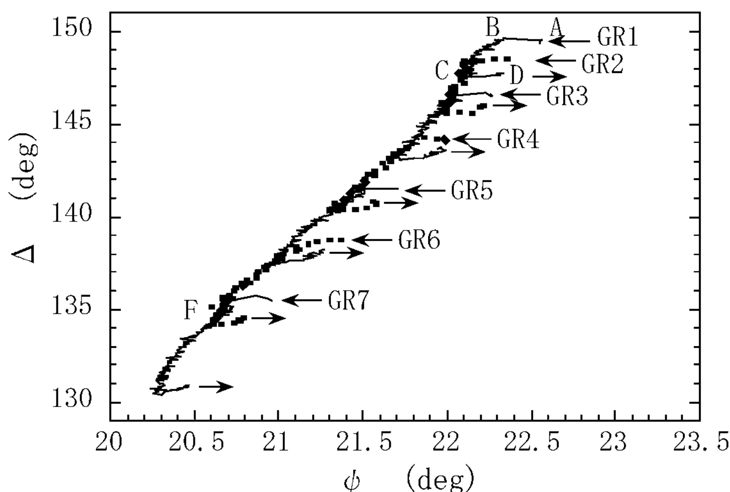

Figure 12. Ψ-Δ trajectories that represent type-II growth on Si(100) surface produced by 15-min cycles of Si_2H_6 exposure and evacuation. For clarity, the trajectories denoted by odd numbers are plotted as thin solid lines and the trajectories denoted by evan numbers are plotted as dotted lines. The ring current decayed from 370 to 280 mA during the seven cycles, and the Si_2H_6 pressure was 3×10^{-3} torr.

Figure 13 shows type-III trajectories produced by five cycles of growth under an SR beam of small flux. The longer trajectory than those of Figures 12 and 13 indicates the greater degree of deterioration in crystallinity from c-Si to a-Si. The fitting simulation curve to the experimental trajectories was obtained by assuming deposition of a 33-Å thick p-Si (50%) and void (50%) layer (trace A → B) followed by deposition of a 75-Å thick a-Si (60%) and void (40%) overlayer (trace B → C → D). The shape of the pseudo-dielectric function changed quickly, i.e., the E_1 and E_2 critical-point features disappeared after GR3 and were replaced by a single broad peak centered on 3.3 eV. A shift in the growth mode from type-II to type-III would occur when imperfections such as point defects and stacking faults involving higher-order hydrides begin to accumulate at a rate greater than that at which they can be repaired to retain crystalline form for the network.

6. Conclusion

Synchrotron-radiation-excited processing has potential for region-selective modification of materials at low temperatures. Real-time monitoring is prerequisite as a vehicle for the understanding of reaction kinetics and identification of reaction products. Radiation effects depend critically on the property of materials. In a-SiO_2, irradiation leads to the formation and annihilation of defects, decomposition of the network into volatile products, and precipitation of Si nanocrystals. The radiation effects on a-SiN_x:H are characterized by compaction of the network and

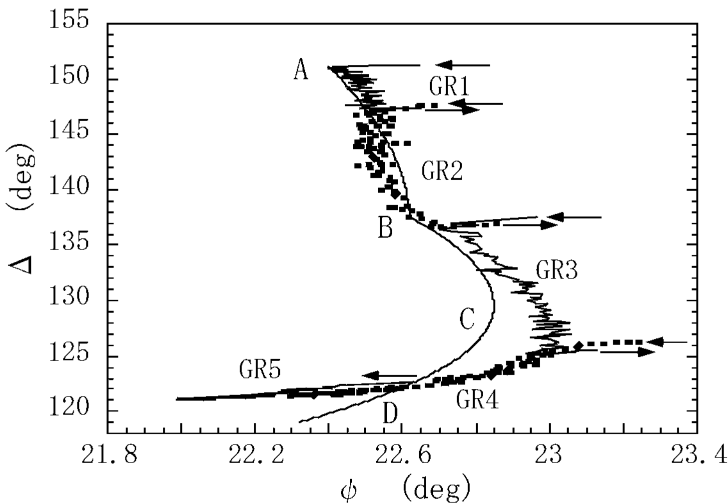

Figure 13. Ψ-Δ trajectories that represent type-III growth on Si(100) surface produced by five 15-min cycles of Si_2H_6 exposure and evacuation. For clarity, the trajectories denoted by odd numbers are plotted as thin solid lines and the trajectories denoted by even numbers are plotted as dotted lines. The ring current decayed from 290 to 270 mA during the five cycles, and the Si_2H_6 pressure was 3×10^{-3} torr.

large changes in the refractive index. In a-Si:H, densification and partial crystallization occur as a result of bond exchange. In synchrotron-radiation-excited homoepitaxy of Si film, evidence for the formation of surface hydride layer and the precursor state of Si-Si network that results in an epitaxial Si layer was presented.

References

1. H. Akazawa and J. Takahashi, *Rev. Sci. Instr.* **69**, 265 (1998).
2. H. Akazawa, *Nucl. Instr. Methods* **B 101**, 227 (1995).
3. B. Drevillon, J. Perrin, R. Marbot, A. Violet and J. L. Dalby, *Rev. Sci. Instr.* **53**, 969 (1982).
4. R. M. A. Azzam and N. M. Bashara, *Ellipsometry and Polarized Light* (Amsterdam: North-Holland, 1986).
5. R. W. Collins, *Rev. Sci. Instr.* **61**, 2029 (1990).
6. B. Drevillon, *Appl. Surf. Sci.* **63**, 27 (1993).
7. M. Niwano, H. Katakura, Y. Takakuwa, N. Miyamoto, A. Hiraiwa and K. Yagi, *Appl. Phys. Lett.* **56**, 1125 (1990).
8. S. Thomas, *J. Appl. Phys.* **45**, 161 (1974).
9. H. Akazawa, M. Nagase and Y. Utsumi, *Nucl. Instr. Methods* **B 91**, 644 (1994).
10. H. Akazawa, *Phys. Rev.* **B 51**, 7314 (1995).
11. H. Akazawa, Y. Utsumi, J. Takahashi and T. Urisu, *Appl. Phys. Lett.* **57**, 2302 (1990).
12. H. Akazawa, *J. Vac. Sci. Technol.* **B 19**, 649 (2001).
13. D. A. G. Bruggeman, *Ann. Phys. (Leipzig)* **24**, 636 (1935).
14. H. Akazawa, *Int. J. Mod. Phys.* **B 15**, 3749 (2001).
15. H. Akazawa, J. Takahashi, Y. Utsumi, I. Kawashima and T. Urisu, *J. Vac. Sci. Technol.* **A 9**, 2653 (1991).
16. M. Hamasaki, T. Adachi, S. Wakayama and M. Kikuchi, *J. Appl. Phys.* **49**, 3987 (1978).
17. D. J. Nesbit, *Appl. Phys. Lett.* **46**, 38 (1986).
18. D. V. Tsu, B. N. Davidson and G. Lucovsky, *Phys. Rev.* **B 40**, 1795 (1989).
19. B. J. Hinds, F. Wang, D. M. Wolfe, C. L. Hinkle and G. Lucovsky, *J. Non-Cryst. Solids* **227–230**, 507 (1998).
20. T. E. Tsai and D. L. Griscom, *Phys. Rev. Lett.* **67**, 2517 (1991).
21. R. A. B. Devine, *Nucl. Instr. Methods* **B 46**, 244 (1990).
22. H. Hosono, H. Kawazoe and N. Matsunami, *Phys. Rev. Lett.* **80**, 317 (1998).
23. R. A. B. Devine, *Nucl. Instrum. Methods Phys. Res.* **B 46**, 261 (1990).
24. K. O. Hill, Y. Fujii, D. C. Johnson and B. S. Kawasaki, *Appl. Phys. Lett.* **32**, 647 (1978).
25. H. Akazawa, *Appl. Phys. Lett.* **80**, 3102 (2002).
26. H. Akazawa, *Nucl. Instr. Methods* **B 116**, 355 (1996).
27. J. P. Bernardin and N. H. Lawandy, *Opt. Comm.* **79**, 194 (1990).
28. C. Fiori and R. A. B. Devine, *Mat. Res. Soc. Symp. Proc.* **61**, 187 (1986).
29. T.A. Dellin, D. A. Tichenor and E. H. Barsis, *J. Appl. Phys.* **48**, 1131 (1977).
30. G. Lucovsky, P. D. Richard, D. V. Tsu, S. Y. Lin and R. J. Markunas, *J. Vac. Sci. Technol.* **A 4**, 68 (1986).
31. L. W. Hobbs, *Nucl. Instr. Methods* b, 30 (1994).
32. D. E. Ramaker, *J. Vac. Sci. Technol.* **A 1**, 1137 (1983).
33. J. J. Chang, C. G. Lee, S. C. Park and C. Lee, *Appl. Phys. Lett.* **51**, 1673 (1987).
34. C. S. Hong and H. L. Hwang, *Appl. Phys. Lett.* **49**, 645 (1986).
35. H. Akazawa, *J. Non-Cryst. Solids* **271**, 73 (2000).
36. R. W. Collins, 'Ellipsometric Study of a-Si:H Nucleation, Growth, and Interfaces', in H. Fritzsche (ed.), *Amorphous Silicon and Related Materials* (Singapore, World Scientific, 1988), p. 1003.
37. S. Kumar, B. Drevillon and C. Godet, *J. Appl. Phys.* **60**, 1542 (1986).

38. N. Layadi, P. Rocca i Cabarrocas, V. Yakovlev and B. Drevillon, *Thin Solid Films* **233**, 281 (1993).
39. V. Nayar, W. Y. Leong, C. Pickering, A. J. Pidduck, R. T. Carline and D. J. Robbins, *Appl. Phys. Lett.* **61**, 1304 (1992).
40. D. E. Ramaker, C. T. White and J. S. Murday, *Phys. Lett.* **89A**, 211 (1982).
41. D. R. Jennison, J. P. Sullivan, P. A. Schultz, M. P. Sears and E. B. Stechel, *Surf. Sci.* **390**, 112 (1997).
42. H. Akazawa, J. Takahashi, Y. Utsumi, I. Kawashima and T. Urisu, *Appl. Phys. Lett.* **60**, 974 (1992).
43. Y. Suda, D. Lubben, T. Motooka, J. E. Greene, *J. Vac. Sci. Technol.* **B 7**, 1171 (1989).
44. S. K. Kulkarni, S. M. Gates, B. A. Scott and H. H. Sawin, *Surf. Sci.* **239**, 13 (1990).
45. Ph. Avouris, F. Bozso and A. R. Rossi, *Mat. Res. Soc. Symp.* **75**, 591 (1987).
46. M. L. Knotek, G. M. Loubriel, R. H. Stulen, C. E. Parks, B. E. Koel and Z. Hussain, *Phys. Rev.* **B 26**, 2292 (1982).
47. L. Hellner, L. Philippe, G. Dujardin, M.-J. Ramage, M. Rose, P. Cirkel and P. Dumas, *Nucl. Instr. Methods* **B 78**, 342 (1993).
48. H. Akazawa, *Phys. Rev.* **B 52**, 12386 (1995).
49. H. Akazawa, Y. Utsumi, T. Urisu and M. Nagase, *Phys. Rev.* **B 47**, 15946 (1993).
50. H. Akazawa and Y. Utsumi, *J. Appl. Phys.* **78**, 2725 (1995).
51. H. Akazawa, M. Nagase and Y. Utsumi, *Appl. Phys. Lett.* **64**, 754 (1993).
52. H. Akazawa and Y. Utsumi, *J. Appl. Phys.* **78**, 2740 (1995).
53. H. Akazawa, *Surf. Sci.* **427–428**, 214 (1999).
54. I. An, R. W. Collins, H. V. Nguyen, K. Vedam, H. S. Witham and R. Messier, *Thin Solid Films* **233**, 276 (1993).
55. H. Yao, J. A. Woollam and S. A. Alterovitz, *Appl. Phys. Lett.* **62**, 3324 (1993).
56. D. E. Aspnes, *Thin Solid Films* **89**, 249 (1982).
57. C. Isobe, H.-C. Cho and J. E. Crowell, *Surf. Sci.* **295**, 99 (1993).
58. H. Akazawa, *Phys. Rev.* **B 59**, 3184 (1999).
59. H. Akazawa, *Appl. Phys. Lett.* **70**, 3528 (1997).

CHAPTER 8

THIN NITRIDE FILMS DEPOSITED BY REACTIVE PULSED LASER ABLATION

Armando Luches* and Anna Paola Caricato
*Università di Lecce, Dipartimento di Fisica and Istituto Nazionale per la Fisica della Materia, 73100 Lecce, Italy (*Author for correspondence, E-mail: luches@le.infn.it)*

ABSTRACT: This chapter reviews the work done in our laboratory and others on synthesis and deposition of thin films of metal nitrides, using the reactive pulsed laser ablation (RPLD) technique. In particular, thin films deposition of transition-metal nitride e.g. TiN and VN, aluminum AlN and boron nitride BN films are detailed. The characteristics of the fabricated films are presented as a function of the deposition parameters, to explain their role and give useful information for the development and application of this innovative deposition technique.

1. Introduction

A challenging problem of modern materials science is to find new materials that can exhibit useful properties and deposit them as thin films on appropriate substrates. Thin film have important applications in advanced technologies such as microelectronics and optoelectronics. They are frequently used also to improve the surface properties, i.e., hardness, chemical inertness and electrical resistivity of bulk substrates. In this endeavor, lasers provide appropriate approaches for synthesis and deposition of materials of interest in modern technology. Laser-assisted surface modification [1], surface nitridation [2], dry etching ablation [3] and chemical vapor deposition [4] are now well established techniques. However, a new laser-based technique is now emerging with great potential: the pulsed laser ablation deposition (PLD) of thin films. In PLD, a powerful laser pulse vaporizes a target material placed in a vacuum chamber. Part of the vapor can be deposited on an appropriate substrate, placed a few centimeters from the target. By using hundreds or thousands of successive laser pulses, a continuos film can thus be grown.

Interest in PLD has experienced an explosive growth since 1987, when it was successfully used to deposit thin films of high critical temperature, T_c, superconductors [5]. This is due to the fact that PLD has the distinctive feature of preserving the stoichiometry of the target material i.e., congruent ablation. Hence, PLD is at present the best-suited technique for the deposition of multicomponent structures like high T_c superconductors, compound semiconductors, alloys, and polymers. The physical properties of the films obtained by the PLD technique are often superior to those obtained by conventional evaporation and electron-beam evaporation. Moreover, the highly non-equilibrium conditions during the PLD process enable the synthesis of metastable phases, unobtainable by conventional fabrication methods.

Aaron Peled (ed.), Photo-Excited Processes, Diagnostics and Applications (PEPDA), 225–250, 2003.
© 2003 *Kluwer Academic Publishers. Printed in the Netherlands.*

In the last years a new PLD variant laser-based technique has been emerging, i.e., the reactive pulsed laser ablation deposition (RPLD) of thin films. In the RPLD method a solid surface collects the material ablated by the laser irradiation of an element target which reacts with a low-pressure ambient gas or vapor. In this way, oxides, nitrides and carbides can be deposited as thin films by ablating an element material in an appropriate low-pressure atmosphere, i.e., O_2 for oxides, N_2 or NH_3 for nitrides, CH_4 or C_2H_2 for carbide film deposition. The RPLD method offers many advantages over traditional techniques, such as: (a) much lower cost of materials since usually elements targets are employed, (b) a low material consumption, (c) short processing times, as long as films of reasonable area and thickness are deposited. Moreover, multilayered films can be deposited by simply changing the process gas and/or the irradiated target. Also, long lasting high temperature post annealing processes are usually not needed. Hence, deep diffusion of the impurities can be avoided. Thus, films can be deposited on any kind of substrate material, even on thermolabile substrates like polymer films and paper [6]. This feature makes RPLD a low thermal budget technique. Note that traditional nitridation/carbidation of materials is done at very high temperatures, of the order of 1000 °C for periods longer than ~1 h. Furthermore, laser light does not introduce pollutants onto the deposition site and the use of corrosive and toxic gases can be avoided. Thus, the ambient gas for nitride film deposition is usually molecular nitrogen, N_2. For carbide film deposition methane, CH_4, is used most frequently, with minimum safety problems. These gases do not pose any pollution problem, in contrast with the gases and vapors currently used in thin film synthesis via chemical vapor deposition (CVD) or plasma enhanced chemical vapor deposition (PECVD).

Properties of the deposited films can be tailored by an accurate selection of the deposition parameters. The laser energy density (fluence) or power density at the target is the most important one. It influences the composition and structure of the deposited film, see e.g. refs. [7, 8]. Variations of the composition and/or structure of the films are due to the variation of the density and temperature of electron, ion and atomic species in the plasma plume [9] created by the interaction of the laser pulse with the target. The plasma plays a key role, since it determines the formation of reactive species and high-energy ions. The particle density, degree of ionization and kinetic energy of the ablated species depend mainly on the power density of the laser pulse. The ion density rapidly increases with increasing laser power density. Above ablation threshold, e.g., 70–100 MW/cm^2 for Ti, ~200 MW/cm^2 for Al, and ~250 MW/cm^2 for W, using an excimer laser [10], a non directional and non stoichiometric evaporation of materials is first observed. Then, a strong forward-oriented plume is created and stoichiometric ablation is observed. In the high-power regime, it is possible to calculate the angular distribution of the ablated materials and the thickness profile of the deposited film [11]. The ablated material is mostly ejected in the forward direction, with an angular distribution of $\cos^n\theta$ type, where θ is the angle to the normal of the target and n is a number between 5–12. By assuming an adiabatic expansion of the plasma plume [9] and a circular laser spot, the film thickness profile is well approximated by

$$h(r) = \frac{Mk^2}{2\pi\rho z^2}\left(1 + \frac{k^2r^2}{z^2}\right)^{-3/2}$$

where M is the mass of the ablated material, ρ is the film density, z is the target-to-substrate distance, k is a tabulated function [12] with a value between 2 and 10, depending on the radius of the laser spot at the target, on the laser pulse duration and on the adiabatic index $\gamma = c_p/c_v$ of the vapor. Here c_p and c_v are the specific heats at constant pressure and constant volume, respectively, of the expanding vapor. For typical deposition parameters, i.e. $\tau = 50$ ns, laser fluence F~1 J/cm^2, $z = 5$ cm, $M = 1$–10 μg, $\rho = 2.5$ g/cm^3 and $k = 2$, the deposition rate is of the order of 0.1–1 nm/pulse at the film center, with a half-thickness radius of ~2 cm. This means, that a monolayer/pulse can be deposited using high power lasers. In the case of an elliptical laser spot, typical of excimer laser beams, the thickness profile of the deposited layer is given by

$$h(\theta_x, \theta_y) = \frac{Mpq^2}{2\pi\rho z^2}\,[p + tg^2\theta_x + q^2tg^2\theta_y]^{-3/2}$$

where p and q are tabulated functions, $tg\theta_x = x/z$ and $tg\theta_y = y/z$ with x and y coordinates with origin at the center of the deposited film of elliptical shape [11].

The ablation rate of most materials increases at the lower laser wavelengths. At a given ablation rate, the deposition rate decreases with increasing target-to-substrate distance.

Noteworthy is the fact that the plasma plume generated by high-power laser pulses greatly differs from the vapor generated by traditional evaporation systems. In fact, the laser plasma plume is much hotter. As a consequence, the laser plasma consists mostly of atomic and ionic species even for molecular targets, and the vapor exhibits the same elemental composition as the target. Moreover, the high kinetic energies of the atomic and ionic species, typically tens of eV, lead to high-density films, frequently with a microcrystalline structure even when deposited on room-temperature substrates. The high kinetic energies of the plasma particles promote also chemical reactions even when ablation is performed in low-pressure atmospheres of poorly reacting gases, like molecular nitrogen.

Unfortunately, PLD and RPLD techniques have also some drawbacks. The main disadvantages of the PLD method are the difficulty in preparing films of homogeneous thickness on large area substrates, and the inclusion of particulate and droplets in the deposited films. Particulate originates from various physical mechanisms such as liquid phase ejection of the target material by the recoiling pressure of the laser produced plasma, explosive dislocation of fragments by the sub-surface overboiling of the target material and gas-phase condensation of the evaporated materials. Surface defects can be produced also in polycrystalline films by multiple orientation of the different crystal domains. However, special procedures and systems have already been developed to overcome these drawbacks, like mechanical shutters, shadow masks and fragmentation of particulate by means of laser pulses propagating parallel

to the target surface [13]. We stress that particulate-free films can be obtained by a proper choice of the laser fluence, of the target-to-substrate distance, and combined rotation and scanning of the compact and smooth targets to ensure uniform laser ablation.

Three main parts form a PLD/RPLD system (Figure 1): a laser, a beam delivery system and a vacuum chamber. Most frequently used are excimer lasers, such as XeCl, λ = 308 nm, KrF, λ = 248 nm, and ArF, λ = 193 nm, since ultraviolet (UV) radiation strongly interacts with almost any material. Their pulse length is in the range 10–50 ns and their repetition rate is 1–100 Hz. Shorter pulses are not convenient for RPLD. In fact, the thermal effect of picosecond pulsed laser ablation is smaller than that of nanosecond pulses and the ablation rate is very low. Higher repetition rates may cause interference between the plasma plume produced by successive laser pulses. The beam delivery system is formed by a set of lenses and mirrors. They have to allow the laser beam focusing on the target surface to achieve the preset fluence for ablation. The laser fluence at the target is usually limited to a few J/cm^2. The laser beam incidence angle at the target is of ~45°.

The deposition is usually done in stainless steel vacuum chambers. It is important to achieve a high vacuum, of 10^{-5}–10^{-6} Pa or better, before starting PLD or introducing the reaction gas for RPLD. Unwanted reactions of the ablated material with the background gas, especially with oxygen, which is highly reactive with almost all elements, must be avoided. The target to substrate distance is usually in the 20–120 mm range. The shorter the distance, the higher is the deposition rate, but the film thickness uniformity increases with increasing distance.

The deposited films are usually submitted to optical and electron microscopy such as SEM, TEM, and AFM, to investigate their surface morphology. The mean

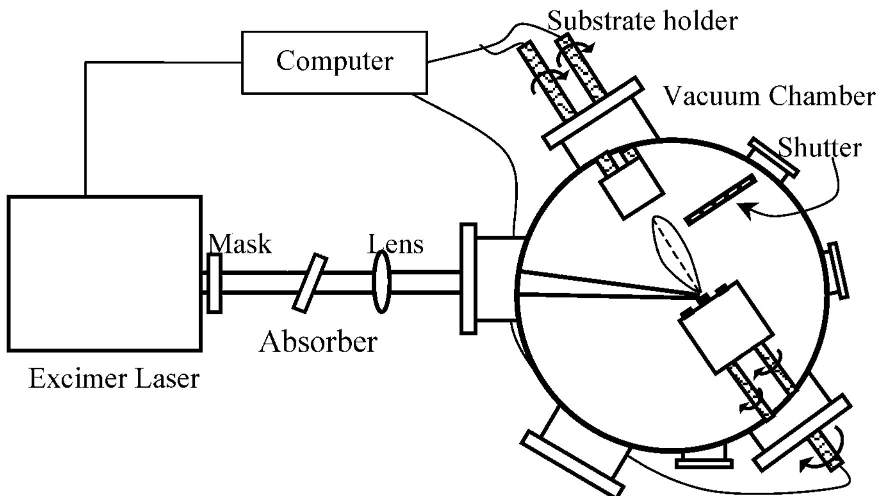

Figure 1. Schematic diagram of a PLD apparatus.

chemical composition of the films is determined with energy dispersive spectroscopy (EDAX) and Rutherford back-scattering spectrometry (RBS). Electron diffraction spectroscopy (EDS) and x-ray diffraction (XRD) are used to investigate the crystalline structure. Electron photoemission spectroscopy (XPS) and Fourier transform-infrared spectroscopy (FTIR) are used to obtain information about chemical bonding. Film thickness is usually determined by simulations of experimental RBS spectra with the Rutherford Universal Manipulation Program (RUMP) [14]. Micro-indentation is performed on films of interest for hard coatings.

Nitride and other ceramic films are usually deposited by PLD/RPLD on small substrates, since areas of ~1 cm^2 are sufficient for characterization purposes. Only recently ceramic films were deposited on large-area ~100 cm^2 and 3-dimensional substrates, to demonstrate that the technique is suitable for industrial applications. This can be done by computer-controlled movement of the large substrates with respect to the target [6].

2. Refractory-metal nitrides for hard coatings and microelectronic applications

In this section, we review the main results on RPLD of refractory metal nitride thin films. In particular, we report on deposition of Ti, V, Zr, Mo, Ta and W nitride thin films.

The nitrides of refractory metals have appealing properties for application in several fields. These compounds combine different properties such as very high hardness, high melting point and high chemical inertness. The reason for their good mechanical and chemical stability is thought to lie in the high directional nature of the metal-nonmetal pd hybrid bonding [15]. Moreover, they exhibit a high electrical conductivity, which accounts for being sometimes called ‘metallic’ compounds. This characteristic makes them ideal in microelectronics VLSI and ULSI applications for contacts and diffusion barriers. In particular, the titanium-nitrogen system has been and is intensively studied for use in mechanics [16] and microelectronics [17]. Much less studied is the vanadium-nitrogen system. Here two phases exist: the hexagonal β-V_2N and the cubic δ-VN. VN is a refractory compound and it is a superconductor with a transition temperature ranging from 2 to 9 K, depending on the nitrogen content [18].

The growth of thin films of transition metal nitrides though presents some problems. In fact, the vaporization of metals is hindered by the high temperatures required to achieve a sufficient vapor pressure. Metallorganic chemical vapor deposition (MOCVD) produces films with a high carbon and oxygen content, due to reactions of the deposited metal with the organic ligands. This is also a good reason why such nonthermal techniques, like sputtering, arc cathodic deposition, and most recently also our technique of RPLD are used.

2.1. *Laser deposition of Titanium nitride films: methods and results*

Particular attention has been paid to titanium nitride films, which were the first to be deposited by RPLD following the high T_c superconductors [19]. The properties of titanium nitride films strongly depend on their crystalline phase and stoichiometry. TiN single-crystals present a face-centered cubic (fcc) structure with a lattice constant $a = 0.424$ nm, a melting point of 2947 °C [7] and an electrical resistivity of 15 μΩ·cm, which increases to 50 μΩ·cm in the polycrystalline phase [20]. Dense, stoichiometric TiN films show hardness values higher than 20 GPa. The dependence of the hardness on the N/Ti ratio and crystalline phase is reported by Sundgren [16]. Serving for diffusion barriers, single crystalline films with a low defect level are required [21, 22]. Thin polycrystalline films provide both corrosion and wear resistance when coated onto metallic substrates. As a bio-compatible material, titanium nitride films may be applied in the coating of hip and knee prostheses.

Congruent laser ablation of TiN targets in vacuum and in N_2 at a pressure of ~5×10^{-2} Pa by an ArF excimer laser was first performed by Auciello et al. [19]. When ablation was performed in nitrogen atmosphere, almost stoichiometric polycrystalline TiN films, with grain sizes of 4–8 nm, were deposited. Substrates were Si (100) crystals at RT positioned at 3 cm from the target. Epitaxial TiN films were deposited by Narayan et al. [23] on MgO and Si (100) heated to 600–700 °C. They ablated TiN targets in vacuum and in N_2 atmosphere with pressures of 0.06–0.11 Pa, using KrF laser pulses with a fluence of 10 J/cm^2 and pulse duration of 25 ns. The electrical resistivity of these films was quite low, 15–17 μΩ cm. An alternative method was used by Chen et al. [24], to fabricate very smooth films and avoid droplet contamination. Ablation of TiN targets was performed in N_2 atmosphere at 6.7 Pa with a pulsed Nd:YAG laser at 335 nm at the fluence of 1 J/cm^2. Besides heating the Si substrates to 700 °C, a mask of appropriate size and location between the laser-induced plasma and the substrate was used. The closer the shadow mask is to the target, the slower the deposition rate is, but the better is the quality of the thin films. In the closest position, 70 mm, the deposition rate was only 2 nm/min at 10 Hz, but the film quality was excellent.

Reactive deposition of TiN films was first accomplished by Craciun et al. [25]. They ablated Ti targets in N_2 atmosphere by XeCl excimer laser pulses at fluences of 4–6 J/cm^2, fabricating polycrystalline TiN films on Si substrates. The RPLD of TiN films was studied in detail by Mihailescu et al. [26–28]. They performed exhaustive studies of the deposition parameters and accurate inspections of samples prepared by ablating Ti targets in nitrogen-containing atmospheres. It was found that molecular nitrogen, in spite of its very high binding energy, works well as a reactive gas. Thus the corrosive and more expensive ammonia was not used. Stoichiometric TiN films were easily formed by irradiation of pure (99.6%) Ti targets with XeCl laser pulses with 30 ns pulse duration, 4–5 J/cm^2 fluence, in N_2 ambient atmosphere at pressures ranging from 10^{-2} to 10^2 Pa. The deposited films exhibit the characteristic gold-yellow color of titanium nitride and a very good adherence to the substrate even when fabricated on substrates at room temperature. Typical

deposition rates are in the range 0.02–0.15 nm/pulse, depending on the ambient pressure and target-to-substrate distance. In particular, the deposition rate increases with increasing pressure up to ~10 Pa, then it decreases rapidly at higher ambient pressure. Surface quality is also better at low nitrogen pressure, up to ~10 Pa. Droplets are rare, with diameters of the order of 1 μm. The droplets density and dimensions increase significantly at higher pressures. From TEM and EDS studies it was observed that the film crystallinity also depends significantly on the gas pressure. Layers deposited at pressures higher than ~5 Pa have a lower content of crystalline phase, with partial amorphization, than the layers deposited at lower pressures. At p ~1 Pa the TiN crystallites have characteristics dimensions of 10–15 nm and the films consist entirely of fcc titanium nitride with a lattice parameter a = 0.424 nm. At pressures in the 10^2 Pa range, the crystallinity and stoichiometry of the compound are poorer than in the samples prepared in the range 10^{-2}–10 Pa. The droplets appearing on the sample surface showed the same composition as the underlying films.

Accurate investigations were made by the same authors about the nitridation process. Generally, the nitridation can be the effect of three subsequent steps of the RPLD process:

(1) direct nitridation on the target surface submitted to the multipulse laser action;
(2) nitridation during the transit of the ablated substance from the irradiated target to the substrate;
(3) nitridation on the collecting support by reaction with nitrogen molecules sticking to the surface of this support.

An evaluation of the relative role played by each of the above-mentioned factors was possible from the experimental evidence reported above, and especially from an accurate analysis of the composition of the droplets [26]. For the reaction during the time-of-flight, calculations show that it cannot significantly contribute to droplet nitridation. If one assumes a droplet velocity of 10 m/s, which is a lower limit for most cases [27], one gets a transit time through the N_2 gas from the metallic target to the Si collecting support for a few cm of ~1 ms. At the used ambient pressure range, one obtains that a metal droplet would be nitridated during its flight to about ten atomic layers from the surface. Thus, most of the metal inside the droplet would remain completely non-reacted. The ~10 atomic layers correspond to a depth of only 2–3 nm of stoichiometrically reacted material, an insignificant part of the droplet dimension which is from 0.1 μm to a few micrometers in diameter. Since droplets are in the micrometer range, their nitridation would also be insignificantly affected by processes taking place after the impact on the Si support. Focusing our attention on the target, the numerical simulation of the heating of target surface indicated that the irradiated area melts during each laser pulse. For 30 ns laser pulses, the duration of melt is ~150 ns, its depth is about ~1.2 μm and the depth of the laser evaporated layer is ~0.5 μm [27]. This means that a layer undergoes a melting process at least twice before its ablation. Thus, chemical reaction of titanium with nitrogen can take place and is enhanced in the hot liquid phase. Moreover, the melt duration is longer than that required for vortices and/or corrugations to develop

in the liquid titanium, events which actively propel fresh gas into the melted material. This is probably the most important contribution to the nitridation process. These results help conclude convincingly, that the titanium is already completely nitridated when it is ablated from the laser-spot area. In fact, this result is in agreement with the observation that the Ti target irradiated area exhibits an intense yellow color, characteristic of TiN layers. In conclusion, it is assumed that the TiN layer, which is deposited on substrates by RPLD, is formed on the target being ablated.

Some authors, to improve film stoichiometry, use radiofrequency (r.f.) discharges in the volume between the target and the substrate. Discharges ionize in part the ambient nitrogen and increase its reactivity. TiN films with good crystallinity and stoichiometry were grown [21] on Si (100) substrates, heated up to 900 °C. Ti targets were ablated with KrF laser pulses of 2–3.5 J/cm^2, in nitrogen atmosphere of 0.1 Pa, ionized by a r.f. discharge of 300–550 W. Well-crystallized films, with a preferred growth of TiN (200) parallel to the Si (100) substrate, were obtained at 700 °C, with 2.5 J/cm^2 and 500 W. These films had an almost stoichiometric composition, N/Ti = 0.97, while films grown in non-ionized molecular N_2 were found Ti-rich with N/Ti = 0.84.

Besides on Si crystals, TiN films were RPLD deposited also on other substrates, like stainless-steel [29]. The ablation source was a pulsed N_2 laser. Peak fluences up to 32 J/cm^2 were used, with laser pulses of 18 ns and repetition rate of 1 Hz. The best results were obtained under nitrogen pressure of 18–20 Pa. EDS patterns showed a cubic structure of the TiN films with a lattice parameter of 0.471 nm. It was also found that TiN can be RPLD deposited on thermolabile supports like teflon and paper [6], since heating of the substrates is not necessary when well crystallized films are not required.

In conclusion, it was found that it is quite an easy task to deposit polycrystalline TiN films within a broad range of laser fluences and nitrogen ambient pressures even on substrates at room temperature. Stoichiometric films are formed either at quite high laser fluences ~5 J/cm^2 or at lower fluences of about 2–3 J/cm^2 aided by RF discharges to generate atomic nitrogen. Heating of the substrates improves the crystallization of the growing films. High temperatures > 600 °C are required for single-crystalline film growth. Smooth and droplet-free layers can be obtained by special arrangements, like a large target-to-substrate distance and using a shadow mask between target and substrate.

2.2. *Growth of Vanadium nitride (VN and V_2N) films*

In contrast to TiN, only two papers reporting on PLD of VN films can be found in the literature. In the first [30], films were prepared on sapphire substrates heated to 450 °C by ablating vanadium metal targets with Nd:YAG laser pulses at a fluence of 2.5 J/cm^2. The ambient atmosphere consisted of a mixture of nitrogen and 3% hydrogen at 200 Pa. In the second work [31] the aim was to deposit stoichiometric and crystalline films and to test the possibility of selective formation of the two different nitrides, i.e. VN and V_2N. To this end parametric studies were performed: the target-to-substrate distance d was varied from 30 to 70 mm, the

KrF laser fluence F from 4.5 to 19 J/cm^2, the N_2 ambient pressure p from 0.5 to 200 Pa and the 3″ Si (111) substrate temperature T from 20 to 750 °C.

The results show that films deposited at low pressures, $p < 5$ Pa, present a gold-like color and are knife-scratch resistant. At higher pressures, p = 5–20 Pa, they begin to assume a brownish color, and are still resistant to scratch tests, while for pressures higher than 50 Pa they become almost black and are easily engraved. This trend is completely independent from the substrate temperature. It could be due to a less compact structure of films deposited at higher pressures, caused by the lower speed of the ablated material impinging on the substrate and the growing film, due to collisions in the gas phase.

RBS analysis showed that at fixed laser fluence, target to substrate distance and substrate temperature, the film deposition rate decreases with increasing ambient pressure. This fact is obviously due to the increase of the scattering rate in the gas phase with increasing ambient pressure. This has the consequence of broadening the material jet. The film deposition rate decreases also with increasing substrate temperature at fixed F, d and p. The effect can be due to desorption of elements from the growing film with increasing temperature. For instance, at F = 17 J/cm^2, d = 40 mm and p = 100 Pa, the deposition rate is 3.6×10^{-3} nm/pulse at T = 20 °C, 3.2×10^{-3} nm/pulse at T = 250 °C and 3.0×10^{-3} nm/pulse at T = 500 °C. The deposition rates are much higher at lower laser fluences. At F = 6 J/cm^2, p = 1 Pa, d = 40 mm and T = 20 °C, the deposition rate is 1.2×10^{-2} nm/pulse. This effect can be attributed to the reduced area of the laser spot at the target with increasing laser fluence, i.e., tighter focusing of the laser beam. Also, the deposition rate decreases naturally with increasing target-to-substrate distance. For instance, it is 8×10^{-3} nm/pulse for d = 50 mm and reduces to 7×10^{-3} nm/pulse for d = 60 mm, in otherwise identical experimental conditions, i.e., F = 5 J/cm^2, p = 1 Pa and T = 20 °C. Besides deposition rate, the N/V atomic ratio can be also inferred from RBS spectra. At fixed laser fluence, ambient pressure and target to substrate distance, the N/V atomic ratio increased with increasing the substrate temperature from 20 to 500 °C. Then, it decreased when the substrate temperature was raised to 750 °C. For instance, for F = 17 J/cm^2, d = 40 mm and p = 1 Pa, we found N/V = 0.29 at T = 20 °C, N/V = 0.36 at T = 250 °C, N/V = 0.41 at T = 500 °C, but N/V = 0.29 at T = 750 °C. This means that moderate heating of the substrate promotes the nitridation processes, while high temperatures have a detrimental effect, possibly because of desorption of nitrogen from the growing film. It should be noticed that very high N/V atomic ratios can be detected in films deposited at T = 250 °C as the N_2 ambient pressure p increases: N/V increases from 0.36 at p = 1 Pa to 0.80 at p = 10 Pa to 1.22 at p = 100 Pa, with the other deposition parameters as above. Films with a high N/V ratio can be deposited on substrates at RT, too: a value N/V = 0.87 was calculated in samples deposited at p = 10 Pa and T = 20 °C, with other ablation parameters as above. At lower fluence, F = 6 J/cm^2 and at T = 20 °C, it was found N/V = 0.82 in samples deposited at p = 1 Pa and N/V = 1 in the ones deposited at p = 2 Pa.

From XRD analyses performed on the above samples, it was found that already at moderate laser fluences an almost stoichiometric polycrystalline vanadium nitride

film was deposited on substrates at RT. For example, the XRD spectra relative to the films deposited at RT with a fluence of 6 J/cm^2, showed well evident, even if quite broad, VN peaks, indicating a vanadium nitride of good stoichiometry with incomplete crystallization. For laser fluences up to $F \sim 12$ J/cm^2 only VN peaks were detected. At relatively high laser fluence, 17 J/cm^2, also V_2N peaks were apparent and predominant. The same results were observed for samples deposited on substrates heated at 250 and 500 °C, in otherwise identical experimental conditions. The reduced peak width of the XRD spectra of the samples deposited with a substrate temperature of 500 °C was an indication of better crystallization of the film.

It can be concluded that VN films can be deposited under experimental conditions similar to those used for TiN deposition. For laser fluences up to ~12 J/cm^2 only the VN phase is formed. At very high laser fluences, 17 J/cm^2, the V_2N phase is dominant.

2.3. *Laser deposition of Zirconium nitride films*

Zirconium nitride (ZrN) has a friction coefficient lower than that of other transition-metal nitrides, while still showing a good hardness [32]. RPLD deposition of ZrN films is particularly attractive, since zirconium gives excellent ablation characteristics. Due to the relatively low mobility and density of its conduction electrons [33], the absorption depth of Zr for 5 eV photons is ~30 nm, more than twice of other transition metals. Its reflectivity at the same photon energy is more than one order of magnitude lower of any other metal. As a consequence, the ablation efficiency of Zr is very high. Moreover, the high melting and boiling temperatures of Zr minimize droplets formation, which hinders film quality.

Recently, ZrN films were RPLD deposited by Spillmann et al. [34] on 25-mm diameter Si (001) wafers and steel disks heated from RT to 600 and 525 °C, respectively. Nitrogen gas was delivered from a pulsed valve at the rate of 8×10^{17} molecules per pulse. The gas and laser pulses were delivered in the crossed-beam configuration [35] to avoid droplets deposition. The KrF laser pulses with τ = 17 ns, had a peak fluence of $F = 9.7$ J/cm^2. Films were grown using 75 000 laser shots, which produced typically film thickness of 350 nm on steel discs, placed at 50 mm from the target, and 125 nm on Si wafers, placed at 90 mm from the target. From XRD patterns only the fcc phase could be detected through the entire range of investigated growth temperatures. XPS analysis showed that the films were fully nitrified. A roughness analysis gave RMS values of ~2.1 nm on 2 μm × 1 μm AFM scans. Nanoindentation tests gave hardness values higher than 25 GPa, while friction measurements gave a coefficient of friction lower than 0.25.

2.4. *Deposition of Tantalum, Molybdenum and Tungsten nitrides*

Recently, thin films of nitrides of other refractory metals, Ta, Mo, W have also been successfully deposited on substrates at T = 25, 250 and 500 °C by RPLD. Pure (99.6%) metal targets were ablated with a KrF excimer laser at fluences of

$F = 7–8$ J/cm^2. Ambient nitrogen pressure was in the range $p = 1–100$ Pa [36]. Stoichiometric polycrystalline, bcc Mo_2N and TaN layers were obtained at $p = 10$ Pa and $T = 250$ °C. Stoichiometric microcrystalline layers entirely formed of bcc W_2N were obtained at the same ambient pressure but at higher substrate temperature, $T = 500$ °C.

We conclude that nitride thin films of all the refractory metals Ti, V, Zr, Ta, Mo and W, were successfully deposited by pulsed laser ablation, mostly with excimer lasers, from pure metal targets in low-pressure N_2 atmosphere. Laser fluence, ambient gas pressure and substrate temperature are the working parameters that need a careful selection to obtain the desired stoichiometric crystalline compounds.

3. Laser deposition of crystalline Aluminum nitride films

Aluminum nitride, AlN, is of great interest due to its outstanding mechanical, electrical, thermal and optical properties. Its wide bandgap, 6.2 eV at 300 K [37], high thermal conductivity, 320 W/mK at 300 K [38], and high surface acoustic wave velocity along the *c*-axis of 6×10^3 m/s [39] make it a promising material for high temperature, high power and high frequency applications. Additionally, AlN in the wurtzite crystal structure, with $a = 0.311$ nm, $c = 0.4982$ nm, which is the equilibrium crystal structure, is piezoelectric [40]. It has a high chemical and thermal stability up to 2200 °C [41], a high electric resistivity of 10^{13} Ω cm [42], high melting point, 3273 K [43], and dielectric strength of 14 kV/mm [44]. Moreover, AlN can be used as a buffer layer for epitaxial growth of high quality GaN films [45]. It has also the ability to accommodate both *n*- and *p*-type dopants [37].

Many different techniques were successfully applied to synthesize AlN films. Metallorganic chemical vapor deposition (MOCVD) [46], molecular beam epitaxy (MBE) [47] and CVD [48] produce layers of good crystalline quality, but at high substrate temperatures, 600–1200 °C. Expensive and corrosive gas mixtures must be used. Also, the corresponding deposition rates are very low. Deposition by reactive magnetron sputtering requires a high nitrogen background pressure and leads to a large surface roughness [49]. PLD and RPLD on the other hand combine the advantages of low-temperature operation and high deposition rates. Thus they became intensely investigated as alternative techniques to prepare crystalline films. Since film properties depend strongly upon deviation from stoichiometry, cristallinity and the nature and concentration of crystalline defects, intensive research has been conducted to find the best growth conditions.

Most of the research work on AlN thin film growth has been done by laser ablation of AlN targets. The most commonly used substrates are Si (100), Si (111), *c*-, *r*-, *a*-, and *m*-cut sapphire and Al_2O_3 with different orientations. In spite of the lattice mismatch between Si or Al_2O_3 substrates and AlN films i.e., 19.3–22.3% and 12.3% respectively, high quality epitaxial aluminum nitride layers have been grown at moderately high substrate temperatures, 700–800 °C [50–55]. Deposition on Si substrates is quite interesting, since the thermal expansion coefficient of AlN, 2.56×10^{-6} K^{-1} at $T = 293$ K, is close to that of silicon [56]. This enables

the integration of AlN thin-films in silicon-based IC technology. Regarding the sapphire substrates, *c*-sapphire is commonly used for materials with hexagonal symmetry, due to its crystalline structure and its relative low price; while *r*-cut sapphire is of particular interest for applications in surface acustic wave (SAW) devices. It must be noted, however, that AlN and Al_2O_3 show different thermal expansion coefficients.

The growth of stoichiometric AlN thin films by RPLD must overcome three major problems: (1) the nitrogen molecule high stability, (2) the low reactivity of nitrogen in comparison to oxygen and the great affinity of aluminum to oxygen and (3) the nitride barrier problems, which prevent attaining the correct film stoichiometry by post annealing treatments.

The problem of oxygen contamination is quite critical because oxygen impurities can lead to *n*-type conduction which influence the electrical and optical properties of the semiconductor [57]. Basillais et al. [58, 59] studied this problem both for laser ablation of an Al metallic target and for laser ablation of a stoichiometric AlN target. The Al target was irradiated with a KrF excimer laser at a fluence $F = 6$ J/cm^2 in nitrogen atmosphere of 1–10 Pa, or in a nitrogen plasma created by a r.f. discharge. The AlN target was irradiated with a frequency-quadrupled Nd:YAG laser either in vacuum or in low-pressure nitrogen, $p = 5 \times 10^{-2}$ Pa. The films were deposited on Si (001), Si (111) or Al_2O_3 (001) single crystals, heated in the range 600-–800 °C.

Irrespective of the method and growth conditions, oxygen atoms were always found in the deposited films. The background atmosphere was considered responsible for this contamination. For background pressures lower than 10^{-4} Pa, the dominant process responsible for film oxidation was considered to be the target oxidation. For background pressure higher than 10^{-4} Pa, the oxygen contamination can occur at each laser pulse due to chemical reactions in the gas phase. Oxides can be also formed at the surface of the growing film during the time interval between laser pulses, because of the great affinity of aluminum to oxygen and the much higher reactivity of oxygen by comparison to nitrogen atoms. Even in the best conditions of vacuum they used, a 10% oxygen contamination was always found in the deposited films, both for AlN and Al target ablation. It was also determined that oxygen concentration in the films depends on the laser fluence, especially for reactive laser ablation. In particular the O/Al atomic ratio in the films decreases as the laser fluence increases. The N/Al ratio is also very sensitive to the laser fluence. At first it increases with increasing fluence, because the electron collision process is favored in hotter plasma. Then it tends to an equilibrium value, due to the competition between the recombination and dissociation processes. A laser fluence of 5–6 J/cm^2 was found a good compromise to obtain an Al/N ratio close to 1. An increase in the nitrogen pressure is not recommended because of the consequent increase in oxygen contamination. In fact, the purest available nitrogen contains usually ~2 ppm of oxygen. Consequently, an increase of nitrogen partial pressure in the ablation chamber causes a proportional increase in the oxygen partial pressure. Due to the extreme reactivity of oxygen with respect to that of nitrogen, the overall result is an increased oxidation. Thus, to grow purer AlN

films by reactive laser ablation of Al it is necessary to boost the reactivity of the nitrogen atmosphere. It can be done by an additional source of atomic nitrogen, i.e., a nitrogen plasma created by an RF discharge. Films grown by Basillais et al. [58, 59] without the r.f. discharge have shown a N/Al ratio ~0.8, due to unreacted Al. Using the r.f. discharge with optimized experimental values, 13.56 MHz, 100–300 W, a N/Al ratio of ~1 was obtained. When deposited on Al_2O_3 (0001) substrates at 800 °C, the resulting films had mainly an orientation of the *c*-axis normal to the substrate. In contrast, polycrystalline films were obtained on (100) Si substrates.

Wu et al. [60] also found that the presence of an additional source of atomic nitrogen is of importance to deposit stoichiometric AlN films. They synthesized AlN films by means of pulsed laser ablation of an aluminum target in nitrogen gas in presence of a microwave discharge. A Nd:YAG laser, λ = 532 nm; τ = 5 ns; f = 10 Hz, at a fluence of 2 J/cm^2 was used for the ablation. The films were deposited on Si (100) substrates held at a temperature below 80 °C. From RBS analyses an Al/N ratio ~1 was observed. The presence of the AlN phase was confirmed by XPS and FTIR characterizations. The spectra of Al 2p and N 1s signals show only one component, at 74 eV and 397.5 eV, respectively, fingerprint of the Al-N bonding [61]. The FTIR spectra, performed in the range 500–3000 cm^{-1}, showed the strong absorption peak at 665 cm^{-1}, characteristic of the transverse optical phonon modes of AlN [62]. The films were highly transparent, with a transmittance of 80%–90% in the visible and near-IR ranges. A bang gap of 5.65 eV was determined.

Nitrogen reactivity can be increased working with a very hot plasma plume. To this end, a very high laser fluence, 25 J/cm^2, was used for AlN thin film deposition by Verardi et al. [63]. They ablated Al targets with a Nd:YAG laser, λ = 1,06 μm, τ = 10 ns. They performed a parametric study by varying in particular the N_2 pressure, 0.1–10 Pa, the substrates, Al_2O_3, Si (100) and (111), and their temperature, 200–400 °C. Depending on the substrates, Al/(Al+N) ratio values ranging from 0.53 to 0.59 were determined for N_2 pressure of 1–5 Pa. Generally polycrystalline films were obtained. The crystalline orientation strongly depends on all varied parameters and on the target-to-substrate distance *d*. In particular, from XRD analyses of the films deposited on Al_2O_3 substrates, it was found that two peaks are present at 2θ = 33.28° and 38.17°, corresponding to AlN (100) and AlN (101) respectively. The second peak is dominant for samples deposited at *d* = 5 cm. The samples deposited at *d* = 4 cm, in otherwise identical experimental conditions, show both peaks with comparable intensity. For the films deposited on Si (100) substrates at an N_2 pressure of 3 Pa, the peak corresponding to the AlN (100) orientation is clearly visible. Reducing the ambient gas pressure to 1 Pa, keeping constant the other parameters, the AlN (110) orientation become dominant, 2θ = 59.40°. At the same pressure, films deposited on Si (111) instead of Si (100) wafer show a higher degree of orientation, exhibiting the (110) peak only.

The first reports on epitaxial growth of AlN films, both on Si (111) and Al_2O_3 (0001) were published by Vispute et al. [50, 52]. For both substrates, the best films were obtained by ablating an AlN target with a KrF excimer laser, 248 nm, τ = 25 ns, at a fluence of 2 J/cm^2. The substrate temperature was 800 °C. The ablation

was performed in vacuum and under low nitrogen pressure to investigate the effect of the gas on film quality. The films deposited on Si (111) were highly oriented along the *c*-axis normal to the Si (111) planes. X-ray diffraction analysis, together with electron diffraction investigations, showed a clear orientation relationship of AlN (0001) and Si (111). The lattice constant *c* found for these films was 0.497 nm, which is close to the value for bulk AlN. The narrowest width of the rocking curve for these films was 1.15°. For the films deposited on Al_2O_3 they found the epitaxial relationship AlN[001]//Al_2O_3[0001] in the direction of growth. The in-plane relationships were also found, the FWHM width of the rocking curve being 0.21°.

Vispute et al. also studied the influence of nitrogen pressure on the film quality. The best films were those grown in vacuum. They suppose that the presence of the nitrogen atmosphere ~0.1 Pa, increases the number of collisions between the gas molecules and the species present in the laser-induced plasma, giving rise to particulate which deteriorate the film surface quality. This effect was reported also by Norton et al. [64]. It seems also that high laser fluences are responsible for deterioration of the surface quality. In fact, films deposited at 10 J/cm^2 showed more particulate than films deposited at 3 J/cm^2, which were quite smooth. Also, they reported that a high laser fluence, 12 J/cm^2, is responsible for the presence of metallic Al inside the films, due to the partial decomposition of AlN during the laser irradiation at high fluence. The presence of metallic Al in the films compromises their crystallinity, stoichiometry and electrical resistivity. In fact, the AlN films prepared at fluences of 2–3 J/cm^2 were highly insulating, with resistivity higher than 10^{13} $\Omega\cdot$cm. Films deposited at fluences higher than 10 J/cm^2 exhibited resistivity in the range 7–25 $\Omega\cdot$cm [52].

In contrast, the presence of metallic Al inside AlN films was ascribed by Gyorgy et al. [65] not to high laser fluence but rather to a gradual decomposition of the AlN compound in the hot target zones beneath and around the laser-induced crater. The phenomenon is attributed to the large duration of the heating process when using nanosecond laser sources. They studied the effects of laser pulse duration and nitrogen pressure on the composition and structure properties of the deposited AlN films. They ablated AlN targets with two KrF excimer laser sources with different pulse duration, 30 ns and 450 fs. Different spot dimensions were used for the two laser beams, 3.3 and 0.16 mm^2 for the nanosecond and the subpicosecond source, respectively. In both cases the laser fluence was 4 J/cm^2. The deposition was carried out in vacuum of 10^{-6} Pa or in nitrogen pressures of 5×10^{-3}, 5×10^{-2} and 0.5 Pa, to partially compensate for the nitrogen loss of the target. Although the films deposited with the shorter laser pulses exhibited not well oriented microcrystals, with dimensions not larger than 20 nm, the XRD spectra showed only one peak at 33°, ascribed to the AlN <100> hexagonal phase. The XRD peak intensity increased with the nitrogen pressure. For deposition performed at 0.5 Pa an undefined peak appeared, too. In contrast, the films deposited with the nanosecond laser source both in vacuum and in low nitrogen pressure, 5×10^{-2} Pa, showed the metallic Al phase together with AlN in many crystallographic orientations.

A study of the dependence of film crystallinity on laser pulse repetition rate was made by Vispute et al. [50] and Six et al. [54]. The first group found no

significant effect on the film quality for the pulse repetition rate up to 30 Hz. The second one found a narrowing of the rocking curve width, indicating a better crystallization, for low repetition rates, i.e., for low deposition rates. Six et al. suppose that the time delay between two pulses should be high enough to allow nucleation and lateral propagation of the epitaxial layer between two successive pulses. They grew AlN films by pulsed laser ablation of an AlN target with a KrF excimer laser with $\tau = 30$ ns. The laser fluence was 3–5 J/cm^2. The films were deposited on Al_2O_3 substrates held at various temperatures in the range from RT up to 850 °C. Beginning the deposition with a laser pulse frequency of 1 Hz for 5 minutes and continuing with 10 Hz, they obtained good-quality epitaxial films. From ERDA analysis they obtained that the films contain around 50 at.% aluminum. The atomic fraction of nitrogen varies between 42 and 49 at.%. Oxygen contamination was also observed. From XRD measurements, highly oriented AlN films with the *c*-axis perpendicular to the surface of the *c*-sapphire substrate were grown at substrate temperatures higher than 450 °C. A complete epitaxial alignment on sapphire was obtained when the substrate was heated to 850 °C. In a further work [55], they reported the very small rocking curve width value of 0.1°. They ascribed this small value to the beneficial effect of the nitrogen/argon ion bombardment of the growing films. The effect of this bombardment is to compress the AlN *a*-axis by 0.6% and to expand the *c*-axis by 1.8%. This lattice distortion reduces the lattice misfit with the *c*-sapphire substrate and improves the epitaxial growth. They found that the lattice distortion is independent of the kind of substrate. The ion bombardment has no significant influence on the film stoichiometry and does not change the texture and phase composition of AlN films.

Meinschien et al. [66] conclude from their own experiments that the orientation of PLD deposited AlN films is driven only by the orientation of the sapphire substrates. They deposited aluminum nitride films with a KrF excimer laser at a fluence of 2 J/cm^2 and repetition rate of 50 Hz. *c*-, *r*-, *m*-, and *a*-cut sapphire substrates heated at 800 °C were used. Highly oriented AlN were obtained on all substrates. In particular, an AlN (11.0) film was deposited on *r*-cut sapphire. It was flat enough to fabricate an r.f. SAW filter.

Kumar et al. in their work [67] stressed the importance of the substrate temperature for the fabrication of high quality AlN films. In general it has been observed that, regardless of the growth technique employed, the growth of AlN films on various substrates at temperatures higher than 500 °C resulted in epitaxial or preferentially-oriented films. Deposition at temperatures below 500 °C produced amorphous films. They report that films deposited at 675 °C are highly textured, having the *c*-axis perpendicular to the Si (100) substrate. The lattice constant *c* for these films is 0.497 nm, very close to the value of bulk material. The relative FTIR spectra show a strong absorption at 665 cm^{-1}, fingerprint of the AlN phase. The film hardness depends on the substrate temperature too, thus increasing with increasing temperature. The greatest value obtained in this work was 33 GPa, which is comparable to the bulk material.

It is worthwhile noting that RT epitaxial growth of AlN films has been recently reported by Ohta et al. [68]. They grew their AlN films on (Mn, Zn)Fe_2O_4 (111)

substrates, because this material gives a lattice mismatch of only 3.6% with AlN and it is available at a reasonable cost. AlN targets were ablated with a KrF excimer laser at a fluence of 3.0 J/cm^2 in a N_2 ambient pressure of $p \sim 1$ Pa. Using reflection high-energy electron diffraction (RHEED) and grazing incidence angle x-ray diffraction (GIXD) measurements, they found that single domain wurtzite AlN (0001) grows epitaxially on (Mn, Zn)Fe_2O_4 (111). The *a*-axis length is 0.3098 nm, which is very close to that of the bulk. They report that the growth at RT is beneficial for the suppression of interface reactions. In fact, grazing incidence angle x-ray reflectivity (GIXR) analysis showed that an abrupt interface between the AlN film and the substrate appears.

Okamoto et al. [69] studied the effect of nitrogen ambient pressure on the growth of PLD AlN films. They found that surface morphology, crystallinity, crystal growth mode and composition of PLD AlN films can be controlled by the nitrogen pressure. Their AlN films were grown on Al_2O_3 substrates heated at 1000 °C. They ablated stoichiometric AlN targets with the fourth harmonic of a Nd:YAG laser, $\lambda = 266$ nm, $\tau = 3$–5 ns, with a fluence of 1 J/cm^2 and 10 Hz pulse repetition rate. The pressure of the N_2 ambient gas was varied from 1.2×10^{-2} to 53 Pa. The film crystallinity improved with decreasing ambient pressure. High quality AlN films were epitaxially grown on sapphire (0001) substrates at an N_2 pressure of 1.2×10^{-2} Pa. The FWHM of the x-ray rocking curve of the AlN (0002) peak was 0.078°, which indicates high crystallinity. The growth mode of the AlN film changed to an *a*-axis orientation at a pressure of 5.3 Pa. The film grown at a pressure of 1.2×10^{-2} Pa was smooth and almost free of particulate. The one grown at 1.2×10^{-1} Pa had a relatively rough and grainy surface. The authors attribute both the rough surface and the change of orientation of films grown at relatively high pressures to increased collisions between the ablated species and the nitrogen gas. This effect causes a large loss of energy of the species impinging on the growing film, which reduces the migration and results in cluster formation. Consequently, the AlN growth mode changes from a *c*-oriented continuous growth to an *a*-oriented island growth. Also the Al/N atomic ratio varies with N_2 pressure. Below 10^{-2} Pa, the composition ratio ranges between 0.95 and 1.05 without appreciable degradation of the film crystallinity. Oxygen contamination was found lower than 1 at.%. As expected, the AlN films were insulating with a resistivity too high to be measured.

To obtain films with a variable electrical resistivity, the same authors [70] grew AlN films doped by incorporation of carbon and/or oxygen impurities. They used the two-beam deposition technique. The laser beam was divided into two equivalent beams with a beam splitter. One beam was directed to the AlN target, while the other to a graphite target. As mentioned above, Al_2O_3 (0001) substrates heated to 1000 °C, placed 4 cm apart from the AlN target, were used. The deposition was carried out in a nitrogen background pressure of 1.2×10^{-2} Pa. For pure carbon doping, the transparent AlN-C film at C concentration < 5 at.% was still of a very high resistivity. At C concentrations > 15 at.% the film was conductive, with a brown color. The AlN-O films showed insulating behavior for [O] ≅ 15 at.%. In contrast, the films doped with both elements, C and O, were conductive and transparent.

The films were prepared with fixed 10 at.% oxygen concentration and various carbon concentrations, 1.9, 3.0 and 3.3 at.%. The samples doped with [C] = 3.0 and 3.3 at.% displayed ohmic conductivity. The conductivity decreased with decreasing carbon concentration. The film with [C] = 1.9 at.% was an insulator, while that with [C] = 3.3 at.% showed a resistivity value of the order of 10^5 Ω cm at room temperature. The increase in conductivity with temperature, in the range 300–400 K, of this sample indicated that the AlN/(C+O) film is a wide-gap semiconductor material. In fact, its optical transmittance showed absorption edges at ~230 nm, to be compared to a sharp edge at ~200 nm of undoped AlN films. Conductivity is tentatively attributed here to an Al_2OC component. However, because of the high dopant concentration, the crystal structure of the doped AlN films was different from that one of the undoped films, showing a mixed structure of two *c*-axis constants. This means that a new phase, with a *c*-axis lattice constant larger than that of stoichiometric AlN was formed.

We conclude that much work has been done on PLD-RPLD deposition of AlN films. The influence of the deposition parameters were carefully investigated. High quality films were fabricated. It was demonstrated that they can be successfully used in technological devices.

4. The case of Titanium Aluminum nitride

The main limitation of TiN, when used as a mechanical protective coating, is its oxidation at temperatures higher than 550 °C, giving rise to a rutile TiO_2 component that induces shearing of the coating film. This fact drastically contributes to the degradation of the film wear resistance. Similar phenomena appear in all transition metal nitrides. The partial substitution of the transition metal with another metal may overcome this drawback and give some better properties to the nitride films used for tribological applications. Non-noble metals like aluminum were proposed to form a ternary solid solution, like TiAlN [71], and are now actively studied. The TiAlN compound should resist oxidation even at high temperatures as 900–1000 °C reached during the high speed mechanical processing of metals. This property is ensured by the formation of a thin surface layer of aluminum oxide, which prevents further oxidation of the underlying TiAlN layer, preventing thus corrosion while still maintaining low friction.

TiAlN films were deposited by excimer laser ablation of TiAl alloys in low pressure N_2 atmosphere [72, 73]. Films deposited by Moromoto et al. [72] were affected by a high content of oxygen, maybe due to the poor background pressure, 2×10^{-4} Pa, in the deposition chamber. In the work of Acquaviva et al. [73] depositions were performed in a chamber first evacuated down to 2×10^{-5} Pa and then filled with a high purity molecular nitrogen at $p = 0.1$, 0.5, 1, 5 and 10 Pa. The target was a TiAl alloy, 47% Al – 43% Ti, disc. The substrates were held at RT. An XeCl laser was used, at a fluence of 6 J/cm^2. The deposition rate was 0.01 nm/pulse at $p = 0.1$ Pa. It halved as the N_2 pressure was increased to $p = 10$ Pa. Films deposited at $p > 1$ Pa show an appreciable content of nitrogen. At 10 Pa the film is made of

hexagonal $Ti_3Al_2N_2$, with a = 0.29875, c = 2.335. The low electrical resistivity, ~30 μΩ·cm, indicates a metallic behavior of these films.

The partial substitution of the transition metal by aluminum and other elements is reported for other nitrides also. Zr_xAl_yN and Zr_xGa_yN films were deposited by Spillmann et al. with the same apparatus and technique used for ZrN film depositions [34].

5. Laser deposition of cubic Boron nitride films

Boron nitride crystallizes mainly in two structures: the hexagonal (h-BN) and the cubic (c-BN). The first is an sp^2-bonded structure, very similar to that of graphite. The second is an sp^3-bonded structure which crystallizes in the zinc-blende configuration. A complete description of the phases and stability of the BN system is reported by Mirkarimi et al. [74]. h-BN is a soft, white and electrically insulating material. The most interesting phase, because of its great technological potential, is certainly c-BN. It has a Vickers hardness of about 5000 Kg mm^{-2} [75], a value that makes it the second hard material after diamond. But, unlike diamond, it has a high oxidation temperature of 1300 °C [75]. It does not react easily at high temperature with ferrous metals, such as iron, cobalt and nickel. Thus, it may be used as protective coating for these elements. It could also find applications for optical coatings, since it is transparent in the infrared [76] and visible [75] parts of the spectrum. c-BN has a crystal lattice very similar to that of diamond. This fact makes it attractive for using as nucleation centers for CVD processes of diamond. Moreover, c-BN can find applications in high-temperature, high-power electronic devices because of its high energy gap, 6 eV, and its good thermal conductivity [75]. c-BN films exhibit a resistivity from 10^9 to 10^{11} Ω cm [77–79]. They can be both *p*- and *n*-doped. A review of the electrical characteristics of c-BN films was recently published by Mohammad [80].

All these promising properties stimulated many efforts for growing c-BN films. The task proved however to be not so easy to perform. To date, single crystalline c-BN have been produced only by high temperature, high pressure synthesis (HTHP). However, the resulting crystallites are too small for most industrial applications [75]. At low pressure, only techniques involving energetic particles and processes far above thermodynamical equilibrium, such as ion-assisted PVD and CVD or pure ion beam deposition, have succeeded in producing c-BN films [74, 81]. Ion bombardment, with nitrogen ions mixed with noble gas ions like Ar, is crucial for c-BN nucleation and growth [82–86]. Without the ion bombardment, only the h-BN phase can be formed. The resulting films have usually a nanocrystalline structure, with a textured h-BN or a h-BN/t-BN interfacial layer [83, 85]. t-BN consists of a mixture of phases ranging from the highly ordered phase and the sp^2-bonded amorphous material.

Another problem arises from the fact that c-BN films suffer from poor adhesion on almost any substrate [87]. Two main reasons have been identified for this behavior [88]:

(1) the poor adhesion strength at the c-BN substrate interface, caused at least in part by the special nucleation sequence of c-BN mentioned above;
(2) the high level of compressive stress, ≥10 GPa, induced by the ion bombardment which is necessary to nucleate and grow c-BN [89].

In consequence, the film thickness is limited to a few hundreds of nanometers. Recently, some papers reported the successful deposition of adhesive c-BN films with thickness of the order of 1–2 μm [90–94]. However, in these cases, some procedures have been used which are not compatible with industrial applications. The characterization of these films is also quite complicated requiring, for a correct phase identification, at least three independent and complementary techniques [74, 81].

Because of the peculiar requirements for the c-BN film growth, PLD and ion beam assisted PLD (IA PLD) are seen as promising techniques for this task. With respect to other ion-assisted PVD methods, ion assisted PLD has the advantage of being a much simpler method. Moreover, the use of separate ion and laser sources permits independent control of the deposition rate, ion flux etc.

Since 1987, several groups started working on the synthesis of c-BN films using PLD and, mostly, ion-assisted PLD [95–112]. The first works were realized by simple un-assisted pulsed laser deposition. With the experimental parameters used, only h-BN or t-BN phases were grown [95, 96]. Only Doll et al. [96] reported growth, on Si (100) substrates at 600 °C, of a thin, 20 nm, epitaxial, yet polycrystalline layer of c-BN by ablating h-BN targets in N_2 atmosphere. These results were confuted by Friedman et al. [97], who performed experiments in the same conditions. They found no evidence of an epitaxial layer of c-BN at all. This material was successfully prepared by IA PLD. The preparation of c-BN films by IA PLD using boron and/or boron nitride targets requires: heating of the substrates at temperatures $T \geq 200$ °C, a strong nitrogen or nitrogen/argon bombardment, to supply sufficient nitrogen at enhanced reactivity, sufficient momentum and energy transfer to the growing film. Boron nitride films have either predominantly a hexagonal or cubic structure, depending on the laser and ion beam parameters and on the substrate temperature. The main results on c-BN synthesis are reported in Table 1.

Friedman et al. [97] explored the effects of ion current, ion energy, growth time and substrate temperature on the c-BN content. They found that stoichiometric

Table 1. Main results on c-BN synthesis.

Maximum film thickness (nm)	Maximum c-BN content (%)	Maximum crystal dimensions (nm)	Maximum hardness value (GPa)	Minimum stress value (GPa)	Ref.
~100	~98	20–100			100
~200	>85	~30		~6	99
400–500	>85	≤40	30–40	4.5	102–108
	~60	Nanocrystals		21.8	110
	~10				111

BN films with high c-BN percentage can be grown between 150 and 500 °C and with ion/atom arrival values near unity for beam energies between 800 and 1200 eV. They also gave an interesting discussion about the limits to the c-BN content and a possible mechanism for the conversion process to c-BN.

Generally, c-BN films are grown in a layered structure. For example, Weissmantel et al. [102] studied the growth of c-BN thin films by ablating both a sintered elemental boron target and an h-BN target. They used KrF excimer laser pulses with repetition rates in the range of 1–50 Hz. Laser fluences were 1–7.3 J/cm^2. The growing films were continuously bombarded with nitrogen/argon ions from an r.f. source with E = 300–700 eV and j = 75–570 μA/cm^2. The films were deposited on heated Si (100) substrates at T = 20–400 °C. The results show that BN films have either predominantly a hexagonal or cubic structure, depending on the laser and ion beam parameters and on the substrate temperature. At optimum laser and ion beam parameters, nearly pure c-BN films could be prepared even at a relatively low substrates temperature of 200 °C. However, the films prepared on Si substrates exhibit the typical layered structure with a 5–10 nm thick amorphous layer formed initially on the substrate, a 10–30 nm thick layer of highly oriented h-BN and the c-BN layer. The c-BN layer consists of nanocrystallites up to 30 nm in diameter. Two types of nucleation of the cubic phase grown upon the hexagonal phase were found: c-BN (111) lattice planes parallel to h-BN (002) lattice planes with a lattice match of 3:2, or c-BN (100) lattice planes parallel to the h-BN (002) lattice planes with a better lattice match. In order to increase the size of c-BN crystallites, with mean size 10–20 nm, the deposited films were irradiated with laser energy densities of F = 0.01–0.19 J/cm^2. Doubling of the crystallite dimensions was obtained only after annealing at laser fluences of F = 0.07–0.11 J/cm^2. They found that, using elemental boron targets, the quality of the films was compromised by the presence of droplets. Surface quality was strictly dependent on the laser fluence. At high fluences a powder-like deposit on the substrate was observed. However, high fluences, $F > 6.4$ J/cm^2, were responsible for a lower particulate density in the case of ablation of h-BN targets. It was also found that, in the beginning, the deposition rate should be low to enable c-BN nucleation. Also, the nucleation of c-BN films requires the ratio of ions I from the ion beam to the ablated atoms and ions A to be I/A ~1. This value can be reduced to 0.6 during further growth.

Klotzbucher et al. [110] report that an ion-to-atom flux of 0.5 was necessary to reveal, by FTIR measurements, the band around 1080 cm^{-1} characteristic of c-BN. They ablated h-BN targets by a hybrid r.f.-PLD technique: ion bombardment of the growing film was performed by igniting a low pressure gas discharge in the processing gas and using a DC self bias of the substrate electrode to accelerate the gas ions onto the substrate. The ion current density to the substrate was of the order of 10 μA/cm^2. The ion energies were some hundreds eV. A KrF excimer laser, λ = 248 nm, τ = 25 ns, was used with a fluence of 2.5 J/cm^2. The substrates were Si (100) and Si (111), heated up to T = 350 °C. Boron enriched films were obtained, probably due to the strong ion bombardment, which caused a preferentially re-sputtering of nitrogen. Increasing the nitrogen partial pressure in the

processing gas led to a boron to nitrogen atomic ratio of ~1. Films deposited in a pure argon atmosphere did not contain the c-BN phase. By adding nitrogen, a c-BN content of about 45% was recorded.

In order to improve the adhesion of c-BN films to substrates, Weissmantel et al. [103–105] have deposited an intermediate layer between the Si or stainless steel substrates and the films. This was obtained by ablating an h-BN target either in the presence of a nitrogen/argon plasma or by a relatively weak ion bombardment of the growing films with $0 \leq E \leq 500$ eV and $0 \leq j \leq 450$ μA/cm^2. For these conditions the ion to atom ratio is low, I/A < 0.5, and the nucleation of c-BN is not allowed. But, the films deposited in such conditions have a high adhesive strength to Si and stainless steel. On these layers, they grew well adhering 400 nm thick c-BN films, the thickness being limited by the increasing density of particulate associated with PLD in their experimental conditions. The Vickers micro-hardness of these films was 30 GPa.

Similar expedients were also used by other groups. Boron or graded BN_x [113], $B_xN_ySi_{1-x-y}$ [114] or turbostratic t-BN [115] were deposited as intermediate layers. From TEM and HRTEM investigations, it was found that, if the intermediate layer is deposited without ion bombardment, the nucleation of c-BN on top of this film occurs only after the formation of a h-BN layer. In contrast, when the intermediate layer is deposited with a sufficiently strong ion bombardment, the nucleation of the c-BN phase takes place immediately after switching to deposition parameters suitable for the nucleation, that is by lowering the growth rate. These intermediate layers have a Vickers hardness, Young's modulus and stress which depend on the substrate temperature, ion bombardment of the growing film and laser fluence. Low substrate temperature, high laser fluences and ion bombardment of the growing film improve the film hardness. Low laser fluences, high substrate temperature and ion bombardment reduce the stress. For instance, the films deposited with a laser fluence of 7.5 J/cm^2 and a substrate temperature in the range of 47–110 °C give a Vickers microhardness of 18.2–18.6 GPa and a Young's modulus of 182 and 165 GPa, respectively, without and with ion bombardment, with $E = 400$ eV and $j = 190$ μA/cm^2. The films deposited at the same laser fluence, without ion bombardment, on substrates heated to 360 °C, give a microhardness of 10.5 GPa and a Young's modulus of 128 GPa. These values decrease to 7.4 GPa and 88 GPa, respectively, in the presence of ion beam bombardment, with $E = 400$ eV and $j = 190$ μA/cm^2 [103, 104]. These features have been explained by the fact that high hardness values are correlated to a great disorder in the material structure. The effect of increasing the substrate temperature and of ion bombardment is to reduce this disorder. For laser fluences higher than 8–9 J/cm^2 the Vickers microhardness values are in the range of 20–25 GPa [105]. Regarding the stress dependence, mentioned above, a low laser fluence and ion bombardment contribute to reduce the stress in the films. Stress values of 8.3 and 1.3 GPa were indeed recorded on films deposited at laser fluences of 10 and 7.5 J/cm^2, respectively. Both films were deposited at a substrate temperature of $T = 360$ °C with ion bombarding parameters of $E = 400$–500 eV and $j = 190$–310 μA/cm^2. Films deposited at a fluence of $F = 7.5$ J/cm^2 and substrate temperature $T = 360$ °C gave a stress

value of 4.7 GPa when deposited without ion bombardment, and of 1.3 GPa when deposited with ion bombardment with $E = 400$ eV and $j = 190$ μA/cm^2 [104, 105].

In a recent work, Weissmantel et al. [106] have shown that the I/A ratio necessary for c-BN film growth can be reduced to 0.14 using very high laser fluences, $F \geq 60$ J/cm^2, since the ablated boron and nitrogen species from the h-BN target have a high mean kinetic energy. It is also worthwhile to mention that boron nitride films containing the c-BN phase were obtained also by RPLD without ion bombardment. Luculescu et al. [111] deposited boron nitride films by laser ablation of h-BN targets in nitrogen atmosphere at $p = 5$ Pa. They used both a nanosecond Nd:YAG laser, with $\lambda = 266$ nm and $\tau = 4$ ns, and a femtosecond Ti:sapphire laser with $\lambda = 780$ nm and $\tau = 100$ fs. The films were deposited on a Si (100) substrate heated to $T = 700$ °C. Laser fluences from 0.3 to 10 J/cm^2 were used. In samples prepared with the nanosecond laser, it appeared from the XPS analysis that the elemental boron peak disappears at fluences of $F > 3$ J/cm^2. In samples prepared with femtosecond laser pulses, the B-N bonding peak became stronger at the highest fluences but the elemental boron peak remained always high. From FTIR spectra, it was observed that the c-BN band appears only for films deposited with nanosecond laser pulses at low fluences. A maximum c-BN content of 10% was recorded. Although the femtosecond laser ablation can provide high energy ions, which is appreciable for the production of c-BN, under the experimental deposition used by Luculescu et al. this technique was not effective, probably because of the generation of a large number of h-BN fragments. Finally, Acquaviva et al. [112] deposited boron nitride films containing the c-BN phase on Si substrates at RT. They used KrF laser ablation of h-BN targets in low pressure (5 Pa) N_2 atmosphere. The laser fluence was 6 or 12 J/cm^2. RBS spectra indicate a deposition rate of ~0.01 nm/pulse and an atomic B/N ratio close to 1. XPS survey spectra in the B 1s and N 1s regions show peaks at 190.7 eV and at 398.1 eV, respectively, characteristic of N-B bonding in boron nitride [116]. The c-BN phase was clearly identified in FTIR spectra, where a relatively narrow and prominent band centered at 1100 cm^{-1} fits well the cubic-BN restrahlen band [76]. The influence of the laser fluence on the film microstructure reflects in a strong variation of the 1100 cm^{-1} peak intensity with respect to the one of the 1378 cm^{-1} peak, attributed to h-BN. The films deposited at 6 J/cm^2 exhibits a cubic-phase content higher than the hexagonal one.

6. Conclusions

The great amount of work done in many laboratories throughout the world demonstrated that RPLD is indeed an effective method for the deposition of thin nitride films.

According to the data available in literature, we conclude that:

(1) Uniform layers of pure polycrystalline fcc TiN can be easily obtained by collecting on RT substrates the substance ejected by RPLD from Ti targets in N_2

ambient atmosphere. Typical laser fluences are 5–6 J/cm^2. Typical N_2 ambient pressures are 0.1–1 Pa. The method allows to achieve TiN films with appropriate characteristics for applications in advanced technologies. VN films also can be deposited at low N_2 ambient pressures of 1 Pa and low laser fluence, 6 J/cm^2, on substrates at RT. To form the V_2N phase, fluences >12 J/cm^2 are needed. The control of the deposition parameters such as laser fluence, ambient pressure and substrate temperature, allows to obtain films with required composition and structure. The nitrides of the other refractory metals, such as Ta, Mo, W, can also be efficiently and easily synthesized.

(2) Much more difficult is the task to deposit pure crystalline aluminum nitride and cubic boron nitride films. In these cases, the heating of the substrate and enhancement of the nitrogen reactivity by r.f. discharges or ion-beam bombardment of the growing film are mandatory. Most important is the fact that the required substrate temperatures are much lower than those required by more traditional deposition techniques.

(3) The RPLD technique offers great versatility, and an appropriate choice of the many adjustable parameters can guarantee almost always the fabrication of desired compounds with required structure.

References

1. I. Ursu, A. M. Prokhorov, V. I. Konov and I. N. Mihailescu, *Laser Heating of Metals*, The Adam Hilger Series on Optics and Optoelectronics, Philadelphia (1990).
2. E. D'Anna, G. Leggieri, A. Luches, M. Martino, A. V. Drigo, I. N. Mihailescu and S. Ganatsios, *J. Appl. Phys.* **69**, 1687 (1991).
3. J. J. Dubowski, A. Compaan and M. Prasad, *Appl. Surf. Sci.* **86**, 548 (1995).
4. G. Auvert, *Appl. Surf. Sci.* **86**, 466 (1995).
5. D. Dijkkamp, T. Venkatesan, X. D. Wu, S.A. Shaheen, N. Jisrawi, Y. H. Min-Lee, W. L. McLean and M. Croft, *Appl. Phys. Lett.* **51**, 619 (1987).
6. S. Acquaviva, M. Fernández, G. Leggieri, A. Luches, M. Martino and A. Perrone, *Appl. Phys.* **A 69**, S471 (1999).
7. T. A. Friedmann, K. F. McCarty, E. J. Klaus, D. Boehme, W. M. Clift, H. A. Johnsen, M. J. Mills and D. K. Ottesen, *Appl. Phys. Lett.* **61**, 2406 (1992).
8. E. D'Anna, M. L. De Giorgi, G. Leggieri, A. Luches, M. Martino, A. Perrone and A. Zocco, *Phys. Stat. Sol. (a)* **166**, 581 (1998).
9. S. Acquaviva, A. P. Caricato, M. L. De Giorgi, A. Luches and A. Perrone, *Appl. Surf. Sci.* **109/110**, 408 (1997).
10. A. Gorbunov, *Laser-Assisted Synthesis of Nanostructured Materials* (Düsseldorf: VDI Verlag, 2002).
11. S. I. Anisimov, B. S. Luk'yanchuk and A. Luches, *JETP* **81**, 129 (1995).
12. S. I. Anisimov, D. Bäuerle and B. S. Luk'yanchuk, *Phys. Rev.* **B 48**, 12076 (1993).
13. E. György, I. N. Mihailescu, M. Kompitsas and A. Giannoudakos, *Appl. Surf. Sci.* **195**, 270 (2002).
14. L. R. Doolittle, *Nucl. Instrum. Meth.* **B 9**, 344 (1985).
15. J. Häglund, A. Fernández Guillermet, G. Grimvall and M. Körling, *Phys. Rev.* **B 48**, 11685 (1993).
16. J.-E. Sundgren, *Thin Solid Films* **128**, 21 (1985).
17. C. Y. Thing, *J. Vac. Sci. Technol.* **21**, 14 (1982).
18. T. B. Massalski, *Binary Alloy Phase Diagram* (ASM Metals Park, Ohio, 1991).

19. O. Auciello, T. Barnes, S. Chevacharoenkul, A. F. Schreiner and G. E. McGuire, *Thin Solid Films* **181**, 65 (1989).
20. R. Chowdhury, R. D. Vispute, K. Jagannadham and J. Narayan, *J. Mater. Res.* **11**, 1458 (1996).
21. K. Obata, K. Sugioka, K. Toyoda, H. Takai and K. Midorikawa, *Appl. Phys.* **A 69**, S715 (1999).
22. K. Obata, K. Sugioka, K. Toyoda, H. Takai and K. Midorikawa, *Jpn. J. Appl. Phys.* **39**, 7031 (2000).
23. J. Narayan, P. Tiwari, X. Chen, J. Singh, R. Chowdhury and T. Zheleva, *Appl. Phys. Lett.* **61**, 1290 (1992).
24. C. Chen, P. P. Ong and H. Wang, *Thin Solid Films* **382**, 275 (2001).
25. V. Craciun, D. Craciun and I. W. Boyd, *Materials Sci. Eng.* **B 18**, 178 (1993).
26. I. N. Mihailescu, N. Chitica, V. Teodorescu, M. L. De Giorgi, G. Leggieri, A. Luches, M. Martino, A. Perrone and B. Dubreuil, *J. Vac. Sci. Technol.* **A 11**, 2577 (1993).
27. I. N. Mihailescu, N. Chitica, L. C. Nistor, M. Popescu, V. S. Teodorescu, A. Andrei, A. Barborica, A. Luches, M. L. De Giorgi, A. Perrone, B. Dubreuil and J. Hermann, *J. Appl. Phys.* **74**, 5781 (1993).
28. I. N. Mihailescu, E. Gyorgy, N. Chitica, V. S. Teodorescu, G. Mavin, A. Luches, A. Perrone, M. Martino and J. Neamtu, *J. Material Sci.* **31**, 2909 (1996).
29. R. Castell, A. Ruiz, C. Castell and C. Suarez, *Appl. Phys.* **A 69**, S521 (1999).
30. Z. N. Dai, A. Miyashita, S. Yamamoto, K. Karumi and H. Naramoto, *Thin Solid Films* **347**, 117 (1999).
31. E. D'Anna, A. Di Cristoforo, M. Fernández, G. Leggieri, A. Luches, G. Majni, P. Mengucci and L. Nanai, *Appl. Surf. Sci.* **186**, 496 (2002).
32. H. Holleck, *J. Vac. Sci. Technol.* **A 4**, 2661 (1986).
33. D. R. Lide, Ed., *Handbook of Chemistry and Physics*, Vol. 72 (London: CRC, 1992).
34. H. Spillmann, P. R. Willmott, M. Morstein and P. J. Uggowitzer, *Appl. Phys.* **A 73**, 441 (2001).
35. P. R. Willmott, R. Timm and J. R. Huber, *Appl. Surf. Sci.* **127–129**, 105 (1998).
36. M. Bereznai, A. P. Caricato, M. Fernández, A. Luches, Z. Tóth, G. Majni, P. Mengucci, P. M. Nagy, A. Juhász, L. Nánai (to be published).
37. S. Strite and H. Morkoc, *J. Vac. Sci. Technol.* **B 10**, 1237 (1992).
38. G. A. Slack, R. A. Tanzilli, R. O. Pohl and J. W. Vandersande, *J. Phys. Chem. Solids* **48**, 641 (1987).
39. M. T. Duffy, C. C. Wang, G. D. O'Clock, S. H. MacFarlane III Jr. and P. J. Zanzucchi. *J. Electron. Mater.* **2**, 359 (1973).
40. A. D. Bykhovski, V. V. Kaminski, M. S. Shur, Q. C. Chen and M. A. Khan, *Appl. Phys. Lett.* **68**, 818 (1996).
41. T. J. Mroz, *Am. Ceram. Soc. Bull.* **71**, 782 (1992).
42. T. Y. Sheng, Z. Q. Yu and G. J. Collins, *Appl. Phys. Lett.* **52**, 576 (1988).
43. G. Radhakrishnan, *J. Appl. Phys.* **78**, 6000 (1995).
44. G. Selvaduray and L. Sheet, *Mater. Sci. Technol.* **9**, 463 (1993).
45. Y. M. Le Vaillant, R. Bisaro, J. Olivier, O. Durand, J. Y. Duboz, S. Ruffenach-Clur, O. Briot, B. Gil and R. L. Aulombard, *J. Cryst. Growth* **189/190**, 282 (1988).
46. A. Saxler, P. Kung, C. J. Sun, E. Bigan and M. Razehi, *Appl. Phys. Lett.* **64**, 339 (1994).
47. K. S. Stevens, A. Ohtani, M. Kinniburgh and R. Beresdorf, *Appl. Phys. Lett.* **65**, 321 (1994).
48. Y. Chubachi, K. Sato and K. Kojima, *Thin Solid Films* **122**, 259 (1984).
49. I. Ivanov, L. Hultman, K. Järrendahl, P. Martensson, J.-E. Sundgren, B. Hjörvarsson and J. E. Green, *J. Appl. Phys.* **78**, 5721 (1995).
50. R. D. Vispute, J. Narayan, H. Wu and K. Jagannadham, *J. Appl. Phys.* **77**, 4724 (1995).
51. J. M. Liu, N. Chong, H. L. W. Chan, K. H. Wong and C. L. Choy, *Appl. Phys.* **A 76**, 93 (2002).
52. R. D. Vispute, H. Wu and J. Narayan, *Appl. Phys. Lett.* **67**, 1549 (1995).
53. J. Meinschien, G. Behme, F. Falk and H. Stafast, *Appl. Phys.* **A 69**, S683 (1999).
54. S. Six, J. W. Gerlach and B. Rauschenbach, *Thin Solid Films* **370**, 1 (2000).
55. S. Six, J. W. Gerlach and B. Rauschenbach, *Surface Coat. Technol.* **142**, 397 (2001).
56. G. Selvaduray and L. Sheet, *Mater. Sci. Technol.* **9**, 463 (1993).
57. B.-C. Chung and M. Gershenzon, *J. Appl. Phys.* **72**, 651 (1992).

58. A. Basillais, C. Boulmer-Leborgne, J. Mathias and J. Perrière, *Appl. Surf. Sci.* **186**, 416 (2002).
59. A. Basillais, C. Boulmer-Leborgne, J. Mathias, N. Laidani, A. Laurent and J. Perrière, *Appl. Phys.* **A 71**, 619 (2000).
60. J. D. Wu, J. Su, Z. F. Ying, W. Shi, H. Ling, F. M. Li, Z. Y. Zhou, K. L. Wang and X. M. Ding, *J. Vac. Sci. Technol.* **A 19**, 299 (2001).
61. J. A. Taylor and J. W. Rabalais, *J. Chem. Phys.* **75**, 1735 (1981).
62. L. E. McNeil, M. Grimsditch and R. H. French, *J. Am. Chem. Soc.* **76**, 1132 (1993).
63. P. Verardi, M. Dinescu, C. Stanciu, C. Gerardi, L. Mirenghi and V. Sandu, *Mat. Sci. Eng. B* **50**, 223 (1997).
64. M. G. Norton, P. G. Kotula, C. B. Carter, *J. Appl. Phys.* **70**, 2871 (1991).
65. E. Gyorgy, C. Ristoscu, I. N. Mihailescu, A. Klini, N. Vainos, C. Fotakis, C. Ghica, G. Schmerber and J. Faerber, *J. Appl. Phys.* **90**, 456 (2001).
66. J. Meinschien, F. Falk, R. Hergt and H. Stafast, *Appl. Phys.* **A 70**, 215 (2000).
67. A. Kumar, H. L. Chan, J. J. Weimer and L. Sanderson, *Thin Solid Films* **308**, 406 (1997).
68. J. Ohta, H. Fujioka, S. Ito and M. Oshima, *Appl. Phys. Lett.* **81**, 2373 (2002).
69. M. Okamoto, M. Yamaoka, Y. K. Yap, M. Yoshimura, Y. Mori and T. Sasaki, *Diam. Relat. Mater.* **9**, 516 (2000).
70. M. Okamoto, Y. K. Yap, M. Yoshimura, Y. Mori and T. Sasaki, *Diam. Rel. Mat.* **10**, 1322 (2001).
71. A. Kimura, H. Hasegawa, K. Yamada and T. Suzuki, *Surf. Coat. Technol.* **120/12**1, 438 (1999).
72. A. Moromoto, H. Shigeno, S. Morita, Y. Yonezawa and T. Shimizu, *Appl. Surf. Sci.* **127–129**, 994 (1998).
73. S. Acquaviva, E. D'Anna, L. Elia, M. Fernandez, G. Leggieri, A. Luches, M. Martino, P. Mengucci and A. Zocco, *Thin Solid Films* **379**, 45 (2000).
74. P. B. Mirkarimi, K. F. McCarty and D. L. Medlin, *Mater. Sci. Eng. R* **21**, 47 (1997).
75. L. Vel, G. Demazeau and J. Etourneau, *Mater. Sci. Eng.* **B 10**, 149 (1991).
76. P. J. Gielisse, S. S. Mitra, J. N. Plendl, R. D. Griffis, L. C. Mansur, R. Marshall and E. A. Pascoe, *Phys. Rev.* **155**, 1039 (1967).
77. C. Ronning, E. Dreher, H. Feldermann, M. Gross, M. Sebastian and H. Hofsass, *Diam. Rel. Mat.* **6**, 1129 (1997).
78. T. Sugino, S. Kawasaki, K. Tanioka and J. Shirafuji, *Diam. Rel. Mat.* **7**, 632 (1998).
79. J. Szmidt, A. Jakubowski, A. Michalski and A. Rusek, *Diam. Rel. Mat.* **1**, 681 (1992).
80. S. N. Mohammad, *Solid-State Electronics* **46**, 203 (2002).
81. C. Ronning, H. Feldermann ad H. Hofsass, *Diam. Rel. Mat.* **9**, 1767 (2000).
82. T. Wada and N. Yamashita, *J. Vac. Sci. Technol.* **A 10**, 515 (1992).
83. D. L. Medlin, T. A. Friedmann, P. B. Mirkarimi, P. Rez, M. J. Mills and K. F. McCarty, *J. Appl. Phys.* **76**, 295 (1994).
84. F. Qian, V. Nagabushnam and R. K. Singh, *Appl. Phys. Lett.* **63**, 317 (1993).
85. D. J. Kester, K. S. Ailey and R. F. Davis, *Diam. Rel Mat.* **3**, 332 (1994).
86. G. Reisse, S. Weissmantel, B. Keiper and A. Weber, *Appl. Surf. Sci.* **108**, 9 (1997).
87. W. Kulisch, R. Freudenstein, A. Klett and M. F. Plass, *Thin Solid Films* **377/378**, 170 (2000).
88. S. Reinke, M. Kuhr and W. Kulisch, *Diam. Rel. Mat.* **5**, 508 (1996).
89. D. R. McEnzie, W. D. McFall, W. G. Sainty, C. A. Davis and R. E. Collins, *Diam. Rel. Mat.* **2**, 970 (1993).
90. S. Matsumoto and W. J. Zhang, *Jpn. J. Appl. Phys.* **39**, L442 (2000).
91. W. J. Zhang and S. Matsumoto, *Appl. Phys.* **A 71**, 469 (2000).
92. K. Yamamoto, M. Keunecke and K. Bewilogua, *Thin Solid Films* **377/378**, 331 (2000).
93. D. Litvinov, C. A. II Taylor and R. Clarke, *Diam. Rel. Mat.* **7**, 360 (1998).
94. K.-L. Barth, A. Lunk and J. Ulmer, *Surf. Coat. Technol.* **92**, 96 (1997).
95. G. Kessler, K.-D. Bauer, W. Pompe and H.-J. Scheibe, *Thin Solid Films* **147**, L45 (1987).
96. G. L. Doll, J. A. Sell, C. A. Taylor II and R. Clarke, *Phys. Rev.* **B 43**, 6816 (1991).
97. T. A. Friedmann, K. F. McCarty, E. J. Klaus, J. C. Barbour, W. M. Clift, H. A. Johnsen, D. L. Medlin, M. J. Mills and D. K. Ottesen, *Thin Solid Films* **237**, 48 (1994).
98. S. Mineta, M. Kohata, N. Yasunaga and Y. Kikuta, *Thin Solid Films* **189**, 125 (1990).

99. T. A. Friedmann, P. B. Mirkarimi, D. L. Medlin, K. F. McCarty, E. J. Klaus, D. R. Boehme, H. A. Johnsen, M. J. Mills and D. K. Ottesen, *J. Appl. Phys.* **76**, 3088 (1994).
100. A. K. Ballal, L. Salamanca-Riba, C. A. Taylor II and G. L. Doll, *Thin Solid Films* **224**, 46 (1993).
101. P. B. Mirkarimi, D. L. Medlin, K. F. McCarty and J. C. Barbour, *Appl. Phys. Lett.* **66**, 2813 (1995).
102. S. Weissmantel, G. Reisse, B. Keiper, A. Weber, U. Falke and M. Roder, *Appl. Sur. Sci.* **127/129**, 444 (1998).
103. S. Weissmantel and G. Reisse, *Thin Soilid Films* **355/356**, 256 (1999).
104. S. Weissmantel, G. Reisse, B. Keiper and S. Schulze, *Diam. Rel. Mat.* **8**, 377 (1999).
105. G. Reisse and S. Weissmantel, *Thin Soilid Films* **355/356**, 105 (1999).
106. S. Weissmantel and G. Reisse, *Diam. Rel. Mat.* **10**, 1973 (2001).
107. G. Reisse, S. Weissmantel and D. Rost, *Diam. Rel. Mat.* **11**, 1276 (2002).
108. G. Lehmann, P. Hess, S. Weissmantel, G. Reisse, P. Scheible and A. Lunk, *Appl. Phys.* **A 74**, 41 (2002).
109. M. B. Guseva, V. G. Babaev, V. S. Guden, V. V. Khvostov, A. U. Bregadze and I. Konyashin, *Diam. Rel. Mat.* **10**, 1385 (2001).
110. T. Klotzbucher, M. Mergens, D. A. Wesner and E. W. Kreutz, *Surf. Coat. Tech.* **100/101**, 388 (1998).
111. C. R. Luculescu, H. Miyake and S. Sato, *Appl. Surf. Sci.* **197/198**, 499 (2002).
112. S. Acquaviva, G. Leggieri, A. Luches, A. Perrone, A. Zocco, N. Laidani, G. Speranza and M. Anderle, *Appl. Phys.* **A 70**, 197 (2000).
113. M. Okamoto, H. Yokoyama and Y. Osaka, *Jpn. J. Appl. Phys.* **29**, 930 (1990).
114. K. Inagawa, K. Watanabe, K. Saitoh, Y. Yuchi and A. Itoh, *Surf. Coat. Technol.* **39/40**, 253 (1989).
115. T. Ikeda, Y. Kawate and Y. Hirai, *J. Vac. Sci. Technol.* **A 8**, 3168 (1990).
116. J. F. Moulder, W. F. Stickle, P. E. Sobol and K. D. Bomber, 'Handbook of X-ray Photoelectron Spectroscopy', edited by J. Chastain and R. C. King Jr, Physical Electronics Inc., 1995.

CHAPTER 9

LIQUID PHASE PHOTODEPOSITION PROCESSES FROM COLLOID SOLUTIONS

Aaron Peled* and Nina Mirchin

*Electrical and Electronics Department, Holon Academic Institute of Technology, 52 Golomb St., Holon 58102, Israel (*Author for correspondence, E-mail: peled@hait.ac.il)*

ABSTRACT: This chapter describes one method used in Liquid Phase Photo-Deposition(LPPD), namely Photodeposition from Colloid Solutions (PDCS). In the introduction, the basic photodeposition processes and their current technological trends are described. In section (2) the PDCS basics are given and in section (3) the photoreactor system and its experimental characteristics are described. In section (4) the significant controlling PDCS parameters are discussed and related to the experimental kinetic investigations. Section (5) describes the currently suggested theories of PDCS processes and section (6) brings typical applications. In section (7) the advantages and weaknesses of PDCS are compared with Gas Phase Photo-Deposition processes and in section (8) conclusions are drawn.

1. Introduction

Photon processing of materials is now a well established field which has been developing for at least three decades in several directions. During this period we have witnessed developments based on photo-excited processes [1] with various nomenclatures. Terms used include photo-assisted processes [2], photodeposition (PD) of thin films [3], photoelectrochemical deposition and etching [4], photodoping [5], laser ablation [6], laser writing and machining [7], chemical processing with lasers and photo-diagnostics [8], laser recrystallization for Thin Film Transistors (TFT) [9], Pulsed Laser Deposition (PLD) [10], and others [11]. Although Gas Phase Photodeposition (GPPD) processes [12, 13] and PLD became the mainstream, stemming from the interest in microelectronics [14], Liquid Phase Photodeposition (LPPD) [15–22] was also investigated by various groups while developing a basic understanding of photo-assisted processes in the more condensed phase. To a lesser extent solid phase photodeposition processes were also developed, such as Laser Induced Forward Transfer (LIFT) [23–25], in which material is transferred to a substrate by the impact momentum of photons. The "photodeposition" term has been used since the early 1960's to emphasize the generic resemblance to the older, well established material deposition technique known as "electrodeposition". In PD, material deposits are obtained by photoelectronic excitation of atoms using light sources as compared to electrochemistry, which uses electrical sources for chemical deposition.

In photo-excited reactions in general and photodeposition processes in particular, lasers and other light sources are used as a directed energy source to produce charged or kinetically excited atoms species in a photoreactor. The photoreactor chamber, besides vacuum processing, may typically contain a gas, liquid or solid

Aaron Peled (ed.), Photo-Excited Processes, Diagnostics and Applications (PEPDA), 251–280, 2003.
© 2003 *Kluwer Academic Publishers. Printed in the Netherlands.*

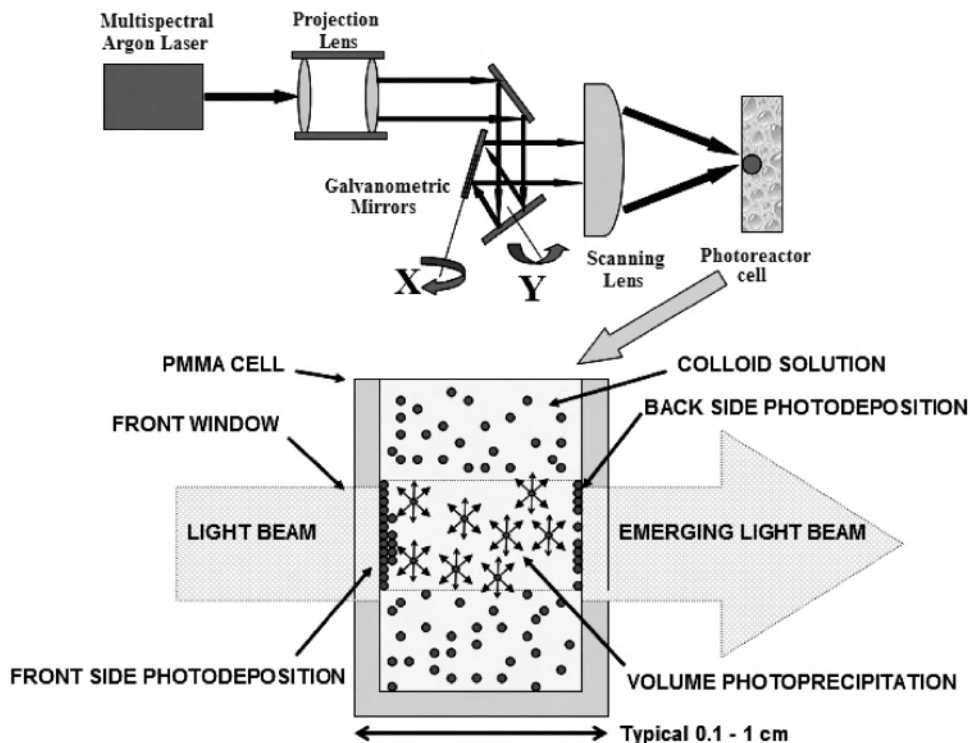

Figure 1. Photodeposition scanner and colloid photo-excited processes schematics.

phase, which interact with the light beam. The light beam is introduced through specially designed optical windows into the system. A typical photodeposition cell is shown in Figure 1.

Quite generally, in photodeposition systems, various schemes of photon interactions with solid/gas/liquid are possible [1–3, 6, 8, 10, 12, 15, 16, 20, 21, 24, 25]. The photon energy transfer to the photo-reacting species may occur in the bulk volume of the photoreactor chamber or directly onto the interfaces of the photoactive media and substrates, depending on the optical penetration properties of the irradiation source into the system and the reacting materials. The photons excite various electronic transfer reactions leading to secondary results such as molecular dissociation, oxidation, desorption, ablation, chemical precipitation, aggregation, adsorption, and film growth. These may lead, under proper conditions, to a controlled film formation on the substrates or other interfaces in the photoreactor. Since the energy for initiating and driving the processes is supplied by light sources such as lasers, a wide range of processing flexibility may be achieved during the deposition processes by varying irradiation parameters such as the wavelength, power, dose and pulse length, or by changing between pulsed and continuous wave excitation. In particular, the possibility of spatial localization of

these processes by scanning and focusing the beam down to the optical resolving power of the system, or even below it by undercutting, is another remarkable feature of material processing by photodeposition [26].

Direct photonic driven deposition methods were used, for instance, to obtain microelectronic devices without the need of using multi-step lithography-based mask processing [27, 28]. They were also used to obtain insulating and semiconducting dielectric optical filters and waveguides for integrated optoelectronic devices [7]. Since 1980, photodeposition techniques from gaseous phases [11, 12, 27] have been investigated by various groups and many papers have appeared on related techniques, materials, applications and theories. Some groups have pursued the investigation of photodeposition techniques from liquid phases [15, 17, 19–22, 29]. In particular, the colloid systems became a subject of investigation for several colloid/solution combinations [17, 30]. In this chapter we focus on the characteristics of liquid-phase colloid photodeposition (PDCS), its underlying physico-chemical principles, experimental results, and potential applications.

2. Features of PDCS systems

2.1. *Basic features*

Photodeposition from Colloid Solutions can be viewed as a process by which photon-material interaction results at the end in the creation of thin film structures or clusters of atoms on surfaces, apart from possible bulk particles nucleation in colloid solutions. As in other photodeposition systems, a PDCS system incorporates three functions: light “harvesting” agents such as colloid particles, which serve as photon absorbing centers, also known as chromophores, dissolved ions which decompose or react due to the electronic photo-excited state of the chromophores, and a substrate or other adsorbing sites. The chromophores may decompose, serve only as catalysts, be precipitated by photoredox reactions or photo-oxidation reactions and create solid phases by agglomeration or direct adsorption on surfaces. Quite generally we may use a solution reaction scheme [29], which specifies the interactions between the ion source M^+, photoelectron e^- or photohole h^+, substrate/colloid used and photon beam properties such as wavelength λ and fluence F, as follows:

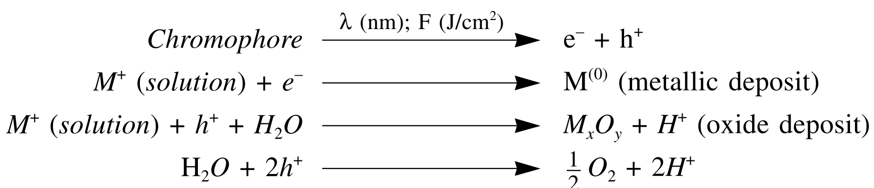

2.2. *Specific PDCS processes*

One of the first photodeposition liquid phase processes investigated since 1975 involved the preparation of a metastable mixture of aqueous colloid solution with solvated Se^{4+} ions and elemental Se particles which are activated by light [29–31]. The process can be described by the following photochemical equation:

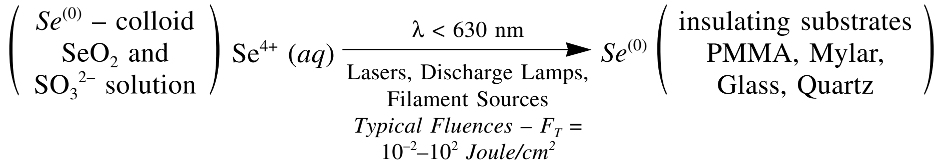

This particular photodeposition system uses amorphous Se (a-Se) colloids prepared in an aqueous reducing solution of SO_3^{2-} or similar reducing agents [32]. Activation by light with $\lambda < 630$ (nm) induces a simultaneous photoprecipitation of additional a-Se from the SeO_2 ion solution. At the same time photoadsorption and Se film growth start on virtually any insulating substrate in the irradiated zone and also on the Se colloid particles in the solution. Moreover, this photo-excited process is autocatalytic, in the sense that the ion source, photoelectron source and adsorption site are all of the same material, i.e., a-Se. The transport of photo-reduced material from the solution bulk to the adsorption sites is believed to be controlled by Brownian motion and the adsorption step itself is thermally and photonically activated [33]. It was observed that the deposition rate, for otherwise identical deposition parameters, is higher by more than an order of magnitude on Se pre-deposited layers as compared to deposition on the foreign material substrate. This phenomenon is observed by the existence of an incubation period occurring before the active deposition stage, and is closely related to the threshold fluence needed before a thin compact layer of a-Se is formed on the foreign substrate [34]. Thus, before the fast deposition rate of a-Se film starts onto the a-Se compact film, there is a delay caused by the unfavorable surface energy conditions existing between the depositing nanoparticles and the foreign substrate material.

Later on, a process, which may be termed a compound photodeposition system, was developed [34–37], in which the colloid chromophore is a binary chalcogenide compound, i.e., of composition XS, where X is a metal and S is Sulphur or more complex molecule. In these systems the depositing material is not of the same species as the chromophore material. The chromophore molecule XS is decomposed by light into its components, where one component is reduced onto the substrate and precipitated in the bulk of the solution, while the other constituent is oxidized, i.e., the Sulphur reacts within the aqueous solution and remains dissolved.

In one system [34], the CdS decomposes by light irradiation with $\lambda < 450$ nm and elemental $Cd^{(0)}$ is precipitated in the bulk and is also growing as a thin film on plastic substrates according to the following equation:

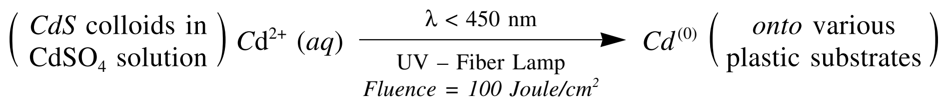

Similar photoreactions have been seen in colloid solutions by other investigators [15–17].

In another chalcogenide system [35], Zn and ZnS were co-deposited from ZnS colloids according to the following photochemical equation:

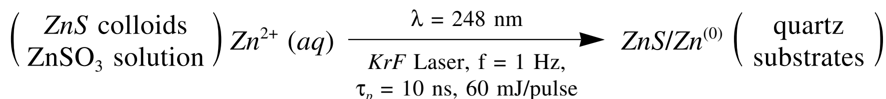

Another photodeposition method involved photo-electrolytical deposition of Gold onto p-Si substrates [36].

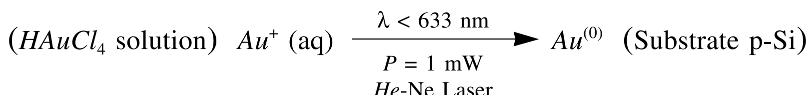

In this process, the chromophore is the Si substrate and the photon-electron excitation across the Silicon bandgap is done by a He-Ne Laser that reduces the gold. The substrate is a photo-electrochemical reducing half cell similar to other investigations in photo-electrochemical liquid media [15–19].

Recently we also investigated photodeposition from bio-organic materials using UV bleaching processes in chlorophyll solutions [37–38], similar to some other works on organic and metallic liquid phase solutions [39–44]. The photochemical scheme of an Chlorophyll-a bleaching process is given by [37]:

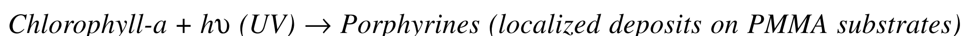

In this process, the chromophore was *Chlorophyll-a* and UV photon energies with wavelengths below 340 nm were needed to activate the deposition process. This variation of the photodeposition method uses a bio-organic material, which bleaches by photolytic processes due to UV photons, and the resulting material is deposited on plastic substrates. This process thus differs from the thermal-pyrolytic type metallization processes of organometallic solutions at solid/liquid interfaces which employ Argon lasers or UV irradiation [45–51] .

3. Photoreactor systems considerations

3.1. *Main requirements of a LPPD system*

A typical liquid phase photodeposition system should optimize the coupling between the incoming photon beams and the photoactive and depositing sites which are either the optical window, substrates immersed in solution, or other interfaces with the solution [26, 28, 29, 39, 42, 45, 48]. The light beam should be shaped in appropriate spatial geometries and accurately controlled and monitored. It must also penetrate into the photoreacting zone through the optical window and solution. A system may employ spatially static deposition modes or scanning modes by moving the laser beam or the substrate relative to each other. For wide area photodeposition, arc, discharge and incandescent light sources are more practical, while for very high radiances needed in fast scanning for pattern-writing, laser systems are the optimal choice.

In early photodeposition investigations [15, 16, 31, 33, 52] conventional incoherent sources were used, but laser sources were soon introduced because of advantages such as high irradiances and accurate wavelength selectivity [2, 8]. The photoreactor chamber requires, similar to CVD or other deposition techniques, a good temperature control and windows which allow the passage of light but which are resistant to both the solution compounds and produced photoexcited species. Finally, the substrate deposition site and bulk zones should be provided with appropriate rate controlling diagnostics instruments in situ or after the deposition [30, 52]. Several other factors are taken also into consideration, such as size, shape and material of the desired substrate. The interaction between the photon beam and photodeposition liquid can be achieved in various forms, to name a few: transmission mode through the substrate, impact mode on immersed substrates, substrate flotation and substrate-less Langmuir Blodgett type deposition on top of the liquid surface [29, 30, 39, 42, 45, 48], see Figure 2. Patterns imaging is performed by wide area masks, maskless exposure or accurate optical projection and high resolution laser line scanning mode.

Stray light shields and specific spectral and spatial filters may be needed to obtain reproducible homogenous deposits of high quality. For fast laser scanning mode and high spatial definition photoreactors, special attention is paid also to beam stability and vibration control. For holographic deposition [53], a wide angle access must be additionally provided for accepting the interfering beams through the photoreactor window. All the above considerations only illustrate some of the photoreactor design considerations encountered also in other liquid phase photodepositon cells [39, 42, 45, 48]. Finally, we mention that several commercial laser photodeposition systems have also been available for some time, mainly for metal pyrolytic deposition for microelectronic chips line repair from organometallic solutions [54].

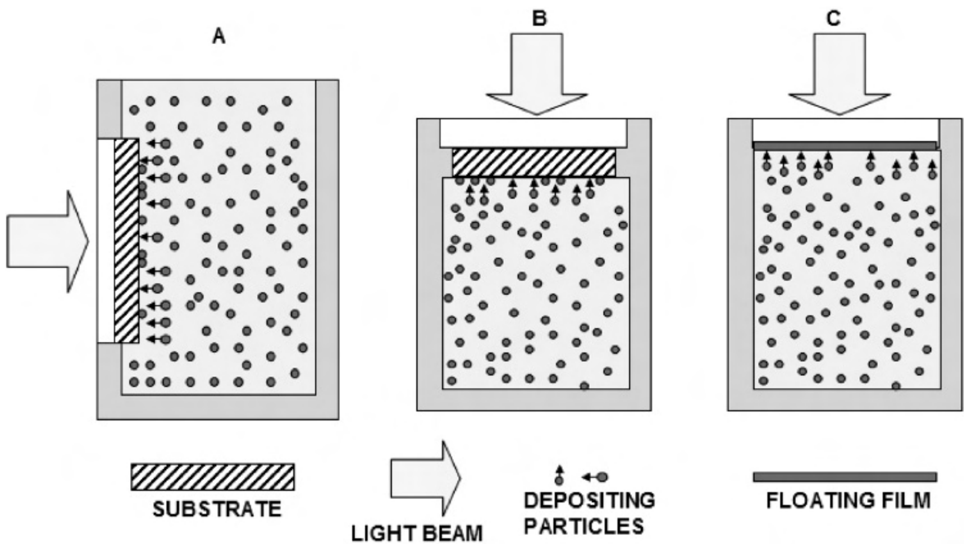

Figure 2. Various modes of photodeposition: A – side projection on substrate; B – top projection on substrate; C – top projection and deposition by flotation (Langmuir Blodgett).

3.2. *Microscopic observations of LPPD*

As detailed in section (2.1) the colloid liquid phase photodeposition processes involve various chemical, photochemical and physical reactions. In those applicable to photodeposition the irradiation with appropriate photons trigger redox or decomposition reactions which lead to photodeposition. This was initially observed as very fine colloidal particles precipitated in the bulk of the liquid phase. This effect was termed Volume Photodeposition (VP) [30]. A second effect which usually follows at a lower rate and accompanies VP, named Surface Photodeposition (SP) [55], consists of processes by which reduced or decomposed nanoparticles are adsorbed and form aggregates at any solution discontinuity boundary such as the substrates, windows, and on other suspended particles in the solution. In time, the nanoscopic colloid particles in the irradiated solution grow radially outwards, becoming large micrometric sized colloid particles, while at the same time adsorption and aggregation processes on the substrates evolve into a growing continuous thin film or aggregates. In Figure 3, one may observe the details of submonolayer photodeposition stages of a-Se films on PMMA [56, 57]. Similar to vacuum deposited films, the morphological structures obtained by PD in the sub-monolayer stages of their growth on a flat substrate consist initially of a discrete random array of individual particles adsorbed onto the surface, see Figure 3(a). These particles grow in size and coalesce during the PD writing process. The pre-compact film growth of a-Se as observed by SEM shows that the deposition is assisted also by material flow through diffusion, growth, bridging and coalescence.

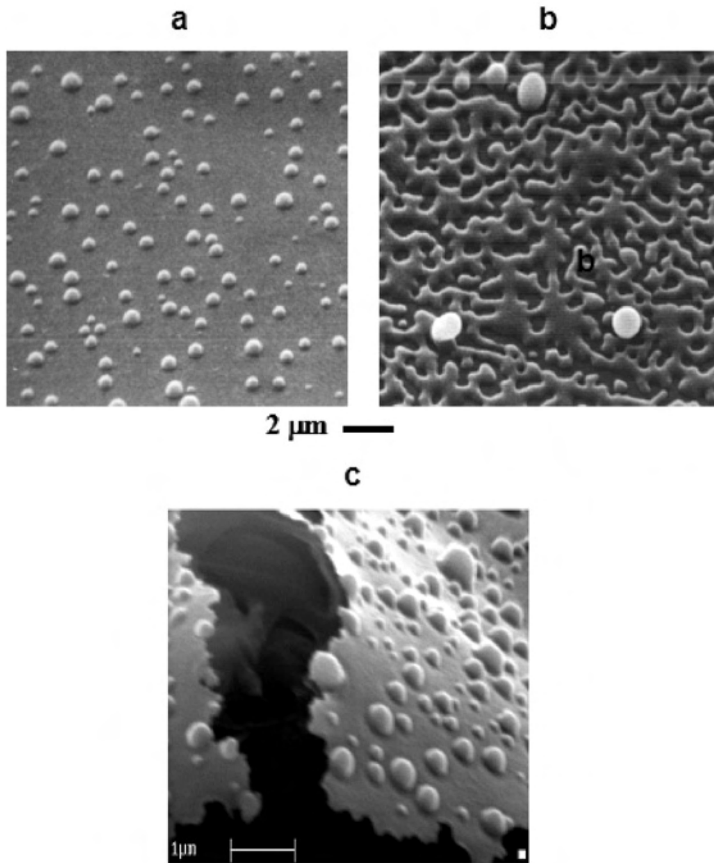

Figure 3. SEM observations of thin film sub – monolayer PD stages – (a) and (b) ; (c) compact layer split by heating to reveal the thickness of the compact layer, from ref. [57].

The particles aggregate and coalesce forming intricate 2D and even 3D topological shapes, depending upon the specific growth deposition parameters such as: temperature of the substrate, concentration of source particles and the adsorbate affinity with respect to the adsorption sites. In Figure 3(a) we show a SEM micrograph exhibiting mostly a morphology of isolated a-Se particles deposited on the substrate. As deposition proceeds one observes that the average particles size increases due to diffusion and material addition, leading to coagulation and aggregation of particles. These particles come into contact as seen in Figure 3(b–c) morphologies, which are typical of later stages of film coalescence when gaps fill up and a continuous film is created.

3.3. *Fundamental diagnostic parameters of photodeposition*

To quantify the SP processes on the substrates, kinetic experiments are usually performed in terms of film thickness and growing rates as a function of controlling parameters such as irradiation time period, light intensity, wavelength, temperature and reagents concentrations. The VP processes have also been investigated but to a lesser extent [30, 37, 38]. To gain a whole picture on the multitude of sub-processes induced by light irradiation in the bulk of the liquid we classify them schematically in Figure 4:

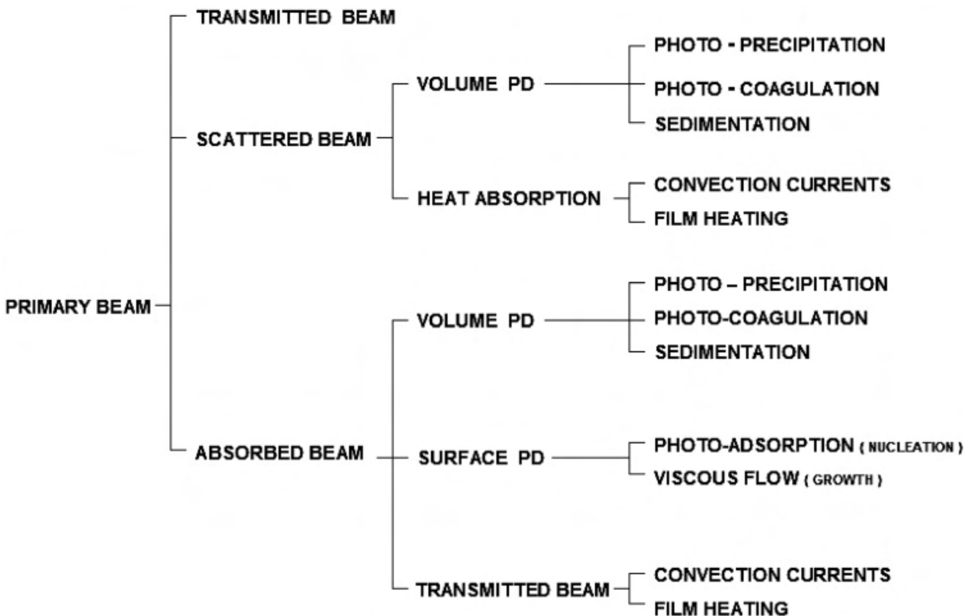

Figure 4. Various processes observed during photodeposition in colloid solutions.

In typical experiments used for PD, the photo-exciting beam is partially transmitted in the colloid cell. Therefore only the absorbed light, and to a lesser extent the scattered light may contribute to photodeposition. The light energy absorption in the solution may lead to various photolytic processes such as photoprecipitation and photoadsorption, or rather simple thermally induced effects such as photocoagulation, sedimentation and heating of the solution and the film. Isolating the various contributions in such complicated circumstances involves simplifying the setups to allow significant kinetic measurements. The simplest method is to measure the film thickness as a function of time for monocromatic light at well defined wavelength and light intensity values.

Even then, the overall conversion of photon energy into photo-precipitated and photo-adsorbed species in colloid solutions involves many mechanisms and the SP film usually grows nonlinearly in time [15, 18, 55, 57]. The dynamics of an

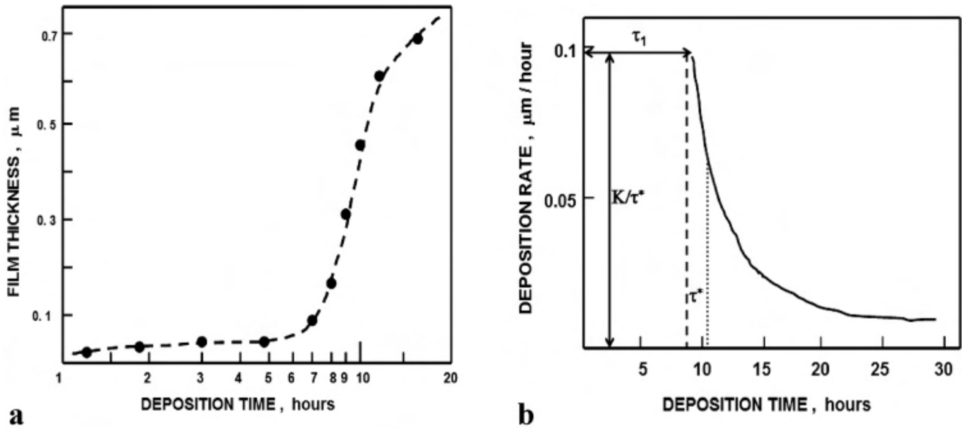

Figure 5. A typical photodeposition a-Se film thickness vs. time-curve (a), and growth rate-curve (b), from ref. [31]; K, τ_1, and τ^* are fitting constants, described in the text.

a-Se PD film thickness growth is shown in Figure 5. The growing rate curve during the active period follows roughly the light absorption in the growing film or the depletion of the ion source and chromophores from the bulk of the liquid solution according to the conditions prevailing in the process.

Since any film growth process depends on the growth mechanisms, one may fit the experimental results to particular rate laws. The most common growth laws are derived from the instantaneous growing rate of the film thickness defined by:

$$\rho = \partial\xi/\partial t. \tag{1}$$

where $\xi(t)$ denotes the time dependent thin film thickness or the deposit weight. In kinetic investigations of thin films growth one commonly finds the following empirical laws:

parabolic	$\xi^2 = 2k_p t + c$	$\rho = k_p/\xi$
cubic	$\xi^3 = k_c t$	$\rho = k_c/3\xi^2$
log*arithmic*	$\xi = (1/b)\ \ell n\ (abt + b)$	$\rho = ae^{-b\xi}$
inverse log	$\xi^{-1} = k_1 - \ell n\ t;$	$\rho = [(k_1 - \ell n\ t)^{-2}]/t$

where k_p, k_c, k_1, a, and b are kinetic constants of the growing mechanisms. Using the test function:

$$S = \frac{\partial \ell n\ (\partial\xi/\partial t)}{\partial \ell n\ \xi}, \tag{2}$$

one may obtain from the experimental growing curves the particular laws i.e., $S = -1$ for the parabolic growth, $S = -2$ for cubic and $S = -\text{const.} \cdot \xi$ for the

logarithmic growth, thus giving a clue to the particular mechanisms involved in the film growth. For photodeposition of a-Se films, a logarithmic growth law was found [31, 33, 55]. An example is seen in the growing curve of Figure 5(a). Hence, the experimental film thickness data, ξ, can be fitted in this case to this logarithmic type equation, also called Elovich equation:

$$\xi(t) = K_{opt} \cdot \ell n \left(1 + \kappa \frac{t - \tau_1}{\tau^*} \right) + \xi_1, \tag{3}$$

and the growing rate is given by the following equation:

$$\frac{d\xi(t)}{dt} = \frac{K_{sol}}{\tau^*} \cdot \exp\left(- \frac{\xi(t) - \xi_1}{K_{opt}} \right), \tag{4}$$

where τ_1 is related to a threshold or a so-called incubation time which refers to the period of time needed to form a compact film layer of thickness ξ_1, for a specific combination of substrate and photon flux. Finally, K_{sol}, K_{opt}, $\kappa = K_{sol}/K_{opt}$ and τ^* are constants of the kinetic equations (3) and (4), see also Figure 5(b), which provide a model for the photodeposition process on the compact layer itself, during the active PD period. This distinction of incubation and active periods during film deposition is of importance to perform significant kinetic experiments since the growing rates are very low during the initial adsorption stage on the foreign substrate, as compared to the later active stages when photodeposition occurs on the already deposited compact film. The incubation time from ref. [59] is given in Figure 6(a) for a-Se photodeposition. Using this division of the overall process into incubation, quasi-linear, and saturation range, we observed that the growing rate is changing with time in a wide range of 0–10 nm/sec for the a-Se case [55, 58], to 0–100 nm/sec for the CdS case[34]. The parameter $\rho = K_{sol}/\tau^*$ in Eq. (4) can be identified as an intrinsic photodeposition rate for film growth starting at $t = \tau_1$, which diminishes in time due to inefficient light absorption in the growing film when deposition is performed in the transmission mode. This parameter may be viewed as the rate which would have prevailed if no photons had been absorbed in the growing film itself. It is called the Quasi Linear Deposition Rate (QLDR) [31, 55]. We also calculated the value of $K_{opt} = 91$ nm which can be compared with the inverse value of the a-Se film optical absorption constant, $1/\alpha \sim 60$ nm at $\lambda = 488$ nm. This result shows indeed that $K_{opt} \sim 1/\alpha$ thus relating the Elovich equation constant K_{opt}, to the optical absorption constant of the depositing material. Regarding the incubation period τ_1, a closely related phenomenon was found in many photo-ablation processes where a threshold fluence value F_T for active photoablation and photoetching was found [60]. Similarly, in experiments of a-Se photodeposition we found a threshold of $F_T \sim 24$ J/cm^2 by fitting the film thickness vs. fluence curve to the following log type form [61], see also Figure 6(b):

$$\xi(F) - \xi_1 = K_F \cdot \ell n \left(\frac{F}{F_T} \right), \tag{5}$$

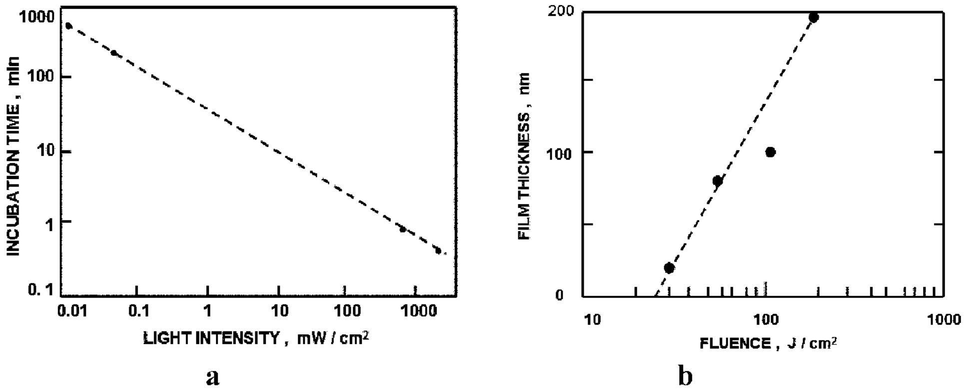

Figure 6. (a) Incubation time τ_1, for a wide range of light intensities for a photon energy of 2.65 eV, at RT, from ref. [59]; (b) Film thickness vs. fluence showing an extrapolated threshold fluence at $F_T = 24.2$ (J · cm^{-2}), from refs. [57, 61].

where K_F is a fitting constant whose value is approximately equal to the inverse of the optical absorption constant of the film. This threshold parameter is related to the Beer Lambert absorption law and accepted in this form in many works on polymer ablation such as Brannon et al., and Braun et al. [60], and mentioned also by Anisimov et al., and Zimmer et al., in this book.

Formally the empirical approximate relation (5) can be obtained from the Elovich mechanism expressed in Eqs. (3), and (4) using the fluence time relation $F = I_0 \cdot t$ where I_0 is the irradiance level entering the photodeposition cell, and $F_T = I_0 \cdot \tau_1$

$$\xi(F) - \xi_1 = K_{opt} \cdot \ell n \left[1 + \frac{\kappa}{\beta} \left(\frac{F}{F_T} - 1 \right) \right] \qquad \text{with} \qquad \beta = \frac{I_0 \cdot \tau^*}{F_T}$$

Then, for the conditions $F \gg F_T$ and $\kappa/\beta \sim 1$, we obtain the approximation of Eq. (5) and an interesting relation connecting between the incubation time τ_1 and the characteristic linear deposition time τ^*, $\tau_1/\tau^* = K_{opt}/K_{sol}$ which for the case of Figure 5(b) gives $K_{opt}/K_{sol} \sim 6.25$.

Moreover, we suggest here that both adsorption and ablation phenomena can be explained by a heterogeneous incubation process prevailing before the homogenous-active process starts, i.e., for photodeposition of Selenium on Selenium, or etching the inhomogeneous upper layer of the material during photo-ablation processes [60, 61]. This incubation process is then followed by an Elovich type hampering mechanism.

4. Controlling photodeposition parameters in liquids

4.1. *Processing parameters*

Several parameters control the film growth and structural properties in photodeposition of thin films. The basic practical problem is that the processes involved are characterized by non-equilibrium and non-linear mechanisms. Therefore, to provide a reproducible base for deposition, one needs accurately defined experimental processing parameters and derived theoretical parameters. The most important controlling parameters in photodeposition are:

a) The irradiation source wavelength λ and its spectral bandwidth $\Delta\lambda$
b) Intensity of the beam and its spatio-temporal profile, $I(x, t)$
c) The energy dose delivered to the system per unit area F, called fluence
d) Optical absorption coefficients profile of the liquid and thin film, $\alpha_k(x, t)$; $k = 1, 2$
e) Chemical and physical surface properties of the substrate such as affinities to adsorption of atoms from the solution
f) Substrate and liquid temperature, T_L, T_S
g) Spatial concentration profile of the reagents $C(x, t)$ with respect to the deposition plane

4.2. *Properties of the light source*

The photons absorbed in typical PDCS systems travel in a straight path, although secondary light scattering effects in the colloid solution may have a considerable effect. In the strong light absorption approximation, which prevails in most cases, the penetration of the laser beam or other light sources into the liquid media may be described quite accurately by the following equation, which ignores scattering:

$$I(x, t) = I(0, t) \cdot (1 - R) \cdot e^{-\alpha \cdot x}$$

Here $I(0, t)$ is the power density of the beam at the window entrance, R is the reflectivity of the photoreactor window and α is the effective optical absorption constant of the photoactive media, which is either that of the colloid solution or of the photoactive substrate. At the end of the film growth most of the photons are absorbed within a range of $X_R \sim 0.1$ µm of the growing film, thus hampering further growth from the solution. However, the absorption path in the colloid solutions used for photodeposition, X_R is much larger, of the order of 0.1–1 cm. This allows photodeposition also on immersed substrates and on the opposite wall of the photoreactor. However, since the optical properties of the solution change in time, during the irradiation, the net photon absorption in a PDCS system may be quite complicated. In these complicated situations one may consider $I(x, t)$ as a function combining the optical properties of the solution and film layer such as:

$$I(x, t) = I_0 \cdot (1 - R) \cdot e^{-\alpha_1 \cdot \xi(t)} \cdot e^{-\int_0^x \alpha_2(x, t)dx}, \tag{6}$$

where I_0 is the photon flux at the photoreactor window, $\xi(t)$ is the deposited film thickness at time t, and α_1 and α_2 are the optical absorption constant of the growing film and the colloid solution optical absorption constant, respectively [31]. It is also advantageous to prepare a diagnostics and controlling system which allows the observation of the photodeposition process in situ. Probing optical elements based on HeNe laser beams which can penetrate the photoreactor in some cases such as in a-Se colloids, were used orthogonal to the excitation beam. These provided a wealth of information regarding the precipitation effects in the solution bulk [30, 37, 38], such as the photodeposited or photobleached particle size and concentration dynamics [30].

4.3. *Substrate surface influence*

The type of substrate material, its cleanliness, topographic structure and optical properties, all affect the incubation period τ_1 or fluence threshold F_T, and also the structure of the photodeposited film and its coverage properties. In several works [62] it has been shown that the quality of the film depends on the presence or absence of structural defects. Quite generally, it was found that τ_1 depends strongly on the relative adsorption affinity A of the depositing material, towards the substrate. For the Se [31] and Cd [34] photodeposition processes the following trend governs the affinities :

$$A(\text{Glass}) < A(\text{Mylar}) < A(\text{PMMA}) < A(\text{Se or Cd}). \tag{7}$$

4.4. *Dependencies of the Quasi Linear Deposition Rate*

The general functional dependence of QLDR is quite complicated due to its many processing variables:

$$\rho = \rho(I, \lambda, T, C, \alpha). \tag{8}$$

However, the photodeposition processes can be monitored one variable at a time, eventually building the full dependence of equation (8). In typical experiments for a-Se, the QLDR dependencies on light intensity and temperature was given by the following equation [31, 33, 55]:

$$\rho(\lambda, I, T) = \rho_0 \cdot \exp\left(\frac{U(\lambda, I)}{kT^*}\right) \cdot \exp\left(-\frac{U(\lambda, I)}{kT}\right), \tag{9}$$

where ρ_0 and T^* are constants of the system with some physical insight discussed in [58]. One may realize that the process in this particular case is a combined photon and thermally activated process with a characteristic activation energy $U(\lambda, I)$.

4.4.1. *Temperature dependence*

Sometimes, the photodeposition is controlled in the liquid by photoreactions in the bulk and by transport of material to the adsorbing site by Brownian motion. The heating of the liquid by the absorption of photons will enhance the homogeneous solid phase nucleation in the liquid and also aid in the diffusive transport to the absorption sites. In many cases, it was found that an Arrhenius thermal activation energy exists i.e., the QLDR has a form $\rho = \rho_0 \exp(-U_D/kT)$ which for the a-Se case has typical activation energies in the range $U_D \approx 0.5 - 1.0$(eV). The low end value is typical of room or low temperature diffusive processes and the higher end involves photonic, non-thermal, high energy activation processes. The parameter T^*, in particular, is of high interest because it defines the temperature above which the photolytic activated process becomes less effective. This observation led to the suggestion of the so-called *compensation effect* [58], between photons and phonons. This effect is a physical realization that in photodeposition processes, the photonic and thermal processes compete and assist each other during the film growth. Their relative contributions cross at a critical temperature T^*, so called *compensation temperature*, which in a-Se is about 303 K [31, 58].

4.4.2. *Light intensity dependence*

By using laser sources with high light intensities [59] one can reduce the incubation period appreciably allowing fast deposition times, suitable for real time, direct laser writing applications [61]. Quite generally, specific power laws were deduced empirically for τ_1 in a wide range of light intensities I [31, 59]:

$$\tau_1 = \tau_0/I^m, \tag{10}$$

where m depends on processing variable parameters other than I, and τ_0 is an appropriate fitting constant. In particular, for the empirical graph given in Figure 6(a), $m = 1/2$.

For the active photodeposition period, the light intensity dependence of QLDR was also found to fit a power law:

$$\rho = \rho_0 \cdot I^m, \tag{11}$$

with m in the range of 0.5–7, thus connected to multiphoton absorption needed for one atom deposition [31, 34, 52, 59].

4.4.3. *Spectral or photon energy dependence*

The photon energy dependence of some photodeposition processes is also of an exponential form [31, 55]:

$$\rho = \rho_0 \cdot \exp - \left(\frac{qh\nu}{kT}\right), \tag{12}$$

where q is a constant and $h\nu$ is the photon energy.

Spectral efficiency curves for the SP processes can be derived from equation (12) and they provide clues for the physical origin and mechanisms involved in photodeposition. The spectral efficiency function [15, 31, 55] can be defined in a simple way by equation (13):

$$QY_{SP} = \frac{M}{I_0 \cdot \tau_d}, \tag{13}$$

where M is the photodeposited mass τ_d the period of film deposition, and I_0 the constant flux of light entering the liquid system.

Equation (13) assumes that the process is linear and hence the best procedure is to apply it only to the initial deposition time, i.e., use the QLDR concept also, for evaluating the intrinsic quantum yield of the process, ε defined by:

$$\varepsilon = \rho / N_\nu, \tag{14}$$

where N_ν is the photons flux with energy $h\nu$ entering the liquid system. The experiments gave typically values of ~10^{-1} atoms/photon for a-Se [55] and about 0.5 atoms/photon for CdS [34]. Some typical curves of the ε dependence on photon energy are given in Figure 7:

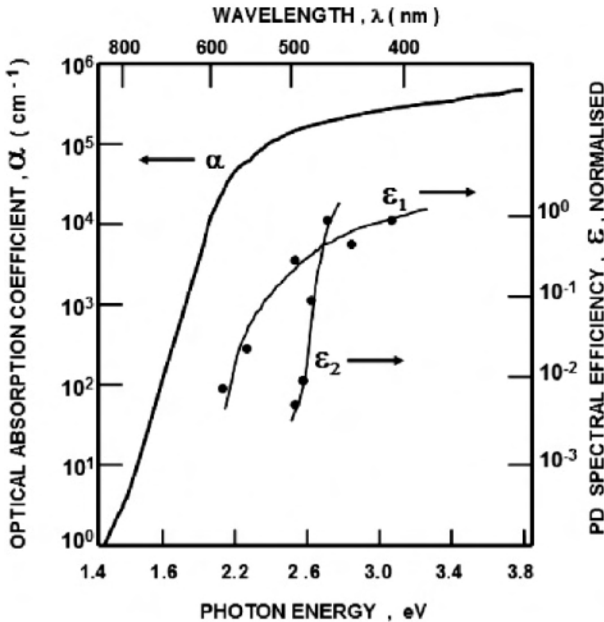

Figure 7. Typical curves of normalized PD spectral efficiency ε vs. photon energy in photodeposition of a-Se [59] for various conditions, along with the optical absorption constant α of a-Se.

The ε_1 curve was obtained for incandescent, low intensity sources, in the range of ~μW/cm^2 while ε_2 was obtained for higher laser beam intensities in the range of ~mW/cm^2. The apparent shift in the curves is only an artifact of the normalization procedure in the wavelength ranges of the two light sources. In fact, both curves follow the optical absorption constant of the depositing material which in this case was a-Se, thus proving that the PD spectral efficiency depends primarily on the bandgap photon absorbing properties of the chromophore.

4.4.4. *Chromophore and ion source concentration dependencies*

The initial concentration of the chromophores C_c and the ion source C_s both influence in principle the QLDR. A priori, the photodeposition processes may be assumed to be non-linear due to chemical amplification [63] or hampering mechanisms such as material depletion [61], possibly having a general power law of the form:

$$\rho(C) = k_0 \cdot [C_c]^n \cdot [C_s]^m, \tag{16}$$

where k_0 is a reaction rate constant, and n and m are the reaction orders of the chromophore and ion source, respectively. Although interesting from a theoretical point of view, practically the concentration dependence is of low importance because photonic properties rather than solution concentration control is sought in liquid photodeposition systems, thus data on chromophore concentration dependencies is scarce. Indeed, from the information available today [30, 31, 45], one may observe that for typical photodeposition systems, n and m are close to first order reactions, i.e., $n \approx m \approx 1$. This almost linear concentration dependence hints to a direct photon-chromophore interaction by which photoexcited particles deposit directly onto the substrate and lead to a proportional mass being deposited by the colloid material onto the substrate.

Probing for any clues on the microscopic mechanisms responsible for a-Se autocatalytic photodeposition, Mirchin et al., 1996 [59] have developed a formalism, expressing the spatial colloid concentration dynamics in the irradiated systems as follows. Let the optical absorption constant of the irradiated system be given by:

$$\alpha(x, t) = \varepsilon(x, t) \cdot C(x, t).$$

The master equation describing the pure electronic photoexcitation and relaxation in the solution is given by:

$$\frac{\partial C^{(*)}(x, t)}{\partial t} = \eta \cdot \varepsilon \cdot C^{(0)}(x, t) \cdot I(x, t) - \frac{C^{(*)}(x, t)}{\tau_c}$$

Here, ε denotes the molar optical extinction coefficient, η is the photoconversion quantum yield for excitation, $C^{(0)}$ is the non-excited chromophore (colloid particles) concentration, $C^{(*)}$ is the photo-excited chromophore concentration, $I(x, t)$ is the local light intensity, and τ_c is the photo-excited particles relaxation time.

The chemically driven precipitation reaction is formally given by another rate equation:

$$\frac{\partial C^{(0)}(x, t)}{\partial t} = k_p \cdot [C^{(\infty)} - C^{(0)}(x, t) - C^{(*)}(x, t)] + \frac{C^{(*)}(x, t)}{\tau_c}$$

where k_p is the precipitation rate constant, i.e., ions dissolved in the solution are photoreduced and $C^{(\infty)}$ is the equilibrium concentration or sometimes the maximum concentration of the colloid particles near the substrate. Solving the above three equations system under simplifying assumptions, and appropriate boundary conditions α_0 and I_0, give a closed expression for the dynamics of the optical absorption constant in the solution as a function of time:

$$\alpha(x, t) = \alpha_0 \cdot \exp[\varepsilon \cdot \eta \cdot I_0 \cdot t - x(\alpha - \alpha_0)],$$

showing that the photoprecipitation may exhibit a positive feedback amplification depending on $\varepsilon \times \eta$ and a negative feedback given by the term $x(\alpha - \alpha_0)$ where α_0 is the initial optical absorption constant of the colloid solution at $t = 0$ at any point x on the beam track, and I_0 is the incident light intensity at the window, $x = 0$.

The above result shows that the chromophores are amplifying in number during photoexcitation, and their concentration increases autocatalytically at the expense of the ion source. However this behavior is limited only to thin layers close to the entrance optical window with typical thicknesses of about $0.1/\alpha_0$.

5. Basic theory of liquid phase photodeposition

Besides the practical aspects of using photodeposition techniques in liquid solutions, there is also a great interest in a better understanding of the processes and mechanisms involved in the various stages of photoexcitation and film deposition. Unfortunately, not many in-depth works are available that address a unified methodology needed to quantify the photodeposition processes. This is however well understood in view of the formidable complexity of quantifying and analyzing empirical functions like those given in equation (8). Among the problems related to a conceptual understanding of photodeposition we find even the uncertainty related to the surface deposition step which may involve either a short range potential barrier activated adsorption by light or an adsorption mechanism by which the Brownian motion assists the barrier penetration process by simple thermal diffusion. In addition, we do not know yet if the surface growth consists entirely of nanoscopic particles adsorbed directly on the surface or also assisted by surface diffusive redistribution of the material which agglomerates on the surface. Finally, no direct evidence exists that light assists material deposition directly in a one step instead of creating proper electrostatic conditions to trigger a two step physical adsorption of a combined transport and adsorption process of colloidal particles on the substrate.

5.1. *The photolytic model of photodeposition in liquid media*

Equation (6) defines the decreasing light intensity law in many photon absorbing media. However, the detailed mechanisms of the absorption processes occurring in the colloid particles during photodeposition are still uncertain. In both photolytic and pyrolitic processes, it is assumed that the absorption of photons occurs primarily by interaction with electrons which are raised to excited states. Then rapidly, in times of the order of 10^{-12} sec, the photons create ions, radicals, free electrons and also give some of their energy to heating the environment, i.e., the absorbing substrate or liquid media. Lacking measurements at these short time scales, mostly phenomenological macroscopic kinetics formalisms were sought to describe the interaction processes in LPPD systems. These interactions cause either electron-photon excitations in the light absorbing chromophores [15–17] or create photo-excited radicals in the solution [55, 64].

The kinetics of the interaction between the photons and photoactive media, i.e., the photoexcitation process can be given formally by a general master equation describing the time space dynamics of the photoexcited species concentration $n^*(x, t)$ in the liquid phase in an uniaxial photon penetration mode:

$$\frac{\partial n^*(x, t)}{\partial t} = G(x, t) - f(n^*), \tag{17}$$

where $f(n^*)$ is a response function which governs the photo-excited chromophore concentration $n^*(x, t)$, and $G(x, t)$ is the photo-excited colloids photogeneration rate governed by the light penetration into the system:

$$G(x, t) = \eta \cdot \alpha_2(x, t) \cdot I^m(x, t), \tag{18}$$

where η is the quantum conversion efficiency of photons into chromophore excited species and m is the photon reaction order mentioned previously in section (4.4.2). The function $f(n^*)$ may have terms which describe various effects of the excited material species such as: agglomeration, de-excitation processes, dissipative diffusion, sedimentation, flocculation etc. [30, 55], given in a typical case by [55, 58]:

$$f(n^*) = k_a(n^*)^2 + D\nabla^2 n^* + \frac{n^*}{\tau}, \tag{19}$$

where k_a is an agglomeration kinetic constant, τ the relaxation time of the photo-excited species, and D the colloid particles diffusion constant. Combining and solving equations (17), (18) and (19), allows in principle to analyze the proper mechanisms applicable to a specific LPPD system. When the final product is a thin film structure or clusters of atoms building upon a surface, we may describe the transport of the photoexcited species to the adsorption sites by a general colloid particles flux transfer equation [55]:

$$J = n^* \cdot \nu + D \cdot \nabla n^* + \mu \cdot n^* \cdot \nabla U, \tag{20}$$

where the first term describes the convection or a free streaming kinetic flow of adsorbing particles with velocity v, onto surfaces. The second term is the particles diffusion term in the system and the third, relates to an electrochemical potential migration term, assumed to be governed by a viscous flow characterized by the particles mechanical mobility μ.

One may develop a particular mechanism of flow and absorption through an energy barrier located in the liquid boundary layer near the substrate as shown in Figure 8.

Under simplifying assumptions [55], this phenomenological theory yields a closed expression predicting the depositing particles flux density $J_p(x, t)$ due to photo-excitation and diffusion by the following equation:

$$J_p = \frac{n^*(x, t) \cdot D}{X_{eff} \cdot \exp(U_0/kT)}, \tag{21}$$

where X_{eff} is the particles depletion layer thickness in the solution close to the substrate and D is their diffusion constant. X_{eff} can be estimated from the particles diffusion characteristic length in the solution $L = \sqrt{D\tau}$, which for Selenium colloids was about 2.3 μm [55]. U_0 is the top of the potential barrier $U(x)$ for the incoming excited particles which adsorb on the surface. For colloid solutions, this potential barrier depends strongly on the electric fields in the colloid particle's double layer charge region. Experimentally, U_0 was resolved into a diffusive term and adsorption term with values ranging between 0.2 and 1.5 eV/atom depending upon parameters such as wavelength and light intensity [30, 55, 58].

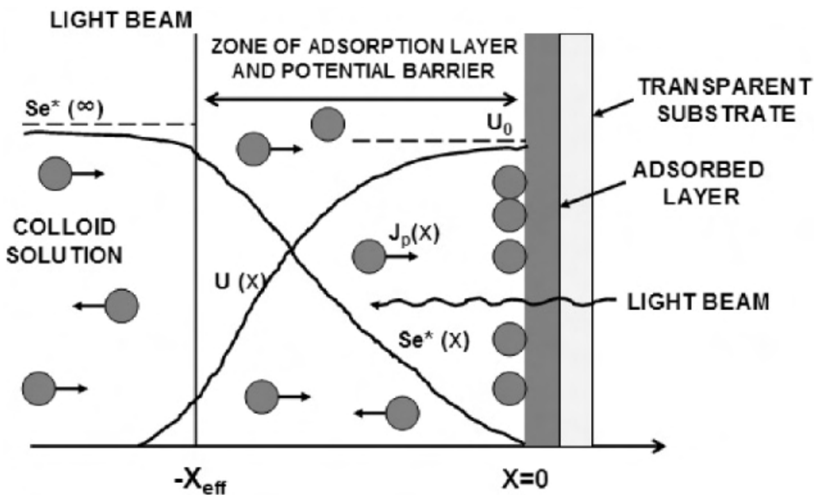

Figure 8. A conceptual mechanism of flow and absorption in photodeposition of a-Se , from ref. [58].

5.2. *The redox model of photodeposition at a semiconductor/liquid interface*

In this section we turn to modeling the photon-material excitation itself using the electrochemists view of redox reactions assisted by light [4, 16, 18]. At the interface between an oxide or semiconductor and an electrolyte, various reactions such as gas evolution [4], corrosion [65], film growth [16, 18], or metal deposition [64, 65], take place just like in regular electrodeposition. Most photoelectrochemical investigators [4, 15–17, 19, 20, 43, 64, 65] favor the somewhat simplistic scheme shown in Figure 9.

Thus in photo-electrochemical systems the photon energy can be converted either into electrical energy, chemical energy, or into the activation energy for driving redox and oxidation reactions. These processes are initiated by first absorbing bandgap photons in oxides or semiconductors immersed in the liquid electrolyte. Electron-hole pairs are created in the space charge depletion layer of the semiconductor, which exists at the semiconductor/electrolyte junction. This depletion layer is created whenever a semiconductor or oxide is immersed in a solution, due to charge transfer caused by the difference in electron affinity or so-called electrochemical potential, also equivalent to Fermi energy level concept, of the two phases. The net result is the formation of a junction electric field at the surface of the semiconductor with a depth of 5–200 nm. The direction of this electric field depends on the relative Fermi levels of the semiconductor and solution. For a p-type semiconductor, the field is directed from the interface towards the bulk of the semiconductor. Now, if electron-hole pairs are formed due to photon absorption in this region of the semiconductor, the electric field will separate them, driving the electrons towards the solution and the holes in the opposite direction. The electric field is seen as a bending of the semiconductor energy level near the interface in Figure 9(a). An opposite result will occur for an n-type semiconductor in contact with an electrolyte. Light will promote thus photoreduction reactions at p-type materials and photo-oxida-

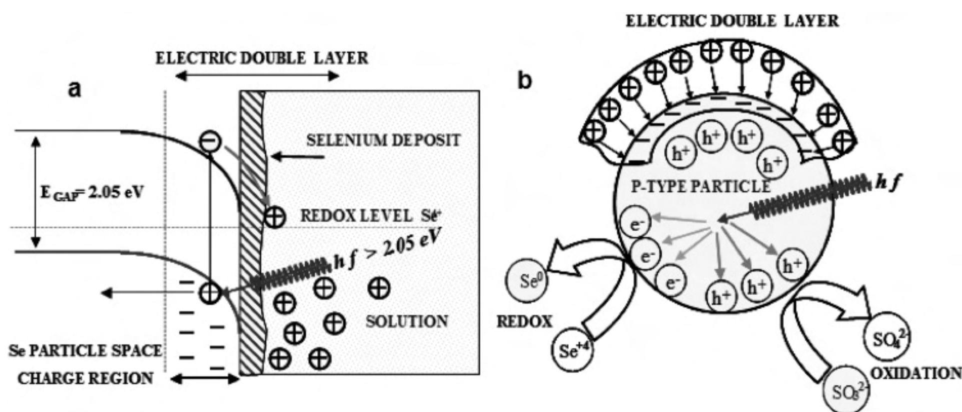

Figure 9. (a) An idealized energy band picture at a semiconductor-electrolyte interface; (b) the conceptual view of a photoexcited colloid particle growing by redox processes in the solution.

tions at n-type surfaces. Hence, for photodeposition, p-type substrates or colloid particles are effective [4].

For electrode photoreactions to occur, electrons should be transferred from the particle to the solution/surface interface. The redox behaviour of the chemical species in the solution will depend on the reactivity of the solution species in the solution towards the surface material. Species with redox potentials within the material bandgap will be oxidized for n-type semiconductors by the minority carriers (holes) while promoting anodic polarization reactions. Conversely, solution species will be reduced at p-type semiconductor interfaces by minority carriers (electrons), thus promoting cathodic polarization reactions see Figure 9(b).

6. Applications of photodeposition processes

6.1. *Photodeposition of optical arrays – parallel recording*

The ability of projecting or masking an image onto substrates and recording in one step by photodeposition from colloids has been demonstrated with a resolution defined by the optical imaging system [26]. Exciting results by masking techniques have been achieved in several laboratories for other techniques, see for example the chapters of Zimmer et al., and Kawaguchi et al., in this book. In all cases the resolution and depth of focus of any photodeposition system behaves as any other lithographic system for which the Rayleigh criterion for linewidth W, and Depth of Focus (DOF) are given by:

$$W = k_1 \cdot \lambda/NA, \tag{22}$$

$$\mathrm{DOF} = k_2 \cdot \lambda/(NA)^2, \tag{23}$$

where NA is the Numerical Aperture of the optical projection system and k_1, k_2 are process dependent constants, usually in the range 0.5–1.0.

Figure 10(a) shows typical resolution test patterns obtained by projection or masking contact methods in colloid photodeposition systems [52]. The 3 fields show several photographic properties of PD patterns, i.e., test charts bars with an optical Modulation Transfer Function (MTF) resolution defined by the optical imaging system, a digital dots recording and an analogue scene recording.

The best line resolution obtained by PD was about 0.5 μm, employing holographic projection interference of an Ar ion laser with $\lambda = 488$ nm, by which line gratings were photodeposited directly in one step [26, 53], see Figure 10(b). The thickness of the gratings fingers was about 9 nm at the tip and the first order grating's diffraction efficiency was about 12% for $\lambda = 628$ nm. An important conclusion drawn from the experiments was that the photodeposition process being *limited intrinsically* by the smallest colloid particles in the solution, may become a method by which submicrometric imaging and near-field imaging can be achieved [26]. The PD wide field projection techniques were used to obtain optical components such as

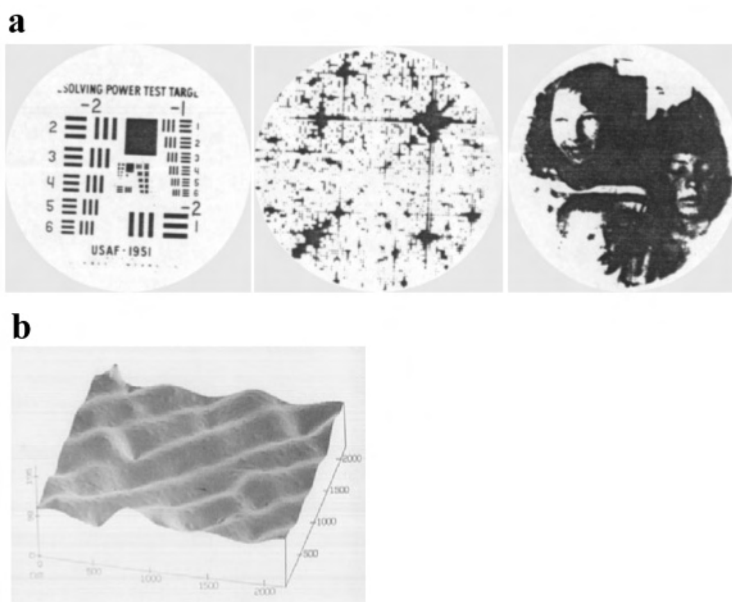

Figure 10. (a) Test patterns obtained by PD with 25 mm diameter each, from ref. [52], (1988) with a best line contact masking resolution of ~8.3 μm; (b) AFM image of a holographic ultra thin film grating obtained by Argon Laser PD, with a line resolution of about ~500 nm; sampled area 200 × 200 nm, from ref. [26] (1994).

filters, zone lenses, mirrors, beam-splitters, birefringent elements, refractive elements, phase-gratings, diffractive optical elements [57, 61], as well as electronic devices contacts [18].

6.2. *Laser photodeposition writing – serial recording*

Scanning systems producing various materials patterns by direct beam writing were tried by many investigators starting with Osgood et al. (1982) [66] and followed by others such as, L. Nanai (1989) [20], H. G. Muller (1990) [11], Y. F. Lu et al. (1991) [18], A. M. Dhote (1992) [22], Brook et al. [22, 45], and since 1995 also by Peled et al. [57, 61]. The scanning methods allows one to deposit conveniently lines and dots, by interactive computer programs in which the operator controls the geometry, number of scanned elements, and exposure time. The scanning can be performed either by using a translating stage moving the entire substrate in the x-y plane, or more conveniently by employing a beam scanner system which is much faster but less accurate. A typical laser beam in a scanning system is focused by a scanning lens of a focal length f and aperture D onto the substrate/active liquid media. The photodeposited linewidths may vary according to the exposure times and other scanning parameters used, but they may be designed by assuming a nominal theoretical laser Gaussian beam spot diameter, given from Gaussian beam waist

theory by the following characteristic parameters for the focused beam diameter-d_{oo}, half angular divergence – θ and Depth of Focus – DOF [57, 61]:

$$\theta = \frac{1}{2}\frac{D}{f} \sim \left(\frac{2\lambda}{\pi d_{oo}}\right) \qquad d_{oo} = \left(\frac{4\lambda}{\pi}\right)\left(\frac{f}{D}\right) \qquad DOF = \frac{1}{2}\frac{\lambda}{\theta^2}. \tag{24}$$

Figure 11(A), and Figure 11(B) show some typical optical elements written by

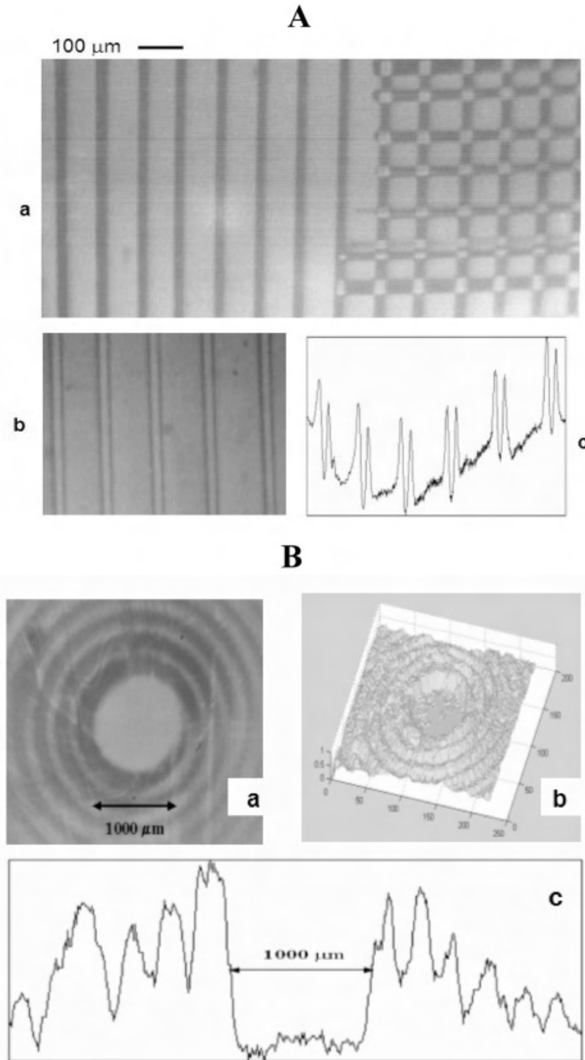

Figure 11. **A.** (a) linear gratings of 25 μm linewidths; (b) ablated grating of 8 μm linewidth; (c) densitometer profile of (b); **B.** (a) typical DOE element obtained by PD; (b) 3D-profile; (c) 1D-densitometer profile of (b) showing a central zone with diameter of ~1000 μm.

PD from colloid solutions [57, 61], with linewidth resolutions in the range W ~ 8–250 μm and DOF ~ 2–5 mm.

6.3. *Write-Erase features by photodeposition in colloid solutions*

A new combination which is of interest today involves write and erase techniques for optical storage of digital information and correction of photodeposited patterns. This technique was investigated in several works [56, 57, 61]. Microscopic elements of linewidths in the range 8–150 μm were written and erased using the combined photodeposition and photoablation effect. Thus PD through its in situ writing and erasing properties promises a multitude of uses ranging from write-only to write-ablate patterning. The fluence threshold for deposition [57] is about $F_T \approx 24.2$ (J/cm^2) and that of ablation ~16.8 (kJ/cm^2). An optimized writing speed reported at room temperature was 150 μm/sec constituting a compromise between several factors such as fluence threshold, heating of the solution and line overflow or undercutting required for the written elements.

7. Comparison with gas phase photodeposition

7.1. *Advantages of liquid phase photodeposition*

Essential to liquid phase photodeposition is that it is performed at much lower substrate temperatures, even below room temperature as compared to gas phase photodeposition [8, 22, 24, 45–49]. Since vacuum or highly controlled pressures in the photoreactor are not demanded for most liquid phase systems, an obvious advantage is obtained in equipment costs and ease of processing [20, 45–47]. Furthermore, the liquid phase material source can usually be prepared as a solution with very long shelf lifetime, up to several years. In comparison, gas phase systems need very accurate in situ mixing of gases leading to obvious higher basic costs for the operation of the photoreactor. Also, specific compounds such as organic materials cannot be easily processed in gas phase at very high temperatures, though several small organic molecules are currenly being vapor deposited for OLEDs. The deposition rates are also much higher for liquid phase photodeposition [20, 45–47] because of the higher concentrations of reagent species in the liquid as compared to the gas phase. Typical film thickness deposition rates for liquid phase photodeposition are of the order of 10 μm/sec, while gas phase photodeposition systems have typically deposition rates of only 10 nm/sec [1–3] i.e., by a factor of 10^3 lower. Also, the lateral writing velocity of gas phase photodeposition systems is about 100 μm/sec [14] while in liquid phase photodeposition systems we find values as high as 100 mm/sec [21, 22, 45–47, 49], giving again, a factor of 1000 in favour of liquid phase photodeposition systems. For comparison purposes, one may define a figure of merit (FM) for the photodeposition efficiency observing that the film thickness growing rate multiplied by the scanning velocity is proportional to the volume or photodeposited mass per unit time. FM thus represents an

overall process efficiency in terms of processing time, keeping other parameters such as spectral, temperature and light dependent efficiencies, constant. Thus we observed that the liquid phase photodeposition FM can be higher by a factor of 10^6 as compared to gas phase photodeposition processes [29]. Nevertheless, specific combinations of very high temperatures and high gas pressures can boost the FM of a gas phase photodeposition process closely to that of liquid phase photodeposition. However, this will be achieved still at the expense of increased complexity and hazardous processing.

7.2. *Shortcomings of liquid phase photodeposition*

The weaknesses of liquid phase photodeposition systems lie in the traditional area where vacuum processing have a leading edge i.e., in critical processing of high purity products, needed for instance in microelectronics semiconductor processing. Also, the high optical absorbance of the liquid cell creates in many cases quite inefficient conditions for the penetration of photons to the deposition sites. However, this problem can be minimized by making extremely thin optical paths at the expense of involving some more complex systems design to circulate fresh chromophores to the deposition zone. Finally, many semiconductor processing technologies are still not compatible with liquid phase processing today. However, this is not a must but rather a technological choice of current microelectronics materials processing.

8. Conclusions

In view of about ~10^5 papers which have appeared in the literature on all phases of photo-assisted processes and applications during the past 2 decades, it is reasonable to expect a continued growth of basic research and subsequent applications in liquid phase photodeposition in particular. This growth will probably be not too rapid. However, it will steadily increase as photonic and laser processing will become more accepted in microelectronics, optoelectronics and other materials science applications. In this chapter we have categorized and described the design, operation, parametric monitoring and theories underlying the liquid phase photodeposition processes in general and colloid systems in particular. Although the principles of operation differ greatly for various types of systems and materials, some fundamental quantifying and processing variables have been defined towards the goal of setting comparable standards in this area.

Acknowledgements

The authors wish to express their gratitude to Ivan Biaggio for editing this chapter, and to C. Ruth Peled and Yael Sharoni for helping with formatting various parts of this book.

References

1. Y. Murata, M. Hanabusa, H. Matsunami and K. Takahashi, Guest Editors, '1-ICPEPA-Photo Excited Processes and Applications', *Appl. Surf. Sci.* (Special Issue), 79–80 (1994).
2. D. J. Ehrlich and J. Y. Tsao, Eds., *Laser Microfabrication: Thin Film Processes and Litography* (Boston: Academic Press, 1989).
3. A. Peled, Guest Editor, 'Photodeposition and Related Photoassisted Thin Film Processes', *Thin Sol. Films* **218** (Special Issue), 1–2, (1992); M. Meunier, V. Craciun, E. Fogarassy and W. Kautek, Eds., 'Laser Materials Processing', *Appl. Surf. Sci.* (Special Issue), 208–209 (2003) .
4. H. Yoneyama, 'Electrochemical Aspects of Light-Induced Heterogeneous Reactions on Semiconductors', *Critt. Rev. in Sol. St. and Mat. Sci.* **18**(1), 69–111 (1993); C. I. H. Ashby, 'Pattern Formation Techniques in Photochemical Etching', *Thin Sol. Films* **218**, 252–258 (1992); M. Wha Shin and J. Gyun Song, 'Study of Photoelectrochemical Etching Process of Semiconducting 6H-SiC Wafer', *Matls. Sci. and Eng.* **B 95**(3), 191–194 (2002).
5. S. A. Lis, J. M. Lavine, 'Ag Photodoping of Amorphous Chalcogenides', *Appl. Phys. Lett.* **42**(8), 675–677 (1983); K. Matsuda, M. Ichida, A. Nakamura, K. Kawamoto, T. Nabatame and I. Hirabayashi, 'Femtosecond Spectroscopic Studies of Photodoping Effects in Insulating $YBa_2Cu_3O_6$ and Nd_2CuO_4 Thin Films', *Physica C* **280**, 84–92 (1997).
6. H. Sato and S. Nishio, 'Polymer Laser Photochemistry, Ablation, Reconstruction, and Polymerization', *Journal of Photochemistry and Photobiology C: Photochemistry Reviews* **2**(2), 139–152 (2001); M. Tejos, R. Schrebler, F. R. Diaz and M. A. del Vallec, 'Thin Amorphous Platinum Films Photochemically Obtained, and Their Potential Sse as Modified Electrodes', *Thin Solid Films* **409**(2), 172–177 (2002).
7. V. Haruna, S. Yoshida, H. Toda and H. Nishihara, 'Laser Beam Writing System for Optical Integrated Circuits', *Appl. Opt.* **26**(21), 4587–4592 (1987); C. A . Sunil, Ye. Gouzhang and H. Gafney, 'Photodeposition of Diffraction Gratings in Glass: A Comparison of Lithographic, Laser Writing and Holographic Deposition', *Applied Spectroscopy* **54**(6), 869–877 (2000).
8. D. Bäuerle, Ed., *Laser Processing and Diagnostics* (Berlin: Springer-Verlag, 1984); D. Bäuerle, *Chemical Processing with Lasers* (Berlin: Springer-Verlag, 1986); D. Bäuerle, 'Laser Processing and Chemistry: Recent Developments', *Appl. Surf. Sci.* **186**(1–4), 1–6 (2002).
9. Y. Helen, R. Dassow, M. Nerding, K. Mourgues, F. Raoult, J. R. Kohler, T. Mohammed-Brahim, R. Rogel, O. Bonnaud, J. H. Werner and H. P. Strunk, 'High Mobility Thin Film Transistors by Nd:YVO_4-Laser Crystallization', *Thin Solid Films* **383**(1–2), 143–146 (2001).
10. K. L. Saenger, 'Pulsed Laser Deposition. I. A Review of Process Characteristics and Capabilities', *Processing of Advanced Materials* **3**(1), 1–24 (1993); D. B. Chrisey and G. K. Hubler, Eds., *Pulsed Laser Deposition of Thin Films* (New York: Wiley, 1994).
11. J. Malinowski and A. Buroff, 'Photostimulated Solid State Reactions', *Contemp. Phys.* **19**, 99–108 (1978); H. G. Muller, 'YAG Laser Direct Writing of Copper from Copper Formate Films', *Appl. Phys. Lett.* **56**(10), 908–906 (1990).
12. R. Alexandrescu, 'Laser-Stimulated Processes in Metal Carbonyls for Metal-Based Film Synthesis', *Appl. Surf. Sci.* **106**, 28–37 (1996).
13. A. Luches, E. D'Anna, G. Leggieri, M. Martino, A. Perrone, G. Majni, P. Mengucci, R. Alexandrescu, I. N. Mihailescu and J. Zemek, 'Excimer Laser Reactive Ablation Deposition of Silicon Nitride Films', *Appl. Surf. Sci.* **86**(1–4), 170–174 (1995).
14. T. H. Baum and P. B. Comita, 'Laser-Induced CVD of Metals for Microelectronics Technology', *Thin Sol. Films* **218**, 80–94 (1992).
15. H. Hada, Y. Yonezawa, A. Yoshida and A. Kurake, 'Photoreduction of Silver Ion in Aqueous and Alcholic Solutions', *J. Phys. Chem.* **80**, 2728–2731 (1976).
16. B. Kraeutler and A. J. Bard, 'Heterogeneous Photocatalytic Preparation of Supported Catalysts Photodeposition of Platinum on Powder and Other Substrates', *J. Am. Chem. Soc.* **100**(13), 4317–4318 (1978).
17. Y. Yonezawa, T. Sato, M. Ohno and H. Hada, 'Photochemical Formation of Colloidal Metals', *J. Chem. Soc., Faraday Trans.* **1**(83), 1559–1567 (1987).

18. R. K. Montgomery and T. D. Mantei, 'UV Laser Deposition of Metal Films by Photogenerated Free Radicals', *Appl. Phys. Lett.* **48**(7), 493–495 (1986)); Y. F. Lu, M. Takai, T. Nakata, S. Nagamoto and S. Namba, 'Laser-Induced Deposition of Ni Lines on Ferrite in Aqueous Solution', *Appl. Phys.* **A 52**, 129–134 (1991); A. K. Al-Sufi, H. J. Eichler and J. Salk, 'Laser Induced Copper Plating', *J. Appl. Phys.* **54**(6), 3629–3631 (1983).
19. T. Inoue, A. Fujishima and K. Honda, 'Photoelectrochromic Characteristics of Photoelectrochemical Imaging System with a Semiconductor/Solution (Metallic Ion) Junction', *J. Electrochem. Soc.* **127**, 1582–1588 (1980); R. J. Phillips, M. J. Shane and J. A. Switzer, 'Electrochemical and Photoelectrochemical Deposition of Thallium Oxide Thin Films', *J. Mater. Res.* **4**(4), 923–929 (1989).
20. R. F. Karlicek, V. M. Donnelly and G. T. Collins, 'Laser Induced Metal Deposition on InP', J. *Appl. Phys.* **53**(2), 1084–1090 (1982); L. Nanai, I. Hevesi, F. Bunkin, B. S. Lukyanchuk, M. R. Brook, G. A. Shafeev, D. A. Jelski, Z. C. Wu and T. F. George, 'Laser-Induced Metal Deposition on Semiconductors from Liquid Electrolytes', *Appl. Phys. Lett.* **54**(8), 736–738 (1989).
21. R. J. von Gutfeld, E. E. Tynan, R. L. Melcher and S. E. Blum, 'Laser Enhanced Electroplating and Maskless Pattern Generation', *Appl. Phys. Lett.* **35**(9), 651–653 (1979); H. K. Kuiken, F. E. P. Mikkers and P. E. Wieranga, 'Laser-Enhanced Electroplating on Good Heat Conducting Bulk Materials', *J. Electrochem. Soc.* **130**, 554–558 (1983).
22. M. R. Brook, K. I. Grandberg and G. A. Shafeev, 'Kinetics of Laser-Induced Au Pyrolytic Deposition from the Liquid Phase', *Appl. Phys.* **A52**, 78–81 (1991) ; A. M. Dhote, S. C. Patil, S. M. Kanetkar, S. A. Gangal and S. B. Ogale, 'Metallization of Glass/Ceramic from Solutions of Organometallic Compounds by Laser Induced Pyrolisis', *J. Mater. Res.* **7**(7), 1685–1689 (1992); Zs. Geretovski, T. Szorenyi, K. Bali and A. Toth, 'Dependence of Deposition Kinetics on Precursor Concentration and Writing Speed in Pyrolitic Laser Deposition from Solution', *Thin Sol. Films* **241**, 67–70, (1994).
23. J. Bohandy, B. F. Kim, F. J. Adrian and A. N. Jette, 'Metal Deposition at 532 nm Using Laser Transfer Technique', *J. Appl. Phys.* **63**(4), 1158–1162 (1988).
24. Z. Toth, T. Szorenyi and L. Toth, 'Ar Laser Induced Forward Transfer (LIFT): A Novel Method for Micrometer Size Surface Patterning', *Appl. Surf. Sci.* **69**(1–4), 317–320 (1993).
25. H. Hidai and H. Tokura, 'Direct Laser Writing of Aluminum and Copper on Glass Surfaces from Metal Powder', *Appl. Surf. Sci.* **174**(2), 118–124 (2001).
26. V. Weiss, A. A. Friesem and A. Peled, 'Inorganic Materials for Archival Holographic Recording', *Journal of Imaging Science and Technology* **41**(4), 355–371 (1997); A. Peled, V. Weiss, D. Rosenblatt and A. A. Friesem, 'Holographic Gratings by Photodeposition Techniques', *Opt. Eng.* **31**(1), 70–73 (1991); A. Peled, V. Weiss, A. Shalgi and A. A. Friesem, 'Resolution Capabilities of Photodeposited Holographic Gratings', *Appl. Surf. Sci.* **79/80**, 393–398 (1994).
27. C. Arnone, M. Rothschild, J. G. Black and D. J. Ehrlich, 'Visible Laser Photodeposition of Chromium Oxide Films and Single Crystals', *Appl. Phys. Lett.* **48**(15), 1018–1020 (1986); H. W. Lee and S. D. Allen, 'High Deposition Rate Laser Direct Writing of Al on Si', *Appl. Phys. Lett.* **59**(19), 2087–2089 (1991).
28. M. Meunier, R. Izquierdo, M. Tabbal, S. Envoy, P. Desjardins, M-H. Bernier, J. Bertomeu, N. Elyaagouby, M. Suys, E. Sacher and A. Yelon, 'Laser Induced Deposition of Tungsten and Copper', *Matls. Sci. And Eng.* **B 45**, 200–207 (1997).
29. A. Peled, 'Review: State of the Art in Liquid Phase Photodeposition Processes and Applications (LPPD)', *Lasers in Engineering* **6**, 41–79 (1997).
30. A. Peled, 'Volume Photodeposition Process in a-Se Hydrosols', *Colloid Polym. Sci.* **262**, 718–820 (1984); N. Borochov and A. Peled, 'Aggregation Kinetics of Photo-Excited Colloid Solutions observed by Dynamic PCS', *Appl. Surf. Sci.* **86**, 533–537 (1995).
31. M. Perakh and A. Peled, 'Photodeposition III: Interpretation of the Structural and Kinetics Studies', *Thin Sol. Films* **50**, 293–300 (1978); M. Perakh and A. Peled, 'Photodeposition II Kinetics Studies', *Thin Sol. Films* **50**, 283–291 (1978).
32. A. Peled, 'Studies of a-Se Dispersions Used in the Photodeposition Process; Part I: Dispersion Properties in the Dark', *J. of Dispersion Sci. and Technol.* **5**(2), 219–226 (1984).
33. M. Perakh and A. Peled, 'Light-Temperature Interference Governing the Inverse/Combined

Photoadsorption and Photodeposition of a-Se Films', *Surf. Sci.* **80**, 430–440 (1979).
34. V. Weiss, A. Peled and A. A. Friesem, 'Photodepositon of Thin Films from CdS Colloid Solutions', *Thin Sol. Films* **218**(1), 193–201 (1992).
35. A. Peled, B. Dragnea, R. Alexandrescu and A. Andrei, 'Laser Induced Photodeposition from ZnS Colloid Solutions', *Appl. Surf. Sci.* **86**, 538–542 (1995).
36. A. K. M. Braga, V. Baranauskas and A. Peled, 'Laser Induced Photodeposition of Gold upon p-Silicon Immersed in Chloroauric Acid Solutions', *Appl. Surf. Sci.* **79/80**, 375–380 (1994).
37. A. Peled, Y. Dror, I. Baal-Zedaka, A. Porat, N. Mirchin and I. Lapsker, 'Photobleaching and Photodeposition in a Chlorophyll Based Solution', *Synthetic Metals* **115**, 167–171 (2000).
38. N. R. Mirchin, A. Peled and Y. Dror, 'Bleaching Processes and Their Reaction Rates in Photo-Excited Chlorophyll Solutions', *Applied Physics* **B 74**, 267–271 (2002).
39. Jan W. M. Jacobs and Chris J. C. M. Nillesen, 'Repair of Transparent Defects on Photomasks by Laser-Induced Metal Deposition from an Aqueous Solution', *J. Vac. Sci. Technol.* **B 8**(4), 635–642 (1990).
40. M. S. Paley, D. O. Frazier, H. Abdeldeyem, S. Armstrong and S. P. McManus, 'Photodeposition of Amorphous Polydiacetylene Films from Monomer Solutions onto Transparent Substrates', *J. Amer. Chem. Soc.* **117**(17), 4775–4780 (1995).
41. A. W. Brinkman, S. Oktik and G. J. Russell, 'Properties of ZnO Layers Deposited by Photoassisted Spray Pyrolysis', *Journal of Crystal Growth* **159**(1–4), 195–199 (1996).
42. D. B. Wolfe, S. J. Oldenburg, S. L. Westcott, J. B. Jackson, M. S. Paley and N. Hallas, 'Photodeposition of Molecular Layers on Nanoparticle Substrates', *Langmuir* **15**, 2745–2748 (1999).
43. M. Tejos, R. Screbler, F. R. Diaz, M. A. Del Valle, 'Thin Amorphous Platinum Films Photochemically Obtained and Their Potentialuse as Modified Electrodes', *Thin Solid Films* **409**, 172–177 (2002).
44. T. Sano, S. Kutsuna, N. Negishi and K. Takeuchi, 'Effect of Pd-Photodeposition over TiO_2 on Product Selectivity in Photocatalytic Degradation of Vinyl Chloride Monomer', *Journal of Molecular Cataltsis A: Chemical* **189**(2), 263–270 (2002).
45. M. R. Brook, K. I. Grandberg and G. A. Shafeev, 'Kinetics of Laser Induced Au Pyrolytic Metal Deposition from the Liquid Phase', *Appl. Phys.* **A 52**, 78–81 (1991); L. Nanai, I. Hevesi, F. Bunkin , B. S. Lukyanchuk, M. R. Brook and G. A. Shafeev, 'Laser Induced Metal Deposition on Semiconductors from Liquid Electrolytes', *Appl. Phys. Lett.* **54**(8), 736–738 (1989).
46. K. Kordas, L. Nanai, G. Galbacs, A. Uusimaki, S. Leppavuori and K. Bali, 'Reaction Dynamics of CW Ar^+ Laser Induced Copper Direct Writing from Liquid Electrolyte on Polyimide Substrates', *Appl. Surf. Sci.* **158**(1–2), 127–133 (2000).
47. K. Kordas, J. Bekesi, R. Vajtai, L. Nanai, S. Leppavuori, A. Uusimaki, K. Bali, T. F. George, G. Galbacs, F. Ignacz and P. Moilanen, 'Laser Assisted Metal Deposition from Liquid Phase Precursors on Polymers', *Appl. Surf. Sci.* **172**(1–2), 178–189 (2001).
48. Z. C. Zhong, P. A. Dowben and D. J. Sellmyer, 'Selective Area Laser-Induced Deposition of Rare Earth Hexaborites from Solution', *Materials Letters* **37**(6), 320–324 (1998).
49. E. J. Lafferty, D. J. Macauley, K. F. Mongey, P. V. Kelly and G. M. Crean, 'Photo-Assisted Metallization: Line Resolution Studies', *Surface and Coatings Technology* **100–101** (1–3), 80–84 (1998).
50. R. Subramanian, P. E. Denney, J. Singh and M. Otooni, 'A Novel Technique for Synthesis of Silver Nanoparticles by Laser-Liquid Interaction', *J. of Mater. Sci.* **33**(13), 3471–3477 (1998).
51. Z. C. Zhong, R. H. Cheng, J. Bosley, P. A. Dowben and D. J. Sellmyer, 'Fabrication of Chromium Oxide Nanoparticles by Laser-Induced Deposition from Solution', *Appl. Surf. Sci.* **181**(3–4), 196–200 (2001).
52. H. Ginsburg, A. Peled and A. Perakh, 'Thin a-Se Films Obtained by Electroless-Photodeposition Phenomenon', Abstracts of the 6th Annual Meeting of the Israel Association of Growth of Crystals and Thin Films, C-2, November 1975; M. Perakh and A. Peled, 'Photodeposited thin Se Films', Annual Meeting Abstracts, Haifa 1976, in *Bull. Isr. Phys. Soc.* **28**(87) (1976); M. Perakh and A. Peled, 'Photodeposition of a-Se films', Electrochem. Soc. Annual Meeting, Philadelphia 1977, The Electrochemical Society, Princeton, New Jersey, 1977, *Extended Abstract* **107**(77-1), p. 288; A. Peled, 'Photodeposition Recording and Display Technology', *Opt. Eng.* **24**(4), 717–718 (1985);

A. Peled and Y. Dror, 'Optical Imaging by the Surface Photodeposition Effect', *Opt. Eng.* **27**(6), 482–485 (1988).

53. V. Weiss, A. Peled and A. A. Friesem, 'Spatial Frequency Response of Holographic Gratings Photodeposited from Inorganic Colloids', *Appl. Optics* **33**(22), 4988–4992 (1994).
54. Malcolm C. Gower, Henry Helvajian, Koji Sugioka and Jan J. Dubowski, Eds., 'Laser Applications in Microelectronic and Optoelectronic Manufacturing VI', *Proceedings of SPIE* **4274**, 1–516 (2001).
55. A. Peled and D. Naot, 'A Phenomenological Model of Photoprecipitation in a-Se Colloid Solutions', *Colloid Polym. Sci.* **265**, 986–992 (1987); A. Peled and M. Perakh, 'On the Theory of Photoadsorption Kinetics of a-Se Colloids: A Simple Model for the Kinetic Parameters', *J. Colloid Interface Sci.* **122**(1), 193–200 (1988).
56. A. Peled, V. Baranauskas, C. Rodrigues, D. Art-Weisman, L.Grantman and A. A. Friesem, 'Characterisation of Photodeposited Se Planar Structures by SFM', *J. Appl. Phys.* **77**(12), 6208–6213 (1995); M. Perakh, A. Peled and Z. Feit, 'Photodeposition of a-Se Films by the Selor Process. I: Main Features of the Process, Film Structure', *Thin Sol. Films* **50**, 273–282 (1978); I. Lapsker, J. Azoulay, M. Rubnov, Z. Regev, R. C. Peled and A. Peled, 'Image Analysis of Structural Changes in Laser Irradiated, Thin Films of Photodeposited a-Se', *Appl. Surf. Science* **106**, 316–320 (1996).
57. I. Baal-Zedaka, S. Hava, N. Mirchin, R. Margolin, M. Zagon, I. Lapsker, J. Azoulay and A. Peled, 'Photodeposition of Optical Elements from Colloid Solutions', *Colloids and Surfaces A: Physicochem. Eng. Aspects* **217**, 191–202 (2003).
58. A. Peled, D. Naot and M. Perakh, 'On the Theory of Photoadsorption Kinetics of a-Se Colloids: the Thermal Activation Energy and Compensation Effect', *Colloid Polym. Sci.* **266**, 958–964 (1988).
59. A. Peled, A. A. Friesem and K. Vinokur, 'CW Laser Photodepositon of a-Se films', *Thin Sol. Films* **218**(1), 201–208 (1992); A. Peled and Y. Dror, 'Optical Imaging by the Surface Photodeposition Effect', *Opt. Eng.* **27**(6), 482–485 (1988); N. Mirchin, J. Gavan and A. Peled 'Theoretical Approach to Optical Response Properties of Photoprecipitation in Irradiated Colloid Systems', *Appl. Surf. Science* **106**, 418–421 (1996).
60. T. Lippert, L. S. Bennett, T. Nakamura, H. Niino and A. Yabe, 'Single Pulse Threshold and Transmission Behaviour of a Triazeno-Polymer During Pulsed UV-Laser Irradiation', *Applied Surface Science* **96–98**, 601–604 (1996); J. H. Brannon, D. Scholl and E. Kay, 'Ultraviolet Photoablation of a Plasma-Synthesized Fluorocarbon Polymer', *Appl. Phys.* **A 52**, 160–166 (1991); A. Braun, K. Zimmer and F. Bigl, 'The Influence of Ambient Temperature on KrF Laser Ablation of Polyimide in Air', *Appl. Surf. Sci.* **154–155**, 73–77 (2000).
61. I. Baal-Zedaka, S. Hava, N. Mirchin, R. Margolin, M. Zagon, I. Lapsker, J. Azoulay and A Peled, 'Diffractive Optical Elements Written by Photodeposition', *Applied Surface Science* **208–209**, 226–232 (2003); A. Peled, L. Grantman, M. Ochayon and A. A. Friesem, 'Investigations of Write/Erase Features by the Photodeposition Technique', *Appl. Surf. Sci.* **106**, 306–310 (1996).
62. A. Peled, 'Transformation Steps of Microstructures in Photodeposited Films of a-Se', *J. Mater. Res.* **4**(1), 177–179 (1989); A. Peled and E. Hadziioannou, 'Thermal Characterization of a-Se Films Obtained by Low Temperature Photodeposition', *J. Mater. Sci.* **26**, 1769–1774 (1991).
63. A. Erdmann, W. Henke, S. Robertson, E. Richter, B. Tollkühn and W. Hoppe, 'Comparison of Simulation Approaches for Chemically Amplified Resists' , *Proceedings of SPIE* **4404**, 99–110 (2001).
64. Y. Yonezawa, T. Sato, S. Kuroda and K. I. Kluge, 'Photochemical Formation of Colloidal Silver: Peptizing Action og Acetone Ketyl Radical', *J. Chem. Soc. Faraday Trans.* **87**(12), 1905–1910 (1991).
65. T. Kobayashi, Y. Taniguchi, H. Yoneyama and H. Tamura, 'Effective Surfaces of Semi-conductor Catalysis for Light-Induced Heterogenous Reactions Evaluated by Simultaneous Photodeposition of Both Oxidation and Reduction Products', *J. Phys. Chem.* **87**, 768–775 (1983).
66. R. M. Osgood, Jr., et al., 'Localized Laser Etching of Compound Semiconductors in Aqueous Solution', *Appl. Phys. Lett.* **40**(5), 391–393 (1982); H. H. Gilgen, T. Cacouris, P. S. Shaw, R. R Krchnavek and R. M. Osgood, 'Direct Writing of Metal Conductors with Near-UV Light', *Appl. Phys.* **B 42**, 55 (1987).

CHAPTER 10

CARBON ALLOTROPES CREATED BY INTENSE IRRADIATION OF FROZEN HYDROCARBONS

M. Okoshi[1, *] and M. Hanabusa [2]

[1] *Department of Electrical and Electronic Engineering, National Defense Academy, 1-10-20 Hashirimizu, Yokosuka 239-8686, Japan;*

[2] *Hamamatsu Industrial Research Institute of Shizuoka Prefecture, 1-3-3 Shin-Miyakoda, Hamamatsu 431-2103, Japan*

*(*Author for correspondence, E-mail: okoshi@nda.ac.jp)*

ABSTRACT: The following chapter describes the processing of frozen hydrocarbons, such as acetone, acetylene, and methanol, by intense irradiation from excimer lasers, femtosecond (fs) laser, synchrotron radiation (SR), and free electron laser (FEL). The main products obtained in these investigations are diamond-like carbon films (DLC), but diamond and possibly one-dimensional carbon (carbyne) microcrystals appear also. Section 2 gives a short review on laser synthesis using frozen gases. In Section 3, the pulsed laser deposition (PLD) conducted to deposit the diamond-like carbon films using excimer lasers is described. Experiments based on novel light sources appear in Sections 4–6 for fs lasers, SR and FEL, then concluding the results in Section 7.

1. Introduction

Carbon allotropes have a rich variety, and many of them are extremely useful for daily and industrial applications. Diamond is probably the best-known example, but recently other interesting carbon allotropes, such as fullerene and carbon-nanotubes, were discovered also.

The artificial production of these carbon allotropes has been a subject of intense investigations, and many efforts have resulted in successful products. For instance, diamond crystals were produced in factories under artificially created high-temperature and high-pressure conditions. More recently, simple schemes were invented to produce diamond films in the gas phase [1].

In particular, lasers have played a key role in the efforts to produce new materials of interest artificially, with carbon allotropes in particular. In fact, fullerene was synthesized initially by lasers processing [2]. Then, even diamond films were created by employing laser methods [3, 4].

For the past 15 years we have conducted many experiments with the goal of synthesizing various carbon allotropes using various light sources. Initially, we conducted pulsed laser deposition (PLD) of diamond-like carbon (DLC) films [5], using a Nd:YAG laser to ablate graphite targets. We were especially interested in DLC, because it is an amorphous material made of sp^3 carbon bonds like diamond and its properties resemble those of diamond, which include a high mechanical hardness, high electrical resistivity, and very good optically transparency.

Then, we used frozen hydrocarbons as targets during PLD experiments, to produce DLC films [6]. The purpose for using frozen hydrocarbon instead of the normal

Aaron Peled (ed.), Photo-Excited Processes, Diagnostics and Applications (PEPDA), 281–300, 2003.
© 2003 *Kluwer Academic Publishers. Printed in the Netherlands.*

graphite target was twofold. First, we intended to decrease the number of particles included in the deposits produced by PLD using the solid target as observed by optical microscopy of the resulting DLC films. These particulates tend to spoil the quality of the deposited DLC films, making their applications quite limited. The particles were generated from the target surface during the intense irradiation of the powerful pulsed lasers. On the other hand, using the frozen gas targets, part of the generated debris is expected to vaporize during the flight towards the substrates or upon their arrival on the substrates. The second reason why we switched to the frozen hydrocarbon was attributed to the fact that from plasma chemical vapor deposition using hydrocarbon gases radicals such as CH_3 play a key role in synthesizing diamond films [7]. In time, it became clear to us that the frozen gas targets offer some unique opportunities for laser synthesis of carbon allotropes for a variety of new reasons other than mentioned above. For instance, we noted that a large number of hydrocarbons with various properties can be used by this method, many of which can be frozen at moderate temperatures. In addition, the choice of frozen hydrocarbon targets matched well with another characteristic of these experiments, namely using various light sources available today for synthesizing the carbon allotropes, as detailed below.

Recent advances in photon generation techniques made it possible to adopt a variety of new light sources for laser processing of materials. Therefore, in addition to excimer lasers with which we started these series of experiments [6], we determined to try out more promising developments by engaging in materials processing using synchrotron radiation (SR) [8] and free electron lasers (FEL) [9]. SR is characterized by the presence of highly energetic photons with short wavelengths, so called hard photons, emerging recently as a versatile powerful light source for materials processing. In particular, SR has been used already for photochemical vapor deposition of Si, Al, and SiO_2 thin films, see for instance ref. [10]. In these applications, the energetic photons generated by SR, which extends as far as the soft X-ray region, are capable of exciting inner core electrons, leading to new types of chemical reactions that lasers have failed to induce by ordinary valence electron excitations. In another experiment, crystalline polytetrafluoroethylene (PTFE) thin films were produced by using SR at a rate unattainable by conventional PLD [11].

As for FEL, it is a monochromatic photon source with a wavelength tunability in a wide range, though this particular feature presents no special advantages for ablation of solid targets used in PLD. However, for our frozen hydrocarbon targets the wavelengths could be adjusted for resonant molecular excitation, thus making FEL a highly desirable light source.

More recently we started also using a femtosecond (fs) laser in our laboratory. The fs lasers have made a substantial progress recently, and they are used not only for diagnostics which require high time resolutions, but also, owing to their increased output power, as new tools for material processing. For instance, the ultra-short pulses can irradiate the target material with such high power densities that extreme nonequilibrium conditions can be achieved, allowing the creation of new materials, unattainable by other lasers. In our experiments, we expected that the frozen

hydrocarbon would be photodissociated differently under the extremely powerful and short laser pulses, thus leading to the production of interesting new carbon allotropes. In addition, the size of the fs laser system has been reduced substantially, making the processing system into a comfortable tabletop size, accompanied also by a substantial reduction of costs. It turned out that the experiments using the fs laser were most rewarding in this series of experiments [12–14], because one of the products obtained had elongated microcystals shaped like a hexagonal pillar. The identification measurements conducted on these crystalline structures strongly suggested we have synthesized one-dimensional carbon crystals, namely carbyne [15–25]. Among carbon allotropes, diamond and graphite possess three-dimensional and quasi two-dimensional structures, respectively [15], while fullerene may be regarded as a material of quasi zero-dimensional structure. In this respect, the presence of one-dimensional carbon crystals (carbyne) has been expected and sought for a long time [26]. The carbon allotrope which seems to satisfy this condition was found in shock-fused graphite gneisses in the Ries Crater [16], and since then, numerous attempts have been made to synthesize these crystals and identify their properties. However, it is very difficult to synthesize high quality carbyne crystals which can be used for reliable identification measurements. Hence, elusive results are still associated today with the carbyne [26].

2. Reviewing laser synthesis in frozen gases

Since the adoption of frozen gases was the key element of our current series of experiments, we review here briefly the previous works related to this subject.

In the past, liquid targets for PLD have been used only occasionally instead of solid materials. Such experiments are indeed limited in number, and they include liquid targets such as molten metals [27, 28], oil [29] and aromatic hydrocarbons [30]. As mentioned, as an alternative to solid and liquid targets, we employed initially frozen hydrocarbons [6, 31]. Soon, other groups followed our experiments based on laser ablation of frozen gas targets [32–35]. Ishiguro and his group [32] irradiated frozen nitrogen gas on a Nb or BN plate at 10 K with a KrF excimer laser, 248 nm, simultaneously with the target. In this case, NbN or BN films were deposited on the substrate heated to temperatures of 300 °C to 400 °C. In another experiment carried by the same group, CH_4 or CO_2 were frozen on graphite carbon plates at 12 K, and both the frozen target and graphite carbon plate were subjected to a simultaneous irradiation from a KrF laser, which led to the deposition of DLC films [33]. Similarly, the simultaneous ablation of frozen CH_4 formed on a Si wafer cooled at 16 K and Si by the second harmonic, 532 nm of an Nd:YAG laser produced SiC films [34]. In another experiment, Niino et al. [35] irradiated frozen nitrogen with a picosecond laser to generate electronic excited nitrogen atoms, used to modify carbon target surfaces and form carbon-nitride layers. For a comprehensive good review on laser ablation of frozen gases see ref. [36].

3. Pulsed laser deposition of diamond-like carbon films using excimer lasers

PLD of diamond-like carbon (DLC) films by excimer lasers was the first in the series of works using frozen hydrocarbons. As mentioned earlier, we used at first graphite as target for the laser, which is still a standard procedure used widely for PLD of DLC. As mentioned, we used frozen acetylene and acetone as targets for the excimer lasers for the dual purpose of eliminating the particles embedded in the films and for increasing the possibility to synthesize diamond.

The experimental arrangement used in our current works is shown in Figure 1. The chamber was made of a stainless steel, 200 mm in diameter and 250 mm high. Either acetylene or acetone was frozen on a copper plate connected to a liquid nitrogen reservoir. The gas was blown through a 1/4 in. stainless steel pipe towards the copper plate. A rotary pump evacuated the chamber during the target preparation. After a frozen gas layer grew into roughly 1–2 mm thick layer, the gas supply was stopped and a turbomolecular pump was turned on to improve the pressure of the chamber to 10^{-6} Torr. The pressure increased to 10^{-5} Torr during deposition. Since the frozen material evaporates quickly by irradiation, the laser beam was moved constantly across the target, to prevent ablation of the copper surface.

A 193-nm ArF laser with a pulsewidth of ~14 ns was used as the light source. The pulse repetition rate was 10 Hz. Using a 248-nm KrF laser, additional experiments were carried out. The laser beam was introduced into the chamber through a quartz plate after passing through a quartz lens with a focal length of 350 mm. The substrate was a quartz plate placed at a distance of 40 mm from the target on a stainless steel holder heated by an electric heater. Before positioning it, the quartz

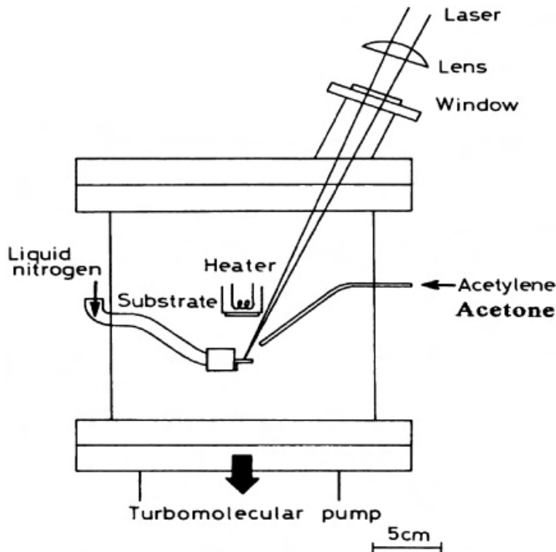

Figure 1. The arrangement used for pulsed laser deposition using excimer lasers and frozen hydrocarbon.

plate was cleaned ultrasonically in methanol and rinsed with distilled water. For further cleaning we used UV ozone cleaning (UVOC), in which the quartz plate was exposed in air to UV radiation generated by a deuterium lamp for 15 min at 200 °C [37].

In Figure 2 we see that for both sources, the films grew almost at the same rate regardless of the substrate temperature for films deposited from frozen acetylene between room temperature and 300 °C. The laser power density was 9×10^8 W/cm^2 and 5×10^9 W/cm^2 for the ArF laser and the KrF laser, respectively.

Raman spectra were measured to identify the deposited films. As shown in Figure 3, a broad peak near 1540 cm^{-1} is observed for films deposited at 200 °C and 300 °C from acetylene targets by the ArF laser and the KrF laser, respectively. This peak is characteristic of the DLC films [5]. We could not observe the sharp Raman peak at 1333 cm^{-1}, which is the signature for the diamond phase. A similar spectrum was observed using frozen acetone and ArF laser at 200 °C. The DLC films thus obtained exhibited a high electrical resistivity and high chemical inertness. The electrical resistivity was typically 3×10^8 Ω·cm, and the films exhibited a good chemical inertness by testing with a HF/HNO_3 (1:1) solution. The optical absorption coefficient in the IR and visible regions, as well as the mechanical hardness, closely resembled that observed previously by us for DLC films produced in laser ablation of graphite targets [5]. It should be emphasized also that during the previous stage of laser ablation by graphite targets, the DLC films were produced at 50 °C and not at room temperature and 100 °C [5]. In contrast, the films produced by the frozen hydrocarbon method were DLC over a much wider range of substrate temperature between room temperature and

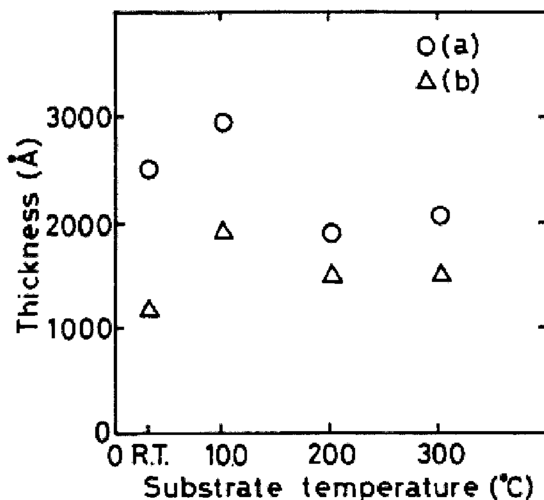

Figure 2. Film thickness as a function of substrate temperature: (a) ArF laser, and (b) KrF laser. The deposition time was 15 min. The laser power density was 9×10^8 W/cm^2 and 5×10^9 W/cm^2 for the ArF laser and the KrF laser, respectively. The substrate temperature was varied from room temperature to 300 °C.

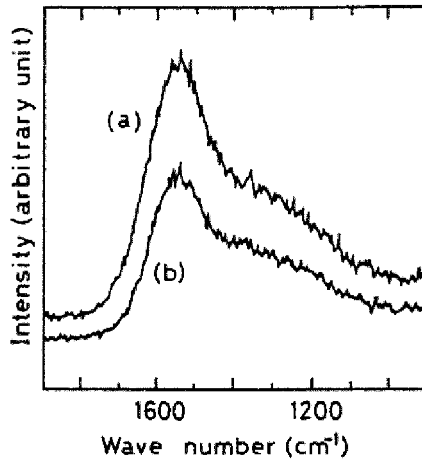

Figure 3. A Raman spectrum showing a broad peak at 1540 cm^{-1}, which is characteristic of DLC films: (a) ArF laser with 9×10^8 W/cm^2, and (b) KrF laser with 5×10^9 W/cm^2. The substrate temperature was 200 °C and 300 °C for the ArF laser and the KrF laser, respectively.

300 °C. Regarding the mechanical hardness of the films deposited, those obtained by the KrF laser were found inferior at 100 °C, as shown in Figure 4. Testing was performed by a ceramic tool with a sharp corner which was used on the films to make scratches. The depth of the scratched dip indicates the film hardness.

We obtained mixed results for the particle appearance in films deposited from frozen hydrocarbon. Although, they had less particulates than those prepared from graphite, the particles density varied even for films deposited under seemingly identical conditions. We ascribe this behavior to the fluence fluctuation of the laser pulses. As for the mechanisms prevailing during the ablation we believe that the extremely powerful laser pulses convert the frozen hydrocarbon into solids, as evidenced by the coloring of the irradiated target area. Subsequent pulses then ablate these solid products, and as in normal PLD processes small particles are incorporated into the growing films.

The DLC films often contain substantial amounts of hydrogen even if graphite target are used [5]. We suspected initially that excessive amounts of hydrogen may be contained in the films formed from the hydrocarbons. To detect the hydrogen content, we measured IR transmission spectra and observed the intensity of the C-H stretching vibration near 2920 cm^{-1} [5]. For films deposited by the ArF laser using frozen acetylene the peak was hardly observed, as shown in Figure 5, but this peak became clearly evident for films deposited by the KrF laser. The observed difference for the two lasers may be ascribed to the fact that the acetylene absorbs ArF laser light stronger than KrF laser light.

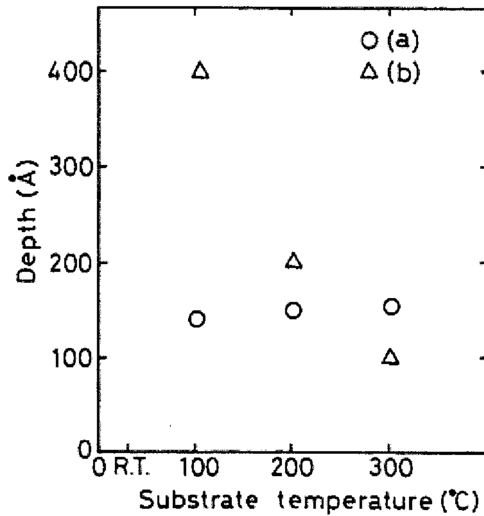

Figure 4. Depth of scratches, indicating the films mechanical hardness as a function of substrate temperature: (a) ArF laser, and (b) KrF laser. The laser power density was 9×10^8 W/cm^2 and 5×10^9 W/cm^2 for the ArF laser and KrF laser, respectively.

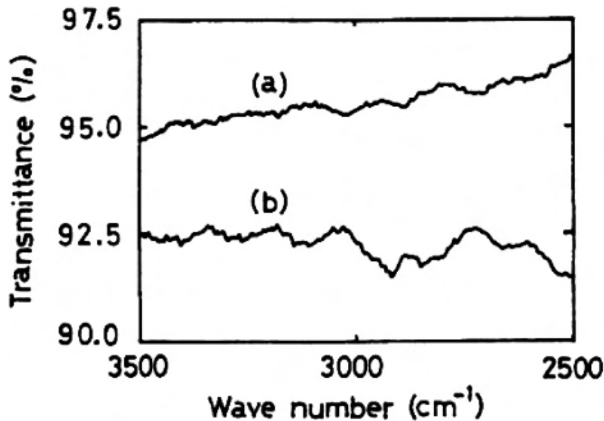

Figure 5. Fourier-transform IR spectra showing a C-H vibrational mode at 2920 cm^{-1}: (a) ArF laser of 9×10^8 W/cm^2, and (b) KrF laser of 5×10^9 W/cm^2. The substrate temperature was 200 °C and 300 °C for the ArF laser and the KrF laser, respectively.

4. The production of carbon allotropes by a femtosecond laser

4.1. *Diamond-like carbon films produced by a femtosecond laser*

A femtosecond laser was used to deposit the DLC films by ablating frozen gas targets. The 10-mJ output pulses from the fs laser with 130 fs duration and wavelength of 790 nm, were generated by a combination of a mode-locked Ti:sapphire

laser and a regenerative amplifier system from Spectra Physics, model-Tsunami and model-TSA-10, respectively.

The experimental arrangement was almost identical to the one used in the previous PLD work with excimer lasers, see Figure 1. The laser beam was introduced into a chamber through a 2.4-mm thick quartz window and focused onto the target by a 17.5-cm focal length lens. The spot shape on the target was elliptical, with an area of about $30 \times 90\ \mu m^2$. The peak power density reached a value as high as 4×10^{15} W/cm^2.

Acetone with a concentration of 99.5%, was frozen on the bottom surface of a liquid nitrogen reservoir made of stainless steel. After the gas condensed into a 3-mm thick layer, the gas supply was stopped, and a 200 l/s turbomolecular pump was turned on to lower the pressure of the chamber to 4×10^{-5} Torr. When the frozen layer was lost, the laser irradiation was interrupted to form new layers. The net irradiation time was 40 min. In some cases, we blew hydrogen gas of 99.99999% purity towards the target surface through a 1/4-in copper pipe and the hydrogen gas pressure was maintained at 0.75 Torr. In addition, an electric heater was used to control the substrate temperature. The laser beam irradiated the surface of the target at an incident angle of 45°. The target was at a 3 cm distance from the substrate. Hydrogen-terminated Si (100) surface was prepared by HF dipping and ultrapure water rinsing after UV ozone cleaning [37, 38].

The DLC films could be produced even at room temperature. The deposited films by fs laser with frozen acetone were 200-nm thick after 40-min irradiation at a laser power density of 4×10^{15} W/cm^2. They were examined by Raman spectroscopy, showing a broad peak near 1540 cm^{-1}, similar to the films deposited by the excimer lasers and shown in Figure 3. Other features that characterize the DLC deposited films include transparency in the visible range and an electrical resistivity higher than $10^7\ \Omega \cdot$cm. Furthermore, the film immersed in an HF/HNO_3 (1:1) solution remained intact, while the silicon substrate dissolved completely.

Using electron energy loss spectroscopy (EELS) we measured the carbon K-edge spectra of the DLC films and estimated the sp^3/sp^2 bonding ratio, which indicates the fraction of the DLC in the films. Figure 6 shows the EELS spectrum measured for a DLC film produced by the fs laser. The area under the π^* peak observed at 285.6 eV is compared with that of a reference graphite [39–41]. Assuming 100% sp^2 bonding for graphite, we estimate that the fraction of sp^3 bonding in the DLC film was about 41%. A wide range of the sp^3 fraction between 26 and 56% was observed for the DLC films produced by PLD using graphite in combination with a KrF laser [42]. It turned out that the fraction of the DLC film produced by the fs laser PLD experiment was fairly high. The films produced at RT were spoiled by the presence of debris of photodissociated hydrocarbons, as shown in Figure 7(a), while the debris disappeared completely for films deposited at 100 °C, see Figure 7(b). However, the deposited films were found to be electrically conductive.

Unfortunately, we failed to produce any deposit for frozen methanol. The reason for the failure may be explained by comparing the optical emission spectra observed from the plume generated by frozen acetone vs. methanol, see Figure 8. For com-

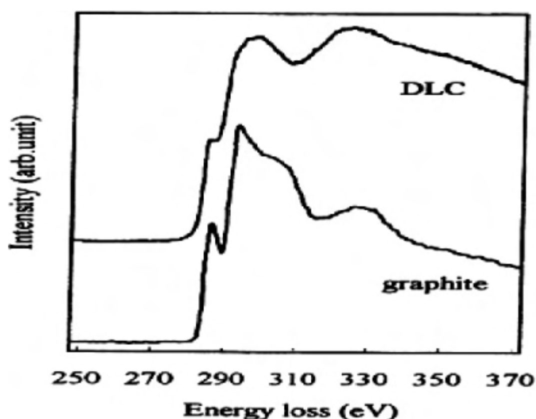

Figure 6. EELS spectra of the DLC film deposited by a fs laser and graphite. The power density of the fs laser was 4×10^{15} W/cm^2. The DLC film was deposited at room temperature for 40 min.

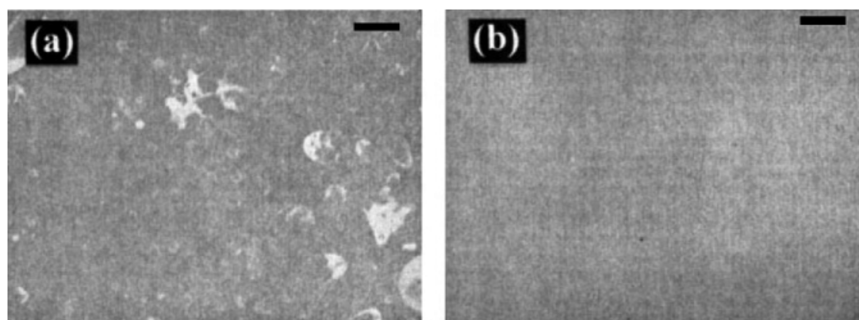

Figure 7. Photographs of deposited films: bars –50 μm; (a) showing debris at room temperature and (b) free from debris at 100 °C. The power density of the fs laser was 4×10^{15} W/cm^2. The irradiation time was 40 min.

parison the spectrum observed from graphite is also shown. The emitted light from the plumes was analyzed by a 25-cm monochromator with a resolution of ~0.2 nm. A 17-cm collection lens was focused 5 mm away from a target surface. The photomultiplier was a Hamamatsu Photonics model-R212UH. The peaks observed from the acetone plume, see Figure 8(a), were identified as the emission of C^+ and C^{2+} ions, as well as C_2, together with a CH line and a CH_2 band [43–45]. The spectrum contains also the emission lines of O^+, CO and H. The lines emitted from the oxygen species are particularly abundant in the spectrum observed from the frozen methanol plume, see Figure 8(b). Based on this observation, we assume that the abundant oxygen radicals removed the deposit generated by the irradiated frozen methanol.

In the case of graphite, see Figure 8(c), a large number of the C^+ emission lines are observed. In addition, the spectrum contains the emission lines of C^{2+}, CH, CO, and O^+. It is not surprising to find species including oxygen and hydrogen in

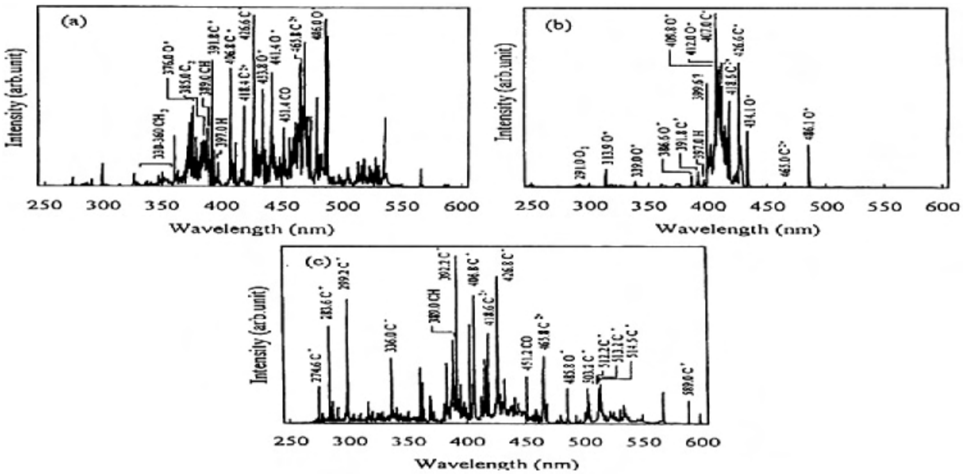

Figure 8. Optical emission spectra of ablation plumes generated by a fs laser: (a) frozen acetone, (b) frozen methanol and (c) graphite. The power density of the fs laser was 4×10^{15} W/cm^2 in all three cases.

the plume generated from graphite, since the DLC films deposited using a graphite target contained a large amount of hydrogen [5]. We assume that the hydrogen atoms were generated by the dissociation of water molecules present in the chamber.

The scanning electron microscope (SEM) photograph given in Figure 9 for a deposit shows the presence of particles with distinct flat surfaces. In this case, the irradiation lasted 45 min, and the substrate temperature was set at 350 °C. We found that the presence of hydrogen was crucial to produce the particles, and they differed from the particles generated from the irradiated target. The shape, size, and number of the particles were not always reproducible. They were not diamond, and we have not yet succeeded in identifying the particles.

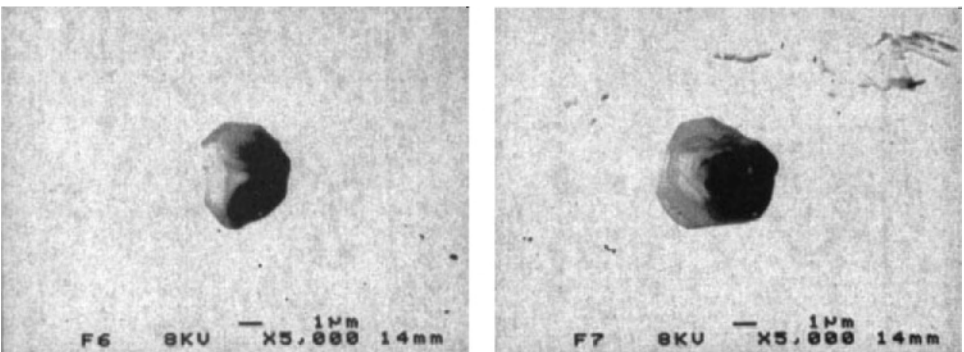

Figure 9. SEM photographs of the deposits formed in hydrogen atmosphere at a gas pressure of 0.75 Torr. The power density of the fs laser was 4×10^{15} W/cm^2, the irradiation lasted 45 min, and the substrate temperature, 350 °C.

4.2. *Synthesis of microcrystals*

Conducting synthesis of DLC films, some elongated microcrystals were discovered in the frozen acetone target irradiated by the fs laser. To minimize the chance of loosing the new synthesized microcrystals, the Si wafer was placed horizontally in direct contact with a liquid nitrogen stainless steel reservoir, as shown schematically in Figure 10. The stainless steel chamber was cylindrically shaped with a diameter of 15 cm and length of 27 cm. The acetone gas was blown through a 1/4 in. copper pipe toward the Si surface. A sorption pump was used to evacuate the chamber during preparation of the target. After the frozen gas was condensed into an ~3 mm thick layer, the gas supply was stopped, and a 200 l/s turbomolecular pump was turned on to improve the vacuum of the chamber to 2×10^{-5} Torr. The pressure increased to 10^{-4} Torr during the laser irradiation. The laser beam was shifted slightly at 5–10 s intervals to avoid the exposure of the underlying stainless to the fs laser beam.

The shape and size of the laser-synthesized microcrystals changed from crystal to crystal. A typical image of crystals observed by SEM is shown in Figure 11(a), with hexagonal pillar shapes. The size of the crystal shown in Figure 11(a), is 4 μm in width and 30 μm in length. Sometimes, many microcrystals were bundled together, as shown in Figure 11(b). This basic crystal shape i.e., the elongated pillar, suggests that the product might be a crystal with a one-dimensional structure, possibly the carbyne.

To identify the microcrystals we measured a micro X-ray diffraction (μ-XRD) pattern using the Cu Kα line for an aggregate of the hexagonal pillar-shaped deposits with the result shown in Figure 12. The X-ray was focused to an area limited to about 30 μm in diameter. The sample was tilted and rotated during the measurement, and therefore the Bragg condition was satisfied for each microcrystal, as well as for the silicon wafer. A position sensitive proportional counter detector

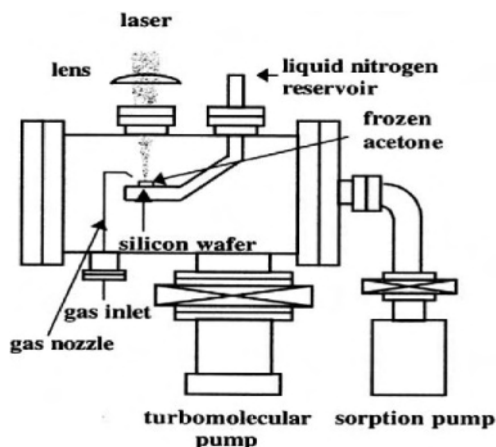

Figure 10. A side view of the arrangement used for fs laser irradiation experiment.

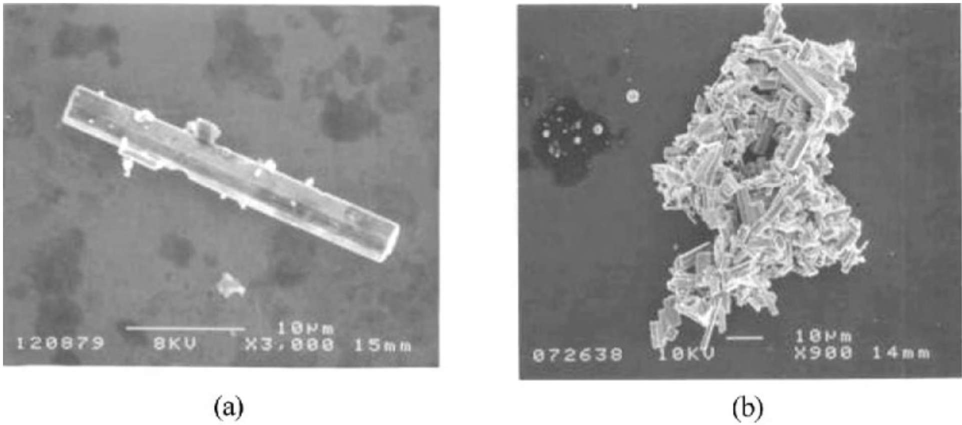

Figure 11. SEM micrographs of deposits on a Si wafer: (a) a hexagonal pillar-shaped microcrystal and (b) an aggregate of microcrystals. The power density of the fs laser was 4×10^{15} W/cm^2.

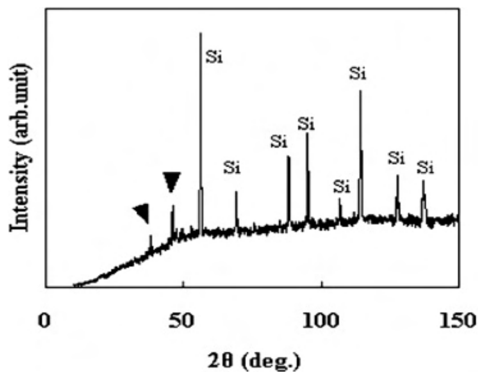

Figure 12. μ-XRD pattern measured from the aggregate of the microcrystals shown in Figure 11(b).

was used to observe the diffracted X-rays. The strong XRD peaks which belong to the diffraction of the Si wafer were observed between 56.2° and 137°. In addition to the silicon peaks, two peaks are visible at diffraction angles of 38.1° and 46.1°, indicated by the arrows in Figure 12. Other peaks are too weak to be claimed as real. From the observed pattern we could determine two *d*-values for the microcrystals as 0.236 nm and 0.197 nm. According to the literature [17–23], the *d*-value of 0.236 nm agrees with one of the diffraction peaks observed for one type of carbyne group allotrope C IX, which was synthesized by heating pyrolytic graphite and with a trigonal symmetry structure [24]. The other peak at 46.1°, however, does not match any diffraction peak associated with any member of the carbyne group [15, 16, 17–23].

We also measured the density of the microcrystals by a gradient liquid method. The observed density was 2.58 ± 0.04 g/cm^3, which lies in the middle for diamond,

3.52 g/cm^3, and graphite, 2.25 g/cm^3. Thus, the experimentally observed value is close to the density of α-carbyne, 2.68 g/cm^3 which possesses alternative single-triple carbon bonds in the chain [25]. However, the μ-XRD pattern shown in Figure 12 did not match any peak associated with α-carbyne [17]. The microcrystals were though heavier than any hydrocarbon polymers, and therefore the possibility of polymers was ruled out. For further confirmation, we tried to measure the hydrogen content in the microcrystals by using elemental analysis based on the combustion method [46]. Unfortunately, we could not collect enough microcrystals to carry out this measurement, due to their small size and poor reproducibility of the synthesis. Nevertheless we confirmed that these crystallites do not dissolve in acetone solution even after a 60 min immersion, giving another support to exclude the possibility of polymers formation. Concluding from all experimental evidence described, we believe that the microcrystals synthesized by the fs laser were some kind of a carbyne, although the characteristics found do not match any of the known single carbyne structures reported in the literature.

It is thus essential to improve the production technique and increase the size of the crystals before further studies can effectively be made to identify the synthesized microcrystals definitively. For this reason, our one-dimensional carbon crystals synthesized remain to date a mystery and we may feel consolation only by the fact that similar problems were encountered previously in other investigations of carbynes [26].

5. Synchrotron radiation used for ablation of frozen acetone

We employed SR with the hope of synthesizing diamond by SR-induced ablation (SRA) of frozen acetone. This expectation was based on a previous report by Eberhaldt et al. [47] that SR can produce the methyl radical and atomic hydrogen ions as dissociation products of acetone, both of which play a crucial role in diamond synthesis.

The light source was Aurora, of Sumitomo Heavy Industries, an SR facility installed at the Synchrotron Radiation Center of Ritsumeikan University. It has a compact, 1-m radius, which by adopting a superconducting magnet is used to accelerate orbiting electrons to an energy of 575 MeV. The used electron beam accumulation current was 300 mA, which dropped typically to 160 mA after 2.5 hours. We were assigned to the beam line BL-14. The radiation spectrum extended over a wide spectral range with a broad peak near a photon energy of about 500 eV. Beyond a photon energy of 2 keV the photon flux decreased rapidly with energy. The SR light passed through an rectangular-shaped iris, and focused to a size of 0.1 mm × 30 mm by a platinum cylindrical mirror. The photon flux was 8.97×10^{15} photons/sec mm^2 (0.576 W/mm^2) at an accumulation current of 300 mA.

Figure 13 shows the experimental setup, which consisted of a stainless steel chamber, 15 cm in diameter and 15 cm high, evacuated by a 150 l/s turbomolecular pump to a base pressure of 1×10^{-6} Torr. Prior to SR irradiation, 98% pure acetone was frozen onto a copper plate connected to a liquid nitrogen reservoir.

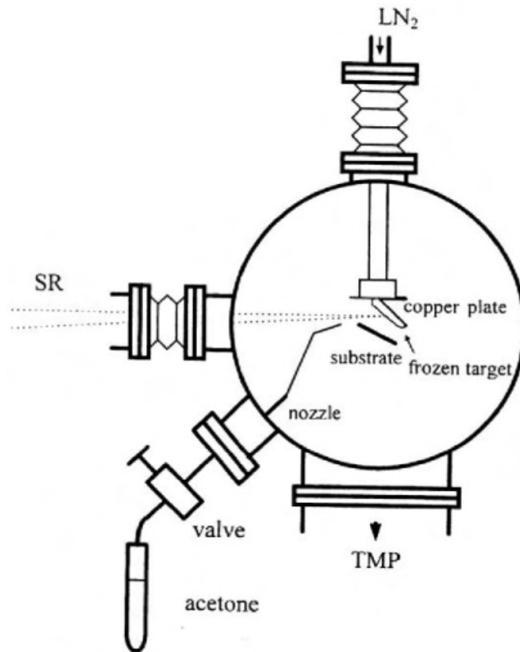

Figure 13. The schematic setup used in the SR experiments.

The average thickness of the frozen target was 2 to 3 mm. The SR beam was incident on the target at an angle of 45°. Although the visible plume characteristic of laser ablation was absent, SR radiation could ablate the frozen gas targets, as evidenced by the formation of holes in the target materials. Also, the pressure in the deposition chamber increased during SR irradiation, reaching about 1×10^{-5} Torr immediately after irradiation started. The target was moved across the SR beam to avoid the exposure of the underlying copper to SR radiation.

Quartz plates and P-doped silicon (100) wafers were used as substrates and located approximately 1 cm from the target. Although sometimes heated to 400 °C, most results were obtained for unheated substrates. The quartz plates were cleaned with methanol and distilled water, followed by UVOC. Silicon was either terminated by hydrogen for protection or by an oxide layer grown on silicon surfaces by heating to 1200 °C for 20 min in a wet oxygen gas atmosphere. In some experiments, a fine sand paper was used to scratch the silicon surface, claimed in the literature to help the formation of diamond on silicon [3].

The first successful results obtained showed a sharp Raman peak at 1333 cm^{-1} in one of the deposits, see Figure 14. The sharp peak characteristic of diamond observed in Figure 14 is for a deposit formed on quartz after 2 hrs and 40 min irradiation with SR. The laser-micro Raman spectroscopy was driven by a 200 mW, 514.5 nm Ar ion laser beam focused to a spot size of about 1 μm in diameter. As seen, the spectrum is characterized by the absence of broad peaks that corresponds to DLC or graphite phases.

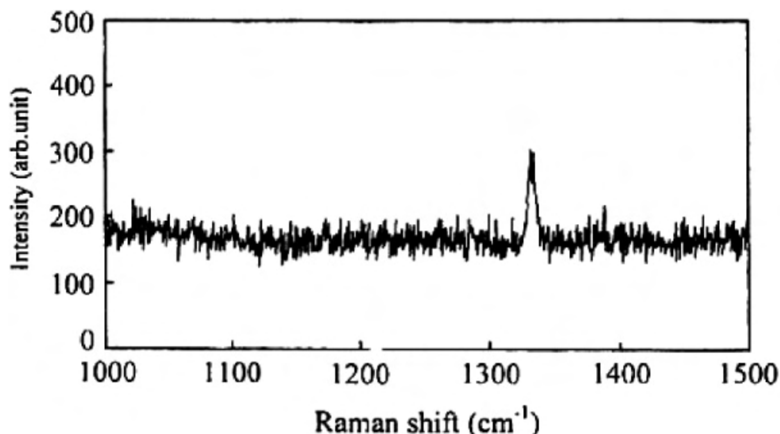

Figure 14. Raman peak observed at 1333 cm^{-1} for a typical deposit. The deposit was synthesized by SRA for 2 hrs and 40 min. The substrate was kept at room temperature.

Unfortunately, the result could not be reproduced, and the successful formation of diamond was confirmed only once. In subsequent experiments the deposits produced by SRA were either film or particles with various forms visible by an optical microscope. Often, the particles were mixed with the films and the shape, size, and density of the particles were hard to control. Figure 15 shows some of the typical shapes of the particles observed by optical microscope. A particle resembling a broken glass piece of 90 μm in size, was found on quartz after 1.5 hours of SR irradiation as shown in Figure 15(a). In this case, the deposit exhibited a sharp Raman peak between 494 cm^{-1} and 517 cm^{-1}, even though the result was not reproducible. For instance, Figure 16 shows a sharp Raman peak observed at 510 cm^{-1} for another broken glass type structure. Another sample shows a needle-like deposit in Figure 15(b), which was found on quartz after 1 hour of SR irradiation. A plate-like deposit was found also on quartz, as shown in Figure 15(c). The deposits shown in Figure 15(b) and (c) did not exhibit any Raman peak, either sharp or broad. Some of the deposits also resemble the pseudo-one dimensional carbon crystal, carbolite [15]. Another possibility of identifying the crystals may be carbon allotropes such as carbyne [16]. We found also that raising the substrate temperature did not affect the deposits. Finally, because of the difficulty to obtain reproducible results, these experimental results should be regarded as preliminary, and more studies are thus required to test the usefulness of SRA as a means of synthesizing carbon allotropes.

6. Free electron laser used for ablation of frozen acetone

By courtesy of the Free Electron Laser Institute (FELI) of the Institute of Free Electron Laser of Osaka University, we employed an FEL in a series of experiments aimed at synthesizing carbon allotropes from frozen hydrocarbons. The output

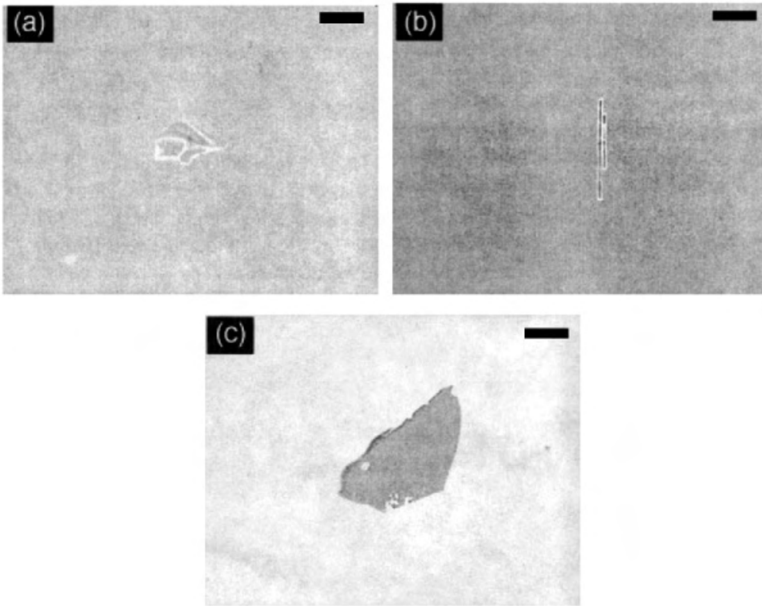

Figure 15. Optical microscope photographs of deposits: bar is 50 μm; (a) glass piece, (b) needle, and (c) flat plate. The deposit was synthesized by SRA during 1 to 1.5 hrs. The substrate was kept at room temperature.

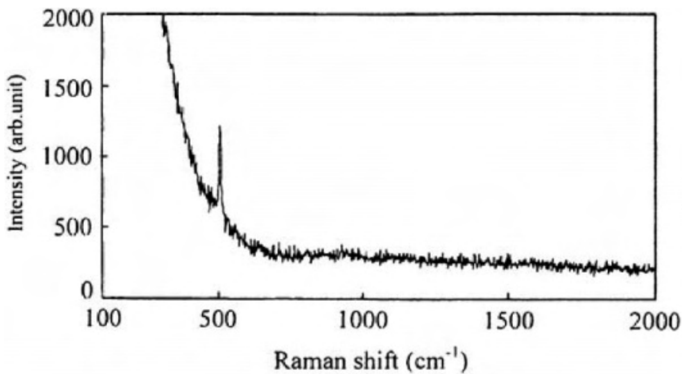

Figure 16. Raman peak observed at 510 cm^{-1} for the glass piece shape deposit shown in Figure 15(a).

of the FEL consisted of 10 Hz-macropulses, consisting each of a train of 22.4 MHz-micropulses. The pulsewidth of the micropulses was 4–6 ps. The average output power was low, normally less than 40 mW, and the beam diameter some 40 mm. The IR wavelengths used were in the range of 5.5–12.5 μm. The laser beam was introduced into the chamber using a similar setup as shown in Figure 13, through a ZnSe window and focused onto the target surfaces by a ZnSe lens with

a focal distance of 35 cm. The beam irradiated the target at an incident angle of 45° and the estimated beam spot size on the target was 0.1 mm.

The frozen acetone was prepared similarly as described in Section 5. P-doped Si(100) or As-doped Si(111) wafers were used as substrates after the hydrogen-termination surface treatment. Finally, the unheated substrate was placed at a distance of 2 cm from the target.

Figure 17 shows the strong mass spectra wavelength dependence while ablating the frozen acetone. The quadruple-mass spectrometer was located in front of the target at a distance of about 20 cm. In the case of Figure 17(a) the FEL wavelength was set at 11.1 μm, which matches the C-H vibration mode of acetone. The observed peaks at the mass numbers (amu) of 58, 56, 54 and 52 were identified with CH_3COCH_3 (parent), CH_2COCH_2, CHCOCH and CCOC, respectively. On the other hand, such peaks were absent from the observed spectrum, Figure 17(b) for 10.0 μm irradiation, which does not match any vibration absorption mode of acetone.

For deposition from the frozen acetone target we used an 8.23 μm wavelength irradiation. This wavelength corresponds to the deformation vibration modes of -C=O. The irradiation time was 40 min, and the average laser power was 50 mW. Although no plume was visible, the frozen acetone target was ablated, as evidenced by the loss of the frozen acetone in the irradiated area. The deposit formed on Si(100) was transparent and shaped like glass-pieces or flat-plates, see Figure 18.

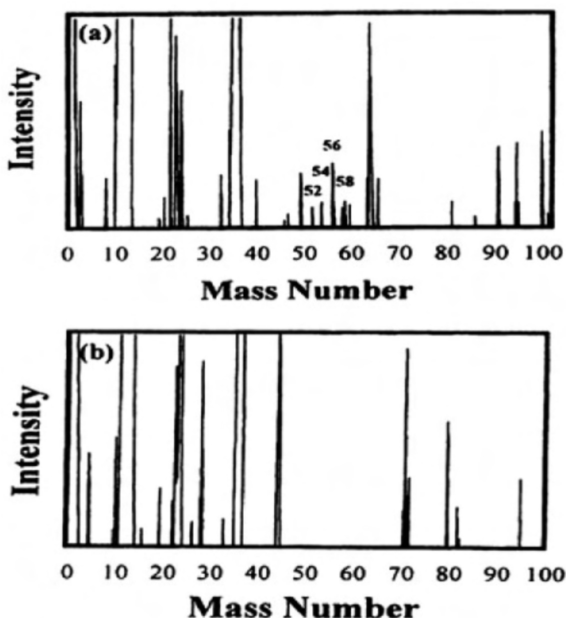

Figure 17. Mass spectroscopy spectra observed from irradiated frozen acetone: (a) 11.1-μm FEL radiation and (b) 10.0-μm radiation. The average laser power was 11 mW and 17 mW for the 11.1 μm and 10.0 μm FELs, respectively.

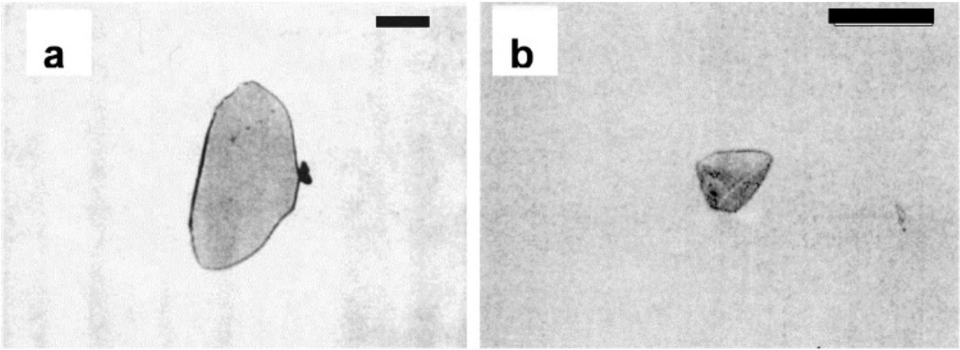

Figure 18. Examples of FEL deposits observed by an optical microscope: bars – 100 μm; (a) flat-plate and (b) glass piece. The irradiation time was 40 min, and the average laser power was 50 mW.

The largest piece was 400 μm long. The observed shape of the deposit is similar to the shape of C_{60} crystals reported in the literature [48]. We tried to confirm this speculation by using micro-Fourier-transform IR spectroscopy, but no infrared peaks could be observed in this case. The other possibility sought was a pseudo-one dimensional structure of carbolite [15] or carbyne [16] for which further studies are required.

7. Conclusions

We irradiated frozen hydrocarbons by various new light sources to synthesize carbon allotropes. The use of frozen hydrocarbon had been rare in laser processing until recently, but we could demonstrate its usefulness through a series of experiments which are described in various publications and here. The light sources included excimer lasers, a femtosecond laser, synchrotron radiation (SR), and a free electron laser (FEL). The comparison of our results obtained from various light sources by a single research group is rare and this work may thus hopefully increase the awareness to photo-induced material processing. ArF and KrF excimer lasers were used for PLD of DLC films. The targets were frozen acetylene and acetone. The quality of the deposited DLC was as good as for those deposited by PLD using a normal graphite target. Less particles incorporated into the deposits using frozen hydrocarbons as compared with graphite. The PLD technique was tested also with an fs laser to irradiate frozen acetone and deposit DLC films. Frozen methanol did not yield any deposit. However, elongated microcrystals were formed in the frozen acetone due to fs-laser irradiation. X-ray diffraction and density measurements suggested that they might be some kind of carbyne, a one-dimensional carbon microcrystal. Because of their small size and poor production reproducibility, the measurement methods available for unambiguous identification of carbyne were limited, thus leaving the task open to further confirmation. Using SR for irradi-

ating frozen acetone, we deposited diamond, as confirmed by Raman spectroscopy. This is also in accordance with previous reports that SR produced CH_3 radicals and hydrogen, which are effective in the synthesis of diamond, upon irradiation of acetone. However, the result was not reproducible to-date. Finally, when the output from FEL was tuned to a vibrational mode of the acetone molecules, many fragments were generated. The deposits were transparent appearing as glass pieces or flat plates. Thus, we have demonstrated the many new interesting possibilities that powerful light sources are offering for the task of synthesizing various carbon allotropes when used in combination with frozen hydrocarbons.

Acknowledgments

The authors are grateful to the graduate students, Kiyohito Tsujihara, Zhengxin Liu, Seiji Ishihara, and Satoshi Higuchi for conducting experiments. Also, we are indebted to Prof. Hidejiro Miki, Dr. Takeo Matsubara and Dr. Takanori Katoh from the Synchrotron Radiation Institute of the Ritsumeikan University, and Mr. Shinji Okuma and Dr. Takio Tomimasu from the Free Electron Laser Institute. We would like to thank Mr. Naoki Nakamura, the Toyota Motor Corporation for the Raman and IR measurements and other valuable assistance, Dr. Tetsuya Sato, Matsushita Electric Industrial Co., Ltd. for the film hardness measurements, Mr. Iwao Matsunaka of Ryukoku University and Mr. Yoshihito Suzuki for Raman measurements, Mr. Seiji Ogino from Sumitomo Electric Industries Ltd. for mass-spectroscopic measurements, and the Rigaku International Corporation for μ-XRD measurements. We also wish to thank Dr. Kiyoshi Miyake, Saitama University, Dr. Mutsukazu Kamo of the National Institute for Materials Science, Dr. Akira Yabe of the Bio Nano Research Institute for valuable discussions, and Mr. Kouta Nakanishi, Mitsubishi Heavy Industries, Ltd. for valuable technical assistance.

This work was partly supported by Special Coordination Funds from the Science and Technology Agency, titled “Development of High-Density Optical Pulse Generation and Advanced Material Control Techniques.” and by The Kazato Research Foundation (JEOL Ltd.).

The experiments described in this chapter were carried out while both authors were affiliated with the Department of Electrical and Electronic Engineering, Toyohashi University of Technology, Tenpaku, Toyohashi 441-8580, Japan.

References

1. S. Matsumoto, Y. Sato, M. Kamo and N. Setake, *Jpn. J. Appl. Phys.* **21**, 183 (1982).
2. H. W. Kroto, J. R. Heath, S. C. O’Brien, R. F. Curl and R. E. Smalley, *Nature* **318**, 162 (1985).
3. M. C. Polo, J. Cifre, G. S·nchez, R. Aguiar, M. Varela and J. Esteve, *Appl. Phys. Lett.* **67**, 485 (1995).
4. M. Yoshimoto, K. Yoshida, H. Maruta, Y. Hishitani, H. Koinuma, S. Nishio, M. Kakihara and T. Tachibana, *Nature* **398**(6734), 340 (1999).
5. T. Sato, S. Furuno, S. Iguchi and M. Hanabusa, *Appl. Phys.* **A 45**, 355 (1988).

6. M. Hanabusa and K. Tsujihara, *J. Appl. Phys.* **78**(6), 4267 (1995).
7. R. Mania, L. Stobierski and R. Pumpuch, *Cryst. Res. and Technol.* **16**, 785 (1981).
8. M. Okoshi, M. Hanabusa, H. Miki, T. Matsubara and T. Katoh, *Appl. Surf. Sci.* **127–129**, 440 (1998).
9. M. Okoshi, M. Hanabusa and S. Okuma, *Nucl. Instr. and Meth. in Phys. Res.* **B 144**, 147 (1998).
10. H. Akazawa and Y. Utsumi, *J. Appl. Phys.* **78**, 2725 (1995).
11. T. Katoh and Y. Zhang, *Appl. Phys. Lett.* **68**, 865 (1996).
12. M. Okoshi, S. Higuchi and M. Hanabusa, *J. Appl. Phys.* **86**(3), 1768 (1999).
13. M. Okoshi, S. Higuchi and M. Hanabusa, *Appl. Surf. Sci.* **154–155**, 376 (2000).
14. M. Okoshi, S. Higuchi and M. Hanabusa, *Jpn. J. Appl. Phys.* **40**(8), 4926 (2001).
15. S. Tanuma and A. Palnichenko, *J. Mater. Res.* **10**(5), 1120 (1995).
16. A. E. Goresy and G. A. Donnay, *Science* **161**, 363 (1968).
17. A. G. Whittaker and P. L. Kintner, *Science* **165**, 589 (1969).
18. A. G. Whittaker and G. M. Wolten, *Science* **178**, 54 (1972).
19. A. G. Whittaker, *Carbon* **17**, 21 (1979).
20. N. Setaka and Y. Sekikawa, *J. Am. Ceram. Soc.* **63**, 238 (1980).
21. Y. P. Kudryavtsev, S. E. Evsyukov, V. G. Babaev, M. B. Guseva, V. V. Khvostov and L. M. Krechko, *Carbon* **30**, 213 (1992).
22. R. B. Heimann, S. Fujiwara, Y. Kakudate, Y. Koga, T. Komatsu and M. Nomura, *Carbon* **33**, 859 (1995).
23. Y. Onuma, Y. Kawai, M. Nakano and K. Kamimura, *Jpn. J. Appl. Phys.* **35**, L1354 (1996).
24. A. G. Whittaker, M. E. Neudorffer and E. J. Watts, *Carbon* **21**, 597 (1983).
25. V. I. Kasatochkin, V. V. Korshak, Y. P. Kudryaavtsev, A. M. Sladekov and I. E. Sterenberg, *Carbon* **11**, 70 (1973).
26. R. B. Heimann, S. E. Evsyukov and L. Kavan, *Carbyne and Carbynoid Structures* (Dordrecht: Kluwer Academic Publishers, 1999).
27. H. Sankur, W. J. Gunning, J. DeNatale and J. F. Flintoff, *J. Appl. Phys.* **65**, 2475 (1989).
28. M. Hanabusa, *Mater. Res. Soc. Symp. Proc.* **285**, 447 (1993).
29. F.-Xiao Rong, *Appl. Phys. Lett.* **67**(7), 1022 (1995).
30. A. A. Lyalin, A. V. Simakin, G. A. Shafeev and E. N. Loubnin, *Appl. Phys.* **A 68**, 373 (1999).
31. M. Hanabusa and K. Tsujihara, *IEEE J. Sel. Top. Quant.* **1**(3), 848 (1995).
32. Y. Hiroshima, T. Ishiguro and K. Esaki, *Jpn. J. Appl. Phys.* **36**(4A), 2267 (1997).
33. T. Ishiguro, K. Esaki and Y. Hiroshima, *Appl. Surf. Sci.* **127–129**, 553 (1998).
34. T. Ishiguro, T. Shoji and H. Inada, *Appl. Phys.* **A 69**, S149 (1999).
35. H. Niino, T. Sato and A. Yabe, *Proc. SPIE* **3933**, 174 (2000).
36. H. Niino, *Photochemistry* **32**(1), 20 (2001) [in Japanese].
37. J. R. Vig, *J. Vac. Sci. Technol.* **A 3**, 1027 (1985).
38. T. Takahagi, I. Nagai, A. Ishitani, H. Kuroda and Y. Nagasawa, *J. Appl. Phys.* **64**, 3516 (1988).
39. F. Qian, R. K. Singh, S. K. Dutta and P. P. Pronko, *Appl. Phys. Lett.* **67**, 3120 (1995).
40. S. D. Berger, D. R. Mckenzie and P. J. Martin, *Philos. Mag. Lett.* **57**, 285 (1988).
41. P. J. Fallon, V. S. Veerasamy, C. A. Davis, J. Robertson, G. A. J. Amaratunga, W. I. Milne and J. Koskinen, *Phys. Rev.* **B 48**, 4777 (1993).
42. K. Yamamoto, Y. Koga, S. Fujiwara and F. Kokai, *Jpn. J. Appl. Phys.* **36**, L1333 (1997).
43. G. R. Harrison, *M.I.T. Wavelength Tables* (Cambridge: M.I.T. Press, 1969), pp. 56–380.
44. G. Herzberg, Electronic Spectra of Polyatomic Molecules (New York, Van Nostrand, 1966), pp. 583–668.
45. D. E. Gray, B. H. Billings, D. F. Bleil, R. K. Cook, H. M. Grosswhite, H. P. R. Frederikse, R. B. Lindsay, J. B. Marion and M. W. Zemansky, *American Institute of Physics Jandbook*, 3rd ed. (New York, McGraw-Hill, 1972), pp. 7–220.
46. S. Atou, *Bunseki kagaku (Analytical Chemistry)* (Tokyo: Baifuukan, 1992), pp. 316–323 [in Japanese].
47. W. Eberhardt, T. K. Sham, R. Carr, S. Krummacher, M. Strongin, S. L. Weng and D. Wesner, *Phys. Rev. Lett.* **50**, 1038 (1983).
48. T. Arari, Y. Murakami, H. Suematsu, K. Kikuchi, Y. Achiba and I. Ikemoto, *Solid State Commun.* **84**, 827 (1992).

CHAPTER 11

EXCIMER LASER MACHINING FOR 3D-SURFACE STRUCTURING

K. Zimmer* and A. Braun
Leibniz-Institut für Oberflächenmodifizierung, Permoserstraße 15, 04318 Leipzig, Germany
*(*Author for correspondence, E-mail: klaus.zimmer@iom-leipzig.de)*

ABSTRACT: This chapter reviews recent developments in the field of 3D-micromachining of surfaces by pulsed laser ablation using different mask projection techniques. The first sections introduce to laser processing and mask projection and summarize the current technology of 3D-laser machining. The basic machining techniques and the design of contour and gray scale masks are described in section 4. In the following sections selected 3D-micromachining techniques and their application in microsystem technology are discussed in detail.

1. Introduction

The demand for micro-sized mechanical [1], fluidic [2] and optical [3] structures in a number of different materials has increased significantly over the past few years. After the success of planar, stepped, or 2.5-dimensional structures, for whose production a considerable number of technologies have been established, future applications now call for real 3-dimensional (3D) topographies with smooth analogous surfaces. Current production steps of such micro structures are based on well-known microelectronic engineering techniques and include lithographic processes such as thermal modification of binary resist structures, dose-dependent beam writing and gray scale lithography [3–5], as well as subsequent etch transfer or replication steps. These approaches are well suited for wafer scale mass production but require a number of processing steps with limitations in materials choice and flexibility.

Lasers in comparison are appropriate for fast, flexible and adjustable material machining. Laser processing is particularly efficient in cases of adaptation of complete systems to specific applications such as machining of small areas, and etching of deep structures. Although used extensively in the production process of electronic devices [6], less experience has been gathered in laser 3D-micromachining. The machining techniques presented here utilize pulsed UV-lasers, e.g. excimer as well as the higher harmonics of solid-state lasers, although cw-lasers have also been used successfully for 3D-machining [7, 8].

The use of excimer laser ablation for polymer structuring became an established technology quite early [9]. Nanometer to micrometer controlled, direct material removal by excimer lasers is now emerging as a universal manufacturing tool for a wide range of materials [10–12]. Using excimer lasers in conjunction with mask projection allows flexible material processing but was limited first only to digital structures. To overcome this basic problem a number of processing methods have

Aaron Peled (ed.), Photo-Excited Processes, Diagnostics and Applications (PEPDA), 301–338, 2003.
© 2003 *Kluwer Academic Publishers. Printed in the Netherlands.*

recently been developed with the aim of machining real 3D-structures with high precision and small roughness values. These machining techniques use specific masks such as contour, gray scale and hybrid masks, together with appropriate high precision workpiece positioning.

The laser ablation techniques that will be discussed in the following sections are grouped according to their technological relevance. Either they feature the high flexibility necessary in rapid prototyping, high efficiency desired for large area processing, or comply with other needs of today's micromachining. Although the techniques are demonstrated for UV-excimer lasers they can also be used with other lasers or beam sources after appropriate adaptation.

For rapid prototyping processes in air, polymers with large optical absorption coefficients remain the material of choice. If there is no sufficient absorption, as with UV-transparent dielectrics, energy deposition in ablation can be achieved by VUV-wavelengths, ultra-short pulses, or by auxiliary means such as using a liquid absorber. To demonstrate the capabilities of the machining techniques, both laser ablation and laser etching are discussed. All approaches utilize the mask projection technique. The details of the appropriate mask and scanning regimes to be used will therefore be discussed in detail.

To achieve our goal of producing 3D-structures appropriate for applications in microsystem technology, much effort was spent to investigate the origin of the roughness evolution in laser based machining processes. To meet this demanding challenge, a number of basic and advanced machining principles are demonstrated. Looking for example at micro-optical applications, the importance of achieving a highly accurate surface as well as small roughness makes the necessary precision of the laser tool more than obvious.

2. Instrumentation for 3D-surface structuring

2.1. *General setup*

In laser micro-technology the purpose of the optical setup is to deliver laser photons in a controlled manner to the workpiece surface where laser-machining processing takes place. The beam properties of today's excimer lasers require downstream beam shaping regardless of the chosen machining regime. Commercial as well as laboratory workstations with incorporated excimer lasers were described by several authors [6, 13, 14]. The essential optical components as depicted in Figure 1 and their functions will be described here briefly.

The excimer laser is the most important unit of the equipment and its characteristics determine to a large degree the qualitative and quantitative parameters of the treatment. Significant characteristics are its energy pulse-to-pulse-stability, energy long and short term stability, maximum pulse repetition rate and its distinctive intensity footprint averaged over several pulses. The energy monitor provides information on the current laser pulse fluence and may, depending on the control mechanism, adjust the discharge voltage of subsequent laser pulses. The cylinder lens adapts

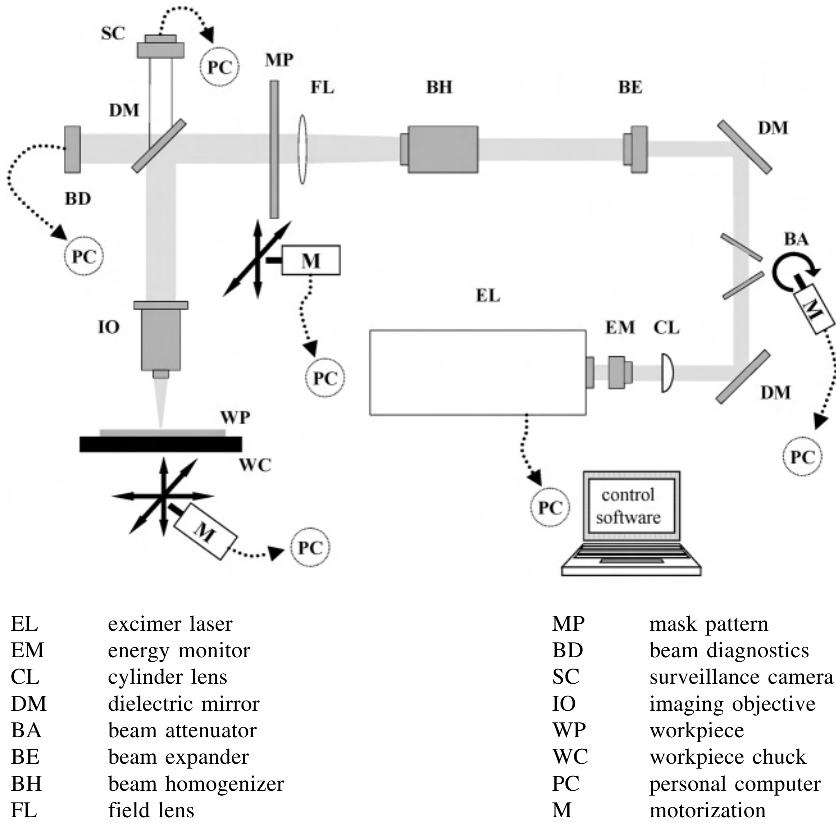

Figure 1. Schematic setup of a typical laser workstation.

the short axis divergence of the laser beam to the downstream optical set-up. Optimized pulse energy can be selected using the beam attenuator. A Kepler telescope serves as a beam expander and allows the adaptation of the short beam axis to fit adequately into the beam homogenizer. The beam homogenizer transforms the raw excimer laser intensity distribution into a laterally homogenized flat top profile. Bi-prism, fly's-eye, and mirror homogenizers are generally used [15, 16]. The additional beam divergence caused by the homogenizing optics is compensated by a field lens. The homogenized beam, including approximately 80% of the pulse energy at a typical energy deviation of 5% (rms), usually illuminates an area of approximately $(20\ \text{mm})^2$ in the object plane or on the mask.

The mask transforms the laser beam profile into a functional shape to provide a desired machining footprint. The mask's families and types are discussed in detail later. The objective projects the mask information, usually demagnified, into the image at the workpiece [15, 17]. The position and motion of the workpiece can be controlled by an *x*-, *y*- and *z*-handling system. In precision micromachining jobs, full control over the handling systems, i.e., both the workpiece and mask

positioning systems, the number of applied pulses, and the laser fluence selected by the beam attenuator are vital prerequisites. Consequently, the better and more comprehensively an integrated computer controls the entire workstation, the better the machining results. For convenience, a unit for beam diagnostics and an online surveillance camera can be installed.

2.2. *Imaging characteristics*

Imaging by optical elements, discussed in textbooks such as [18], is described by theories based on geometric and diffraction optics, Fourier transformation, and ray tracing. For ideal imaging conditions, all the light that is scattered at the mask must be projected onto the workpiece. Since not all of the scattered light is collected by the aperture of the projection optics, the image is a filtered image of the mask rather than an ideal copy. We will briefly discuss this effect for the case of a repeating mask structure such as an optical grating. Here the propagation of individual Fraunhofer diffraction orders must be taken into account. The angle of diffraction β is given by $\sin\beta = m \cdot \lambda / g$, where m, λ and g denote the order of diffraction, the excimer laser wavelength, and the grating period respectively. Only if the diffracted angle β is less then the solid angle of the optics β_s, higher $(2m + 1)$ diffraction orders will contribute to the image formation, see Figure 8. Hence, cutting off higher diffraction orders corresponds to an extreme low pass filtering as discussed in ABBE's theory of microscopy. If the structural information of the object in addition to the transmitted intensity is desired in the projection, at least the ±1st orders of diffraction must fall into the entrance radius of the imaging objective, i.e. $\beta \le \beta_s$.

The projection of a non-repeating mask structure is more complex but can be discussed similarly. For practical purposes, the resolution of an objective $r_{\min}$ is the most interesting attribute and can be approximately calculated using

$$r_{\min} = k \cdot \frac{\lambda}{NA} \tag{1}$$

where the numerical aperture $NA = n \cdot \sin\beta_s$ and the factor k are influenced for example by the radiation properties [19]. Due to chromatic and spherical aberrations as well as other shortcomings of the optical set-up, the resolution of the projection optics is lower than the diffraction limited value $r_{\min}$ and is consequently often determined experimentally.

After imaging acute angled triangles of equal height h_i but different angles γ, the resolution can be calculated from the real height h_r of the ablated images [14], see Figure 2. Since the height is easy to measure one can deduce the curvature radius r_i using the simple geometrical consideration $r_i = \sin\gamma \cdot (h_i - h_r)/(1 - \sin\gamma)$. For excimer laser material processing, values of r_i are about 1.5 µm. Since the fluence distribution after diffraction at the internal mask edges is disregarded at this point, r_i gives only the magnitude of the optical resolution.

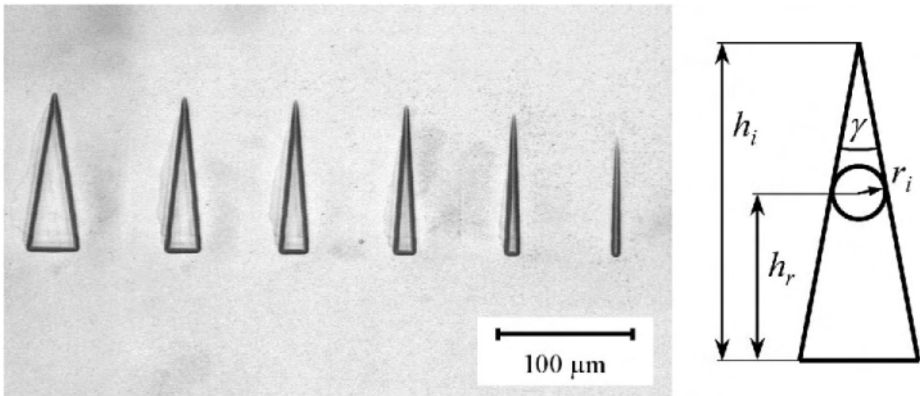

Figure 2. Ablated structures on polyimide with geometric considerations for the evaluation of optical resolution.

3. Remarks on excimer laser materials processing

Laser micromachining employs various physical and chemical methods and processes. The basic processes of interaction between laser radiation and matter and their applications to material processing have been summarized in several books, monographs, and reviews [6, 19, 20]. The interaction of the laser photons usually takes place at the materials surface. Laser etching and laser ablation are the most important processes used in micromachining because of their ease of implementation in material structuring and thin film processing. Sometimes specific conditions such as temperatures, specific reactive gasses, vacuum, or absorbing liquids are required or recommendable.

3.1. *Ablation of polymers*

The interaction of pulsed high intensity UV-laser radiation results in a photo-etching process usually called ablation. Depending on the laser pulse parameters and the material properties, photochemical and photothermal ablation mechanisms can be distinguished [10, 19, 21, 22]. In the first case, the energy of the photons is high enough to cause direct bond breaking, causing the ablation of the material. In the second case, laser photons rapidly heat a certain amount of material up to the point where thermal processes result in the decomposition and ejection of material. In practice, both these primary processes are responsible for laser ablation. If, as in most polymers, the thermal diffusion length is very small compared to the absorption length of the laser light, the extent of material excitation is mainly determined by the optical absorption of the laser photons.

This leads to a commonly used model for the ablation rate based on Beer's law.

$$Ra = \frac{1}{\alpha_{eff}} \cdot \ln\left[\frac{F}{F_{th}}\right] \tag{2}$$

The ablation rate *Ra* increases logarithmically if the laser fluence *F* exceeds the threshold fluence F_{th}. The effective optical absorption coefficient α_{eff} describes the modified optical absorption of the utilized polymer under intense laser photon irradiation. Although some other models describing the etch rate dependency exist [see e.g. 30], material parameters are often given according to the model of equation 2. Some of the experimentally measured material parameter values are summarized in Table 1. Differences in the measured values of their ablation parameters are quite common due to factors such as inconsistent chemical structures in the polymer and dissimilar experimental conditions. The determination of the actual ablation rate is therefore necessary in precision machining.

Also, photon irradiation of materials often changes the material properties, e.g., the absorption caused by the formation of color centers or radiation induced defects etc. This and similar processes influence the ablation rate, which may increase or decrease during the first pulses, resulting in incubation and depletion effects [28, 31, 32].

3.2. *Etching of dielectric materials*

The ablation of dielectric materials such as certain types of glass, fused silica, and sapphire is more difficult due to the low absorption at UV-wavelengths. Only VUV- and ultra-short-pulse lasers can be used for direct etching of these materials [33, 34]. Some characteristic problems associated with the ablation of inorganic materials are: incubation effects, irregular etch pits, and rough surfaces due to melting effects, debris formation, and local material defects.

Laser etching caused by other physical and chemical effects also allows the

Table 1. Threshold fluences and effective absorption coefficients of selected polymers.

Material	Wavelength [nm]	α_{eff} [10^4 cm^{-1}]	F_{th} [mJ/cm^2]
polyimide (PI)	248	30 [23] 22 [24] 14 [26]	19 [23], 36 [25] 54 [24] 67 [26]
polyethyleneterephthalate (PET)	248	15 [24]	30 [24]
polytetrafluorethylene (PTFE)	248 193	0.0158 [27, 28] 0.026 [19]	
polymethyl-methacrylate (PMMA)	248 193	0.04 [29], 0.057 [22] 0.2 [22]	650 [22] 65 [22]
polycarbonate (PC)	248	1 [24] 16 and 6 [26]	40 [24] 74 and 84 [26]

removal of dielectric materials [19]. Specifically, the laser-induced backside wet etching (LIBWE) of dielectric materials by excimer laser radiation is a promising machining method for many transparent, brittle, hard, and chemically resistant materials [35]. The threshold fluence for LIBWE-etching is essentially lower than that for conventional laser ablation [35]. Due to the lower energy deposition in the etched material, the thermal effects on the surface are milder. This results in a smooth etched surface achieved even in deeply etched structures [36]. The etch rate of the LIBWE process increases linearly in the low fluence region for many materials:

$$Ra = s \cdot (F - F_{th}) \tag{3}$$

F_{th} denotes the material specific threshold fluence and s is the slope of the linear etch rate. Unfortunately, at very low laser fluences a small incubation effect has been detected. A negligible debris deposition at the surface has been observed. This process is described in more detail by Kawaguchi et al., in chapter 12 of this book.

3.3. *Roughness of laser machined surfaces*

The purpose of 3D-machining is not only the generation of the desired topography but also the retention of a smooth surface. This is particularly important for applications in micro-optics and micro-fluidics. To meet this challenge the laser machining process must be optimized or a tailored post process is needed. Even under ideal processing conditions, the multi-shot laser ablation limits the attainable quality and the smoothness of the surface. The deviations of the laser ablated pit from the desired topology can be cast into two categories: distortions in the central area and distortions towards the edges.

In general, if the laser pulse hits a surface with a locally varying composition, different ablation depths are unavoidable. Occasional shadow effects, e.g. from re-deposited debris, may lead to the formation of macroscopic cones [37]. Also, in the scanning mode the laser beam hits the debris deposited in the scanning direction. A considerable reduction in the debris deposition was observed when light gases e.g., He, low gas pressures [38, 39] or higher temperatures [40] were used.

In addition, self organizing microstructures [41, 42] and surface instabilities [19] on laser ablated polymers lead to the development of surface roughness. For many materials, laser-induced periodic surface structures (LIPSS) have been described for polarized laser beams [43, 44] in early works. In laser ablation with excimer lasers, however, LIPSS plays only a minor role.

At the edges of etch pits, additional processes are involved in the roughness evolution. Most significant are the expansion dynamics of the developing plasma plume [45]. Here the expansion dynamics change from one-dimensional to two- or three-dimensional. This leads to altered interactions between the plume and the material such as re-deposition and recoil pressure. Also, the diffracted and reflected light on already ablated structures is involved in the formation of trenches and roughness at the bottom surface [46, 47]. Diffraction patterns at the edges of the projected

contour masks leading to an ablated depth modulation have been published [48, 49].

Technical and technological limitations of the machining process also result in the buildup of surface structures. Despite major efforts at beam homogenization and shaping, the remaining fluence inhomogeneities influence the accuracy of the machining process due to fluence distribution effects on the etch rate of the chosen process, e.g., the ablation rate given in equation 2.

The geometrical precision of gray scale and contour masks and therefore their functionality is mainly limited by their fabrication process. Solid metal masks provide only limited precision, may expand thermally under laser irradiation, and have a high edge roughness arising from the cutting process, e.g. laser cutting, but are not prone to mask degradation. On the other hand, chromium-on-quartz masks can be processed very precisely, e.g., in a mask shop, but have a low laser damage threshold, less than about 100 mJ/cm^2, depending on the excimer laser wavelength used [50, 51, 52].

To reduce the roughness of microstructured surfaces there are at least three different post-processing methods. The first group of techniques uses an additional layer of material for the planarization process. Planarization is based on the reduction of the surface energy of a viscous film applied to the rough surface. In practice, the additional liquid layer is spread over the entire surface and dried afterwards [53]. A second group of techniques uses the re-flow of material either by the softening of the material at increased temperatures, or by melting a thin surface layer by pulsed application of energy (e.g. laser pulse) [54]. A third group of new techniques for reducing the roughness is based on high energy ion beam bombardment of surfaces [55]. A planarization process reduces the high spatial frequencies by nearly the same amount whether they originate from the desired topology or from the roughness. Thus, current planarization processes are incapable of producing simultaneously smooth and angled surface topographies with sharp edges, necessary in micro-prisms.

4. Machining techniques for 3D-surfaces

4.1. *Overview of basic techniques and masks used in 3D-machining*

3D-machining requires local etching of the workpiece to a predetermined depth, often by multiple laser shots. Due to the digital nature of laser ablation, the desired depth is often approximated in steps. All 3D-machining techniques use specific mask designs. In principle, two basic mask families are employed in 3D-processing: the contour mask and the gray scale mask [13, 57]. When projected onto a workpiece, both, along with other parameters, control the machining process of the 3D-topographies to be etched. The contour mask defines an area on the workpiece with a homogenous fluence where laser etching takes place. It can be used either at one location or scanned over the workpiece. The gray-scale mask locally controls the transmitted laser fluence onto the workpiece and consequently the local etch

rate of the material. The fundamental 3D-machining techniques are depicted in Figure 3.

Sometimes 3D-machining needs to be accomplished on areas much larger than the focused beam or the projection area. Specific machining techniques were thus developed to deal with today's needs for the production of microsized functional devices [56].

a) Stationary contour mask method:
The simplest method for excimer laser machining is using one or a set of contour masks containing the complete 2D-shape of the 2.5D-element to be ablated. Patterning large areas with repetitive elements may be achieved by a step-and-repeat process.

b) Direct writing with small spot laser beams:
The 3D-structure is produced by scanning a small laser spot along a carefully designed path across the workpiece. The number of overlapping laser pulses of all successive scans controls the final etch depth. This extremely flexible approach can handle CAD data but is rather slow and produces a crude and rough surface.

c) Scanned contour mask:
When a contour mask is scanned along a path the topography profile is determined by the contour mask shape. Different mask regions account for different numbers of overlapping laser pulses which in turn determine the locally ablated depth. Following this approach real 3D-microstuctures of high quality can be produced continuously in a time efficient manner. Intersecting single scans increases the variety of structures that can be ablated. Because contour masks contain specific structural information, one mask can ablate only one type of scan profile, which reduces their flexibility.

d) Stationary gray scale mask:
The stationary gray scale mask approach is the only technique that enables the continuous ablation of real 3D-microstuctures with single or sequential laser pulses. This is achieved by adjusting the local laser fluence to the desired topography depth by the mask. Since the complete 3D-information is stored within the mask, each microstructure requires a gray scale mask carefully designed for each individual device. With a proper series of masks, high quality microstructures with a high filling factor can be ablated.

e) Hybrid masks:
The combination of contour and gray scale masks has the advantages of both techniques thus eliminating their specific weaknesses. Arrangements of a contour and a gray scale mask in one optical set-up [59] and the usage of hybrid masks featuring both contour and gray scale characteristics in one mask have been successfully demonstrated for scanned laser ablation [58].

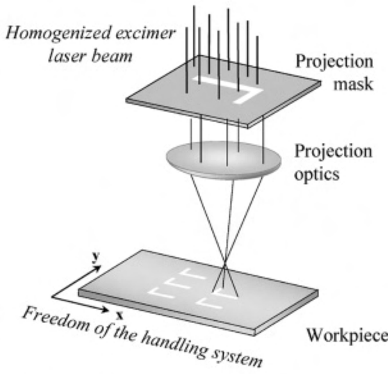

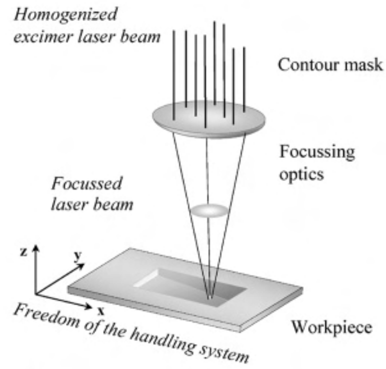

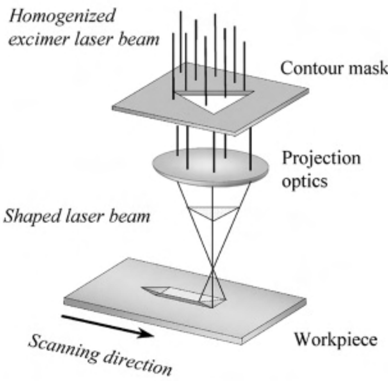

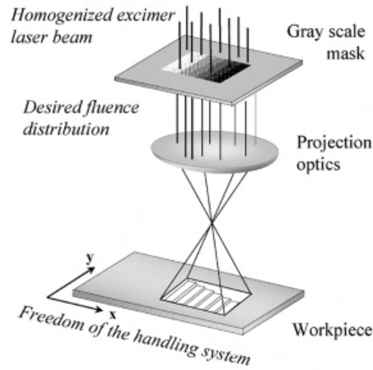

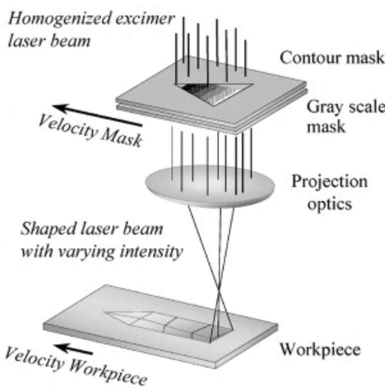

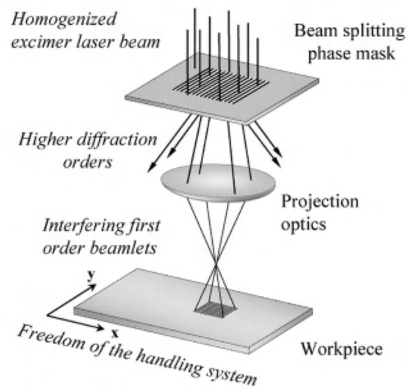

Figure 3. Overview on excimer laser machining techniques used for 3D-micromachining of surfaces based on mask projection.

f) Beam interference by mask projection:
As in holography, optical gratings split the laser beams preferably into two identical beams that pass through an objective and interfere on the workpiece surface. If the resulting sub-micrometric interference pattern exceeds locally the material specific threshold fluence, material processing commences. The utilization of sophisticated masks here allows the etching of more complex structures rather than simple line gratings.

4.2. *The approach of 3D-surface machining*

Technical applications require well-defined surface structures. Optimizing the machining process requires a quantified concept of machining in terms of the influence of the laser beam, the material parameters, and mask design. In General, the final ablation depth d is the sum of the individual material removal steps obtained by N_{app} laser pulses with etch rates Ra_i

$$d = \sum_{i}^{N_{app}} Ra_i. \tag{4}$$

A simple summation of the ablation rate for the applied pulses is not always accurate because laser parameters and material properties change during processing by various laser-material interactions. Neglecting incubation effects and fluctuations in the laser fluence, using equation 2 gives the following expression for the ablated depth:

$$d = N_{app} \cdot \frac{1}{\alpha_{eff}} \cdot \ln\left(\frac{F}{F_{th}}\right). \tag{5}$$

For constant laser and material parameters, only the pulse number determines the ablation depth. Some 3D-machining techniques use this fact and achieve the control of the local number of pulses either by directly triggering the laser, see Figure 3a, or by the contour of a moved mask, see Figure 3c.

4.2.1. *One dimensional scanning*

The projection of a homogenized laser beam onto the workpiece surface results in an even, material dependent ablation rate over the whole area of the mask. When scanning techniques are used, the contours of the mask, together with the pulse-to-pulse distance, control the locally applied pulse number. The laser pulse number needed at a selected surface point can be calculated from the scanning velocity v_s, the repetition rate of the laser f_{rep}, and the length of the mask in scanning direction at the selected point. Using equation 2, the depth $d(x)$ of the cross section of a single scan can be expressed by

$$d(x) = \frac{1}{\alpha_{eff}} \cdot \ln\left(\frac{F_0}{F_{th}}\right) \cdot \frac{f_{rep}}{v_s} \left[f_{K1}(x_{pM}) - f_{K2}(x_{pM})\right] \tag{6}$$

where the functions f_{K1} and f_{K2} define the frontside and the backside mask contour at the workpiece and consequently the height of the mask image in the scan direction.

4.2.2. *Two dimensional scanning*
More complex structures can be achieved by applying the contour mask technique several times successively. If the machining parameters and the etch rate remain unchanged for all machining steps and are not effected by topographies already etched, the locally achieved depth of a 3D-topography is only determined by the set of contour masks applied. For a machining process in two orthogonal directions using different masks, the local depth $d(x, y)$ of the topography is given by

$$d(x,\ y) = \frac{1}{\alpha_{eff}} \cdot \ln\left(\frac{F_0}{F_{th}}\right) \cdot \frac{f_{rep}}{v_s} \cdot [(f_{K1}(x_{pM}) - f_{K2}(x_{pM})) + (f_{K1}(y_{pM}) - f_{K2}(y_{pM}))]. \quad (7)$$

In principle, all surface topographies which can be given as a sum of linear functions can be machined by this method. However, in technological applications with complex shapes such as blazed profiles and spherical element topographies, mathematical terms such as $d(x, y) = x \cdot y$ are required. To make use of the advantages of mask scanning, as discussed in section 5.3, an improved scanning technique was developed and demonstrated [59].

In order to make use of mask scanning, the function $d(x, y) = x \cdot y$ must be transformed into a sum of functions depending on only one coordinate. In this example, a coordinate transformation $f(x, y) \rightarrow F(x', y')$ such as a rotation must be carried out on the function using the equations $x' = x \cdot \cos\alpha + y \cdot \sin\alpha$ and $y' = -x \cdot \sin\alpha + y \cdot \cos\alpha$. The result of this transformation for a rotation angle of 45° is shown in equation 8 after some simplifications.

$$d(x',\ y') = \frac{1}{2} \cdot (y'^2 - x'^2) \quad (8)$$

This modified function of the topography agrees with the structure of equation 7 for the multi step scanning contour mask technique. Two scans using two masks are necessary. Both masks possess a quadratic contour (y'^2 and $-x'^2$) and are scanned along the directions (x' and y') of the rotated coordinate system. According to the applied coordinate transformation the scans are carried out at an angle of 45° with respect to the axis of the non-rotated coordinate system or against the borders of the desired structure. In addition to the contour mask, an aperture mask with rectangular openings is used to limit the processing area to a single topographical unit as shown in Figure 4. This aperture mask is also the result of the rotation of the coordinate system. The borders of the desired topography are no longer parallel to the scan axis of the laser processing as is accepted in mask scanning. The aperture mask is placed directly on the workpiece, as seen in the example of Figure 4, or the image of the aperture mask is moved in step with the workpiece.

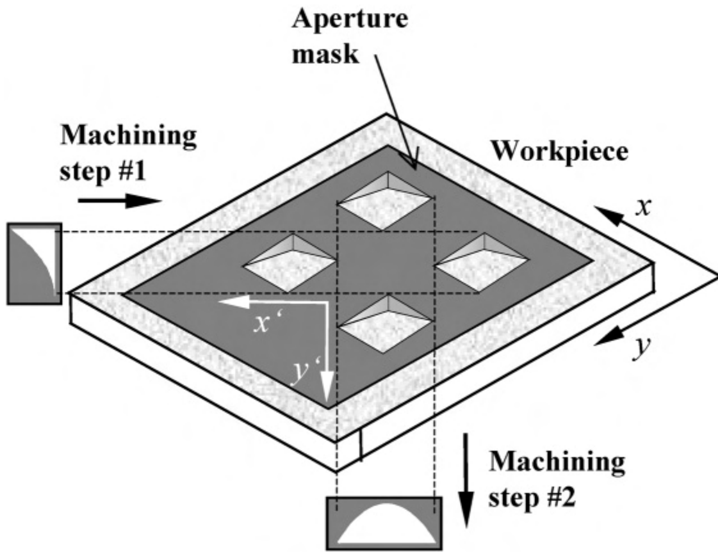

Figure 4. Scheme of the modified contour mask scanning technique.

4.2.3. *Gray scale techniques*

The gray scale techniques shown in Figure 3d use the laser fluence dependency of the ablation rate. The gray scale mask with local varying grades of transparencies transforms the constant laser fluence ahead of the mask into the spatial fluence distribution necessary to etch the desired topology. The projection of the modulated fluence distribution onto the material surface of the workpiece results in locally different ablation rates. Hence, the gray scale mask with a transmittance $T(x, y)$ controls the transmitted laser fluence to the workpiece and allows the machining of 3D-surfaces with an appropriate number of pulses according to

$$d(x, y) = N_{app} \cdot \frac{1}{\alpha_{eff}} \cdot \ln\left(T(x, y) \cdot \frac{F_0}{F_{th}}\right). \tag{9}$$

For known material properties and assuming a constant laser fluence, the ablation depth is determined only by the local transparency of the gray scale mask and the number of pulses. From equation 9, the distribution of the grades of transparency of the mask must be calculated. Although a gray scale mask can only be properly used with the set of parameters for which it was calculated, equation 9 shows that slight changes in the material properties F_{th} and α_{eff} can be compensated to a certain limit by an adjustment of the applied laser fluence F_0 and pulse number N_{app}.

For full technological accessibility to all ablation rates, the lowest grade of transparency $T_{\min}$ needed is calculated using the laser fluence at the mask plane F_M, the threshold fluence of the material F_{th} and the projection ratio Γ to $T_{\min} = F_{th}/F_M \cdot \Gamma^2$. The projection ratio considers the reduction of the image size and hence the quadratic increase of the fluence.

4.2.4. *Combinations of gray scale and contour mask techniques*
In order to combine the already discussed advantages of gray scale masks and scanning techniques, the combination of gray scale and contour masks has been proposed and demonstrated [59]. The processing scheme of this technique is shown in Figure 3e. As shown in the figure, both masks are projected simultaneously onto the surface. In the contour mask technique, the projected contour mask is moved relative to the workpiece. This is usually realized by scanning the workpiece. In addition to scanning the workpiece, the fluence distribution, i.e. the gray scale mask, is moved in step with the workpiece. This can be achieved by adjusting the velocity ratio of the workpiece and the gray scale mask to fit the magnification of the projection optics. Equation 10 gives the ablation depth $d(x, y)$ expression for this method.

$$d(x, y) = \left[\frac{f_{rep}}{v_s} \cdot (f_{K1}(y_{pM}) - f_{K2}(y_{pM}))\right] \cdot \left[\frac{1}{\alpha_{eff}} \cdot \ln\left(T(x) \cdot \frac{F_0}{F_{th}}\right)\right] \qquad (10)$$

The first term of the equation is a function of the y-coordinate, only describing the contour mask $[f_0(y) - f_1(y)]$ which determines the applied pulse number in the scanning direction. The second term describes the ablation rate as a function of fluence which varies locally according to the transparency grade $T(x)$ of the gray scale mask (varying only in x-direction). Since the x- and y-terms above are multiplied by using both masks simultaneously, 3D-machining of surfaces with composite terms (e.g. $x \cdot y$) can be realized using this approach.

4.3. *Design of masks for 3D-machining*

4.3.1. *Contour masks*
According to equation 6, the contour of a scanned mask determines the cross section of the resulting groove. Incubation effects usually influence the machining accuracy in a negative manner, particular at low etch depths that require only a few laser pulses. A solution is to attach a rectangular open bar to the mask design perpendicular to the scan direction. The added rectangular makes no functional changes in the topography and serves only as a homogenous pre-illumination which eliminates the incubation effect. Also, an open bar can be used to improve the projection of sharp pointed mask contour details whose image is insufficient due to the limited resolution of the objective.

Additional difficulties should be overcome when large areas are structured with non-repeating patterns. If the intended structure requires a mask pattern larger than the illuminated area in the mask plane, the pattern must be subdivided into a set of individual masks. In many cases it is advisable to select a point of shallow ablation for subdividing a mask. At rims of shallow ablation depths, adjoining scans fit together easily. In order to further reduce trenches between adjoining scans, both masks may be supplied with an extra complementary mask feature reducing the slope and consequently trench formation at the scan border. Overlapping regions can be used in both contour and gray scale approaches. A simple approach for a contour

mask overlap region is to add or remove triangular shaped areas at etch mask ends, see Figure 5.

4.3.2. *Gray scale masks*
Simple contour masks can produce only 2.5D-structures or require the relative workpiece-laser-motion at optimized ablation conditions to produce real 3D-topologies. An alternative for ablating complex surface structures is to use a mask with a locally variable transparency that determines the controlled ablation process at the workpiece. Thus, complete structures may be machined by single laser shots, making gray scale masks favorable for time restricted processing schemes such as marking on the fly with fast moving workpieces.

First approaches for gray scale masks used in photolithography consisted of a stack of several layers of a moderate absorber [60]. Thin metal film mirrors with a graded attenuation have been used as a gray scale mask at very low fluences, < 10 mJ/cm^2 [61]. In addition to the difficult fabrication process, they suffer from degradation under laser illumination. Currently, the variation of the optical density within a thin, energy sensitive layer has reached a notable degree of maturity, in photolithography down to wavelengths of 365 nm [62, 63]. Unfortunately, the absorption of HEBS- and LDW-glass increases dramatically with shorter wavelengths, making these masks inappropriate for excimer lasers in the far UV. In addition, thermal effects from the absorbed laser radiation can damage the mask.

An alternative approach is to use standard manufacturing techniques employed for advanced binary masks in microelectronics, such as chromium-on-quartz, and apply half-tone methods for producing variable chromium dot densities and consequently transparency grades. These half-tone masks form an image by varying the local area density of chromium dots, each of which is too small to be resolved individually. Together, however, they produce an image with various shades [13, 57].

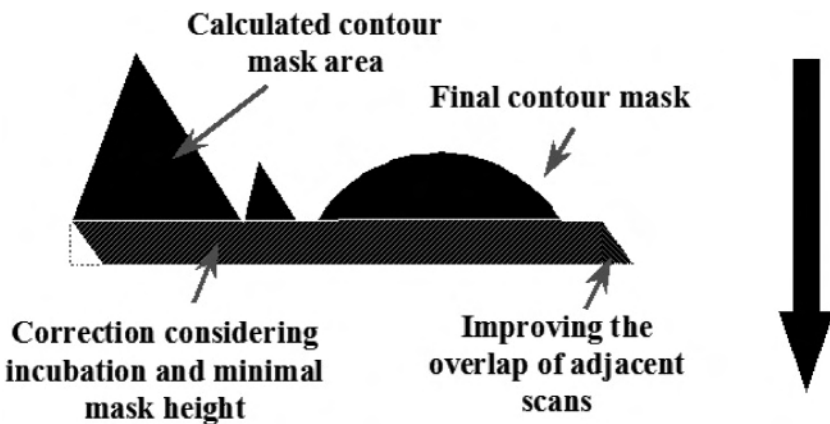

Figure 5. Design of a contour mask for overlapping successive scans in order to reduce topography distortions at the transient area. The black arrow denotes the scan direction.

The two possible arrangements of chromium dots discussed here are shown in Figure 6. The first approach uses chromium dots of equal size but randomly distributed according to the desired local transparency. Their individual positions are computed by various dithering algorithms [64]. The local grade of transparency is determined by the average density of chromium dots at this mask position. Implementing masks of this type leads to unsatisfactory results, namely uneven and roughened surface after ablation. This fact can be attributed to undesired clusters of chromium dots, as seen in the inset of Figure 6a, which macroscopically still retain the required dot density but fail from the imaging point of view as they can be large enough to be projected entirely onto the workpiece surface.

The second approach uses regular structures such as two-dimensional amplitude gratings in reticule masks to rule out the occurrence of the aforementioned shortcomings. The local grade of transparency is determined by the local ratio of crossed chromium lines and quartz open spaces. Not only is the evolution of dot clusters prevented in this case, but the diffraction patterns are even more regular and can be filtered easily by apertures compared to the case of randomly distributed dots.

The grade of the transparency can be treated formally in two ways. The less accurate approximation uses the local area density of geometrically open sub-units. The second based on the accurate diffraction approach, considers primarily only the transmitted intensity of the zeroth diffraction order. The transmitted fluence of an optical amplitude grating is given by:

$$F \approx A^2 = A_0^2 \frac{\sin^2 \xi}{\xi^2} \frac{\sin^2 N\eta}{\sin^2 \eta} \text{ with } \eta = \pi \frac{g}{\lambda} \sin \beta = \frac{g}{b} \xi \text{ and } \xi = \frac{\pi b \sin \beta}{\lambda}. \quad (11)$$

The relative transmitted intensity (or pulsed laser fluence) F and linewidth (grating period less slit width) g-b are normalized [65]. The principal maxima behind the

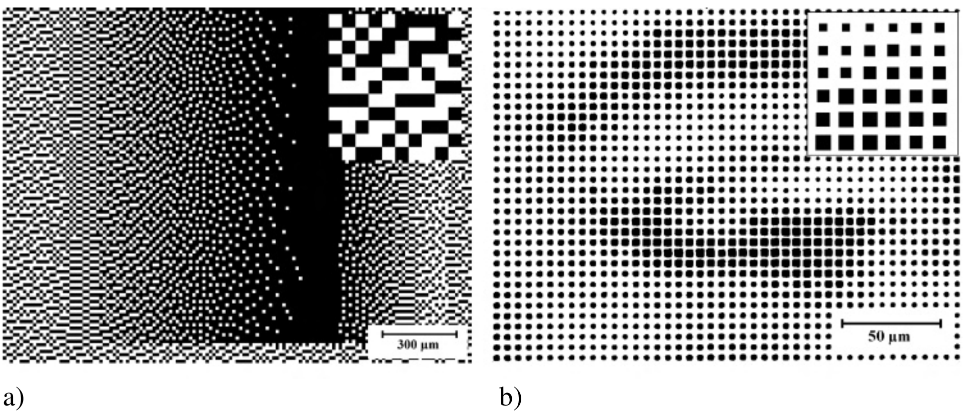

a) b)

Figure 6. a) Half-tone mask representing a gray scale transition through a dithered (irregular) arrangement of chromium dots of equal size. b) Half-tone mask representing a human right eye and eyebrow through a regular arrangement of chromium dots of varying size.

grating can be found at the angle β according to conditions $g \cdot \sin \beta = 0, \lambda, 2\lambda, 3\lambda, \ldots = m\lambda$ where m is the diffraction order. Although the transmitted light relates to the geometrical areas of the open quartz spaces, it is also influenced by the diffraction of the grating. Selecting certain grating periods according to the optical setup and using equation 2 for the ablation process, the local linewidths for the desired grades of transparency on the gray scale mask should be calculated from equation 11. Typical transmitted laser fluences and the resulting etch rate dependence on the width of the quartz spaces are shown in Figure 7a for a set of machining parameters. The grade of transparency of amplitude gray scale masks is only coded in the width of the grating lines. Hence, the thinnest lines and spaces that can be fabricated limit the range of continuous transparency adjustments, excluding zero and full transparency. For more advanced masks, crossed gratings are used.

Structures of dielectric bilayers are also used for gray scale masks. Masks of this type consist of a stack of dielectric bilayers which serve as a dielectric mirror at high numbers of bilayers. Following laser ablation [66] or wet chemical etching [67] of a number of pairs of dielectric layers, the principle of constructive interference works only to a limited degree and a level of transmission can be adjusted. The advantage of those masks however, is their suitability to high laser fluence ranges up to several J/cm^2. Their disadvantage though is that only stepped transmitted laser fluences can be selected.

To overcome the drawbacks of known gray scale mask approaches, e.g. low damage threshold, difficult and costly fabrication, and discontinuities/limitations in the reproducibility of certain grades of transparency, an alternative approach was recently introduced [68]. The new approach uses diffractive masks of the phase grating type with adjustable phase shifts. Masks of this type are made purely of a single transparent material such as quartz and have high physical durability.

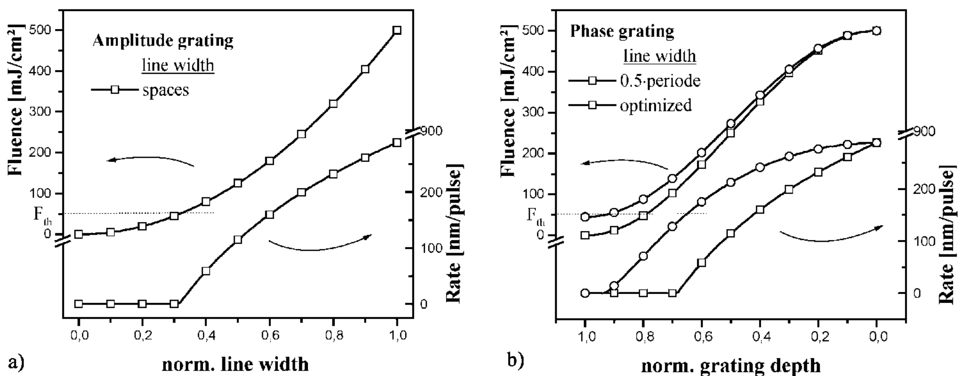

Figure 7. Transmitted laser fluence and corresponding ablation rate of gray scale masks consisting of a) amplitude or b) phase gratings. The line width or the grating depth is used to control the grade of transparency. For rate calculations, the ablation parameters $\alpha_{eff} = 8 \cdot 10^4$ cm^{-1} and $F_{th} = 50$ mJ/cm^2 were used.

Here, only the zeroth order of diffraction of an optical phase grating is used to form the image, see Figure 8. Since higher diffraction orders do not contribute to image formation the line grating itself is not resolved by the objective as mentioned in section 2.2. Grades of transparency (gray levels) are adjusted via the local phase shift, which in turn is determined by the local groove depth d_g [69]. Since the grating period g determines the diffraction angle β it must be selected so as to ensure that no scattered light falls into the objective's aperture. Hence, the laser fluence distribution F_z in the zeroth order and the angle of diffraction, are independently controlled by the groove depth and the gratings period, respectively.

Since the grating depth can be etched, e.g. via ion beam milling, very precise, continuous gray scale distributions can be achieved. In an optical grating with a rectangular groove profile of width w, the transmitted intensity or pulsed laser fluence in the zeroth diffraction order F_z is calculated by $F_z \approx 1 + 4 \cdot w \cdot (w - 1) \cdot \sin^2(\delta/2)$. The phase shift δ is determined by $2 \cdot \pi \cdot d_g \cdot (n - 1)/\lambda$ where n is the refractive index of the grating material. The adjustment of transparency in the range from 0 to 1 by the depth of the gratings is not limited by the fabrication technique. If a high contrast ratio between the dark and illuminated regions in the image plane, which is typical for contour masks, is desired, phase shifts of π or $\lambda/2$ are needed. This is accomplished by groove depths of $\lambda \cdot (n - 1)/2$ [70].

The controlled tuning of the groove width w at a constant grating period and a constant phase shift of π also yields transparency grades as shown in Figure 7a. The masks share setbacks of amplitude grating masks [71], such as low fabrication reproducibility of minimal line widths.

The influence of the grating depth of phase masks on the transmitted laser fluence and ablation rate is shown in Figure 7b. A 0.5 line width may reduce the transmitted fluence to nearly zero. Since laser ablation is characterized by a threshold

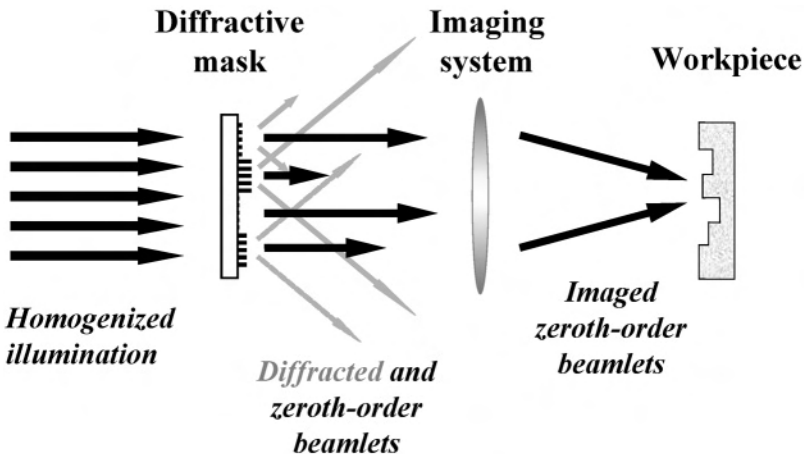

Figure 8. Diffractive mask in the optical beam guidance setup. Certain areas on the mask deflect individually a certain amount of laser light outside the solid angle of the imaging system, whereas, the zeroth diffraction order passes through the imaging system and accomplishes laser ablation.

fluence, fluence values below this threshold are not required. By reducing the grating line width to an optimized value, the ablation rate can be varied within the full range using a grating depth between zero and $\lambda \cdot (n - 1)/2$.

4.3.3. *Masks for producing interference patterns*
High resolution laser techniques enable the fabrication of sub-micrometric features by lithographic techniques [72], holographic techniques [73, 74], and by gratings imaging [75]. In this section, the imaging of gratings is described. By coherent illumination of a transmission grating, the two side first orders of the diffraction pattern are projected onto a normally oriented surface by a Schwarzschild-type reflective objective. Thus, the laser beam is split up into two parts which recombine on the surface and result in an interference pattern. The line spacing g of the produced pattern is calculated by the relation $g = \lambda/[2 \cdot \sin \theta]$ with 2θ being the angle between the two incident beams and λ the selected wavelength, see Figure 3f.

5. Some laser 3D-machining techniques and their applications

The need for micro-machined 3D-elements consistently increases for applications in microsystems technology. Considerable advances were made in research and industry, especially with analytical devices [76] and micro-reactors [77]. Micrometric and sub-micrometric structuring of materials is obtained by standard techniques such as wet or dry etching [78]. Both methods require photolithographic masking of the material surface prior to etching and the removal of the mask afterwareds [79] hence, these processing schemes do not offer great flexibility and are not useful in rapid prototyping. For a number of applications, polymers offer an attractive alternative to the traditional glass and Si/SiO_2, materials, e.g., for the fabrication of microfluidic devices, being less expensive and fragile than classical materials used in microelectronics or precision optics. An additional cost reduction is achieved for mass production schemes based on replication of micro structured polymer devices [80].

5.1. *Laser machining for the microsystems technology*

Laser beam machining proved a versatile tool for micromachining of solid materials. Laser beams are widely used today for drilling, welding, and cutting of materials for applications in precision engineering, microelectronics, and microsystem technology. Specific attention is paid to thin film micromachining, e.g., trimming, scribing, cutting, etc. [6]. For these applications Nd:YAG-lasers and their higher harmonics are used extensively for some time due to their good beam quality, low costs and ease of handling.

Due to improved design and extended functionality of today's microsystems, there is an increased demand for surface topography and especially for the fabrication of 3D-elements. However, one of the main obstacles to a more rapid development of new technologies is the deficiency of suitable processing methods, e.g., real

3D-machining. Since most attention was paid to the classical tasks of laser machining such as drilling and cutting, relatively few works were published on 3D-surface machining. Some works using laser micromachining for the fabrication of 3D-elements will be summarized in the following sections. Material based approaches to 3D-machining are only touched briefly, such as micro-lenses, which are fabricated by melting a laser ablated pre-formed polymer at elevated temperatures [81] or by sub-threshold laser illumination [82].

5.2. *Stationary regimes*

Stationary ablation is successfully implemented in the production of bubble jet printer nozzles, the etching of via holes [83] in flexible printed boards, and the fabrication of specially formed spinnerets [84]. More complex, multilevel structures are ablated using step and repeat techniques or a set of contour masks. The application of a contour mask set, which consists of masks having various, complex shapes, results in a stepped multilevel topography of multilevel diffractive optical elements in photoresist. Once the mask set is designed, the approach suffers from low flexibility and the alignment problems of subsequent masks.

5.2.1. *Step and repeat techniques*

The simplest and most flexible method for 3D-machining is to utilize a small spot beam for local etching in sequential steps, also known as step and repeat processing. This technique is based on computer-controlled positioning of the focused laser onto the workpiece surface, and the local application of a preset number of laser pulses to etch precisely to the desired topology depth. In technological applications, the total depth of the 3D-topography is subdivided into a number of machining layers. Laser etching itself is accomplished by a small, often square shaped mask with an applied fixed number of pulses needed to attain the required layer depth. For many materials, the resulting surface roughness is unacceptably high [85]. The reasons for the high level roughness are the overlay of ablation irregularities such as trench and rim formation.

5.2.2. *Gray scale masks for 3D-machining*

The stationary gray scale mask approach is the only technique enabling a continuous ablation of real 3D-microstuctures with single or a sequence of laser pulses. The gray scale mask stores the entire information needed for the ablation of the desired microstructure within the mask's structure, e.g., the local laser fluence necessary to perform ablation at the specific rate for the material used. Using one or a set of gray levels masks, large area 3D-machining with a high filling factor and satisfactory quality can be easily achieved by means of a step and repeat or synchronized movement approach [86].

A conventional bitmap file with 86 × 86 pixels and 265 gray tones, see Figure 9a, was processed into a reticule mask. A cutout of the mask can be seen in Figure 6b. Every original bitmap pixel was translated into a square mask subunit consisting of 3 × 3 grating periods at a 4.85 μm grating constant. The width vari-

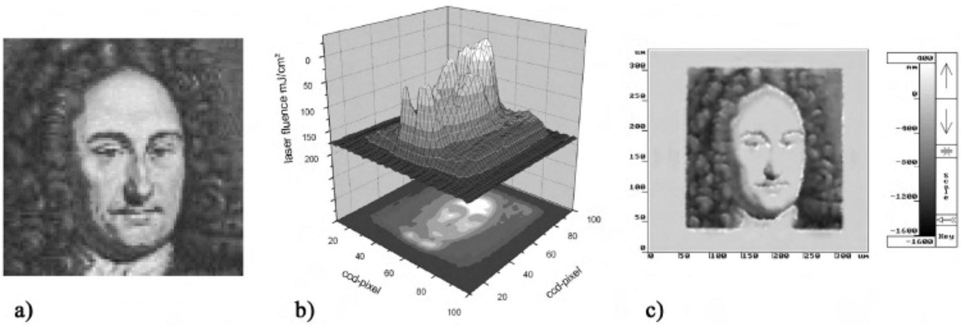

Figure 9. a) Portrait of G.W. Leibniz (1646, Leipzig – 1716, Hannover) to be processed into a reticule mask, b) the measured laser fluence distribution in the image plane after transmission through the reticule mask, and c) white light interferometric measurement of the ablated polymer surface, displaying gray color depth reconstruction of the original portrait.

ation of the crossed chromium lines yields 265 gray levels or grades of transparency. The laser fluence distribution in the image plane is shown in Figure 9b. It ranges from ca. 20 mJ/cm^2 to 175 mJ/cm^2. After a 30-pulse laser ablation of polyimide in a helium atmosphere, the surface topography was measured with white light interferometry. The gray color-coding into ablated depths clearly reconstructed the human portrait on an area of 250 μm × 250 μm, see Figure 9c.

Using specially designed phase shift gray scale masks, some 3D-microstructures have been ablated into thin polymer layers. According to the theory, the grating constant must be smaller than the value necessary for diffracting the first diffraction orders beyond the aperture of the imaging objective, thus g = 5 μm was chosen. To achieve the high accuracy needed, the mask's gratings were e-beam written. The groove depth, controlling the mask's transparency grade, was adjusted by ion beam etching techniques [69]. For the calculation of the mask's transparency, the experimentally determined ablation rates of photoresist AZ4562 were fitted to equation 2 yielding F_{th} = 80 mJ/cm^2 and $\alpha_{eff} = 8.5 \cdot 10^4$ cm^{-1}. On the mask, a small rectangular semi-transparent area embeds the functional gray level area coding the desired microstructure. With this semi-transparent area the fluence was set slightly above the ablation threshold leading to a reduction of debris deposition during the ablation. Figure 10 shows a SEM image of an array of tapered blind-holes etched by such a single gray scale mask. The array was created with a step a repeat process using the same mask. A smooth surface is visible on almost all surface parts ablated with different laser fluences. Some irregularities or surface humps visible in the enlarged inset repeat at every 3D-element, resulting from tiny gray level mask contaminations which change the local transparency. White light interferometry was used to check the conically tapered sidewalls, vertical sidewalls, and the flat bottom all of which were encoded into the gray level mask. The roughness at different etch depths in the range of 2 to 10 μm was measured to be less than 100 nm (rms). The independence of the roughness from the etch depth indicates that the roughness originates from the pure ablation process rather than from microstructural assembly on the gray level mask. Thus gray scale mask can

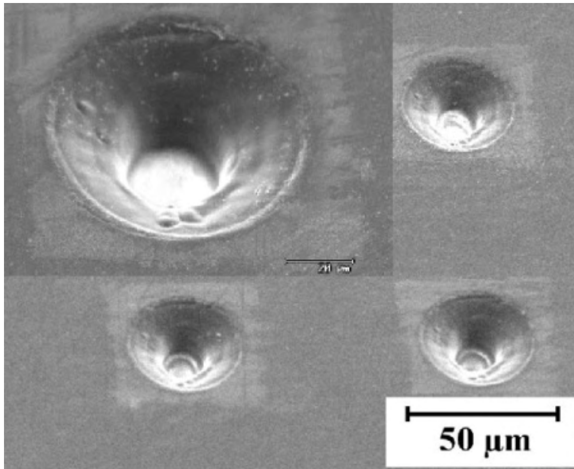

Figure 10. SEM image of tapered holes etched by a gray scale mask. A well-defined border and a smooth surface characterize the element.

provide steep sidewalls, well-defined edges, and a clear outer border of the machined elements. Gray scale masks are thus also suitable for ablating both binary and continuous surface profiles.

5.2.3 Sub-micrometric structuring

Sub-micrometric surface relief structures can be achieved by means of laser beam interference, see Figure 3e. Amplitude line gratings allow easy beam splitting, but the zeroth order needs to be blocked [75]. Phase gratings diffract a greater portion of energy into the diffraction orders and suppress the zeroth order of diffraction if they are carefully designed [18, 65]. To achieve a sinusoidal fluence distribution, only ± first diffraction orders were allowed to pass the objective. In order to suppress the zeroth order of diffraction, a binary phase grating made of quartz by photolithographic means and ion etching with a period of 22 μm and a depth of ~270 nm was used. Applying this technique in conjunction with the approach of backside etching, i.e., the LIBWE technique, periodic gratings in quartz with a sub-micrometric period have been machined [87].

A solution of acetone and pyrene served as the laser photon absorbing liquid and was in permanent contact with the quartz workpiece backside. Sub-micrometric surface relief gratings have been etched with a measured period of 787 nm, which is in good agreement with the calculated value 730 nm using a 15 × demagnifying Schwarzschild-type objective. The applied laser fluence determines the surface grating's relief profile depending on the etch rate of the local fluence according to the LIBWE mechanism. Using an illuminating average fluence of ca. 400 mJ/cm^2, the etching starts at the maximum fluence of the sinusoidal interference intensity distribution. In the intensity minima, the fluence does not exceed the threshold fluence and laser etching is not activated. As a result, the surface gratings become distorted. In some cases, plateau-like crests could be seen. Here,

the periodic sub-micrometric structures exhibit deep, acute-angled grooves, whereas the grating depth increases with increasing pulse number. An average laser fluence of about 1 J/cm^2 etches a sinusoidal surface grating to a depth of about 100 nm, see Figure 11. The surface roughness of these gratings measured by AFM was calculated after passing the Fourier transformed images through a high pass filter to remove spatial frequencies longer than 0.2 μm. For all processing conditions, the rms roughness of the grating surface was below 10 nm and reached a value of less then 3 nm for optimized conditions.

5.3. *Scanned mask regimes*

The profile of the machined groove of a scanned contour mask is determined by the contour mask shape. Pulse repetition rate and workpiece velocity only affect the geometrical distance between individual laser pulses and, together with the applied laser intensity, control the depth of the groove. In this way, the desired topology is approximated by superimposing individual mask images, i.e. shape defined material ablation processes. In many cases, the bottom of the scanned groove exhibits images of individual mask rims and undesired regular periodic structures appear. Here, pulsed laser ablation displays its digital nature. Reducing the ablation depth per laser pulse and lowering the workpiece feed between subsequent pulses improves the surface quality. Pulse distances of about 1–2 μm were found to yield low bottom roughness values.

Some effects associated with laser ablation, such as trench formation and light reflection at the walls, can also arise while using scanning techniques. Although the scanning contour mask technique produces less complex 3D-structures, it is easy to use since it needs relatively simple equipment.

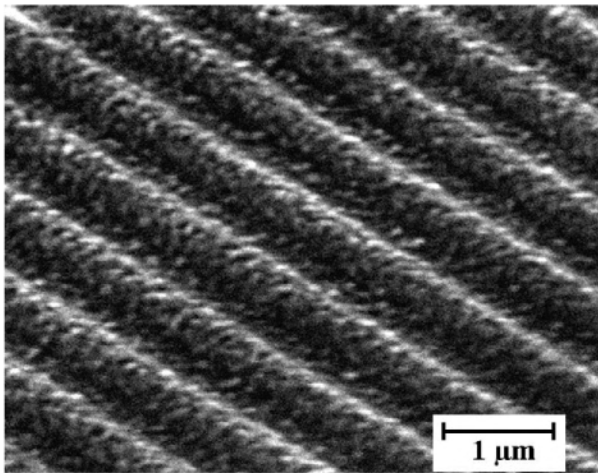

Figure 11. SEM image of an etched grating in quartz, laser fluence: 960 mJ/cm^2 at 248 nm, 10 pulses.

Advanced scan techniques were developed to overcome the limitation of projection optics in terms of limited field of homogeneous mask illumination. This is the case when larger mask patterns need to be imaged and it is not advisable to separate the mask into a set of sub-masks. The preferably stretched but slim mask pattern is then moved through the object plane while the workpiece is moved in a synchronous manner [56]. Large area structures can be efficiently machined with one single mask and without lowering the projection ratio. This synchro-move technique is especially useful when high laser fluences are necessary to ablate inorganic materials. It can also be used for 3D-machining in conjunction with gray scale masks.

5.3.1. *General considerations of mask scanning*

As experimental results demonstrate, the roughness of a laser machined surface depends on the set of processing parameters [57]. The influence of various processing parameters shall be discussed in order to optimize the process and reduce surface roughness evolution.

Mask scanning can be achieved either by moving the mask, the workpiece, or both, depending on the technical equipment available. Figure 12a shows a typical excimer laser fluence distribution and a mask inserted to be used for mask scanning. Mask scanning is performed by moving either b) the mask through the mask plane or c) the workpiece under the mask shaped laser beam. The ablated topology was investigated by white light interferometry. Although the same laser fluence and geometrical pulse-to-pulse-distance was used, a significant difference in the surface roughness can be seen. Moving the mask results in a rough surface due to an inhomogeneous fluence distribution. When moving the workpiece, typical grooves appear in scan direction which originate from either fluence inhomogeneities or mask inaccuracies. Traces of the mask rims are also clearly observed. The white area in the center of Figure 12c represents a higher etch depth resulting from a slightly more intense laser pulse, consistent with the standard deviation of the pulse-to-pulse

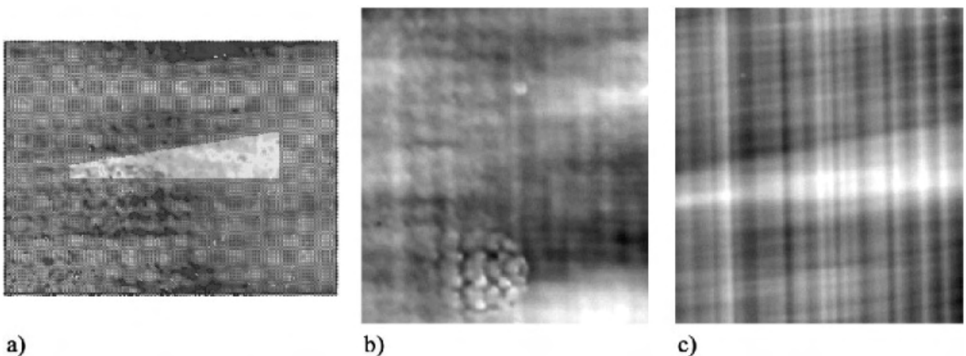

Figure 12. a) Fluence distribution and inserted mask used to compare the surface roughness development measured by white light interferometry using the scanning contour mask technique by either moving b) the mask or c) the workpiece.

stability. If the workpiece was moved, the roughness measured was up to 3 times lower than with the mask moving. In the case of scanning the workpiece, inhomogeneities are partially leveled out in scan direction. As this cannot be achieved with a mask moved through a stationary beam profile over an equally stationary workpiece, the measured roughness values are higher.

Further, in mathematical considerations the influence of the mask footprint on the roughness evolution is investigated. Three different footprint border types are used. They differ in the type of fluence transition from the inner mask area to the outer surrounding non-illuminated area. Footprints with step, ramp, and sine-like transitions have been considered. The footprints used and the calculated surface topography after machining with the selected footprints are shown in Figure 13. Roughness evolution by the ablation process itself is not regarded in this evaluation.

The calculations emphasize the drastic influence of the footprint characteristic. Binary footprint rims turn out to be least advantageous for 3D-processing. In general, a steady and smooth rim transition yields smoother surfaces. Increasing the width of the rim transition tends to result in the reduction of the roughness as shown in Figure 13. In a first approach, low resolution projection systems might be exploited to achieve such smooth footprint rims, but they are not advantageous. The adjustment of a suited fluence transition in scan direction, however, can be achieved by a specific mask design, see section 5.3.3. In this case, the fluence transition can be controlled independent of the optical projection system and can be selected according to the specific application via gray scale attachments.

Low surface roughness values can be expected if (i) the mask footprint used for scanning shows a smooth transition at the rim, (ii) the width of fluence transition at the footprint rim is equal to the geometrical pulse-to-pulse distance or a multiple thereof, (iii) the fluctuations of the processing parameters are kept as low

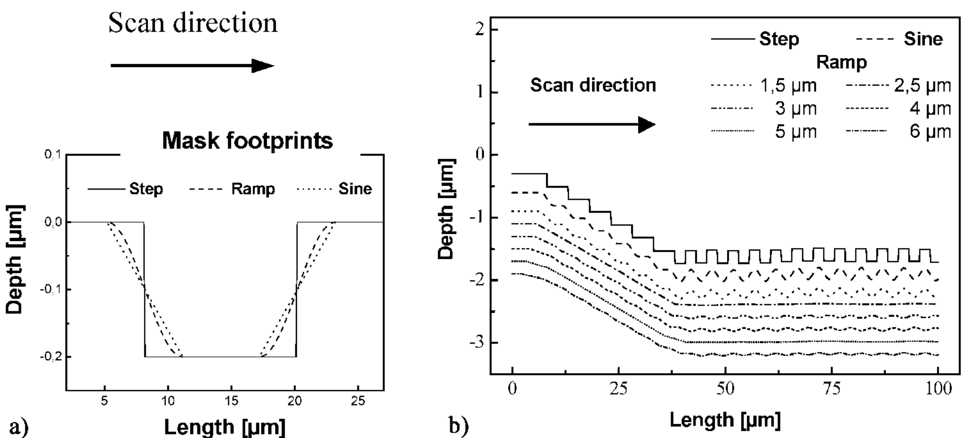

Figure 13. a) Stationary cross sections of different mask footprints applied to calculations of mask dragging along the indicated scan direction. b) Calculated topography of laser machined surfaces using the scanning contour mask technique caused by different mask footprints.

as possible. Unfortunately, the greatest contribution to roughness evolution, however, must be attributed to the fluence inhomogeneities and intensity fluctuations of the laser beam, compare Figure 12.

5.3.2. *Application of scanning contour masks*
Applying contour mask techniques results in 3-D microstructures such as blazed gratings, saw-tooth structures, and cylinder lenses with lateral dimensions from 10 to 1000 μm and profile heights up to 10 μm [57]. With refinements, these techniques were used to machine specific free shape optics, e.g., micro-prisms, which can be used in optical data processing [88]. To achieve high quality, adaptable, and fast surface machining, the scanning contour mask technique was selected.

To ablate large areas of micro prisms, a contour mask was calculated according to equation 6, projection optics with a demagnification factor of 5 and a geometric pulse to pulse distance of 1 μm were used. Surface distortions due to incubation effects and a limited mask resolution were avoided by adding a rectangular bar with a width of about 15 μm to the nominal mask, see Figure 5. The e-beam written chromium mask consists of different sub-masks. Using an aperture close to the contour mask, a set of 3 or 4 sub-masks was selected for separate writing scans. Then, both mask and workpiece positions were reselected to scan the next set of micro-prisms. Large area machining was thereby achieved. By choosing the parameters and machining aspects ratios mentioned above, a final etch depth of up to 170 μm, wall angles up to 75°, and curvature radii as small as 5 μm were achieved. In spite of the remarkably great etch depth a surface roughness as low as 160 nm (rms) was measured on the planes of the micro-prisms. Micro-prism arrays of this type have been replicated and are described more in section 6 [88, 89].

The techniques we have considered are not limited to standard laser ablation processes but can be exploited also in conjunction with other radiation based etch and deposition techniques. For example, the contour mask technique was used in conjunction with the backside etching technique, see Chapter 7 of this book. Figure 14a represents an SEM picture of an etched fused silica workpiece with a concave cylindrical topography useful for micro-lenses. The applied laser fluence was about 750 mJ/cm^2, which is remarkably low for ordinary laser ablation of fused silica. This allows for using low demagnification ratios i.e., large processing areas. The measured micro-roughness of the machined surface by microscopic white light interferometry was below 10 nm (rms) for an etch depth of more than 50 μm [36]. The low roughness values are probably related to the low rate of the backside etching process.

This etching process can be extended to other transparent materials of high importance to microsystem technologies as demonstrated in [90]. A number of glasses such as Pyrex, Corning 7059, Schott D263, and AF45 are of great industrial importance due to their exceptional physical and chemical properties. Using pulsed XeF-excimer laser radiation (351 nm) at moderate laser fluences of less than 1 J/cm^2, these glasses have been etched with remarkably low roughness values. At an etch depth of a few microns, roughness values as low as 4 nm (rms) were measured by AFM. Recent results show that very smooth surfaces can also be achieved in

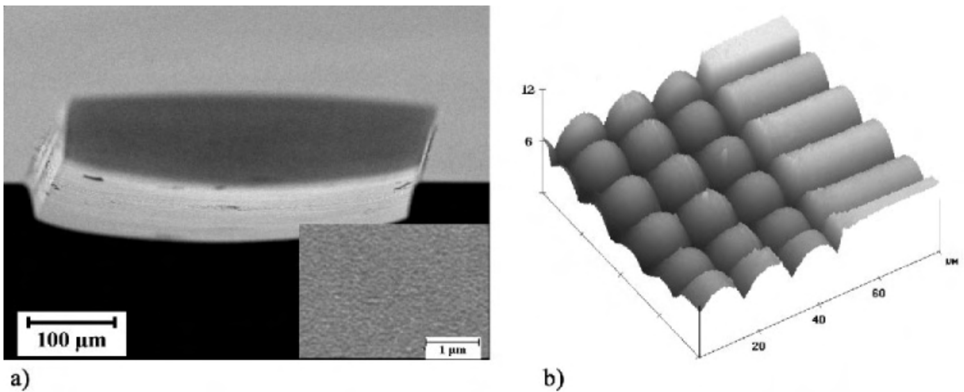

Figure 14. Laser machined 3D-topographies: a) SEM picture of a cylindrical structure etched into fused silica employing the scanning contour mask technique. Note the very smooth bottom of the structure as shown in the inset [36]. b) AFM view on a micro lens array in polyimide accomplished by using the scanning contour mask technique twice [57].

Pyrex. The machining of Pyrex, which is a glass developed specifically for anodic bonding to silicon, holds an especially great potential in microsystem technology for the integration of optical structures such as micro-lenses, prisms and gratings.

More complex 3D-micro-topographies were machined by applying the same or other contour mask scans in consecutive machining steps. An early publication demonstrated the process capability [57] as depicted in Figure 14b. The array was fabricated by scanning in two orthogonal directions with a semi-circular contour mask using the same processing parameters i.e., 150 mJ/cm^2 laser fluence, 20 Hz repetition rate and 20 µm/s scan velocity for both scans. The final lens diameter is 15 µm and the structure height is 2.5 µm. Structuring a similar, but larger lens array with an area of 1.7×1.7 cm^2 consisting of more than 900 individual lenses with lateral dimension of 500 µm and height of 7 µm took about 11 minutes with a laser pulse repetition rate of 80 Hz. Since the estimated cumulative temperature rise due to laser pulses at 80 Hz is well below the glass transition temperature of the used polyimide (~350 °C) a further increase of the machining speed without thermal distortion of the microstructure is possible by increasing the repetition rate.

To demonstrate the machining of surface topographies of type $d(x, y) = x \cdot y$, the modified scanning contour mask technique described in section 4.2.2 was applied [59]. Such surfaces are useful for beam steering applications. In addition to the designed contour masks, such as e-beam written chromium-on-quartz masks, a metal foil was used as aperture mask directly on top of the workpiece surface to restrict the laser machining area to a single topographic region. The fabricated structures, depicted in Figure 15a, show the desired surface topography. The rough border lines of all individual micro-structures can be attributed to the aperture metal foil, which had poorly defined border lines.

In comparison to gray scale techniques, which are also capable of machining these elements, the described machining technique utilizes scanning techniques, which

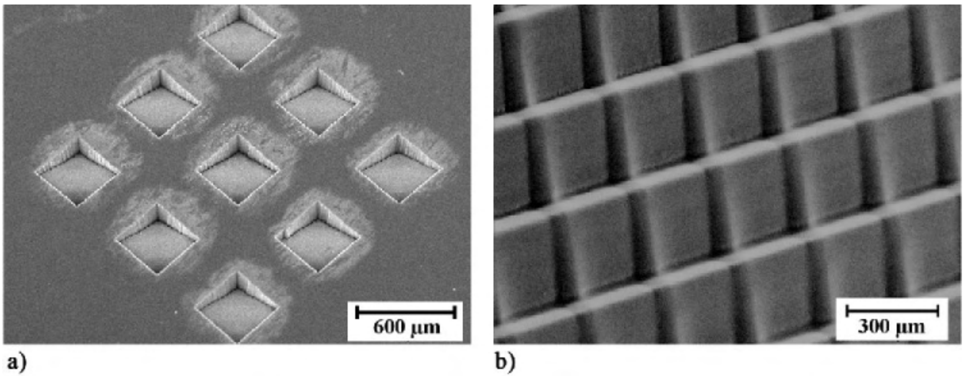

Figure 15. SEM images of 3D-topographies of the type "$x \cdot y$": a) machined squares by the modified contour mask technique and b) machined structures by the combination of gray scale and contour mask technique [59].

were shown to have considerable advantages in producing low surface roughness values. Both the intensity fluctuations between subsequent laser pulses, and the characteristic intensity profile of each individual laser pulse influence the roughness and shape fidelity of the fabricated structures. Scanning techniques level out these irregularities in the direction of the scan to some degree. By switching to static techniques such as gray scale techniques, these advantages are lost. As long as laser micromachining copes with intensity deviations of the beam profile of about 5%, scanning techniques should be preferred over static approaches.

Topographic surface structures of the type $d(x, y) = x \cdot y$ have also been fabricated using a combined grayscale and contour mask technique as described in section 4.2.4 and depicted in Figure 3e. According to equation 10 the gray scale mask in this experiment changes the laser fluence in the y-direction, whereas a triangular contour mask is scanned in the x-direction [59]. Due to the high accuracy needed, e-beam written chromium-on-quartz masks were used. The gray scale mask is composed of quadratic openings on an equidistant grid of various dimensions in the range of 2 to 5 μm. In front of the gray scale mask, the stationary triangular contour mask was mounted in such a manner that both masks were projected onto the workpiece. During machining, the gray scale mask was moved with a velocity equal to the workpiece speed multiplied by the demagnification of the projection optics.

Polymer samples of polycarbonate ablated at processing parameters $F_{th} \approx 70$ mJ/cm^2, $\alpha_{eff} \approx 1.1 \cdot 10^4$ cm^{-1}, and UV-cured acrylic blends at $F_{th} \approx 220$ mJ/cm^2; $\alpha_{eff} \approx 2.5 \cdot 10^4$ cm^{-1} on a glass plate were used in these investigations. Fluences in the image plane of 200–500 mJ/cm^2 were used to fabricate these samples. Figure 15b shows an array of fabricated 3D-structures that were also characterized by microscopic white light interferometry. The measured topography corresponds to the mathematical description predicting a linear dependence along the coordinate axis, and a quadratic dependence in the diagonal direction. The roughness and surface irregularities over a surface area of about 300 μm^2 were determined

to be about 200 nm (rms) at an etch depth of about 50 μm. This relatively high value must in part be assigned to the remaining inhomogeneities of the beam profile intensity.

5.3.3. *Hybrid masks*

Calculations on the influence of the mask footprint on the processed surface after contour mask scanning have shown, see section 5.3.1, that a smooth fluence transition at the mask rim reduces the resulting surface roughness notably. To take advantage of this fact, a new mask concept helps to improve the quality of pulse laser machined topographies. The task of this new mask is to generate a fluence gradient across the projected contour mask rim in a defined and adjustable manner as compared to conventional contour mask projection where only the optical imaging system determines the fluence gradient. This gradient adaption can be accomplished by attaching a graded gray scale mask to the outside border of the contour mask, see Figure 16 [91]. If properly employed, the attached gray scale mask implements a graded transition from full to zero laser intensity while the transmitted intensity function across the gradient can be tuned to a specific task, e.g., to minimize the roughness. In order to preserve the possibility of fabricating vertical sidewalls, the graded transition only needs to be attached to the contour mask in the direction of the laser scan. The hereby enlarged etch depth must be attributed to the gray scale attachments and needs to be considered when designing such hybrid masks [58]. An example of a simple hybrid mask implementation that consists of repeating isosceles triangles (200 × 5 μm^2) on either side of a simple contour mask core is depicted in Figure 16.

Conventional contour masks and the hybrid mask technique were used in comparative experiments at fixed processing parameters, i.e., f_{rep} = 150 Hz, F_{th} = 210 mJ/cm^2 [92]. In all cases the hybrid masks employing a graded fluence transition in the scan direction outperformed the conventional contour masks in terms of resulting surface quality at the bottom of the ablated scan as shown in Figure 17.

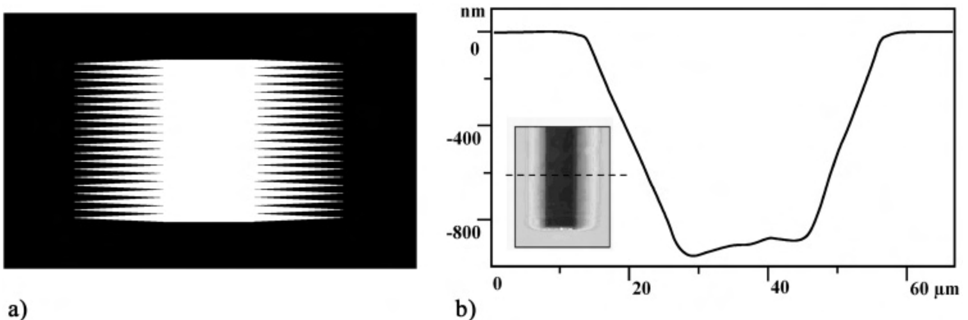

Figure 16. a) Schematic representation of a contour mask core partially surrounded by a series of isosceles triangles implementing the transition from full to zero laser intensity. b) Surface profile of the ablated topography of Pyralin-Polyimide after 10 pulses at 210 mJ/cm^2 (λ = 248 nm) using the mask in stationary ablation processing. The inset shows a false color contour plot of the ablated depth.

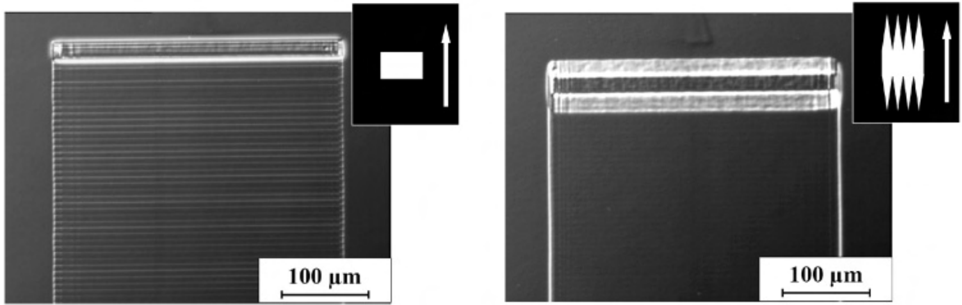

Figure 17. Nomarski image of scanned laser ablation of polyimide with 210 mJ/cm^2, 150 Hz repetition rate and 1000 μm/s scan velocity in a Helium atmosphere, left: using a regular contour mask, right: using a partly gray-scale surrounded contour mask. The spatial differences between single laser pulses are significantly less visible than in the left picture.

More detailed studies show the important influence of the spatial pulse distance to the bottom roughness. A significant reduction of the roughness value up to a factor of 3 as well as a minimum roughness value at a certain spatial pulse distance, here about 6 μm, have been observed. The residual deviations from the perfect surface result mainly from an inhomogeneous laser beam. Such irregularities increase with the number of overlaying laser pulses and give rise to a non-uniform ablation depth over large areas. This effect is the main limiting factor in the increased roughness values observed for increasing ablation depth.

5.4. *Laser direct writing using a small spot*

This technique is the most flexible technique for 3D-machining and is preferably applied to rapid prototyping. In contrast to step and repeat approaches, see section 5.2.1, here we only consider techniques using a permanently translated or scanned small spot laser beam. The 3D-structure is produced by translating the laser spot along a designed path across the workpiece to etch the material. Advanced CAD/CAM programming with a small laser spot is used to calculate the laser path in order to achieve the desired surface topology. It is helpful to sub-divide the depth axis of the desired topology into several machining planes. Starting with the original surface level, each machining plane is subsequently ablated. Depending on the depth of focus, repositioning of the workpiece along the z-axis may be required. Square masks moving in a circular fashion were utilized to achieve multi-stepped diffractive patterns [93]. This direct write process was used to fabricate binary, multilevel, and blazed diffractive optical structures [61] and 3D-microstructures [94].

The shape of the small laser spot crucially influences the quality of the machined 3D-structure. Beside unfocused beams, circular and quadratic shapes have been used. The region of two adjacent laser scans is the most critical area. Compare Figure 18a for an often found mismatch of adjacent laser scans, each having U-like groove geometry utilizing a quadratic shaped small laser spot.

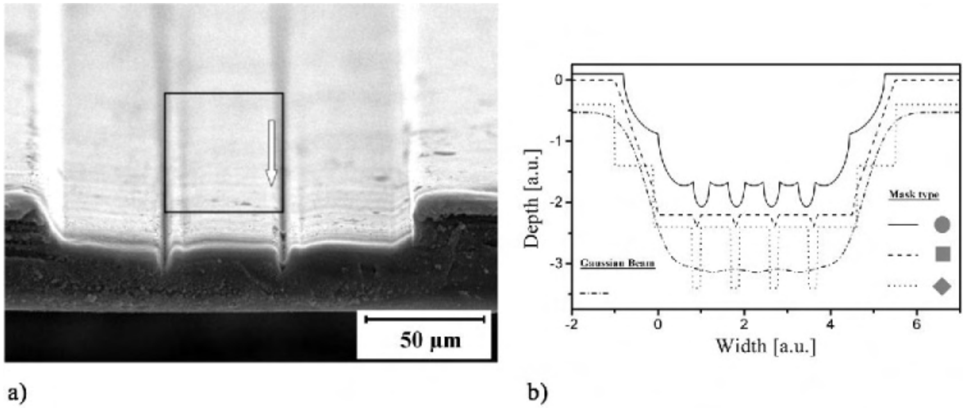

Figure 18. a) Micrographs of ablated polyimide after three parallel scans using a small quadratic laser spot as shown in the picture. The scans were performed along one side of the quadratic laser spot with a scan offset of 1 µm shorter than the mask dimension. b) Surface topography resulting from a set of intertwined machining scans using various tool shapes.

Similar to the influence of the laser footprint on the resulting surface topography, the attainable depth distribution at the border of two adjacent laser scans dramatically affects the surface quality. Calculated results of scanned surfaces using various small masks-quadratic, or circular, with a homogenized beam, and using a focused Gaussian laser beam are shown in Figure 18b. The aforementioned mismatch of adjacent laser scans was also taken into account. The lowest deviations from the perfect plane can be achieved when a Gaussian laser beam profile is used or the projected quadratic mask is scanned parallel to one of its diagonals.

The approach of quadratic mask machining with a scan direction rotated by 45° shall be discussed next in more detail. Single scanned masks lead to isosceles V-shaped groove geometries. The overlap of equally left and right-sloped topologies in adjacent parallel scans produces normally oriented groove bottoms. As a result of the shallow slopes of the V-groove geometries, trenches do not form. A lower roughness can thus be achieved. With a being the base of the quadratic laser spot, simple geometric considerations show that a $2a^{-1/2}$-separation of adjacent scans lead to a maximum width of the ablated bottom plateau. Figure 19 reveals the evolution of single V-grooves into more complex 3D-structures.

A refinement of the method of quadratic mask machining with a 45°-scan rotation helps override inherent and permanent inhomogeneities within the laser spot which often result in regular bottom structures at greater depths after multi-shot scanned material ablation. These refinements include alternating scan directions, shifts of $2a^{-3/2}$ for entire groups of scans belonging to the next machining level and 90°-rotation of scan direction for subsequent machining levels [95]. The implementation of all these refinements yields up to 5 times smoother laser written surfaces as compared to conventional approaches. See Figure 19 for a plateau etched to a depth of 25 µm having a roughness of less the 150 nm (rms) measured by white light interferometry.

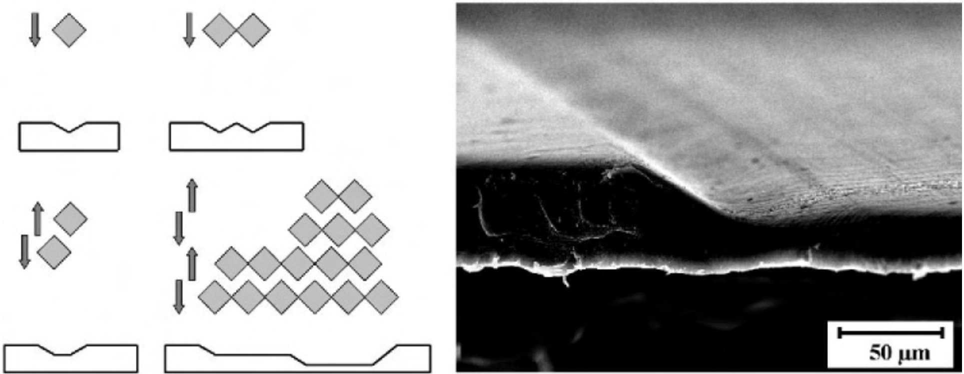

Figure 19. Schematic representation and micrograph of laser direct writing of complex 3D-geometries. Small V-grooves from quadratic machining spots are added to plateaus and walls with different slopes.

Using this small spot writing technique, micro-fluidic structures have been machined into polymer surfaces as shown in Figure 20. The designed microfluidic element consists of a reservoir (1) a micro filter unit (2) and a supply channel (3). The reservoir has an overall diameter of 0.5 mm and a depth of about 50 µm. The smallest widths were achieved for a filter with 15 µm. Various mask dimensions were used for machining and were included thus into the CAD-programming. After subdividing the overall depth into seven machining layers, the element was written by the aforementioned method into polycarbonate using a wavelength of 248 nm and a laser fluence of ~4 J/cm^2. Besides the high complexity of the details of the written element, Figure 20 also demonstrates the attainable low surface roughness [96].

6. Replication and transfer of laser machined surfaces

Typical methods of pattern generation like e-beam writing, laser writing, gray tone lithography etc. are time and cost ineffective [79, 97]. Replication techniques are the main issue in cheap mass production of 3D-elements and hold the key to commercial success of new 3D-products. It is thus favorable to combine the flexibility of the laser writing process with an appropriate replication technique.

The most common replication techniques are hot embossing, injection molding and casting. Since 3D-elements are first written in soft polymers such as photoresist, the additional step of forming an intermediate replica in a hard, robust material is often necessary. A common process is electroforming in a galvanic bath [98]. The replication technique and the purpose of the 3D-elements define the type of polymers to be used for replication. Based on the standard LIGA process Arnold et al. [99] demonstrated the replication of excimer laser machined binary and stepped

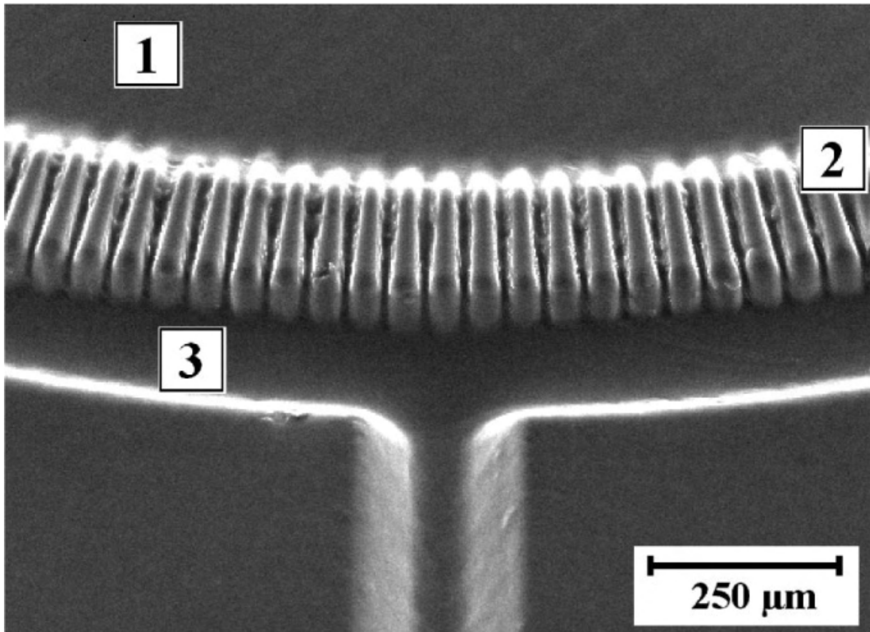

Figure 20. SEM image of an micro-fluidic element etched by writing with a small contour mask into polycarbonate at 4 J/cm^2.

elements for microsystem technology. Due to final replication by injection molding, time consuming electroforming of Ni-shims was employed [100].

A faster, one-step replication process based solely on a laser machined polymer master was developed [88]. A safe and reliable replication process requires an adequate master and a gentle replication process. For one-step replication, a negative master is necessary. Replication based on acrylate casting followed by UV-curing requires an insoluble, stabile polymer master. Also, the master polymer used must meet the requirements of laser ablation. In order to optimize ablation, reduce debris formation, and improve surface quality, an acrylic polymer blend was selected [89]. With the aim of protecting the master copy and to secure a safe and non-destructive separation of the master copy from its replica, the master copy was homogeneously coated with a Teflon-like, high fluorine content layer. This technique was successfully applied to replication of laser machined large area (> 10 cm^2) acrylic polymer masters, which in turn were prepared using the scanning contour mask technique. Figure 21 shows the cross section of the laser processed master consisting of a series of micro prisms and the 6th replica. Thanks to the Teflon-like anti-adhesion layer, the master surface shows no failures, see Figure 22.

Depending upon the desired surface topography, to minimize the etched volume and to retain an unprocessed surface outside the laser machined 3D-structures, one

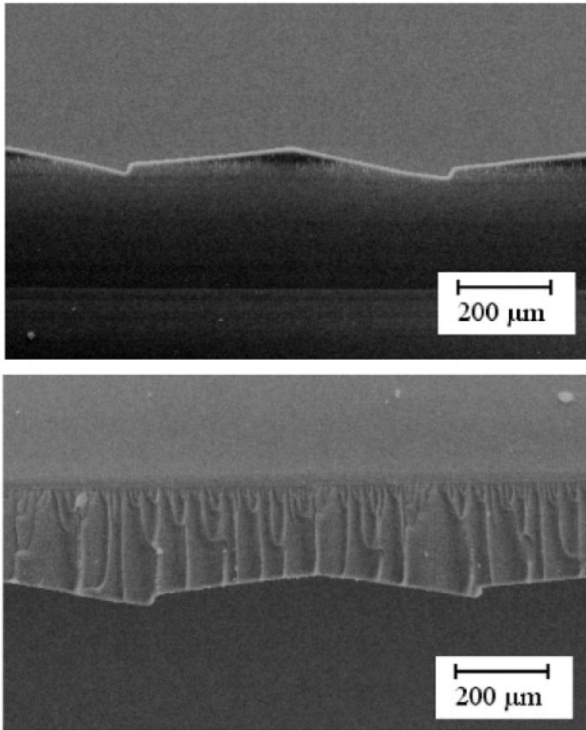

Figure 21. SEM-picture of the laser machined master and 6th replica [88].

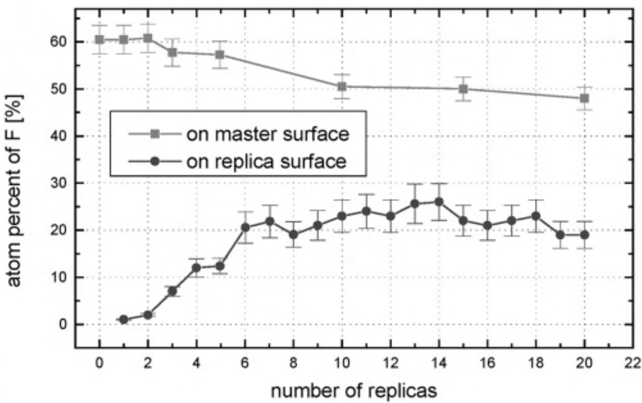

Figure 22. X-ray photoelectron spectroscopy measured fluorine concentration on master and replica surface, as in Figure 21, versus number of replication cycles [88].

has to decide between a simple one-step and a two-step replication, i.e., with an intermediate polymer copy. In general, the simple replication process is favorable if convex structures are fabricated. The two-step replication approach should be used for replicating deep concave 3D-elements such as micro channels or cavities used for subsequent bonding steps [96].

If high quality surface structures are necessary in semiconductor material or glass, an etch transfer process from laser structured polymer to said materials may be advantageous. Reliable transfer process schemes well known from microelectronics engineering and microsystem technology [79, 97] should be applied.

A cylinder lens which was laser machined by the scanning contour mask technique in a polyimide layer was transferred into crystalline silicon by plasma etching using a commercial plasma etcher. At non-optimized plasma etching conditions with a CF_4/O_2-gas mixture, a polymer topography with a depth of ~3 µm was transferred within 20 min, see Figure 23. By adapting plasma etch selectivity, the silicon topography can be shrunk or stretched in relation to the laser machined surface. At optimized selectivity the plasma etching process even reduces the roughness of the transferred surface. In the documented case the surface roughness of the transferred cylinder lens was between 10 and 20 nm (rms), and topography deviations of about 100 nm were found.

7. Conclusions

The emerging field of 3D-surface structuring by excimer laser processing was reviewed. Starting with basic principles, various machining techniques were presented and applied to the fabrication of true 3D-microstructures. Under optimized conditions, the surface accuracy of 3D-microelements was repeatedly improved with roughness values as low as 10 nm (rms). Many examples demonstrate that laser micromachining is capable of producing high quality 3D-topographies for application in microsystem technology. The presented laser machined topographies can also be used in replication and etch transfer processes. Therefore, laser 3D-

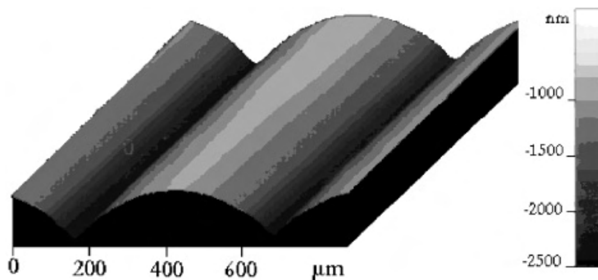

Figure 23. Cylinder lens transferred into silicon by reactive ion etching after mask fabrication by the scanning contour mask technique.

machining stands on the cusp of modern applications in different fields of micro technology.

Acknowledgements

We express our gratitude to many colleagues who shared information with us. In particular we would like to thank F. Bigl, and P. Rhone for their help with this manuscript and D. Hirsch, R. Böhme, and E. Salamatin for technical assistance in the experiments. The support of the BMBF and the DFG are also greatly acknowledged.

References

1. S. Fatikov and U. Rembold, *Microsystem Technology and Microrobotics* (Berlin: Springer, 1997).
2. C.-M. Ho and Y.-C. Tai, *Annu. Rev. Fluid Mech.* **30**, 579 (1998).
3. St. Sinzinger and J. Jahns, *Microoptics* (Weinheim: Wiley-VCH, 1999).
4. S. M. Shank, *Diffractive Optics: Design, Fabrication, and Applications*, Vol. 11, Technical Digest Series, Optical Soc. Amer. 302 (1994).
5. Chr. Gimkiewicz, D. Hagedorn, J. Jahns, E.-B. Kley and F. Thoma, *Appl. Opt.* **38**, 2986 (1999).
6. S.M. Metev and V.P. Veiko, *Laser-Assisted Microtechnology*, Springer Series in Mat. Sci. 19 (Berlin: Springer, 1994).
7. D. J. Ehrlich, *Appl. Surf. Sci.* **69**, 115 (1993).
8. O. Lehmann and M. Stuke, *Appl. Phys.* **A 53**, 343 (1991).
9. F. Bachmann, *Chemtronics* **4**, 149 (1989); D. Basting and U. Stamm, *Z. Phys. Chem.* **215**, 1575 (2001).
10. R. Srinivasan, 'Interaction of Laser Radiation with Organic Polymers', in J. C. Miller (ed.), *Laser Ablation*, Springer Series in Mat. Sci. 28 (Berlin: Springer, 1994).
11. J. Ihlemann and B. Wolff-Rottke, *Appl. Surf. Sci.* **106**, 282 (1996).
12. H. K. Toenshoff, F. von Alvensleben, H. Kappel and C. Graumann, *Production Engineering* **IV/1**, 25 (1997).
13. E. C. Harvey, P. T. Rumsby, M. C. Gower and J. L. Remnant, *Proc. of SPIE* **2639**, 266 (1995).
14. K.-H. Gerlach, J. Jersch, K. Dickmann and L. J. Hildenhagen, *Optics & Laser Technol.* **29**, 439 (1997).
15. H. J. Kahlert, U. Sarbach, B. Burghardt and B. Klimt, *Proc. of SPIE* **1835**, 110 (1993).
16. K. Jasper, P. Berger and H. Huegel, *Proc. of SPIE* **3618**, 403 (1999).
17. P. T. Rumsby and M. C. Gower, *Proc. of SPIE* **1598**, 36 (1995).
18. M. V. Klein and T. E. Furtak, *Optik* (Berlin: Springer, 1988).
19. D. Bäuerle, *Laser Processing and Chemistry* (Berlin: Springer, 2000).
20. J. C. Miller (Ed.), *Laser Ablation* (Berlin: Springer, 1994).
21. J. H. Brannon, J. R. Lankard, A. I. Baise, F. Burns and J. Kaufman, *J. Appl. Phys.* **58**, 2036 (1985).
22. R. Srinivasan, B. Baren, D. E. Seeger and R. W. Dreyfus, *Macromol.* **19**, 916 (1986).
23. S. Küper, J. Brannon and K. Brannon, *Appl. Phys.* **A 56**, 43 (1993).
24. S. Lazare, J. Lopez and F. Weisbruch, *Appl. Phys.* **A 69**, 1 (1999).
25. P. E. Dyer and J. Sidhu, *J. Appl. Phys.* **57**, 1420 (1985).
26. H. Frerichs, *Theses, Aachen Shaker* (1996).
27. S. Küper and M. Stuke, *Appl. Phys. Lett.* **54**, 4 (1988).
28. S. Küper and M. Stuke, *Appl. Phys.* **A 49**, 211 (1989).

29. H. Schmidt, J. Ihlemann, B. Wolff-Rottke, K. Luther and J. Troe, *J. Appl. Phys.* **83**, 5458 (1998).
30. see e.g. R. E. Russo, D. B. Geohegan, R. F. Hagelund and K. Murakami (Eds.), *Proc. 4th Conference on Laser Ablation* (Elsevier, 1998).
31. R. Srinivasan, B. Braren and K. G. Casey, *J. Appl. Phys.* **68**, 1842 (1990); R. Srinivasan, K. G. Casey, B. Braren and M. Yeh, *J. Appl. Phys.* **67**, 1604 (1990).
32. T. Lippert, L. S. Bennett, T. Nakamura, H. Niino and A. Yabe, *Appl. Surf. Sci.* **96–98**, 601 (1996).
33. J. Zang, K. Sugioka, T. Takahashi, K. Toyoda and K. Midorikawa, *Appl. Phys.* **A 71**, 23 (2000).
34. S. Ameer-Beg, W. Perrie, S. Rathbone, J. Wright and W. Weaver, *Appl. Surf. Sci.* **129**, 875 (1998).
35. J. Wang, H. Niino and A. Yabe, *Appl. Phys.* **A 68**, 111 (1999).
36. R. Böhme, A. Braun and K. Zimmer, *Appl. Surf. Sci.* **186**, 276 (2002).
37. R. S. Taylor, K. E. Leopold, D. L. Singleton, G. Paraskevopoulos and R. S. Irwin, J. *Appl. Phys.* **64**, 2815 (1988).
38. S. Küper and J. Brannon, *Appl. Phys. Lett.* **60**, 1633 (1992).
39. M. Mendes and R. Vilar, *Appl. Surf. Sci.* **206**, 196 (2003).
40. A. Braun, K. Zimmer and F. Bigl, *Appl. Surf. Sci.* **154–155**, 73 (2000).
41. W. Kesting, T. Bahners, D. Knittel and E. Schoellmeyer, *Angew. Makromol. Chem.* **212**, 129 (1993); L. Wefers, D. Bosbach, W. Rammensee and E. Schollmeyer, *Appl. Surf. Sci.* **69**, 418 (1993).
42. J. Heitz, J. D. Pedarnig, D. Bäuerle and G. Petzow, *Appl. Phys.* **A 65**, 259 (1993).
43. H. M. van Driel, J. E. Sipe and J. F. Young, *Phys. Rev. Lett.* **49**, 1955 (1982).
44. M. Birnbaum, *J. Appl. Phys.* **36**, 3688 (1965).
45. B. Wolff-Rottke, J. Ihlemann, H. Schmidt and A. Scholl, *Appl. Phys.* **A 60**, 13 (1995).
46. P. E. Dyer, S. D. Jenkins and J. Sidhu, *Appl. Phys. Lett.* **49**, 453 (1986).
47. T. W. Hodapp and P. R. Fleming, *J. Appl. Phys.* **84**, 577 (1998).
48. B. Braren and R. Srinivasan, *J. Vac. Sci. Technol.* **B3**, 913 (1985).
49. R. Braun, R. Nowak, P. Hess, H. Oetzmann and C. Schmitt, *Appl. Surf. Sci.* **43**, 352 (1989).
50. J. R. Lankard Sr. and G. Wolbold, *Appl. Phys.* **A 54**, 355 (1992).
51. U. Sarbach and H.-J. Kahlert, *Lamda Highlights 40, Lamda Physik AG* (1993).
52. J. Siegel, K. Ettrich, E. Welsch and E. Matthias, *Appl. Phys.* **A 64**, 213 (1997).
53. L. F. Johnson, K. A. Ingersoll and D. Kahng, *Appl. Phys. Lett.* **40**, 636 (1982).
54. A. Bosseboeuf, J. Boulmer and D. Débarre, *Appl. Surf. Sci.* **109–110**, 473 (1997).
55. F. Frost, A. Schindler and F. Bigl, *Appl. Phys.* **A 66**, 663 (1998).
56. E. C. Harvey and P. T. Rumsby, *Proc. of SPIE* **3223**, 26 (1997).
57. K. Zimmer, D. Hirsch and F. Bigl, *Appl. Surf. Sci.* **96**, 425 (1996).
58. A. Braun, K. Zimmer and F. Bigl, *Appl. Surf. Sci.* **168**, 178 (2000).
59. K. Zimmer, A. Braun and F. Bigl, *Appl. Surf. Sci.* **154**, 601 (2000).
60. J. E. Cronin, P. A. Farrar Sr., C. W. Kaanta, J. G. Ryan and A. J. Watte, *US 5334467* (1993).
61. G. P. Behrmann and M. T. Duignan, *Appl. Opt.* **36**, 4666 (1997).
62. W. Daschner, P. Long, R. Stein, Ch. Wu and S.H. Lee, *Appl. Opt.* **36**, 4675 (1997).
63. Canyon Materials Inc., *LDW-Glass Photomask Blanks*, product information (1995).
64. M. Mes and P. P. Vaidyanathan, *IEEE Trans. Ima. Proc.* **9**, 691 (2000).
65. F. A. Jenkins and H. E. White, *Fundamentals of Optics* (Singapore: McGraw-Hill Book Company, Int'l Ed., 1981).
66. K. Rubahn and J. Ihlemann, *Appl. Surf. Sci.* **127**, 881 (1998).
67. L. H. Kaplan, *US 5254202* (1993).
68. K. Zimmer, A. Braun and F. Bigl, *DE 10026960.5* (2000).
69. A. Braun and K. Zimmer, *Appl. Surf. Sci.* **186**, 200 (2002).
70. A. H. Smith, R. O. Hunter Jr. and B. B. McArthur, *US 5501925* (1994).
71. A. H. Smith, R. O. Hunter Jr. and B. B. McArthur, *US 5538817* (1994).
72. T. Ohfuji, T. Ogawa, K. Kuhara and M. Sasago, *J. Vac. Sci. Technol.* **B 14**, 4203 (1996).

73. S. Pissadakis, L. Reekie, M. Hempstead, M. N. Zervas and J. S. Wilkinson, *Appl. Phys.* **A 69**, 739 (1999).
74. K. Kawamura, T. Ogawa, N. Sarukura, M. Hirano and H. Hosono, *Appl. Phys*. **B 71**, 119 (2000).
75. P. Simon and J. Ihlemann, *Appl. Phys.* **A 63**, 505 (1996).
76. A. Manz and H. Becker, *Microsystems Technology in Chemistry and Life Science, Topics in Current Chemistry* **194**, 263 (Berlin: Springer, 1998).
77. W. Ehrfeld, V. Hessel and H. Löwe, *Microreactors* (Weinheim, Wiley-VCH, 2000).
78. A. Heuberger, *Mikromechanik* (Springer Verlag, 1991);
00. S. Büttgenbach, *Mikromechanik* (Teubner Verlag, 1994).
79. Rai-Choudhury, *Handbook of Microlithography, Micromachining and Microfabrication*, SPIE PM39 (1997).
80. R. Konrad, *Proc. of 1st Conf. on Microreaction Technol.* (1997).
81. S. Mihailov and S. Lazare, *Appl. Opt.* **32**, 6211 (1993).
82. F. Beinhorn, J. Ihlemann, K. Luther and J. Troe, *Appl. Phys.* **A 68**, 709 (1999).
83. A. H. Smith, B. B. McArthur and R. O. Hunter Jr., *US 5539175* (1994).
84. C. Lammers and K. Dickmann, *Chem. Fibers Intern.* **1**, 50 (2001).
85. H. Schmitt, *Opto & Laser Europe* **13**, 35 (1994).
86. G. Gal, *US 5310623* (1992).
87. K. Zimmer, R. Böhme, A. Braun, B. Rauschenbach and F. Bigl, *Appl. Phys.* **A 74**, 453 (2002).
88. A. Braun, K. Zimmer, B. Hösselbarth, J. Meinhardt, F. Bigl and R. Mehnert, *Appl. Surf. Sci.* **127**, 911 (1998).
89. A. Braun, J. Meinhardt, K. Zimmer, B. Hösselbarth and F. Bigl, *Appl. Surf. Sci.* **138**, 206 (1999).
90. K. Zimmer, A. Braun and R. Böhme, *Appl. Surf. Sci.* **208–209**, 199–204 (2003).
91. A. Braun, K. Zimmer and F. Bigl, *DE 19919009A1* (1999).
92. A. Braun and K. Zimmer, *Proc. of SPIE* **4236**, 213 (2001).
93. M. T. Duignan, *Diffractive Optics: Design, Fabrication, and Applications*, Vol. 11, Technical Digest Series, Optical Soc. Amer. 129 (1994).
94. C. P. Christensen, *Proc. of SPIE* **2045**, 141 (1994).
95. A. Braun, *Thesis*, Fakultät für Physik und Geowissenschaften der Universität Leipzig (2002).
96. K. Zimmer, A. Braun and M. Kostrzewa, *Proc. of SPIE* **4236**, 58 (2001).
97. E.-B. Kley, *Microelectronic Engineering* **34**, 261 (1997).
98. T. M. Gale, Replication, in H.P. Herzig (Ed.), Mikrooptic, Taylor & Francis (1997).
99. J. Arnold, U. Dasbach, W. Ehrfeld, K. Hesch and H. Löwe, *Appl. Surf. Sci.* **86**, 251 (1995).
100. R. A. Lawes, A. S. Holmes and F. N. Goodall, *Microsys. Technol.* **3**, 17 (1996).

CHAPTER 12

MICROFABRICATION OF TRANSPARENT MATERIALS BY LASER PROCESSING

Yoshizo Kawaguchi*, Hiroyuki Niino and Akira Yabe

Photoreaction Control Research Center, National Institute of Advanced Industrial Science and Technology (AIST), Tsukuba Central 5, 1-1-1 Higashi, Tsukuba, Ibaraki 305-8565, Japan

*(*Author for correspondence, E-mail: y-kawaguchi@aist.go.jp)*

ABSTRACT: Microfabrication of transparent materials by laser processing is challenging due to the high transparency of many materials of interest in the near ultraviolet (UV)-visible region. This chapter gives the processing details of fused silica and other transparent materials by pulsed-laser irradiation involving: (1) Direct excitation of transparent materials with high-intensity UV lasers, femtosecond lasers, vacuum ultraviolet (VUV) lasers, and (2) Indirect excitation of the substrate by conventional nanosecond pulsed lasers. The indirect-excitation method using laser-induced backside wet etching (LIBWE) to etch transparent materials by laser ablation of an organic solution is described in detail.

1. Introduction

Materials processing with lasers is effective for the microfabrication and surface modification of various materials. Because of their good beam quality, laser beams can be easily focused to the order of microns. Thus, micro-patterns of any shape can be fabricated directly by scanning a focused laser beam or by using a photomask and a projection system. The quality and throughput of laser processing is influenced mainly by the laser parameters and properties of the target material. Typical key parameters of the laser include wavelength, pulse-width, repetition rate, pulse number, energy density, fluence, scanning rate, and ambient atmosphere. Optical, electronic, and thermal properties of the material also affect the laser-material interaction and the resulting laser processing. The absorption coefficient of the material at the wavelength of the laser is one of the most important properties because it determines the degree of absorption of the laser beam by the material.

On the other hand, dielectric materials such as fused silica, calcium fluoride, and sapphire have excellent optical transparency and high thermal, chemical, and mechanical stabilities. As a result, transparent materials, particularly fused silica, are widely used to prepare optical components. Thus, microfabrication of transparent materials is desirable in the fields of optoelectronics, micro-optics, and fiber-optics technology. The fabrication of these materials by using mechanical and chemical processes is, however, difficult due to the above-mentioned specific properties of the materials. Furthermore, the excellent optical transparency of these materials makes it difficult to employ microfabrication by laser processing.

To develop methods that overcome these difficulties, many studies on transparent materials processing methods that use pulsed-laser irradiation have been performed.

Aaron Peled (ed.), Photo-Excited Processes, Diagnostics and Applications (PEPDA), 339–357, 2003.
© 2003 *Kluwer Academic Publishers. Printed in the Netherlands.*

Figure 1 shows a conceptual classification of several methods, which can be broadly classified as either direct interaction using a special pulsed laser or indirect interaction using a conventional pulsed laser. Direct irradiation involves photo-absorption and processing with special lasers, such as high-intensity, nanosecond UV lasers [1–3], femtosecond (fs) lasers [4–19], vacuum ultraviolet (VUV) lasers [20–24], or a combination of multi-wavelength lasers [25–35]. However, microfabrication of transparent materials can also be done with a conventional, nanosecond pulsed laser by using an indirect excitation method in which laser ablation of another material is used to excite a transparent substrate indirectly. Two such methods are *laser-induced plasma-assisted ablation* (LIPAA), which involves laser ablation of a metal target [36–42], and *laser-induced backside wet etching* (LIBWE), which involves laser ablation of an organic solution [43–57].

In this chapter, a review of various methods for microfabrication of fused silica and other transparent materials by pulsed-laser irradiation is given with emphasis on the characteristics of the LIBWE process, which was recently developed by Niino et al. [43–54].

2. Microfabrication of transparent materials by pulsed-laser irradiation

2.1. *Direct interaction between the substrate and the pulsed laser*

Figure 2 shows a schematic for etching fused silica by direct irradiation with an intense excimer laser, fs-laser, and an F_2 laser. The bandgap of fused silica is about

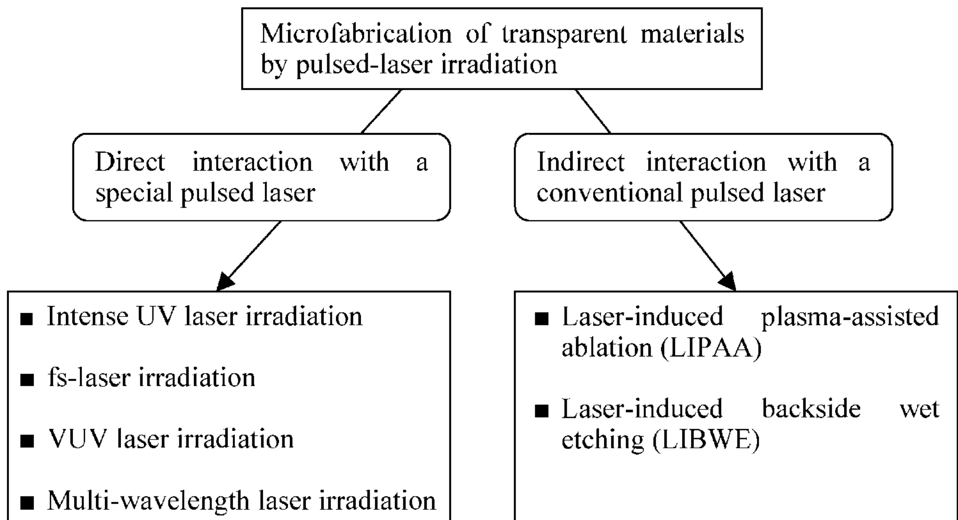

Figure 1. Conceptual classification of transparent-materials microfabrication techniques that use pulsed-laser irradiation.

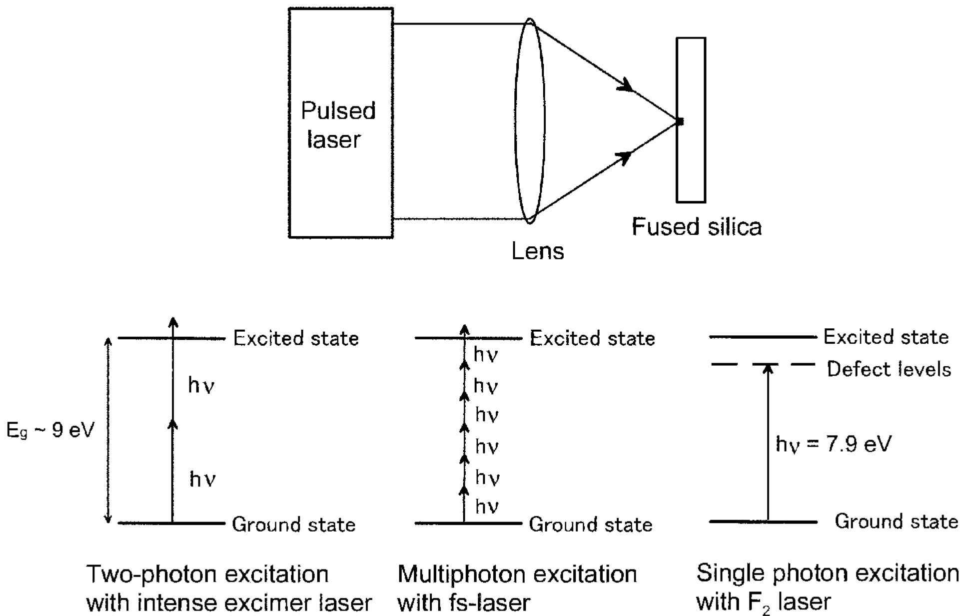

Figure 2. Etching of fused silica by direct irradiation with a special pulsed laser.

9 eV, and thus photo-absorption in the near UV-visible region is negligible. To process fused silica with a conventional nanosecond UV laser, the laser-material interactions should consist mainly of two-photon absorption to overcome the large bandgap. Therefore, a high fluence is required.

Ihlemann et al. reported that the threshold fluence for etching fused silica with a KrF excimer laser at $\lambda = 248$ nm, FWHM = 28 ns, was as large as 11 J cm^{-2} $pulse^{-1}$ [1, 2]. Because this high threshold fluence requires a tightly focused laser beam, only relatively small areas can be processed at a time, resulting in a low throughput. Furthermore, obtaining a smooth, etched surface is difficult due to large thermal damages.

Technologies for processing transparent materials with fs-lasers are developing rapidly [4–19]. A typical fs-laser for material processing consists of a regenerative amplified Ti:sapphire laser operating at $\lambda = 780$–820 nm, FWHM = 100–200 fs, and repetition rate = 10 Hz–200 kHz. Because of the short pulse width, the large irradiance necessary for multiphoton excitation can easily be achieved by focusing the laser beam. Because the unfocused laser beam is not absorbed by transparent materials, only a limited region irradiated by the focused laser beam is selectively processed with the fs-laser. Thus, three-dimensional fabrication inside transparent materials can be achieved.

Ashkenasi et al. drilled fused silica by using laser ablation with 120 fs pulses at $\lambda = 790$ nm [4, 5]. Because focusing the fs-laser causes dielectric breakdown in air, which affects the processing performance, the drilling was done in a vacuum.

A pulsed beam with an energy of 330 μJ $pulse^{-1}$ was focused onto an area of 680 μm^2, corresponding to a fluence of 49 J cm^{-2} $pulse^{-1}$. This permitted drilling a channel depth of 1 mm with 1600 pulses at a frequency of 160 Hz. Although cracking occurred around the hole, the damage was less than that when either picosecond or nanosecond lasers are used.

Hirao et al. reported the fabrication of optical waveguides inside various types of glasses [6–11]. Irradiation with focused fs-laser pulses disrupted the Si-O bonds, generated defects, and increased the refractive index, thus enabling waveguide formation.

By creating small periodically damaged regions inside silica glass with a spacing comparable to the wavelength of the laser, Misawa et al. fabricated various types of three-dimensional photonic crystals with an fs-laser [12–15]. The fs-laser-induced damage was due to multiphoton excitation, which limited the laser-affected zone, enabling this type of fabrication of sub-micrometer structures.

Another advantage of fs-laser beams is their excellent coherence. Kawamura et al. used a two-beam holographic method with two fs-laser pulses to fabricate a surface relief grating on fused silica with a spacing as small as 0.43 μm [16–18]. By interference of two fs beams, a periodic modulation of the laser intensity was generated on the surface of the substrate, forming a grating with sub-micrometer pitch, even smaller than the wavelength of the laser. This technique was applied to many types of transparent dielectrics, such as sapphire, TiO_2, ZrO_2, $LiNbO_3$, ZnO, SiC, MgO, CaF_2, and fused silica. Furthermore, two cross-superposed holographic gratings were patterned by rotating the substrate by 90° between the first and second irradiation. A variety of periodic nanostructures, from one-dimensional wire arrays to two-dimensional arrays of holes or islands, were formed by changing the laser energy and incident angle of the fs-laser beams [19].

In addition to fs-lasers, F_2 lasers are also capable of processing fused silica.

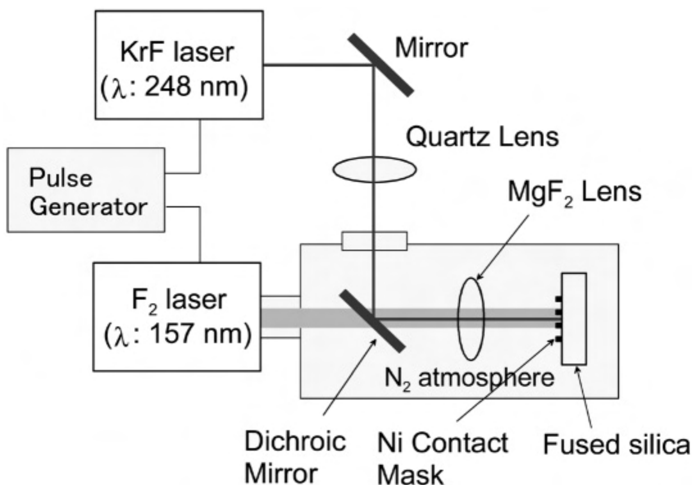

Figure 3. Etching of fused silica by simultaneous irradiation with KrF and F_2 laser beams.

The photon energy of an F_2 laser is 7.9 eV at $\lambda = 157$ nm. Although the bandgap of fused silica is about 9 eV, significant photo-absorption occurs at 7.9 eV due to defect centers and the Urbach optical absorption tail [58]. Thus, F_2 laser beams are absorbed by single photon absorption and etching of fused silica can be achieved. Because the transmission of the F_2 laser beam is stopped by the absorption of O_2 in the air, the optical path of the beam must be evacuated or purged with pure N_2 gas. Herman et al. prepared a special chamber for F_2 lasers that included a homogenizer and Schwarzschild optics, and successfully used this laser for microfabrication of surface relief gratings and buried gratings on fused silica [20–24].

Sugioka et al. used simultaneous irradiation with a UV laser and a VUV laser to achieve micropatterning of fused silica [25–35]. Figure 3 shows a schematic of the typical system. The VUV laser beam generated transient defect centers, thus promoting etching by the intense absorption of the KrF laser beam. Compared to etching with the KrF laser alone, the throughput and etching equality were significantly improved.

Besides microstructuring, three-dimensional sculptures have been engraved by focusing a pulsed laser inside a glass and forming small cracks at the designated positions. These products are commercially available as ornaments and pendants – so called "3D Laser Art Crystals". Figure 4 shows an example.

2.2. *Indirect interaction between the substrate and a conventional pulsed laser*

2.2.1. *LIPAA process*

Sugioka et al. developed a method to etch transparent materials by using laser ablation to generate plasma from a metal target, i.e. LIPAA process [36–42]. Figure 5 shows a schematic of the LIPAA process in which an excimer laser beam is passed through a photo-mask, then focused with a lens, and finally irradiates a metal target through a transparent substrate.

The laser-induced plasma was generated from the metal target. This plasma, together with the laser pulse, then attacked the backside of the transparent substrate, thus etching the substrate with high efficiency. Metals that have been used

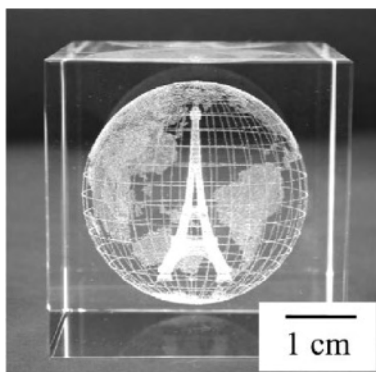

Figure 4. Three-dimensional sculpting inside a glass block.

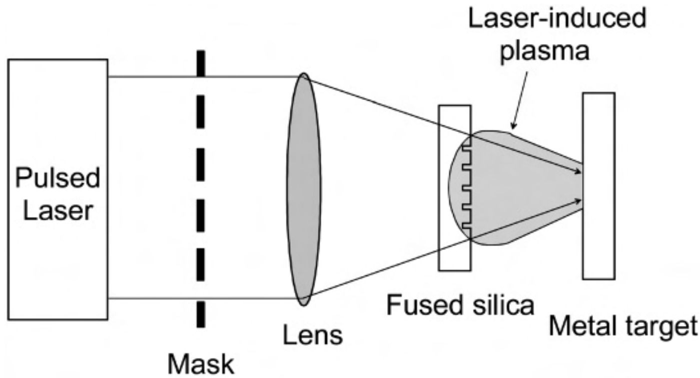

Figure 5. Microetching fused silica by the LIPAA process.

as the target material include stainless steel, Ag, Cu, Ti, and Cr. The distance between a metal target and the transparent substrate was typically 100 μm–1 mm, depending upon the pressure of the ambient gas. Following the etching, a thin film of the metal was deposited onto the etched region of the substrate, and this film could be easily removed by cleaning with an HCl solution. A surface grating on the fused silica surface, with a period of 1.06 μm and grating depth of 200 nm, was fabricated by using 40 pulses of a KrF excimer laser at a fluence of 1.3 J cm^{-2} $pulse^{-1}$ in a vacuum with a phase mask. The distance between the stainless steel target and the fused silica plate was 200 μm [36].

Because a metal target absorbs UV, visible, and even near infrared (NIR) light, the LIPAA process can also be done with a Q-switched Nd:YAG laser operating at λ = 1064, 532, and 266 nm [37–41]. Micropatterning was achieved with a photo-mask setup similar to the excimer laser setup shown in Figure 5. Microetching of complex structures was possible by scanning a tightly focused beam of a diode-pumped solid-state Nd:YAG laser operating at λ = 532 nm by using a computer-controlled galvanometer mirror system. Character and picture engraving on a fused silica plate without microcracks were typical applications demonstrated by this technique [41, 42]. Prior to cleaning with acid, a thin metal film remained on the etched region, and the color of the film could be adjusted by selecting the metal target; for example, Cu for red and SiC for black. Thus, the LIPAA process is useful in color marking and selective metallization of the glass.

In the LIPAA process, the etch rate strongly depends on the pressure of the ambient gas. When the ambient N_2 pressure was increased from 10^{-2} to 760 Torr, the etch rate decreased by about 90% [38] due to the confinement and deactivation of the laser-induced plasma by the ambient N_2 gas.

2.2.2. *LIBWE process*

The LIBWE process was recently developed for etching fused silica and other transparent materials by using laser ablation of an organic solution [43–54]. Figure 6 shows a schematic of the LIBWE process used to etch fused silica.

Organic molecules were chosen because they show strong absorption at the

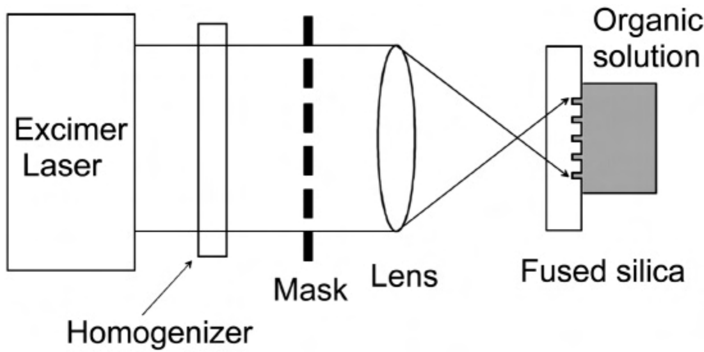

Figure 6. Microetching of fused silica by the LIBWE process.

UV laser wavelength yet are stable against UV laser irradiation. The organic molecules were dissolved in either organic or aqueous liquids. A nanosecond-pulsed UV laser beam irradiates the organic solution through a fused silica plate. UV laser absorption by the fused silica is negligible, and the UV beam is transmitted through the plate and strongly absorbed by the organic molecules. The laser energy is consumed by rapid heating and vaporization of the solution, and the thermal energy is transferred to the rear surface of the fused silica plate under high pressure, causing etching. This etching condition is characterized by the structure and concentration of the organic solution, the wavelength and fluence of the UV laser, and the number of laser pulses.

Compared with other etching techniques, the advantages of the LIBWE process are as follows:

- The fluence necessary for etching is less than 10% of the fluence needed for direct etching with a conventional excimer laser. This enables the processing of large areas by a single-step treatment, as shown in Figure 7.
- Etching is achieved in a single step, compared to conventional photolithography methods that involve multiple, complex steps.
- Etching is achieved at atmospheric pressure; a vacuum system is not necessary.
- The etched surface is free from cracks and debris.
- The etched surface is smooth, and the etch depth can be controlled on a nanometer scale by adjusting the fluence and the number of laser pulses.
- The etching pattern can be varied with a mask projection technique.
- This method is applicable not only to fused silica but also to other transparent materials, such as quartz crystal, calcium fluoride, sapphire, and fluorocarbon polymer [46, 47].

More detailed characteristics of the LIBWE process are described in the next section.

Closely related studies have been reported on etching of transparent materials by laser ablation of inorganic solutions. Ikeno et al. reported drilling a fused-silica

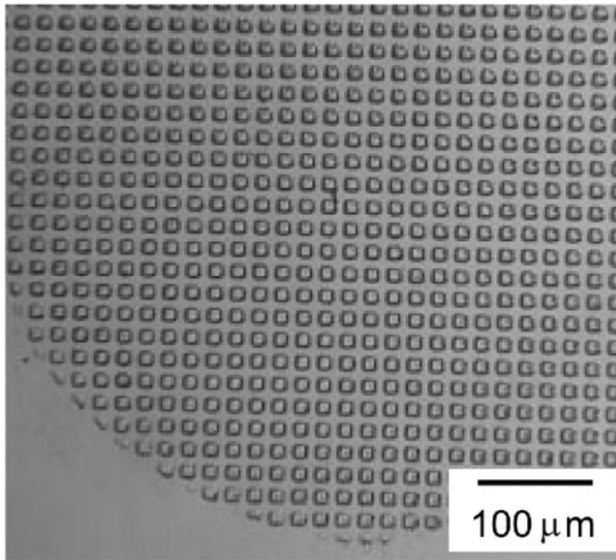

Figure 7. Micropatterning of a large area on a fused-silica surface by the one-step LIBWE process.

plate by ablation, using an $NiSO_4$ aqueous solution with a pulsed Nd:YAG laser operating at λ = 1064 nm [59]. The nickel ion strongly absorbs the NIR laser beam, and heats the rear surface of the glass plate, resulting in thermal damage and formation of a shallow hole. A hole 1.5-mm deep and 0.2 mm in diameter was drilled by cumulative irradiation of Nd:YAG laser pulses. The etched surface was rough and consisted of needle-like structures scattered radially, showing melting and localized emission of ejected materials.

Shafeev et al. reported the etching of sapphire and fused silica by scanned irradiation of a focused copper-vapor laser beam (λ = 510 nm, FWHM = 10 ns, repetition rate 8 kHz) [60–62]. They irradiated the beam through transparent substrates in aqueous solutions of CrO_3, $FeCl_3$, and $KMnO_4$, which have intense absorption at 510 nm. Upon etching of a sapphire substrate with an aqueous solution of CrO_3 at a fluence of 10 J cm^{-2} $pulse^{-1}$, the etch rate was as high as 2 mm s^{-1}, i.e., 0.3 μm $pulse^{-1}$, with a spatial resolution of 3 μm. After etching, an opaque film 30- to 40-nm thick was deposited on the etched surface consisting of CrO_2, Fe_2O_3, and MnO_2 for aqueous solutions of CrO_3, $FeCl_3$, and $KMnO_4$, respectively. An epitaxial film was deposited on the sapphire substrate, whereas an amorphous film grew on the glass substrate. After the laser irradiation, there was a time delay of about 30 ms before the onset of etching. This delay corresponds to the film deposition time, which assists laser absorption and enhances the etching of the substrate. These observations suggest that the etching process proceeds according to the following steps:

1. The laser beam is absorbed by the metal ions, leading to the growth of an oxide thin film on the substrate.

2. The laser beam is strongly absorbed by the opaque thin film, causing heating and removal of the thin film, followed by the removal of the surface layer of the substrate.
3. Etching proceeds by repetition of steps 1 and 2.

3. Microetching of transparent materials by the LIBWE process

3.1. *Micropatterning of fused silica*

By using a mask-projection technique, any fine pattern can be etched by the LIBWE process. Figure 8 shows an image and cross-sectional profile of a grid pattern observed with a confocal scanning laser microscope. The pattern was etched on a fused silica plate by irradiation with a KrF excimer laser using an aqueous solution of a naphthalene derivative. As a demonstration of the LIBWE process, an array of 10 × 10 μm holes, each with a depth of 0.5 μm was etched on fused silica. Each hole had well-defined sharp edges and a smooth bottom, and no cracks or debris on the nearby surface of the etched area [50, 51]. The surface roughness in the etched regions was about 30 nm, similar to that of the virgin surface within the resolution of the confocal scanning laser microscope.

Using a fly's-eye type homogenizer, micropatterning on a fused-silica plate was fabricated on an area as large as 1 × 1 mm^2 with a resolution of 1 μm by using a single-step treatment. Figure 9 shows images of the fabricated 1-μm-scale grating

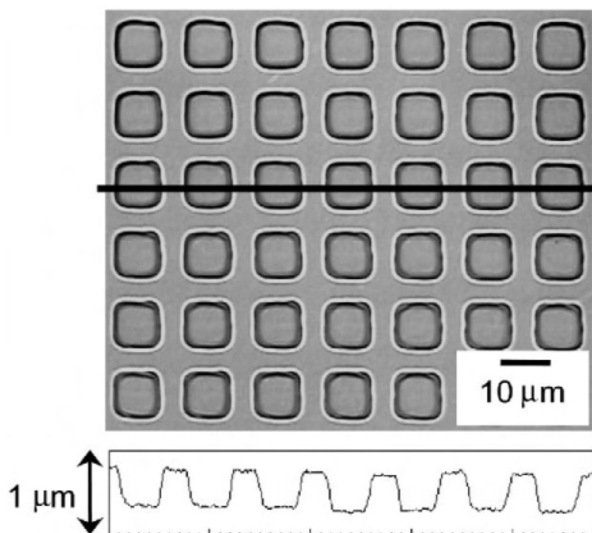

Figure 8. Microscopic image of a grid pattern etched on fused silica showing an array of 10 × 10 μm holes with a depth of 0.5 μm, and the cross-sectional profile along the black line. The sample was irradiated with a KrF excimer laser using an aqueous solution of a naphthalene derivative. (Reprinted from Figure 8 in [51] by permission from Springer Verlag.)

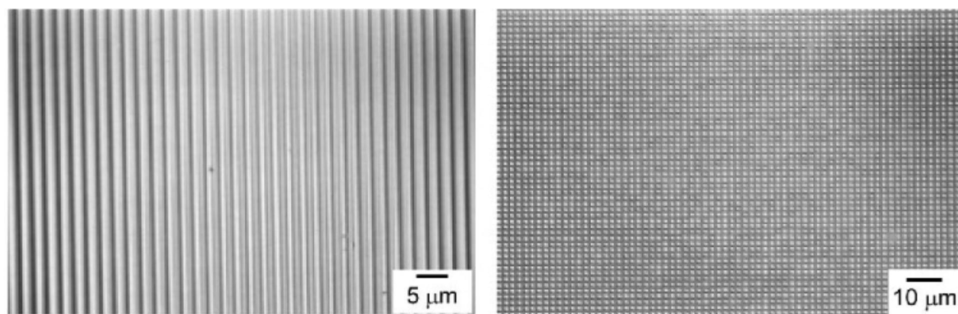

Figure 9. Microscopic images of etched patterns on the surface of fused-silica plates fabricated with a KrF excimer laser in an aqueous solution of a naphthalene derivative: (left) line-and-space pattern (each line or space is 1 µm wide), (right) grid pattern with an array of 1 × 1 µm holes. (Reprinted from Figure 5 in [52] by permission from SPIE.)

and grid patterns [52]. A surface relief grating with sub-micron pitch was fabricated by applying a phase mask and a Schwarzschild objective [55].

By either scanning a contour mask or using a gray scale mask, three-dimensional structuring on fused-silica surfaces can be fabricated with KrF excimer laser irradiation by adjusting the distribution of the number of pulses. A concave cylindrical lens structure was fabricated on the surface of fused silica, as shown in Zimmer et al., in this book [56].

3.2. *Characteristics of the LIBWE process with various organic solutions*

A variety of concentrated organic solutions were tested in the LIBWE process. Figure 10 shows the chemical structures of the organic molecules tested. Pyrene molecules were chosen for testing because they show strong absorption at the wavelengths of the excimer laser and are chemically stable to UV laser irradiation [43–49]. Pyrene dissolves well in acetone, and therefore a concentrated solution could be used. However, from an industrial-application viewpoint, comparison to volatile organic solvents such as acetone, aqueous solutions are safer. Therefore, water-soluble pyrene and naphthalene derivatives were tested because they showed strong photo-absorption at the wavelength of the laser [50–52]. Pure toluene, without additional organic molecules, was also tested in the LIBWE process [53]. Toluene also shows strong photo-absorption in the UV region, is cost effective for industrial applications, and therefore fundamental research on laser ablation of toluene has also been reported [63]. Toluene was therefore chosen as a suitable medium for testing and understanding the mechanism of the LIBWE process.

Figure 11 shows the dependence of the etch depth on the number of pulses for irradiation with a KrF excimer laser in a pyrene/acetone solution at a concentration of 0.4 mol dm^{-3}. The etch depth was proportional to the number of incident laser pulses, and the slope of the straight line gives an etch rate of 23.5 nm $pulse^{-1}$ for the test conditions. A linear relationship was obtained for other organic solutions

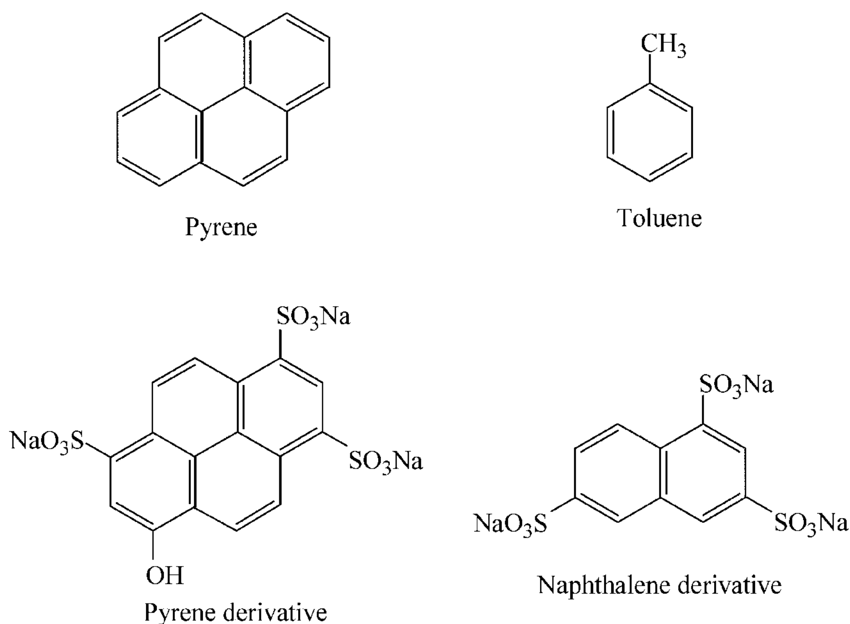

Figure 10. Chemical structures of organic molecules tested in the LIBWE process.

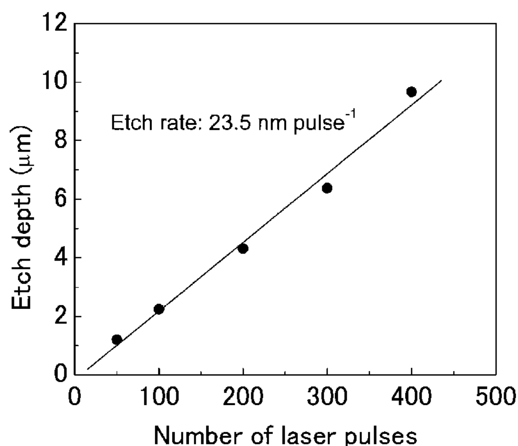

Figure 11. Etch depth vs. number of laser pulses on fused silica, for irradiation with a KrF excimer laser at 1.1 J cm^{-2} $pulse^{-1}$.

as well, showing that etch depth can be precisely controlled by the number of laser pulses.

Figure 12 shows the etch rate in fused silica as a function of laser fluence for various combinations of excimer laser beams and organic solutions. A linear relationship was observed for all combinations within the fluence range used.

The etch rate ranged from about 3 nm to 40 nm per pulse for the pyrene/acetone

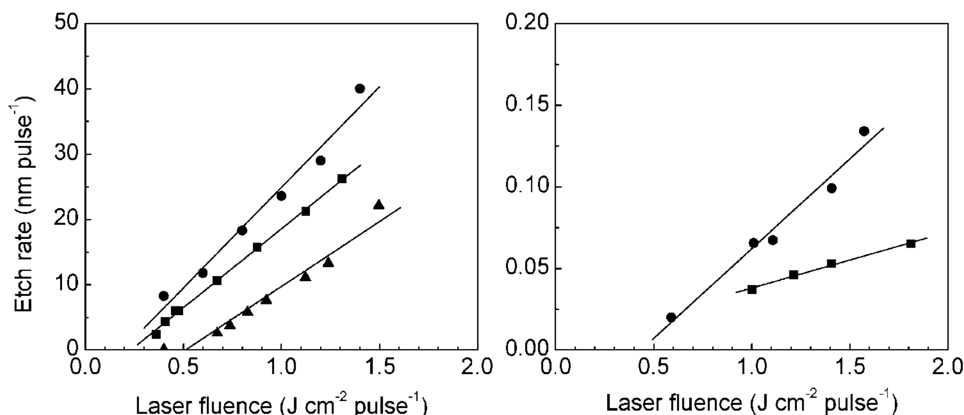

Figure 12. Etch rate vs. laser fluence on fused silica using various combinations of excimer laser beams and organic solutions: (left) ● toluene and KrF laser, ■ pyrene/acetone solution (0.4 mol dm^{-3}) and KrF laser, ▲ pyrene/acetone solution (0.4 mol dm^{-3}) and XeCl laser; (right) ● aqueous solution of pyrene derivative (0.8 mol dm^{-3}) and KrF laser, ■ aqueous solution of naphthalene derivative (0.4 mol dm^{-3}) and KrF laser.

solution of 0.4 mol dm^{-3} and for pure toluene, demonstrating that the etch depth could be linearly controlled in the nanometer range by adjusting the laser fluence and number of pulses. The threshold fluence was 0.19 J cm^{-2} pulse^{-1} for toluene and 0.24 J cm^{-2} pulse^{-1} for the pyrene/acetone solution, both of which are 40 times lower than that when etching was done with conventional KrF excimer laser ablation. The etch rate for toluene was about 30% larger than that for the pyrene/acetone solution, thus yielding a higher throughput for toluene.

Low concentrations of pyrene and naphthalene derivatives in aqueous solutions gave etch rates in the range of 0.05–0.1 nm pulse^{-1}, two orders of magnitude smaller than that for either toluene or pyrene/acetone solutions. However, for concentrated aqueous solutions of naphthalene derivatives, the etch rate increased rapidly to about 1 nm pulse^{-1} with increased laser fluence, and the roughness of the etched surface increased correspondingly [51]. By optimizing the solution concentration and the laser fluence, switching from slow etching to fast etching was made possible with an aqueous solution of the naphthalene derivative.

Besides using the KrF excimer laser at λ = 248 nm, etching fused silica with the pyrene/acetone solution could be achieved with a XeCl excimer laser at λ = 308 nm [49]. Because the lifetime of the gas in XeCl lasers is several times longer than that in KrF lasers, the use of a XeCl laser with the LIBWE process is desirable for commercial applications. Moreover, other lasers with different wavelengths, such as Nd:YAG lasers, can be used in the LIBWE process. The etch rate obtained by using the XeCl laser was half of that obtained by using the KrF laser. This is due to the lower photon energy of the XeCl laser of hν = 4.0 eV, compared to hν = 5.0 eV for KrF lasers, which activate a different excitation process in the organic molecules. In addition to fused silica, etching of other transparent materials was achieved with the LIBWE process by using a pyrene/acetone solution [46].

Figure 13 shows the dependence of the etch rate on laser fluence for various transparent materials upon irradiation with a KrF excimer laser using a pyrene/acetone solution at a 0.4 mol dm^{-3} concentration. Similar to the relationship between laser fluence and etch rate for fused silica, linear relationships were also observed for quartz crystals, calcium fluoride crystals, and a UV-transparent fluoro-polymer film (fluorinated ethylene-propylene copolymer: FEP). By extrapolating the straight lines, the following threshold fluences for etching the various materials were estimated: 0.24 J cm^{-2} pulse^{-1} for fused silica, 0.33 J cm^{-2} pulse^{-1} for quartz crystal, 0.74 J cm^{-2} pulse^{-1} for calcium fluoride, and 0.05 J cm^{-2} pulse^{-1} for FEP.

3.3. *Mechanism of the LIBWE process*

Figure 14 shows a schematic of the LIBWE process. When an excimer laser beam irradiates an organic solution through a transparent material, most of the laser beam is absorbed by the solution within the optical penetration depth, L ~ α^{-1}, where α is the optical absorption coefficient of the solution at the wavelength of the laser.

The calculated penetration depth of a KrF laser is about 0.7 μm for a pyrene/acetone solution (0.4 mol dm^{-3}), 8.9 μm for toluene, 0.5 μm for an aqueous solution of the pyrene derivative (0.8 mol dm^{-3}), and 7.9 μm for an aqueous solution of the naphthalene derivative (0.4 mol dm^{-3}). Thus, most of the laser energy is deposited in a thin layer of the solution (≈ 1 μm) from the rear surface of the transparent material. The energy is mainly consumed by heating it. In the estimation of the maximum temperature of the solution at the threshold fluence, T_{th}^{max},

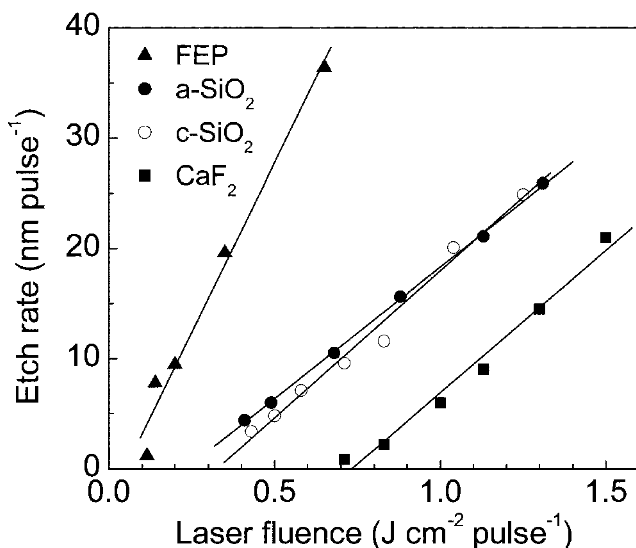

Figure 13. Etch rate vs. laser fluence by irradiation of various transparent materials by using a KrF excimer laser and a pyrene/acetone solution at a concentration of 0.4 mol dm^{-3}.

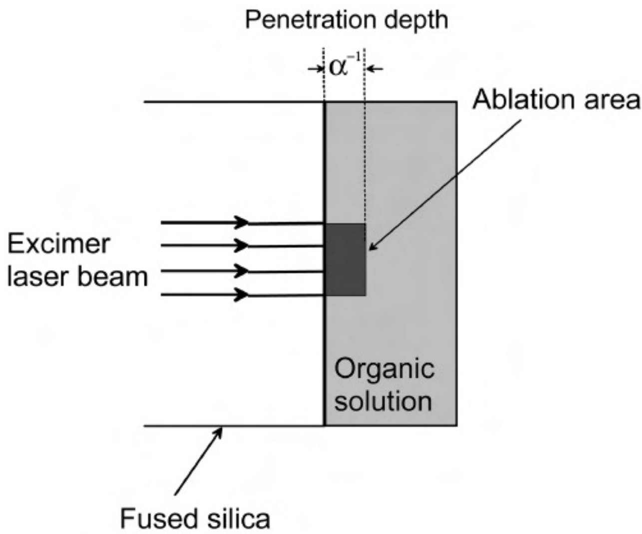

Figure 14. The LIBWE process.

two assumptions were made: (1) all the incident photon energy is converted into heat, and the rate of thermal diffusion is slow compared to the duration of the laser pulse, and (2) the vaporization of the solvent can not be ignored. Thus, T_{th}^{max} can be calculated as [63, 64]:

$$T_{th}^{max} = T_0 + \alpha_{th} F_{th}/\rho C \quad (1)$$

where T_0 is the room temperature, F_{th} is the threshold fluence, and ρ and C are the density and heat capacity of the solvent, respectively. Typical values of T_{th}^{max} are on the order of 1000 K. The generated heat is transferred to the transparent substrate and thus softens the surface. Because T_{th}^{max} is much higher than the boiling point of the solvent, the solution vaporizes and creates high pressure.

To quantify the pressure generated during the LIBWE process, time-resolved imaging of laser-induced liquid ablation at the interface between the liquid and the fused-silica plate was done by using a back-illumination technique [51–53]. Figure 15 shows images of laser ablation in toluene by KrF excimer laser irradiation at a fluence of 1.6 J cm^{-2} $pulse^{-1}$. A shock wave formed and propagated hemispherically within 1 μs from the onset of ablation. Simultaneously, a flat vapor bubble was generated and expanded to a hemispherical shape within 10 μs (shown in Figure 15 as a dark shadow at the interface between the substrate and the solution). The bubble reached a maximum size of 600 μm at 50 μs, and the vapor gradually shrank about 150 μs after ablation. Measured initial velocities of the shock wave and the vapor bubble were 1.4 km s^{-1} and 200 m s^{-1}, respectively.

The impact pressure of the liquid jet can be roughly estimated as [65, 66]:

$$P = \rho \cdot c \cdot V_{jet} \quad (2)$$

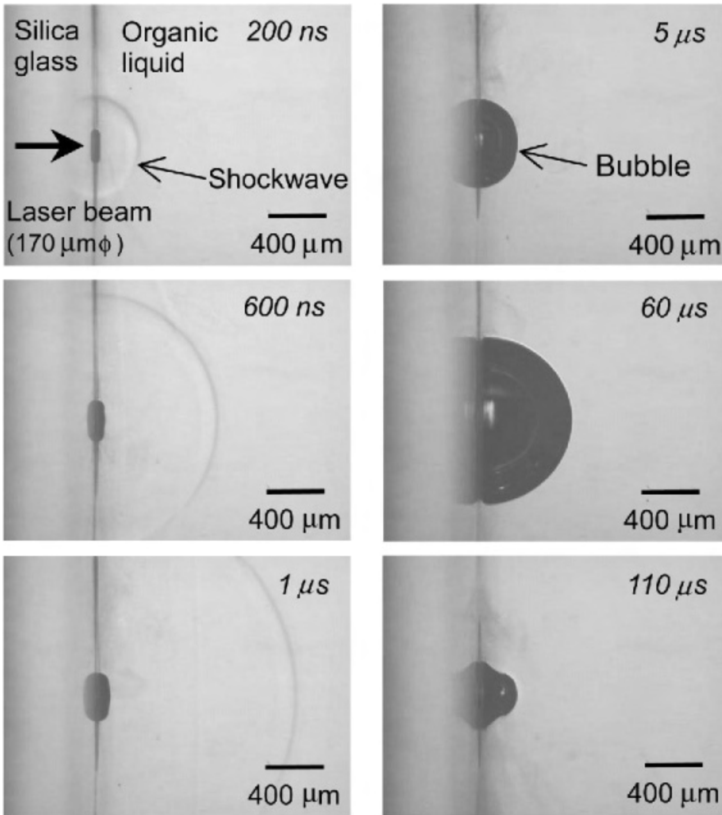

Figure 15. Time-resolved images of laser-induced ablation in toluene at the interface with a fused-silica plate. Images were acquired by using a back-illumination technique.

where ρ is the density of toluene, c is the acoustic velocity in toluene (ρ = 0.86 g cm^{-3}, c = 1300 m s^{-1} at 300K), and V_{jet} is the velocity of the liquid jet. Equation (2) indicates that V_{jet} = 200 m s^{-1} corresponds P = 220 MPa [53]. For an aqueous solution of the naphthalene derivative (0.4 mol cm^{-3}), P ≈ 300 MPa [52]. The high-temperature, high-pressure vapor bubble attacks the softened surface of the transparent material, removing a cluster of SiO_2 from the bulk substrate, and then the cluster moves into the liquid. At the end of the laser pulse, rapid cooling occurs in the laser-irradiated area, preventing thermal damage of the substrate.

4. Conclusions

Figure 16 summarizes the characteristics of various methods used in the microfabrication of transparent materials by using pulsed-laser irradiation. Although current trends point towards using more recently developed lasers such as fs-lasers

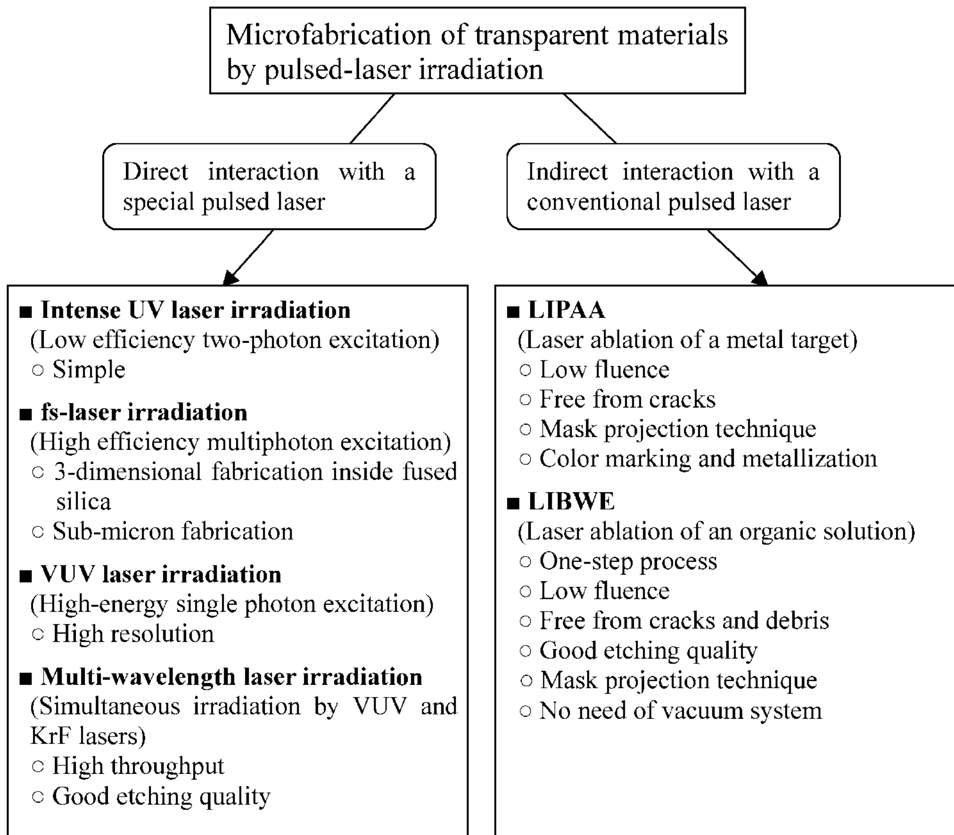

Figure 16. Characteristics of methods for microfabrication of transparent materials by pulsed-laser irradiation.

and F_2 lasers, these lasers are still evolving, and therefore more testing is needed before they can be used in industrial applications. On the other hand, conventional nanosecond-pulsed lasers are also suitable for microetching transparent materials by using sophisticated methods, such as the LIBWE process. By using the advantages of each method, microfabrication of transparent materials by pulsed-laser irradiation will be widely used in industrial processes, and will play an important role in new technologies such as Micro-Electro Mechanical System (MEMS).

Acknowledgments

The authors thank Drs. T. Sato and A. Narazaki for their collaboration and fruitful discussions, and are deeply indebted to Drs. J. Wang, Y. Yasui, and X. Ding for their diligence in doing the microetching experiments.

References

1. J. Ihlemann, 'Excimer Laser Ablation of Fused-Silica', *Appl. Surf. Sci.* **54**, 193–200 (1992).
2. J. Ihlemann, B. Wolff and P. Simon, 'Nanosecond and Femtosecond Excimer Laser Ablation of Fused-Silica', *Appl. Phys.* **A 54**, 363–368 (1992).
3. J. Ihlemann and B. Wolff-Rottke, 'Excimer Laser Micro Machining of Inorganic Dielectrics', *Appl. Surf. Sci.* **106**, 282–286 (1996).
4. H. Varel, D. Ashkenasi, A. Rosenfeld, M. Wahmer and E. E. B. Campbell, 'Micromachining of Quartz with Ultrashort Laser Pulses', *Appl. Phys.* **A 65**, 367–373 (1997).
5. D. Ashkenasi, M. Lorenz, R. Stoian and A. Rosenfeld, 'Surface Damage Threshold and Structuring of Dielectrics Using Femtosecond Laser Pulses: The Role of Incubation', *Appl. Surf. Sci.* **150**, 101–106 (1999).
6. K. Miura, J. R. Qiu, H. Inouye, T. Mitsuyu and K. Hirao, 'Photowritten Optical Waveguides in Various Glasses with Ultrashort Pulse Laser', *Appl. Phys. Lett.* **71**, 3329–3331 (1997).
7. K. Hirao and K. Miura, 'Writing Waveguides in Silica-Related Glasses with Femtosecond Laser', *Jpn. J. Appl. Phys.* **37** (Suppl. 1), 49–52 (1998).
8. K. Miura, H. Inouye, J. R. Qiu, T. Mitsuyu and K. Hirao, 'Optical Waveguides Induced in Inorganic Glasses by a Femtosecond Laser', *Nucl. Instrum. Meth.* **B 141**, 726–732 (1998).
9. K. Hirao and K. Miura, 'Writing Waveguides and Gratings in Silica and Related Materials by a Femtosecond Laser', *J. Non-Cryst. Solids* **239**, 91–95 (1998).
10. K. Miura, J. R. Qiu, T. Mitsuyu and K. Hirao, 'Preparation and Optical Properties of Fluoride Glass Waveguides Induced by Laser Pulses', *J. Non-Cryst. Solids* **257**, 212–219 (1999).
11. K. Hirao, 'Internal Modification of Glass Materials with a Femtosecond Laser', *SPIE Proceedings* **4088**, 33–39 (2000).
12. A. Marcinkevicius, S. Juodkazis, M. Watanabe, M. Miwa, S. Matsuo, H. Misawa and J. Nishii, 'Femtosecond Laser-Assisted Three-Dimensional Microfabrication in Silica', *Opt. Lett.* **26**, 277–279 (2001).
13. T. Kondo, S. Matsuo, S. Juodkazis and H. Misawa, 'Femtosecond Laser Interference Technique with Diffractive Beam Splitter for Fabrication of Three-Dimensional Photonic Crystals', *Appl. Phys. Lett.* **79**, 725–727 (2001).
14. H. B. Sun, Y. Xu, S. Juodkazis, K. Sun, M. Watanabe, S. Matsuo, H. Misawa and J. Nishii, 'Arbitrary-Lattice Photonic Crystals Created by Multiphoton Microfabrication', *Opt. Lett.* **26**, 325–327 (2001).
15. V. Mizeikis, H. B. Sun, A. Marcinkevicius, J. Nishii, S. Matsuo, S. Juodkazis and H. Misawa, 'Femtosecond Laser Micro-Fabrication for Tailoring Photonic Crystals in Resins and Silica', *J. Photochem. Photobiol. A: Chem.* **145**, 41–47 (2001).
16. K. Kawamura, N. Sarukura, M. Hirano and H. Hosono, 'Holographic Encoding of Permanent Gratings Embedded in Diamond by Two Beam Interference of a Single Femtosecond Near-Infrared Laser Pulse', *Jpn. J. Appl. Phys.* **39**, L767–L769 (2000).
17. K. Kawamura, T. Ogawa, N. Sarukura, M. Hirano and H. Hosono, 'Fabrication of Surface Relief Gratings on Transparent Dielectric Materials by Two-Beam Holographic Method Using Infrared Femtosecond Laser Pulses', *Appl. Phys.* **B 71**, 119–121 (2000).
18. K. Kawamura, N. Sarukura, M. Hirano and H. Hosono, 'Holographic Encoding of Fine-Pitched Micrograting Structures in Amorphous SiO_2 Thin Films on Silicon by a Single Femtosecond Laser Pulse', *Appl. Phys. Lett.* **78**, 1038–1040 (2001).
19. K. Kawamura, N. Sarukura, M. Hirano, N. Ito and H. Hosono, 'Periodic Nanostructure Array in Crossed Holographic Gratings on Silica Glass by Two Interfered Infrared-Femtosecond Laser Pulses', *Appl. Phys. Lett.* **79**, 1228–1230 (2001).
20. R. Herman, R. S. Marjoribanks, A. Oettl and K. Chen, 'Laser Shaping of Photonic Materials: Deep Ultraviolet and Ultrafast Lasers', *Appl. Surf. Sci.* **154–155**, 577–586 (2000).
21. P. R. Herman, K. P. Chen, M. Wei and J. Zhang, 'F_2-Lasers: High Resolution Optical Processing System for Shaping Photonic Components', *SPIE Proceedings* **4274**, 149–157 (2001).
22. J. Zhang, P. R. Herman, C. Lauer, K. P. Chen and M. Wei, '157-nm Laser-Induced Modification of Fused-Silica Glasses', *SPIE Proceedings* **4274**, 125–132 (2001).

23. X. M. Wei, K. P. Chen, D. Coric, P. R. Herman and J. Li, 'F_2-Laser Microfabrication of Buried Structures in Transparent Glasses', *SPIE Proceedings* **4637**, 251–257 (2002).
24. J. Li, P. R. Herman, X. M. Wei, K. P. Chen, J. Ihlemann, G. Marowsky, P. Osterlin and B. Burghardt, 'High-Resolution F_2-Laser Machining of Micro-Optic Components', SPIE Proceedings **4637**, 228–234 (2002).
25. K. Sugioka, S. Wada, A. Tsunemi, T. Sakai, H. Takai, H. Moriwaki, A. Nakamura, H. Tashiro and K. Toyoda, 'Micropatterning of Quartz Substrates by Multiwavelength Vacuum-Ultraviolet Laser-Ablation', *Jpn. J. Appl. Phys.* **32**, 6185–6189 (1993).
26. K. Sugioka, S. Wada, H. Tashiro, K. Toyoda and A. Nakamura, 'Novel Ablation of Fused Quartz by Preirradiation of Vacuum-Ultraviolet Laser-Beams Followed by 4th Harmonics Irradiation of Nd:YAG Laser', *Appl. Phys. Lett.* **65**, 1510–1512 (1994).
27. K. Sugioka, S. Wada, H. Tashiro, K. Toyoda, Y. Ohnuma and A. Nakamura, 'Multiwavelength Excitation by Vacuum-Ultraviolet Beams Coupled with 4th-Harmonics of a Q-Switched Nd-YAG Laser for High-Quality Ablation of Fused Quartz', *Appl. Phys. Lett.* **67**, 2789–2791 (1995).
28. K. Sugioka, S. Wada, Y. Ohnuma, A. Nakamura, H. Tashiro and K. Toyoda, 'Multiwavelength Irradiation Effect in Fused Quartz Ablation Using Vacuum-Ultraviolet Raman Laser', *Appl. Surf. Sci.* **96–98**, 347–351 (1996).
29. J. Zhang, K. Sugioka, S. Wada, H. Tashiro and K. Toyoda, 'Ablation of Fused Quartz by Ultraviolet, Visible or Infrared Laser Coupled with VUV Laser', *Jpn. J. Appl. Phys.* **35**, L1422–L1425 (1996).
30. J. Zhang, K. Sugioka, S. Wada, H. Tashiro and K. Toyoda, 'Dual-Beam Ablation of Fused Quartz Using 266 nm and VUV Lasers with Different Delay-Times', *Appl. Phys.* **A 64**, 477–481 (1997).
31. K. Sugioka, J. Zhang, S. Ruschin, S. Wada, H. Tashiro and K. Toyoda, 'Vacuum-Ultraviolet Laser-Induced Refractive Index Change of Fused Silica', *Appl. Surf. Sci.* **129**, 843–847 (1998).
32. K. Sugioka, J. Zhang, S. Wada, H. Tashiro and K. Toyoda, 'Novel Ablation of Wide Band-Gap Materials by Multiwavelength Excitation Using a VUV-UV Laser System', *Nanotechnology* **9**, 99–103 (1998).
33. K. Sugioka and K. Midorikawa, 'Novel Technology for Laser Precision Microfabrication of Hard Materials', *SPIE Proceedings* **4088**, 110–117 (2000).
34. J. Zhang, K. Sugioka, T. Takahashi, K. Toyoda and K. Midorikawa, 'Dual-Beam Ablation of Fused Silica by Multiwavelength Excitation Process Uusing KrF Excimer and F_2 Lasers', *Appl. Phys.* **A 71**, 23–26 (2000).
35. K. Obata, K. Sugioka, T. Akane, N. Aoki, K. Toyoda and K. Midorikawa, 'Influence of Laser Fluence and Irradiation Timing of F_2 Laser on Ablation Properties of Fused Silica in F_2-KrF Excimer Laser Multi-Wavelength Excitation Process', *Appl. Phys.* **A 73**, 755–759 (2001).
36. J. Zhang, K. Sugioka and K. Midorikawa, 'Direct Fabrication of Microgratings in Fused Quartz by Laser-Induced Plasma-Assisted Ablation with a KrF Excimer Laser', *Opt. Lett.* **23**, 1486–1488 (1998).
37. J. Zhang, K. Sugioka and K. Midorikawa, 'High-Speed Machining of Glass Materials by Laser-Induced Plasma-Assisted Ablation Using a 532-nm Laser', *Appl. Phys.* **A 67**, 499–501 (1998).
38. J. Zhang, K. Sugioka and K. Midorikawa, 'Laser-Induced Plasma-Assisted Ablation of Fused Quartz Using the Fourth Harmonic of a Nd^+:YAG Laser', *Appl. Phys.* **A 67**, 545–549 (1998).
39. J. Zhang, K. Sugioka, and K. Midorikawa, 'High-Quality and High-Efficiency Machining of Glass Materials by Laser-Induced Plasma-Assisted Ablation Using Conventional Nanosecond UV, Visible, and Infrared Lasers', *Appl. Phys.* **A 69**, S879–S882 (1999).
40. M. H. Hong, K. Sugioka, Y. F. Lu, K. Midorikawa and T. C. Chong, 'Optical Diagnostics in Laser-Induced Plasma-Assisted Ablation of Fused Quartz', *SPIE Proceedings* **4088**, 359–362 (2000).
41. M. H. Hong, K. Sugioka, Y. F. Lu, K. Midorikawa and T. C. Chong, 'Laser Microfabrication of Transparent Hard Materials and Signal Diagnostics', *Appl. Surf. Sci.* **186**, 556–561 (2002).
42. M. H. Hong, K. Sugioka, D. J. Wu, L. L. Wong, Y. F. Lu, K. Midorikawa and T. C. Chong, 'Crack-Free Laser Processing of Glass Substrate and Its Mechanisms', *SPIE Proceedings* **4637**, 270–279 (2002).
43. J. Wang, H. Niino and A. Yabe, 'Microfabrication of a Fluoropolymer Film Using Conventional XeCl Excimer Laser by Laser-Induced Backside Wet Etching', *Jpn. J. Appl. Phys.* **38**, L761–L763 (1999).

44. J. Wang, H. Niino and A. Yabe, 'One-Step Microfabrication of Fused Silica by Laser Ablation of an Organic Solution', *Appl. Phys.* **A 68**, 111–113 (1999).
45. J. Wang, H. Niino and A. Yabe, 'Micromachining of Quartz Crystal with Excimer Lasers by Laser-Induced Backside Wet Etching', *Appl. Phys.* **A 69**, S271–S273 (1999).
46. J. Wang, H. Niino, and A. Yabe, 'Micromachining by Laser Ablation of Liquid: Super-Heated Liquid and Phase Explosion', *SPIE Proceeding*s **3933**, 347–354 (2000).
47. J. Wang, H. Niino and A. Yabe, 'Micromachining of Transparent Materials by Laser Ablation of Organic Solution', *SPIE Proceedings* **4088**, 64–69 (2000).
48. J. Wang, H. Niino, and A. Yabe, 'Micromachining of Transparent Materials with Super-Heated Liquid Generated by Multiphotonic Absorption of Organic Molecule', *Appl. Surf. Sci.* **154–155**, 571–576 (2000).
49. Y. Yasui, H. Niino, Y. Kawaguchi and A. Yabe, 'Microetching of Fused Silica by Laser Ablation of Organic Solution with XeCl Excimer Laser', *Appl. Surf. Sci.* **186**, 552–555 (2002).
50. X. Ding, Y. Yasui, Y. Kawaguchi, H. Niino and A. Yabe, 'Laser Induced Backside Wet Etching of Fused Silica with an Aqueous Solution Containing Organic Molecules', Appl. Phys. **A 75**, 437–440 (2002).
51. X. Ding, Y. Kawaguchi, H. Niino and A. Yabe, 'Laser-Induced High Quality Etching of Fused Silica Using a Novel Aqueous Medium', *Appl. Phys.* **A 75**, 641–646 (2002).
52. X. Ding, Y. Kawaguchi, H. Niino and A. Yabe, 'Fabrication of 1 μm Patterns on Fused Silica Plates by Laser-Induced Backside Wet Etching (LIBWE)', *SPIE Proceedings* **4830**, 156–161 (2003)
53. H. Niino, Y. Yasui, X. Ding, A. Narazaki, T. Sato, Y. Kawaguchi and A. Yabe, 'Surface Micro-Fabrication of Silica Glass by Laser-Induced Backside Wet Etching with Toluene Solution', *J. Photochem. Photobiol. A: Chem.* **158**, 179–182 (2003).
54. X. Ding, T. Sato, Y. Kawaguchi and H. Niino, 'Laser-Induced Backside Wet Etching of Sapphire', *Jpn. J. Appl. Phys.* **42** L176–L178 (2003).
55. K. Zimmer, R. Böhme, A. Braun, B. Rauschenbach and F. Bigl, 'Excimer Laser-Induced Etching of Sub-Micron Surface Relief Gratings in Fused Silica Using Phase Grating Projection', *Appl. Phys.* **A 74**, 453–456 (2002).
56. R. Böhme, A. Braun and K. Zimmer, 'Backside Etching of UV-Transparent Materials at the Interface to Liquids', *Appl. Surf. Sci.* **186**, 276–281 (2002).
57. K. Zimmer, A. Braun and R. Böhme, 'Etching of Fused Silica and Glass with Excimer Laser at 351 nm', *Appl. Surf. Sci.* **208**, 199–204 (2003).
58. D. L. Griscom, 'Optical Properties and Structures of Defects in Silica Glass', *J. Ceram. Soc. Jpn.* **99**, 923–942 (1991).
59. J. Ikeno, Y. Masugi, O. Horiuchi, T. Kasai and A. Kobayashi, 'Crack-Free and 3-Dimensional YAG Laser Processing of Glass-Ceramics', *J. Jpn. Soc. Precision Eng. (Japanese)* **64**, 1062–1066 (1988).
60. S. I. Dolgaev, A. A. Lyalin, A. V. Simakin and G. A. Shafeev, 'Fast Etching of Sapphire by a Visible Range Quasi-cw Laser Radiation', *Appl. Surf. Sci.* **96–98**, 491–495 (1996).
61. S. I. Dolgaev, A. A. Lyalin, A. V. Simakin and G. A. Shafeev, 'Etching of Sapphire Assisted by Copper-Vapor Laser Radiation', *Quantum Electron.* **26**, 65–68 (1996).
62. S. I. Dolgaev, A. A. Lyalin, A. V. Simakin, V. V. Vornov and G. A. Shafeev, 'Fast Etching and Metallization of Via-Holes in Sapphire with the Help of Radiation by a Copper Vapor Laser', *Appl. Surf. Sci.* **109–110**, 201–205 (1997).
63. Y. Tsuboi, K. Hatanaka, H. Fukumura and H. Masuhara, 'The 248 nm Excimer Laser Ablation of Liquid Benzene Derivatives: A Relation between Ablation Threshold and Molecular Photochemical Reactivity', *J. Phys. Chem.* **98**, 11237–11241 (1994).
64. H. Fukumura and H. Masuhara, 'The Mechanism of Dopant-Induced Laser Ablation. Possibility of Cyclic Multiphotonic Absorption in Excited States', *Chem. Phys. Lett.* **221**, 373–378 (1994).
65. D. Kim, M. Ye and C. P. Grigoropoulos, 'Pulsed Laser-Induced Ablation of Absorbing Liquids and Acoustic-Transient Generation', *Appl. Phys.* **A 67**, 169–181 (1998).
66. J.-C. Isselin, A.-P. Alloncle and M. Autric, 'On Laser Induced Single Bubble Near a Solid Boundary: Contribution to the Understanding of Erosion Phenomena', *J. Appl. Phys.* **84**, 5766–5771 (1998).

This page intentionally left blank

INDEX

Ablated images, 304
Ablated topology, 324
Ablation of polymers, 139, 151, 305
Ablation depth, 307, 311, 313, 314, 323, 330
Ablation front, 125, 126, 130, 133–135, 141, 145, 152–154
Ablation kinetics, 121, 128, 138, 139, 145, 149
Ablation of dielectrics, 306
Ablation of metals, 121, 130, 156
Ablation of PMMA, 139, 142–144
Ablation of polyimide, 129, 150, 151, 280, 321, 330
Ablation rate, 122, 123, 131, 133, 134, 136, 146, 227, 228, 305, 306, 308, 311, 313, 314, 317–319, 321
Ablation threshold, 134, 137, 138, 144, 149, 150, 152, 226, 321, 357
Ablation velocity, 135, 136, 151, 153, 154
Absorption coefficient, 31–34, 36–38, 40, 41, 43, 44, 63, 71, 72, 90, 91, 123, 126, 130, 140, 142, 143, 145, 148, 150, 151, 173, 191, 263, 285, 302, 306, 339, 351
Absorption constant, 66, 69, 72, 146, 261–264, 266–268
Absorption cross-sections, 153, 183
Absorption grating, 86
Absorptivity, 126, 134, 145, 148
Acetone, 280, 281, 284, 285, 288–291, 293, 295, 297–299, 322, 348–351
Acetylene, 279, 281, 284–286, 298
Activation energy, 115, 135–137, 143, 144, 148, 152, 153, 155, 172, 206, 264, 265, 271, 280
Adaptive interconnection, 88, 89
Adiabatic potential, 51
Adiabaticity ratio, 14
Adsorption, 252–254, 257–259, 261–264, 268–270, 279, 280
Adsorption affinity, 264
Adsorption mechanism, 268
AFM, 139, 180, 182, 228, 234, 273, 323, 326, 327
Ag, 277, 344
Aggregates, 206–209, 211, 257, 258, 291, 292
All-optical light control, 65
Aluminum nitride, 191, 235, 239, 241, 247
Amorphous film, 208, 239, 346
Amorphous semiconductors, 25, 38–41, 43, 50, 53, 54, 183
Amplitude grating, 316, 318
Anatase, 181, 182
Angle Resolved Photoelectron Spectroscopy (ARPES), 1, 3–7, 9–17, 19–22
Angular distribution, 226
Argon lasers, 191, 255, 273
ARPES, *see* Angle Resolved Photoelectron Spectroscopy
Arrhenius coordinates, 122
Arrhenius tail, 123, 137, 138
a-Se, 254, 257, 258, 260, 261, 264–267, 270, 278–280
a-Si:H, 41, 43, 51, 53, 183, 201, 213–315, 223
a-SiN: H, 201, 210–212, 222
a-SiO, 201, 204, 205, 208, 210, 212
Atomic layer epitaxy, 218
Au, 190, 191, 255, 278, 279
Auger decay, 206, 213
Auger-stimulated mechanism, 215
Avalanche ionization,150

Back-illumination technique, 352, 353,
Backside etching, 322, 356, 357
Band gap, 27, 29, 34, 36–39, 41, 44, 49, 50, 57, 63, 101, 104, 150, 174, 235, 255, 267, 271, 272, 340, 341, 343, 356
Band transport model, 57
Bandgap, *see* Band gap
Bandtailing, 37, 38
Band-to-band absorption, 25, 34, 53
Band-to-band transitions, 25, 34, 53
Barium titanate ($BaTiO_3$) crystal, 57, 63, 64, 84, 93, 97, 119
Barrier penetration, 268
Beam coupling, 86, 88, 89, 93
Beam diagnostics, 303, 304
Beam fanning, 62, 89, 90
Beam homogenizer, 303, 308
Beam interference, 311, 322, 355
Beam processing, 79, 201
Beam profile, 77, 303, 325, 328, 329, 331
Beer Lambert, 262

$Bi_{12}SiO_{20}$, 63, 65, 105, 115, 116, 119, 120
Bi-directional link, 88, 92, 94
Bi-excitons, 50
Bifurcation boundary, 133
Bio-organic materials, 255
Bi-prism, 303
Bird-wing phased conjugator, 88, 91
Blazed grating, 326
Bleaching, 140, 141, 255, 279
Boltzmann kinetic equation, 32, 150
Bond breaking, 122, 143, 215, 216, 305
Bond exchange, 213, 215, 223
Boron nitride films, 225, 242, 243, 246, 247
Boundary conditions, 68, 126, 127, 136, 137, 140, 143, 146, 147, 153, 268
Bragg angle, 89, 102, 118
Bragg diffraction, 79, 90
Breathing period, 69, 71, 72, 76
Breathing soliton, 70, 73
Bridge phase conjugator, 88
Broken bonds, 135, 136, 138, 141–143, 152
Brownian motion, 254, 265, 268
Bruggeman EMA, 206, 210, 215
Bulk models, 121, 137, 139, 151, 152
Bulk photothermal model, 135, 137, 143, 144, 151
Buried grating, 343
Burstein-Moss shift, 37

Calcium fluoride, 339, 345, 351
Carbon allotropes, 281–283, 285, 287, 295, 298, 299
Carbyne, 281, 283, 291–293, 295, 298, 300
Carrier mobility, 61, 101–104, 108, 113, 114, 116, 119
CCD camera, 74
Cd, 254, 255, 264
CdS, 254, 255, 261, 266, 279
CDW, 2, 3, 5, 7–14, 18–22
Ceramic films, 229
CF_4/O_2 gas, 335
Chalcogenide, 41, 254, 255, 277
Characteristic exchange time, 145
Characteristic thermal length, 127, 132
Charge-carrier diffusion, 103, 104, 107, 115, 117
Charge-carrier grating, 51
Charge-carrier injection, 101
Charge-carrier lifetime, 102, 115
Charge-carrier mobility, 61, 101, 104, 114, 116
Charge density waves, 2
Charge displacement, 101, 102, 104–108
Charge pattern, 104
Charge transport, 101–104, 106, 107, 116–120
Chemical amplification, 267
Chemical energy, 271
Chemical inertness, 225, 229, 285
Chemical laser processing, 139
Chemical vapor deposition, 44, 218, 225, 226, 229, 235, 282
Chlorophyll, 255, 279
Chromophores, 144, 150, 151, 153, 253–255, 260, 267–269, 276
Clusters, 182, 189, 192, 206, 253, 269, 316
Coalescence, 257, 258
Coherence length, 5, 16, 20
Colloid, 171, 252–255, 257, 259, 263, 264, 267–272, 275–280
Colloid solution, 251, 253–255, 257, 259, 263, 264, 268, 270, 271, 275, 278–280
Color center, 212, 306
Color marking, 344
Compact film, 254, 257, 261
Compaction, 212, 222
Compensation, 32, 64, 71, 265, 280
Compensation effect, 265, 280
Compensation temperature, 265
Complex refractive index, 25, 27, 28
Complex relative permittivity, 25, 27, 28
Compositional change, 205, 206
Compound semiconductors, 63, 225, 280
Confinement soliton, 65, 70–73
Confocal scanning laser microscope, 347
Conjugated reflectivity, 57, 63
Conservation law, 122, 140
Constructive interference, 317
Continuous ablation, 309, 320
Continuous random network (CRN) model, 209
Contour mask, 308, 309, 312–315, 318, 320, 323–330, 333, 335, 348
Coordination number, 209, 213
Copper-vapor laser, 346, 357
Core electronic state, 201
Corning 7059, 326
Coulombic repulsion, 1, 216
Coupled wave theory, 62, 63, 92
Coupling transmission efficiency, 50, 90–94, 96, 97
Covalency, 213
Coverage, 216, 264
Cr, 64, 344
Critical point, 130, 206, 214, 218, 222

CrO_3, 346
Cross-linking, 212
Crystal orientation, 62, 70
Crystallographic direction, 74, 76
Cu, 190–193, 291, 344
Cubic boron nitride films, 242, 247
Cubic oxides, 63
CV characterization, 171
Cylinder lens, 302, 303, 326, 335

Dangling bond, 212, 215, 218, 219
Dark conductivity, 61, 62, 80, 84
Darkening, 140, 141
Debye screening, 61
Defect annealing, 161, 166, 168–171, 174–179, 181, 182, 189, 210, 226, 236, 244
Degenerate four-wave mixing, 104, 105, 120
Densification, 179, 213, 215, 223
Dephasing of excitons, 44, 78, 86
Depletion effects, 306
Depletion layer, 270, 271
Deposition chamber, 241, 294
Deposition of thin films, 225, 246, 263, 277
Depth of focus, 272, 274, 330
Diamond, 27, 129, 242, 281–285, 287, 290, 292–295, 299, 355
Diamond-like carbon, 281, 284, 287
Dielectric bilayers, 317
Dielectric constant, 38, 42, 52, 53, 61, 109, 161, 167, 168, 176, 179, 185–188, 210, 218
Dielectric deposition, 183
Dielectric mirror, 303, 317
Dielectric permittivity tensor, 66, 67
Diffraction, 3, 57, 64, 65, 69, 71–75, 79, 81–90, 97, 102, 103, 118, 180, 206, 207, 229, 238, 240, 272, 277, 291, 292, 298, 304, 307, 316–319, 321, 322
Diffraction angle, 292, 318
Diffraction efficiency, 57, 85–88, 272
Diffraction length, 75
Diffraction optics, 304
Diffraction regime, 79, 81, 84, 87
Diffractive mask, 317, 318
Diffusion, 57, 60, 61, 65, 80, 84, 92, 103–106, 108, 109, 111, 112, 114–116, 119, 138, 154, 157, 169, 189, 205, 208, 226, 229, 230, 257, 258, 268–270, 305, 352
Diffusion space charge field, 80
Diffusion time, 105, 109, 111, 112, 114
Diffusion transport, 3, 7, 8, 20, 32, 57, 59–61, 63, 66, 101–107, 115–120, 147, 170, 188, 190, 254, 265, 268, 269
Digital information, 275
Direct beam writing, 273
Direct excitation, 339, 340
Direct interaction, 340, 343
Direct transition, 34–37, 150
Direct writing, 277–280, 309, 330, 332
Dispersion relations, 26, 27
Dispersive charge transport, 117, 118
Dithering, 316
Donor, 57, 59, 61, 66, 101, 104–107, 109, 119
Doping, 12, 31, 32, 37, 63, 85, 87, 90, 107, 116, 201, 240, 251, 277
Double phase conjugation (DPC), 57, 88–97
Drift, 30, 57, 59–61, 64, 66, 101–105, 108–111, 114–119, 203
Drift mobilities, 101, 102, 119
Drift transport, 57, 59–61, 66, 101–107, 115–120
Drift velocity, 109, 111, 114, 116, 117
Dynamic grating, 63, 79, 88, 99
Dynamic holography, 60, 103
Dynamic interconnection, 57, 88, 95, 97
Dynamic waveguide, 57, 64, 65, 97

EDC, *see* Energy Distribution Curve
Effective modulation ratio, 80
Electric dipole, 212
Electrical energy, 271
Electrical resistivity, 6, 225, 230, 238, 240, 242, 281, 285, 288
Electrochemical potential, 270, 271
Electroless plating, 190
Electro-phonon interaction, 1, 2, 4, 7, 14, 22, 145
Electron affinity, 271
Electron energy loss spectroscopy (EELS), 288, 289
Electron spin resonance, 212
Electron storage ring, 201, 202
Electron subsystem, 145
Electron temperature, 146–148
Electro-optic coefficient, 80, 81, 84, 87–90, 120
Electro-optic effect, 80, 103, 107
Electro-optic linear effect, 80, 103, 107
Electro-optic tensor, 67
Ellipsoid index, 67
Elovich equation, 261
Energy band gap, 39, 101, 104
Energy Distribution Curve (EDC), 5
Epitaxial film, 239, 346

Equilibrium concentration, 268
Etch depth, 141, 142, 309, 314, 321, 324, 326, 329, 345, 348–350
Etch rate, 185, 193, 306–308, 311, 312, 317, 322, 344, 346, 348–351
Etch transfer, 301, 335
Etching, 15, 117, 121, 141, 161, 166, 177, 186, 189, 193–195, 202, 205, 212, 225, 261, 262, 277, 280, 286, 301, 302, 305–308, 311, 317, 319–322, 326, 335, 339–347, 350, 351, 354, 356, 357
Evaporation, 121, 122, 125, 126, 130, 132, 136, 137, 146, 148, 153, 190, 205, 206, 209, 211, 225–227
Excimer complexes, 161, 162, 195
Excimer lamp properties, 161, 165, 184, 188, 193, 194
Excimer lamp supply, 162, 164
Excimer lamps, 161–167, 170, 182–184, 187–189, 191–195, 199
Excimer lasers, 125, 128, 137, 138, 156, 157, 161, 162, 193, 195, 226–228, 230, 234–241, 244, 277, 281–284, 288, 298, 301–305, 307–309, 311, 324, 326, 332, 335, 340, 341, 343–345, 347–352, 355–357
Excimer spectra, 163
Excitation, 4, 5, 7, 8, 14, 15, 22, 25, 29, 30, 33, 34, 38, 46, 50, 54, 57, 60, 62, 101–111, 115–120, 122, 162, 163, 167, 201, 209, 210, 213, 215, 316, 351, 352, 255, 264, 267–271, 282, 305, 339–342, 350, 356
Excited states, 14, 15, 103, 118, 150, 151, 153, 154, 178, 188, 253, 269, 357
Exciton adsorption peaks, 44
Exciton-phonon interaction, 44
Explosive decomposition, 142
Explosive vaporization, 121, 134
Extended states, 39, 40, 42, 43, 53
Extinction coefficient, 25, 26, 30, 31, 37, 142, 211, 267
F_2 laser, 139, 340, 343, 354–356
$FeCl_3$, 346
Femtosecond laser, 156, 246, 287, 298, 339, 355
Fermi electron velocity, 147
Fermi energy, 271
Fermi liquid, 1, 4–7, 14, 22
Fermi Surface, 3, 7–10, 13, 17, 20–22
Ferroelectric oxides, 63
Ferroelectric perovskite, 116
Figure of merit (FM), 275, 276
Filling factor, 309, 320
Film crystallinity, 231, 238, 240
Film growth, 190, 219, 232, 235, 243, 246, 252, 254, 257, 260, 261, 263, 265, 271
Film quality, 230, 234, 238, 239
Film thickness, 139, 189, 201, 226, 228, 229, 234, 243, 259–262, 264, 275, 285
Fluence threshold, 121, 264, 275
Fluence transition, 325, 329
Fluorinated ethylene-propylene copolymer (FEP), 351
Fluoro-polymer, 351
Fokker-Planck equation, 150
Footprint Mask, 302, 303, 325, 329, 331
Formation soliton, 64, 65, 69, 73–75
Fourier transform infrared spectroscopy (FTIR), 170, 173, 176–178, 186, 189, 229, 237, 239, 244, 246
Fourth harmonic generation (FHG), 240, 356
Four-wave mixing, 63, 88, 103, 118, 120
Fowler-Nordheim (FN) tunneling, 175
Fraunhofer diffraction, 304
Free carrier attenuation coefficient, 30
Free carrier density, 101, 102, 107, 111
Free carrier lifetimes, 101, 102, 108, 109, 111, 112, 115, 116
Free carrier mobility, 101, 108, 113, 116
Free electron laser (FEL), 281, 282, 295–299
Frenkel excitons, 38, 39
Frenkel pair, 209
Frenkel-Wilson boundary conditions, 136, 137, 141
Fresnel reflection, 93, 204
Fresnel's equations, 29
Fringe contrast, 80
Fringe modulation, 84, 87
Fringe pattern, 79, 80, 84
Fringe spacing, 80
Frozen hydrocarbon, 281–286, 295, 298, 299
Fs-laser, 152, 281–283, 287–293, 298, 340–342, 353
FTIR, *see* Fourier transform infrared spectroscopy
Fused silica, 27, 306, 326, 327, 339–353, 355–357

Galvanometer mirror, 344
Gas Phase Photodeposition (GPPD) processes, 251
Gauss equation, 109
Gaussian beam, 69, 273
Ge oxidation, 161, 162, 188, 189

Glass, 51, 98, 117, 120, 164, 165, 167, 185, 191, 254, 264, 277, 278, 295–299, 306, 315, 319, 326–328, 335, 337, 342–344, 346, 355–357
Grating, 57, 59–63, 79–92, 97, 99, 102–104, 110, 112, 118, 120, 147, 210, 272–274, 277, 278, 280, 304, 311, 316–323, 326, 327, 342-344, 347, 348, 355–357
Grating period, 60, 61, 85, 87, 304, 316–318, 320
Grating temperature, 61, 112, 118, 120, 147, 210, 320, 327
Gray color-coding, 321
Gray scale mask, 301, 308, 309, 313–315, 317, 320–322, 324, 328, 329, 348
Gray tones, 320, 322
Growing rates, 259–261, 275
Growth mechanisms, 260
Gyration constant, 66, 67

Hagen Rubens relation, 31
Half tone mask, 315, 316
Hardness, 225, 229, 230, 234, 239, 242, 243, 245, 281, 285–287, 299
Heat capacity, 126, 134, 146, 352
Heat equation, 127, 131, 135
Heavy carriers, 216
HEBS, 315
HeNe laser, 264
Hologram, 104
Holographic data storage, 103
Holographic deposition, 256, 277
Holographic grating, 103, 110, 278, 280, 342, 355
Holographic methods, 103, 342, 355
Holographic Time of Flight (HTOF), 101, 104–107, 111, 114–119
Homoepitaxy, 216, 223
Homogenizer, 303, 343, 347
Hopping decay, 213
HTOF, *see* Holographic Time of Flight
Hybrid masks, 302, 309, 329
Hydrodynamics model, 130, 158
Hydrogen content, 286, 293
Hydrogen-terminated defect site, 210, 215, 288

Image amplification, 63
Image processing, 304, 352
Imaging, 256, 272, 278, 280, 304, 316, 318, 319, 321, 352
Imaging system, 272, 278, 318, 329
Imidization, 187
Impact ionization, 150
Impact pressure, 352
Impurity centers, 101, 107, 108
Incubation, 254, 261, 262, 264, 265, 306, 307, 311, 314, 326, 355
Incubation period, 254, 261, 264, 265
Incubation time, 261, 262
Indirect excitation, 339, 340
Indirect interaction, 340, 343
Indirect transition, 34, 36, 37
Induced birefringence, 67
Inorganic materials, 278, 306, 324
Insulating liquid cell, 74
Inter-atomic separation, 40, 43
Interband excitation, 101
Interband relaxation process, 48
Interband transitions, 18, 46, 101
Interconnection, 57, 88–97
Interconnects, 79, 89, 185
Interference pattern, 57, 59, 60, 62, 79–81, 102, 104, 107, 108, 110–118, 311, 319
Interfering beams, 60, 61, 79, 81, 83, 84, 86, 256
Interferometry, 79, 97, 139, 321, 324, 326, 328, 331
Intermediate asymptotic technique, 134, 157
Intermediate threshold, 134
Interpolation formula, 125, 134
Intraband processes, 46
Ionic crystals, 27, 29, 38, 55, 116
Irradiation source, 252, 263
Irradiation time period, 202, 259, 288, 289, 297, 298

$K_{0.3}MoO_3$, 2, 4, 9, 10, 13, 17, 18, 20–22
Keldysh parameter, 150
Kepler telescope, 303
Kinetic experiments, 259, 261
Kinetic investigations, 251, 260
$KMnO_4$, 346
$KNbO_3$, 63, 105, 116, 119, 120
Kramers-Kronig relations, 29, 212
KrF excimer laser, 137, 138, 234, 236–240, 244, 283, 298, 341, 344, 347–352, 356
Lagrange extinction coefficient, 142
Langmuir Blodgett, 256, 257
Large polarons, 116, 120
Laser ablation, 121–123, 125, 127–130, 133–135, 139, 142, 145, 146, 151–156, 225, 226, 228, 230, 235–237, 239, 241, 246, 251, 280, 283, 285, 294, 301, 302, 305, 307, 308, 317,

318, 320, 321, 323, 326, 330, 333, 336, 337, 339-341, 343–345, 348, 350, 352, 355-357
Laser ablation deposition, 225, 226
Laser arrays, 355
Laser beam, 57–60, 62, 74, 79, 82, 84, 85, 88–92, 97, 102, 118, 139, 227, 228, 233, 240, 256, 263, 264, 267, 273, 277, 284, 288, 291, 294, 303, 307, 309, 311, 319, 322, 324, 326, 330, 331, 339, 341–343, 345–347, 349–351, 356
Laser deposited films, 230, 234, 235, 242, 243, 251, 277, 278, 281, 284
Laser diode, 89
Laser direct writing, 277, 278, 330, 332
Laser etching, 280, 302, 305, 306, 308, 320, 322
Laser Induced Forward Transport (LIFT), 251, 278
Laser intensity, 64, 137, 150, 153, 303, 323, 329, 342
Laser micromachining, 305, 320, 328, 335, 355
Laser photodeposition writing, 273
Laser processing, 156, 199, 276, 277, 282, 298, 301, 312, 333, 335, 336, 339, 356, 357
Laser pulse duration, 122, 147, 149, 227, 238
Laser pulse shape, 125, 129, 145
Laser pulses, 101, 116, 121–123, 125, 126, 129–131, 133, 134, 145, 147–152, 154, 156, 225–228, 230–232, 234, 236, 238, 239, 244, 246, 283, 286, 302, 305, 307–309, 311, 314, 320, 323, 324, 327, 328, 330, 342, 343, 345, 346, 348-357
Laser recrystallization, 251
Laser scanning, 256, 329–331
Laser workstation, 303
Laser writing, 251, 265, 277, 278, 331, 332
Laser-induced backside wet etching, 307, 339, 340, 356, 357
Laser-induced periodic surface structures, 307
Laser-induced plasma-assisted ablation, 340, 356
Lattice temperature, 45, 46, 146–148
LDW glass, 315, 337
LIBWE, 307, 322, 339, 340, 344–352, 354, 357
Light intensity, 62, 64, 66, 68, 80, 110, 140, 259, 264, 265, 267–270
Light intensity modulation, 110
Light scattering, 84, 263
$LiNbO_3$, 63, 64, 191, 342
Linear regression analysis, 210, 214
LIPAA, 340, 343, 344
LIPSS, 307
Liquid jet, 352, 353
Liquid phase, 19, 227, 231, 251, 253–257, 268, 269, 275, 276, 278, 279
Liquid Phase Photodeposition (LPPD), 251, 256, 257, 269, 278
Lithographic processes, 301
Lithographic techniques, 319
Lithography, 167, 253, 301, 315, 332, 338, 345
Logarithmic growth, 261
Lorentz-Lorenz relations, 212
Low temperature epitaxy, 201
Luttinger liquid, 4

Machining techniques, 301, 302, 308–311, 319, 327, 335
Mask, 191, 192, 227, 230, 232, 253, 256, 272, 273, 278, 279, 301–304, 308–333, 335, 337, 339, 343–345, 347, 348
Mass-loss kinetics, 137
Master equation, 267, 269
Material depletion, 267
MDC, *see* Momentum Distribution Curve
Mechanical stresses, 142, 144
Metal nitrides films, 225, 229, 234, 241
Metal target, 232, 234, 235, 340, 343, 344
Metallization, 190, 255, 278, 279, 344, 357
Metallo-organic decomposition, 191
Metastable, 209, 225, 254
Methanol, 281, 285, 288–290, 294, 298
MgO, 28, 168, 230, 342
Microcrystal, 227, 235, 238, 281, 291–293, 298
Micro-Electro Mechanical System (MEMS), 354
Microetching, 344, 345, 347, 354, 357
Microfabrication, 277, 338–340, 343, 353–357
Micro-fluidics, 307, 319, 332, 333
Micro lens array, 327
Micromachining, 301–303, 305, 310, 319, 320, 328, 335, 338, 355, 357
Micro-optical, 302
Micro-prisms, 308, 326, 333
Micro-roughness, 326
Micro structures, 55, 201, 280, 301, 307, 309, 319, 321, 326, 327, 330, 335
Microsystems technology, 319, 338
Migdal theorem, 14, 22
Migdal-Eliashberg, 5
Mixing of diffraction orders, 79
Mobility, 39, 40, 61, 63, 101–109, 113–117, 119, 120, 234, 270, 277
Mobility anisotropy, 103, 119

Mobility edge, 39, 40
Mobility tensor, 103
Modified scanning contour mask technique, 327
Modulation, 7, 8, 11, 60, 62, 64–66, 79–82, 84–87, 92, 96, 97, 102, 103, 105, 108–116, 118, 272, 308, 342
Modulation charge carrier density, 46, 102, 106, 116
Modulation index, 82, 84–86
Modulation ratio, 80
Modulation Transfer Function, 272
Molybdenum, 9, 234
Moments method, 125, 127–130, 137, 144, 147, 155, 157
Momentum Distribution Curve (MDC), 9, 20, 21
Morphology, 139, 179, 191, 193, 228, 240, 258
Moving interface, 141
Multi-beam coupling, 89
Multiphoton absorption, 265
Multiphoton excitation, 341, 342
Multi-photon ionization, 150
Multiphoton processes, 150
Multi-photon transition, 150
Multiple-wave mixing, 63
Multiple-wavelength irradiation, 340, 356
Mutual coherence, 88
Mutually incoherent beam coupling, 57, 88–90, 97
Mutually pumped phase conjugation (MPPC), 88
N_2O photodecomposition, 190, 191
Nanocrystalline Si, 207
Nanoparticles, 189, 254, 257, 279
Nanoscopic particles, 268
Naphthalene derivative, 347, 348, 350, 351, 353
Nd:YAG laser, 190, 230, 232, 236, 237, 240, 246, 281, 283, 344, 346, 350, 356
Near-field imaging, 272
Negative feedback, 268
Nesting, 9
NIR laser, 346
$NiSO_4$, 346
Non-bridging oxygen hole center, 209
Non-centrosymmetric materials, 101, 103, 104, 110
Noncentrosymmetry, 44, 101, 103, 104, 110
Non-equilibrium, 122, 145, 162, 225, 263, 282
Nonequilibrium molecular excitation, 122
Nonlinear absorption, 93
Non-linear anisotropic material, 66
Non-linear material, 65, 79
Non-linear mechanisms, 263
Nonlinear recording, 79, 81
Nonlinearity recording, 79, 81
Non-radiative recombination, 50
Nonradiative relaxation, 50, 150, 151
Nucleation, 220, 223, 239, 242–245, 253, 265
Numerical aperture, 272, 304

One-photon process, 201
Optical absorption, 25, 67, 140, 264, 266–268, 285, 302, 305, 306, 343, 351
Optical absorption coefficient, 140, 263, 285, 302, 306, 351
Optical activity, 57, 65–69, 71, 72, 77, 84
Optical data processing, 326
Optical elements, 264, 273, 274, 280, 304, 320
Optical emission spectra, 288, 290
Optical gap, 40, 41, 43
Optical interference pattern, 108, 110, 112–114,
Optical projection, 256, 272, 325
Optical resolution, 304, 305
Optical storage, 275
Optical transparency, 339
Optical waveguide, 77, 210, 342, 355
Organic molecule, 275, 344, 345, 348–350, 357
Organic solution, 339, 340, 344, 345, 348-351, 357
Organometallic solutions, 255, 256
Oscillations, 30, 62, 63, 68, 111, 112, 114, 117, 130, 133
Oxide charge, 171, 174, 181, 189
Oxygen activation, 201
Oxygen photodissociation, 201
Oxygen vacancy, 205, 209
Oxygen-vacancy defect, 205
Ozone, 167, 168, 178, 188, 194, 285, 288

Parabolic growth, 260,
Patterns, 57, 59–62, 79–81, 84, 102, 104–108, 110–118, 161, 180, 181, 186, 190–192, 196, 207, 232, 234, 256, 272, 273, 275, 277, 278, 291–293, 303, 307, 309, 311, 314, 316, 319, 324, 330, 332, 339, 342–348, 356, 357
Pd acetate, 190
Pd nucleation, 193
Peak temperature, 132
Peierls, 1–4, 7–9, 11–13, 17–20, 22, 23
Penetration depth, 127, 202, 351
Periodic nanostructure, 342, 355
Permanent grating, 355

Peroxylinkage, 209
Peroxyradical, 209
PET, *see* Polyethyleneterephthalate Phase conjugate,
Phase conjugation, 57, 63, 88, 89, 91, 93, 94, 97, 99
Phase gratings, 79–83, 97, 273, 317, 318, 322, 357
Phase mask, 318, 344, 348
Phase modulation, 79, 81
Phase shift, 61, 62, 110, 317, 318, 321
Phase-separation, 208
Photoablation, 261, 262, 275, 280
Photoactive media, 252, 263, 269
Photoadsorption, 254, 259, 279, 280
Photo-assisted processes, 170, 171
Photobleaching, 279
Photochemical ablation, 139
Photochemical bond breaking, 122
Photochemical modification, 141, 144
Photochemical reactions, 139–141, 161, 201, 210
Photoconductivity, 61, 62, 80, 101, 103, 119
Photoconversion, 267
Photocopier, 102
Photo-CVD, 167, 169–173, 175–177, 181–183
Photodeposition, 251–257, 259–273, 275–280
Photodeposition efficiency, 275
Photodeposition from Colloid Solutions (PDCS), 251, 253, 254, 263
Photodeposition processes, 251, 257, 261, 264, 265, 267, 268, 272, 276, 278
Photodeposition systems, 252–254, 256, 267, 272, 275, 276
Photodesorption, 201
Photodiagnostics, 251
Photodissociation, 201
Photo-electrochemical, 251, 255, 271, 277, 278
Photoelectron, 1, 3, 5, 10, 22, 118, 205, 250, 251, 253, 254, 334
Photo-etching, 193, 261, 305
Photo-excitation, 25, 29, 34, 62, 101–110, 115, 116, 119, 120, 210, 213, 267-270
Photo-excited, 57, 59, 63, 84, 97, 104–108, 112, 115, 117, 118, 120, 204, 210, 251–254, 256, 267, 269, 271, 277–279
Photohole, 10, 16, 17, 253
Photoionization, 66, 101, 107, 151, 217, 218
Photolithography, 315, 345
Photoluminescence, 25, 46, 50–53, 189
Photolysis, 178, 201, 203, 217–219
Photolytic,172, 194, 202, 208, 210, 212, 215, 255, 259, 265, 269
Photolytic processes, 255, 259
Photon flux, 161, 220, 261, 264, 293
Photon-material interaction, 253
Photon-stimulated desorption, 215
Photo-oxidation reactions, 189, 253
Photophysical ablation, 121, 152–155, 157
Photoprecipitation, 254, 259, 268, 280
Photoreactions, 187, 190, 255, 265, 272, 339
Photoreactor, 251, 252, 256, 263, 264, 275
Photoreactor systems, 251, 256
Photoredox reactions, 253
Photorefractive coupling strength, 92
Photorefractive crystal (PRC), 57, 59, 64–67, 71, 74, 79, 88, 97
Photorefractive effect, 57, 58, 64, 66, 67, 92, 97, 98, 119, 120
Photorefractive materials, 57, 59–64, 88, 89, 97–99, 106, 199, 120
Photorefractive organic materials, 63
Photorefractivity, 57–67, 88, 89, 99
Photothermal ablation, 154, 155, 305
Photothermal reactions, 136, 144
Photovoltaic effect, 58, 60, 63
Pixels, 320
Planarization, 308
Plasma, 18, 30, 140, 161, 163, 164, 168, 169, 171, 175, 176, 196, 197, 210, 212, 226–228, 245, 280, 282, 307, 335, 340, 343, 344, 356
Plasma frequency, 18, 30
Plasma plume, 226–228, 237, 307
PLD, *see* Pulsed Laser Deposition
PMMA, *see* Polymethyl-methacrylate
Pockels cell, 76
Pockels effect, 101, 103
Poincaré sphere, 76, 78
Polarons, 2, 5, 13–19, 22, 55, 116, 120
Polyamic acid, 186, 187
Polycarbonate (PC), 306, 328, 332, 333
Polyethyleneterephthalate (PET), 193, 306
Polyimide (PI), 124, 125, 128, 129, 137–139, 144, 150, 151, 185–187, 191, 193, 279, 280, 305, 306, 321, 327, 329–331, 335
Polymer structuring, 301
Polymers, 63, 98, 116, 117, 119–121, 135, 136, 138–140, 142–144, 150, 151, 157–159, 161, 166, 171, 180, 186, 191–195, 199, 225, 226, 262, 277, 279, 280, 293, 301, 302, 305–307, 319–321, 328, 332, 333, 335, 336, 345, 351, 357

Polymethyl-methacrylate (PMMA), 139, 142–144, 193, 254, 255, 257, 264, 306
Polytetrafluorethylene (PTFE), 193, 282, 306
Porous silica, 185, 187
Power density, 226, 263, 285, 287–290, 292
Precipitation, 207, 210, 222, 252, 254, 259, 264, 268, 280
Pre-formed polymer, 320
Probe pulse, 104, 110, 115, 118
Projection mask, 301, 302, 310, 311, 329, 345, 347
Projection optics, 304, 314, 324, 326, 328
Projection ratio, 313, 324
Pseudo-dielectric function, 213, 214, 218, 219, 222
Pseudogap, 3, 4, 9, 18, 21, 22
p-Si, 169, 206, 207, 214, 221, 222, 255
PTFE, *see* Polytetrafluorethylene
Pulse length, 108, 123, 228, 252
Pulse repetition rate, 238–240, 284, 302, 323, 327
Pulsed laser ablation, 121, 133, 156, 225, 226, 228, 235, 237, 239, 301, 323
Pulsed laser ablation deposition, 225, 226
Pulsed Laser Deposition (PLD), 174, 177, 225–229, 232, 235, 239–241, 243–245, 281–284, 286, 288, 298
Pulse-to-pulse stability, 302
Pump-probe technique, 104, 105, 151
Pyralin, 329
Pyrene, 322, 348–351
Pyrene/acetone solution, 322, 348–351
Pyrex, 326, 327
Pyrolytic deposition, 256, 278
PZT, 167, 168, 180

Quantum yield, 140, 144, 266, 267
Quartz, 163, 173, 180, 191, 192, 255, 284, 285, 288, 294, 295, 308, 315–317, 322, 327, 328, 345, 351, 355–357
Quartz crystal, 345, 351, 357
Quasi Linear Deposition Rate (QLDR), 261, 264–267
Quasiparticle, 2–6, 13–18, 22, 23
Quasi-stationary model, 122, 142, 143, 149

Radiation effect, 153, 201, 203, 204, 210, 213, 222, 356
Radiation induced defects, 306
Radiative recombination, 50–52
Radiative tunneling, 51
Raman spectra, 285, 286, 288, 294, 299
Raman-Nath diffraction, 79, 84
Random chain scission, 136
Rare gas dimers, 162
Rare gas halides, 162, 163
Rarefaction wave, 143,
Ray tracing, 304
Rayleigh criterion, 272
Reaction rate constant, 267
Reactive ablation, 277
Reactive pulsed laser (RPL) ablation, 225–232, 234–236, 241, 246, 247
Reactive pulsed laser ablation deposition, 225, 226
Real-time holography, 79, 97
Real-time monitoring, 204, 222
Reflectance, 25, 26, 29–31
Reflection coefficient, 123, 142, 146, 204
Reflectivity, 57, 63, 90–94, 97, 126, 139, 234, 240, 263
Refractive index, 25–28, 31, 34, 40, 43, 57–60, 62–67, 79–81, 84, 86, 89, 92, 101–104, 108, 110, 118, 167, 184, 185, 210–212, 223, 318, 342, 356
Refractive index grating, 60, 62, 63, 81, 86, 102, 104, 110
Refractive index modulation, 64–66, 84, 92, 103, 108, 110, 118
Relative permittivity, 25, 27–30
Relaxation of excitons, 48
Relaxation time, 6, 30, 48, 63, 144, 148, 149, 151–155, 219, 267, 269
Relief structures, 322
Renormalized activation energy, 137
Repetition rate, 163, 228, 232, 238–240, 244, 284, 302, 311, 323, 327, 330, 339, 341, 346
Replication, 301, 319, 332, 333, 335, 338
Resolution, 1, 3, 6, 12, 65, 101, 102, 104, 116, 118, 139, 145, 203, 204, 216, 217, 256, 272, 273, 275, 278, 279, 282, 289, 304, 305, 314, 319, 325, 326, 346, 347, 355, 356
Resolving power, 253
Response, 8, 14, 18, 62, 63, 97, 115, 118, 120, 122, 139, 150, 151, 153, 203, 206, 209, 210, 213, 216, 218, 269, 280
Reticule mask, 316, 320, 321
Rhodium-doped barium titanate (Rh:$BaTiO_3$), 57, 84–86, 88–93, 97
Richardson constant, 146, 148
Richardson law, 146
Rotating power, 63, 66, 97

Sapphire, 27, 191, 232, 235, 236, 239, 240, 246, 287, 306, 339, 341, 342, 345, 346, 357
Scanned laser ablation, 309, 330
Scanning, 228, 253, 256, 273, 275, 290, 302, 307, 309, 311–314, 323–329, 333, 335, 339, 344, 347, 348
Scanning contour mask, 312, 323–327, 333, 335
Scanning electron microscope (SEM), 228, 257, 258, 290–292, 321–323, 326–328, 333, 334
Scanning mask, 324
Scanning systems, 273
Scanning velocity, 275, 311
Schott D263, 326
Schwarzschild optics, 343
Screening, 2, 3, 14, 22, 61, 64, 123, 125, 128, 134, 145
Screening effect, 128, 145
SDW, *see* Spin density-waves
Se, 254, 257, 258, 260, 261, 264–267, 270, 278–280
Sedimentation, 259, 269
Self-diffraction spectra, 97
Self-focusing, 65, 74
Self-limiting, 216, 220
Self-pumped phase conjugation (SPPC), 88, 94, 95
Self-trapped exciton, 51
Sellmeier coefficients, 27
Sellmeier dispersion equation, 27
SEM, *see* Scanning electron microscope
Semiconductors, 2, 25, 27, 30–32, 34, 37–41, 43, 44, 48, 50, 51, 53–55, 63, 101, 146, 161, 163, 167, 183, 197, 198, 225, 236, 241, 271, 272, 276–280, 335
Serial recording, 273
Shadow bands, 11, 22
Shallow traps, 103, 105, 109, 115, 119, 120
Shock wave, 158, 352
Si, 28, 34, 36–39, 41, 43, 51, 53, 161, 166–172, 174–183, 185, 188, 189, 191, 196, 198, 201, 205–223, 230–239, 243–246, 255, 278, 282, 283, 288, 291, 292, 297, 319, 342
Si oxidation, 180
SiC, 183, 283, 342, 344
SiGe oxidation, 161, 188, 189
SiH_6, 183–185, 211, 212, 215–221
Silent discharge, 163–165
Silicon dioxide, 201
Silicon hydride, 216, 218
Silicon nitride, 185, 210, 277
Silicon oxynitride, 210, 277
Sillenite crystals, 71, 74, 119
Single-bunch mode, 203
Singlet excitons, 52, 53
Singular point, 130, 132
SiO_2, 27, 63, 65, 105, 115, 116, 119, 120, 167, 176, 177, 179, 181, 183–186, 188, 189, 201, 204–210, 212, 213, 222, 282, 319, 353, 355
Sol gel processing, 167, 170, 174, 179
Solid-phase crystallization, 207
Space charge distribution, 58, 105
Space-charge field, 58, 59, 61, 65, 66, 80–82, 84, 102– 105, 107, 109–119
Spatial filters, 76, 256
Spatial frequencies, 81, 280, 308, 323
Spatial harmonics, 81
Spatial localization, 252
Spatial period, 68, 83, 102, 104, 112, 113, 116, 117
Spatial soliton, 57, 59, 63–65, 74, 76, 77, 97, 98
Spatio-temporal profile, 263
Spectral bandwidth, 263
Spectral efficiency, 266, 267
Spectroscopic ellipsometry, 204
Spherical aberrations, 304
Spin density-waves (SDW), 2
Stainless steel, 170, 228, 232, 245, 284, 288, 291, 293, 344
Stationary ablation, 122, 137, 320, 329
Stationary contour mask method, 309
Stationary evaporation wave, 130, 132, 146
Stationary gray scale mask, 309, 320
Stefan boundary condition, 136
Step and repeat, 309, 320, 330
Stimulated emission, 150, 151
Stokes parameters, 76–78
Stray light, 256
Structural defects, 264
Structural freedom, 213
Sub-micrometer structure, 342
Sub-micrometric, 272, 311, 319, 322, 323
Sub-micrometric structuring, 319, 322
Submonolayer, 257
Suboxide phase, 207
Sub-picosecond laser ablation, 145
Subthreshold process, 123, 125, 131, 134
Superheating, 130, 132
Surface cleaning, 167
Surface growth, 268

Surface Photodeposition (SP), 257, 259, 266, 280
Surface relief grating, 322, 342, 343, 348, 355, 357
Surface roughness, 193, 206, 214, 221, 235, 307, 320, 323–326, 328, 329, 332, 335, 347
Surface-roughness layer, 206, 214
Surface vaporization model, 121
Switching and routing, 55
Synchrotron radiation, 23, 201, 202, 216, 222, 223, 281, 282, 293, 298, 299

Ta_2O_5, 167–172, 174–179, 182, 198
Tail states, 37, 39, 40, 42–44, 51
Tantalum, 168, 170, 171, 174, 175, 177, 179, 234
Tantalum pentoxides, 168
Tauc's constant, 41
Tauc's relation, 41
Temporal dynamics, 103
Thermal diffusion, 103, 105, 268, 305, 352
Thermal diffusion length, 305
Thermal excitation, 57, 62, 111, 117
Thermal model, 122, 125, 130, 135, 137, 143, 145, 147, 149, 151, 153–155
Thickness profile, 226, 227
Thin polymer layers, 321
Three-dimensional photonic crystals, 342, 355
Three-dimensional sculpture, 343
Three-dimensional structuring, 348
Three-level model, 150
Threshold fluence, 123, 139, 193, 254, 261, 306, 307, 311, 313, 322, 341, 350–352
Ti, 5, 145–148, 167, 168, 179, 182, 226, 229, 230, 232, 235, 241, 246, 287, 341, 350–352
Ti: Sapphire laser, 246, 341
Time-of-flight (TOF), 101, 102, 104, 106, 107, 115, 117–120, 203, 231
Time-of-flight method, 118
Time-of-flight mass spectrometry, 203
Titanium Aluminium nitride films, 241
Titanium nitride films, 230, 231
Titanium oxide TiO_2, 167, 168, 179–182, 241, 279, 342
TOF, *see* Time-of-flight
Toluene, 348, 350–353, 357
Trajectory, 76, 77, 205, 206, 219, 221, 222
Transfer of laser machined surface, 332
Transient oscillations, 63, 133
Transient stresses, 143
Transit time, 102, 117, 231
Transition-metal nitrides, 225, 229, 234, 241
Transmission electron microscopy, 208
Transparency grade, 314, 315, 318, 321
Transparent dielectric, 149, 302, 342, 355
Transparent material, 317, 326, 339–341, 343–345, 347, 350, 351, 353, 354, 357
Transparent substrate, 279, 340, 343, 344, 346, 352
Transport length, 101, 102, 104, 105, 115–117
Traps concentration, 80
Trap effective density, 61
Trap-limited mobility, 109, 115
Trapping mechanism, 109
Traps, 58, 80, 103,, 105, 107, 115, 117, 119, 120
Trial function, 127, 130, 147
Trions, 50
Triplet excitons, 52, 53
Tungsten nitride films, 234
Two-beam coupling, 86, 88, 93
Two-beam holographic method, 342, 355
Two-phase model, 209
Two-photon absorption, 341
Two-photon excitation, 341
Two-temperature model, 121, 145–147, 149, 155
Two-wave mixing, 57, 60, 62, 79, 84, 97

Ultra-short pulses, 282, 302, 306
Unzipping process, 144
Urbach rule, 38
Urbach's tail, 38, 44, 343
UV, 30, 139–141, 144, 161–175, 177–182, 186–195, 197, 199, 228, 255, 278, 280, 285, 288, 301, 302, 305, 306, 315, 328, 333, 339-341, 343–345, 348, 351, 356, 357
UV annealing, 171, 174, 175, 177–179, 181, 182, 189
UV bleaching, 255
UV cleaning, 167
UV-curing, 182, 186, 187, 194, 199, 333
UV-excimer laser, 302
UV laser, 139, 140, 161, 278, 280, 301, 305, 339–341, 343, 345, 348, 356
UV metallization, 190, 255, 278, 279, 344, 357
UV photons, 144, 161, 255
UV printing, 194
UV transmittance, 172, 173, 177, 178
UV-transparent dielectrics, 302
UV windows, 162, 163, 165, 166, 170

Vacuum ultraviolet (VUV), 139, 161, 162, 165, 167, 169, 170, 183, 188, 189, 191, 194, 195, 302, 306, 339, 340, 343, 356
Valence electron, 41, 43, 201, 206, 282
Van Hove singularities, 37
Vanadium nitride, 232–234
Vaporization, 121, 123, 126, 134, 229, 345, 352
Volume photo-deposition (VP), 257, 259
VUV laser, 139, 339, 340, 343, 356
VUV Raman laser, 285, 294, 356
VUV-wavelengths, 161, 195, 302

Wannier excitons, 38
Wannier-Mott excitons, 38, 39, 51
Wave of modification, 140, 141
Wave-mixing, 57, 60, 62, 63, 79, 84, 88, 97, 101, 103–105, 118, 120
Weak bonds, 43, 135, 136, 187
Weak coupling theory, 12
Wet chemical etching, 317
White light interferometry, 321, 324, 326, 328, 331
Windowless lamps, 162, 163, 165, 195
Write and erase techniques, 275

XeCl excimer laser, 194, 230, 350, 356, 357
XeF excimer laser, 326
XPS, 170, 172, 173, 176, 178, 189, 229, 234, 237, 246
X-ray, 3, 11, 180, 201, 204, 205, 229, 238, 240, 250, 282, 291, 292, 298, 334
X-ray diffraction (XRD), 180, 181, 229, 233, 234, 237–240, 291–293, 298, 299,
X-ray photoelectron spectroscopy, 205, 250, 334
XRD, *see* X-ray diffraction

Zhurkov's formula, 143
Zirconium nitride, 234
Zn, 239, 240, 255
ZnO, 32, 279, 342
ZnS, 255, 279
ZrO_2, 167, 168, 182, 342